TRANSIENT FLOW AND TRANSPORT IN UNSATURATED HETEROGENEOUS MEDIA: FIELD EXPERIMENTS IN MINE WASTE ROCK

BY

CRAIG FERGUSON NICHOL

B.A.(Hons.), Cambridge University, 1990

M.Sc., University of Birmingham, 1992

A THESIS SUBMITTED IN PARTIAL FULFILLMENT OF

THE REQUIREMENTS FOR THE DEGREE OF

DOCTOR OF PHILOSOPHY

in

THE FACULTY OF GRADUATE STUDIES

Department of Earth and Ocean Sciences

We accept this thesis as conforming

to the required standard

THE UNIVERSITY OF BRITISH COLUMBIA

March 2002

In presenting this thesis in partial fulfilment of the requirements for an advanced degree at the University of British Columbia, I agree that the Library shall make it freely available for reference and study. I further agree that permission for extensive copying of this thesis for scholarly purposes may be granted by the head of my department or by his or her representatives. It is understood that copying or publication of this thesis for financial gain shall not be allowed without my written permission.

Department of Earth & Ocean Sciences

The University of British Columbia
Vancouver, Canada

Date 21/3/02

ABSTRACT

It is essential to understand how water is transported and stored in mine waste rock to predict the rates and quantities of mineral weathering products released to the environment. The lack of understanding of flow mechanisms is the largest of the difficulties facing efforts to predict waste rock leaching. A large scale (8m x 8m x 5m high) constructed waste rock pile experiment (CPE) has been built upon a contiguous grid of 16 drainage lysimeters to better characterize the flow of water in unsaturated waste rock.

The measurement of water flow parameters in a waste rock experiment required the development and testing of new instrument methods to determine water content, using time domain reflectrometry (TDR), and matric suction, using thermal conductivity sensors. The use of a resistive coating on the TDR probe conductors is found to be a successful strategy for obtaining measurable TDR signals and hence water contents. The thermal conductivity sensors are successful in certain soil conditions, but not those present in the CPE.

Water flow data from the first two and a half years of the experiment are examined. Average net infiltration to an uncovered waste rock pile is 55% of precipitation. Large rainfall events have net infiltration of 55% to 85%. Water flow is spatially heterogeneous at scales less than 2m. In-situ instrumentation is found to be a poor (non-conservative) predictor of water flow. Data are analysed from the first year of a tracer test carried out under transient infiltration. Physical mechanisms of water flow are identified including non-capillary flow, flow in macropores, and water flow in the granular matrix. Water chemistry is different between different pore sizes, and between spatially distinct areas of the pile. The residence time distribution has an estimated mean of 3.0 to 3.9 years under average infiltration conditions.

TABLE OF CONTENTS

APPENDIXES:

LIST OF TABLES

LIST OF FIGURES

ACKNOWLEDGEMENTS

This project is part of the Waste Rock Hydrology Research Program, a joint research program initiated between the University of British Columbia, the University of Saskatchewan, Cogema Resources Incorporated, Cameco Corporation, and the Natural Sciences and Engineering Research Council of Canada. Additional funding was provided through an NSERC Postgraduate Fellowship, and a University of British Columbia Graduate Fellowship.

I would like to thank the many people who assisted with the construction and operation of the experiments at Cluff Lake and at UBC: Lloyd Daigneault, Leonard Mineault, Ray Kirkland, Tracy Bellehumeur, Nakib Ahmed, Sara Harrison, Keely Bright, Julie-Ann Moore, Pamela Fines, Bonnie Sjoberg, and Joe Marcoline. The assistance of the site staff at the Cogema Resources Cluff Mine operation, and in particular the Environment group, made this work possible. I am grateful to Del Fredlund and Fangsheng Shuai for the opportunity to use the thermal conductivity sensors.

I am grateful to Leslie Smith and Roger Beckie for their support, guidance and for having doors that are always open (before 4:30). Thanks to Ward Wilson, Lee Barbour and Jim Hendry for their help from Saskatchewan and Vancouver. Thanks to all the members of the hydrogroup over the years for their friendship and good humour.

"....."

"Yes, Christopher Robin?"

"I'm not going to do Nothing any more."

"Never again?"

"Well, not so much. They don't let you."

Pooh waited for him to go on, but he was silent again.

"Yes, Christopher Robin?" said Pooh helpfully.

"Pooh, when I'm - *you* know - when I'm *not* doing Nothing, will you come up here sometimes?"

"Just Me?"

"Yes, Pooh."

"Will you be here too?"

"Yes, Pooh, I will be, *really*. I promise I will be, Pooh."....."

A.A. Milne

The House at Pooh Corner

For Christine, Hamish, Alan and Heather

CHAPTER 1: INTRODUCTION

1.1 PURPOSE

This thesis describes research undertaken to investigate the infiltration and flow of water within unsaturated mine waste rock. Mine waste rock is barren or low-grade material removed from an open pit or underground mine to gain access to the ore-grade material. Typically, waste rock is dumped in large unsaturated piles immediately adjacent to the mine workings. Fresh waste rock weathers after excavation, which may lead to the release of poor quality drainage water from the base of the dump into the receiving environment. The most common weathering reaction is the oxidation of metal sulphide minerals to produce sulphate, acidity and free metal ions. It is essential to understand how water is transported and stored in waste rock to predict the rates and quantities of mineral weathering products released to the environment.

Waste rock is a more complex granular material than most natural soils. The grain size varies from clay to boulders, and the textures range from cobbles and boulders supported in a granular matrix to areas which are clast-supported with little or no granular matrix. This extreme variation in grain size, combined with a range of large-scale structures created within waste dumps by the haulage process, make water flow in waste rock very difficult to monitor experimentally, or simulate numerically. Water flow in waste rock is not well understood and represents the largest source of uncertainty in current efforts to predict the loadings of weathering products from existing piles, or to make predictions of potential future loadings prior to pile construction.

Examination of the previously conducted field experiments on mine waste rock and data sets from operating mines (Chapter 6, Appendix A) indicated that existing data sets of

observations of flow and tracer were insufficient to allow a detailed study of flow mechanisms. This work therefore focussed on the collection of detailed observations of the flow of water in waste rock. When later combined with information on primary and secondary geochemical reactions, this will permit insight to the coupling between fluid flow and the release of metals from waste rock. The experimental work in this thesis is focussed on waste rock, but the mechanisms of water flow and solute transport discussed are also relevant to any unsaturated heterogeneous porous media.

1.2 STUDY OBJECTIVES

The key questions that are addressed by this research are:

- What is the duration of the initial wetting of a waste rock pile before any release of water is to be expected?
- Which physical measurements of waste rock properties are critical to the characterization of flow in waste rock, and how are these best achieved?
- What is the fate of precipitation onto a waste rock pile surface and how is the flow of water initiated?
- What mechanisms control the flow of water within a waste rock pile, and how does water outflow at the base relate to water stored in the granular matrix within the pile?
- What is the degree of spatial variability in unsaturated flow through waste rock?
- What is the variation in residence times of water in waste rock?
- What changes in pile construction practices may be beneficial in reducing the generation of acid rock drainage, or improving the ability to predict acid rock drainage.

1.3 SUMMARY OF RESEARCH PROGRAM

The research program undertaken had two broad themes. The first was the development of instrumentation for the measurement of the hydrogeological parameters necessary to study water movement in waste rock. The second major focus was two experiments on waste rock: a specially constructed waste rock pile (CPE) at an active mine site and a laboratory column experiment.

1.4 INSTRUMENTATION

The time domain reflectrometery method (TDR) of water content measurement was selected as the best means of making automated measurements of water content. The method measures the velocity of an electromagnetic pulse propagating in a probe placed in contact with the soil. The pulse velocity is related to the dielectric properties of the soil, and hence to the water content of the soil. Initial testing revealed that existing TDR instrumentation technology was not adequate in mine waste rock due to the high electrical conductivity of the soil water solutions present. This leads to degradation of the signal used by the TDR instrument, causing both inaccuracy and eventual failure of conventional TDR methods. Several previously proposed methods of improving signal quality were combined to design a new TDR probe. This probe was successful in obtaining interpretable measurements of the pulse velocity (Chapter 3).

Further work was undertaken to calibrate the measurements of TDR pulse velocity to the actual water content of waste rock (Chapter 4). Both field and laboratory experiments were undertaken to calibrate TDR velocity measurements to water content. The final calibration work undertaken was to derive a correction for changes in ambient temperature

based upon the data collected during the constructed pile experiment. TDR probes were installed in both the laboratory column and constructed pile experiments.

The measurement of water suction was undertaken using tensiometers (Appendix D) and thermal conductivity sensors (Chapter 5). Tensiometers and manometer tubes were used in the laboratory column experiment. Tensiometers equipped with pressure transducers were used in the CPE. Further automated measurements of soil matric suction in the CPE were undertaken using thermal conductivity (TC) sensors. These sensors are composed of a porous ceramic material which is heated using a controlled heat pulse. The thermal properties of the ceramic are measured, and hence the water content of the ceramic is estimated. Using calibrated measurements, this is related to the matric suction of the soil surrounding the probes. A new theoretical correction for changes in the ambient temperature of the soil is derived and applied to the field data. The performance of the thermal conductivity sensors is compared to that of tensiometers to determine the long term accuracy.

1.5 EXPERIMENTS

Two experiments were conducted using waste rock obtained from the Cluff Lake mine located in Northern Saskatchewan. The main experiment is a large scale constructed waste rock pile experiment (CPE), undertaken at the Cluff Lake mine site. The experiment core is 8m x 8m x 5m in height. The CPE was constructed in the fall of 1997 and the summer of 1998. The experiment was operational from September 1998. Flow experiments were conducted in 1999 and 2000, and the results of analysis of water flow include data up to March 2001. A conservative tracer test was started in September 1999, and the results of monitoring up to October, 2000 are presented in this thesis. The CPE experiment is ongoing, and additional monitoring of water flow and tracer transport have been conducted but are not

presented in this thesis. Analysis of the results of flow measurements are presented in Chapter 6, and results of a conservative tracer test are presented in Chapter 7.

A small scale laboratory column experiment (1m diameter, 2m height) was constructed at the University of British Columbia, using material transported from the mine. The experiment was built in the spring of 1998, and several flow experiments were conducted. The experiment was then allowed to drain between the summer of 1998 and the spring of 1999. Another series of flow experiments were conducted in the spring of 1999, leading up to a conservative tracer test started in June, 1999. This experiment was used primarily as a testing ground for technologies and ideas prior to the construction and testing of the CPE. Detailed results from these experiments are not included in the main body of this thesis, but a summary of construction details, experiments and results are presented in Appendix M.

1.6 STRUCTURE OF THESIS AND PRESENTATION OF RESEARCH PROGRAM

The results to date of this research are presented in the five main chapters. Chapters 3 to 7 are in the form of manuscripts submitted or prepared for submission to journals. All references between manuscripts have been updated to reflect the thesis structure.

Chapter 2 presents a brief overview of the constructed pile experiment and its construction, and serves as background for instrument development detailed in Chapters 3 to 5. Some of the introductory material is repeated in the introduction to Chapter 6.

Chapters 3 and 4 present the work undertaken to develop instrumentation to monitor water content in mine waste rock using the time domain reflectrometry (TDR) method. Chapter 3 describes the new TDR probe design, and the overall success of the strategies adopted to improve the quality of TDR measurements in high conductivity systems. Chapter

4 presents the details of the specific calibration of our waste rock material, and the derivation of field-based temperature corrections. There is some repetition of the background of the TDR method in the introductory sections of these two manuscripts.

Chapter 5 presents the results of study of thermal conductivity sensors for the measurement of soil matric suction. The thermal conductivity sensors used for this research were prototype sensors purchased from Dr. Del Fredlund and his research group at the University of Saskatchewan. The sensors were calibrated by Dr. Fredlund's group prior to their installation in the CPE in 1998. During data collection, Dr. Fredlund's group provided additional information on sensor hysteresis and a preliminary temperature compensation equation. In return, several suggestions were made to improve the data collection and interpretation.

Chapter 6 presents the first part of the results obtained from the constructed pile experiment. This includes a summary of the design and construction of the constructed pile experiment similar to Chapter 2. The results of water flow in the constructed pile are discussed, including: the overall water balance and calculation of net infiltration; spatial heterogeneity of water flow; temporal changes in water flow; evidence for preferential flow in waste rock; water balances from individual flow events; conditions which increase of decrease preferential flow; and the style and spatial scale of flow behaviour observed during winter drainage.

Chapter 7 presents the results of the conservative tracer test carried out on the constructed pile. Data from September 1999 to October 2000 have been analysed. The results include an overall summary of the progress of the tracer test. This is followed by the presentation of a generic conceptual model of flow and transport in unsaturated porous

media. This framework is used as context to interpret the breakthrough curves and hydrographs of individual lysimeters. This includes discussion of the spatial and temporal variability of tracer transport mechanisms. The results from in-situ tracer measurements are then used to demonstrate the manner in which the generic transport model presented is characterized by the measurement methods used.

Chapter 8 presents the conclusions of this thesis and a summary of the major contributions of this research. A series of thirteen Appendices are attached to this thesis. Appendix A presents the full text of the Nichol et al. (2000) paper which is referenced in several chapters and is summarized for Chapter 2. Appendix M provides the construction details, experimental outline and brief results summary from the laboratory column experiment. These two appendices provide additional information about the research program that directly contribute to the research presented in the main body of the thesis.

Appendices B to L provide a permanent record of the details necessary for continued operation of the experiment. The constructed pile experiment has been taken over by other researchers. Many of the details of the construction of the CPE and the methods used to calibrate and operate equipment at the CPE are required for its continued operation. These Appendices provide: (B) detailed notes on the construction of the CPE, including photographs; (C) details of the preparation and operation of the suction lysimeters; (D) details of the installation and operation of the tensiometers and pressure transducers; (E) calibration details of the temperature probes installed in the CPE; (F) details of the datalogging equipment and programming for the CPE; (G) details of the construction and calibration of the rainfall simulators developed for both the laboratory column and CPE; (H) instruction for operation of the rainfall simulator at the CPE; (I) calibration measurements

taken for the TDR probes installed in the CPE; (J) calibration measurements taken for the thermal conductivity sensor installed in the CPE; (K) calibration details for the tipping bucket gauges used to monitor flow rate at the CPE; and (L) details of the method development and analysis protocol for the analysis of dissolved chloride in water from the CPE. Appendices D, G, J, K and L include more in-depth analysis of experiments required to develop and calibrate the methods contained in these appendices.

CHAPTER 2: INTRODUCTION TO THE CONSTRUCTED PILE EXPERIMENT

2.1 INTRODUCTION

A brief description of the constructed pile experiment is presented in this chapter to provide an introduction to the experiment sufficient for understanding the information on instrument development included in Chapters 3 through 5. These chapters refer to the paper by Nichol et al. (2000) for background information. The full text of this paper is included in Appendix A. A brief summary of the pile construction and early results is presented here. A more comprehensive review of waste rock issues, and further details of the experiment construction are included in Chapter 6.

2.2 EXPERIMENTAL DESIGN

The CPE was built at the Cluff Lake Mine in northern Saskatchewan, owned and operated by Cogema Resources Inc. of Saskatoon. The location of the Cluff Lake site is shown in Figure 2.1. Mean annual air temperature at Cluff Lake is 0°C. Average annual precipitation is 455 mm, with 305 falling as rainfall.

The CPE foundations were constructed in 1997, and the remainder of the pile built from June to September, 1998. Automated and manual monitoring of the pile commenced in September 1998. A conservative tracer test was started in September, 1999, and is ongoing. Simplified plan views and cross sections of the pile are shown in Figures 2.2 and 2.3. The instrumented core of the pile has a footprint of 8 m by 8 m. Outflow from the base of the pile is collected in a contiguous grid of 16 gravity drainage lysimeters (Figure 2.3). Maintaining the lysimeters under suction was not considered to be technically feasible. Accordingly, a design leading to the formation of a water table at the base of the pile was chosen. Outflow

from each 2 m by 2 m lysimeter is separately piped to an instrumentation hut where outflow is monitored using tipping-bucket rain gauges.

The top surface of the pile was finished to resemble other existing piles on site which were free-dumped and then contoured to a smooth surface. No attempt was made to create a trafficked dump surface nor any type of compaction or artificial cover, although these may be options for later study. Detailed notes, drawings and photographs detailing the construction of the pile are provided in Appendix B.

2.2.1 Waste Rock Composition And Internal Pile Structure

The waste rock for this study was mined from the DJ Extension open pit at the Cluff Lake mine in the fall of 1996, and placed in the CPE in 1998. The grain size distribution of the 0.6m minus fraction of the waste rock is shown in Figure 2.4. Further details of the methods of grain size analysis and the material characteristics are discussed in Chapter 6. Grain size is highly heterogeneous, ranging from 1.5 m diameter boulders to clay, with areas that are matrix supported and areas with matrix-free cobbles and boulders.

2.2.2 Instrumentation

The instrumentation used to measure water content, matric suction, temperature and matrix soil water chemistry were placed in three instrument profiles (Figures 2.2, 2.3). Water content is monitored continuously using time domain reflectrometry (Chapters 3 and 4). Matric suction is monitored year round using thermal conductivity sensors (also known as heat dissipation sensors) with laboratory-derived temperature and sensor hysteresis corrections (Fredlund and Shuai 1999, Feng 1999, Chapter 5). Tensiometers with pressure transducers were installed in 1999 to provide independent measurements of matric suction

when air temperatures are above freezing. Temperatures are measured using commercial pre-calibrated thermistors.

Outflow water samples are collected in a cascade of mixing cells, where the water is directed through containers of increasing volume (0.2L, 2.0L and 25L) before final overflow to waste. Both instantaneous grab and longer term composite samples can be obtained without post-sampling compositing. Matrix water chemistry is monitored through the periodic manual extraction of water samples from suction lysimeters (also called soil water samplers) placed within the pile during construction. Approximately 12,000 samples have been collected during this research. Selected samples of outflow and soil-water were analysed for dissolved chloride to monitor the progress of a conservative tracer test (Chapter 7).

Pile surface evaporation will be calculated using data from a full weather station and surface mini-lysimeters by other researchers involved in this project. Processed and calibrated data are not yet available.

2.3 INITIAL RESULTS

A summary of rainfall and outflow measured during the initial wetting-up period of the pile from September, 1998 to July, 1999 is presented in Figure 2.5. Snowfall over the winter is generally blown off the top of the pile. Snow depth was measured to be 80 to 100 mm, which was included as 9 mm of rainfall in mid-March. The CPE was initially very dry due to intense evaporation from the soil surface during construction. Between September 1998 and July 1999, approximately 7000 litres of water fell as precipitation on the pile, and 220 litres of water exited as outflow. Details of the outflow records and water balance after the wetting up period are given in Chapter 6.

Preliminary estimates of water content by TDR and matric suction by thermal dissipation sensor from instrument profile A are shown in Figure 2.6. The TDR response down to a depth of 1 m was affected by ground freezing, and low measurements from November to March indicate the conversion of free water to ice, which does not register as water content. During freezing conditions the matric suction sensors do not operate, and data are absent, or erratic. The progress of the first wetting front in the capillary-dominated matrix material can be followed by observing increases in water content and changes in matric suction. The TDR data show that the initial wetting front from fall and spring precipitation events took 9 months to travel the 5 m depth to the base of the pile. An increase in water content at 4.5 m depth immediately preceded the first lysimeter outflow. The relationship of measured water contents and outflow behaviour are discussed further in Chapter 6.

Initial matric suction measurements were high due to intense evaporation from the pile surface at each instrument level during the time required to install each set of instruments. Matric suction measurements from the thermal dissipation sensors show declines at all levels. The matric suction values reported in this figure are based on raw measurements to demonstrate the initial trends. Further details of calibrations, hysteresis effects and temperature corrections are included in Chapter 5.

2.4 CONCLUSION

The CPE experiment was designed and built to provide a detailed, long-term data set of water flow and solute transport and geochemistry in a mine waste rock pile. The early experience presented here indicates the five meter high experiment required a wetting-up period of 11 months until the disturbances created by construction were overcome. This re-

equilibration time implies short term results from large lysimeters installed to monitor net infiltration to waste rock piles cannot be relied upon. At least one full season would be required in the northern Saskatchewan climate to equilibrate such an experiment.

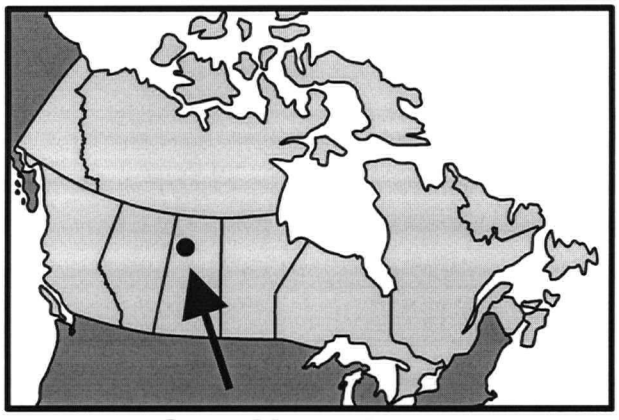

Figure 2.1: Site of the constructed pile experiment. Location of the Cluff Lake Mine (Lat. 58 22', Long. 109 32'), owned and operated by Cogema Resources Incorporated of Saskatoon.

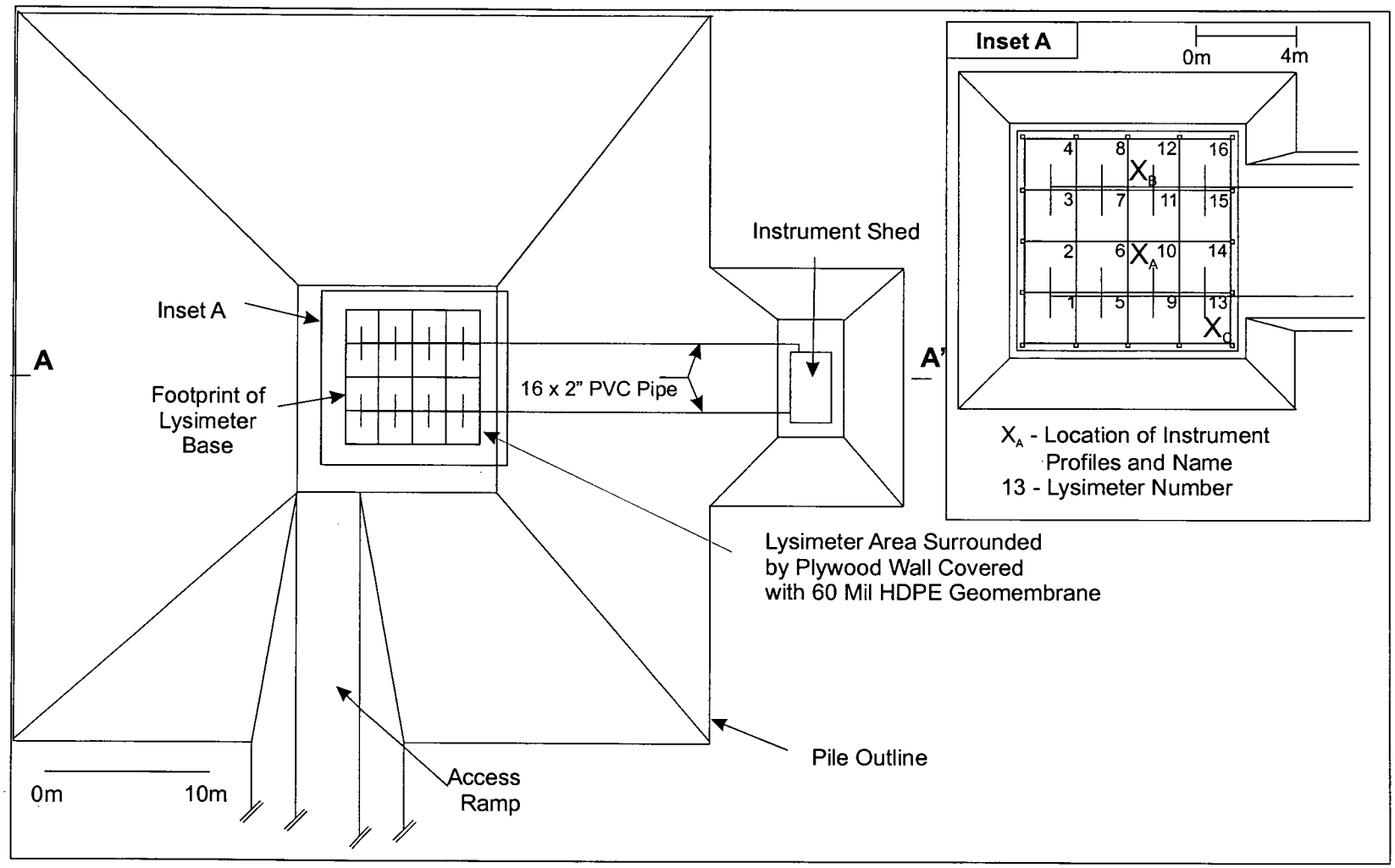

Figure 2.2 : Simplified plan view of constructed pile experiment

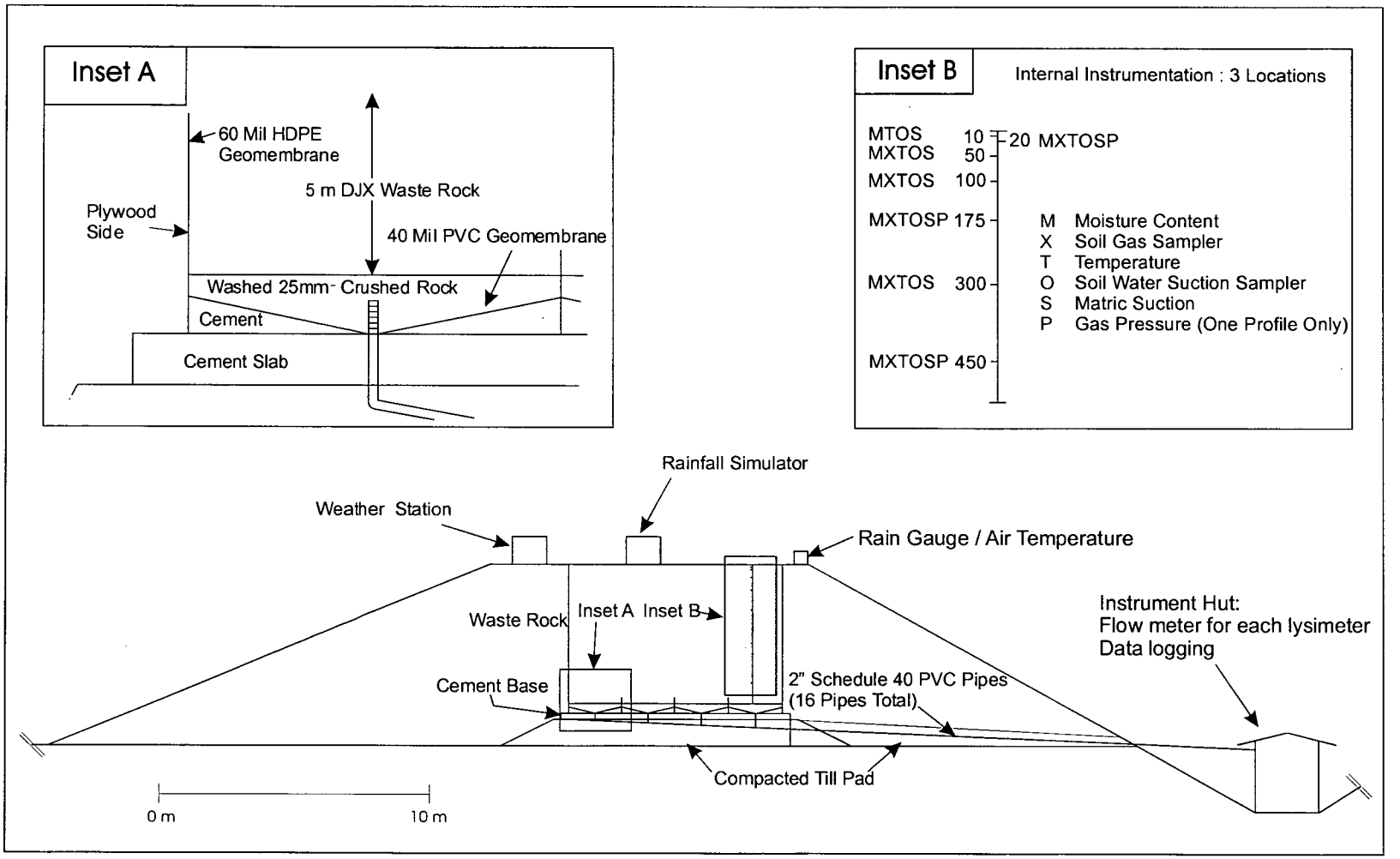

Figure 2.3: Simplified cross-section A-A' of constructed pile

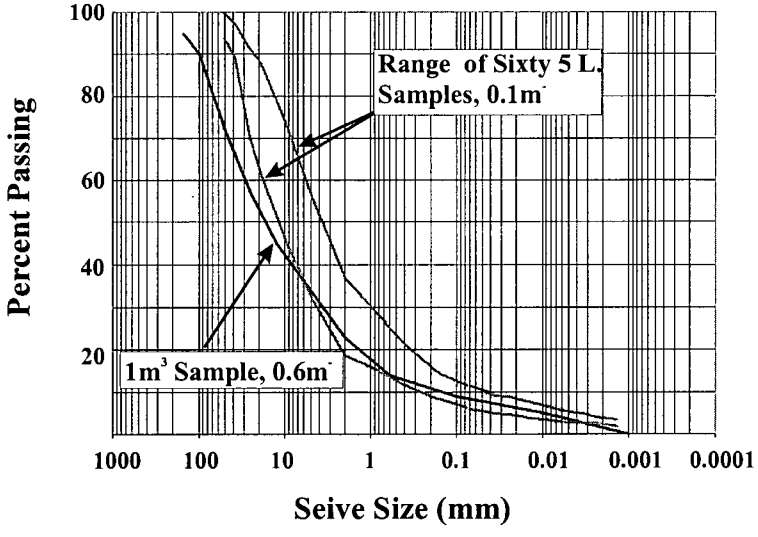

Figure 2.4: Grain size of waste rock in constructed pile

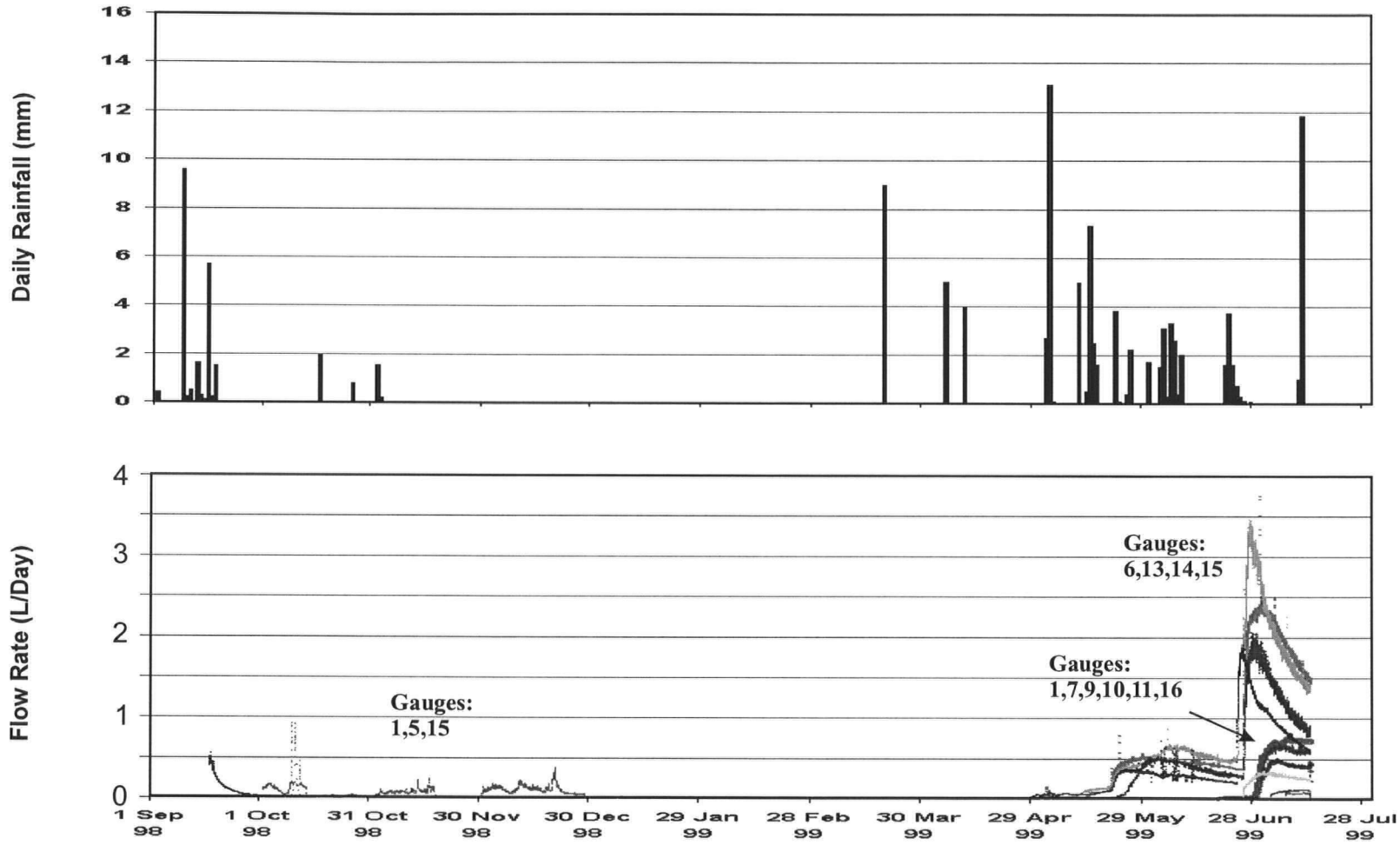

Figure 2.5: Daily rainfall volume and outflow rate summary

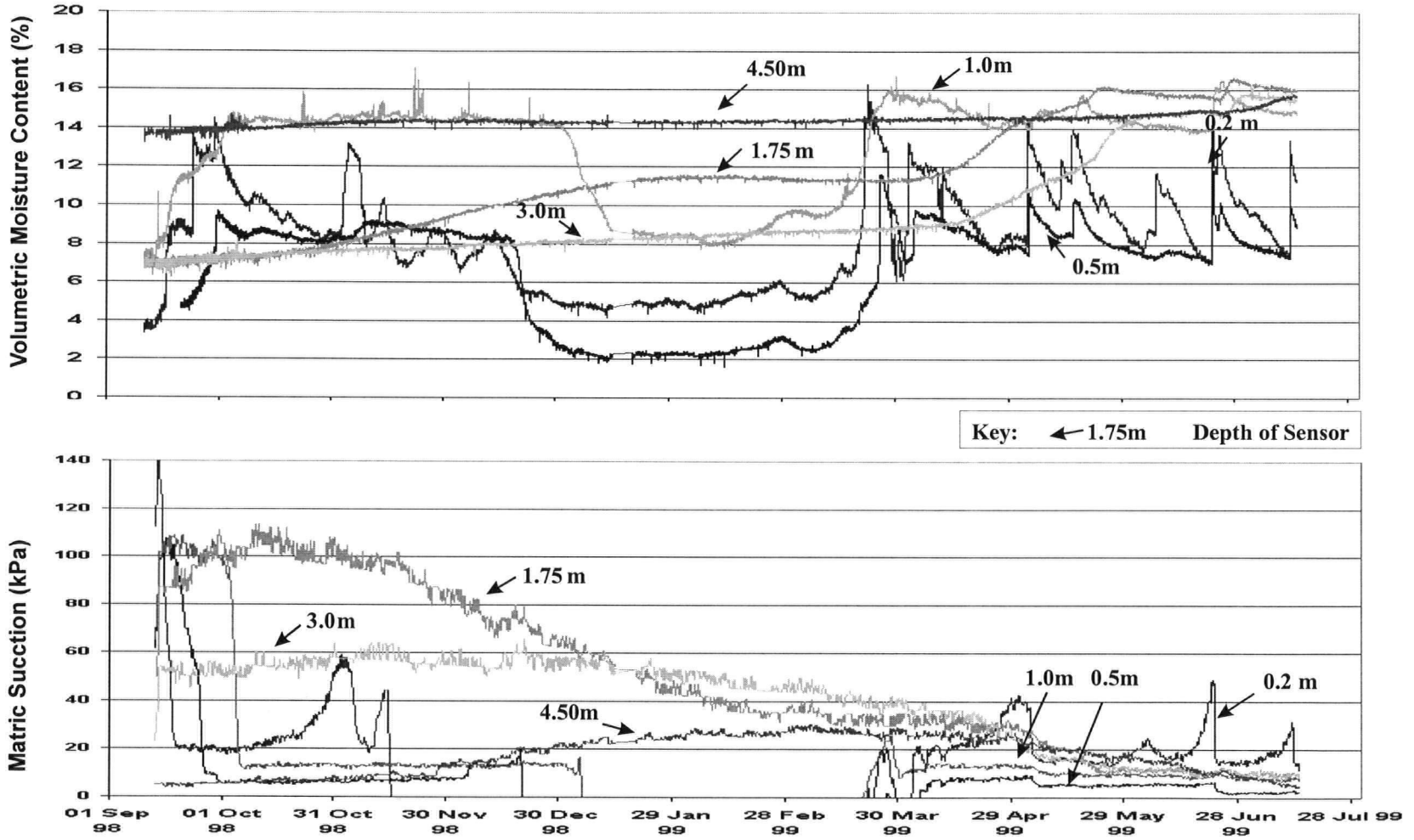

Figure 2.6: Summary of volumetric water content and matric suction profile at pile center

CHAPTER THREE: EVALUATION OF UNCOATED AND COATED TDR PROBES FOR HIGH ELECTRICAL CONDUCTIVITY SYSTEMS

3.1 ABSTRACT

The effects of high sample electrical conductivity upon time domain reflectrometry (TDR) measurements are investigated. High sample electrical conductivity reduces the quality of a TDR waveform through the loss of signal amplitude. Two strategies to obtain higher signal-to-noise waveforms are examined: waveform differencing by remote diode shorting and covering probe conductors with resistive coatings. Experiments using electrically conductive water solutions show conventional dual-tangent line waveform analysis is accurate for solution electrical conductivities up to 5 dS m^{-1}. Waveform differencing using manual short circuits is accurate, but the remote diode shorting method is systematically biased for three-rod probes in electrically conductive water solutions. The bias is related to the electrical properties of the diodes used. Three-rod Zegelin-type probes with a high resistance coating on the central rod are capable of returning analyzable waveforms for solutions with electrical conductivities at least as high as 70 dS m^{-1}. Travel time in a coated probe determined by the remote diode shorting method was constant in solutions up to 5 dS m^{-1}, but varied in an inconsistent manner at higher electrical conductivities. Travel time estimates using a coated probe and remote diode shorting in silica sand saturated with electrically conductive water solutions are less accurate in comparison to conventional waveform analysis. Current theoretical descriptions of the relationship between the apparent dielectric permittivity estimated using a coated probe to the actual sample apparent dielectric permittivity for three-rod probes do not lead to a simple

analytical expression to account for the presence of a coating. Samples of known dielectric permittivity were measured using a coated probe. An empirical fit of the experimental data is obtained using an equation of the form for a coated coaxial cell. A three rod coated probe with a single diode at the probe head is a practical means to collect interpretable waveforms in media with high electrical conductivity.

3.2 INTRODUCTION

Soil water content can be measured in the field using gravimetric methods, neutron scattering, or techniques based upon the thermal or electrical properties of soil-air-water mixtures. Electrical methods are advantageous because they are easily automated to conduct unattended measurements with high sampling rates at multiple locations. Time domain reflectrometry (TDR) is a commonly used electrical technique. With knowledge of the electrical properties of soil-air-water mixtures, and appropriate experimental calibrations, the bulk soil dielectric permittivity can be related to the volumetric water content and the bulk soil electrical conductivity can be related to the soil water electrical conductance.

While TDR methods have gained wide acceptance and usage in soils, relatively less attention has been given to TDR's application to high electrical conductivity materials such as mining waste. In these materials, conventional TDR probe designs and signal analysis techniques fail to provide sufficiently accurate estimates of the sample dielectric properties. This chapter describes an approach to design an automated TDR system for the measurement of water content in unsaturated mine waste rock. The TDR system is used in both a laboratory column experiment and a field-scale experiment (Nichol et al., 2000, Appendix A). In this application, a high soil water electrical conductivity (5 to 20 dS m^{-1}) caused by oxidizing sulphide minerals in the mine waste lead to poor signal quality using conventional

TDR techniques. Sufficient signal amplitude could not be reliably obtained using a short probe of conventional design. Two techniques for obtaining improved signals were selected: waveform differencing using remote diode shorting (Hook and Livingstone, 1992), and the use of a resistive probe coating (Kelly et al., 1995; Ferré et al., 1996, Mojid et al., 1998). The aim is to derive a method to reliably collect waveforms that can be interpreted by automated waveform fitting to derive an estimate of travel time and hence apparent dielectric permittivity.

In this chapter, both techniques are tested for the collection of interpretable waveforms in high electrical conductivity media. A brief summary of the TDR method is provided which discusses how it is affected by bulk soil electrical conductivity. The relevant theory of waveform differencing by remote diode shorting and the use of probes covered with a high-resistance coating are described. A series of experiments are then presented. The first examines the performance of a short (160mm) uncoated probe using water solutions of variable electrical conductivity. The second experiments analyse the performance of the waveform differencing method using the remote diode shorting method and manual short circuits under the same conditions as the first experiments. This chapter then examines the performance of a coated probe under the same conditions for both conventional TDR waveform collection and analysis, and using the remote-diode shorting method. The performance of a coated probe in silica sand saturated with water solutions of varying electrical conductivity is presented. A last experiment demonstrates a practical means of compensating for the effect of a probe coating on the estimation of sample dielectric permittivity.

3.3 THEORY

TDR can be used to determine the apparent relative bulk dielectric permittivity (ε_{app}), the bulk electrical conductivity (σ_{DC}), and in certain circumstances, the frequency-dependent real and imaginary parts of the complex sample dielectric permittivity (Hoekstra and Delaney, 1974, Dalton et al., 1984, Topp et al., 1988, Heimovaara et al., 1996, Friel and Or, 1999). TDR measures the propagation of a fast rise time, step voltage pulse through a coaxial cable to a waveguide (probe) in contact with the sample. Part of the incident pulse energy reflects back to the TDR instrument from each impedance change in the transmission line and probe, with a full reflection of the remaining pulse energy at the end of the probe. The sum of the incident voltage and reflected pulse voltage measured at the TDR instrument is plotted in time and presented as a waveform. The arrival of reflected energy at the TDR instrument causes a change in voltage over time, and thus a deflection of the waveform. The apparent velocity (v_{app}) of the pulse along the probe is determined from the probe length (L) and the arrival times of the reflections from the head and end of the probe (t_o, t_l). The dielectric permittivity of the medium surrounding the probe is related to the velocity of an electromagnetic wave propagating in the transverse electric and magnetic mode (TEM) along a waveguide by:

$$\varepsilon_{app} = \varepsilon_o \left(\frac{c}{v_{app}} \right)^2 \left(\frac{\mu_o}{\mu} \right)^2 \qquad [3.1]$$

where ε_o is the permittivity of free space and c is the velocity of light in a vacuum. It is assumed that the magnetic permeability of soils and soil-air-water solutions (μ) equals that of

free space (μ_o) and therefore (μ_o/μ) is unity (Topp et al., 1980). In this thesis, all dielectric permittivities are expressed relative to the permittivity of free space, and the term relative is taken as understood.

Successful TDR measurement of the sample dielectric permittivity requires collecting a waveform in which the pulse travel time at the probe head and probe end can be accurately determined. In conventional waveform analysis, the timing of a reflection is determined using two lines fitted to the deflection of the waveform caused by the arrival of reflected pulse energy. The first is a tangent-line fit to the steepest slope of the rising or falling limb of the deflection. The second line is either a horizontal line fit to the pre-deflection waveform (flat-tangent method), or a tangent fit to the slope of the pre-deflection waveform (dual-tangent method) (Hoekstra and Delaney, 1974, Topp et al., 1982). The time of the intercept of the pre- and post- deflection lines is the arrival time of the reflected pulse energy. The dual-tangent method is more accurate for high electrical conductivity solutions (Wraith and Or, 1999) and is used as the reference method for the alternate methods examined.

The dielectric permittivity estimated by tangent-line analysis of a TDR waveform is termed the apparent dielectric permittivity (ε_{app}) because the estimate of dielectric permittivity is not obtained for a single frequency. Frequency domain analyses of TDR waveforms using Fourier transform techniques (Hoekstra and Delaney, 1974, Heimovaara et al., 1996, Friel and Or, 1999) demonstrate that the incident TDR pulse generated by common TDR instruments contains energy in a range of frequencies up to 1.5 GHz. The deflection of the waveform is the integration of the arrivals of all of the frequencies reflected. Tangent-line methods of waveform analysis are biased towards the higher frequencies as these create the sharpest waveform deflections. The frequencies which dominate travel time estimates

from tangent-line waveform analysis are in the range of 700 MHz to 1.0 GHz. (Hoekstra and Delaney, 1974, Heimovaara et al., 1996, Friel and Or, 1999).

3.3.1 Effect of solution electrical conductivity

Ions in solution affect both the waveform quality and the pulse velocity. DC conductance and ohmic losses due to current between the probe conductors dissipate the pulse energy within the waveguide. The energy reflecting from the end of the probe is reduced, the waveform deflection becomes less distinct, contributing to greater uncertainty in tangent-line fitting and travel time determination. In samples with high electrical conductivity, the amplitude of the signal reflected from the probe end may be fully dissipated within the exposed probe conductors and no travel time can be determined. The effect of electrical conductivity on the signal amplitude decreases with a shorter length of probe. The practical lower limit for probe length with common TDR instruments is 0.1 to 0.15 m (Kelly et al., 1995).

Dissolved ions directly decrease the dielectric permittivity of a water solution by reducing the number of highly polarizable water molecules per unit volume and indirectly by the interaction of ions with the electrostatic bonding structure of liquid phase water molecules (Hasted, 1973). In contrast, the DC conductance resulting from ions in solution contributes to the imaginary component of the complex valued dielectric permittivity, leading to an increase in dielectric permittivity. However, at the frequencies which contribute most to tangent-line analysis of a TDR waveform, the DC conductance of water has negligible effect on the pulse velocity (Or and Wraith, 1999). Tabulated experimental measurements of $\varepsilon(\omega)_{solution}$ for common electrolytes are available in Hasted (1973) and Robinson and Stokes (1959).

The dielectric properties of the water phase in soil differs from that of water in a water solution. Both polar water molecules and dissolved ions interact with mineral surfaces. The dielectric and conductive properties of these diffuse, bonded layers are different from the rest of the water solution (Or and Wraith, 1999). Experiments in saturated and unsaturated soils have shown that increasing the concentration of dissolved ions in soil water increases the measured travel time when soil water content is constant (Wyseure et al., 1997; Sun et al., 2000; Topp et al., 2000). The measured increases in travel time are larger than can be explained by the direct effect of the increased bulk electrical conductivity on the real and imaginary parts of the complex dielectric permittivity (Topp et al., 2000). This indicates that increasing the concentration of dissolved ions in the soil water solution affects other components of the complex-valued dielectric permittivity of the soil/air/water/bound water/dissolved ions mixture in a manner that is not fully understood.

3.3.2 Waveform Differencing and Remote diode shorting

Hook et al. (1992) describe a method to improve TDR signal quality using waveform differencing. A raw waveform is first collected from the probe. A short circuit then is created between the signal and ground conductors at the probe head. A second waveform is then collected, termed the shorted waveform. The incident pulse energy will leave the signal conductor and return to the TDR instrument along the ground conductor. This causes a sharp downwards deflection in the shorted waveform. The difference waveform is the difference between the raw waveform and shorted waveform. The timing of the deflection in the difference waveform is determined by tangent-line fitting to derive the travel time for the pulse through the short circuit and back to the instrument. The same process is then repeated with a short circuit created at the probe end.

Positive-intrinsic-negative diodes (PIN) can be used to create the short circuits remotely, and thus allow the waveform differencing method to be automated. PIN diodes have a low resistance under a forward-bias DC current and a high resistance under no current or a reverse-bias DC current. Hook et al. (1992) do not provide details or specifications for the diodes used. MPN3404 diodes were used, as suggested by the manufacturers of the MoisturePoint TDR system (Environmental Sensors Inc, Victoria, B.C.) which incorporates the remote diode method (Young, 1998a). The impedance of these diodes, measured at 100 MHz, switches from greater than 5MΩ to less than 0.8Ω under a forward bias current (On Semiconductor, 2000).

Our experimental waste rock pile allowed for direct burial of the TDR probes on an open soil surface. This removed the requirement for an open-ended probe design that can be inserted into in-situ soil materials. The probe construction is based upon a three rod Zegelin-type probe design (Young, 1998a), with the inclusion of a single PIN diode at the probe head, and two PIN diodes at the probe base. A schematic of the probes is shown in Figure 3.1. The velocity of the TDR pulse within in the sample is determined from the difference between the time for the TDR pulse pass through the probe head diode, and the probe end diode. Calibration measurements in materials of known dielectric permittivity allow the measured time to be corrected for the distance between the diodes located within the probe head and end termination structures and the start of the exposed conductors.

3.3.3 Resistive Probe Coatings

The ohmic loss of signal voltage between the signal conductor and the ground conductors can be reduced by introducing a high resistance coating (Kelly et al., 1995). In this work, a polyolefin heat shrink resistive coating is applied on the center rod (Livingstone,

1997, pers. comm., Mojid et al., 1998). The energy of the travelling TEM wave will still extend outside the coating. The inclusion of an additional dielectric material complicates the relationship between the measured electrical properties and the electrical properties of the sample (Annan, 1977a, Knight et al., 1997). The polyolefin heat shrink used has an apparent dielectric permittivity of approximately 3, lower than most soils materials, and therefore the estimate of apparent dielectric permittivity using a coated probe (ε_{cp}) will always be less than the apparent dielectric permittivity that would have been estimated using an uncoated probe (ε_{app}).

Three-rod or multi-rod probes are designed to emulate a coaxial cell (Zegelin et al., 1989). A simple analytical solution for the effect of a dielectric material of uniform thickness around the central conductor of a coaxial cell can be derived from Annan (1977a).

$$K_{cp} = K_s \left[\frac{\frac{K_c}{K_s} \ln\left[\frac{r_o}{r_i}\right]}{\ln\left[\frac{r_c}{r_i}\right] + \frac{K_c}{K_s} \ln\left[\frac{r_o}{r_c}\right]} \right] \qquad [3.2]$$

K_{cp} = Apparent dielectric determined from travel time in coated probe
K_c = Dielectric constant of coating
K_s = Dielectric constant of sample
r_c = Outer radius of coating
r_i = Outer radius of inner conductor
r_o = Radius to outer conductor

Equations have been derived which exactly describe the effects of coatings applied to three-rod or multi-rod probes, but these equations do not have analytical solutions and are

solved numerically (Zegelin et al.,1989; Knight et al., 1994, 1997). A simpler analytical solution is therefore tested.

All probe designs with a fixed dielectric material within the sampling zone have a non-linear relationship between the apparent dielectric permittivity estimated directly from the measured travel time and the actual sample dielectric permittivity. This non-linear relationship means that the sample dielectric permittivity must be uniform along the probe length to properly determine the sample dielectric permittivity (Ferré et al., 1996).

3.4 MATERIALS AND METHODS

The primary objective of this research is to obtain reliable TDR signals and therefore estimates of the apparent dielectric permittivity in samples with high electrical conductivity. A series of experiments were conducted to compare the results of traditional methods of TDR signal collection and analysis with alternative methods that have been proposed for increasing signal quality. The probes used for the experiments (Figure 3.1) are unbalanced, Zegelin-type three-conductor probes constructed using 3.2 mm diameter 316 stainless steel rods of varying length. Coated probes include a polyolefin heat shrink, carefully applied to the center conductor to ensure no air gaps between rod and coating. The average thickness was 0.40 mm. Probe designs are quoted in the remainder of the chapter as three numbers a/b/c where a is the length of exposed rods in mm, b is the rod diameter in mm, and c is the center rod to outer rod spacing in mm.

Reference raw waveforms with 5000 points in time were collected using a Tektronics 1502C instrument (TTDR) connected to a PC running WAT TDR Version 3.11 (Waterloo Center for Groundwater Research, Waterloo, Ontario). All waveform analysis of TTDR waveforms was performed manually using the dual-tangent analysis method. All waveforms

are presented as the reflection coefficient displayed against the two-way travel time. This approach represents the currently accepted practice of TDR measurement against which the alternate methods are compared.

Raw waveforms and diode-shorted waveforms with 256 points in time were collected using a MoisturePoint™ TDR (MTDR) instrument (Environmental Sensors Inc., Victoria, B.C., Canada) with firmware Version 1.27. The MTDR instrument was purchased with proprietary software and hardware specifically designed for conducting automated, diode-shorted TDR measurements. Travel times were measured using the automated waveform fitting routines which are included in the instrument firmware. Additional waveforms for presentation and for detailed waveform analysis were collected manually using a PC connected to the MTDR and running the instrument control software ViewPoint™ Version 1.34. For all measurements, all instrument settings and waveform fitting parameters in the instrument firmware and software were optimized for maximum accuracy and stability of tangent-line fitting. The MTDR instrument warm up time was set to 15 seconds and a minimum of 5 measurements were discarded prior to all recorded measurements to ensure the instrument returned a stable value of travel time.

The first experiments determine the effect of solution electrical conductivity on conventional travel time analysis and on the performance of the remote diode shorting method. Waveform and travel time analysis was carried out for a 160/3.2/25 uncoated probe immersed in isothermal water of variable solution electrical conductivity. The probe was connected to the TTDR and MTDR using 6 metres of Commscope F660BEF 75Ω RG6 coaxial cable, a male F-connection termination, and an F-to-BNC adapter. Solution electrical

conductivity was altered from 0 to 5 dS m^{-1} using potassium chloride. Raw waveforms and probe head and end diode-shorted waveforms were manually collected for each solution.

The effectiveness of the MPN3404 diodes as short circuits was assessed by taking waveform measurements using manually-created short circuits. For distilled water and for a solution electrical conductivity of 2 dS m^{-1}, 6 gauge copper wire was used to create a short circuit at the start of the exposed rods and then at the end of the exposed rods. Shorted waveforms of each short circuit were collected using both TTDR and MTDR.

The second set of experiments address the effect of a resistive coating; waveform and travel time analysis was carried out for a 281/3.2/25 coated probe using the same experimental setup as the uncoated probe. The electrical conductivity of the solution was altered from 1 to 70 dS m^{-1} using sodium chloride. The measurements for 30 to 70.8 dS m^{-1} solutions have some conductive amplitude loss of signal, and different overall probe impedance due to failure of the probe head seal and invasion of electrically conductive water into the probe head. Conclusions can still be drawn from these results and they are included in the following analysis. No manually created short circuits were tested in these probes due to the presence of the probe coating.

The performance of a 281/3.2/25 coated probe and remote diode method was then assessed for silica sand saturated with electrically conductive water solutions. Water electrical conductivity was altered from 0 to 20 dS m^{-1} using sodium chloride. Raw and diode shorted waveforms were collected using the MTDR. Travel time was determined using automated remote diode shorting at the probe head and end. Water solution and bulk soil electrical conductivity were measured independently using a four electrode conductivity cell and conductivity meter.

The effect of the resistive coating on the estimation of sample dielectric permittivity was determined in the final set of experiments. Travel time measurements were made using a coated probe and materials of known dielectric with low electrical conductivity, the latter determined using a calibrated 295/3.2/25 uncoated probe. Measurements were conducted using the MTDR instrument and averaging a minimum of 15 measurements. For the purposes of these experiments, the best dielectric materials are liquids, which allow simple probe immersion, uniformity of sample and a controlled range of dielectric properties. Organic liquids can be used to obtain a range of dielectric properties. However, the 281/3.2/25 coated probe used in this study was required for other calibration work and the compatibility of the probe construction materials with various organic liquids was not known. To prevent damage to this probe, a more limited range of inert materials was used. Air, oven-dried silica sand, wetted silica sand, methanol and water were used as dielectric media. Liquids were placed in a 15.2 cm diameter PVC container. Granular materials were packed within a 12 cm x 12 cm x 63 cm watertight container.

3.5 RESULTS AND DISCUSSIONS

3.5.1 Uncoated Probes

The conventional method of TDR raw waveform analysis is first demonstrated for an uncoated probe in water. Raw waveforms are presented in Figure 3.2 for solution electrical conductivities from 0 to 5 dS m^{-1}. The reflection from the probe head is virtually identical for all solution electrical conductivities. The negative slope on the probe segment of the waveform decreases and the probe end reflection shows a decrease in the final amplitude as solution electrical conductivity increases. Manually-determined tangent-lines to the end reflections are presented for 0 and 2 dS m^{-1}. The signal quality is significantly degraded at

5.0 dS m^{-1} making manual waveform fitting challenging. In the range of 0 to 5.0 dS m^{-1}, no changes in travel time greater than the method uncertainty were detected. By definition, the transition time of a reflection is half the time for the signal to rise from the pre-reflection tangent to the maximum amplitude and is related to the highest frequencies contained within the reflected signal (Hook and Livingstone, 1992). The transition time of the probe end reflection was consistently 1.2 nanoseconds (ns) from 0 to 5 dS m^{-1}. These water solution electrical conductivities do not contribute to either increased transition time or decreased amplitude of the high frequency components of the TDR pulse.

Signals obtained using remote diode shorting are shown in Figure 3.3. The gain- and offset-corrected MTDR raw waveforms, diode-shorted waveforms, and diode difference waveforms are shown for distilled water (panels A, B) and a solution electrical conductivity of 2 dS m^{-1} (panels C, D). Waveforms are separated for when the diode is located at the probe head (panels A, C) and at the probe base (panels B, D). The probe head and probe end diode-shorted waveforms for distilled water both drop rapidly due to the short circuit created by the diodes. The resulting diode difference waveforms have distinct signals, with sharp waveform rises and short transition times, making tangent-line fitting both simple and accurate. Note that the vertical position of the difference waveforms in this figure, and following figures, has been shifted vertically for greater clarity of presentation. However, at 2 dS m^{-1}, both the probe head (panel C) and probe end (panel D) diode-shorted waveforms more closely follow the raw waveform. As a result, the diode-difference waveforms demonstrate reduced total amplitude, increased time to maximum amplitude, and a less distinct shape than those in distilled water. The 2 dS m^{-1} probe head and probe end diode-

difference waveforms are more difficult to analyse by tangent-line fitting than the raw waveforms presented in Figure 3.2.

The performance of the MPN3404 diodes can be understood by examining the data for near-perfect short circuits created with copper wire. Figure 3.4 presents the waveforms obtained using manually created short circuits in distilled water (panels A, B) and in a 2 dS m^{-1} water solution (panels C, D) for the probe head (panels A, C) and probe end (panels B, D). The shorted waveforms at the probe head and end are similar for both solution electrical conductivities. The difference waveforms have different amplitudes due to the difference in amplitude of the raw waveform, but similar transition times. The poor signal quality of the difference waveforms in Figure 3.3 is therefore not the result of the waveform differencing method itself, but results from the MPN3404 diodes not creating adequate short circuits.

At the probe head, the multi-frequency incident TDR pulse encounters two possible transmission paths when a short circuited is present. Wave energy will be reflected and transmitted along the waveguide or into the short circuit in proportions determined by the frequency dependent complex impedance of each path. The impedance of the manual short circuit is near zero, and thus all wave energy diverts from the signal conductor to the ground conductor. After 85 ns, the manually shorted waveforms in Figure 3.4A and 3.4C are both are flat, illustrating that there are no reflections present in the shorted waveform from any energy that passed the short circuit and entered the probe.

In contrast, the pathway created by the remote diode short has a low, but finite impedance. Pulse energy does divide between the diode pathway and the probe pathway when it encounters the two impedances in parallel. The diode-shorted waveform collected at 2 dS m^{-1} at the probe head closely follows the raw waveform (Figure 3.3C), indicating that

significant signal energy continued past the location of the diode in the probe head, entered the probe and returned reflections from impedance changes within the probe. The transition time of the probe-end reflections in the diode-shorted and the raw waveforms indicates that the frequency spectra of the energy pulse transmitted into the probe was similar. The difference between the diode-shorted waveform and the raw waveform represents the energy that returned via the diode. The gradual departure of the diode-shorted waveform from the raw waveform indicates the energy passing through the diode was dominated by lower frequencies. The probe impedance at low frequency (Z_∞) was calculated from the reflection coefficient at long times using the method of Mallants et al. (1996). The probe impedance is 4000 Ω in distilled water and 20 Ω in 2 dS m^{-1} water. The MPN3404 PIN diodes used have a rated impedance of 0.8Ω at 100 MHz. It is clear from Figure 3.3 that the MPN3404 diode and the impedance of the probe design used are more similar at higher frequencies, and thus shorting becomes less effective.

At the probe end, a similar division of pulse energy occurs as at the probe head. Connecting diodes across the end of the probe conductors requires the presence of a probe termination structure, similar to the probe head, to house the diodes. Energy is reflected and transmitted at both the end of the exposed waveguides, and again at the diodes, which connect the end of the center conductor to ground within the probe end termination structure. At 2 dSm^{-1} (Figure 3.3D), the higher final amplitude of the diode-shorted waveform than in distilled water (Figure 3.3B) indicates a greater proportion of the energy was reflected back along the signal conductor, instead of through the diode short.

In high electrical conductivity systems, the combination of the effects of imperfect diode shorting at the probe head and end leads to large errors in travel-time estimation, and

hence water content. The automated, instrument-determined travel time for varying solution electrical conductivity is shown in Figure 3.5, with the theoretical travel time calculated from Equation 3.1, and the travel time estimated from the manually created shorts in Figure 3.4. The travel time estimated using manually created shorts does not include travel time within the probe head and end termination structures from the diodes to the ends of the exposed conductors. The automated determination of travel time increased by 6 ns. Remote-diode shorting hinders travel time estimation under the conditions examined. In contrast, manually fitted tangent-line analysis of the manual short circuit data presented in Figure 3.4 determined no change in travel time greater than the uncertainty in the analysis, similar to the results of manual tangent-line fitting to the raw waveforms in Figure 3.2.

The method of waveform differencing does not significantly extend the range of waveform analysis to media with higher electrical conductivities. At the probe end, waveform differencing by either manual short circuits, or diode short circuits relies upon the collection of a raw waveform with non-zero reflected signal amplitude. This method will therefore only be successful up to similar solution electrical conductivities as conventional raw waveform analysis, or approximately 5 dS m^{-1} for a 0.16 m probe.

3.5.2 Coated Probes in Water

The performance of coated probes is first assessed using conventional waveform analysis. Raw waveforms for solution electrical conductivities between 1 to 70.8 dS m^{-1} collected using the TTDR are shown in Figure 3.6. The raw waveforms from 1 to 20 dS m^{-1} indicate little signal amplitude loss and a consistent trend in probe impedance. The transition time of the probe head reflections is similar for 1 to 70.8 dS m^{-1}. No attempt was made to precisely match the impedances of the cable, connectors and probe head. Multiple

reflections are seen between 67 and 73 ns caused by these impedance changes and the start of the exposed conductors. The accidental penetration of high electrical conductance water into the probe head causes the sharp drop in probe-head impedance observed in the lowest three waveforms. The multiple internal reflections originating from within the probe base are smoothed out at higher electrical conductivities.

The dual-tangent method of waveform analysis was assessed by manual tangent-line fitting. The better preservation of probe head internal reflections in coated probes does not affect manual tangent-line fitting, but would make automated tangent-line analysis of the probe head reflection more difficult. The signal from the end reflection of a coated probe has lower transition times than the signal from the uncoated probe, more signal amplitude and therefore tangent-lines are easier to fit to the waveform. Manually-determined tangent-lines to the probe end reflection are presented on Figure 3.6. Between 1 dS m^{-1} and 70.8 dS m^{-1} the travel time determined by the tangent-line method decreases by 0.4 ns. This decrease in travel time will be discussed in final section. The signal attenuation encountered in uncoated probes, caused by high sample electrical conductivity, is reduced in coated probes and raw waveforms are interpretable to >70 dS m^{-1}.

The waveform differencing method was assessed for coated probes using only the remote diode shorting method as no manual short circuits could be created due to the presence of the probe coating. The diode waveforms collected at 1 (panels A, B) and 20 dS m^{-1} (panels C, D) are presented in Figure 3.7, with the probe head waveforms on the left (panels A, C) and the probe end waveforms on the right (panels B, D). In contrast to the uncoated probes, the overall probe impedance calculated from the final reflection coefficient remains high throughout the range of solution electrical conductivities presented. The probe

impedance at low frequency changes from 6000 Ω to 1000 Ω from distilled water to 20 dS m^{-1}. The impedance contrast between the shorted diode and the probe remains high and therefore the diode acts as a better short circuit than in uncoated probes. The probe head diode waveforms indicate negligible changes in the slope and intercept of the diode waveforms between 1 and 20 dS m^{-1}. The probe head diode-difference waveforms eliminate internal reflections within the probe head, and are smoother and more easily interpreted using tangent-line analysis than the raw waveforms in Figure 3.6.

The diode-shorted waveform for the probe end diode in a 1 dS m^{-1} solution shows a very small reflection from the conductor to probe end transition; none is visible at 20 dS m^{-1}. The probe end diode-shorted waveform at 20 dS m^{-1} has a 4 nS longer transition time than the 1 dS m^{-1} waveform due to frequency-dependent transmission by the diode and frequency filtering by the solution. The automated measurements of travel time using remote diode shorting from 1 to 70 dS m^{-1} are presented in Figure 3.8. The travel time calculated using the tangent-line method remains constant up to 5 dS m^{-1}. Between 5 dS $m^{-1}$and 20 dS m^{-1} the travel time rises by 0.5 ns, beyond which it decreases. The combined effects of the longer diode waveform transition times and the raw waveform smoothing contribute to the inconsistent estimation of travel time. The decrease after 20 dS m^{-1} may be the result of the invasion of water into the probe head. The probe coating therefore allows collection of a waveform interpretable by travel time analysis in samples with electrical conductivities that are much higher than uncoated probes. Waveform differencing improves accuracy of travel time determination at the probe head, even with the MPN3404 diodes. The success of the waveform differencing method with manual short circuits in uncoated probes implies that either manual short circuits or perfect remote diode short circuits created would be similarly

successful in a coated probe, but the well preserved end reflection removes the necessity for waveform differencing at the probe end.

3.5.3 Coated Probes in Saturated Sand

The first experiments presented used electrically conductive water solutions to isolate the effects of DC conductance on signal quality from any other effects arising from the interaction of water and soil particles. The data collected in a saturated silica sand are now examined to determine the quality of the waveforms collected by a coated probe using a sample material closer to the expected field conditions. Figure 3.9 presents waveforms collected in silica sand saturated with distilled water (panels A, B), and saturated with a water solution with an electrical conductivity of 19.6 dS m^{-1} (panels C, D). Waveforms are displayed for the probe head (panels A, C) and probe end (panels B, D). When the saturating solution was 19.6 dS m^{-1}, the bulk electrical conductivity of the saturated silica sand, measured with a four electrode conductivity probe, was 8.3 dS m^{-1}. The diode-difference waveforms at the probe head are good quality, and again, probe head travel time is more easily estimated from the difference waveform than the raw waveform. The difference waveforms have the same rise time and waveform fitting derives the same travel time. At the probe end, the waveforms in the silica sand saturated with 19.6 dS m^{-1} water (panel D) are significantly more rounded, with longer transition times. The transition time of the probe end reflection is the same as in 20 dS m^{-1} water (Figure 3.7D), but the final amplitude is actually lower.

Figure 3.10 presents the two way travel times estimated from the waveforms in Figure 3.9 using automated remote diode shorting at both the probe head and end (A) and manual dual-tangent fitting to the raw waveforms (B, open circles). The measured travel

times for both the remote diode method, and the manual method both increase, but the remote diode method overestimates the increase. Curve C presents the travel time measured in water of the same bulk electrical conductivity, taken from Figure 3.8. This indicates that the increase in travel time determined by curves A and B is not directly the result of increased electrical conductivity of the water solution, but arises from the interaction of that water solution with the mineral particles.

The measured apparent dielectric permittivity increases in both the manual and remote diode waveform analysis methods and it can be therefore inferred this is a real increase in apparent dielectric permittivity similar to observations by Wyseure et al. (1997), Sun et al. (2000) and Topp et al. (2000). As discussed in the theory section, the apparent dielectric permittivity is not an actual physical property of the sample media , but is an average measurement over a non-specific range of frequencies defined by the tangent-line method of waveform analysis. An increase in apparent dielectric permittivity may therefore be the result of either changes in the frequency range used to define the apparent dielectric permittivity or actual changes in the dielectric properties of the media. It is clear from the waveform smoothing in Figure 3.7 and 3.9 that changes in the frequency content of the TDR pulse reflections are occurring with increasing electrical conductivity. Changes in the actual dielectric permittivity of the soil-water mixture may also be occurring.

Detailed investigation of changes in frequency content of the TDR pulse, and changes in the dielectric permittivity of soil/water/air/bound water/dissolved ion mixtures are best determined using frequency domain techniques where it is possible to determine both the real and imaginary parts of the complex dielectric permittivity across all the frequencies in the TDR pulse (Hoekstra and Delaney, 1974; Heimovaara et al., 1996; Friel and Or, 1999). This

type of analysis, using both uncoated and coated probes, would increase our understanding of the effects of high concentrations of dissolved ions on dielectric permittivity, TDR signal frequency content and on the apparent dielectric permittivity derived from tangent-line analysis.

These methods are not currently suited to automation in a field situation, and therefore this study has focussed the analysis on conventional travel time measurements. The primary concern is with signal quality, and obtaining a waveform interpretable by automated waveform fitting. The results obtained in saturated silica sand indicate that a coated probe is sufficient to determine a measurement of travel time and hence apparent dielectric permittivity, but that apparent dielectric permittivity alone is not sufficient to determine the water content of a soil containing a high electrical conductivity water solution. Calibration of the apparent dielectric permittivity to water content for mine waste material is presented further in Chapter 3.

3.5.4 Effect of probe coating

The apparent dielectric permittivity estimated using a coated probe must be related to the apparent dielectric permittivity of the soil to accurately estimate water contents. The third set of experiments determined the measured travel time for both a coated probe and an uncoated probe in materials with different dielectric permittivity. Apparent dielectric permittivity for coated and uncoated probes were estimated from these measured travel times using Equation 3.1. The apparent dielectric permittivity (ε_{cp}) derived from a coated probe is plotted against the apparent dielectric permittivity (ε_{app}) determined with an uncoated probe in Figure 3.11.

The dielectric permittivity of the probe coating can be estimated from where the apparent dielectric permittivity from the coated probe and the actual apparent dielectric permittivity coincide. This is estimated to be at a dielectric permittivity of 2.8. Three fitted curves are shown. Curve A represents a two-point linear correction for the presence of a coating material using the air and water measurements as suggested by Young (1998b). The maximum overestimation of the apparent dielectric permittivity using curve A occurs at a dielectric permittivity of 30, which corresponds to the apparent dielectric permittivity of saturated silica sand. The estimate of apparent soil dielectric permittivity using curve A would be double the true value. Curve B is derived from Equation 3.2 using the known probe dimensions and the estimated probe coating dielectric permittivity. Experiments by Friel and Or (1999) demonstrate that three-rod probes may emulate coaxial cells up to frequencies of 0.7 GHz. Equation 3.2 may be appropriate up to that frequency, but based upon the poor fit between the measured data and curve B, it is not applicable at the 0.7 to 1GHz that is estimated to dominate the travel time analysis of TDR waveforms. Curve C is the best-fit equation to the measured data obtained by modifying Equation 3.2. The rod and coating dimensions are retained as the known values, but r_o is used as a fitting parameter. Using the form of Equation 3.2, the correct curve shape is captured while using a relatively simple fitting equation.

It is now possible to assess the accuracy of a coated probe for the determination of the apparent dielectric permittivity of a high electrical conductivity sample. A 0.4 ns change in the measured travel time was noted in the previous discussion of the performance of coated probes in solutions between 1 and 70 dS m^{-1} (Figure 3.6). The highest solution electrical conductance, 70.8 dS m^{-1}, corresponds to a sodium chloride concentration of 0.77 mol/L

(Mojid et al., 1998). Using the data tabulated in Hasted (1973), the dielectric constant would be expected to decrease from 80.7 to 69. Using Equation 3.1, the two-way travel time in an uncoated probe of the same length as the coated probe should decrease by 1.3 ns. The actual decrease in measured travel time for the coated probe is affected by the probe coating. Using the best fit curve (Figure 3.9, Curve C), this calculated change of dielectric permittivity would correspond to a change in measured apparent dielectric permittivity from 29.3 to 27.3 and a travel time difference of 0.38 ns. This corresponds to the measured 0.4 ns change in travel time between 1 and 70 dS m^{-1}. The coated probes are therefore sensitive enough to determine small changes in the dielectric permittivity.

3.5.5 Recommendations

The method of waveform differencing for determination of the travel time is accurate for high electrical conductivity samples (Figure 3.4) when the waveguides are perfectly shorted. As this method requires a raw waveform with an end reflection, it has the same upper limit of solution electrical conductivity as does the interpretation of raw waveforms. The remote diode method of creating short circuits using the MPN3404 diodes recommended by Young (1998) is inaccurate for media with high electrical conductivities. The MPN3404 diodes have frequency-dependent impedances that are incompatible with the probes design used. The results obtained for the remote diode method may be improved by the use of diodes other than the MPN3404 that have lower impedance characteristics at frequencies of 700 MHz to 1GHz. Alternate diodes have not been investigated , but can recommend that any diodes selected can be easily checked for performance by measuring diode waveforms of an uncoated probe in an electrically conductive water solution. The presence of significant

signal amplitude in the diode-shorted waveform is an indication of unsuitable diode characteristics.

Measurement of apparent dielectric permittivity in high electrical conductivity systems requires the use of a probe coating to obtain an interpretable waveform. The three-rod Zeglin type probe with a coating on the center rod obtained interpretable waveforms in both water solutions and saturated silica sand. The accuracy of the probe head measurements for coated probes (Figure 3.7) demonstrates that probe head travel time for coated probes is more easily determined using remote diode shorting, even with the MPN3404 diode. The accuracy of locating the probe end reflection using conventional waveform analysis (Figure 3.6) indicates that probe base travel time should be determined from the raw waveform using a dual-tangent method. No probe end diodes or terminal block (Figure 3.1) are therefore required. An empirical correction (Figure 3.9) for the probe coating should be derived by TDR measurements in liquids of known dielectric properties. The calibration media should have dielectric permittivities close to the range of expected dielectric permittivities in the soil and calibration of individual probes is required. The use of a resistive coating permits the determination of travel time and hence apparent dielectric permittivity in high electrical conductivity systems. Further work using frequency domain techniques is required to investigate the changes in apparent dielectric permittivity with both soil water content and soil water electrical conductivity.

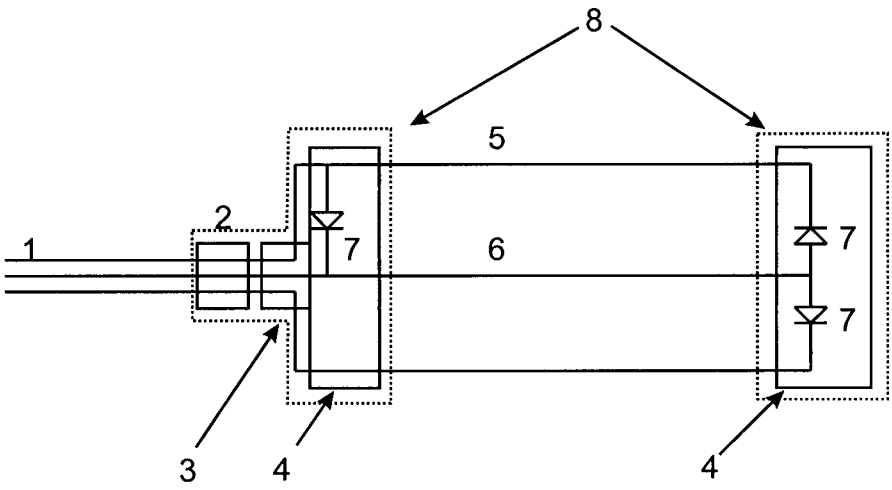

1. RG6 coaxial cable: F660 BEF CommScope 75 ohm cable
2. Female F-connector
3. Male F-Connector to plug
4. Polyethylene terminal block
5. Outer rod: unshielded 3.2 mm dia. 316 stainless steel.
6. Center rod: uncoated 3.2 mm dia. 316 stainless steel. Optionally coated with 0.4 mm thick polyolefin heat shrink
7. Motorola MPN3404 PIN diode
8. Terminal block sealed with silicon sealant

Figure 3.1: Schematic of TDR probe design.

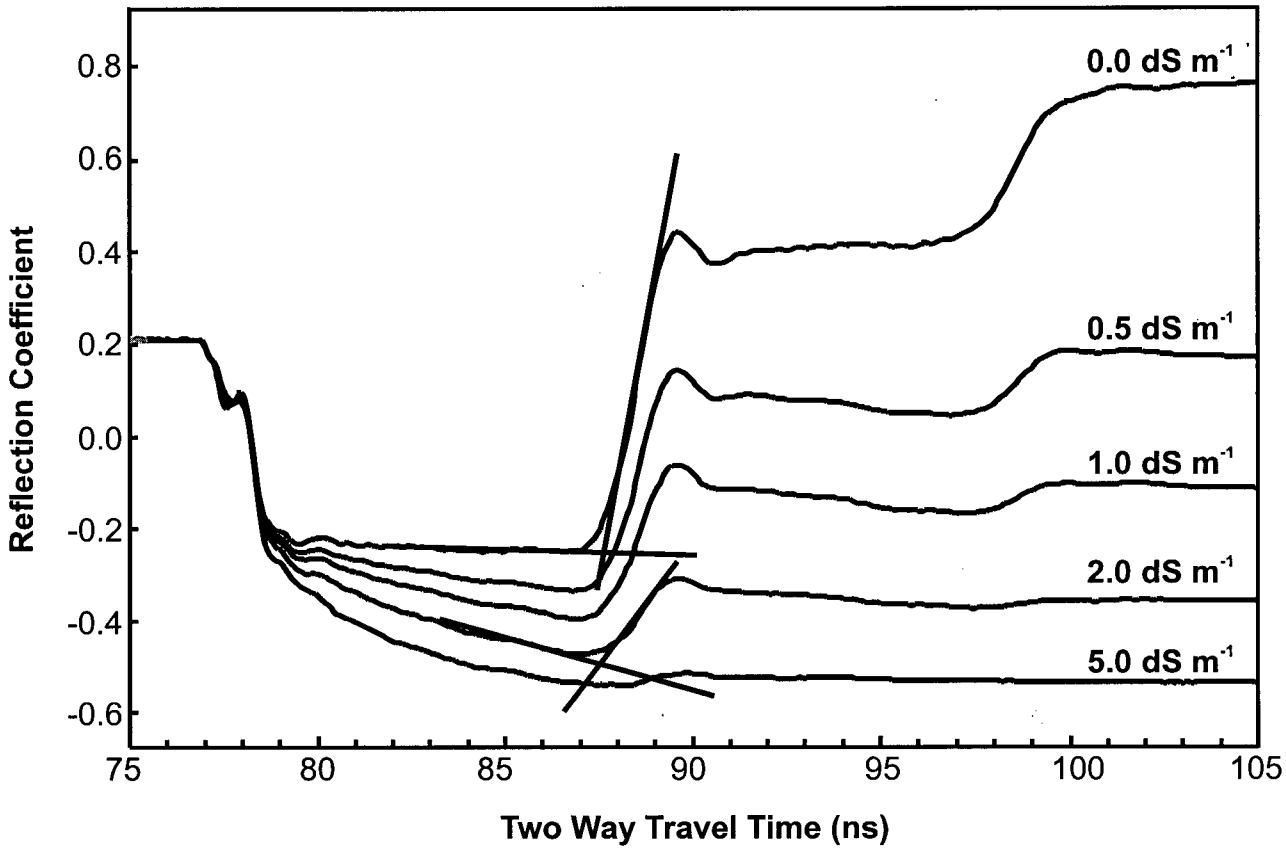

Figure 3.2: Raw time domain reflectrometry waveforms with manually determined tangent-lines to the probe end reflection: 160 mm length uncoated probe.

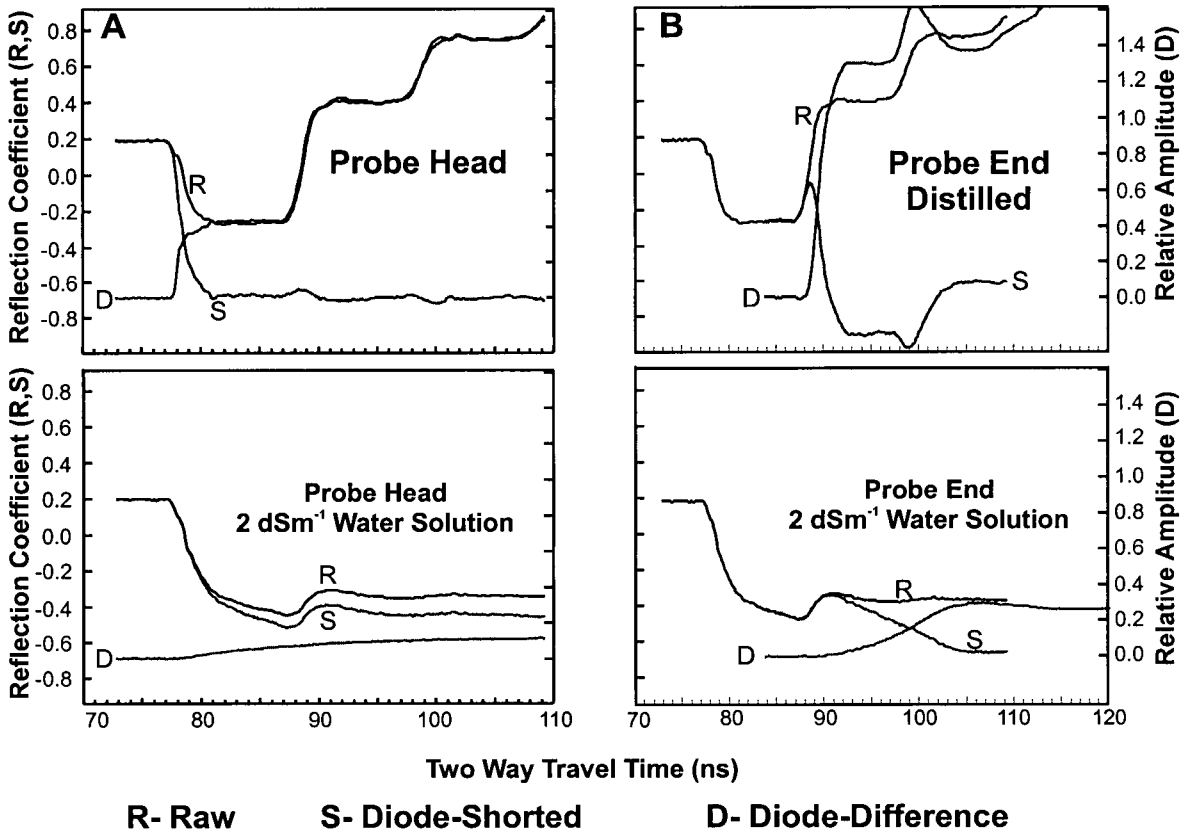

Figure 3.3: Remote diode shorting method waveforms for diodes located: (AB) at the probe head and (CD) at the probe base: 160 mm length uncoated probe in water solutions of varying conductivity

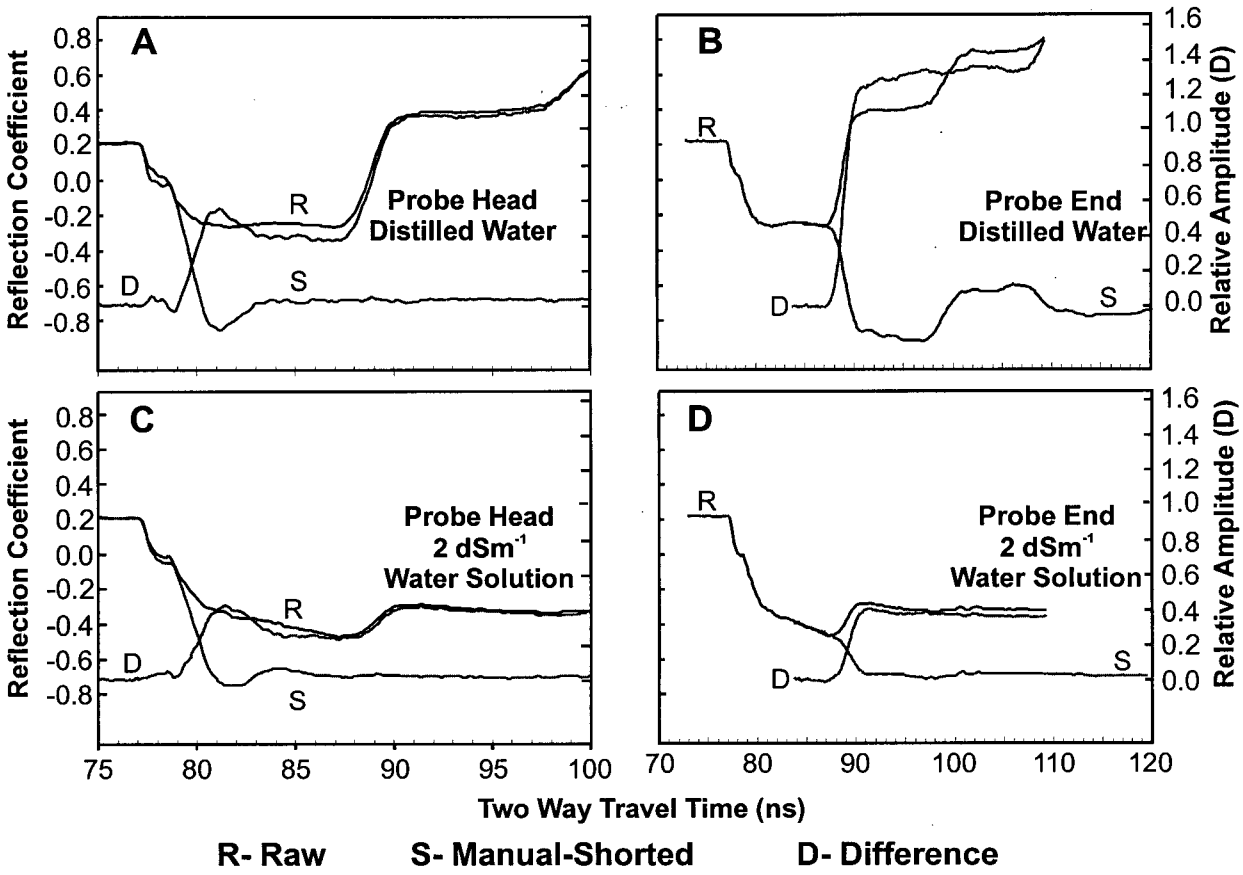

Figure 3.4: Manual probe shorting method waveforms for short circuits using copper wire located: (AB) at the probe head end of the exposed conductors and (CD) at the probe base end of the exposed conductors: 160 mm length uncoated probe in water solutions of varying conductivity

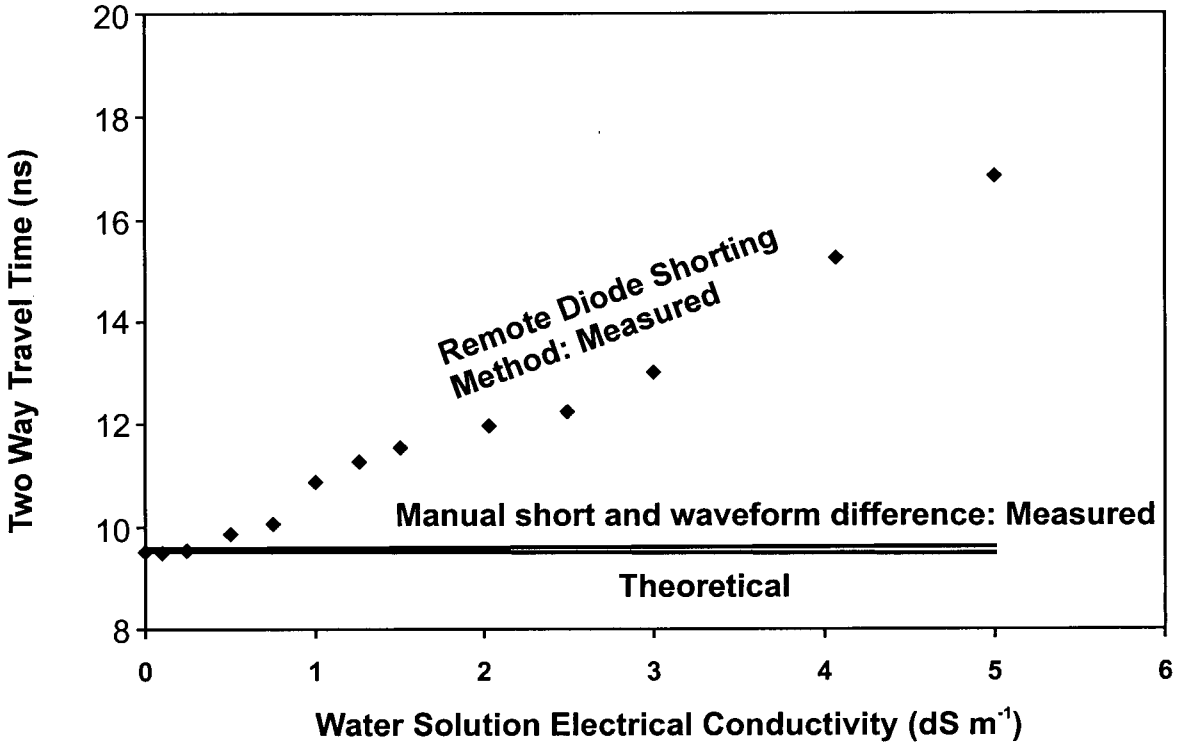

Figure 3.5: Automated remote diode shorted method measured two way travel time, travel time measured using manual probe shorting and waveform differencing and travel time calculated from Hasted (1973) data: 160 mm length uncoated probe in water solutions of varying electrical conductivity.

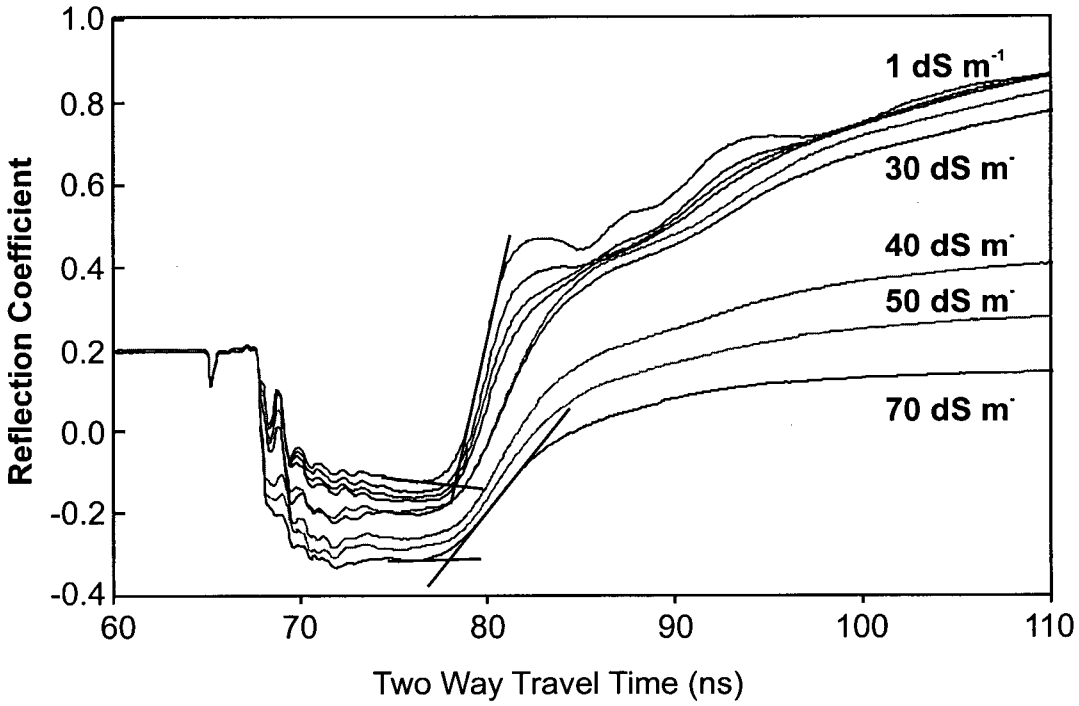

Figure 3.6: Raw time domain reflectrometry waveforms with manually determined tangent lines to the probe end reflection: 281 mm length coated probe in water solutions of varying electrical conductivity

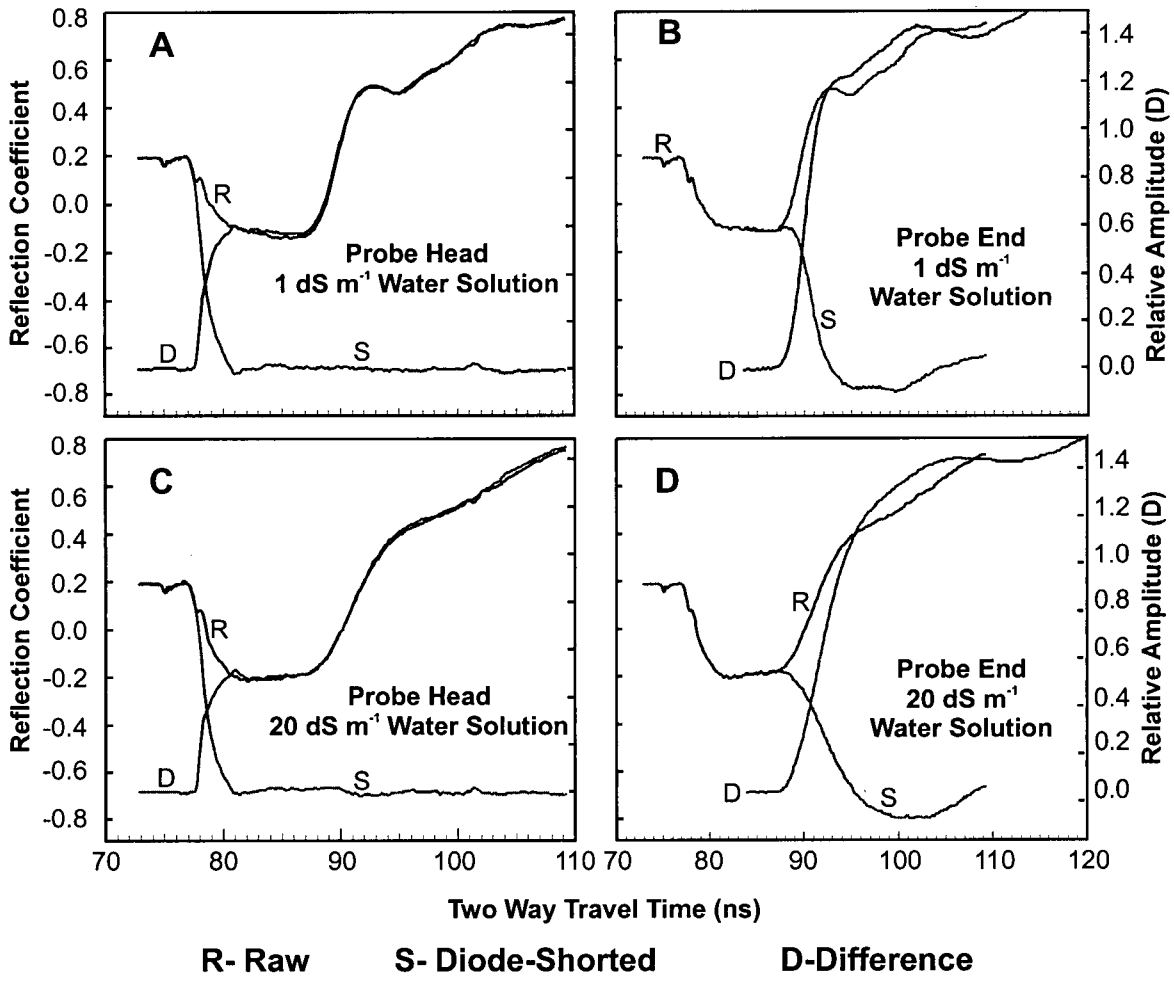

Figure 3.7: Remote diode shorting method waveforms for diodes located: (AB) at the probe head and (CD) at the probe base: 281 mm length coated probe in water solutions of varying electrical conductivity.

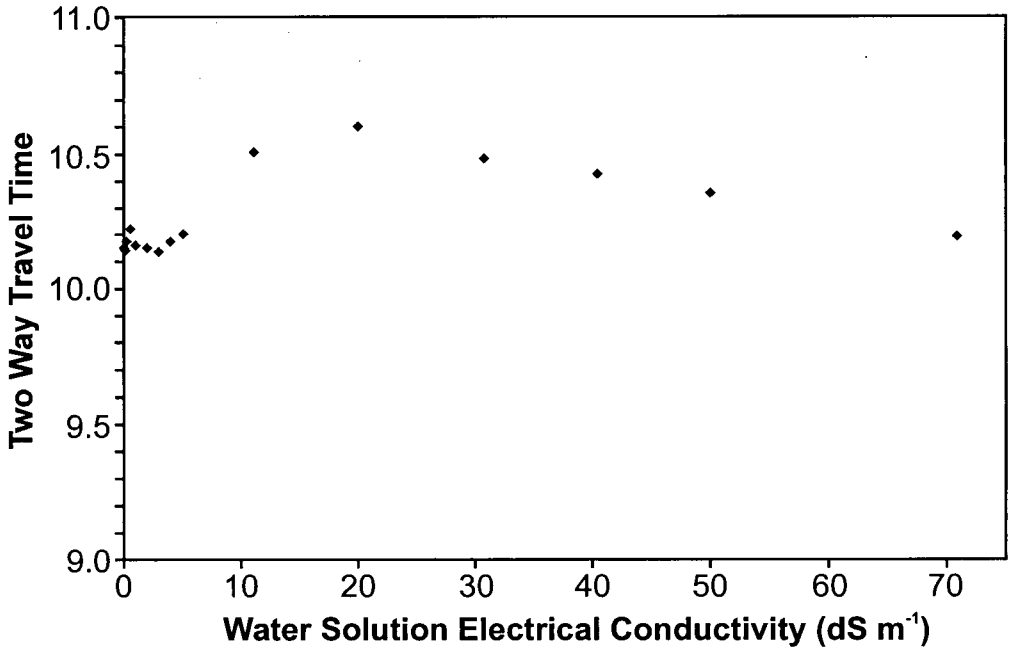

Figure 3.8: Automated remote diode shorted method measured two way travel time: 281 mm length coated probe in water solutions of varying electrical conductivity

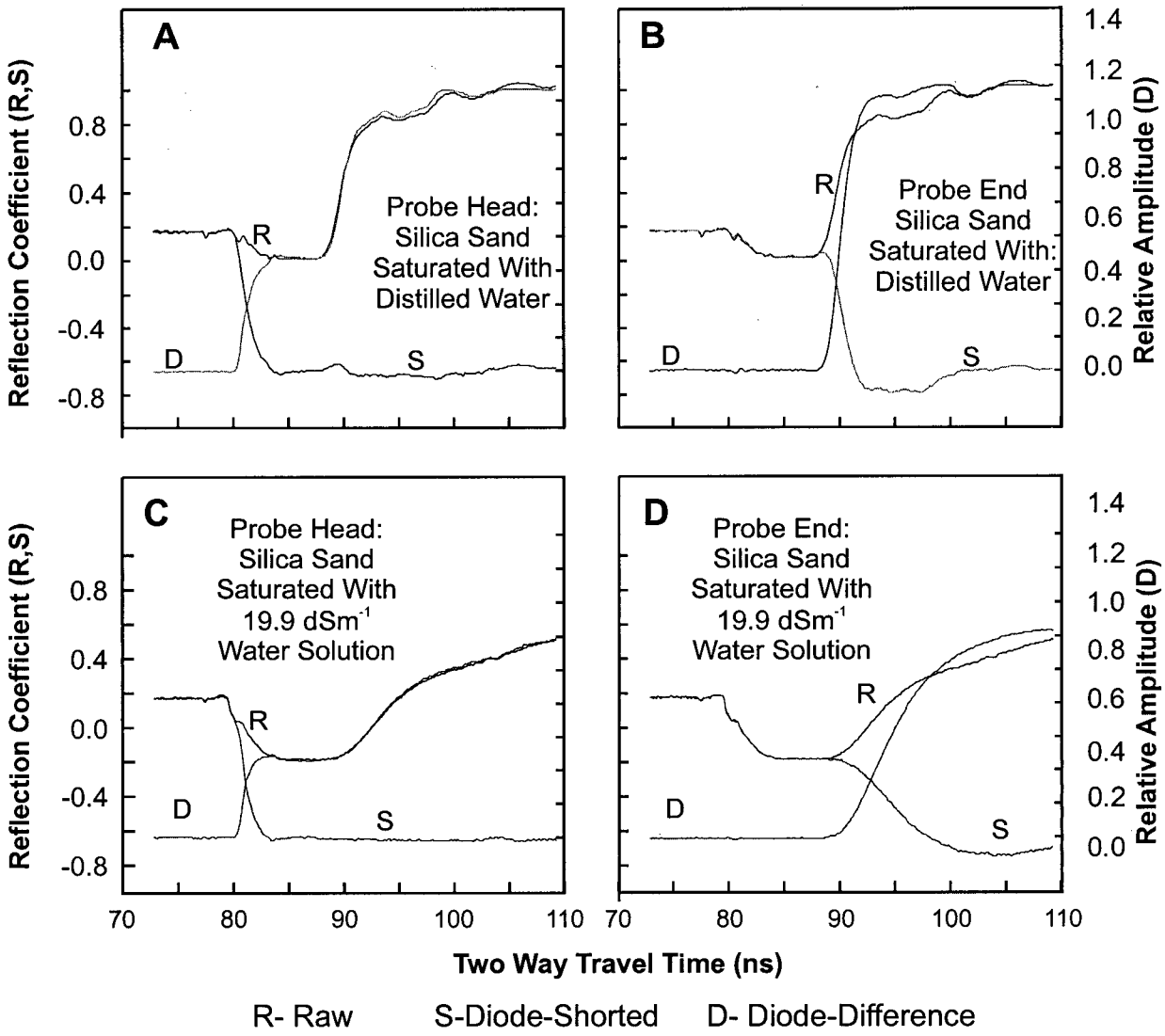

Figure 3.9: Remote diode shorting method waveforms for diodes located: (AB) at the probe head and (CD) at the probe base: 281 mm length coated probe in silica sand saturated with water solutions of varying electrical conductivity

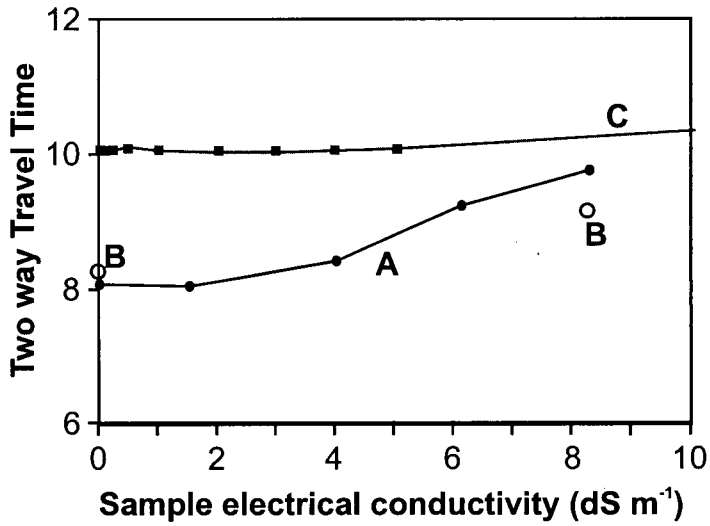

Figure 3.10: Automated remote diode shorted method measured two way travel time: 281 mm length coated probe in silica sand saturated with water solutions of varying electrical conductivity.

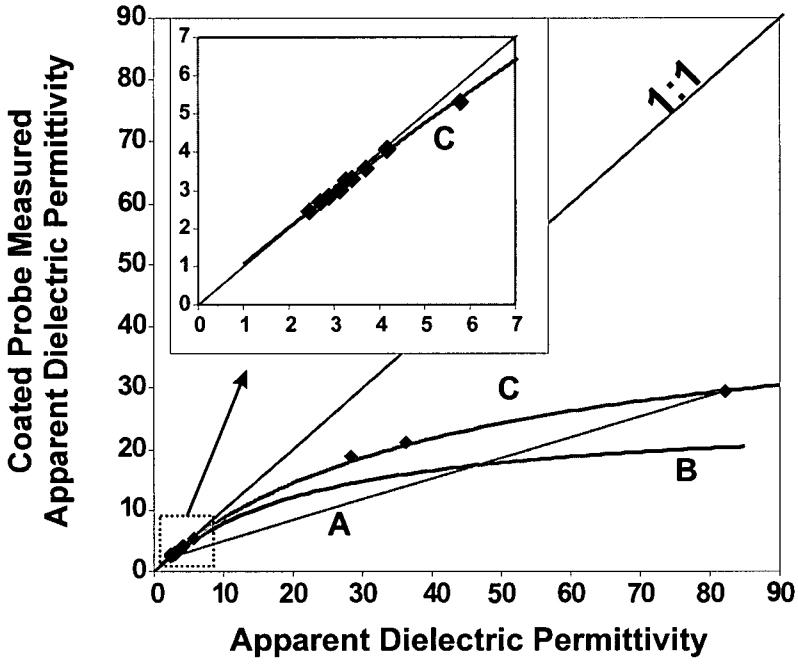

Figure 3.11: Relationship of coated probe measured apparent dielectric permittivity to apparent dielectric permittivity. A) Linear correction B) Equation 3.2 using known probe dimensions: r_o= 12.5 mm., Kc=2.8 C) Equation 3.2 using r_o as fitting parameter: r_o= 53.5 mm., Kc=2.8

CHAPTER 4: TIME DOMAIN REFLECTROMETRY MEASUREMENTS OF WATER CONTENT IN COARSE WASTE ROCK

4.1 ABSTRACT

The TDR method is calibrated and applied to determine the water content of mine waste rock in a large scale field experiment. High electrical conductivity of the soil water in waste rock reduces the quality of a TDR waveform through the loss of signal amplitude. Two strategies are used to obtain higher signal-to-noise waveforms: waveform differencing by remote diode shorting and covering probe conductors with a resistive coating. The TDR pulse travel-time measured in soils containing electrically conductive water solutions increases systematically, partly due to bias in the remote diode and tangent-line measurement methods. This bias affects the experimental calibration data, and is larger than the variations in the calibration data caused by variations in probe construction, grain size, or cable length. Two empirical calibrations are derived for waste rock with low and high electrical conductivity soil water, respectively. An ambient temperature correction is derived from measured field data based upon the diurnal fluctuation of measured travel time with temperature. The variation of apparent dielectric permittivity with temperature is positively correlated with temperature at low water content, and negatively correlated at high water content. This trend indicates a significant influence of water bound to mineral surfaces on the variation of apparent dielectric permittivity with temperature. Examination of the field data indicates the effect of electrical conductivity of the soil water on the accuracy of the remote diode method is larger than the ambient temperature effect.

4.2 INTRODUCTION

Long-term measurements have been made of the water content of mine waste rock in a large scale field experiment (Nichol et al., 2000, Appendix A). Automated measurements of soil water content are most easily achieved using methods based upon the electrical properties of soils, with time domain reflectrometry (TDR) being the most common method. TDR measures the propagation of a fast rise time, step voltage pulse through a coaxial cable to a waveguide (probe) composed of parallel conductors in contact with the sample. TDR can be used to determine the dielectric properties of the sample and the bulk soil electrical conductivity. With appropriate calibrations, the bulk soil dielectric permittivity can be related to the soil water content, and the bulk soil electrical conductivity can be related to the electrical conductivity of the soil water solution.

The measurement of water content in coarse, heterogeneous mine waste rock presents a challenge when using the TDR method. Oxidation of sulphide minerals within waste rock leads to soil water with high electrical conductivity. This can lead to high signal attenuation, and subsequent difficulty in the estimation of soil electrical properties. Several strategies have been proposed to overcome this limitation, including using short probes (Kelly et al., 1995), resistive probe coatings (Knight et al., 1997, Mojid et al., 1998), and waveform differencing using remote diode shorting (Hook et al., 1992). A review of the success of these strategies is presented in Chapter 3.

In this chapter, work undertaken to relate the measured electrical properties of mine waste rock to the volumetric water content is presented. These experiments demonstrate that while TDR measurement of water content is well accepted in theory, its practical application to difficult soil material can be challenging. This required three issues to be addressed.

Firstly, the effectiveness of the probe design deployed in the constructed pile experiment (CPE) is determined. This design differs from the design recommended in Chapter 3. Two potential sources of error are highlighted: design deficiencies in the probe head and end connections; and a systematic bias of the remote-diode method used in soils with high electrical conductivity soil water solutions. Secondly, laboratory and field calibrations are undertaken to relate the electrical properties of mine waste rock to the water content. Thirdly, the effects of ambient temperature upon the measured electrical properties are corrected for using an algorithm derived from two and a half years of field data. The processed field data are then presented to demonstrate the relative effects of probe design errors, calibration variation, and the effect of ambient temperature on the final calculated values of water content, and the overall performance of the TDR measurement system.

4.3 THEORY

4.3.1 Dielectric Properties of Soil-Air-Water Mixtures

The measurement of soil water content using electrical methods is related to the change in the dielectric permittivity of soil-air-water mixtures as a result of the variation in the proportion of water. The complex dielectric permittivity of a substance, $\varepsilon(\omega)$, is dependant upon the angular frequency (ω) of the electrical field. It has a real component, $\varepsilon'(\omega)$, which expresses recoverable energy storage, and an out-of-phase imaginary component, $\varepsilon''(\omega)$, which describes both ohmic losses arising from the electrical conductivity (σ_{DC}) and polarization losses, $\varepsilon_p(\omega)$. The dielectric permittivity is (Topp et al., 1980):

$$\varepsilon(\omega) = \varepsilon'(\omega) - i\varepsilon''(\omega) \qquad [4.1]$$

$$\varepsilon''(\omega) = \varepsilon_p(\omega) + \frac{\sigma_{DC}}{\omega} \qquad [4.2]$$

The dielectric constant (K) is defined as the static dielectric permittivity relative to the permittivity of free space ($\varepsilon'(0)/\ \varepsilon_o$). The dielectric constant is often used, sometimes inappropriately, in place of $\varepsilon(\omega)$, as it allows the dielectric properties to be expressed as a single value. The dielectric constant of soil changes as water (K~80) replaces air (K~1) in the pore space of dry soil (K~3 to 5).

The relationship of the soil dielectric permittivity to the soil water content can be described using either a theoretical mixing model, or by direct calibration. Various theoretical mixing models have been proposed to relate the electrical properties of soil-air-water mixtures to the electrical properties of the individual components (Birchak et al., 1974, Dobson et al., 1985; Roth et al., 1990; Herkelrath et al., 1991; Dirksen and Dasberg, 1993; Heimovaara et al., 1994, Ferré et al., 1996, Yu et al., 1997). However, the dielectric permittivity of water within a soil environment may not be the same as that of water as a free phase. Water close to mineral surfaces, especially clays, is bound by electrostatic forces. Similarly, the presence of high concentrations of dissolved ions in water constrains liquid water molecules by partly binding them to the dissolved ions. (Robinson and Stokes, 1955; Hasted, 1973). The dielectric and electrical conductance properties of bound water are therefore different from those of free-phase water (Hoekstra and Delaney, 1974, Topp et al., 1980; Herkelrath et al., 1991; Dirksen and Dasberg, 1993; Or and Wraith, 1999). Several studies have attempted to relate the amount and influence of bound water to theoretical

descriptions of the water bonding processes, and measurements of clay mineralogy, surface area or hygroscopic water content (Dirksen and Dasberg, 1993; Or and Wraith, 1999). Work is progressing, but no theoretical description or experimental correlation exists to reliably account for bound water independent of actual measurements of the soil dielectric permittivity. A significant silt and clay fraction (10% of the <600mm fraction or 20% of the <5mm fraction) is present in the CPE waste rock, in addition to high total dissolved solids in the soil water. It was therefore assumed that a fraction of bound water would be present, and work proceeded directly to an empirical calibration between measurements of the apparent dielectric permittivity of the waste rock material, and the volumetric water content of the waste rock.

4.3.2 Measurement of Dielectric Permittivity using Time Domain Reflectrometry

A TDR instrument propagates a fast rise time, step voltage pulse through a coaxial cable to the probe. Part of the incident pulse energy reflects back to the TDR instrument from each impedance change in the transmission line and probe, and a full reflection of the remaining pulse energy occurs at the end of the probe. The sum of the incident voltage and reflected pulse voltage measured at the TDR instrument is plotted in time and presented as a waveform. The arrival of reflected energy back at the TDR instrument causes a change in the measured voltage over time, and thus a deflection of the waveform. Figure 4.1 illustrates a representative waveform for a TDR probe immersed in an electrically conductive water solution.

The simplest analysis of a TDR waveform is to determine the times that the waveform is deflected by the arrival of energy from the probe head and probe end reflections (t_0, t_1) and use the difference to estimate an apparent pulse velocity within the probe (v_{app}):

$$v_{app} = \frac{2L}{(t_1 - t_o)} \qquad [4.3]$$

where L is the length of the probe.

Two forms of line-fitting for wave form analysis are commonly used to determine the locations in time of the reflections within the TDR waveform (Hoekstra and Delaney, 1974, Topp et al., 1980, Wraith and Or, 1999). One line is fit to the pre-deflection waveform and this can either be a horizontal line (flat-tangent method) fit to the lowest point on the pre-deflection waveform, or a tangent to the pre-deflection waveform (dual-tangent method). The second line in both methods is a tangent fit to the falling (probe head) or rising limb (probe end) of the deflection. The time of the intercept of the pre-deflection and post-deflection fitted lines is the arrival time of the reflected pulse energy. A comparison of the flat-tangent and the dual-tangent methods by Wraith and Or (1999) indicated the dual-tangent method is more accurate for high electrical conductivity samples.

The dielectric permittivity of the medium surrounding the probe is related to the velocity by:

$$\varepsilon_{app} = \varepsilon_o \left(\frac{c}{v_{app}} \right)^2 \left(\frac{\mu_o}{\mu} \right)^2 \qquad [4.4]$$

where ε_o is the permittivity of free space and c is the velocity of light in a vacuum. It is assumed that the magnetic permeability of soils and soil-air-water solutions (μ) equals that of free space (μ_o) and therefore (μ_o/μ) is unity (Topp et al., 1980).

The dielectric property calculated by interpreting the arrival times of reflections in the waveform by tangent-line analysis is termed the apparent dielectric permittivity, (ε_{app}), not the dielectric permittivity, $\varepsilon(\omega)$, because the apparent dielectric permittivity is not derived for a single frequency. The TDR equipment deployed at the CPE was not capable of automated recording of full waveforms with sufficient detail to permit the interpretation of dielectric properties in the frequency domain. All the TDR interpretations presented are therefore based upon travel time analysis and are measurements of apparent dielectric permittivity only.

Tangent-line methods of waveform analysis to determine travel time may be impossible to apply in systems with high electrical conductivity. Conduction of energy between the central signal conductor and the outer ground conductors leads to signal voltage loss, a weak reflection from the probe end, and ultimately a waveform on which tangent-lines cannot be accurately fitted. This is demonstrated in Figure 4.1, where the waveform descends between t_o and t_1, and the end reflection after t_1 is small. The conductive loss of signal between the signal and ground conductors can be reduced by the use of resistive coatings on the conductors (Knight et al., 1997, Chapter 3). The signal energy is retained, and the amplitude of the reflection from the end of the probes is increased.

Waveform differencing using remotely shorted diodes has also been proposed as a method to improve waveform interpretability and obtain improved estimates of the arrival times (t_o, t_1) (Hook et al., 1992). The TDR pulse is selectively diverted from the signal conductor to the ground conductors by positive-intrinsic-negative (PIN) diodes. Travel times to the probe head (t_o) and end (t_1) are estimated from the arrival of the diverted signal

returning along the ground conductor. Hook et al. (1992) and Chapter 3 provide further discussion of the remote diode and waveform differencing methods.

4.3.3 CPE Probe Design

The probes that were installed in the CPE (Figure 4.2) are based upon a probe design suggested by Young, 1998a, for use with the MoisturePoint ^{TM} TDR (MTDR) instrument (Environmental Sensors Inc., Victoria, B.C., Canada). The probes are Zegelin-type, three-conductor probes constructed using 3.2 mm diameter 316 stainless steel rods (Zegelin et al., 1989). The coated probes include a 0.4 mm thick polyolefin heat shrink on the center conductor. Probe designs are quoted in the remainder of the chapter as three numbers a/b/c, where a is the length of exposed rods in mm, b is the rod diameter in mm, and c is the center rod to outer rod spacing in mm. The probe design includes a single positive-intrinsic-negative (PIN) diode (On Semiconductor, MPN3404) at the probe head, and two PIN diodes at the probe end. The presence of diodes at the probe end required the use of a terminal block, a probe termination structure at the probe end, which is not normally included in a TDR probe. The TDR probes were manually buried within the waste rock pile as it was being constructed and thus the terminal block did not interfere with the TDR probe installation, as it would in a more standard soils application where the probe is pushed into the soil to avoid disturbing the natural soil structure.

The PIN diodes used for the remote diode shorting method are located within the probe head and end termination structures, which are manufactured out of polyethylene terminal blocks coated with industrial silicon sealant (Figure 4.2). The diodes are located immediately prior to the start of the exposed TDR rods at the probe head, and immediately after the exposed rods at the probe end. The remote-diode method determines the time that

the propagated voltage signal passes through the diodes when they are short-circuited, and the signal returns along the ground conductor. To determine the travel time in the soil only, a probe head/end offset correction must be applied to account for the signal travel time within the termination structures between the diodes and the conductors exposed to soil (Young 1997).

The probes were installed July of 1998. Several difficulties with the probe design and waveform interpretation method were subsequently uncovered after the probes were irretrievably installed: (1) it was determined that the two-point linear calibration of Young (1998b) was insufficient to describe the effects of the coating on the calculated sample apparent dielectric permittivity; (2) the MPN3404 diodes do not create short circuits of sufficient quality for the remote diode method to be successful; and (3) the probe head and end structures were found to be inadequate. Problems 1 and 2 are discussed in Chapter 3. Problems 2 and 3 are further investigated in this chapter.

4.3.4 Temperature Dependence

The waste rock in our experiment undergoes variations in ambient temperature from -20 to 25 °C. Measurements below 0 °C are not considered in this work due to ice formation. The effect of ambient temperature upon the measured soil apparent dielectric permittivity must be determined prior to the final calculation of soil water content. The dielectric permittivity of a wetted soil changes with ambient temperature as a function of two competing processes. First, the dielectric of liquid water in the free phase decreases with increasing ambient temperature. Second, the volume fraction of water bound to mineral surfaces decreases with increasing temperature (Hoekstra and Delaney, 1974; Wraith and Or, 1999; Or and Wraith, 1999). The dielectric constant of the bound fraction (~3) is lower than

that of free water (~80) and thus the conversion of bound water to unbound water with increasing temperature leads to a higher dielectric permittivity at the same water content. Both the dielectric permittivity and conductive properties of water that remains bound to the surface of clay minerals and of water bound in hydration layers of dissolved ions can also be expected to vary with temperature (Or and Wraith, 1999).

Soils with a significant bound water fraction can therefore be expected to have a positive trend of dielectric permittivity with temperature at low water contents and a negative trend of dielectric permittivity with temperature at high water contents, when the relative contribution of the bound water fraction is lower. The cross-over point will be a function of the clay fraction and porosity of the sample.

The effect of temperature can be measured empirically by controlling the water content of a sample, then progressively changing the ambient temperature of the sample (Pepin et al., 1995; Halbertsma et al., 1995; Wraith and Or, 1999). The calibration is repeated for different water contents, and over the full range of ambient temperatures expected in the field. An alternative method is presented based upon the field data, using the measured daily variations of the apparent dielectric permittivity and ambient temperature at the same location.

4.4 EXPERIMENTAL METHODS

Experiments were first conducted to investigate the ability of the TDR system used to collect valid measurements of the apparent dielectric permittivity, secondly to relate the measured apparent dielectric permittivity to the water content of the waste rock, and thirdly to determine a correction for ambient soil temperature.

4.4.1 TDR Instruments and Waveform Collection

For the laboratory experiments, raw waveforms and diode-shorted waveforms with 256 points in time were collected using a MTDR instrument with firmware Version 1.27. Travel times were measured using the automated waveform fitting routines which are included in the instrument firmware. Additional waveforms for detailed waveform analysis were collected manually using a PC connected to the MTDR and running the instrument control software ViewPoint^{TM} Version 1.34. For all measurements, all instrument settings and waveform fitting parameters in the instrument firmware and software were optimized for maximum accuracy and stability of tangent-line fitting. For all laboratory calibration work, a minimum of twenty measurements of travel time were obtained in each media, and averaged.

The CPE experiment required the use of 34 m coaxial cables (Commscope F660BEF RG6) and up to two Campbell Scientific SDMX-50 coaxial multiplexers in series to connect multiple TDR probes to the TDR instrument. Long cables and multiplexers may increase the measured travel time slightly by changing the frequency content of the TDR pulse. This effect was checked during our calibration experiments, and was found to be small enough to be ignored. Laboratory calibration work was conducted using 6 m cables (Commscope F660BEF RG6) to connect the TDR instrument to the TDR probe.

4.4.2 Probe Head/End Offset

To determine the probe head/end offset, automated travel time measurements were taken using a 291/3.2/25 uncoated probe in air and in methanol and water contained in a 15 cm diameter PVC chamber. In addition, prior to installation of the TDR probes into the CPE, travel time measurements were conducted for each probe in oven dried silica sand, and de-ionized water contained within 30 cm diameter PVC containers. These measurement were

taken in accordance with the two-point probe calibration procedures described in Young (1998b). These measurements were indicated to be sufficient to parameterize the probe head/end offset and a linear correction equation to compensate for the presence of the probe coating.

4.4.3 Performance in electrically conductive media

Measurements of travel time using the automated curve fitting routines of the MoisturePoint instrument were carried out to determine the performance of a 281/3.2/25 coated probe and the remote diode shorting method using MPN3404 diodes in electrically conductive media. Measurements were taken in a water solution in which the electrical conductivity was varied from 0 to 70 dSm^{-1} using NaCl. Measurements were also conducted in silica sand (K~27) saturated with water solutions of with varying electrical conductivity. The electrical conductivity of the water solutions saturating the silica sand was varied from 0.24 to 17.5 dSm^{-1} using NaCl. This caused the bulk soil electrical conductivity to vary from 0.029 to 8.3 dSm^{-1} which represents the variation of soil-water conductivities expected in the field experiment.

Travel time in the water solutions (Curve A, K~80) was determined using the remote diode shorting method for both the probe head and end (Chapter 3). In the saturated silica sand, three methods were used to measure t_1 at the probe end. The travel time was measured using remote diode shorting for both the probe head and probe end. The travel time was also measured using the remote diode method to determine the probe head travel time (t_o) and using the automated curve fitting routine of the MoisturePoint TDR system to perform flat-tangent fitting to the raw waveform collected at the probe end. The travel time was also measured by manual determination using the dual-tangent method.

4.4.4 Laboratory Calibration Measurements for CPE waste rock

An empirical calibration of the travel time-water content relation was obtained by packing waste rock into a box at known water contents, and measuring the travel time using coated probes. Three sets of calibrations were performed. First, calibrations were performed using two different probes, 281/3.2/25 and 376/3.2/25, using waste rock collected from the CPE during construction, to assess the magnitude of variation between probes. Secondly, two calibrations were conducted to determine the effect of variable grain size on the measured travel time using a 281/3.2/25 probe. CPE waste rock samples were sieved to obtain two fractions, <5mm and <25mm.

Thirdly, calibrations were performed on two different waste rock materials to encompass the range of soil water electrical conductivities expected in the field. Measurements were conducted using both 281/3.2/25 and 376/3.2/25 probes in washed waste rock material. This waste rock was flushed with many pore volumes to remove stored weathering products. Upon saturation, the measured electrical conductivity of the soil water solution was <0.8 dSm^{-1}. The second material was waste rock sampled as the waste rock pile was constructed, which included a reserve of stored weathering products. Measurements were obtained using a 281/3.2/25 probe.

Waste rock was first oven dried for 24 + hours at 110 °C. It was progressively wetted using a hand spray bottle and thoroughly mixed prior to packing. At each water content, the soil was repacked three times and the measurements replicated to determine variability caused by the packing arrangement. Repeated calibrations from oven-dried soil to wetted soil were made. The travel time was measured with automated remote diode shorting for both the probe head and end. Volumetric water content was determined for each packing

from the difference of total mass and dry mass, and the volume of the packed sample. The dry density of the material was kept similar to that obtained with waste rock at the water contents measured during construction of the experimental waste rock pile.

The container used was 12 cm x 12 cm in cross section, representing 2.4 times the outer rod to outer rod spacing. The size of the container was checked prior to use. Measurements of the travel time for an uncoated probe in water in a 35 cm diameter cylindrical container and the 12cm x 12cm container were found to be within 0.7%, confirming that the container was adequate to contain the majority of the wave energy of the TDR pulse. Coated probes do not correctly average water content if the water is not evenly distributed along the probe length (Ferré et al., 1996, Knight et al., 1997). All measurements were therefore taken with the TDR probe and soil container horizontal to minimize vertical gradient in water content. Wetting was stopped when it was clear that water was redistributing within the soil container during the time taken to measure the travel time.

Measurements were also conducted for saturated waste rock. A coated TDR probe was placed into a 15 cm diameter PVC pipe, and soil was packed around the probe at residual water content. The pipe was slowly flooded from the bottom upwards over 24 hours by equilibration of the water level in the pipe with a large external water reservoir.

4.4.5 Field Measurements

Two and a half years of measured TDR travel times are available from 21 probes installed within the constructed pile at depths from 0.1 m to 4.5 m. Instrumentation was placed within the CPE during construction of the waste rock pile. The TDR probes were manually placed upon a leveled waste rock surface and buried by hand to 20 cm depth. Further waste rock was placed upon the probe using a tracked excavator with a $1m^3$ bucket.

It was necessary to remove larger grain size particles (>25mm) from the vicinity of the TDR probes to prevent damage to the TDR probes during burial.

Automated TDR measurements are conducted using an MTDR instrument connected to a Campbell Scientific CR10X datalogger. The TDR probes are connected using 34 metres of cable, and either one or two Campbell Scientific SDMX-50 multiplexers connected in series. Measurement intervals range from 20 minutes to 60 minutes with the time of year. Travel time is measured using the automated remote diode measurement routine of the MTDR at both the probe head and end. Five measurements of travel time are discarded at the start of each round of measurements to ensure the instrument is properly warmed up and stable. During a single measurement round, each probe is measured three times in succession and the average and standard deviation of the three measurements are recorded. Ambient soil temperature is recorded every 15 minutes at each instrument location using commercially available thermistors. Separate dataloggers are used to collect TDR and temperature data, and the measurements are not synchronized. The soil ambient temperature corresponding to each TDR measurement was determined by linear interpolation between the nearest temperature measurements.

4.5 RESULTS AND DISCUSSION

For all measurements of travel time, the raw measured travel time (t) is converted to an adjusted travel time (t*) by subtraction of the probe head/end offset (t_{off}). The adjusted travel time (t*) is then divided by the calculated travel time in air (t_{cair}), calculated from the probe length and the dielectric constant of air. Division by t_{cair} allows comparison of raw travel time measurements of probes of varying length. All measurements are presented as t^*/t_{cair}, referred to in the remainder of this chapter as the corrected travel time.

4.5.1 Probe Head/End Offset

The results of the measurements of travel time in air, methanol and water are presented in Figure 4.3. The dielectric properties of these substances are known (CRC Press, 1994), and a theoretical travel time can be estimated from Equations 4.3 and 4.4 using the length of the exposed conductors. The difference between the calculated travel time and the measured travel time is the probe head/end offset (t_{off}). The results show that t_{off} increased with increasing sample medium dielectric constant. This behaviour indicates that the electromagnetic field of the TDR signal traveling within the probe head and end termination structures was not contained within the termination structures and its velocity is affected by the dielectric permittivity of the surrounding medium.

This difficulty with the probe design was not discovered until after probes were installed in the field. To correct for this effect, it was necessary to derive an empirical equation, relating t_{off} to measured travel time based upon the data in Figure 4.3 and measurements from the probe calibrations performed before installing the probes (Appendix I). t_{off} can be expected to vary between probes depending upon the exact dimensions of the probe head and end, and upon the thickness and nature of the silicon coating. The apparent dielectric permittivity of the oven-dried silica sand (2.7) used in the two-point calibration of the probe coatings is very close to the dielectric permittivity of the probe coatings (2.8) (Chapter 3). The travel time measured by a coated probe in oven-dried silica sand will therefore be equal to the travel time that would be measured in the absence of the coating. Using the probe length, a theoretical travel time in oven-dried silica sand was calculated, and a value of t_{off} determined for each probe. t_{off} in oven dried silica sand ranged from 0.464 to 0.696 nanoseconds (ns), with an average of 0.571 for 21 probes. The empirical correction

uses the measurement of t_{off} in silica sand for each individual probe, and increases t_{off} from that value based upon the slope of data in Figure 4.3.

The connection of the coaxial signal conductor to the central probe rod is relatively direct, leading to minimal opportunity for interaction of the propagating signal with the medium surrounding the probe head or end. The remote diode method short circuits the signal propagating along the signal conductor at the probe end. The signal must then travel through the un-shielded wire connecting the central rod to the ground conductors at the probe end (Figure 4.2, Item 8), then from the ground conductors to the coaxial cable shield at the probe head (Figure 4.2, Item 9). This gives increased opportunity for interaction of the signal with the surrounding medium. Had the wiring connecting the inner and outer conductors in the probe head and end structures been properly shielded, the t_{off} correction would not have been dependant upon the dielectric permittivity of the sample material.

4.5.2 Effect of Electrical Conductivity

Figure 4.4 presents the variation of corrected travel time (t^*/t_{cair}) for the measurements conducted in electrically conductive water solutions (Curve A), and in silica sand saturated with electrically conductive water solutions (Curves B,C, Open Circles D). Curve B presents the travel time measured using remote diode shorting for both the probe head and probe end. Curve C presents measurements taken using the remote diode method to determine the probe head travel time (t_o) and using the automated curve fitting routine of the MoisturePoint TDR system to perform flat-tangent fitting to the raw waveform collected at the probe end. Points at D presents the manually determined measurements of travel time using the dual-tangent method.

There should be no measureable change in the measured travel time over this range of electrical conductivities for water solutions (Or and Wraith, 1999). Chapter 3 determined that travel times determined using remote diode shorting and MPN3404 diodes in coated probes was biased in electrically conductive water solutions. This systematic bias was introduced because the MPN3404 diodes did not create short circuits of sufficient quality for the remote diode shorting method to be successful. This bias is small over the electrical conductivity range presented in Figure 4.4 (Curve A).

Curves B,C and D indicate that a systematic change occurs in the measured travel time in saturated silica sand. Similar results were obtained by Wyseure et al. (1997). Both the automated and manual measurements of travel time increase with increasing electrical conductivity of the saturating solution. However, both the automated measurements methods overestimate the magnitude of this change. Figure 4.4 indicates the flat-tangent method is no better than the remote diode method for the probe design used.

The increase in measured travel time determined by manual measurements may relate to a real change in the complex dielectric permittivity of the soil-air-water-bound water mixture present in electrically conductive soil. Changing ionic strength may alter both the dielectric and conductive properties of water bound in mineral and ionic hydration layers (Or and Wraith, 1999). It may also relate to the changes in frequency content of the TDR pulse during passage through the soil. As discussed in the theory, the apparent dielectric permittivity is an average measurement which integrates dielectric permittivity over an unspecified range of frequencies. Changes in the frequency content of the TDR pulse brought about by the interaction of the probe design with the electrically conductive soil will therefore cause variations in the measured apparent dielectric unrelated to changes in the soil

itself. The precise reasons for the increase in travel time cannot be investigated without using frequency domain analysis of the TDR waveforms, which is not the purpose of this chapter. For the practical measurement of water content in the field, commercially available equipment is based upon travel time measurement. This result indicates that the measurement of travel time alone may not be sufficient to determine water content in soils with both bound water, and highly electrically conductive soil-water solutions.

Figures 4.3 and 4.4 indicate the travel time measured using the probe design installed in the CPE and the remote diode method using MPN3404 diodes varies with both sample dielectric permittivity and electrical conductivity of the soil water solution. To compensate for and eliminate these errors empirically would require unwieldy calibrations. In addition, the use of coated probes means that the probes cannot be used for the measurement of in-situ bulk soil electrical conductivity by analysis of the raw waveform. It is not possible, with the system used, to perform simultaneous measurement of travel time and electrical conductivity, and thus it is not possible to deterministically correct the field travel time measurements for the bias introduced by the electrical conductivity of the soil water. These results provided the justification for measuring two end-member empirical calibrations for a washed (low soil water electrical conductivity) and unwashed (high soil water electrical conductivity) waste rock.

4.5.3 CPE Waste Rock Calibration

4.5.3.1 Probe Variability and Grain Size

The effects of probe variability and grain size on the measured calibrations using unwashed waste rock are presented in Figure 4.5. The use of a probe coating implies a unique relationship between measured travel time and the true sample apparent dielectric

permittivity that was not fully characterized by the two-point calibration performed for each probe prior to installation (Chapter 3). Combined with the previously noted variation in the probe head/end offset, it was expected that there would be variation between probes. Figure 4.5A indicates a slight shift in the calibration curve upwards to higher travel times between the 281/3.2/25 probe and the 376/3.2/25 probe. The magnitude of the shift in the calibration between these two probes was smaller than the range of variability of measurements between different replicates at the same water content with a single probe. From these results, it appears that variations in the texture or nature of the waste rock are larger than the variations in the probe characteristics caused by the coatings and probe head and end termination structures. The unaccounted for inter-probe variation will lead to some uncertainty in the absolute value of calculated water content within the CPE experiment.

The results shown in Figure 4.5B indicate that the difference between the measured travel times for <5mm and <25mm fractions was small compared to the variability between replicates of the same soil at the same water content. This indicates that the water content measured by TDR will not be affected by the grain size of the material around the probe.

However, it should be noted that while the TDR probes will correctly measure the water content of the waste rock around the probe, that waste rock is not representative of the bulk waste rock contained within the entire experiment. The TDR probes only measure the water content in the finer grain size fraction of the pile as a result of the grain size selection during placement of the probes. The water content measurements derived for the field installed probes will represent water in the finer grained (< 5mm) fraction over a scale of approximately 40 cm. The actual waste rock contains particles up to 1.5 m in diameter. An investigation of the conversion of water contents to account for larger grain size fractions can

be found in Yazdani et al. (2000). This work indicates that particles > 5mm occupy volume with impermeable material, but do not contribute to water retention under capillary tension. In unsaturated material, they act to lower volumetric water contents under the same matric suctions. The actual value of volumetric water content of the bulk waste rock that includes all grain size fractions, will thus be some lower fraction of the TDR measured water content to account for the presence of particle sizes greater than 5mm.

4.5.3.2 Soil Water Electrical Conductivity

The results of the calibrations conducted in waste rock with varying soil water electrical conductivity are presented in Figure 4.6. The empirical Topp equation, reformulated as a square root mixing model by Ferré et al. (1996), is presented as a reference comparison only. The Topp equation has been calculated using the non-linear calibration of the effect of the probe coating on the measured apparent dielectric permittivity presented in Chapter 3. The data for unwashed (Figure 4.6A) and washed (Figure 4.6B) soil are similar between 10 to 20 % water content. Near saturation, the effects of soil water electrical conductivity on the measurement of travel time is stronger, and the curve for the unwashed soil trends upwards. In contrast, the washed soil calibration converges to the Topp equation as higher water contents (>15%). At low water contents (<10 to 15%), both calibrations fall above the Topp equation, with the washed material at a slightly higher travel time. The differences between washed and unwashed waste rock calibrations are significant enough to justify separate calibrations.

In-situ water samples extracted from the field experiment indicated that water to 1 m depth reaches electrical conductivities of 2 to 3 dSm^{-1} (Nichol et al., 2000, Appendix A). Figure 4.4 indicates that the systematic increase in travel time did not commence until after

the bulk soil electrical conductivity exceeded 1.5 dSm m^{-1}, which corresponds to a soil water solution of 4 dSm^{-1} in saturated material. It is expected therefore that the measurements in washed material will be representative of probes installed near surface (<1m) where the electrical conductivity of the soil water is low.

Measurements of soil water electrical conductivity during the waste rock calibration experiments using saturated, unwashed waste rock indicated soil water electrical conductivities of 10 to 20 dSm^{-1}. This range of electrical conductivities is similar to the range of electrical conductivities measured for in-situ soil water samples extracted from the experimental pile using suction lysimeters between 1.75 m and 4.5 metres below the surface of the pile. Travel time measurements conducted in unwashed waste rock matches the most electrically conductive soil water solutions near the base of the constructed pile and are expected to be more representative of probes installed at 1.75 m and below.

4.5.4 Field Measurements

4.5.4.1 Field Temperature Correction

Data from three TDR probes installed at 20 cm depth, located immediately adjacent to temperature probes, were analysed to derive a field based temperature correction. A maximum daily temperature variation of approximately 7 °C was recorded. All travel times were corrected for probe head/end offset, and t^*/t_{cair} was determined. A 24 hour moving window average of t^*/t_{cair} was calculated, and the difference between each individual measurement and the average ($t^*/t_{cair} - (t^*/t_{cair})_{24avg} = \Delta\, t^*/t_{cair}$) was calculated. Figure 4.7A presents individual measurements of t^*/t_{cair} and the calculated $(t^*/t_{cair})_{24avg}$. This figure indicates significant daily fluctuation in measured travel time.

A 24 hour moving window average was calculated of ambient in-situ temperature (T_{24avg}) and the deviation of each individual temperature measurement from the average ($T-T_{24avg}=\Delta T$) was calculated. Figure 4.7B presents the variation in measured travel time, $\Delta t^*/t_{cair}$ with the variation in measured temperature, ΔT. For this water content range, the systematic daily variation of the measured travel time is in phase with the in-situ temperature. This behaviour is consistent with the presence of a significant water fraction bound to mineral surfaces, or within the hydration layers of dissolved ions. This variation would not be correctly described by a temperature correction based upon the properties of free phase water only.

For each of the three probes, the ratio of $(\Delta t^*/t_{cair})/(\Delta T)$ was calculated, which represents the change in travel time with temperature. Figure 4.8 presents a plot of the temperature correction factor, $(\Delta t^*/t_{cair})/(\Delta T)$ against t^*/t_{cair} for a probe at 20 cm depth. The data have been filtered to remove all data where the soil water content was changing rapidly, and the 24-hour moving window average is a poor representation of water content. Only those measurements where $\Delta T>1.5$ °C are shown in Figure 4.8. This temperature filter was varied, and 1.5 °C was found to be optimal for the field data.

Figure 4.8 indicates that the correction factor is positive at low travel times (low water content) and negative at higher travel times (high water contents). The highest corrected travel time on Figure 4.8 is ~2.6. Analysis of daily variation of measured travel times at higher water contents was not possible as these water contents only exist during short-lived rainfall events, where determination of a 24 hour average of travel time is not possible. A linear equation has been fitted to the data describing the change in the temperature factor with travel time. The positive correction factor at low water contents

indicates that the apparent dielectric permittivity of the water increases with temperature due to the unbinding of bound water. The influence of bound water decreases with increasing water content as the relative fraction of bound water to free water decreases. The crossover from a positive to negative correction factor for this probe location occurs at approximately $t^*/t_{cair} \sim 2.65$, or approximately 15% water content. At higher water contents, the correction factor becomes negative, implying the higher temperature lowers the free water dielectric permittivity, and this trend is now larger than the unbinding of bound water

The slope of the temperature correction factor $(\Delta t^*/t_{cair})/\Delta T)$ against t^*/t_{cair} was similar for all three probes, and an average value of 0.006 was chosen. The cross-over point from positive to negative was different, and varied from 2.6 to 2.9. This behaviour indicates the influence of bound water varies from location to location due to variations in the grain size and clay content of the material immediately surrounding the probe. The correction factor will therefore vary for each probe location. An average empirical equation was derived to be applied to the other probes:

$$(\Delta t^* / t_{cair}) / \Delta T = -0.006 * \left(\frac{t}{t_{cair}} \right) + (2.65 * 0.006) \qquad [4.5]$$

This equation is applied to t^*/t_{cair} as shown in Figure 4.9, for a probe at 20 cm depth, which presents the measured travel time (A,t^*/t_{cair}), the 24 hour moving window average of the measured travel time (B, $(t^*/t_{cair})_{24avg}$), and the temperature corrected travel time (C). All three time periods have similar magnitudes of daily temperature fluctuation. The data from June and April, 1999, indicate the correction is sufficient to remove the diurnal variation of measured travel time to below the measurement precision. The data in

September are at a higher water content, near the cross-over point, and demonstrate little diurnal variation in both the raw (A) and corrected (C) data.

4.5.4.2 Corrected Field Data

The magnitude of the differences between the effects of electrical conductivity and temperature on the final calculated value of water content can be assessed by examination of the corrected field data. The raw time is corrected for probe head/end offset, then ($\Delta t^*/t_{cair}$)/ ΔT) is calculated using Equation 4.5. ΔT is determined as the difference in ambient temperature from 21 °C, the temperature of the laboratory during calibration. t^*/t_{cair} is adjusted based upon Equation 4.5, or upon the probe specific calibrations for the three probes used. The water content is then calculated using either the washed or unwashed waste rock calibration equation appropriate for the depth of the probe.

Figure 4.10 presents calculated water contents for a probe located at 20 cm depth following a large rainfall event in September, 1999, and for a probe located at 3.0 m depth as it underwent the cooling portion of a yearly temperature cycle in the winter of 1999/2000. Three curves are presented for each probe: the calculated water content with no temperature correction using the washed (0.2 m depth) or unwashed (3.0 m depth) calibration (A); the same waste rock calibration including the temperature correction (B); and the ambient temperature (C). The difference between the washed and unwashed calibrations is shown by curve D, which represents the water content calculated using the opposite (washed or unwashed) calibration to that used for curves A and B.

The data for both shallow and deep probes indicate the effect of temperature (A,B) is smaller than the variation in the calculated water content caused by the effect of electrical conductivity on the remote diode method (D). For the probe at 20 cm depth, using no

temperature correction (A) underestimates water content at low water contents, but only overestimates water content for very short periods during short-lived peak water flow. The difference between calibrations (A,D) for electrical conductivity is more pronounced at low water contents where the two calibrations diverge. Near the peak water contents measured in the field, 17 to 20%, the two calibrations are quite similar. At 3 m depth, the water content is generally higher. By coincidence, the water content is close to the cross-over range where the ambient temperature correction is very small and the uncorrected and temperature corrected data are indistinguishable (A, B). The two calibrations for different electrical conductivities also coincide at these measured travel times, and the two calibrations are very close (A, D).

4.6 CONCLUSIONS

The TDR method using travel time analysis has been empirically calibrated and applied to determine the water content of coarse grained waste rock. This required consideration of the effects of poor probe design, electrical conductivity of the soil water solution, and grain size of the waste rock. The effects of grain size and inter-probe variation (Figure 4.5) alter the relative position of the measured calibration curves, but have little effect on the slope of the either the unwashed or washed calibration curves. These effects are averaged by including all these data in the calibrations derived in Figure 4.6. An estimate of the total error in absolute water content is difficult because the variability of the probe coatings and the probe head/end offsets were not properly measured prior to installation, but a single measurement of t^*/t_{cair} in Figure 4.6 corresponds to a spread of +/- 2% water content in the range of 0 to 15% water content. The approximate calibrations required to compensate for electrical conductivity will increase the error estimation. At saturation, the same

measured travel time corresponds to a 12% difference in volumetric water content due to the effects of electrical conductivity on the remote diode method. The timing of the arrival of wetting fronts and the transition time for measurements relate directly to the measured travel time, and thus will be accurate. In addition, the change in water content at any give probe location will be more accurately described.

The measurement of water content using TDR is promoted as a simple and effective means of water content estimation using commercially available, automated equipment. This work has demonstrated that the practical application of TDR can be more difficult. Based upon this experience with probe design, calibration and field installation, and the knowledge gained from the literature, the following recommendations can be made for the practical usage of coated probes in materials with high electrical conductivity soil water solutions:

1) Three-rod Zegelin-type probes with a resistive coating are a reliable means of determining the travel time in media with high sample electrical conductivity. A successful design is recommended in Chapter 3. A check of the performance of any design should be undertaken in soil saturated with solutions of differing electrical conductivity prior to probe deployment.
2) Measurement of travel time alone may not be sufficient to characterize the dielectric properties of water-soil-air mixtures where the soil water has a high electrical conductivity.
3) The construction of the probe head/end should be such that the propagating TDR pulse is fully contained within the probe head. All wiring should be properly shielded. Travel times should be measured in both air and water. The theoretical travel time can be

determined, and the probe head offset determined. Only those probes that show no variation in probe head/end offset should be used.

4) Remote diode shorting can be used to determine the timing of the signal arrival at the probe head (Chapter 3)

5) Remote diode shorting should not be used at the probe end. The dual-tangent analysis method should be used to determine the timing of the probe end reflection with no probe end termination structure or diodes present (Chapter 3)

6) Coated probes installed in the field should be matched with short uncoated probes which are used solely for the determination of bulk soil electrical conductivity. This will enhance the capability for soil calibration and provide information on the electrical conductivity of the soil water solution.

7) All coated probe calibrations and field installations should ensure uniform water distribution along the probe length. Coated probes should not be installed vertically.

8) All field measurements should include the simultaneous measurement of ambient in-situ temperature to permit correction for the effects of changes in temperature.

9) The effects of ambient temperature can be compensated for by the examination of field data or by laboratory calibration. The temperature compensation is dependent upon the clay fraction and varies with water content.

10) The measurement of the difference in water content is more accurate than that of the absolute water content in coarse, heterogeneous waste rock. The measured water content is representative of the water content in the finer (<5 mm) fraction.

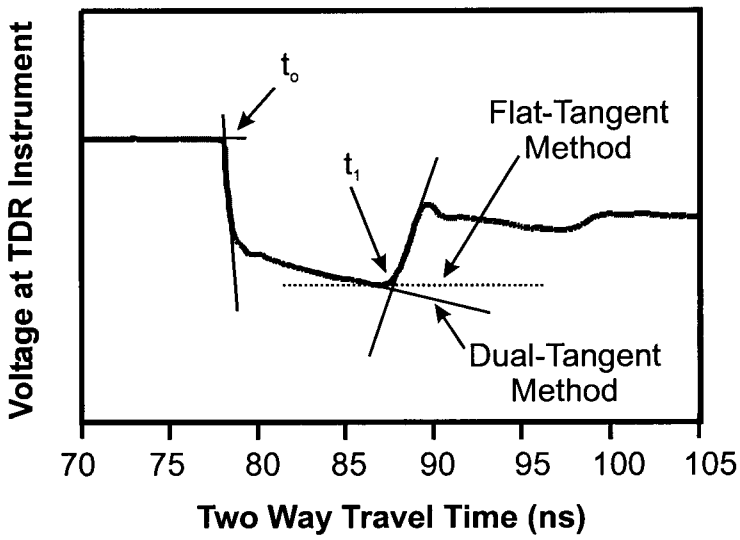

Figure 4.1: TDR waveform collected using uncoated TDR probe in water with 1 dSm^{-1} electrical conductivity. Tangent-line methods are used to determine the timing of the probe head (t_o) and probe end (t_1) reflection.

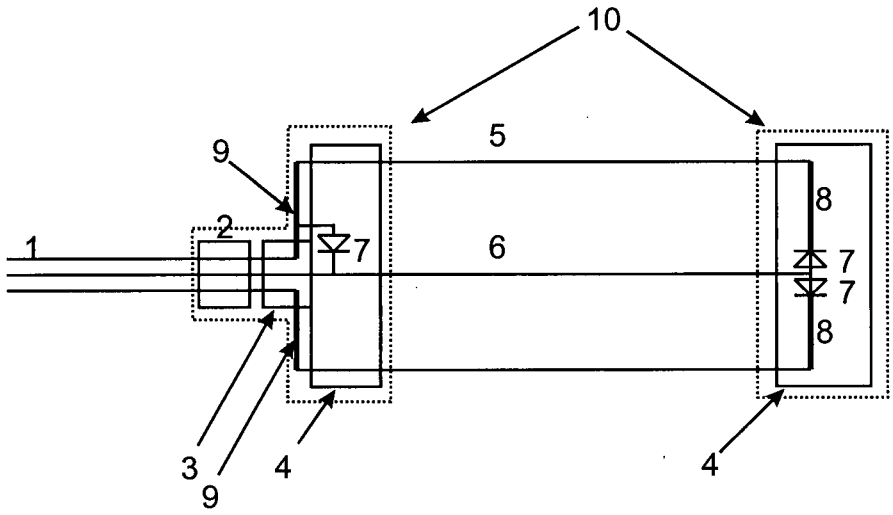

1. RG6 coaxial cable: F660 BEF CommScope 75 ohm cable
2. Female F-connector
3. Male F-Connector to plug
4. Polyethylene terminal block
5. Outer rod: unshielded 3.2 mm dia. 316 stainless steel.
6. Center rod: 3.2 mm dia. 316 stainless steel coated with 0.4 mm thick polyolefin heat shrink
7. On Semiconductor MPN3404 PIN diode
8. 22 gauge un-insulated bus wire
9. 22 gauge un-insulated bus wire
10. Terminal block sealed with silicon sealant

Figure 4.2: Design of TDR probes installed in field experiment.

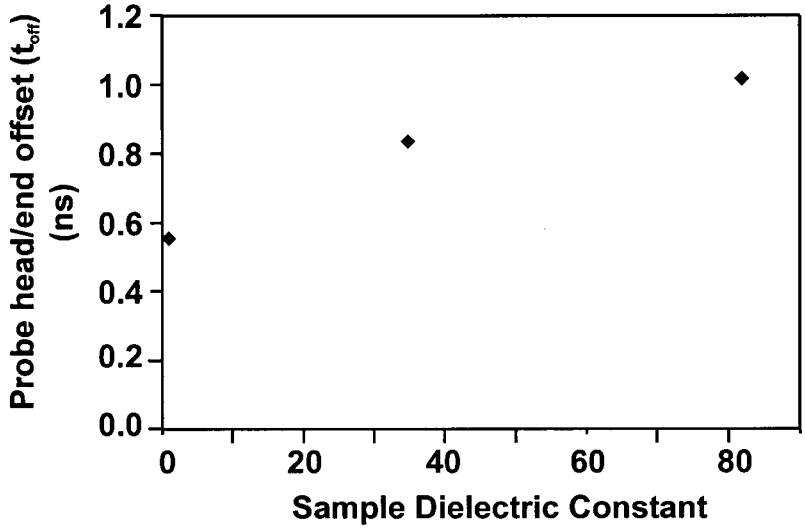

Figure 4.3: Variation of probe head/end offset (t_{off}) with sample dielectric constant.

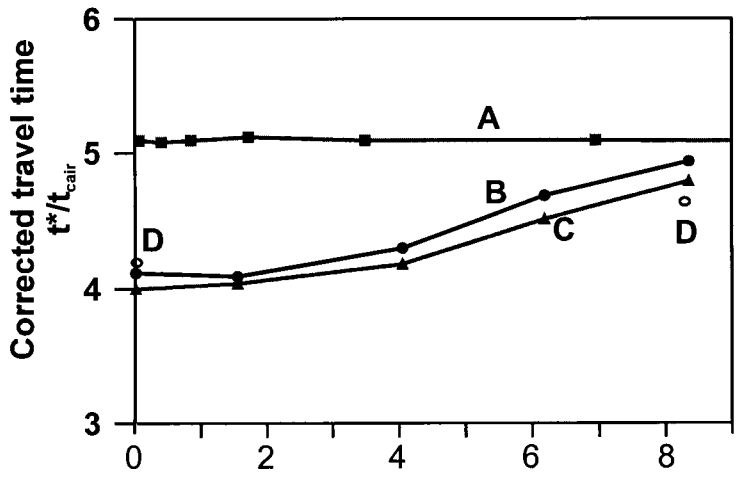

Figure 4.4: Corrected travel time (t^*/t_{cair}) measured using a coated probe in water solutions of varying electrical conductivity (A), and silica sand saturated with electrically conductive water (B,C,D). Probe head travel time determined using remote diode method. Corrected travel time determined using the remote diode method at probe end (A,B), the flat-tangent method at the probe end (C), or manually determined dual-tangent method at probe end (D).

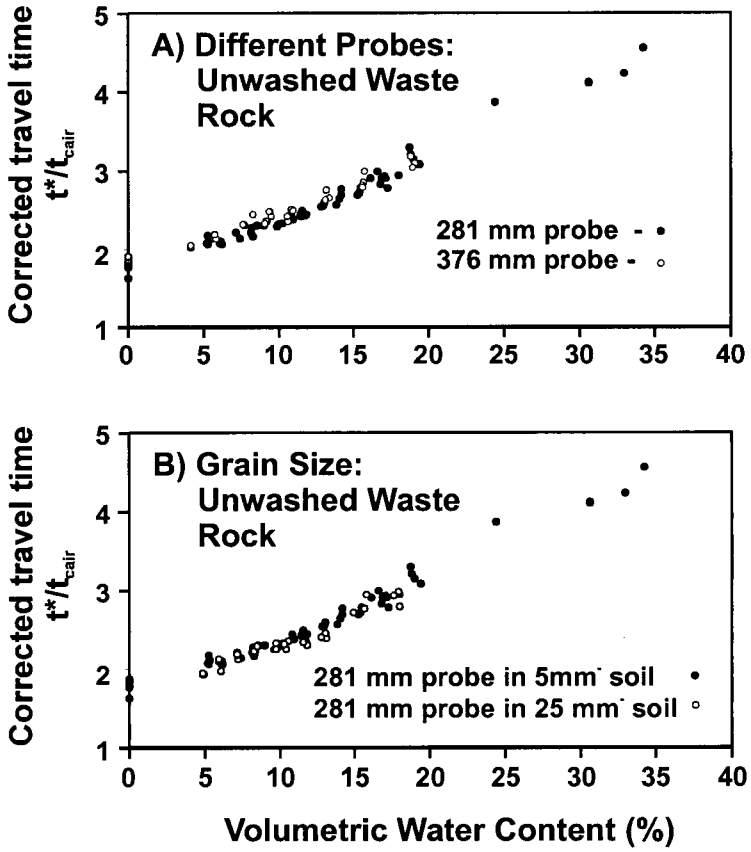

Figure 4.5: Effects of probe variability and grain size on the relationship of corrected travel time (t^*/t_{cair}) to volumetric water content.

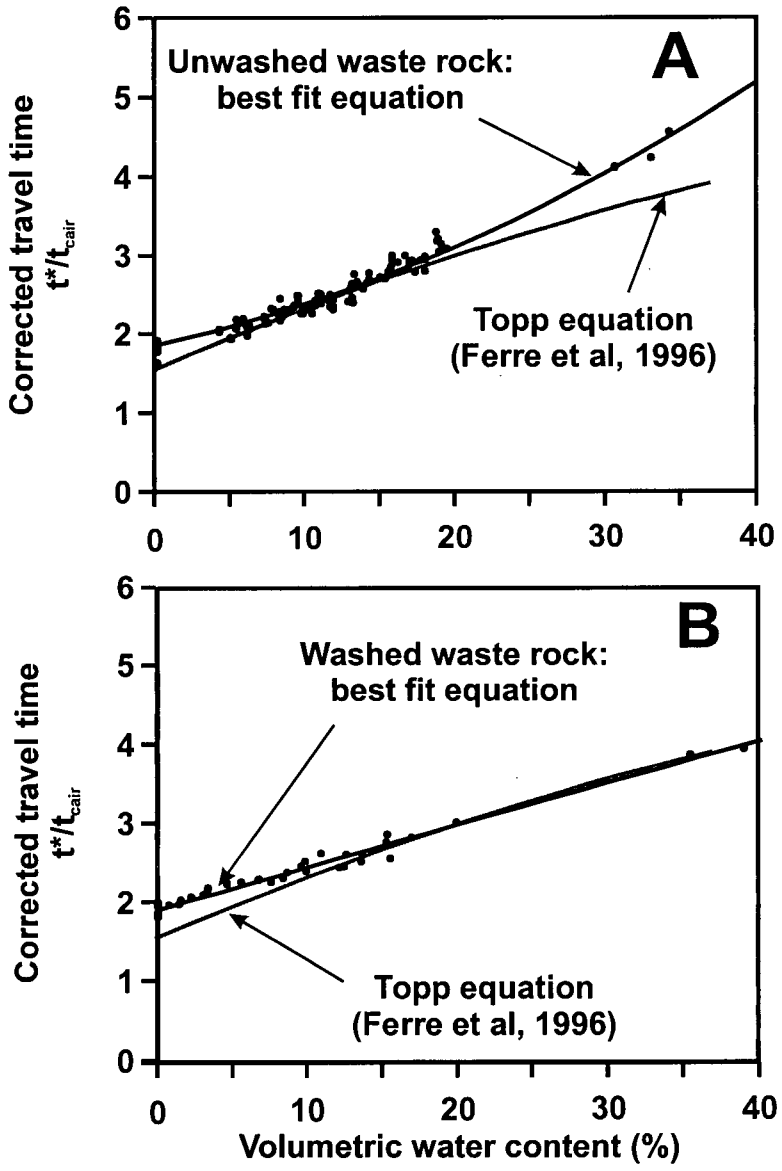

Figure 4.6: Calibration curves relating corrected travel time (t^*/t_{cair}) to volumetric water content for waste rock with high soil water electrical conductivity (A) and low soil water electrical conductivity (B).

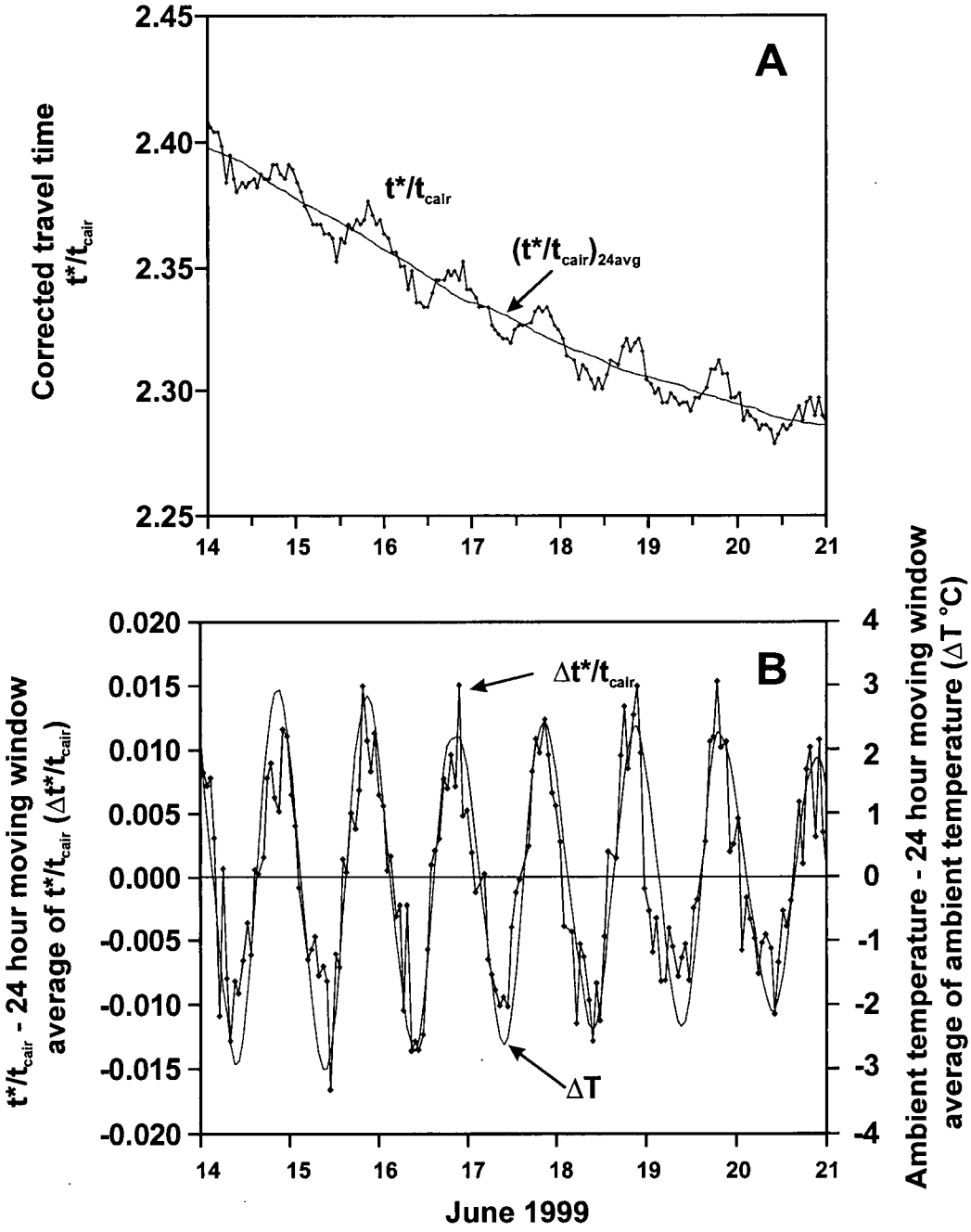

Figure 4.7: Daily variation in measured corrected travel time (t^*/t_{cair}) for a probe at 20 cm depth (A). Comparison of corrected travel time variation with temperature variation (B).

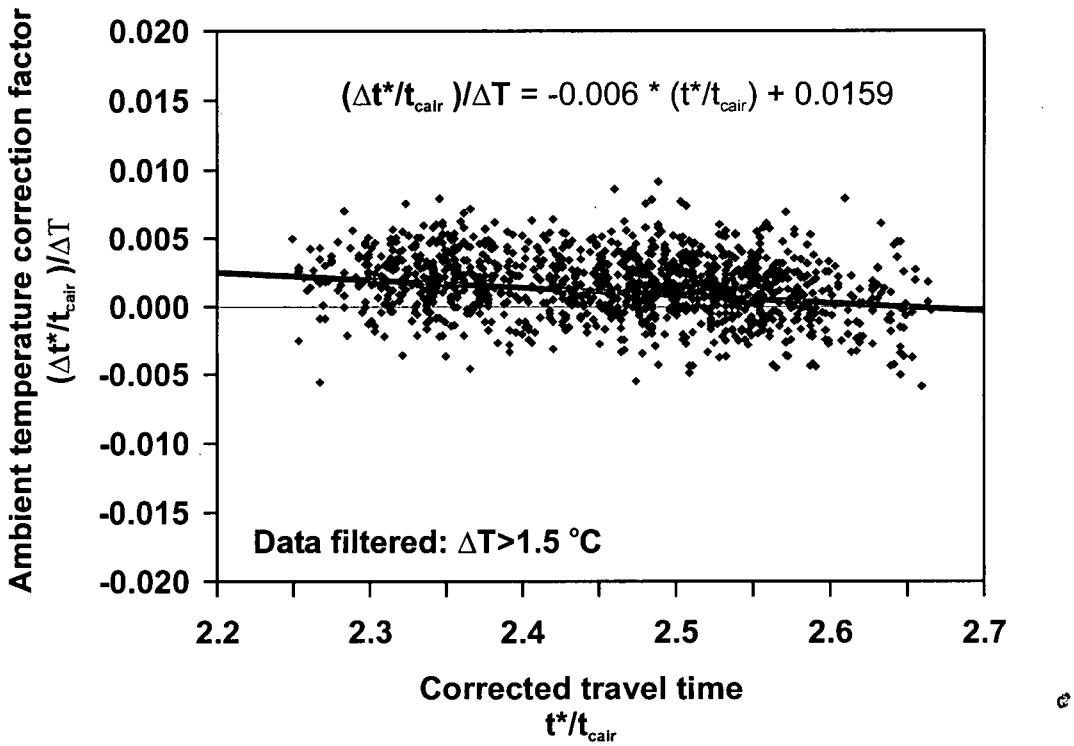

Figure 4.8: Field determined ambient temperature correction, $(\Delta t^*/t_{cair})/\Delta T$, as a function of corrected travel time, (t^*/t_{cair}), for a probe at 20 cm depth.

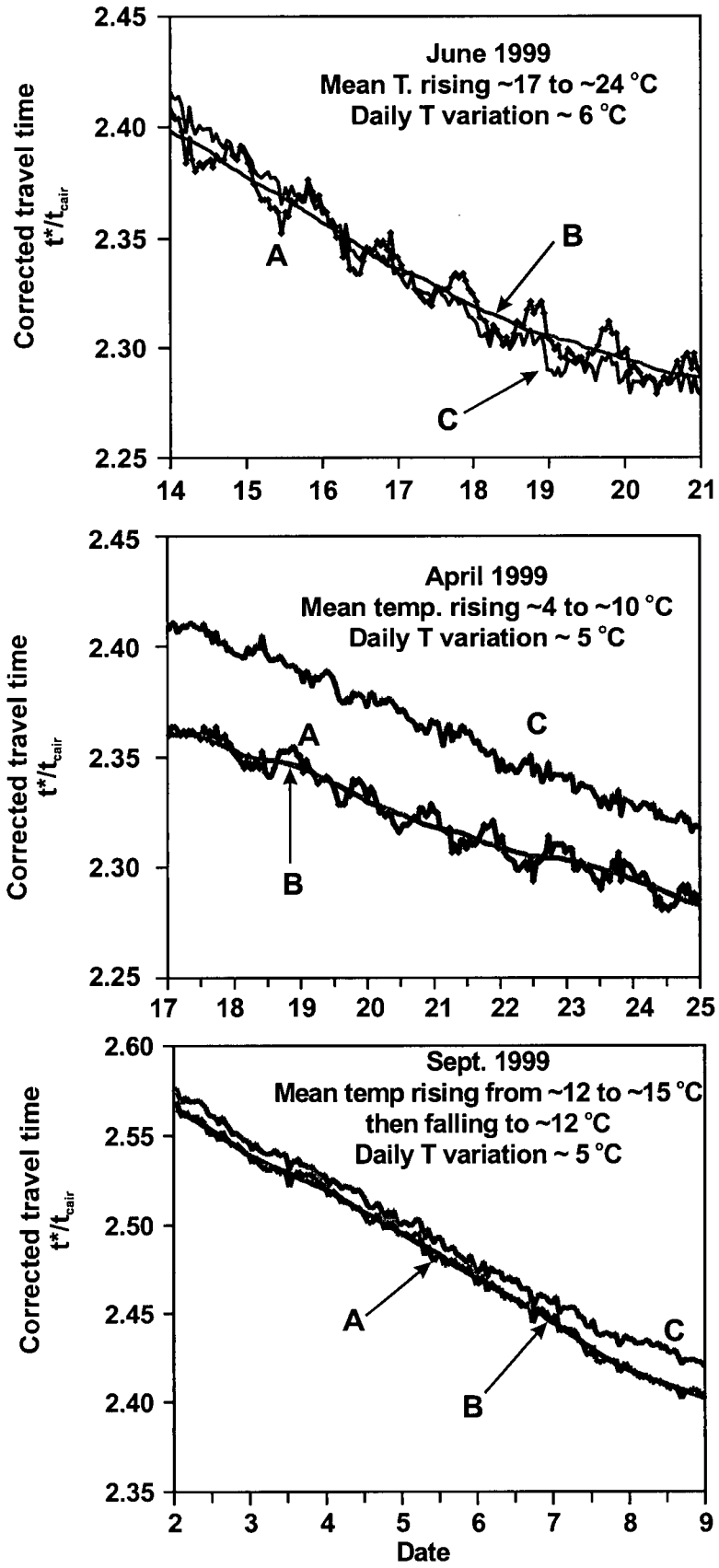

Figure 4.9: Application of field determined ambient temperature correction to field data: (A) corrected travel time (t^*/t_{cair}); (B) 24 hour moving window average of corrected travel time $(t^*/t_{cair})_{24avg}$; and (C) temperature corrected travel time $(t^*/t_{cair})_T$

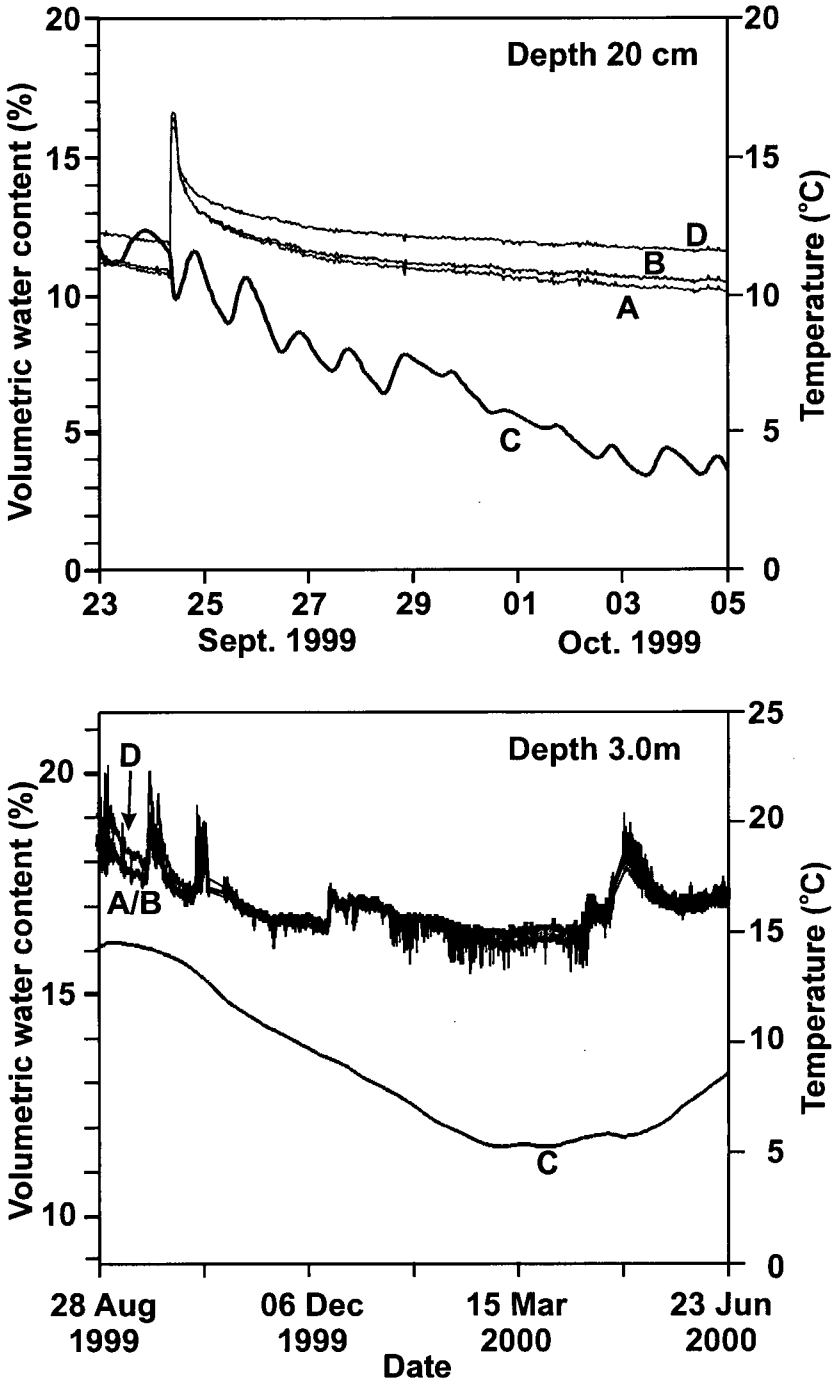

Figure 4.10: Effect of ambient temperature correction and remote diode shorting bias on measured water contents: (A) volumetric water content using appropriate calibration for soil water electrical conductivity; (B) temperature corrected travel time $(t^*/t_{cair})_T$; (C) ambient soil temperature; and (D) volumetric water content using wrong calibration for soil water electrical conductivity.

CHAPTER 5: FIELD EVALUATION OF THERMAL CONDUCTIVITY SENSORS FOR THE MEASUREMENT OF MATRIC SUCTION.

5.1 ABSTRACT

Thermal conductivity (TC) sensors indirectly measure matric suction in a material through its effect upon the water content and hence thermal properties of an engineered ceramic probe. TC sensor output must be corrected for sensor hysteresis and for ambient temperature. The effects of hysteresis are described and an equation presented to correct for ambient probe temperature. Two years of monitoring data from a field site are assessed to determine long-term sensor performance and accuracy. Air entrapped in the sensors during initial wetting has led to unpredictable long-term drift in those sensors continually exposed to matric suctions less than 20 kPa. Comparison of uncorrected field measurements to values corrected for both sensor hysteresis and ambient sensor temperature indicates the magnitude of these corrections can be similar. Corrected TC sensor measurements of matric suction are compared to tensiometer measurements. The field results demonstrate that TC sensor accuracy is highly variable in the low matric suction range. Initial sensor response lags 1 to 4 days behind tensiometer measurements and the transition time of TC sensor measurements is significantly greater than tensiometers. It is recommended that TC sensors only be installed where the matric suctions are expected to exceed a limiting value of matric suction determined from the hysteresis characteristics of the sensor. The expected rates of change of matric suction in a field application should be estimated prior to sensor installation, and TC sensors installed only if the expected matric suction changes are slower than the response time of the TC sensors.

5.2 INTRODUCTION

Nichol et al. (2000) (Appendix A) describe a field experiment to characterize unsaturated flow within waste rock at a mine site in northern Saskatchewan. As part of that experiment, matric suction has been monitored over a two year period. The experimental pile, which is 5 m high, is composed of waste rock from an open pit operation. The material is highly heterogeneous, with boulders up to 1.5 m in diameter, 20-30% by mass less than 2mm in size, and a silt size fraction less than 5% by mass. Spatially and temporally detailed measurements of volumetric water content and matric suction are being collected on an ongoing basis to understand the transport of sulfide mineral weathering products from the pile.

Measurements of matric suction can be obtained using tensiometers, gypsum blocks, granular matrix sensors, filter paper methods, psychrometers, and thermal conductivity (TC) sensors. Fredlund and Rahardjo (1993) provide an excellent review of most methods. Filter papers and psychrometers are not appropriate for long term in-situ field monitoring. Granular matrix sensors and gypsum blocks rely upon measuring the electrical conductivity of a water solution within the probe and both sensors contain probe components constructed of sulphates. Both of these factors are incompatible with the waste rock at the field study site. In addition, granular matrix sensors are not sufficiently accurate or reliable for long-term monitoring (Thomson and Armstrong, 1987, McCann et al., 1992 and Spaans and Baker, 1992). Thermal conductivity sensors and tensiometers were therefore chosen to measure matric suction in this study. The use of tensiometers is reviewed elsewhere (Cassel and Klute, 1986, Fredlund and Rahardjo, 1993) and their accuracy and limitations are

understood within their range of operation (matric suctions between 0 to ~85 kPa). In contrast, thermal conductivity sensors are a developing technology.

TC sensors measure the thermal conductivity of a ceramic probe in hydraulic contact with the soil water. The water content of the ceramic changes in response to the matric suction and therefore the thermal properties of the ceramic change. A laboratory calibration determines the relationship between matric suction, the water content of the ceramic, the thermal properties of the ceramic, and the sensor measurements recorded by a datalogger. The modern design of a thermal conductivity sensor was first proposed by Phene et al. (1971a; 1971b). Histories of the development of TC sensors and discussions of previously available commercial sensors are provided by Fredlund (1992), Reece (1996) and Feng (1999).

The experimental waste rock pile provides the opportunity to examine long-term TC sensor performance under field conditions. In this chapter, TC sensor operation and calibration is reviewed. The raw sensor output must be corrected for both hysteresis in the relationship between matric suction and water content of the ceramic (Feng, 1999; Feng and Fredlund, 1999), and for the effect of ambient temperature on the thermal properties of water. A new correction factor for the ambient temperature effect is derived. Methods used to collect TC sensor and tensiometer measurements at the experimental site are then presented. The TC sensors are used to conduct year-round, automated measurements of matric suction. Manual tensiometer measurements and automated measurements using pressure transducers were conducted to provide independent estimates of matric suction. The raw and corrected TC sensor data are presented to demonstrate the effects of hysteresis and ambient in-situ

temperature. The corrected data are then compared with the measurements of matric suction by tensiometer to assess the performance of the TC sensors.

5.3 THERMAL CONDUCTIVITY SENSORS

A TC sensor is composed of a heating element and a temperature measurement device encased in an engineered ceramic body. A diagram of the sensors used in this study is shown in Figure 5.1. These prototype sensors (Beta-98 Sensors) were made at the University of Saskatchewan (U. of S.) by D.G. Fredlund and F. Shuai. The thermal conductivity of the ceramic body is determined by measuring the dissipation of a known heat pulse. The core of the ceramic is heated by controlled activation of the heating element. The temperature at the core is measured before, during and after heating. The temperature rise at the core changes as the rate of dissipation of heat away from the probe center or its thermal diffusivity changes. The temperature rise is used to determine the thermal conductivity of the ceramic probe. The thermal conductivity of the ceramic skeleton is constant while the thermal conductivity of a wetted sensor will change as water and air exchange within the pore spaces. The thermal conductivity of water (~0.6 W $m^{-1}K^{-1}$) is much greater than that of air (0.026 W $m^{-1}K^{-1}$) and thus thermal conductivity increases from a dry sensor to a wet sensor. The thermal conductivity is primarily affected by volumetric water content in conjunction with the degree of interconnection of the water phase in the engineered ceramic. The water content of the ceramic, and the distribution of the water phase, is in turn controlled by the matric suction applied to the outside of the sensor and, as in any porous material, is a function of the pore size distribution of the ceramic.

Laboratory-based calibration curves relating the temperature rise at the sensor core to an applied matric suction are derived by equilibrating the sensors to known matric suctions

using a pressure plate apparatus and measuring the temperature in the probe over the heating cycle (Feng and Fredlund, 1999). The temperature rise-matric suction relationship is not unique due to hysteresis of the ceramic's water content to matric suction relationship (Feng, 1999; Feng and Fredlund, 1999) and is also a function of changes in ambient temperature (Shuai, 1998, pers. comm.).

5.3.1 Sensor hysteresis

The hysteretic nature of the relationship between water content and matric suction in the ceramic TC sensor leads to a hysteretic relationship between measured thermal conductivity and matric suction. To interpret the sensor output, it is necessary to know the hysteresis behaviour of the ceramic, and the wetting and drying history of the sensor. To follow is a review of hysteresis corrections that will later be applied to the field data

Feng (1999) and Feng and Fredlund (1999) conducted experiments to record the water content and thermal properties of the sensors under different wetting and drying regimes. The curves shown in Figure 5.2 are based upon the measured curves in Feng (1999) but they have been simplified here for clarity. Four curves define the primary wetting and drying characteristics of the sensors. The ceramic has an initial drying curve derived by saturation under vacuum, followed by drying. The investigated range of sensor calibration was restricted to a matric suction of 400 kPa for practical purposes. Once the sensor equilibrates at 400 kPa matric suction, the sensor is re-wetted to 0.1 kPa to produce the main wetting curve, then re-dried to 400 kPa to produce the main drying curve. A further curve can be measured by air drying the sensor, then wetting the sensors to 0.1 kPa. This curve is termed the boundary wetting curve and is not shown, but it lies slightly below the main wetting curve.

The scanning curves shown on Figure 5.2A describe the water content-matric suction relationship that is followed between the main drying and main wetting curves. The scanning curves are also hysteretic. To correct for hysteresis it is therefore necessary to know the main wetting and drying curves as well as the shape of the scanning hysteresis curves. The wetting/drying history of the sensor is then used to determine whether any given measurement lies on a main curve or a scanning curve. No measurements were conducted of the main wetting curves for the Beta-98 sensors used in this study. The ceramic of the Beta-97 and the Beta-98 sensors is identical and therefore the main wetting curves are estimated from the Beta-97 data of Feng (1999) and Feng and Fredlund (1999). They experimentally determined the scanning curves and provided empirical functions to fit the measured curves.

Two points should be noted from Figure 5.2. First, the core temperature rise is a non-linear function of matric suction, with the smallest changes recorded at low matric suctions. The sensors will therefore be least sensitive to changes at low matric suctions and high water contents. The second important feature is the large difference in saturation between the initial drying curve and the main wetting curve at 1 kPa. This difference is due to air trapped within the sensors during re-wetting on the short time scale of the measurement of the main drying and wetting curves during laboratory calibrations (Feng, 1999). Experiments by Feng (1999) indicate this entrapped air is gradually released through diffusion and dissolution, a process called relaxation, and the sensor water content steadily increases with time. Relaxation is slow; a submerged sensor achieved 60% saturation within 1 hour, but only 70 % saturation at the conclusion of the one month test. To achieve 100% saturation would take years. The relaxation process raises concerns for the long term stability of sensor

measurements at low matric suctions. This point will be addressed in conjunction with the presentation of field results.

5.3.2 Correction Factor for Ambient Temperature

Sensors deployed in the field experiment undergo variations in ambient temperature from –10 to +25 °C, with the operational range restricted to temperatures above freezing. The thermal conductivity of water and hence the thermal conductivity and core temperature rise of a wetted sensor are functions of temperature. The aim is to correct the field-measured core temperature rise to the temperature rise that would have been measured at the ambient temperature of the laboratory during calibration (23 °C).

Phene (1971a) and Xing and Fredlund (1994) present an analysis of the core temperature increase in the sensor, based upon the representation of the sensor ceramic and the heater element core as spherical bodies. In practice, the sensor ceramic is not spherical, but if it is large enough, the heat pulse does not reach the outer boundary during the heating cycle and the actual sensor shape does not affect the core temperature rise. They solved for the temperature rise ($\Delta T(t)$) inside a spherical sensor as a function of the time since heating began (t). They conclude that at long times the effects of the finite heat capacity of the heating element, wire and epoxy become small and the full equation can be reduced to its first two terms (Phene, 1971a; Xing and Fredlund, 1994):

$$\Delta T(t) = \frac{Q}{4\pi r \lambda}\left[1 - \frac{r}{\sqrt{\pi D t}}\right] \qquad [5.1]$$

where Q is the heating rate (W), r is the radius of the heating element core (m), λ is the thermal conductivity ($Wm^{-1}K^{-1}$) and D is the thermal diffusivity (m^2s^{-1}). The thermal

diffusivity is the thermal conductivity divided by the density and specific heat capacity (Phene 1971a). Equation 5.1 can simplified:

$$\Delta T(t,r) = A - B\frac{1}{\sqrt{t}}, \qquad [5.2]$$

Where :

$$A = \frac{Q}{4\pi\lambda r}$$

$$B = \frac{Q}{4\pi\lambda\sqrt{\pi D}}$$

From these relations :

$$\lambda = \frac{Q}{4\pi r A}$$

$$D = \left(\frac{Q}{4\pi^{3/2}\lambda B}\right)^2$$

A plot of $\Delta T(t)$ vs $1/\sqrt{t}$ can be used to derive A and B.

A correction for ambient temperature can be derived by taking the ratio of Equation 5.1 at two temperatures and considering the thermal conductivity and diffusivity as functions of temperature, T. If :

$$\lambda_{Sensor}(T,\psi) = \lambda_{Dry\_Sensor} + F(\psi)\lambda_w(T) \qquad [5.3]$$

where $F(\psi)$ is the fractional contribution to the total thermal conductivity from the water phase as a function of the matric suction (ψ), then the temperature rise ΔT at time t and calibration temperature T_o can be expressed as a function of the temperature rise (ΔT) at time t at ambient temperature T_1:

[5.4] $$\Delta T(t,T_o) = \Delta T(t,T_1) * \left[\frac{\lambda_{Dry} + F(\psi)\lambda_w(T_1)}{\lambda_{Dry} + F(\psi)\lambda_w(T_o)} \right] * \left\{ \frac{\left[1 - \frac{c''}{\sqrt{D(T_o)}} \right]}{\left[1 - \frac{c''}{\sqrt{D(T_1)}} \right]} \right\}$$ [5.4]

where

$$c'' = \frac{r}{\sqrt{\pi t}}$$

Values for λ and D for the TC sensors at 23 °C were estimated using Equation 5.1 and the values of A and B collected during the calibration of Beta 97 sensors (Shuai et al., 1998). Thermal conductivity and diffusivity were calculated using values of 2 watts for the rate of heating (Shuai, 1998, pers. comm.) and estimating the radius of the heater element and temperature sensing integrated circuit at the sensor core (ie: r = 0.002 m). No laboratory calibrations exist at other ambient temperatures to directly determine the changes in thermal diffusivity. Therefore, the effect of temperature upon the thermal diffusivity was estimated by making the conservative assumption that the density and heat capacity of the sensor are that of water and calculating thermal diffusivity from the thermal conductivity divided by the density and specific heat capacity. The magnitude of the third term of Equation 5.4 ranges from 1.000002 to 0.999999 over the range of ambient probe temperatures measured in the field. The third term in Equation 5.4 can therefore be set to a value of 1.0.

The correction for ambient temperature depends upon the F(ψ) function in Equation 5.4. It can be derived from the laboratory calibration data by recording the full heating curve and using Equations 5.1 and 5.2. If λ_{dry} is measured, then at each subsequent calibration measurement , the values of $\lambda(T_o,\psi)$, A, B and $\Delta T(t,T_o)$ are all known and Equations 5.3 and 5.4 are fully determined for both wetting and drying. The second term of Equation 5.4 can

then be calculated. This term, which can be termed the correction factor, represents the ratio by which the measured core temperature rise must be multiplied to correct for ambient sensor temperature.

$F(\psi)$ is a non-linear function that is dependent upon the distribution and continuity of the water phase within the sensor. The function $F(\psi)$ is expected to be hysteretic as the relationship between water content and matric suction is hysteretic. The parameters required to derive $F(\psi)$ and the correction factor from the laboratory calibration are not available for the sensors used in this study. The estimates of $\lambda(\psi)$ derived from Shuai et al. (1998) and the equation for $\lambda(\psi)$ from Reece (1996) were used to estimate $F(\psi)$ and hence to calculate the temperature correction for different matric suctions. The ambient temperature correction factor derived as a function of matric suction during drying is shown in Figure 5.3. The Shuai et al. (1998) data required using an estimated λ_{dry} of 0.15 $Wm^{-1}K^{-1}$. Estimates of matric suction corrected for ambient temperature are determined using recursion as the correction factor is a function of ψ.

The ambient temperature correction is applied directly to the measured change in sensor core temperature during the heating cycle ($\Delta T(t,T_1)$). Figure 5.3 indicates the correction is largest near 0 kPa when the sensor has the highest water saturation. It was previously noted that the calibration curves are least sensitive at matric suctions near 0 kPa. Ambient temperature corrections will have the largest effect on the calculated matric suction between 0 and 15 kPa.

5.4 FIELD INSTRUMENTATION

This section describes the details of the measurements that were conducted to assess the performance of the TC sensors. The experimental pile was constructed in the summer of

1998 and measurements between September 1998 and October 2000 are analysed in this study.

Eighteen TC sensors were calibrated by the U. of S. to determine the main drying curve. The sensors were installed in three instrument profiles at depths from 0.2 to 4.5 metres. Probe bodies were briefly wetted immediately prior to installation to improve initial equilibration time (Fredlund,1992). Each sensor ceramic was coated with approximately 5mm of saturated silica flour paste to improve sensor-soil contact. The controlled heat pulse is delivered using a 10 volt constant voltage supply. This power supply was used in the laboratory calibration. More recent versions of the U. of S. TC sensor are calibrated and deployed using a constant current supply (Shuai, 2000, pers. comm.). Sensor internal temperature is measured using the integrated circuit (IC) temperature-sensing chip installed in each probe. All IC output voltage measurements and heating power control is performed using a Campbell Scientific CR-10X datalogger. The datalogger and voltage supply are located in an insulated and heated instrumentation hut. The datalogger is located approximately 20 metres from the sensors, and the lead wires are located in an above-ground cable duct.

Measurements are collected from the sensors at intervals of four hours. This provides sufficient time for the previous heat pulse to dissipate, and the sensor body to re-equilibrate to the ambient in-situ temperature. The average ambient temperature within the center of the ceramic body is measured before the heat pulse. The regulated power is supplied to the heater element within the sensor core for a fixed time period (50 seconds). The temperature is recorded each second during the heating cycle. A second-order polynomial is fit by least-squares regression to the data for the last twenty seconds of the heating cycle (Devore, 1987).

The final heating voltage reading is calculated at a fixed time equal to the time used in laboratory calibration (50.225 seconds) using the polynomial equation. The temperature rise is calculated by subtracting the ambient voltage measurement from the calculated voltage at the end of the heating cycle.

Nine Jetfill tensiometers (SoilMoisture Equipment Corp., Model 2725) were installed in three profiles in August 1999 at depths of 20, 50 and 100 centimeters. Tensiometers were installed within 0.5 m of the TC sensors. Each tensiometer ceramic was coated with approximately 5mm of saturated silica flour paste to improve sensor-waste rock contact. Tensiometers were monitored during August to October, 1999. The tensiometers were measured manually using a digital vacuum gauge with the double-puncture technique of Greenwood and Daniel (1996). Additional manual measurements were obtained using direct measurement with a mechanical vacuum dial gauge.

Tensiometers were also measured using automated pressure transducers (Motorola 5100DP) at time scales of every 15 minutes. The pressure transducers were individually calibrated prior to installation using a variable hanging water column to apply an equal vacuum to all sensors. Three sets of readings were taken with increasing, decreasing and increasing vacuum applied to the sensors. The maximum vacuum applied was 23kPa. A correlation between tranducer output signal and ambient temperature was observed despite the on-chip temperature compensation (Motorola, 1998). The transducers were allowed to collect data for 15 days at 0 kPa and variable air temperature to determine the temperature dependent drift in output voltage for each sensor. The recorded output signal from each transducer was corrected for ambient temperature based upon the individual calibrations. All manual or automated measurements of pressure were corrected for the height of the water

column within the tensiometer to determine the matric suction in the material surrounding the tensiometer tip.

5.5 RESULTS

The main features of the TC sensor measurements are first described using the uncorrected field measured data prior to hysteresis and temperature corrections. The effects of hysteresis and ambient temperature upon the measured data are then assessed. The corrected data are then compared to the tensiometer measurements to make an assessment of sensor accuracy under field conditions.

5.5.1 Uncorrected Measurements

Uncorrected matric suctions for three sensors are presented in Figure 5.4. These matric suction estimates are calculated using the laboratory calibration based upon the main drying curve with no hysteresis or ambient temperature correction. Three dominant features can be seen: near surface measurements are absent or erratic in winter; estimated matric suctions follow clear trends, but the individual measurements appear "noisy"; and estimated matric suctions at deeper sensors have steadily declined over time and estimates are no longer possible. Examination of the ambient in-situ temperature data indicates that the erratic measurements in early winter correspond to freezing temperatures. Once freezing conditions start, the sensors are not meant to provide reliable results, as the heat pulse is absorbed by the latent heat of fusion of water frozen in the sensor. All of the near surface sensors have frozen for two winters, up to 6 months each, but all have recovered and operated normally when in-situ temperatures recovered above zero in the spring.

Closer examination of the "noise" in the raw data for a probe buried at 4.5 m depth indicates systematic daily variation of sensor output. Figure 5.5 presents the uncorrected

matric suction calculated using the main drying curve (A), a 24-hour moving window average of the values of calculated matric suction (B), air temperature (C), the in-situ temperature (D), and the variation of matric suction defined as the difference between an individual measurements and the 24-hour moving window average (E). The probe temperature at this location is isothermal and air pressure measurements within the pile indicate no daily variation during the 10 day interval. The daily variation of calculated matric suction is systematic, and is much larger than the measurement resolution. The variations appear to be opposite phase of the measured air temperature. Several components of the TC measurement system experience daily temperature fluctuation. The observed variation in measurement may result from air temperature effects on the resistance of the heater element wiring and the resistance of the sensor output wiring within the above-ground cable duct, or the effect of temperature within the instrumentation hut on the performance of the datalogger and voltage supply.

Attempts were made to compensate for this daily variation. The variation of measured core temperature rise for each individual measurement from a 24-hour moving window average of the core temperature rise was plotted against the variation in individual measurements of air temperature from the 24 hour moving window average air temperature. A weak negative correlation was found, but when this correction was applied it did not remove the daily variation seen in Figure 5.5. The variation of individual core temperature rise measurements from the 24-hour moving window average was plotted against the absolute air temperature, but no correlation was found. Similarly, no clear correlation was found to the temperature of the instrument enclosure. It is assumed the daily variation is related to the use of a constant voltage source and includes effects of both air temperature

and datalogger enclosure temperature. This method of heating is not recommended. U. of S. TC sensors manufactured after the Beta-98 sensors were all calibrated and deployed with a constant current source. Data from these sensors do not exhibit the same daily variations (Shuai, 2001, pers. comm.).

The field readings are averaged using a 24-hour moving window average of the measured core temperature rise to smooth the daily fluctuations. This does not address the possibility of a systematic bias due to the absolute values of average air temperature or whichever factors lead to the daily variation. The calculated matric suction values may therefore be systematically too high or low.

The long-term decline in calculated matric suction (Figure 5.4, 4.5 m depth) can be related to the gradual saturation of the sensors as previously noted. The sensors located deep within the pile are constantly exposed to matric suctions less than 20 kPa. Air entrapped in the sensors during initial wetting causes the difference between the main wetting curve and the initial drying curve (Figure 5.2) measured in the laboratory. Over time, the air trapped within the sensors is replaced by water. The increased degree of saturation of the sensors while exposed to a constant matric suction is calculated incorrectly as a decrease in matric suction. The calculated matric suction drifts towards zero as the degree of saturation approaches the highest value reached during the laboratory calibration on the main drying curve. The laboratory calibrations can no longer be used to calculate a matric suction value from the sensor measurements once the degree of saturation exceeds the main drying curve. The relationship between sensor water content and the external matric suction was slowly changing during the entire installation period for those sensors exposed to low matric suctions. The laboratory calibration curves are only valid immediately following installation.

After two years, 15 of the 18 sensors installed have saturated to water contents above the main drying curve and calculation of matric suction is not possible.

5.5.2 Sensor Hysteresis and Ambient Temperature

The data can now be examined to determine the effect of sensor hysteresis and ambient waste rock temperature on the measured data. Post-processing of the data was carried out in the following sequence. A 24-hour moving window average of measured core temperature rise was calculated. Approximations for the matric suction using the drying calibration curve were derived from this average. The appropriate $F(\psi)$ ambient temperature correction curve was chosen from Figure 5.3 based upon this preliminary estimate of matric suction. The individual raw measurements of core temperature rise were then recalculated using the ambient temperature correction factor and the ambient probe temperature. The individual, corrected, core temperature rise measurements were used to calculate a 24-hour moving-window average of core temperature rise to remove the daily variation. The averaged core temperature rise was then used to calculate a matric suction using both the sensor drying calibration curve and the sensor wetting calibration curve. Comparison of these two calculated values gives an indication of the magnitude of hysteresis effects.

Figure 5.6 presents the non-temperature corrected matric suction calculated using both the main drying (1) and wetting (3) calibration curves. The estimates shown are the individual measurements, prior to the application of a 24-hour moving-window average. There is considerable daily variation that masks the underlying changes in matric suction. The effect of daily averaging can be seen in the matric suctions calculated after application of the ambient temperature correction, and using the drying (2) and wetting (4) calibration curves. The data have been smoothed by the application of the 24 hour moving window

average. The data presented are for the 0.2 m depth probe shown in Figure 5.4. The probes at 0.2 m depth experience the largest changes in both matric suction and ambient waste rock temperature. The importance of sensor hysteresis can be illustrated by comparing the preliminary matric suctions calculated using the main drying calibration curve (1) and the main wetting calibration curve (3). The initial estimate of the matric suction calculated using the drying calibration curve ranges from 35 to 50 kPa, while the matric suction calculated from the wetting calibration curve ranges from 20 to 30 kPa. This demonstrates that sensor hysteresis must be addressed, or significant errors will result in the estimate of matric suction.

The magnitude of the effect of ambient temperature is also seen in Figure 5.6 by examining the data in curves 1, 3 and 5. As shown in curve 5, the ambient probe temperature at 0.2 m depth drops from ~20 °C to ~3 °C over the period presented. The uncorrected matric suction calculated with the drying calibration curve (1) increases over this period from 35 to 50 kPa, while the uncorrected matric suction calculated with the wetting calibration curve (2) increases from 20 to 30 kPa. The matric suctions calculated by correcting for ambient temperature and averaging to remove the daily variation (2, 4) rise only slightly during the same period. There are several large rainfall events in August, 1999, which is the wettest month of the year at the site. There are rainfall events of similar magnitude on both October 10th and 20th, 1999, and therefore the matric suctions near surface at these times are expected to be similar to the August values. The increase in the uncorrected matric suctions (1,2) is therefore due to the long-term trend in ambient temperature. The 10 to 15 kPa differences in uncorrected matric suctions between August and October are similar in magnitude to the 20 kPa difference between the wetting and

drying curves. The application of an ambient temperature correction is necessary, particularly at lower matric suctions. The combination of hysteresis and ambient temperature corrections would correct a drying calibration curve (1) estimate of matric suction during the October 20, 1999 rainfall from 43 kPa to an actual value of 18 kPa (Curve 4).

5.5.3 Comparison to Tensiometer Data

The corrected matric suctions calculated from the main wetting curve and main drying curve are now compared to tensiometer data in Figure 5.7. Data from two of the three sensors installed at a depth of 20 cm depth within the pile and the rainfall records for the same time period are shown in Figure 5.7. The upper graph shows the sensor response presented in Figures 5.4 and 5.6. The middle graph represents the TC sensor data which most closely matched the tensiometer data. The total rainfall volume (mm), and the timing of the rainfall are shown by the vertical lines in the bottom graph. These graphs indicate the matric suction calculated from the drying (1) and wetting (2) laboratory calibration curves, with correction applied for ambient temperature, and averaged using a 24-hour moving window average. The use of a 24-hour moving window average causes some smearing of changes in the measurements, but this is a small effect compared to the scattering in the unaveraged data seen in Figure 5.6. The manual tensiometer measurements (3, solid squares) and the automated pressure transducer tensiometer measurements (4, solid diamonds) are also shown.

The data indicate TC sensor accuracy, time to first response, transition time and response to similar rainfall events are all highly variable. Sensor accuracy is easily determined by comparison of the middle and upper graphs. In the middle graph, the matric suction calculated using the wetting calibration curve approximates the tensiometer data

during periods of waste rock wetting, such as August 23rd. The matric suction calculated using the drying curve follows the trend in tensiometer data during the drying period prior to September 12th. This demonstrates the validity of using wetting and drying curves to describe sensor hysteresis. However, this TC sensor generally overestimates matric suction, and underestimates the magnitude of the changes in matric suction. The upper graph represents a more typical degree of agreement between TC sensor and tensiometer data observed at the other TC sensors. The upper graph indicates poor agreement in both the magnitude of matric suction, and the magnitude of changes in matric suction between the TC sensor and tensiometer measured matric suction.

TC sensor response time and transition time can be assessed by examining the rainfall events labeled as A, B and C. Response time refers to the time to the first change in the measurement following a rainfall event. By definition, the transition time of a change in the sensor signal is the time required for the sensor measurement to have changed by 50% of the overall difference from the initial value to a final measured matric suction. The three rainfall events marked by (A) indicate rapid response of both TC sensors to the rainfall events. The apparent early response of the TC sensor readings is an artifact of the 24-hour averaging. The non-averaged readings indicate the TC sensors responded within hours to the onset of rainfall and their first response occurs at the same time as the tensiometers. In comparison, neither TC sensors responded to the September 9th rainfall event (B) for 12 and 48 hours after the rainfall event. This compares to 2 hours for the tensiometers. The TC sensors transition time was approximately 48 hours for event B, compared to 2 hours for the tensiometers. There was a strong drying trend after September 9th, as evidenced by the increase in matric suction recorded by the tensiometers. The matric suction estimated by both TC sensors

continued to fall, even when the matric suction measured by tensiometer had been rising for 96 hours.

The unpredictable response to similar events can be assessed by examining rainfall event C on September 24th, in comparison to three events in August, 1999 marked as A. This event, C, represents the largest rainfall event monitored during this period. The matric suction measured with the tensiometers indicate similar matric suctions prior to the rainfall events for both the A and C events. The changes in matric suction during these rainfall events, as measured by the tensiometers, are also similar. The data in the top graph indicate three clear responses to the August rainfall events (A). However, a TC sensor response is not discernable in the top graph during the September 24th rainfall (C). The estimated matric suction actually increases. In the middle graph, the TC sensor clearly responds to each of the three August events (A). The TC sensor response on September 24th (C) appears to lead the rainfall event. Examination of the unaveraged data on the 24th indicates no changes in TC sensor output greater than the systematic daily variations noted earlier. The apparent decrease in matric suction in the averaged data shown in Figure 5.7 is unrelated to the rainfall event.

5.6 DISCUSSION

The results presented imply that TC sensors will provide accurate and responsive results only for certain materials and conditions. As described below, properties of the TC sensor ceramic must be matched to the properties of the surrounding material. Improper matching will result in problems with long term saturation of the sensors, and slow or erratic sensor response.

The observed long-term saturation of the sensors will affect any of the TC sensors designs currently available, although the timing and magnitude of the effect will vary for each ceramic. The point of significant departure of the initial drying curve from the main drying curve (Figure 5.2) should be determined and represents the limiting matric suction for long-term operation, even if short-term laboratory calibration is possible at lower suctions. The limiting value for long-term operation of the sensors used in this study is 15-20 kPa. Long-term results will be possible if sensors are installed in materials in which the matric suction is expected to always exceed the limiting matric suction. The magnitude of the drift in sensor measurement is represented by the difference between the initial and main drying curves. Above the limiting matric suction, this drift is small compared to the differences caused by hysteresis, which is the difference between the main drying and wetting curves. Sensors may provide interpretable results if the sensors are placed in materials where the matric suction exceeds the limiting value on a weekly or perhaps monthly basis. A sensor will drain to a water content close to the main drying curve if it is dried out to matric suctions greater than the limiting value, it will. The majority of the pores which entrap and exchange air are emptied and the re-wetting process will then more closely follow the main wetting curve. If this occurs regularly, then sensor drift will be removed sufficiently often to allow the data to be interpreted. Sensors should not be installed in materials where the matric suction is constantly below the limiting value. Sensors will over-saturate, and interpretation of the output will be difficult. A method to restore the sensors used in this study, which are currently over-saturated, by over-heating the sensors and drying them out beyond the limiting matric suction value in-situ has been proposed to the U. of S. and will be tested in the laboratory in the future.

The field data indicate that matric suction calculated from the TC sensors is a damped, delayed, and sometimes unpredictable response to the matric suction in the CPE waste rock. This can be partly explained by the differences in the time scales of changes in matric suction, and the response time of the matric suction sensors.

Matric suction in the CPE waste rock changes rapidly, as demonstrated by the tensiometer measurements, and wetting fronts propagate to five metres depth in as little as three hours. The waste rock behaves similarly to other coarse materials in which hydraulic conductivity drops rapidly with increasing matric suction. The hydraulic conductivity is $\sim 10^{-3}$ to $\sim 10^{-4}$ ms^{-1} near saturation and drops to $\sim 10^{-10}$ ms^{-1} at 20 to 30 kPa with an air entry value of <1 kPa. The rapid decrease of hydraulic conductivity with increasing matric suction means increases in matric suction are self-limiting as water phase movement of water downwards slows dramatically.

The response time of a TC sensor is determined by the rate of water movement into or out of the ceramic. This is controlled by the hydraulic conductivity of the ceramic and the matric suction contrast between the sensor core and the surrounding material. The sensor hydraulic conductivity has been estimated to range between 2×10^{-6} ms^{-1} at 1 kPa to 10^{-8} ms^{-1} at 30 kPa and 10^{-12} ms^{-1} at 400 kPa (Shuai et al., 1998). In the CPE waste rock, the matric suction changes are small, leading to low driving forces in or out of the ceramic. Experiments on sensor response time by Feng (1999) indicate 30 to 70 hours for sensor equilibration to a change in matric suction between 0 and 7 kPa, 20 to 100 hours for a change between 55 and 103 kPa change, and 100 to 200 hours for a change between 200 and 400 kPa. The shorter time corresponds to drying, and the longer times to wetting. In the CPE experiment, some wetting fronts arrive and recede faster than the equilibration time and the

sensor ceramic may be imprinted with first a wetting, then a drying trend. The distribution of water within the sensor ceramic is therefore a complex integration of the matric suction over the equilibration time.

TC sensors will work best in materials where the sensor response time is always faster than the changes in matric suction brought about by the arrival and recession of wetting fronts in the material. It is advisable, but not sufficient to require that the permeability of the sensor always exceed the permeability of the surrounding material because both the geometry and driving forces of flow in the sensor, and the downward propagation of a wetting front in the surrounding material are different. An estimate of the hydraulic properties of the material at the intended installation should be acquired, and this used to conduct preliminary modeling of the anticipated rate of change in matric suction.

The slow response time of the TC sensors has one further implication. Matric suction is often monitored in conjunction with in-situ water content. Water content measurement methods such as time domain reflectrometry (TDR) respond immediately to changes in the water content of the surrounding material. TC sensor matric suction data should not be matched to water content data to estimate field soil water characteristic curves unless the response times and transition times of the two measurements are similar.

5.7 RECOMMENDATIONS

The theoretical analysis of the effects of ambient temperature and the experience from two years of field application suggests the following:

1) Laboratory calibrations and field deployments should avoid the use of a constant voltage for powering the heating pulse.

2) The full heating and cooling curves for all laboratory calibrations should be recorded and kept for later use.

3) An ambient temperature correction factor can be calculated from thermal conductivity measurements during calibration.

4) Air temperature and datalogger / power supply enclosure temperature should be recorded during field measurements.

5) A second order polynomial is used to fit the last twenty data points of the heating curve, and to calculate the final temperature during field measurements. The three coefficients of the fitted curve should be recoreded to subsequently determine field thermal conductivity and diffusivity values.

6) TC sensor measurements should be corrected for both sensor hysteresis and ambient temperature.

7) The initial drying curve and main drying curve of the sensors should be determined. TC sensors should not be installed in material where the matric suction is expected to be always less than the point where the initial drying curve and main drying curve diverge at low matric suctions.

8) Preliminary estimates of the range in the rate of change of matric suction should be obtained for the material at an intended installation site either by modeling or experiment. Sensors will operate best in materials where the changes in matric suction occur on longer time scales than the sensor response time.

9) Volumetric water content data and TC sensor matric suction data should not be matched to create field soil water characteristic curves unless the response times and transition times of the two measurements are similar.

10) Automated, unattended TC sensor measurements should be periodically confirmed by independent measurement of the matric suction using an alternate method.

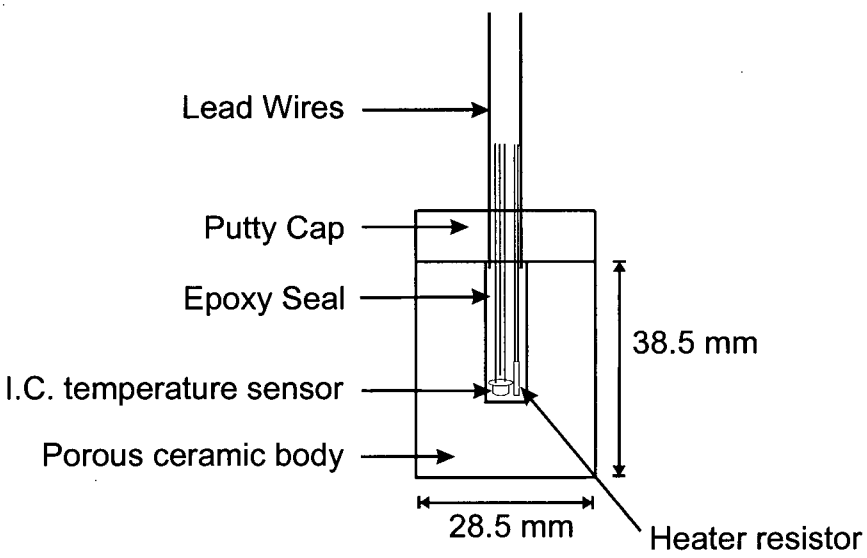

Figure 5.1: Schematic of TC sensor design (after Feng, 1999).

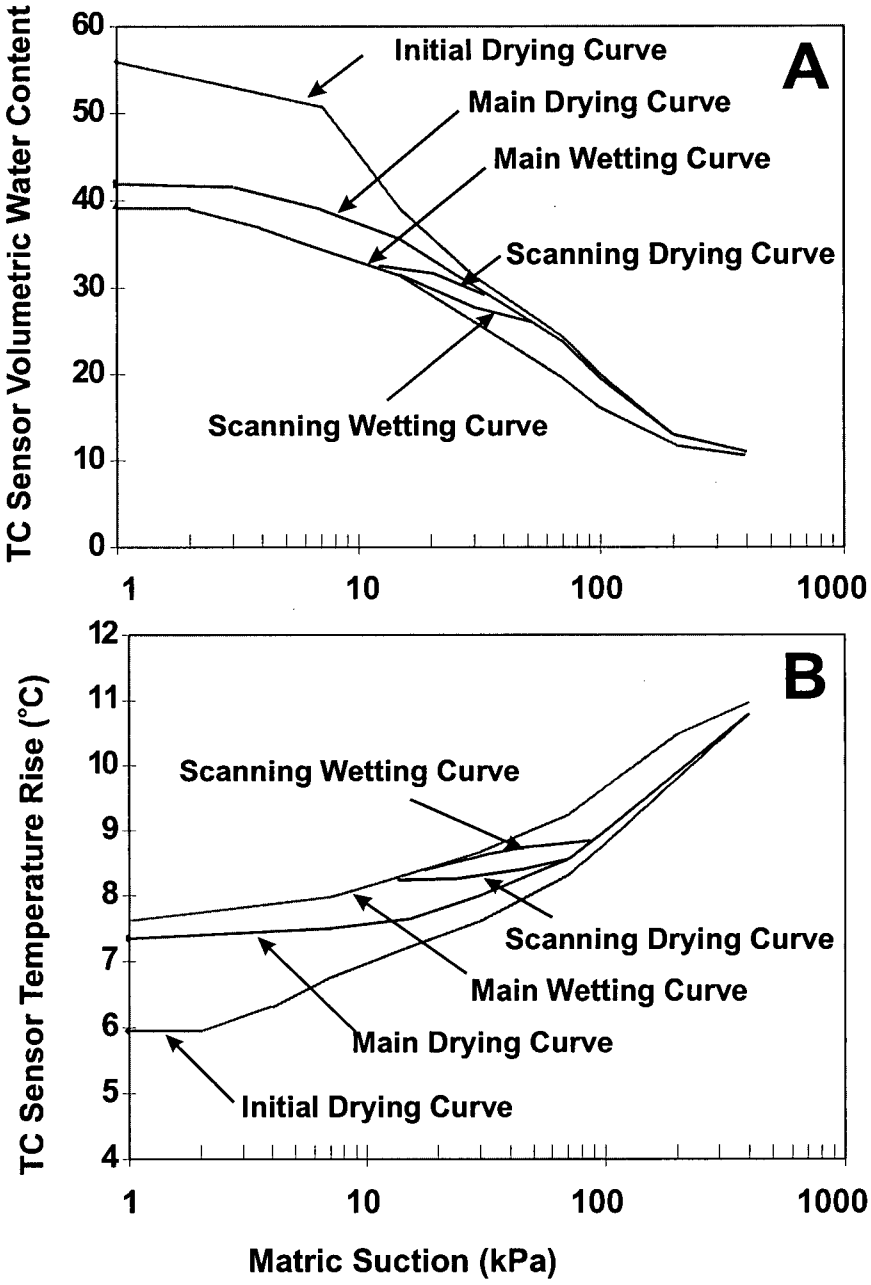

Figure 5.2: Effects of hysteresis on: (A) TC sensor volumetric water content and (B) measured TC sensor core temperature rise.

Simplified from data in Feng (1999).

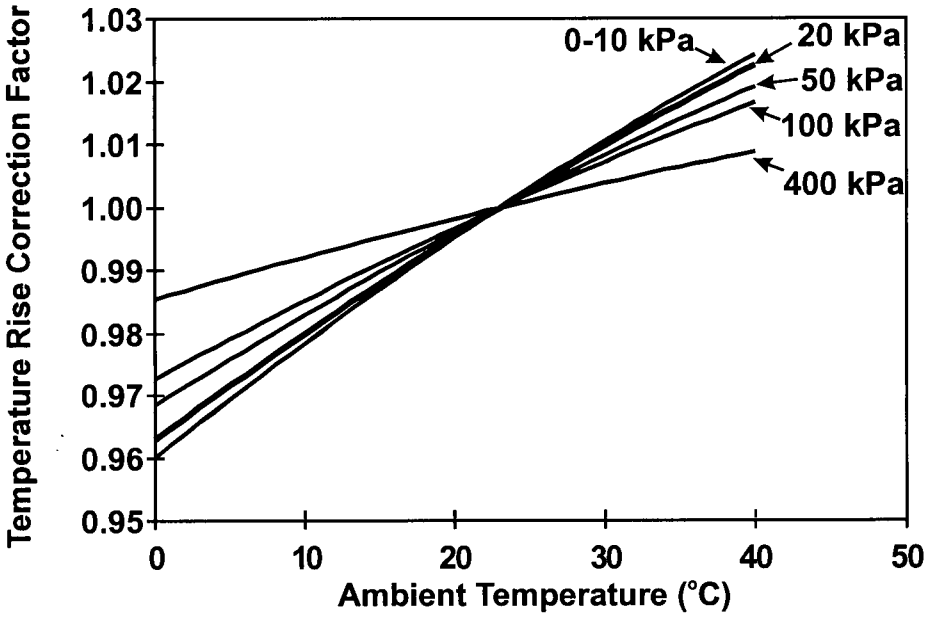

Figure 5.3: Correction factor for ambient soil temperature. The field measured TC sensor core temperature rise is multiplied by the correction factor to obtain the core temperature rise that would have been measured at 23 °C.

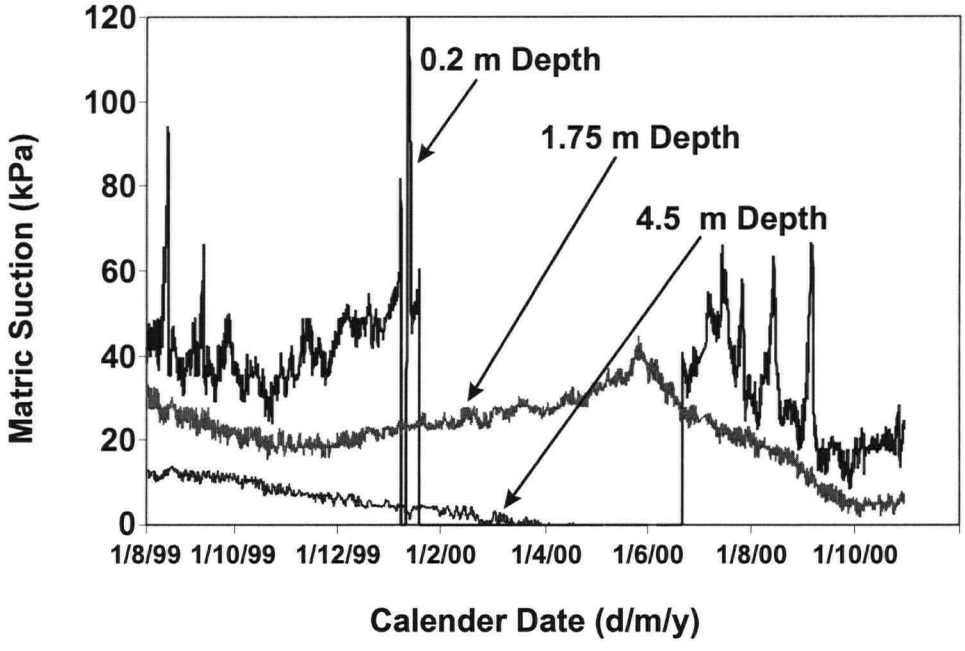

Figure 5.4: Preliminary estimate of matric suction based upon laboratory calibration curve for a drying TC sensor.

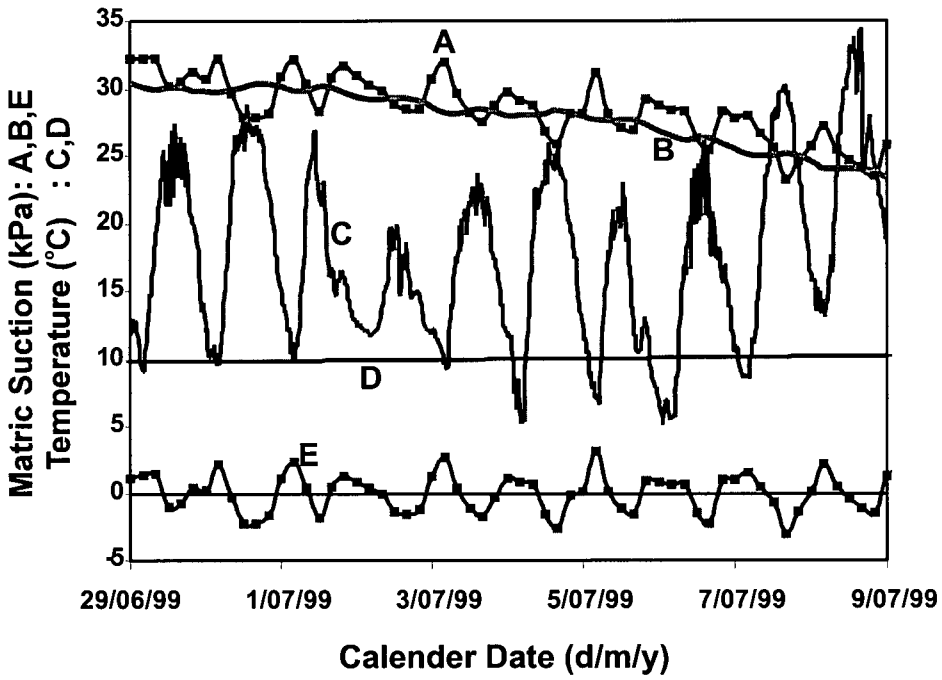

Figure 5.5: Daily fluctuation of estimated matric suction for a TC sensor installed at 4.5 m depth: matric suction calculated using laboratory calibration curve for a drying sensor (A, kPa); 24-hour moving-window average of estimated suction (B, kPa); air temperature (C, °C); ambient waste rock temperature (D, °C) and variation of estimated matric suction from the 24-hour moving-window average of estimated suction (E).

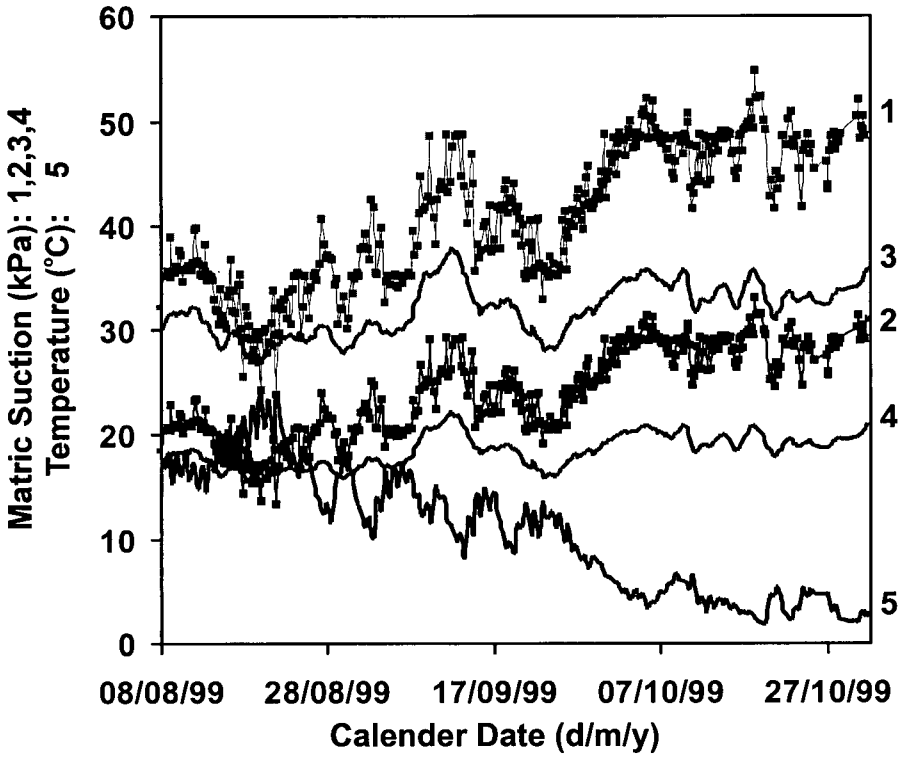

Figure 5.6: Demonstration of the effects of 24-hour moving window averaging, sensor hysteresis, and ambient temperature correction for a sensor at 0.2 m depth. Matric suction is calculated from individual readings using the laboratory calibration curve for a drying sensor (1) and a wetting sensor (2). Corrected matric suction is calculated using a 24-hour moving-window average of TC sensor output and using a drying calibration curve (3) and wetting calibration curve (4) and ambient soil temperature (5).

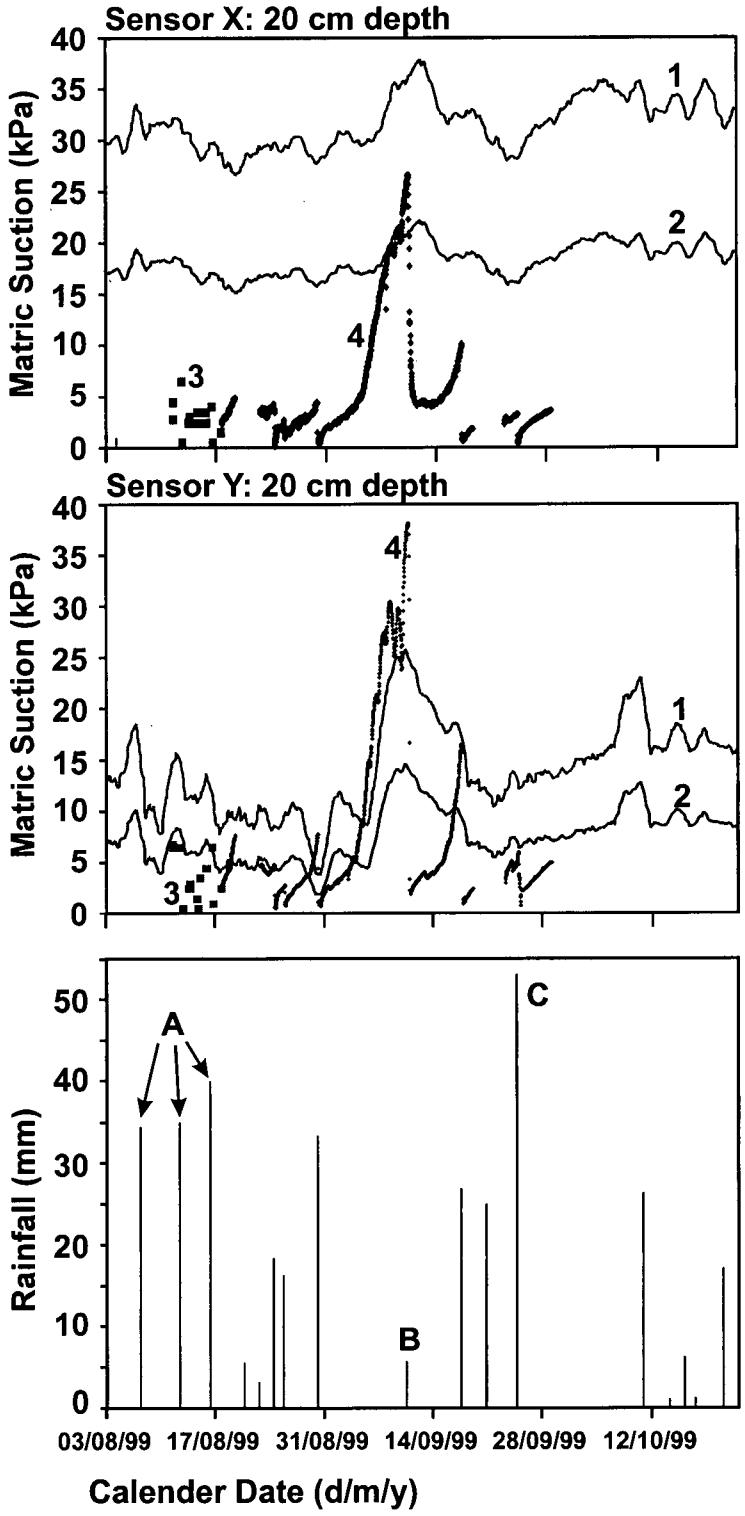

Figure 5.7: Assessment of TC sensor accuracy, precision and response time for two sensors (X and Y) located at 0.2 m depth: estimated matric suction suction based upon a 24-hour moving-window average of sensor output and a drying sensor calibration curve (1) and a wetting sensor calibration curve (2); matric suction measured manually using a tensiometer (3, closed squares); matric suction measured using a tensiometer and pressure transducer (4, closed diamonds); and rainfall amount and timing.

CHAPTER 6: WATER FLOW IN UNSATURATED HETEROGENOUS POROUS MEDIA: A CONSTRUCTED WASTE ROCK PILE

6.1 ABSTRACT

Weathering of minerals in mine waste rock can lead to mobile, water soluble weathering products. The flow of water through waste piles is one of the primary controls on the timing and rate of environmental loading. Preferential flow in an unsaturated heterogeneous porous medium such as waste rock leads to the potential for large spatial variation in leaching rates which prevents accurate prediction of loading rates. A large scale (8m x 8m x 5m high) experiment has been built upon a contiguous grid of 16 lysimeters to better characterize the flow of water in waste rock. The experiment has been operated for two and a half years. Material characterization from laboratory and in-situ data indicate strong hysteresis effects, and that measurement of representative unsaturated material properties is difficult. In-situ measurements of wetting front propagation are found to be a poor predictor of outflow timing and volume. The whole pile water balance indicates an average of 55% of precipitation is measured as outflow. Analyses of hydrographs and outflow volumes from individual lysimeters indicate the number of preferential flow paths and the total water outflow volume within preferential flow paths increases with increasing rainfall event magnitude but the total water outflow volume is more evenly spatially distributed. The scale of spatial averaging required to determine effective unsaturated flow parameters increases with increasing flow rate.

6.2 INTRODUCTION

The exposure of minerals in mine waste materials to atmospheric oxygen leads to the weathering of primary minerals and the formation of secondary minerals and dissolved weathering products. The most common process is the oxidation of metal sulfides to produce sulphate, acidity and free metal ions. The mineralogy and geochemistry of the weathering process have been studied in detail (Jambor and Blowes, 1994; Malstrom et al., 2000), as have the processes of gas and heat movement in waste rock piles (eg: Pantielis and Ritchie, 1990, 1992, 1993; Bennet et al., 1995, Birkham et al., 2001, Lefebvre et al., 2001a/b). In comparison, water flow in waste rock is less well understood and represents the largest source of uncertainty in current efforts to predict environmental loadings of weathering products (Smith et al., 1995; Ericksson and Destouni, 1997; Malmstrom et al., 2000). Waste rock piles are typically placed and stored under unsaturated conditions. It is essential to understand how water is transported and stored in waste rock to predict the rates at which weathering products are released to the environment. The focus of this study is on obtaining detailed observations of the flow of water in waste rock. When later combined with information on primary and secondary geochemical reactions and solute transport properties of waste rock, this should permit insight to the coupling between fluid flow and the release of metals. A study of water movement in waste rock is also relevant to the general question of flow and transport in any heterogeneous porous medium.

Mine waste rock is uneconomic or barren material moved from an underground or open-pit mining operation and typically deposited in piles adjacent to the mine workings. It is composed of broadly graded material from clay up to boulders several metres in diameter (Herasymuik et al., 1995; Smith et al., 1995; McKeown et al., 2000). Waste rock textures are

highly heterogeneous, from cobbles and boulders supported in a granular matrix, to clast-supported cobbles and boulders completely free of matrix (Herasymuik et al., 1995; Wilson et al., 2000). Piles may be constructed in lifts, and hence may also include internal compacted layers from haul truck traffic. Waste rock may be dumped on a flat surface (free-dumped) leading to random grain sizes and textures for each dump load. Alternately, waste rock may be dumped or pushed off the edge of the pile (end- or push- dumping) leading to cross-bedded structures down the face of the pile with interbedded layers of varying grain size. End- or push-dumping creates a grain size gradation from finer material near the lip of the lift to coarser material at the base (Herasymuik et al., 1995; Smith et al., 1995). Waste rock piles typically range from ten's of metres to several hundred metres high.

Previous studies of water flow in coarse rock include small scale lab experiments (El Boushi, 1975; Dexter, 1993), large column experiments (Ward et al., 1983a,b; Frostad, 1999; Li, 2000), field studies of full scale piles (Gelinas et al., 1994; Smith et al., 1995; Ericksson et al., 1997), and numerical studies (Davis et al., 1986a/b; Ericksson and Destouni, 1997; Lopez et al., 1997; Newman et al., 1997; Gerke et al., 1998). Closely related to the problem of environmental leaching of waste rock is heap leaching, where ore minerals are purposefully leached from granular materials as the method of resource recovery (eg: Murr et al., 1981; Dixon and Hendrix, 1993ab; and Decker and Tyler, 1999). A review of these studies indicates there is no comprehensive data set with sufficient temporal and spatial detail to build and test mechanistic models for describing infiltration and metal transport through coarse-grained waste rock.

The non-specific term preferential flow is typically applied to describe either any mechanism leading to flow or tracer movement faster than expected by an observer, or the

concentration of flow into spatially distinct areas. Preferential flow has been confirmed in waste rock by quick responses after the start of rainfall events: rapid changes of water flow rates in pile toe-drains; increases in water table elevations beneath piles; and changes in water pressure or temperature deep within waste piles (Smith et al., 1995). Channeling of flow to spatially distinct areas has been observed in small scale lab experiments on coarse materials by Elboushi (1975) and Dexter (1993), in larger scale column experiments by Murr et al.(1981) and Li (2000), and in dye tracer tests on waste rock piles by Bellehumeur (2001). The presence of preferential flow implies the potential for a significant spatial variation of leaching rates for different areas of a pile. The nature of this preferential flow is poorly characterized and creates uncertainty in efforts to predict leaching from existing piles or to make predictions prior to pile construction.

Some degree of preferential flow in unsaturated porous media is common enough to be the rule rather than the exception (Flury et al., 1994). The mechanisms leading to preferential flow in natural soils include: variable infiltration at the soil surface; flow in macropore features such as large pores, cracks, wormholes and root holes; film flow in non-filled pore spaces; surface flow over large particles; instability of infiltrating wetting fronts and fingering of flow in homogeneous materials; soil hydrophobicity; spatial heterogeneity of soil properties; hysteresis effects; and the focussing of flow through the presence of large boulders or zones of fine grained materials. In this chapter, the non-specific term flow path is used to describe a location or mechanism of water flow when the exact nature is not known.

A range of experimental methods have been used to study preferential flow. Small columns, or isolated soil blocks, have been used both for quantitative studies of flow and

transport (eg: Seyfried and Rao, 1987; Jardine et al., 1993; Sassner et al., 1994; Wildenschild and Jensen 1999a) and for qualitative visualisation of preferential flow mechanisms (eg: Booltink and Bouma, 1991). Some studies have investigated the spatial variability of flow using grids of contiguous collection lysimeters installed at the base of columns or soil blocks (eg: Wildenschild et al., 1994; Phillips et al., 1995; Boll et al., 1997; Kranz et al., 1998). Small scale studies, however, do not encompass the patterns and mechanisms of preferential flow that are present in larger field plots (Schulin et al., 1987).

Large scale studies of unsaturated flow in natural materials have been carried out in agricultural fields and hill slopes. In some studies, water movement is deduced from changes in water content and pressure monitored by intensive in-situ instrumentation, and tracer movement from in-situ methods or destructive sampling (eg: Jury et al., 1982; Biggar and Nielsen, 1976, Schulin et al., 1987; Butters et al., 1989; Wierenga et al., 1991; and Rudolph et al., 1996) Other studies have been performed in fields with tile drains that capture outflow (Mohanty et al.1998; Villholth et al., 1998; Lennartz et al., 1999) or in hillslopes using cross-slope trenches to intercept flow (Feyen et al., 1999). The outflow at a tile drain or a hill slope base is a spatial average of all fluxes passing through the vadose zone to the base of the experiment and a correction must also be made for lateral transport at the base of the experiment (eg:Jury, 1975).

It was decided to construct a large scale waste rock dump on a collection system composed of contiguous lysimeters. This design combines a large area experiment to investigate flow processes with direct measurement of flow and flux-averaged water chemistry at the pile base. By constructing the pile, both the difficulties associated with attempting to install instrumentation into an existing waste rock pile and trying to estimate

outflow at the pile base are avoided. Few conventional methods of drilling, coring or instrument insertion are successful in coarse, rocky waste rock. As the natural state of waste rock is a deposit formed randomly by large haulage equipment, this experiment mimics the textures found in existing waste rock.

This chapter describes the design and construction of the waste rock pile. The pile has been monitored for a period of 2.5 years, during which time data were collected from natural infiltration events, a series of artificial rainfall experiments, and from a tracer test in which a conservative tracer was released during one of the rainfall experiments. After presenting the experimental design and instrumentation, the material properties are reviewed. The water balance for the pile is calculated and net infiltration is estimated. The changes in the patterns of infiltration over time are assessed, as is the flow behaviour observed at different spatial scales. Analysis of the outflow response to varying infiltration rates and the conditions that increase or decrease both flow rate and flow volume is undertaken. In Chapter Seven, the results of the tracer experiment are presented which permits a detailed analysis of the time scales of interaction of transient flow through the different hydrologic regimes of an unsaturated waste rock pile.

6.3 EXPERIMENTAL DESIGN AND CONSTRUCTION

The constructed pile experiment (CPE) was built at the Cluff Lake Mine in northern Saskatchewan. Air temperature at Cluff Lake ranges from –40 °C to +35 °C with a mean annual temperature of 0 °C and an average annual precipitation of 455 mm, of which 305 mm occurs as rainfall. The site is semi-arid, with precipitation typically occurring as intense summer thundershowers or spring and fall frontal systems of lower intensity but longer

duration. Snow fall on the top of the waste rock piles is typically removed by wind and thus accumulations are low (<0.1m).

The CPE is intended to mimic the behaviour of the upper 5m of a much larger unsaturated waste rock pile. A simplified cross sections of the pile is shown in Figure 6.1 with a partial plan view of the experiment core in Inset C. The photograph in Figure 6.2 presents a side view of the CPE, including the instrument hut. The instrumented core of the pile has a footprint of 8 m by 8 m and is 5 m high. A height of 5 m is typical for lifts in existing waste rock piles at Cluff Lake. Outflow from the base of the pile is collected in a contiguous grid of 16 lysimeters each 2m x 2m (Insets A and C). The lysimeter base represents a compromise between the need to collect outflow from both the granular matrix material and from coarse grained areas with no matrix material. Water moves through the finer material under the influence of capillary forces and gravity. In contrast, the experiments by El Boushi (1975), Prazak et al. (1992), Dexter (1993) and Bellehumeur (2001) all demonstrate water flow by surface flow over large particles. In regions of the pile where capillary forces dominate, water cannot flow freely from unsaturated material unless either a water table is formed or water is removed by suction. Maintaining the pile base under controlled suction was not technically feasible. Accordingly, a design leading to the formation of a water table at the base of the CPE was chosen (Figure 6.1, inset A). The pile is built on a contoured cement pad lined with a PVC geomembrane. Within each lysimeter is a layer of 9.5 to 25 mm washed gravel. Outflow from each lysimeter is separately piped to an instrumentation hut. The finer waste rock immediately above the gravel will wet to a higher saturation than would normally be encountered in a thicker unsaturated pile. Those flow paths dominated by capillary forces will therefore be affected by the base of the pile,

and these flow paths may vary from those in a higher pile. The gravel is coarse enough to not retain or delay water which flows from any free-draining flow pathways where capillary forces do not control the rate or direction of flow. The presence of the lysimeter base will have no effect on these non-capillary flow paths, and these flow paths will be the same as if the pile was higher.

The CPE includes impermeable sides from the base of the lysimeter grid to the pile surface to ensure a complete water balance. Only by limiting lateral diversion using these walls will a zero-pressure lysimeter successfully capture capillary dominated water flow (Bews et al., 1997). Plywood lined with a 60 mil HDPE geomembrane isolates the central core of the CPE. The walls may limit the lateral range of spatially-distinct flow pathways. Closed cell polyethylene foam strips were attached to the geomembrane to reduce gaps at the waste rock-wall contact and re-direct any water flowing down the wall back into the waste rock. A skirt on the exposed wall prevents any water flowing down the wall from above the pile surface. Although these measures cannot guarantee the absence of wall flow, they act to minimize it.

The top surface of the CPE was finished to resemble other piles on site which were free-dumped and then contoured to a smooth, level surface. No attempt was made to create a sloped or compacted surface, no vegetative growth was allowed, nor was any cover material used to alter infiltration.

6.3.1 Waste Rock Composition And Internal Pile Structure

The waste rock was mined from the DJ Extension open pit at the Cluff Lake mine in the fall of 1996. It is composed of aluminous gneisses and granitoids from the Precambrian Earl River and Peter River Gneiss Formations. Associated with the target uranium

mineralization are sulphides of iron, copper, lead, zinc and molybdenum, with localized concentrations of nickel and arsenic minerals. Despite low overall sulphide content, < 0.64%, the total dissolved solids concentrations of in-situ water samples are as high as 50,000 mg/L. Further information on the composition and weathering of the material is available in Hollings et al. (1999,2001). The waste rock was exposed to natural weather conditions from mining, until placement in the CPE.

Waste rock was placed within the CPE during July and August of 1998. Delicate instrumentation within the pile, and the construction of the impermeable walls around the lysimeter grid required reworked placement of previously dumped waste rock. Final placement of the rock within the experimental core was undertaken using a tracked excavator (1 m^3 capacity). The waste rock was randomly placed and the texture approximates the range of textures seen in excavations of existing waste rock piles on site (Bellehumeur, 2001). The pile contains regions that are matrix-supported and regions with matrix-free cobbles and boulders. The internal structure of the CPE represents the simplest grain arrangement possible for randomly dumped waste rock. No attempt was made to reconstruct haul truck traffic surfaces, or the cross-bedding structures and the extreme separation of grain sizes down dump faces that result from end- or push-dumping.

Prior to pile construction, a backhoe was used to make a 15 m^3 blended composite from thirty 0.5 m^3 sub-samples of the 2600 m^3 of waste rock used to build the CPE. A 1 m^3 sample of this composite was collected using the backhoe bucket (0.1 m^3), stored in five 200 L drums and analysed for grain size (Rowlett et al., 1999). The maximum grain size of this sample, ~0.6 m., was determined by the diameter of the drum opening. Sixty 5 litre samples were collected on a regular grid during pile construction using a hand shovel. Maximum

grain size in these samples was ~0.1 m. The range of grain size distributions of the grab samples is shown in Figure 6.3, along with the full grain size curve of the composite sample. The $1m^3$ composite appears coarser as it has a larger sample support volume and grain size cut-off and therefore includes greater numbers of particles greater than 0.1m. When the data are re-plotted for the <5mm fraction only, the composite sample plots in the middle of the grab samples. The waste rock contains boulders up to 1.5 metres in diameter, and thus any practical measurement of samples for grain size necessitates the selection of sub samples. A large number of small volume grab samples better defines the envelope of grain sizes in the <5mm size fraction, but poorly represents the larger fractions. Any comparison of grain size curves for waste rock requires knowledge of the sampling method, support volume, and the maximum grain size sampled. According to the grain size classification system adopted by Dawson and Morgenstern (1995), this pile falls at the boundary between a soil-like and rock-like pile.

6.3.2 Instrumentation

The CPE was instrumented to permit the determination of water movement across the soil-atmosphere boundary, within the waste rock, and out of the waste rock at the experiment base. An automated weather station is located on top of the pile to determine wind speed and direction, air temperature, relative humidity, net radiation and rainfall. Nine pairs of mini-lysimeters were installed across the surface to permit periodic direct measurement of actual and potential evaporation to complement and calibrate evaporation calculated from the weather station.

A rainfall simulator was deployed to create artificial rainfall events of controlled rate and duration, and the later application of a conservative tracer. An oscillating lawn sprinkler

was found that supplied rainfall rates with a uniformity better than that obtained with a spray nozzle simulator (eg: Holden et al., 1995) . The interruption in application rate caused by the sprinkler oscillation is acceptable if the interruption interval is small (Barnett and Dooly, 1972; Young and Burwell, 1972; Holden et al., 1995). Artificial rainfall events were constrained to periods of very low wind speed to minimize systematic drift of the spray pattern. Water was supplied from a nearby lake.

Instrumentation within the pile was installed during waste rock placement within three profiles during waste rock placement (Figure 6.1). Water content, matric suction, in-situ temperature, matrix water chemistry, pore gas pressure and pore gas chemistry are monitored. The instrumentation used to measure water content, matric suction, temperature and matrix soil water chemistry (Figure 6.1, inset B) either require direct contact with finer waste rock as part of their principle of operation, or would be damaged during construction by cobbles or boulders. Some grain size selection was required to remove particles >25 mm immediately adjacent to instrument locations and thus these instruments monitor conditions in the matrix-supported waste rock. There are no existing instrument technologies for clast-supported, matrix-free areas. Instruments were only placed on one side of the CPE to permit unrestricted placement of waste rock on the other side.

Automated measurements of volumetric water content are conducted using time domain reflectrometry (TDR). Monitoring is carried out at a 20 to 60 minute interval depending on the time of year. The high concentrations of dissolved solids in the soil water necessitated the use of three rod TDR probes employing a high resistance coating to overcome high signal attenuation. Details of the TDR design, calibration and temperature corrections are presented in Chapter 3 and 4. Water content is monitored manually using a

neutron probe through aluminum access tubes placed during pile construction. Matric suction is monitored year round using thermal dissipation sensors (Feng and Fredlund, 1999; Feng 1999, Chapter 5). Tensiometers with pressure transducers were installed near surface to provide independent measurements of matric suction when air temperatures are above freezing. Tensiometers are measured both manually and using automated pressure transducers.

Water outflow rate and water outflow chemistry are monitored within the instrumentation hut. The outflow pipes leading from the experimental base to the instrumentation hut are heat-traced to permit year-round operation. Water outflow rate is monitored using sixteen tipping bucket rain gauges. Outflow water is passed through a cascade of mixing cells, where the water is directed through containers of increasing volume (0.2 L, 2 L, 25 L). The outflows are then combined and directed through a 2 L, then 100 L container prior to discharge to waste. Both instantaneous grab and longer term composite samples can be obtained without post-sampling compositing. In-situ water chemistry is monitored through the periodic manual extraction of water samples from suction lysimeters placed within the pile during construction.

6.4 FIELD ACTIVITIES AND DATA ANALYSIS

During placement of the waste rock, no rainfall was recorded at the CPE, and significant evaporation occurred from waste rock surfaces exposed during pile construction. The pile instrumentation was connected in August and September 1998, and the CPE was fully operational in September, 1998. Automated data collection has been running continuously since then. The top surface is left open to natural precipitation. Limited outflow from three lysimeters was recorded from September to December, 1998 and outflow

recommenced in April 1999 (Nichol et al., 2000, Appendix A). All lysimeters were not flowing until August 8, 1999. The CPE surface freezes in November and thaws in March with the melting of the winter snow cover. Temperatures measured deeper within the pile indicate the advance of freezing conditions to 1.75 m depth within the pile, with the deeper waste rock freezing in February and thawing by April.

On September 24, 1999, a conservative tracer (LiCl) was applied to the surface of the pile as a single rainfall event of three hours duration. Intensive outflow sampling was carried out following the tracer application at times scales as short as 5 minutes. Unlabelled rainfall events were created on October 10^{th} and 20^{th}, 1999. Four additional unlabelled rainfall events were created in July 2000 with similar sampling intensity. The pile surface is always uncovered, and additional natural rainfall events occur. Outside of the main field work periods, the CPE was maintained by on-site staff. Outflow chemistry was sampled on a weekly or three-times-weekly depending on the flow rate variability.

6.4.1 Analysis Methods

Rainfall data were compiled from the two rain gauges located on top of the pile, with additional information from another nearby automated weather station at the site airport (~500 m away), from manually determined snow depth estimates, and from artificial rainfall amounts measured using rainfall collection cups deployed on the pile surface. The uniformity of artificial rainfall events was measured calculated using the Christensen Uniformity Coefficient (CUC) (Christensen, 1942) which approaches 100 for uniform application:

$$Cu = 100\left(1 - \frac{\frac{1}{n}\sum_{i=1}^{n}\left|Xi - \overline{X}\right|}{\overline{X}}\right) \quad [1]$$

where Xi is the ith measurement, $\overline{X}$ is the mean rainfall and n is the number of measurements.

Time domain reflectrometry measurements of water content were estimated to be accurate to within 4%, partly due to variability in the TDR probe design (Chapter 4). Relative changes in water content are more accurate, and changes < 0.5 % are detectable. The measurements of matric suction using thermal conductivity sensors were corrected for hysteresis and variation in ambient in-situ temperature using laboratory-derived correction equations (Feng and Fredlund, 1999; Feng 1999, Chapter 5). Short term sensor responses were sometimes unrepresentative of in-situ conditions and long term accuracy was poor due to sensor drift. Response times of the thermal dissipation sensors was varied from hours to days, but generally was too slow to match the rapid movement of wetting fronts through the CPE (Chapter 5). Tensiometer measurements were successful, and response times were rapid (seconds to minutes). Raw measurements of the timing of individual tips of the tipping bucket rain gauges were converted to outflow rate using moving window averaging and gauge specific calibrations.

6.5 RESULTS AND DISCUSSION

6.5.1 Material Characterization

Any study of water flow in unsaturated material requires the measurements of the soil water characteristic curve (SWCC) and hydraulic conductivity curves (HCC) of the material. Estimates of the SWCC and HCC of the waste rock have been made from both laboratory

and field data (Figure 6.4). These estimates emphasize the difficulty in measuring the properties of heterogeneous waste rock. SWCC's of the <5mm fraction of the coarsest, middle and finest grab samples of the 60 collected were measured in a large diameter (0.15m) tempe cell. The <5mm fraction was selected as the effect of particles greater than 5 mm on the SWCC can be empirically corrected for using the method of Yazdani et al. (2000). Samples were placed in the tempe cell as a saturated slurry. Figure 6.4A presents the drying curves (solid symbols) obtained during drying from saturation to 80 kPa matric suction, and the re-wetting behaviour (open symbols) obtained from 80 kPa to 2 kPa. Continuous functions were fit to the drying data using the method of Fredlund and Xing (1994). Saturated porosity ranges from 21 to 23%, and air entry values range from 1.0 to 3.3 kPa. Water contents remain at 10-12% by volume (50% saturation) at 100 kPa, indicating significant water retention by the waste rock forming the fine grained tail of the grain size curve (Figure 6.3). The wetting curves show a large displacement from the measured drying curves, indicating the potential for significant hysteresis at low matric suctions.

In-situ SWCCs were derived by combining water content measurements by TDR and matric suction measurements by tensiometer for instrument pairs installed near the surface of the CPE. Figure 6.4B presents an example of typical field data recorded at a single instrument location over a three week period in August 1999. The right hand edge of the clustered data represents the conditions recorded during extended drying periods, and a boundary drying curve was manually fitted this data. This data set incorporates wetting trends from multiple wetting events, shown by the sparser data to the left of the boundary drying curve. The duration of wetting events was often short compared to the sampling interval of automated TDR and tensiometers measurements (15 to 20 minutes) and thus

fewer data points could be collected. Short term wetting and drying during rainfall events progressed exclusively on wetting and drying scanning hysteresis curves, and no boundary wetting curves could be determined at any of the probe locations examined.

Detailed examination of the matched data collected during wetting events indicates trends in the data which are not possible in the case of a uniform wetting front. For example, in response to an infiltration event, water content increases while matric suction is increasing. These responses are created when the wetting front arrives separately at the tensiometer and TDR instruments located approximately 0.2 m apart. Wetting or drying scanning hysteresis curves can therefore not be reliably determined from in-situ instrumentation during short term infiltration given the possibility for mismatch of the data.

Figure 6.4C presents the estimated boundary drying curves from eight instrument locations for the same period as Figure 6.4B. Using the right-hand boundary limit of the matched data should remove the short-term mismatches in water content and matric suction data observed during wetting events (Figure 6.4B). Only partial curves can be determined from the range of conditions occurring at each location. All of the in-situ drying curves are located to the left of the laboratory curves, indicating changes in water contents at lower matric suctions. This indicates the presence of larger pore spaces in the field waste rock than in the tempe cells. Water contents are also generally lower than the laboratory data which is consistent with the presence of particles greater than 5mm. These particles do not contribute to water retention at higher matric suctions but replace porous granular matrix with impermeable material and therefore lower total water content (Yazdani et al., 2000). Data are sparse below 1 kPa for all curves and the data in this region represent wetting and drying

scanning behaviour. Although some curves exhibit breaks in slope at suctions of 0.2 to 0.6 kPa this does not indicate the an accurate air entry value.

Comparison of the laboratory and field measured SWCC's indicates both the laboratory SWCC method, and the field SWCC data fail to adequately represent near-saturated conditions. Bellehumeur (2001) measured in-situ dry densities of 1630 to 1690 kg/m^3 and porosities of 36 to 39% for a nearby pile at Cluff Lake. Measurements of 1550-1800 kg/m^3 dry density and 31to 34% porosity were made in laboratory calibrations of TDR probes (Chapter 4). When the waste rock is mixed and compacted at typical field measured water contents (10-15% by volume) the smallest sized particles tend to form into 1 to 2mm diameter aggregates that resist compaction and create inter-aggregate porosity. Placement of the waste rock sample as a slurry, or vacuum saturation of the waste rock, is required to measure the boundary drying curve from saturation to ensure no entrapped air in the sample and a repeatable starting point. Placement of the laboratory samples as saturated slurries in the tempe cells led to de-flocculation of these aggregates, no clast supported textures, higher dry densities (1980 kg/m3), lower saturated porosities (22%), and higher air entry values than in-situ waste rock Vacuum saturation of samples compacted at residual water contents (10-15%) led to similar de-flocculation of the fines aggregates and the collapse of the additional porosity created by these aggregates. The saturated conditions necessary to measure the boundary drying curve destroy the waste rock texture. Further pores with larger diameters are created under field conditions by particles greater than 5mm diameter, which create pores greater than 1mm when these particles are clast-supported (Kenny et al., 1985). Field SWCC curves indicate highest measured water contents of 20 to 23%, implying greater than 10% air filled porosity even under the highest flow conditions. This pore space may still

permit water flow by film flow and flow in partially filled pores (Tuller and Or, 1999) but these flow processes are not represented in the SWCC.

The hydraulic conductivity curve (HCC) relating water content or matric suction to the unsaturated hydraulic conductivity can be estimated for a granular porous medium from a SWCC and an estimate of saturated hydraulic conductivity using methods based upon the representation of the porous medium as a continuum of capillary tubes (Fredlund et al., 1994). Measurements of saturated hydraulic conductivity were conducted on waste rock from several waste piles at the Cluff Lake site with similar grain size distributions using constant head and falling head tests. The results varied over 7 orders of magnitude from 4.6 x 10^{-5} ms^{-1} at 1660 kgm^{-3} to 10^{-12} ms^{-1} when compacted to 2300 kgm^{-3}. Saturated permeability measured in the laboratory is a poor representation of field conditions without detailed knowledge of in-situ densities. Therefore, estimates of field HCC curves were derived from selected SWCC field curves by matching the HCC curves to field measured unsaturated conductivities, rather than laboratory measured saturated conductivities. In-situ field measurements were examined for artificial rainfall events where the moisture and matric suction measurements reached steady state during the event. Water contents between 12% and 23%, and matric suctions between 0.1 and 1 kPa, were recorded by in-situ probes near surface under rainfall at 4.9 x 10^{-6} m/s. The measured partial SWCC field curves were fit with an estimated SWCC using Fredlund and Xing (1994), then an unsaturated permeability estimation was performed using the method of Fredlund et al. (1994) (Figure 6.4D). The saturated permeability used to generate the HCC was adjusted until the curves matched the in-situ field data. As these data are collected under wetting conditions, it represents scanning hysteresis behaviour, not boundary drying behaviour. These curves are

for the matrix supported areas of the pile and are valid for permeabilities below the match point with field data, 5 x 10^{-6} m/s. Near saturation, the unsaturated permeability is not well estimated by these methods of calculation and is better measured empirically.

6.5.2 Whole Pile Water Balance

The water balance of the CPE, and its variation in space and time, can be used to assess flow mechanisms in waste rock, and to determine long-term estimates of net infiltration. A summary of the average rainfall and precipitation statistics and the precipitation during the experimental period is provided in Table 6.1. The periods when artificial rainfall events were created in 1999 and 2000 exceed the monthly maximums recorded for these months under natural rainfall conditions by up to 20%, but monthly rainfall is still low in comparison to more temperate climates. Yearly totals indicate both 1999 and 2000 were below average precipitation years without the added artificial rainfall and 2000 was a below average year with the artificial rainfall.

Figure 6.5A presents the daily precipitation record over the experimental period. Artificial rainfall events are shown as lines in bold. A summary of the artificial rainfall events created in 1999 and 2000 is presented in Table 6.2. The sprinklers used for artificial rainfall events proved successful if used during low wind conditions. The CUC's compare well with the CUC's obtained in other field studies using large arrays of overlapping spray nozzles (eg: Miller, 1987; Chow and Rees, 1994). The intensities and durations of artificial rainfall events were based upon the rainfall rates delivered by the sprinklers used in the rainfall simulator, rainfall return period statistics for the Cluff Lake site, and rainfall return statistics for other wetter climates. The application rates are similar to the range of rates used in heap leaching (eg: Murr et al., 1981; Pantelis and Ritchie, 1993; Decker and Tyler, 1999).

The return periods (Hogg and Carr, 1985) for the artificial events shown in Table 6.2 indicate these events represent large storms for the semi-arid Cluff Lake site. It is the duration of these events that makes them statistically large events, not the rate. Natural rainfall events with similar daily rainfall totals (eg: August 28 & 29, 1999, 35 mm; August 26, 2000, 31.3 mm) occur as three or four intense thundershowers of 15 to 30 minutes duration with rainfall rates up to 80 mm/hr, spread over a period of several hours and joined by low rate (<1-2mm/hr) rainfall or no rainfall. Low rainfall rates (<1-2 mm/hr) occur under natural conditions during spring and fall frontal rains of 12 to 24 hours duration.

Figure 6.5B presents the outflow flux of the whole pile as a flux rate, equal to flow rate per unit area ($m^3s^{-1}m^{-2}$). A summary of the outflow volumes for the CPE on a monthly basis is shown in Table 6.1. The outflow starts at 10^{-11} ms^{-1} during the wetting up period prior to August 1999 when not all lysimeters were flowing. Following August 1999, the flow rate varies over three orders of magnitude (10^{-9} to 10^{-6} ms^{-1}) between peak summer flow and the lowest flow at the end of winter. The highest flow rates generally correspond to the periods during which artificial rainfall events were created but several natural rainfall events created outflow responses of similar magnitude indicating the outflow rates created by the artificial events are realistic for the Cluff Lake site.

Yearly water balances are calculated for 1999 and 2000 using the cyclic period for flow behaviour. Water drains slowly from November until late March following spring thaw. To estimate net infiltration, precipitation from March to November was matched to the outflow from mid-March to the following mid-March. Measured water contents indicate no net change in water content between March 2000 and March 2001 and thus recorded outflow equals net infiltration. Outflow was 57% of precipitation in 2000. Outflow was 56% of

precipitation for 1999, but net infiltration is estimated to be higher as storage within the pile was being replenished following drying during construction in 1998. Net infiltration was also estimated for natural rainfall only. An estimated drainage curve (under the assumption of no subsequent infiltration) was derived from the last artificial rainfall event on July 23, 2000 to March 2001. The estimated drain down was subtracted from the measured outflow for the period from July 23, 2000 to March 15, 2001. Net infiltration was estimated as 55% of precipitation for this northern Saskatchewan climate. These estimates represent long term average net infiltration to an uncompacted waste rock surface with no vegetation cover. Net-infiltration estimates for specific rainfall events are presented in later sections.

6.5.3 Individual Lysimeter Data

The division of the pile base into sixteen lysimeters allows for the investigation of smaller scale processes occurring within a larger volume of waste rock. Outflow volume data show a large degree of spatial variability at the 2m x 2m scales. Figure 6.6A illustrates the variability in rainfall and snowmelt on the surface of the CPE for the period from September 1998 to March 2001. This plot is calculated by including the measured spatial variability of artificial rainfall events, and assuming natural rainfall events are evenly distributed. The variation in total outflow volume for each lysimeter is shown in Figure 6.6B for the same period. The data indicate a variation of 8% between the lowest and highest recording lysimeters for rainfall, and of 400% for outflow. Individual estimates of net infiltration range from 30% to 121% of precipitation for the sixteen different lysimeters with a standard deviation of 23%. This wide range of net infiltration estimates between 2m x 2m areas of the pile indicates that the individual 2m x 2m lysimeters are poor predictors of net infiltration.

The spatial distribution of outflow was examined to determine changes in the distribution of outflow volume between lysimeters with time. Figure 6.7A presents the monthly total outflow per lysimeter as a percentage of the monthly total for all sixteen lysimeters. The wetting up period from September 1998 to August 1999 and has been excluded. Spring snowmelt and early spring rainfalls occur when the pile is under the driest conditions. Outflow responses to these events can be weeks apart for different gauges, leading to wide variability in outflow volume on a monthly basis. Between 1999 and 2000, lysimeters 6 and 13 increased their share of the cumulative outflow at the expense of the slower flowing lysimeters. Their monthly outflow volume shows greater variability at the higher water flow rates experienced during summer months than at the low flow rates recorded during the winter drain down. Figure 6.7B presents the same calculation as Figure 6.7A, with lysimeters 6 and 13 removed. The overall range of variation in outflow volume for the remaining lysimeters is similar throughout the experimental period. Within the range, individual lysimeters show greater variability between 1999 and 2000.

These data indicate at least one process leading to greater outflow volume reporting to lysimeters 6 and 13 that is more active at the higher flow rates during summer months and that increased from 1999 to 2000. Outflow as 120% of precipitation at lysimeter 6 can only be caused by redistribution of precipitation falling on other areas of the pile surface to within the footprint of this lysimeter. This may occur at or below the pile surface. Surface runoff and the subsequent infiltration at low elevation points on the waste rock surface is one possible mechanism. Minor surface ponding was observed at the highest flow rates created during artificial rainfall events (16 to 19 mm/hr), indicating these rainfall rates exceeded the local infiltration capacity at points on the pile. No significant ponding or runoff was

observed at lower rates. No runoff was allowed to exit the isolated central block of the experiment and any runoff generated infiltrated at lower elevations on the pile surface. Intense physical weathering due to freezing and thawing conditions leads to rapid disintegration of the larger particles exposed at the waste surface. This may have led to decreased surface infiltration rates, and increased run-off between 1999 and 2000.

A surface survey was conducted in August 2001, and the topography of the pile surface is presented in Figure 6.8. Boundaries between surface catchments are shown by thick grey lines. Settlement of the waste rock surface around the fixed neutron access tubes indicates approximately 0.15 m of average surface settlement has occurred over three years. The footprints of lysimeters 6 and 13 correspond to two of ten lower spots on the pile surface but this is not conclusive evidence that increased outflow volume is due to runoff. The two next highest flowing lysimeters, 10 and 11 do not have low elevations within their boundaries. Lysimeters 7 and 15 contain low elevation points with catchments of greater area than lysimeter 13, but are within the middle range of total outflow volume. The lowest volume, and slowest flowing lysimeters, 3, 5, 8 and 9 do not all correspond to higher elevations. Lysimeters 6 and 13 response faster and with greater volume to all precipitation events, even when rainfall intensity is below the infiltration capacity of the surface. Surface runoff is therefore a contributing, but not dominant, mechanism creating variation in the volume of outflow.

6.5.4 Outflow Hydrographs

Outflow hydrographs for all thirteen artificial rainfall events, and the larger natural rainfall events were examined to investigate variations of flow rates and flow volumes between lysimeters in response to individual events. The time to the first hydrograph

response, peak flow rates, volumes produced and flow recession behaviour all vary. Figure 6.9 presents the flow response recorded within three lysimeters following the artificial rainfall event on July 18, 2000. Note that outflow rate is presented on a logarithmic scale to fit the three curves on a single graph. This event represents the CPE under high flow rate conditions but the general character of the outflow response is typical of all of the artificial rainfall events and of the larger natural rainfall events. Lysimeters 6 and 9 are included as they represent the fastest and one of the slowest flowing lysimeters, respectively. Lysimeter 10 represents the third highest volume lysimeter, and is typically within the highest five for peak flow rate.

Three important features are illustrated in Figure 6.9. First, the initial changes in outflow rate, and the peak flow rate occur at different times at each lysimeter. Lysimeter 6 rises to peak flow within 4.5 hours of the start of the rainfall event, lysimeter 10 after 22.5 hours and lysimeter 9 after 33.5 hours. Those lysimeters recording the lowest flow rates and total volumes are the slowest to respond to any given event. The slowest responses to an artificial rainfall event were recorded October 20, 1999. The flow rate at lysimeter 6 rose after 9 hours to a peak after 13 hours. In comparison, lysimeter 12 rose after 43 hours to a peak at 151 hours.

Second, the pre-event flow rates are also different, ranging by a factor of 3.5 from 2 to 7 x 10^{-8} ms^{-1} (Figure 6.9). This range rises to a factor of 18 at the peak flow. Figure 6.10 presents the ratio of maximum flow rate in the fastest flowing lysimeter to the slowest flowing lysimeter (open triangles) for the thirteen artificial rainfall events and several natural events. The ratio of the fastest flowing four lysimeters and the slowest flowing four lysimeters is calculated as measure of how the spread in measurements changes are a larger

cross sectional area of the pile is considered. This ratio is shown as open circles. These ratios are plotted against the average maximum flow rate calculated from the maximum flow rates of all sixteen lysimeters. This measure combines the effects of rainfall intensity, total rainfall volume and prior wetting conditions and is representative of the overall flow state of the pile. The ratio of maximum flow rate between the single fastest and slowest lysimeters varies between 4 and 30 at peak flows and from 4 to 6 for the four fastest and slowest lysimeters. The same ratios were calculated for the whole experimental period, which includes data at the end of long flow recessions. The ratio of the fastest and slowest lysimeter ranges from 4 at a whole pile flow rate of $2x10^{-8}$ ms^{-1} to 2 at the lowest flow rate of 10^{-10} ms^{-1} at the end of the winter period. The same ratio calculated for the fastest and slowest four lysimeters varies from 3.2 at $2x10^{-8}$ ms^{-1} to 1.3 at 10^{-10} ms^{-1}. Figure 6.10 demonstrates that higher peak flowrate lysimeters are always flowing at higher flow rates and the spread of flow rates is larger during high rainfall, wetter conditions.

The third distinct feature of Figure 6.9 is the presence of multiple arrivals. The non-specific term arrival refers to an identifiable increase in the outflow rate. Two distinct increases in flow rates are present in the hydrographs for lysimeters 9 and 10. Closer examination of the hydrographs reveals seven distinguishable outflow arrivals in lysimeter 6, and six in each of lysimeters 9 and 10. Multiple arrivals are present in all lysimeters and for all events examined. The number of distinguishable arrivals within individual lysimeters ranges from 3 to 12 between different lysimeters for the artificial rainfall events where influx rate is constant. During natural rainfall events, multiple arrivals may be the result of varying rainfall rate. The majority of distinguishable arrivals are prior to the peak flow, on the rising limbs of the hydrographs. In some of the early arrivals, it is possible to distinguish an arrival,

peak and the start of a recession curve prior to the next arrival. Changes in observed slope of the recession curve are present that indicate arrivals after the hydrograph peak. The lysimeter hydrograph is the integration of all these separate arrivals at scales below that of the lysimeter.

These multiple arrivals suggest at least as many spatially distinct flow paths as there are discernable arrivals. The number of faster arriving preferential flow paths within each of the 2m x 2m lysimeters is small enough to produce an integrated response that is not a single smoothed curve. The number of distinct arrivals is higher in faster flowing lysimeters than slower flowing lysimeters, and the number increases between events with increasing maximum flow rate. In the unsaturated zone, the imposition of a higher input flux increases the geometry of the water-filled pore space into larger, more conductive pore spaces. The fastest arrivals may result from preferential flow due to spatial heterogeneity of properties, non-capillary flow or saturation on boulder surfaces, but the mechanism cannot be determined from flow data alone. The physical mechanisms leading to the early arrivals in the hydrograph are further investigated using the results of a conservative tracer test in Chapter 7.

The outflow data from individual lysimeters were combined to determine the outflow response at larger spatial scales. Figure 6.11A presents the outflow hydrographs for four adjacent lysimeters added together to represent the four quarters of the pile, and Figure 6.11B presents the outflow for halves of the pile. Both figures include the flow rate calculated for the whole pile from all sixteen lysimeters. Note the scale on the flow axes is arithmetic. The range of pre-event and maximum flow rates decreases with increasing spatial averaging, as does the range in first arrival times. The maximum flow rates for the quarters span a range of

a factor of 6, and the halves span a range of a factor of 1.5. The whole pile hydrograph still contains distinguishable multiple arrivals. For the artificial rainfall events, averaging between 50 and 110 distinguishable arrivals in sixteen individual hydrographs leads to between 10 to 15 separate arrivals in the whole pile hydrograph. The 8m x 8m area of the CPE was therefore not sufficient to average enough of the preferential flow paths active at highest flow rates to produce a smooth outflow hydrograph for the whole pile.

6.5.5 Event Based Outflow Volume

The data for specific rainfall events can be examined to learn more about the short-term net infiltration and distribution of outflow. The outflow volumes attributable to single rainfall events were estimated using recession curve data. Both the net infiltration rate, and the spatial variability in net infiltration are found to be functions of the rainfall event magnitude. Examination of the recession curves indicates that the hydrographs for each lysimeter converge to a similar recession curve unique to that lysimeter. Figure 6.12 presents the recession curves for lysimeters 6 and 9 for the artificial events which created the highest flow rate, September 24, 1999, and the lowest flow rate, October 20, 1999. The curves have been translated laterally such that the first rises in the hydrograph are coincident. Each event has a different short term behaviour, but all events converge to the same recession curve at longer times. The curve for lysimeter 6 converges to a common curve after five days, whereas in lysimeter 9 the recession curves become coincident after 10 days.

These estimated recession curves were used to extend the pre-event hydrographs for selected artificial and natural rainfall events. The post-event hydrograph was extended to eliminate the volume from rainfall events after the selected event. The total volume between these curves represents the outflow from the individual event. Only those rainfall events

where the measured outflow rate preceding the selected rainfall event was declining along a similar recession curve to the outflow rate after the event were analysed. Hydrographs that were still rising from the previous rainfall event were excluded. For some periods, several rainfall events were combined into a single estimate when the hydrographs from adjacent events could not be separated. An estimate for outflow from the whole pile was obtained by the same method from the whole pile hydrograph.

The results are presented in Table 6.3. Estimated total volumes for each event from the whole pile hydrograph, and from the sum of the sixteen lysimeters are within 4% agreement. Net infiltration for each event was calculated from the whole pile hydrograph. Estimated net infiltration ranges from 85% for the artificial rainfall event on August 16, 1999 to 51% for natural rainfalls in August 2000. The data from the spring of 2000 represent rainfall and snowmelt introduced under the driest, slowest outflow conditions where this analysis was possible. The estimated net infiltration rate from this event was 52%. The long term estimate of 55% net infiltration is composed of high net infiltration during short duration intense storms (50 - 84%), coupled with low net infiltration from low intensity, low duration rainfalls. Large rainfall events similar to those considered for this analysis account for 50% of precipitation. Events of less than 5 mm daily rainfall account for 25% percent of the total precipitation.

Figure 6.13 presents the variability in total volume between lysimeters for the different events. Percentage deviation from the average value is plotted against lysimeter number, with data from individual events connected by lines The heavy line indicates the deviation of total volume over the entire experimental period from Figure 6.6. The pattern of water volume reporting to each lysimeter shows consistency between the precipitation events

monitored, from the smallest event in the spring of 2000 to the largest on September 24, 1999. The fastest flowing lysimeters 6 and 13 returned the highest volumes in each event and lysimeters 3,5,8 and 9 were consistently lower volume in each event. Others vary from event to event. Figure 6.13 indicates that the variation in outflow volume created by increased surface run-off to lysimeters 6 and 13 during high rainfall rate events is small in comparison to the variation between lysimeters caused by spatial heterogeneity of the waste rock below the surface. Figure 6.14 presents the ratio of the volumes produced by the lysimeters reporting the highest and lowest volumes (open triangles) and the ratio of volumes from the four lysimeters reporting the highest and lowest volumes (open circles) as a function of the average maximum flow rate of the pile. The ratio of the highest and lowest decreases from 6 at the lowest flow rates to 3.5 at the highest and the ratio of the four highest and lowest decreases from 2.5 to 2. The range in maximum flow rate increases with event intensity for large rainfall events but the range of variation in outflow volume between lysimeters decreases.

Newmann et al. (1997) and Wildenschild and Jenson (1999a/b) demonstrated that preferential flow due to spatial variability in material properties occurs in different spatial locations as a function of flow rate. Coarser grained areas conduct greater flow under higher infiltration rates and wetter conditions. As previously noted, the total number of distinct arrivals in large rainfalls increases with increasing event intensity, indicating more fast preferential flow paths are active. The spatial distribution also changes. The number of distinct arrivals in the fastest four lysimeters is twice the number in the slowest four lysimeters for the smallest events. As the flow rate increases, the ratio of the number of distinct arrivals in the fastest and slowest four lysimeters is reduced to 1. With increasing

flow rate, more fast preferential flow paths are active and the spatial distribution of preferential flow paths becomes more even between lysimeters, the lateral redistribution of water is reduced, and lysimeter volumes become more even.

The preceding observations of the changes in preferential flow behaviour and volume for individual events have been derived only for those events large enough to cause distinct flow arrivals. Preferential flow occurs in those areas of the pile with the highest unsaturated hydraulic conductivity under the given infiltration rate. Under dryer, higher matric suction conditions, it is the finer grained sized fractions that retain water and have a higher unsaturated hydraulic conductivity (Newmann et al., 1997; Wildenschild and Jensen, 1999a/b). In the CPE, the smaller infiltration events cannot be analysed because they create slow wetting fronts in the granular matrix. These are overtaken by the rarer, larger events before they reach the pile base. It is therefore not possible to directly determine the distribution of volume and the hydrograph responses from single rainfall events with low infiltration rate and duration. However, the winter drain down data can be examined for evidence that the spatial distribution of water within the pile may be different at lower flow rates. Each lysimeter has a different recession curve at higher flow rates and each lysimeter starts the winter drain down period at different flux rates due to the spatial re-distribution of water at higher summer flow rates. The outflow flux rate for the fastest flowing lysimeter, the slowest flowing lysimeter and the whole pile are shown in Figure 6.15A and 6.15B for the winter of 1999-2000 and 2000-2001. These hydrographs have been translated laterally so that they match at the lowest flow rate recorded. For both years, all three curves are indistinguishable at flux rates lower than 2.2×10^{-9} ms^{-1}. Comparison of the 1999-2000 and 2000-2001 data for the whole pile (Figure 15C) indicates the two are identical for flux rates

below 2.0 x10^{-9} ms^{-1}. The drain down behaviour of the pile below 2.0 x10^{-9} ms^{-1} is identical between different lysimeters, and at different physical scales. The flow rate of 2.2 x 10^{-9} ms^{-1} corresponds to an evenly applied net infiltration of 63 $mmyear^{-1}$ net infiltration which corresponds to 14% of average annual precipitation or 21% of rainfall.

At the end of winter, flow will only be occurring in the finest grain sized portions of the granular matrix material, where capillary forces dominate. It is inferred from the convergence of the drain down curves that at low flow rates, the spatial scale of variation in flow within the granular matrix is reduced and a 2m x 2m footprint is sufficient to average these variations in flow rate.

6.5.6 In-situ measurements and direct measurements of outflow.

We now compare the progress of changes in water content through the pile with changes in outflow at the base of the pile. TDR measurements of water content of the granular matrix (Chapter 4) have been recorded in three profiles in the CPE. When the field data are examined in detail, TDR measured water content is found to be a poor predictor of changes in the outflow hydrograph and the volume of water outflow.

For the thirteen artificial rainfall events and selected natural rainfall events, the arrival and peaks of wetting fronts at each TDR probe location were compared to the arrival and peak of the outflow recorded from the lysimeter underlying the instrument profile. Selected results from this analysis are presented. In the majority of the artificial rainfall events, where the time to the first change in outflow rate was hours to days, the outflow rate increased before the TDR measured water content at the base of the pile increased, and the outflow rate at the base peaked before the water content at the base of the pile peaked. Figure 6.16 presents the data measured in Profile A following an artificial rainfall event on September

20, 1999. It shows water contents from TDR instruments located in Profile A (Figure 6.16A), and the outflow hydrograph from lysimeter 10, located beneath the TDR profile (Figure 6.16B). Water content changes are generally larger near surface (5 to 7%) in comparison to deeper probes where water content changes in response to the largest rainfall events may be 1% to less than 0.5%. At the scale presented, the change in water content at 1.75 m is barely visible, but is clearly defined when examined in detail. Increases in water content are seen to progress in order down the pile, from 0.1 m to 3 m depth. The first increase in water content at 3 m depth occurs 16 hrs after the start of rainfall, and the peak is reached after 55 hrs. The flow hydrograph increases 4.75 hours after the start of the rainfall event and reaches a first peak after 9 hrs with a second peak after 33 hrs. The flow arrival and first peak occur when increases in water content are noted to 1 m to 1.75 m depth. Delayed response of the TDR in comparison to water outflow was consistent between profiles A, B and C for all larger rainfall events. The arrival and peak of the hydrograph typically occurred when the measured wetting front had reached 1.75 or 3m depth.

We can infer that the spatially distinct preferential flow paths at high flow rates did not correspond to the majority of TDR probe locations. However, the TDR probe located at 4.5m in Profile A (Figure 6.16A) records a change in water content prior to changes in water content at the probes installed at 1.0 and 1.75 metres and immediately prior to changes in outflow. This response was consistent for all examined flow events. This probe location falls within a stable and predictable preferential flow path. Other TDR probes in all three profiles recorded early responses that were observed for single events only, indicating the TDR probe was located within a preferential pathway, but the location of the preferential pathway was not consistent between different precipitation events.

The measured water content is a marginally better predictor of flow behaviour at the low end of the outflow flux range. In two profiles (A and C), the progress of a wetting front down the instrument profile, and the subsequent increase in outflow rate followed a smooth progression during some, but not all, of the low rate infiltration events under low water content and outflow conditions, such as spring snowmelt, or small rainstorms after long dry periods in the summer. During these events, the first change in outflow occurs days to weeks after the precipitation event. A wetting front in the granular matrix could be traced through the pile, and soon after the increase in water content at 4.5 metres was recorded, the outflow rate increased. These low flow events were the only events where in-situ water content matched the timing of outflow. In profile B, the water content response was always delayed in comparison to the outflow response, even at the lowest flow rates.

The late response of the instrumentation to the observed outflow implies the estimation of water flow through waste rock based solely upon the information derived from in-situ instrumentation would underestimate both the average wetting front velocity and the total volume of outflow to the base of the pile. The progress of the TDR monitored wetting front was plotted against time, and estimates derived for the predicted wetting front arrival and peak at the base of the experiment for all the artificial rainfall events. These data were combined with the outflow recession data to derive the volume of water in outflow that had discharged prior to the predicted arrival of the wetting front from the TDR data. Between 10 to 60% of the event outflow volume, with an average of 31%, arrives prior to the predicted TDR wetting front arrival, and an average of 44% of the event volume arrives prior to the predicted peak of the TDR wetting front. It was not possible to determine quantitative estimates for the lowest infiltration rates, as these events were always overprinted by the

responses to larger events. However, as previously indicated, qualitative observations indicate the better agreement between the timing of the movement of the wetting front observed using TDR, and the timing of changes in outflow at the base lower infiltration events. The TDR measurements may be better quantitative predictors of outflow timing and volume at lower flow rates.

The TDR probes are located only in granular matrix, and the responses outlined above indicate they monitor the slower wetting front velocity portions of the pile. It is not clear if the TDR data represent something close to the median wetting front velocity, or if the minor grain size selection necessary to place instrumentation may have biased the material around the probes towards consistently slower flow conditions than average waste rock.

6.6 CONCLUSIONS

The primary aim of this experimental work is to provide a comprehensive data set of water flow, transport and geochemical observations to assist in the understanding of the leaching of mineral weathering products from mine waste rock. Only the water flow data have been presented here, which is the starting point to understand the processes of leaching.

Prediction of environmental loadings from waste rock requires both an understanding of the total net infiltration which determines the overall water volume, and an understanding of the contact of net infiltrating water with reactive surface area of the waste rock. The results presented indicate net infiltration under bare surface conditions is high, 50-85% of rainfall during storms, and an average of 55% long term. The variability of net infiltration calculated between different lysimeters indicates either a single large lysimeter (larger than the CPE), or a large number of smaller scale lysimeters is required to accurately determine net infiltration to bare waste rock. Commonly constructed lysimeters for field monitoring of

net infiltration include large plastic tanks (~4 m^2 area) and 200 L drums (~0.4 m^2 area). The variation in net infiltration data between the 2m x 2m lysimeters indicates that several of the tank lysimeters, or a larger number of 200L drum lysimeters would need to be installed and the data averaged to provide a similar estimate of net infiltration as a single large lysimeter such as the CPE.

The measurements of water flow demonstrate preferential flow in spatially distinct flow pathways under these infiltration conditions. At least some of these pathways exist in the matrix supported waste rock. Some appear stable in space between flow events, whereas others are active only during specific flow events. Preferential flow behaviour increases with increasing water content and rainfall event intensity. The spatial distribution of preferential flow paths is also flow rate dependent. Increased numbers of preferential flow paths at the highest flow rates are more evenly distributed and lead to a slight decrease in the spatial variability of outflow. Based on the possible mechanisms identified in the introduction, it is postulated that these flow pathways are the result of infiltration and ponding at surface, ponding on large boulders beneath surface, surface flow in clast-supported areas, heterogeneity of the granular matrix or hysteresis effects, but the exact mechanism cannot be determined from flow data alone.

Two strategies have been used to describe flow and transport behaviour in heterogeneous media. Approaches such as the transfer function approach of Jury et al. (1982) start with field scale observations of flow and transport and work backwards to derive a single set of parameters that describe the cumulative effects of all possible flow mechanisms. These averaged parameters are thus descriptive of some average material over the scale of the whole experiment. The hydrograph for the whole pile shows evidence that it

integrates the response of individual flow mechanisms but that the 8m x 8m experiment may not have been a large enough spatial scale to average sufficient numbers of preferential pathways occurring at high flow rates. This implies experiments larger than the CPE may be required to determine a single set of averaged parameters for randomly placed waste rock.

A second strategy is to start from detailed descriptions of flow mechanisms at small scales and use extensive databases of measured parameters and appropriate spatial averaging or statistics to work upwards to the field scale behaviour (eg: Butters et al., 1989; Wierenga et al., 1991; Russo and Bouton, 1992; Shouse and Mohanty, 1998). It is clear that this second approach will also be difficult in this waste rock. The material characterization results indicate that simple laboratory methods fail to preserve in-situ textures and that the currently measured in-situ measurements of water content and matric suction will not be sufficient to define the necessary unsaturated flow characteristics for the granular matrix. Hysteresis effects are large, and field flow events are too short lived to derive adequate data from in-situ instrumentation. Immediately adjacent instruments may record different flow behaviours due to preferential flow. The response of TDR measured water contents during large rainfall events suggests that a substantial proportion of the outflow volume propagated in areas of the pile that bypass the three profiles of TDR probes. No in-situ parameters will be measured in those areas leading to the fastest propagation of wetting fronts, and 30 to 40% of the outflow volume. A careful program of in-situ measurement during pile deconstruction and laboratory testing using in-situ textures will be required if this strategy is to succeed.

The nature of waste rock piles allows a third strategy to be applied. Waste rock is an engineered material and therefore changes in surface texture are possible by altering haulage and deposition practices during pile construction. In addition, re-vegetation and re-sloping of

piles is often a required component of mine closure plan. Thus both within construction and post-construction changes to the pile surface may be possible. The observed convergence of recession curves at annual average net infiltrations of less than 69 mmyear^{-1} at Cluff Lake presents the possibility that a surface treatment of the pile capable of reducing net infiltration to a steady infiltration below this figure may also reduce the spatial scale required to predict flow behaviour. This observation does not imply that no heterogeneity in flow exists at this scale and flow rate, just that the physical scale of preferential flow is reduced and thus experimental size and cost can be reduced. Observation of the results of a tracer test would be required to determine if the spatial scale required to observe residence time distributions is also reduced. As flow is dominated by the finer grain sized fraction of the granular matrix, predictions derived from laboratory characterizations of small samples are also more likely to be successful. Plans for future experimentation at the CPE include the compaction of the surface and the installation of a sand cover to reduce surface infiltration. These experiments will confirm if low net infiltration does reduce the spatial scale of flow and transport behaviour and if the variability of net infiltration estimates at the 2m x 2m scale is reduced. While reduction of net infiltration may decrease the necessary physical size of an experiment, it will increase the time scale necessary to conduct experiments by lengthening of the initial wetting-up period .

This chapter has presented the observed responses of the pile outflow to changing infiltration and the overall success of the CPE experiment. The mechanistic reasons for these changes have not yet been addressed. The results of the first year of a transient tracer test conducted on the CPE are presented in Chapter Seven. These data are used to determine specific information about the nature of specific flow pathways. The results of the tracer test

also indicate the average residence time, the residence time distribution, and the spatial variability in these measures of water-rock contact time.

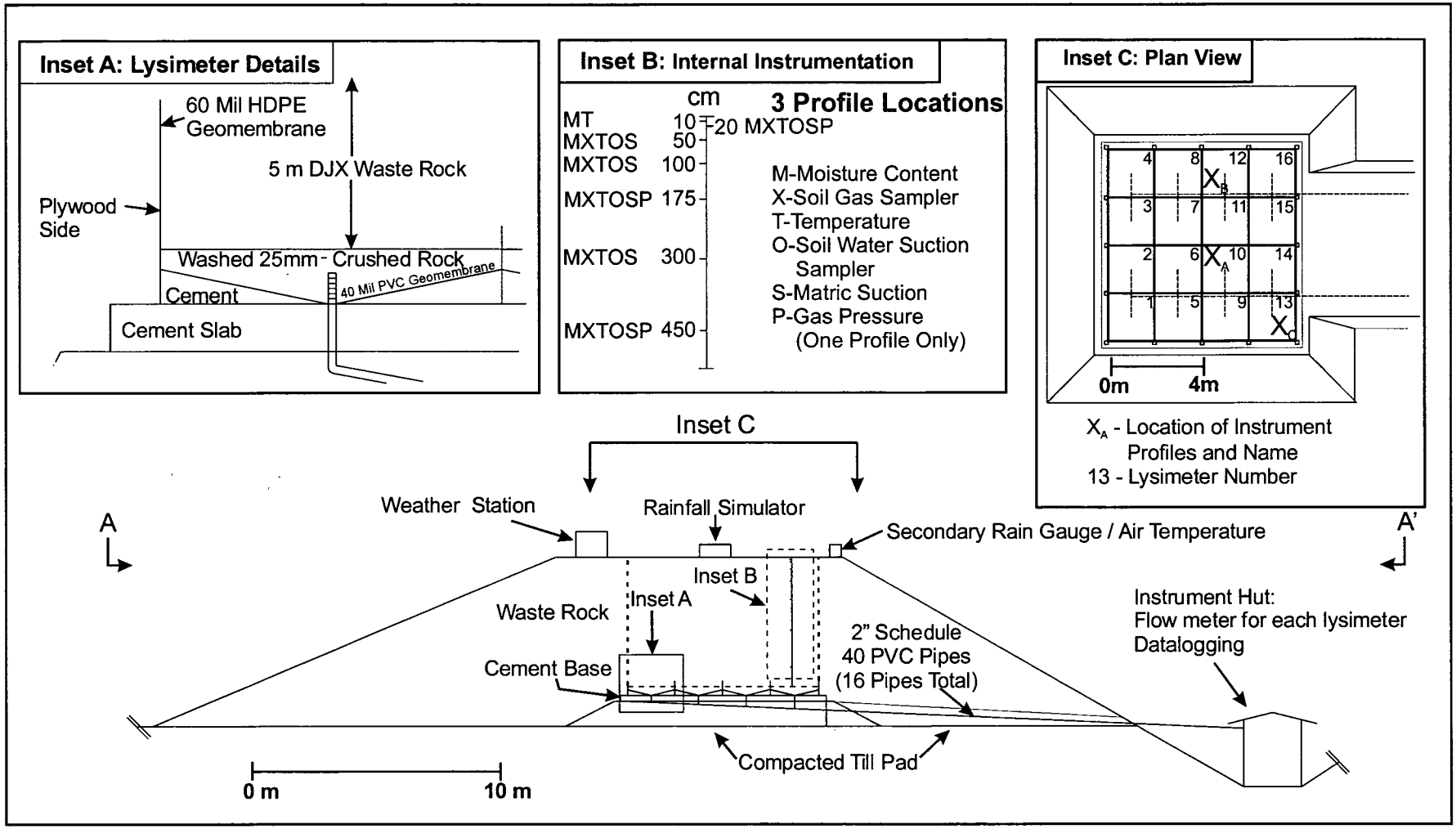

Figure 6.1: Simplified cross section of constructed pile experiment including details of basal lysimeters (Inset A), instrument profiles (Inset B) and a plan view of experiment core (Inset C)

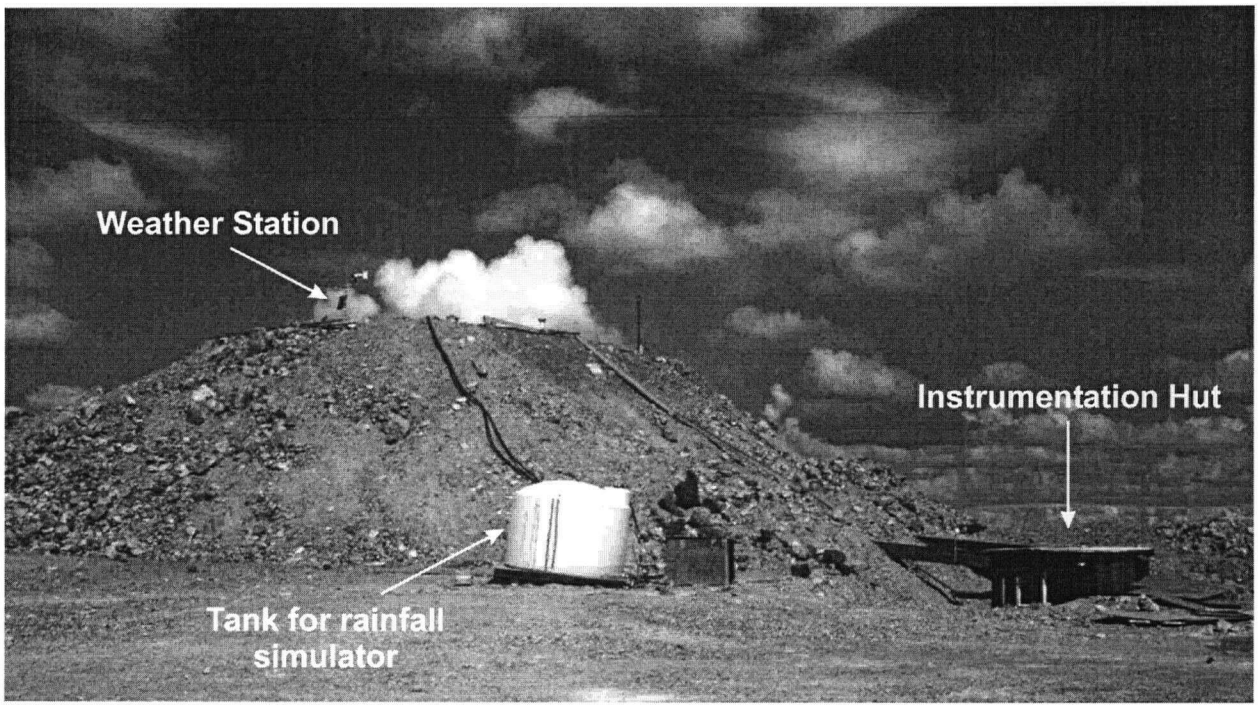

Figure 6.2: Side view photograph of constructed pile experiment.

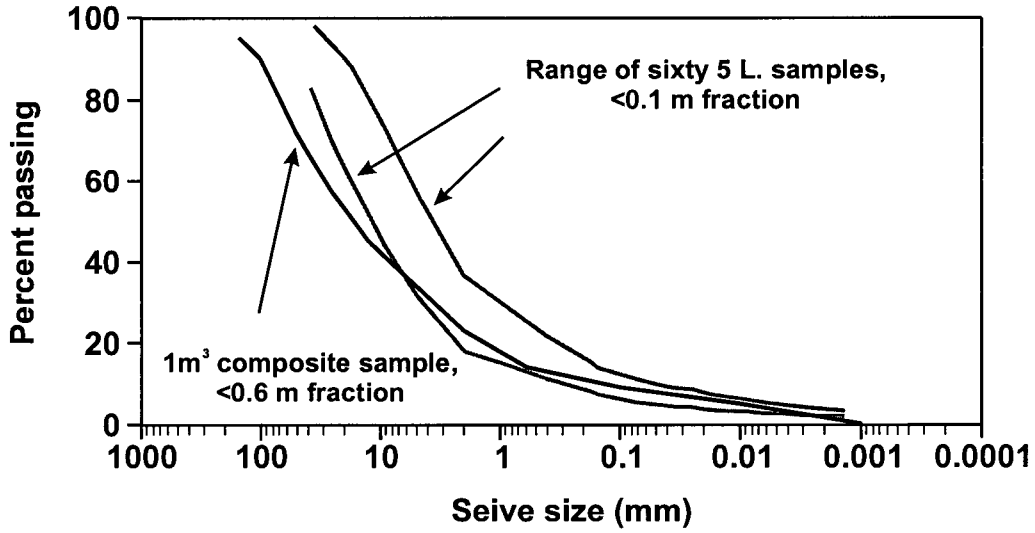

Figure 6.3: Grain size analyses of waste rock samples collected during pile construction

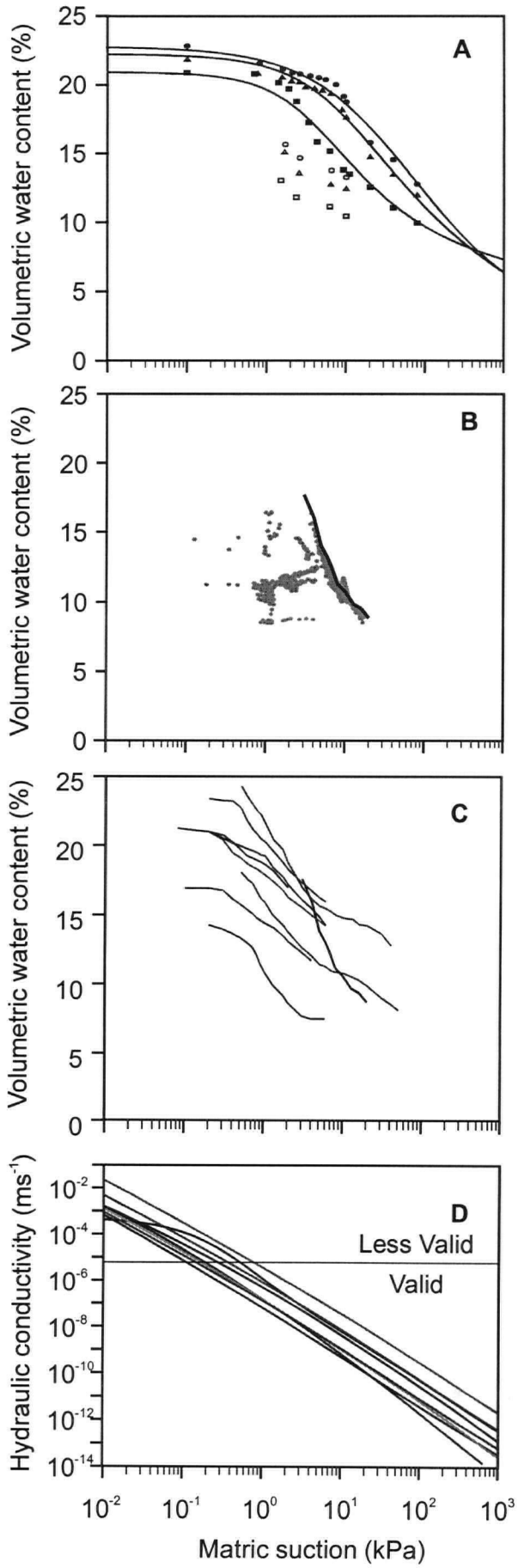

Figure 6.4: Laboratory and field derived soil water characteristic curves and hydraulic conductivity curves.
A) Laboratory data for the coarsest (squares), medium (triangles) and finest (circles) of 5 L grab samples for drying (closed symbols) and wetting (open symbols).
B) Typical field measured data and estimated boundary drying curve
C) Estimated boundary drying curves from 8 instrument profile locations.
D) Estimated unsaturated hydraulic conductivity curves derived from field estimates of unsaturated hydraulic conductivity and the SWCCs presented in (C) using the method of Fredlund and Xing (1994).

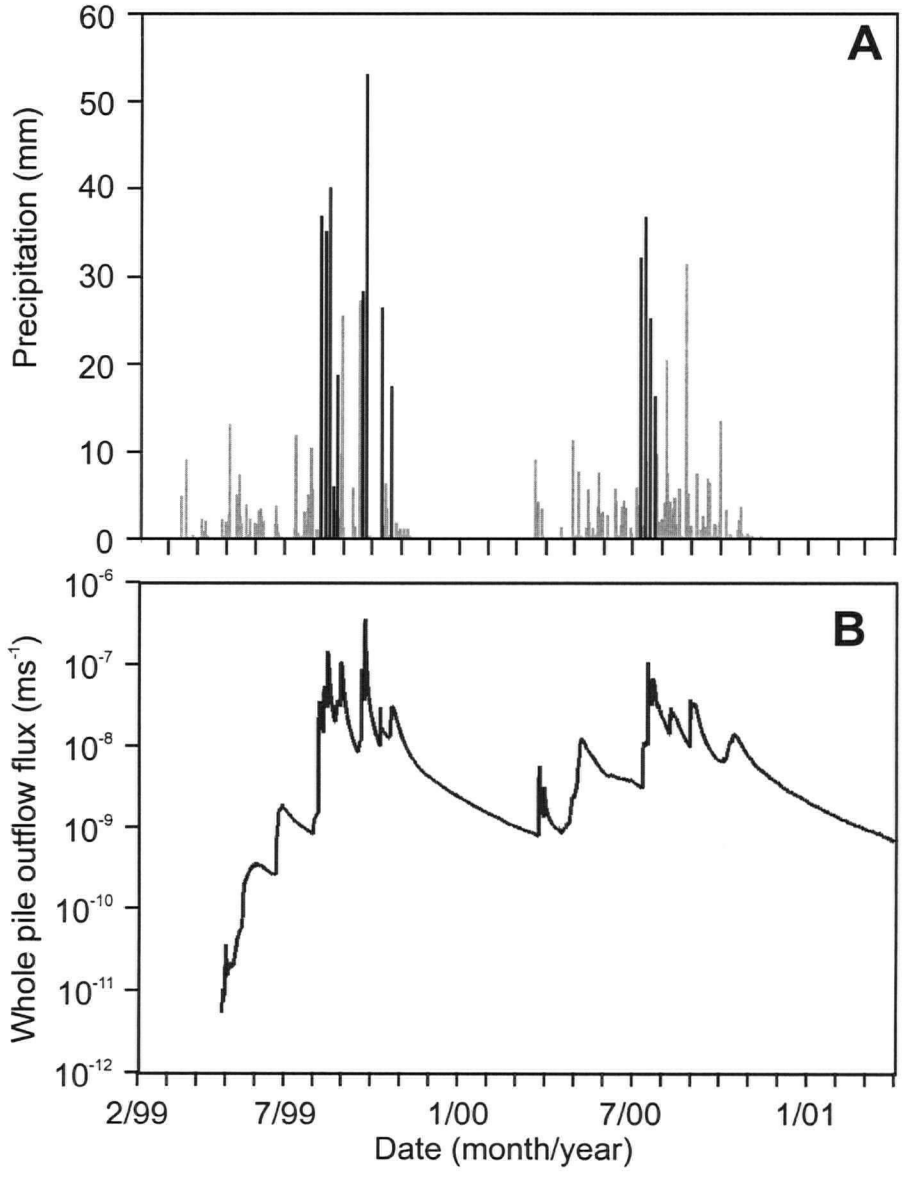

Figure 6.5: Daily precipitation totals and whole pile outflow rate for March 1999 to March 2001.

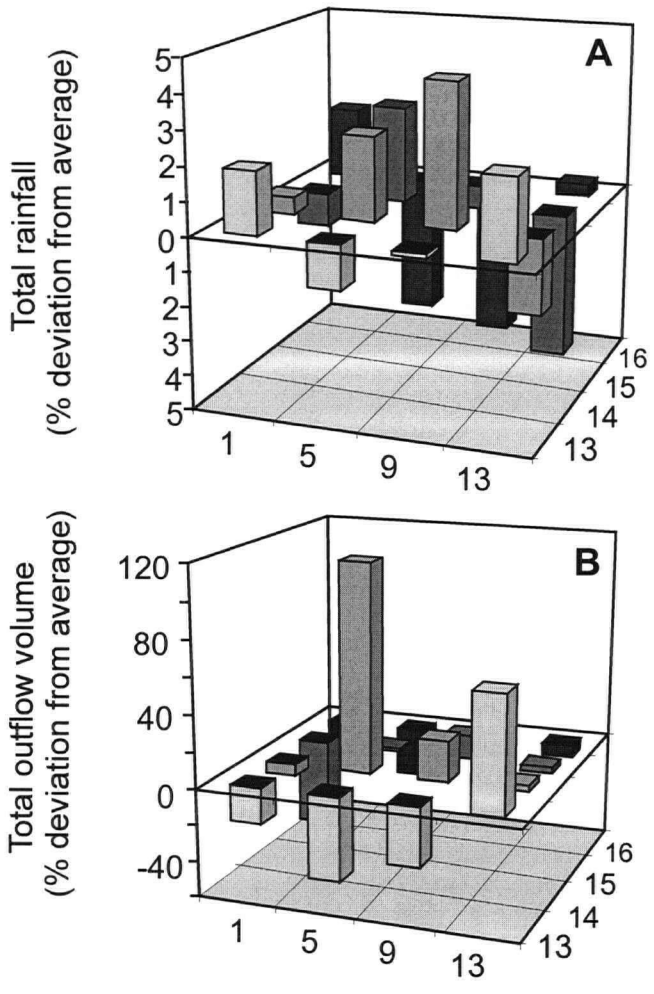

Figure 6.6: Variability in total accumulated precipitation (A) and total outflow volume (B) between lysimeters from September 1998 to March 2001.

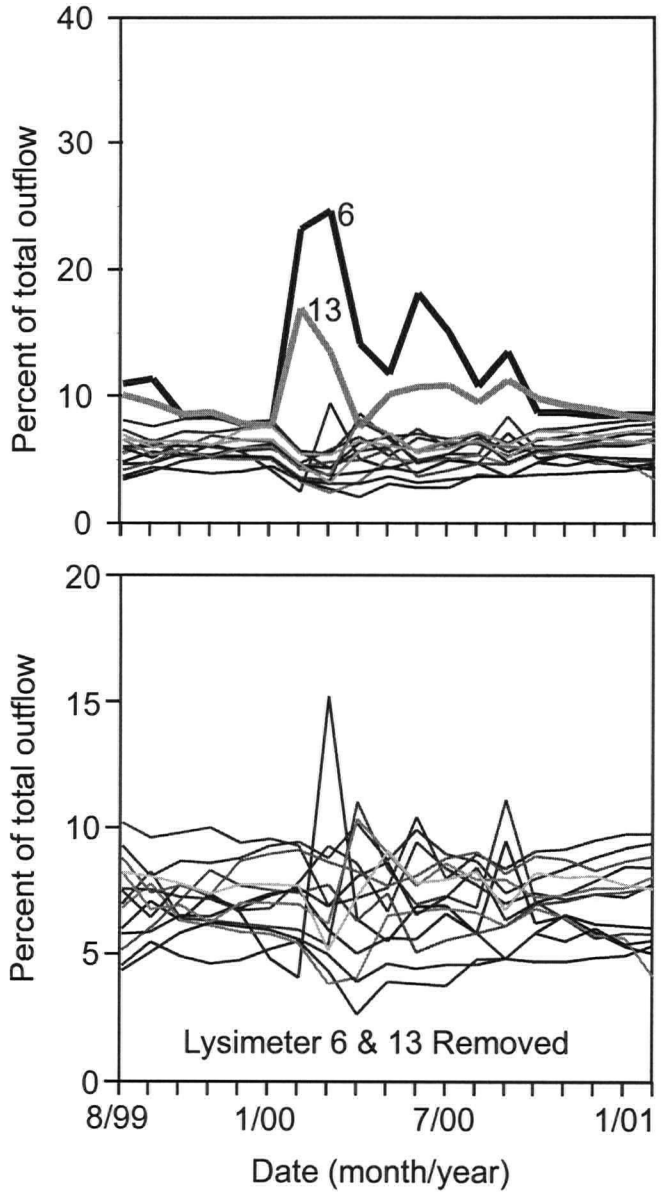

Figure 6.7: Monthly total outflow volume for the period of August 1999 to March 2001 expressed as percentage of total monthly outflow volume for A) all lysimeters and B) with lysimeters 6 and 13 removed

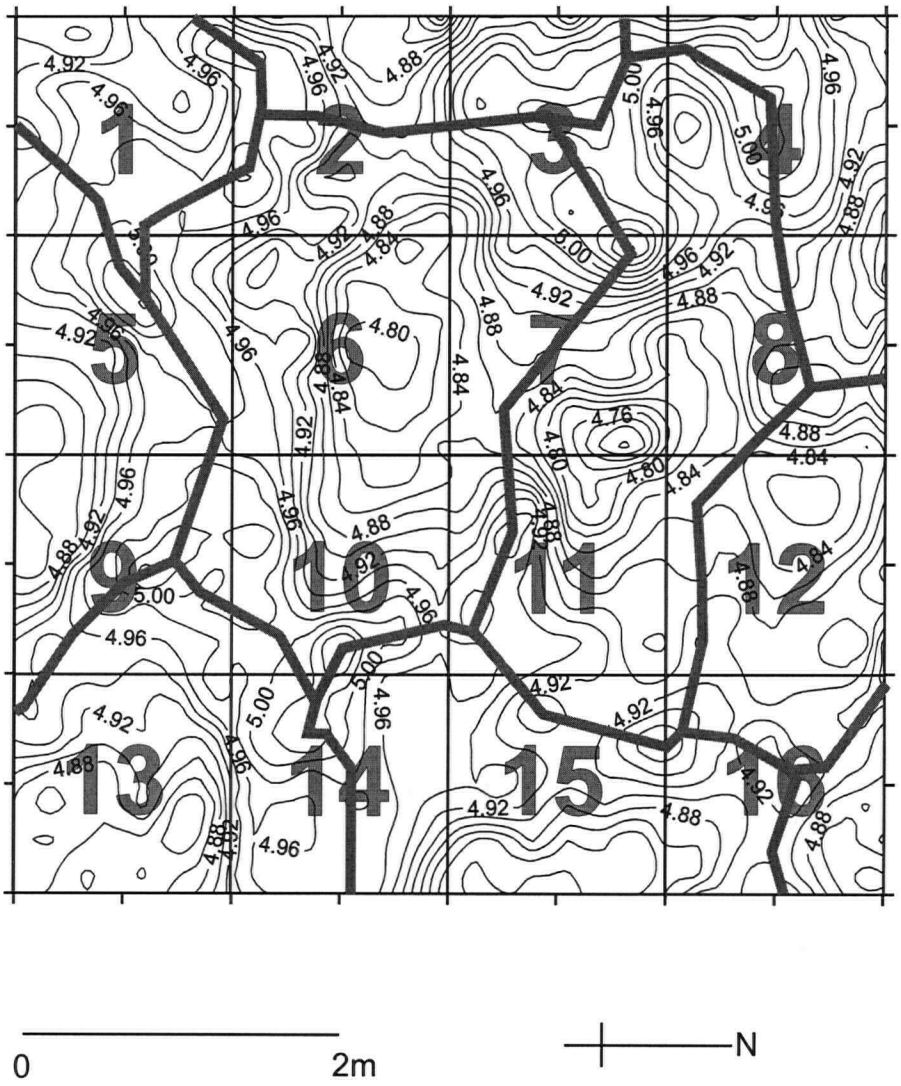

Figure 6.8: Topographic survey of pile surface conducted August 2001 using 0.3 m x 0.3 m survey resolution. Drainage catchments are outlined in heavy shaded lines. Lysimeter numbers are indicated.

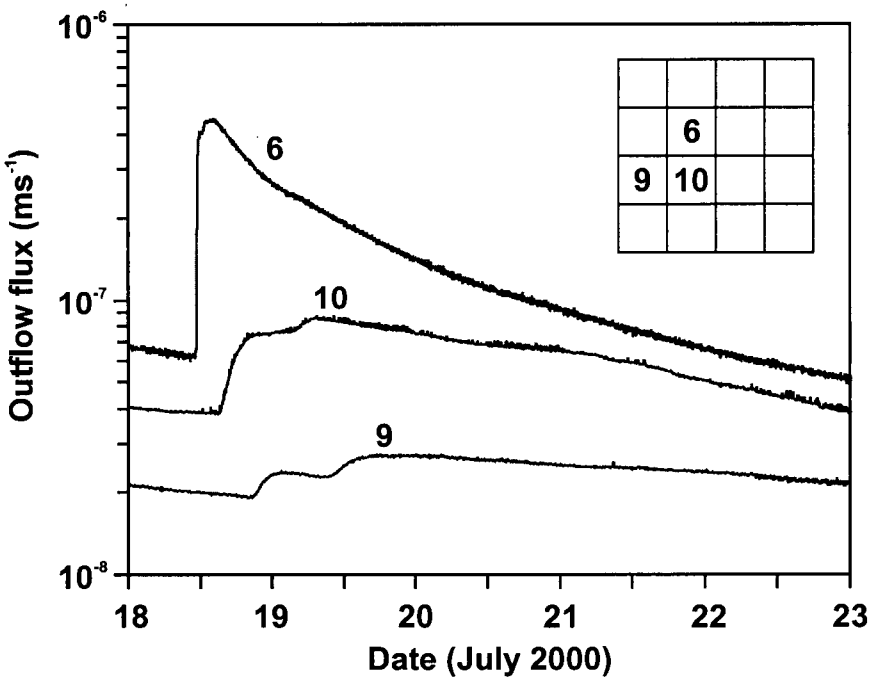

Figure 6.9: Outflow hydrographs of lysimeters 6, 9 and 10 in response to the July 18, 2000 artificial rainfall event.

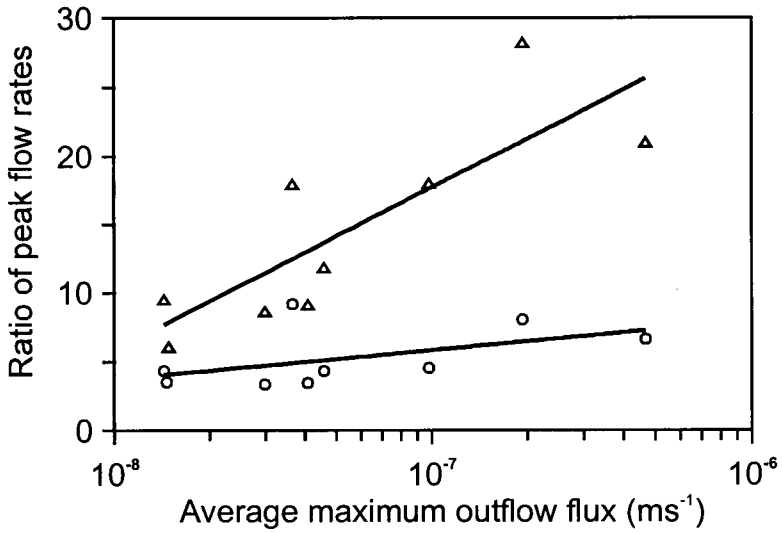

Figure 6.10: Variation of peak flow rates during large rainfall events with the event magnitude expressed as the average maximum flow rate of all lysimeters. Highest flow rate divided by lowest flow rate (triangles) and average of the four highest rates divided by the average of the four lowest rates (circles)

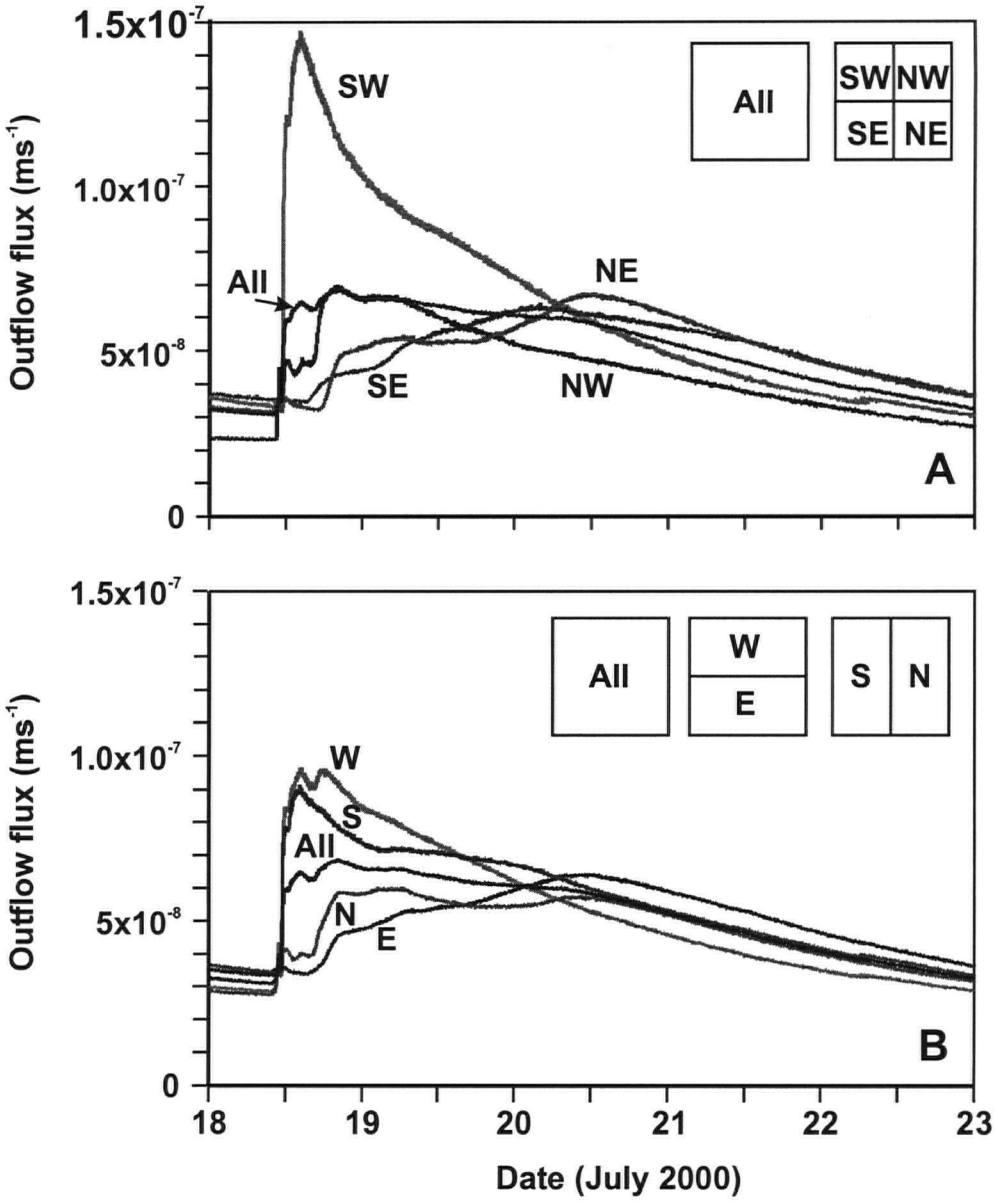

Figure 6.11: Outflow hydrographs for individual lysimeters combined into quarters (A) and halves (B), and all of the pile (A and B) in response to the July 18, 2000 artificial rainfall event.

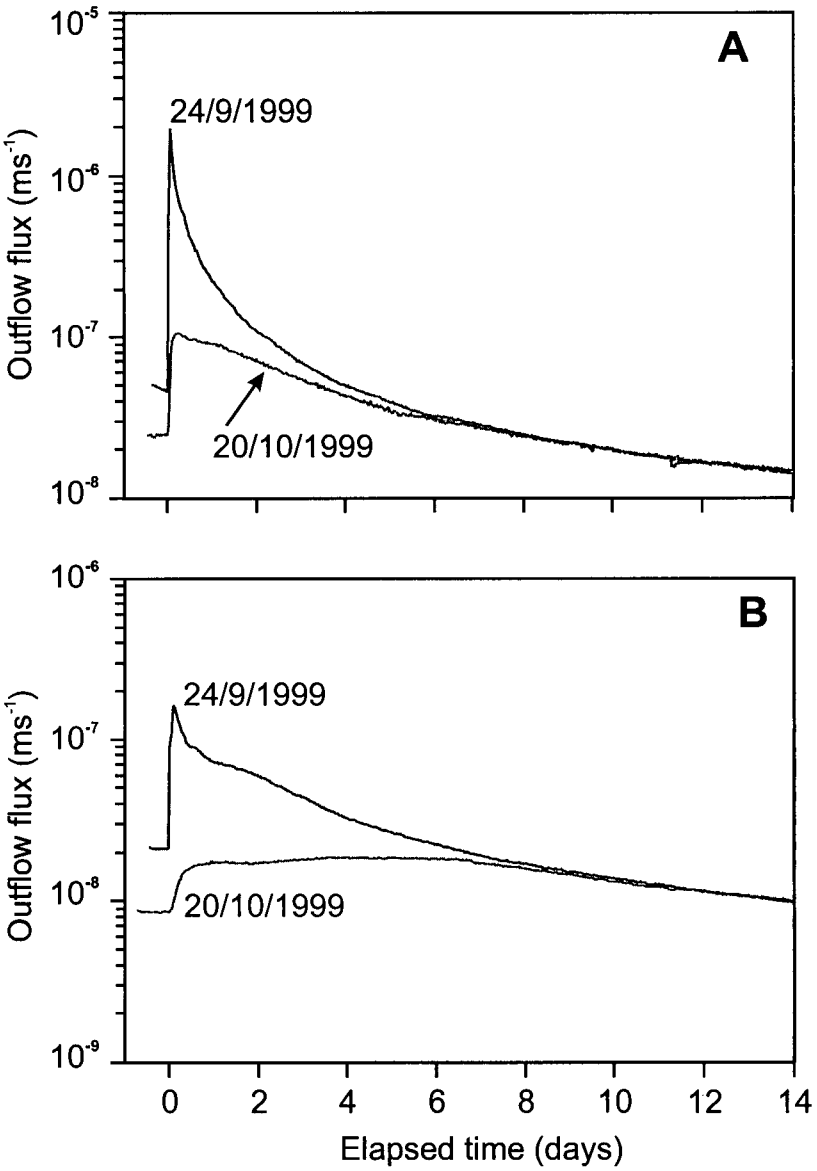

Figure 6.12: Outflow hydrographs for A) lysimeter 6 and B) lysimeter 9 in response to the September 24, 1999 and October 20, 1999 artificial rainfall events. Hydrographs are translated laterally such that the first increases in flow are coincident.

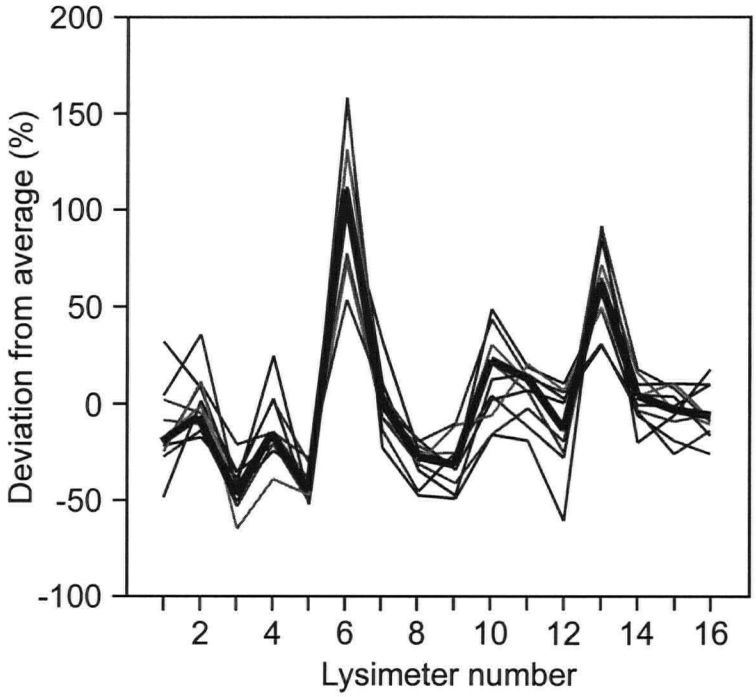

Figure 6.13: Distribution of outflow volume between lysimeters expressed as percent deviation of outflow volume from the average outflow volume for different rainfall events (light lines) and the whole experimental period (heavy line).

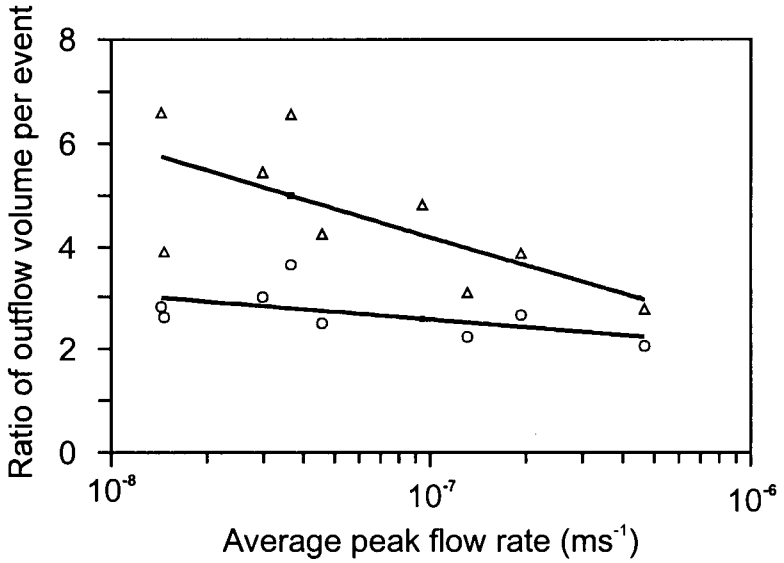

Figure 6.14: Variation of spatial distribution of outflow volume for varying rainfall event magnitude. Ratio of volume of highest volume lysimeter to lowest volume lysimeter (triangles) and total volume of highest four volume lysimeters to lowest four volume lysimeters (circles) plotted against the average maximum flow rate of the rainfall events as a measure of rainfall event magnitude.

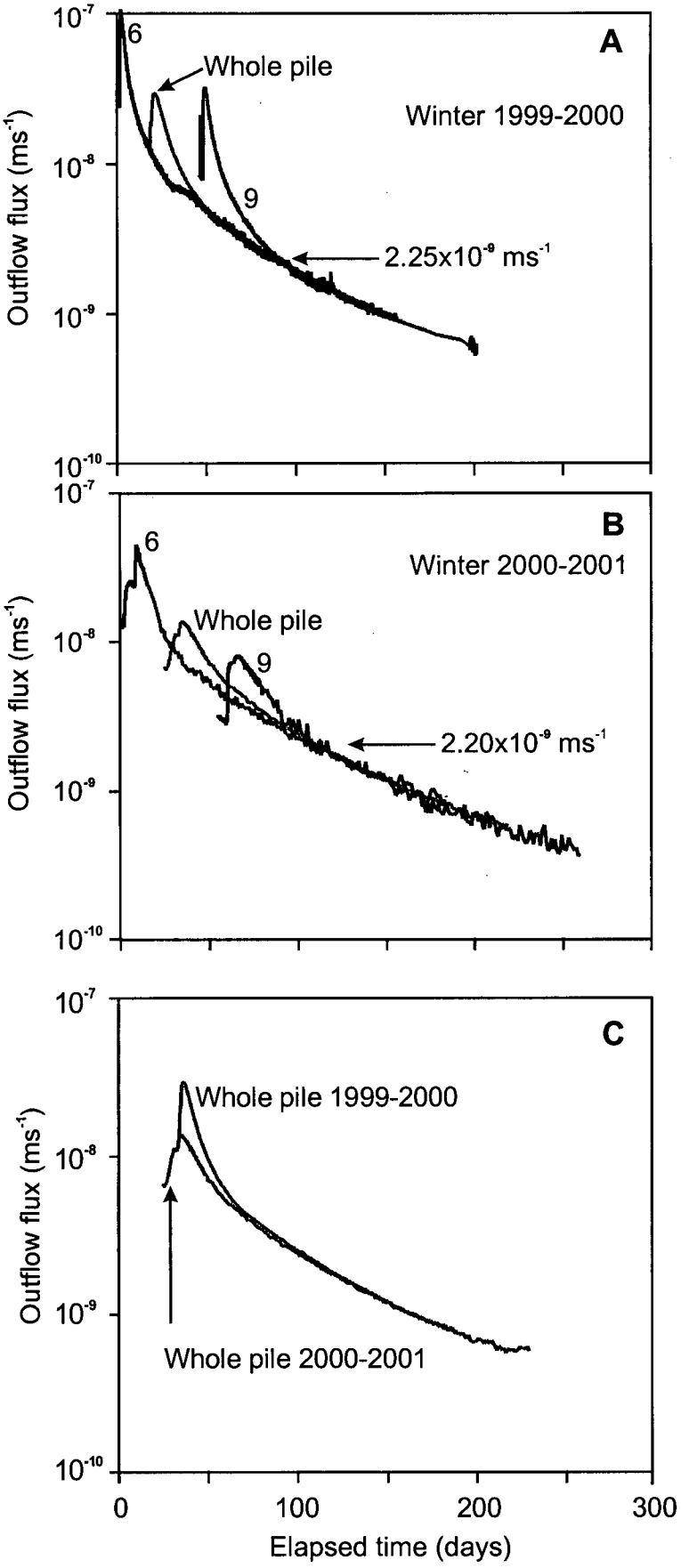

Figure 6.15: Flow rate recession curves of whole pile, slowest flowing lysimeter and fastest flowing lysimeter for A) winter 1999-2000 and B) 2000-2001. Comparison of winter 1999-2000 and 2000-2001 data for whole pile outflow (C).

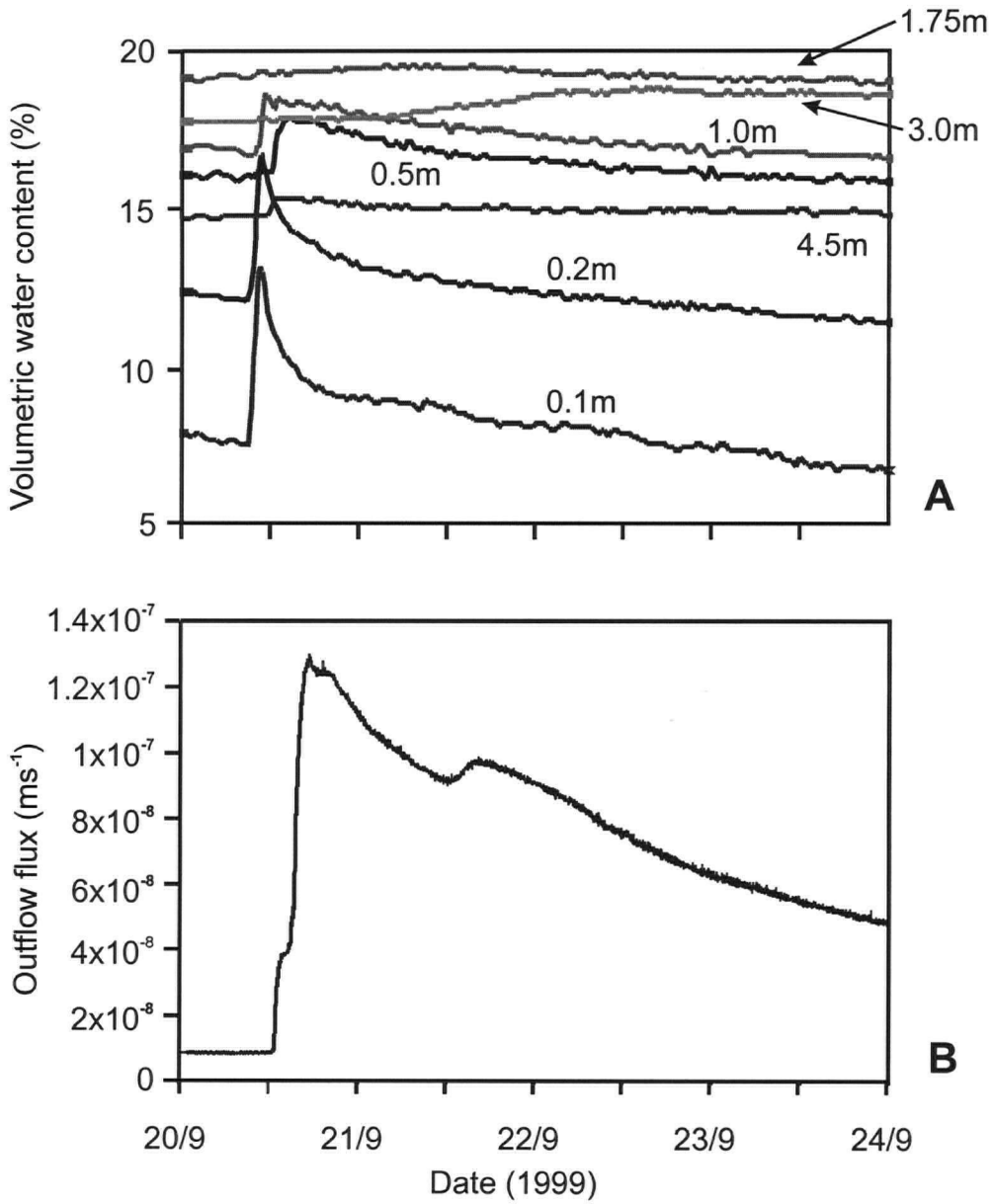

Figure 6.16: Volumetric water content in instrument profile A and outflow hydrograph of lysimeter 10 in response to the September 20, 1999 artificial rainfall event.

		Jan	Feb	Mar	Apr	May	Jun	Jul	Aug	Sep	Oct	Nov	Dec	Year
Site Rainfall Statistics														
1981 - 1996 Rainfall (mm)														
Average		0.2	0.5	1.9	5.9	24.8	55.7	81.0	72.3	44.5	16.9	0.8	0.7	305
Max		1.5	6.2	10.2	16.0	61.2	90.7	125.1	191.8	151.7	50.3	9.3	7.9	519
Min		0.0	0.0	0.0	0.0	9.0	17.9	39.4	14.2	7.0	2.1	0.0	0.0	232
Site Precipitation Statistics														
1981 - 1996 Precipitation (mm)														
Average		18.1	17.1	22.4	16.2	26.9	55.7	81.0	72.3	66.6	30.4	28.1	20.4	455
Max		36.1	29.4	37.0	42.4	61.2	90.7	125.1	191.8	367.0	51.5	63.2	33.9	696
Min		8.7	6.4	8.9	2.4	9.0	17.9	39.4	14.2	7.0	7.4	8.9	7.3	361
Constructed Pile Experiment (mm)														
Artificial Rainfall	1998									0.0	0.0	0.0	0.0	0
Total Rainfall	1998									48.8	4.3	1.7	0.0	55
Artificial Rainfall	1999	0.0	0.0	0.0	0.0	0.0	0.0	0.0	136.4	81.1	43.7	0.0	0.0	261
Total Rainfall	1999	0.0	0.0	14.2	9.4	43.2	21.3	42.0	194.0	116.8	59.8	2.6	0.0	503
Artificial Rainfall	2000	0.0	0.0	0.0	0.0	0.0	0.0	109.9	0.0	0.0	0.0	0.0	0.0	110
Total Rainfall	2000	0.0	0.0	17.4	3.7	51.3	28.3	147.4	95.4	47.2	13.9	0.6	0.0	405
Constructed Pile Experiment (L)														
Artificial Rainfall	1998									0.0	0.0	0.0	0.0	0
Total Rainfall	1998									3123.2	275.2	108.8	0.0	3507
Artificial Rainfall	1999	0.0	0.0	0.0	0.0	0.0	0.0	0.0	8729.8	5193.3	2796.4	0.0	0.0	16719
Total Rainfall	1999	0.0	0.0	908.8	601.6	2764.8	1363.2	2688.0	12416.2	7478.1	3826.8	166.4	0.0	32214
Artificial Rainfall	2000	0.0	0.0	0.0	0.0	0.0	0.0	7032.1	0.0	0.0	0.0	0.0	0.0	7032
Total Rainfall	2000	0.0	0.0	1113.6	236.8	3283.2	1811.2	9433.4	6105.6	3020.8	889.6	38.4	0.0	25933
Constructed Pile Experiment (L)														
Whole Pile Outflow	1998									1.7	1.8	1.2	3.0	
	1999	0.03			1.6	17.7	85.2	200.0	5799.8	6213.4	2930.5	1126.2	519.9	16894
	2000	309.2	188.9	207.1	212.8	1235.0	655.5	4196.5	3263.4	1900.7	1574.4	706.1	410.4	14860
	2001	258.5	160.0	129.6										548

Notes: Winter snowfall is blown off the top of the waste rock piles by wind.
March 1999-2000 data includes 9 mm water equivelant of snowfall still remaining on pile at snow melt in March

Table 6.1: Summary of monthly rainfall and precipitation statistics, measured monthly precipitation and measured monthly outflow of the whole CPE

Date	Start Time	End Time	Duration (hrs)	Average (mm)	Rate (mm/hr)	Christiansen Uniformity Coefficient	Return Period (yr)
7/8/99	9:39	14:45	5:06	36.8	7.2	92	1 in 12
12/8/99	10:10	14:30	4:20	35.0	8.1	84	1 in 12
16/8/99	8:33	10:53	2:20	40.0	17.1	88	1 in 30
20/8/99	16:42	16:57	0:15	5.9	23.8	56	1 in 1
24/8/99	9:49	11:00	1:11	18.6	15.7	90	1 in 4
20/9/99	9:11	10:56	1:45	28.2	16.1	89	1 in 18
24/9/99	8:00	11:00	3:00	53.0	17.7	85	1 in 100+
10/10/99	8:17	9:47	1:30	26.3	17.6	87	1 in 10
20/10/99	8:30	10:30	2:00	17.4	8.7	82	1 in 3
8/7/00	9:00	13:20	4:20	32.0	7.4	91	1 in 7
13/7/00	9:00	11:20	2:20	36.6	15.7	91	1 in 30
18/7/00	9:05	10:35	1:30	25.1	16.7	94	1 in 10
23/7/00	8:03	10:03	2:00	16.2	8.1	83	1 in 2
Average						86	

Table 6.2: Summary of artificial rainfall events.

	Date Start	Date End	Artificial Rainfall (mm)	Total Rainfall in period (mm)	Rainfall Volume (L)	Whole Pile Outflow Estimate (L)	Sum of 16 Lysimeter Estimates (L)	Net Infiltration From Whole Pile %	Average Maximum Flow Rate m/s
1999	16/8	24/8		40.0	2561	2162	2180	84	1.9 E-07
	24/8	17/9	44.0	71.5	4576	3216	3195	70	1.3 E-07
	24/9	10/10	53.0	53.0	3390	2642	2656	78	4.7 E-07
	10/10	20/10	26.3	26.3	1685	985	971	58	3.7 E-08
2000	1/3	3/6		70.3	4499	2320	2262	52	1.4 E-08
	18/7	23/7	25.1	26.9	1719	1405	1460	82	9.4 E-08
	4/8	26/8		48.2	3085	1560	1557	51	3.0 E-08
	26/8	17/9		47.2	3021	2222	2189	74	4.6 E-08
	1/10	30/10		47.2	3021	1794	1809	59	1.5 E-08

	Date Start	Date End	Lysimeter Outflow Volume (L)																
			1	2	3	4	5	6	7	8	9	10	11	12	13	14	15	16	Whole Pile
1999	16/8	24/8	70	138	88	107	72	272	180	103	93	202	162	150	203	128	110	101	2161
	24/8	17/9	165	198	112	171	121	345	185	148	148	261	223	171	343	230	195	178	3215
	24/9	10/10	169	158	106	168	114	294	161	130	113	201	176	124	274	161	151	157	2642
	10/10	20/10	80	65	35	76	31	157	47	32	31	51	49	24	116	49	57	71	984
2000	1/3	3/6	106	157	50	86	74	327	139	98	126	133	170	151	212	147	156	130	2320
	18/7	23/7	72	75	56	94	44	211	101	60	48	103	105	93	119	90	90	100	1405
	4/8	26/8	89	87	46	77	48	249	90	67	57	82	95	78	185	114	105	88	1560
	26/8	17/9	99	118	68	115	69	288	135	111	90	140	146	137	223	150	151	150	2221
	1/10	30/10	118	153	62	86	69	240	97	62	84	118	100	82	208	118	117	95	1793

Table 6.3: Estimated outflow volumes for individual rainfall events and individual lysimeters

CHAPTER 7: SOLUTE TRANSPORT IN AN UNSATURATED HETEROGENEOUS MEDIUM: A CONSTRUCTED WASTE ROCK PILE

7.1 ABSTRACT

A long duration conservative tracer test has been carried out on a heterogenous, unsaturated waste rock pile (8m x 8m x 5m high) to determine the physical mechanisms by which water flows in waste rock, and the resulting distribution of water residence time. Tracer was applied during a single rainfall event, which was followed by unlabelled rainfall in the form of natural and artificial rainfall events. Progress of the tracer is monitored using in-situ suction lysimeters and a contiguous grid of 16 lysimeters at the experiment base. A conceptual framework of the processes of solute transport under transient infiltration are presented to clarify the components of the hydrographs and breakthrough curves presented. Data from the first year have been analysed, and the long term spatial heterogeneity of flow and transport properties are presented. Data from the lysimeters demonstrate the presence of matrix flow in a heterogeneous granular porous medium and preferential flow in macropores and non-capillary pathways. Data from the in-situ suction lysimeters are used to determine transport processes at the pore scale, and the effectiveness of these instruments for monitoring the progress of tracer. Tracer transport is dominated by water flow in a small fraction of the total water content. Peak tracer concentration was observed in the lysimeters at 0.3 pore volumes, and the arrival of the center of mass is anticipated at 0.5 to 0.65 pore volumes. Median residence time is 3.0 to 3.9 years at the average annual rainfall rate. Residence time is underestimated by data from suction lysimeters due to systematic bias in the water sampled.

7.2 INTRODUCTION

The movement of water through unsaturated mine waste rock must be understood to better predict the rates and timing of metals and acidity loadings to the environment. The grain size and textures of a waste rock pile can vary widely; the resulting porous medium is highly heterogeneous. A long duration experiment has been conducted on a 5m high waste rock pile with an 8m x 8m footprint. The pile is constructed on a contiguous grid of sixteen lysimeters (Chapter 6). The constructed pile experiment (CPE) was designed to provide a detailed set of observations of infiltration and water flow, tracer transport, and the evolution of the geochemistry of the leaching process in a waste rock pile under varying infiltration conditions. Details of the design, construction, instrumentation and operation of the CPE and the results of water flow in the first two and a half years of its' operation are presented in Chapter 6. In-situ and laboratory measurements of waste rock properties indicated the waste rock within the CPE is spatially heterogeneous. Measurements of matric suction and water content within the CPE indicated this heterogeneity occurred at scales as small as ~0.2 m. This heterogeneity is expressed in the lysimeter hydrographs by the presence of multiple changes in the outflow hydrograph (arrivals) in response to single rainfall events. This was noted for both for the hydrographs of individual lysimeters (2m x 2m) and the whole pile. The spatial distribution of water outflow was also heterogeneous.

In this chapter the data from the first year of a conservative tracer test are presented. The tracer test was carried out to resolve the mechanisms of water flow within the CPE, and determine the residence time distribution of water flowing through the pile. This information is needed to better understand the time-scales of water-rock interaction, and the manner in which the outflow geochemistry may be altered by the rate and duration of individual

infiltration events and subsequent changes in the outflow rate. Infiltration was not maintained at steady state as the tracer test formed only part of the CPE's purpose and transient infiltration conditions were required for the other objectives. Tracer was applied in a single rainfall event, after which the surface of the pile was subject to both natural and artificial rainfall events in which no further tracer was added.

In this chapter, the aim is to achieve: (1) a description of the effects of both heterogeneity and transient infiltration on the transport of solutes in unsaturated heterogeneous porous media; (2) an evaluation of flow mechanisms active in waste rock; (3) the effectiveness of in-situ instrumentation and lysimeters for the measurement of tracer transport in waste rock under transient infiltration conditions, and (4) an estimate of the distribution of solute travel times within the CPE.

7.3 SOLUTE TRANSPORT IN AN UNSATURATED MEDIUM

Chapter 6 discussed the effects of spatial heterogeneity within waste rock using the non-specific term "flow path" to describe water flow that occurred either in a location or by a mechanism of which the exact nature was not known. Water flow in coarse, heterogeneous waste rock may proceed by a variety of physical mechanisms including: capillary-dominated porous medium flow in granular matrix material; capillary or non-capillary flow in macropores; surface flow over clast-supported cobbles and boulders; and by ponding on the surface of large cobbles and boulders (Chapter 6). The analysis of flow data alone cannot distinguish between these types of flow paths. In this section, more specific descriptions are developed of the possible physical mechanisms of water flow in waste rock material, and the manner in which they can be expected to affect the transport of solute. A conceptual framework is first introduced to describe transport under transient infiltration in unsaturated

porous media. This conceptual model is later used to frame the discussion of the results from the CPE.

7.3.1 Homogeneous Porous Media

In an ideal unsaturated homogeneous porous medium, water is held in capillary tension, and water flow can be described by the Richards equation, which relates capillary tension and gravity driving forces to the Darcy water flux by the unsaturated hydraulic conductivity function. An increase in the infiltration rate at surface creates an increase in the water velocity within the medium, and hence a change in water content. The interface between the higher water content and water velocity, caused by the infiltration, and the lower water velocity and water content deeper within the soil, is termed a wetting front, which propagates downwards through the soil profile. The velocity of the wetting front is determined by the kinematic velocity (Smith , 1982; Yamada and Kobayashi, 1988; Rasmussen et al., 2000). To first approximation, the kinematic velocity (c) is equal to the derivative of the Darcian flux (q) with respect to the water content (θ), which represents the slope of the hydraulic conductivity to water content curve if gravity gradients dominate (Rasmussen et al., 2000). The hydraulic conductivity of a porous medium increases as water content increases, and thus the wetting front will propagate faster than the Darcian advective velocity, v, of the soil water:

$$v = \frac{q}{\theta} \qquad [7.1]$$

$$c = \frac{\partial q}{\partial \theta} \qquad [7.2]$$

When the wetting front arrives at the base of the soil profile, in our case the CPE lysimeters, the outflow rate increases. Two factors compete at the wetting front. The increase in wave velocity with saturation means that any small perturbations in the wetting

front caused by variations in hydraulic properties tend to self-correct and keep the wetting front sharp, whereas capillary pressure gradients act to widen the wetting front (Smith, 1982). The wetting front represents equilibrium between these two processes (Rasmussen et al., 2000). The end of the infiltration event starts a drying front, which also propagates faster than the Darcy water velocity. When this arrives at the base of the pile, the outflow rate recedes. Both variations in hydraulic properties and capillary gradients act to widen the drying front into an elongate trailing wave, rather than a sharp front (Smith, 1982), thus creating the faster rise and long recession of a typical hydrograph. The wetting and drying front velocities determine the advective velocity of the water within storage. The advective velocity field under transient infiltration is therefore a highly non-linear, time-varying function of the infiltration rate and duration, and the water content / matric suction / unsaturated hydraulic conductivity relationships.

7.3.2 Transport

One-dimensional-solute transport in a porous medium has been described using the advection-dispersion equation:

$$\frac{\partial C}{\partial t} = D\frac{\partial^2 C}{\partial z^2} - v\frac{\partial C}{\partial z} \qquad [7.3]$$

where C is the solute concentration, z is the depth and D is the dispersion coefficient. The advective component of tracer movement is described by the second term on the right hand side. The center of mass of the solute, the first moment, travels at the mean water velocity, v. As noted above, this lags the wetting front velocity. Experiments by Rasmussen et al. (2000) noted a three orders of magnitude difference between the wetting front velocity and the average tracer velocity.

The first term on the right hand side describes the process of dispersion, a term which encompasses all processes by which some solute moves faster than the Darcy velocity, and some slower. Dispersion is caused by heterogeneity of the water velocity field at spatial scales smaller than the scale used to describe that average water velocity. In the advection-dispersion equation, the dispersion process is quantified using a Fickian diffusion term and the dispersion coefficient. This approximation assumes that the variation in water velocities can be described by a single mathematical term which is defined and is measurable at the same physical scale as the measurements used to define the advective components of water flow. This matter is discussed below. The dispersion coefficient must be measured experimentally for any given porous medium. For a saturated porous medium, it has been found experimentally to be linearly related to average advective velocity (Matsubayashi et al., 1997). In unsaturated porous media, experimental evidence shows it is a non-linear function of water saturation that is not linearly related to velocity, and that dispersion is higher in unsaturated media than saturated media. The dispersion coefficient has been found to increase with saturation and velocity to a peak near, but prior to, saturation, and then to decrease to the saturated values (Smiles and Phillip, 1978; Sharma and Tanaguchi, 1991; Maraqa et al., 1997; Matsubayashi et al., 1997).

7.3.3 Preferential Flow, Heterogeneity, Macropores and Non-capillary Flow

The term preferential flow was introduced in Chapter 6 to describe water or solute movement either concentrated spatially, or faster than expected, in unsaturated media. For solute transport at the pore scale, preferential flow is a loosely defined term used to refer to water or solute movement faster than expected. Several physical mechanisms account for preferential flow.

Heterogeneity of soil properties at a macrosopic scale leads to spatial concentration of flow into areas with different properties. Under low infiltration and higher matric suction, water flow is concentrated into finer-grained areas where water is held under capillary tension, the water-filled pore space is more interconnected and hydraulic conductivity is higher. Under high infiltration rates, water fills more pore space and enters the larger pores. These pores have higher hydraulic conductivity, and thus carry a larger fraction of the water volume (Bews et al., 1997, Birkholzer and Tsang, 1997, Wildenschild and Jensen, 1999a). When these areas of varying properties occur at a field scale, and the variations in properties can be measured deterministically, then the process is assigned to the term heterogeneity.

If water flow is concentrated at the scale of single, or several pores, then the term macropores is applied. In this case the heterogeneity is at a small scale, typically too small for the changes in properties between the macropores and the remainder of the porous medium, the matrix, to be easily measured and hence described deterministically. The loosely-defined term macropores is used to describe single pores or textures made of collections of pores within an unsaturated porous medium which are hydrologically effective at channeling water through the soil in a manner in which the water contained within them does not interact well with the water in the surrounding porous medium (Beven and Germann, 1982). Physical examples of single pores include root holes, worm holes, cracks, or larger pore spaces created by large grained particles, or open soil textures. The characterstics which describe them are (1) low or no air entry value (2) large size (3) some degree of vertical continuity within the soil profile (4) large variation in hydraulic conductivity from neighbouring pores and (5) poor mixing of water within macropores with the remainder of the porous medium. The range of physical definitions spans from -0.1 to -

10 kPa when defined by the air entry pressure or 0.03 mm to 2 mm minimum using size (Beven and Germann, 1982), but the threshold between micropores and macropores is a matter of convention rather than physical principle (Germann and Beven, 1981). They may contain water under tension, under atmospheric pressure, or under positive pressures depending on the flow regime (Beven and Germann, 1982). They need not be filled for flow to occur. Flow can occur in films and rivulets on the pore wall sides (Germann et al., 1997; Tuller and Or, 2001).

It should be made clear that macropores are not necessarily distinct from the porous medium but are part of it. Macropores are an extension of the pore space continuum to those pores that are filled near or at saturation. They may be singular in space, and easily identifiable, such as a worm hole, but they may also simply be a term to describe the largest pore spaces within the continuum.

The propagation of a wetting front through a porous medium occurs when water content and hydraulic conductivity in the porous medium increases at surface. Water from the infiltration event is introduced into larger pore spaces at surface. If these pore spaces terminate in a short distance in a collection of finer pores, then the pressure wave continues in other large pores, but the water is matrix water. When water is introduced to pores large enough, and vertically continuous enough to be termed macropores, the infiltrating water flows in these pores at, or faster than, the wetting front in the finer matrix. What distinguishes them for the purposes of solute transport is their increased degree of vertical connection, and the manner in which the water they carry mixes poorly with water held in other pores.

Conceptual models of water flow and solute transport in macropores consider that water flows within the macropores, and gradually loses or exchanges water with the rest of the porous matrix (Beven and Germann, 1982). If the macropore is continuous, and the infiltration event is long enough, then water within the macropore at the base of the soil profile is event water. In this case, the hydrograph response corresponds to an increase in the solute break through curve (BTC) in the application event. If the macropore dead ends within the soil, the water is dispersed back into the matrix, which is termed internal catchment (Hatano and Booltink, 1992).

As clast size and the resulting pore spaces are increased, the same processes used to define the term macropore extend to the larger pore space resulting from clast-supported gravel, cobbles or boulders with no matrix between. In these environments, the pore space is sufficiently large that water is never under tension, and non-capillary water flow may occur as surface flow over part or all of the clast surface. Between episodes of water flow in these pathways, small volumes of water are held in tension only at grain contacts (El Boushi, 1975, ElBoushi and Davis, 1969). This latter behaviour has been confirmed in waste rock by Bellehumeur (2001). These pathways would have even less interaction between the event water and the water resident in the granular matrix.

7.3.4 Conceptual Model of Effects of Heterogeneity During Transient Infiltration

An unsaturated porous medium is described as heterogeneous if the properties of the porous medium required to describe the Darcy velocity change between spatial locations, and measurement scales. The results presented in Chapter 6 indicate that material properties of the CPE waste rock vary in space, and water flow varies in space at scales less than 2m x 2m. The laboratory and in-situ measurements of material properties (Figure 6.4) indicated that

coarser waste rock had lower air-entry values and overall lower water contents than finer waste rock. Lower air entry values indicate the presence of larger pore spaces, and thus higher conductivities at lower water contents. Thus, if the same wetting front velocity ($\partial q/\partial\theta$) was recorded in both a coarse and fine sample, the coarse sample would have a lower water content, and thus a higher average advective velocity (q/θ). Similarly, under the same Darcy flux, the coarser area will have both higher wetting front, and advective velocities.

The effects of average advective velocity, wetting front velocity, dispersion, and spatial heterogeneity of porous medium properties can now be combined to demonstrate a typical hydrograph and BTC response to a single rainfall event. This is used later to address the results of the CPE tracer test. A conceptual explanation can be made by imagining that at least three distinct arbitrary classes of flow and transport pathways occur within the waste rock: fast, medium and slow, which refers to the velocity of the wetting fronts that propagate in each pathway. At this point, no further characterization of the actual nature or scale of these pathways is required. Figure 7.1 presents conceptual in-situ tracer profiles (panel A), the outflow hydrograph (panel B), and the BTC (panel C) that result from a single infiltration event at some time after the start of the tracer test. In our case, the plane of observation is at the base of the CPE at 5 meters depth. The time considered is after the original tracer application event, and sufficient infiltration has occurred such that the tracer has reached the lysimeters in two of the three flow pathways.

The outflow hydrograph (panel B) is the integration of the wetting fronts that propagate within each pathway, and the hydrograph from each pathway. Wetting fronts will propagate to the base the experiment in the fast, medium and slow pathways with different kinematic velocity and arrival times (t_f, t_m, t_s).

The average movement of water resident within each pathway is much slower (panel A), moving at the average Darcy velocity, which matches the velocity of the center of mass of the solute mass contained within each pathway. As discussed above, the observations in Chapter 6 indicate that the average advective velocity is higher in the pathways which generate the fastest moving wetting fronts. Thus, the tracer profile has advanced further in the fast pathway. Each rainfall event contributes to the downwards migration of the tracer profile, shown as the solid (pre-event) and dashed (post event) profiles. The vertical distribution of tracer in each pathway is subject to dispersion, which is here represented by a Gaussian distribution for simplicity.

The BTC (panel C) measures the flux-averaged concentration in outflow. This is the result of the outflow rate and the concentration of each pathway. Prior to the event, the flux-averaged tracer concentration is a mix of the outflow from the three paths. The tracer concentration starts to rise at t_f with the arrival of a wetting front within the fast flow path. Tracer in this pathway has moved further downward, and has a greater concentration at the outflow. The flux-averaged tracer concentration in outflow will rise as the proportion of the outflow composed of water from the fast flow path increases. The BTC tracer peaks at a concentration below that contained within the fast flow path, and then starts to drop with the arrival of lower tracer concentration outflow contained within the medium pathway. The BTC drops further as the flux from the fast and medium pathways decreases, and the proportion of water from the slow pathway increases. At some long time after the infiltration event, the water flux from each pathway will be similar to the proportions prior to the event. The final concentration in the outflow is higher than the pre-event concentration, as the peak concentration within each pathway has moved downward (panel B).

7.3.5 Heterogeneity and Transient Infiltration

In a saturated porous medium, or an unsaturated porous medium under constant infiltration, the advective velocity field, the geometry of the saturated pore space, and the processes causing dispersion are constant in time. Under transient infiltration, water content, average water velocity, the geometry of the saturated pore space and dispersive processes are all time-variant and non-linear. It is not clear what the long-term average effect of a given transient infiltration regime will be in comparison to the same net infiltration applied at steady state.

Several long-term, large-scale field experiments of solute transport under transient infiltration conditions have been conducted in unsaturated heterogeneous soils. These experiments have produced conflicting results. Experiments by Wierenga (1977) and Destouni (1991) found good agreement between the average water velocity, and the velocity of the first moment of the tracer mass. The BTC could be modeled using methods based upon steady state infiltration, by re-formulating the transient infiltration into a time-averaged measure. For example, the steady-state advection-dispersion equation can be re-written using either cumulative net infiltration or outflow instead of time (Wierenga, 1977). In these experiments, the effects on advection and dispersion from the changing soil conditions under transient infiltration averaged out in a manner that could be represented by the methods used to describe transport and solute dispersion under steady infiltration. Other experiments have noted differences in the velocity of the first moment of tracer mass, and the time-averaged water velocity under transient infiltration. Experiments have recorded average solute velocity both faster (Bowman and Rice, 1986; Roth et al., 1991) and slower (Jury et al., 1982; Butters et al., 1989) than the time-averaged pore water velocity.

The results of several experiments demonstrate that under transient infiltration conditions, the timing of the initial infiltration of the pulse is also a stochastic variable (Destouni, 1991). In comparison, the timing of the tracer application is not important in steady state experiments. Schulin et al. (1987) determined that the tracer velocity under a given flow regime was a function of the application date. They followed two tracers applied separately during summer and winter, and observed greater transport (as a function of cumulative net infiltration) for the tracer applied at the start of a wet season. Jury et al. (1982) observed slower than expected tracer transport for a tracer applied in which a 25 to 35 day delay occurred prior to rainfall. Both authors attribute the slower transport to the tracer being more mixed between large and small pores by evaporative cycling near surface.

7.3.6 Monitoring Methods at the CPE

Data to describe the movement of tracer through unsaturated soils, and ultimately to parameterize predictive unsaturated transport models, are derived from measurements of in-situ tracer concentrations (eg: Rudolph et al., 1996), or from BTC's measured at tile-drains or lysimeters underlying the field plot (eg: Mohanty et al., 1998). Any observations of tracer concentrations or movement using instruments or lysimeters implies that the measurement is made over a particular physical scale, matching the sampling area of the instrument. Description of the movement of solute cannot be made independently of the scale of measurement (Butters et al., 1989a). At the CPE, the progress of tracer movement is monitored by two methods. Within the pile, tracer is monitored using in-situ suction lysimeters. The arrival of the tracer at 5 m depth is monitored in the lysimeter grid.

Suction lysimeters were installed during construction of the pile. These samplers collect soil water from centimeters to tens of centimeters around the tip of the porous cup.

Destructive sampling followed by soil water extraction (Jury et al., 1982) was not an option. Nor was the use of TDR to monitor bulk soil conductivity, and hence ionic tracer concentration (Rudolph et al., 1996, Caron et al., 1999), due to the high background conductivity of the soil water (5 to 20 dSm^{-1}) caused by weathering of sulphide minerals. (Chapters 3 and 4).

It is known that suction lysimeters sample a biased fraction of the water present in a soil and they measure neither volume-averaged nor flux-averaged concentration (Parker and van Genuchten, 1984, Litaor, 1988). They extract water from the soil around the ceramic tip by the application of an artificial pressure gradient. The water obtained is therefore a flux-averaged sample of the soil water immediately around the suction lysimeter, based not upon the flux resulting from natural matric suction and gravity gradients, but upon the flux generated by the applied suction and the geometry of the suction lysimeter tip. The exact nature of the suction lysimeter samples is therefore not well defined.

The lysimeters at the base of the CPE allow direct measurement of flux-averaged concentration (Parker and van Genuchten, 1984) at the spatial scale of a single lysimeter (2m x 2m) or data can be combined to derive flux-averaged tracer concentration at larger scales up to 8m x 8m. As noted in Chapter 6, these lysimeters are at zero tension, and thus create a zone of increased water saturation in the waste rock immediately above the lysimeters. This may lead to mixing of water from different flow paths within the zone of increased water saturation that may not have occurred in a pile without the lysimeters.

7.4 FIELD METHODS AND DATA ANALYSIS

7.4.1 Rainfall Record and Tracer Application

The CPE was operational in September 1998 and has been exposed to both natural rainfall and artificial rainfall events. A series of artificial rainfall events was conducted between August and September, 1999. On September 24th, a single rainfall event of 53 mm depth and 3 hours duration was labeled with 2100 mg/L chloride as LiCl. At the time of the tracer test, the pile water content and outflow rate was similar to that recorded during typical wet season (July/August) conditions. In our experiment, the initial application of tracer was during a period of relatively high water flow and resident water contents. The application event was also a large precipitation event for the northern Saskatchewan climate. This choice was made to maximize the possibility of activating non-capillary flow paths (Shipitalo and Edwards, 1996). This initial condition likely increased the participation of high flow rate pathways in the initial application event.

Chloride ion was introduced with lithium to reduce disturbance to the geochemistry of the pile due to cation exchange or other geochemical reactions with the weathering sulfide minerals. Data from the tracer test have been analysed up to October 24, 2000. In this period, 154 mm of artificial rainfall has been added in six additional artificial rainfall events and 313 mm of natural rainfall has occurred. Average yearly rainfall at the site is 305 mm with a standard deviation of 76 mm and a maximum of 518 mm (1981-1997 site data).

7.4.2 In-situ and Outflow Water Sampling

In-situ water samples are collected for geochemical and tracer analysis from suction lysimeters located in three instrument profiles (Figure 6.1). These were installed during construction in matrix supported areas of the pile, with a thin paste of silica flour to ensure

good hydraulic contact between the ceramic cup and the granular waste rock. Suction lysimeters installed at 0.2, 0.5 and 1.0 m depth are composed of a 0.022 m diameter x 0.05 m length ceramic cup connected to a 100 mL reservoir. The deep samplers are a 0.05 m diameter x 0.05 length ceramic cup connected to a 500 mL reservoir. During low flow rate periods, suction lysimeters were typically placed under 50 kPa suction, and left overnight. For samples collected during high flow rate conditions, the suction lysimeters were emptied within three hours. The timing of samples was assigned to the mid-point of the sample collection interval. Typical sample recoveries were 20 to 60 mL in the small suction lysimeters and 100 to 300 mL in the large suction lysimeters. Samples could not be collected during winter months from November to March when air temperatures are consistently below 0°C. Sampling restarted in April when near surface waste rock had thawed.

Outflow chemistry in the lysimeter grid was sampled on a variable time scale. Immediately following artificial rainfall events, high frequency sampling of outflow was carried out by directly collecting samples from the sixteen tipping bucket gauges used to the monitor flow rate. Sampling of outflow during lower flow rate periods ranged from daily to weekly depending on flow rate. Between extensive field programs, long-term sampling carried out by site staff was performed tri-weekly or weekly. These samples were collected from a 0.2 L container placed in line after the tipping bucket gauge and therefore represent composite samples of varying duration depending on flow rate. At the lowest flow rates recorded at the end of the five month winter periods (0.1 to 0.2 $Lday^{-1}$), this volume represented 1 to 2 days of outflow.

7.4.3 Data Analysis

Water samples were analysed for dissolved chloride using a modification of the mercuric thiocyanate / ferric nitrate spectrophotometric method for chloride (Standard Methods, 1995) using a Hach 2100 portable spectrophotometer. The high and variable concentrations of other dissolved ions led to background interferences that varied between suction lysimeters and outflow gauges. These interferences were partly removed by adjusting the ratio of reagent to sample to 30:1, to optimize performance over the range of 0 to 400 mgL^{-1}. Interferences were further minimized using calibration standards created by known addition of chloride to samples collected prior to tracer application. Outflow samples from the detailed sampling periods were selected for analysis based upon the rate of change of flow rate and tracer concentration. A total of 4420 outflow samples were analysed, with 900 duplicates. Between 216 and 312 samples were analysed per lysimeter, with an average of 275. Tracer concentration measurements have been processed up to October 24, 2000.

Measurements of outflow rate were calculated from individual tipping bucket outflow tips using gauge specific calibration. Data were linearly interpolated to determine flow rates and cumulative outflow volumes at fixed intervals, every 30 seconds during summer, and every 15 minutes during winter. Water flow data have been processed up to March, 2001. Chloride concentration in the outflow was linearly interpolated between measurements to derive chloride concentration estimates at the same fixed time intervals as the flow rate estimates. Chloride mass flux and cumulative mass were determined using flow rate and chloride data from the individual lysimeters. Tracer mass flux and cumulative tracer mass were estimated by subtracting the background chloride concentrations estimated from samples collected prior to tracer application. Background chloride in outflow was assumed

to be constant. The values for flow rate and cumulative volume in individual lysimeters were combined to form the outflow record of the whole pile. Total chloride mass flux rates from individual lysimeters were combined with cumulative outflow volume data to derive flux-averaged chloride concentration for the whole pile.

7.5 RESULTS AND DISCUSSION

7.5.1 Whole Pile Tracer BTC and Mass Recovery

Figure 7.2 presents the record of precipitation (panel A), the outflow hydrograph for the CPE (panel B) and the flux-averaged chloride concentration in outflow for the whole pile (panel C). Note that the vertical scale in panel B is logarithmic. Artificial rainfall events are shown as darker lines and the date of the tracer application event is indicated. Outflow rates are presented as fluxes ($m^3s^{-1}m^{-2}$) to allow direct comparisons between measurements at different physical scales. BTC's under transient infiltration conditions can also be presented plotted against the cumulative net infiltration, or outflow volume (Wierenga, 1977). In Figure 7.3, the outflow hydrograph (panel A), and the flux-averaged chloride concentration (panel B) are presented plotted against cumulative outflow volume, normalized by cross sectional area and calculated relative to the start of the tracer application. Key events on Figure 7.3 have been labeled with their dates. In this figure it is possible to see multiple arrivals in each hydrograph response that indicate that the hydrograph responses to individual events are composed of the integrated arrivals from several flow paths (Chapter 6). The outflow rate climbed over five orders of magnitude during the wetting up of the pile from April to August, 1999. During this time, water storage depleted by evaporation during construction was replenished. Subsequently, flow rate varies over three orders of magnitude. Background chloride concentration ranged between 24 to 27 mgL^{-1} prior to August, 1999.

Several key features of the BTC can be noted in Figures 7.2 and 7.3. Firstly, tracer reaches the base of the CPE during the application event. The flux-averaged chloride concentration rises quickly to 350 mgL^{-1} within hours of the tracer application, beginning with the first wetting front arrival. At this peak, the discharge is composed of 17% by volume of water applied in the infiltration event (event water). Secondly, the duration of this high tracer concentrations in the first event is short-lived. The flux-averaged chloride concentration peaks early, on the rising limb of the outflow hydrograph (Figure 7.3). The BTC falls much more rapidly than the flow recession curve, reaching an inter-event concentration of ~50 mg L^{-1}, or 1% event water by volume. This result indicates that the outflow in this first event is dominated by water already in storage within the pile, termed resident or pre-event water. Thirdly, during subsequent artificial rainfall events on October 10 and 20 (no tracer input), the flux-averaged chloride concentration again rises sharply with each flow peak, and falls to a progressively higher inter-event concentration during flow recession. These early events indicate that the flux-averaged BTC is composed of outflows from different pathways within the pile that contain tracer in different concentrations. At the start of the experiment, those pathways that contribute a greater proportion of the outflow volume in the earlier parts of the hydrograph response to each infiltration contain higher tracer concentrations. The pattern of the hydrograph and BTC is similar to the conceptual framework discussed in the preceding section.

Lastly, the early pattern of short-lived increases in flux-averaged concentration during peak flow and a gradually increasing inter-event concentration continues until July 18, 2000 at which time the flux-averaged chloride concentration reaches a second experiment peak of 332 mgL^{-1}, or 16% of the applied tracer concentration. After this time, the pattern changes.

A small drop in flux-averaged chloride concentration occurs at the start of each event response, followed by a rise to a peak concentration, and a more gradual fall to the inter-event flux-averaged chloride concentration. The inter-event flux-averaged chloride concentration also begins to decline. Later in the experiment, those pathways that contributed a greater proportion of the outflow volume during earlier parts of response to each infiltration now contain lower tracer concentrations. These issues are discussed in sections 7.5.3 to 7.5.7 using the BTC's from individual lysimeters, where the relationships of tracer concentration and water outflow are more easily demonstrated.

Comparison of Figures 7.2 and 7.3 indicates that several features of the outflow BTC in Figure 7.2 are distorted by the presence of the long winter period from November to May in which there is little infiltration and low outflow flux. This period represents 40% of the time period presented in Figure 7.2, but only 10% of the cumulative outflow in Figure 7.3. Over the winter, the BTC rises from November to January, then declines prior to two increases in April and May, 2000. In Figure 7.3, the changes over the winter period can be seen to be minor contributions to the overall BTC, and the changes in flux-averaged concentration from the small volume rainfall events in the April 2000 become less prominent. In general, plotting the BTC against cumulative outflow (Figure 7.3) better represents the relative magnitude of infiltration events.

There were four larger precipitation events after July, 2000 that led to significant flow responses and rises in the BTC. It should be noted that these events appear to have smaller changes in chloride concentration over the event, but this may be a sampling artifact. These events occurred during tri-weekly sampling of outflow by site staff. This sampling frequency

was not adequate to measure the peak chloride concentrations, which are typically only hours in duration.

The cumulative fraction of applied tracer recovered in the CPE outflow is plotted against cumulative outflow volume in Figure 7.4, reaching 34% by October 24, 2000. The first moment of the tracer pulse has not reached the base of the pile. Also shown along the x-axis are the approximate pore volumes of outflow. This is calculated from the resident pore water volume and the cumulative outflow. Resident pore water volume is not constant as in-situ water contents change rapidly following infiltration events (Chapter 6). Changes of 6 to 7% in water content occur near surface, which reduce to approximately 1% below 1m depth. The pore volumes were calculated by assuming a long-term average water content of 16%, based on monitoring of water contents by TDR. By this method, approximately 0.5 pore volumes of water have flowed through the pile.

The peak slope in the cumulative mass recovery curve is between 0.15 and 0.2 m^3m^{-2}, or 0.3 pore volumes, which corresponds to the peak in chloride concentration in July 2000 (Figure 7.2C). After this time, the cumulative tracer curve flattens out as the inter-event chloride concentration decreases after July 2000. The peak chloride concentration arrives well in advance of one pore volume, and prior to the first moment. The declining concentration of chloride in the outflow after July 2000 implies a gradual decrease in the mass flux that will lead to a long tail on the cumulative breakthrough curve.

7.5.2 BTCs and Tracer Mass Recovery in Individual Lysimeters

The division of the pile base into sixteen contiguous lysimeters allows for investigation of transport at smaller scales (2m x 2m). The BTC's of the sixteen lysimeters are presented in Figure 7.5, plotted as chloride concentration against time. In four lysimeters,

(2,3,7,8), single concentration peaks exceed the maximum scale of 600 mgL^{-1}, and the peak concentration is noted. The cumulative outflow volume varies by a factor of 4 between lysimeters, and plotting the BTC's against cumulative volume makes discussion of specific rainfall events difficult.

The differences in BTC's indicate a wide range of spatial and temporal responses at the 2m scale within the CPE. Varying transport between each lysimeter footprint results from the spatial variability of surface infiltration and the spatial variability of medium properties. The effects of spatial variability on the long-term transport between lysimeters is presented in Figure 7.6. Figure 7.6A presents tracer mass recovery to October 24, 2000, expressed as the fraction of the total tracer mass applied to each lysimeter footprint. Tracer recovery ranges from 11% to 117%, with an average of 34% and a standard deviation of 26%. For comparison, the spatial distribution of cumulative outflow volume is presented in Figure 7.6B. The spatial variation in tracer recovery is much greater than that of outflow volume, but those lysimeters recording the highest outflow volumes generally recover greater tracer mass (Figure 7.6C). For example, lysimeter 6 recorded the highest tracer recovery (117%) and recorded 120% net infiltration, compared to the average of 55%. This indicates substantial lateral transfer of water flow and tracer mass within the CPE. Heterogeneity of material properties at the macroscale (2m) leads to variations in both outflow volume and residence time.

The relative transport in each lysimeter can be illustrated by introducing a dimensionless recovery ratio, Figure 7.6D, which expresses the mass of tracer recovered in a lysimeter as a fraction of the tracer mass applied at surface, divided by the total outflow flux per lysimeter (m^3m^{-2}). Differences in total water volume represents the variation in advective

movement of tracer mass among the lysimeters and is the first-order control of tracer recovery (Figure 7.6B). Variation in the recovery ratio represents the second-order variations in tracer movement caused by differences in dispersive properties between lysimeters. In general, faster flowing, higher volume lysimeters such as 6 and 13 have higher recovery ratios, thus higher dispersion. The effect of dispersion on the tracer recovery can be seen by comparing lysimeters 1, 5 and 9 in Figure 7.6B and Figure 7.6D. They have similar volumes of outflow, but different recovery ratios. Lysimeter 1 has a tracer recovery ratio similar to lysimeter 6. Lysimeters 5 and 9 have opposite rankings of outflow volume and tracer recovery. The mechanisms that govern flow volume, and solute dispersion are weakly linked.

7.5.3 Summary of the Character of Individual BTC's

The high temporal sampling rate of the data collected from individual lysimeters in the CPE provides an opportunity to examine BTC's in greater temporal detail than typical field-scale studies. These can be used to determine the nature of flow mechanisms operating in the CPE, and their variation in space. The character of the BTC's of individual lysimeters at early times, prior to July 2000, can be grouped into three classes (Figure 7.5): (1) lysimeters 2,3,8,12 and 16 exhibit distinct spikes in chloride concentration; (2) lysimeters 1,4, 6,13 and 15 show a rise in tracer concentration to a peak with rising flow rate, which tails off to a gradual rise in inter-event chloride concentration, similar to the BTC of whole pile; and (3) lysimeters 5,9,10,11 and 14 exhibit dips in chloride concentration during the tracer application event, followed by later slow increases. The character of the BTC's after the peak in chloride concentration also involve several classes: (1) lysimeters 3 and 12 continue to exhibit higher chloride during flow events, and rising inter-event chloride

concentration; (2) lysimeters 2,4,5,7,9,10,11,14 and 15 exhibit higher event chloride concentrations, yet gradually decreasing inter-event chloride concentrations; and (3) lysimeters 1,6,8,13 exhibit a third character where rainfall events lead to lower chloride concentrations during peak flows, which return to a higher, but steadily decreasing inter-event chloride. Each of these classes is examined, and the flow mechanisms responsible are identified.

7.5.4 Flow and Tracer Spikes

The first class of early time behaviour is seen in Figure 7.7. This presents the tracer concentration and outflow hydrographs from lysimeters 2 (panels A, B) and 12 (panels C, D), which exhibit distinct spikes in flow rate and tracer concentration at early times. Tracer concentration is presented in the top plots (A, C) and outflow hydrographs in the bottom plots (B, D). The application event and the next two rainfall events of the tracer test are presented, with the September 24, 1999 tracer application event expanded in the inset of each graph. Examination of lysimeter 2 in panels A and B indicates a distinct spike in the flow response prior to the main rise in the outflow hydrograph in each of the three rainfall events presented. The outflow rate rises rapidly within 1.5 to 2 hours of the start of the rainfall event, reaches a short lived peak, and then returns to the outflow rate recorded prior to the rainfall event within 3 to 12 hours. Further changes in the flow rate occur later with the arrival of multiple wetting fronts typically 14 to 48 hours later. This character of response has been observed following both natural and artificial rainfall events in several lysimeters. Tracer concentration during the spike in the flow rate reaches 1124 mgL^{-1} during the tracer application event, and 400 and 253 mgL^{-1} during the following two rainfall events. The tracer concentration falls to the pre-application concentration with the fall in flow rate. The

inter-event tracer concentration does not begin to rise above background until after the October 20th event. In lysimeters 2,3 and 16, the second and third events both contain tracer during the spike in flow rate. A similar spike in flow rate and tracer concentration is seen after 1 hour in lysimeter 12 but the only during the tracer application event, and not in subsequent events.

This response is indicative of flow and transport through a high conductivity pathway, which has little storage capacity, and little exchange of water or tracer with the remainder of the granular matrix. The water which creates the hydrograph response is predominantly composed of event water. These conditions could be met by either water flow down the walls of the experiment or by water flow as surface flow over clast-supported cobbles and boulders. As indicated in Chapter 6, considerable effort was made to prevent wall flow by the inclusion of skirts around the edge of the experiment both above and below ground surface to re-direct water flow back into the waste rock. Flow directly down the wall from above ground is minimized. If water is flowing down the wall, it is being introduced beneath the ground surface, perhaps by ponding on the upper surface of large clasts in contact with the wall. The four lysimeters located in the center of the experiment not bounded by one or more walls did not show this type of early response. The response recorded in lysimeter 12, where tracer only appeared during the application event may indicate wall flow.

The presence of high tracer concentrations in lysimeter 2 during the second and third unlabelled rainfall events indicates some interaction between the water in this pathway and the tracer introduced in the application event. This outflow and tracer response would also be characteristic of non-capillary flow over clast-supported particles with small amounts of

water stored at grain to grain contacts, or on the upper surface of large particles (El Boushi, 1975, El Boushi and Davis, 1969). Non-capillary water flow over larger particles could be generated either at surface by localized ponding, or by sub-surface ponding of resident or event water on the top surface of larger clasts. This latter mechanism would re-mobilize water containing high tracer concentration from near the CPE surface into non-capillary flow paths if the large clast was located near the pile surface. This would generate BTC peaks during the second and third rainfall events which contain significant tracer chloride, as seen in Figure 7.7A.

Calculation of the total outflow volume produced from this pathway indicates approximately 0.1% of the total outflow volume between September 1998 and March 2001 flowed within this pathway, and 1.3% of the total tracer applied was recovered during flow spikes. A waste rock pile with greater than 20% of a sand size fraction can be classified as soil-like (Smith et al., 1995), which indicates that the majority of larger clasts are matrix supported. The grain size analysis of the CPE indicates approximately 25% sand sized (>2mm) grains. Areas of clast-supported texture with no matrix filling voids, were observed during construction. The tracer data suggest that few of these paths reach from the pile surface to 5m depth without interacting or dead-ending within matrix material. Under different circumstances, if surface runoff to clast-supported areas of the pile were to occur, or the fraction of finer-sized material was reduced, then this mechanism may be more important for both infiltration past the evaporative zone and the duration of water-rock contact, which is a fundamental process in the development of water chemistry deeper within the pile.

7.5.5 Tracer Arrival with the Wetting Front

Lysimeters 1,4, 6,13 and 15 show a rise in tracer concentration with the first wetting front arrival, indicating event water was able to flow at the velocity of the wetting front (Figure 7.8). The tracer concentration increases distinctly after each infiltration event in the fall of 1999. The typical maximum tracer concentration reached 100 to 150 mgL^{-1}, or 0.5% to 7% event water at the flow peak. Figure 7.8 presents the tracer concentration (panel A) and the outflow hydrograph (panel B) measured in lysimeter 13 after the tracer application event. The arrival of chloride is simultaneous with the first wetting front arrival (insets). The hydrograph rises sharply, and this arrival has started to recess by the time a second broader arrival can be seen. The arrival of chloride is part of the main hydrograph and chloride is present through the whole hydrograph response. The BTC starts to drop sharply with the second large wetting front arrival, and then levels out to a steadier figure (70 to 80 mgL^{-1}). In Figure 7.8, the first three rainfall events have hydrograph and BTC patterns similar to the conceptual model presented earlier, where the hydrograph and BTC can be explained using multiple flow paths.

Event water containing tracer is able to flow from surface to the base of the experiment during the application event as part of the wetting front. Unlike the spikes in flow rate and tracer concentration described in Figure 7.7, these flow paths are part of the porous medium in the granular matrix. Tracer labeled water accounts for a maximum of 6% of the outflow hydrograph, indicating the majority of the hydrograph response is resident water from within the granular matrix. This BTC response results from macropores, or spatially distinct zones of high conductivity material. As stated before, both of these flow path types are part of the continuum of the heterogeneous porous medium. At the 2m x 2m

scale, there is no way to distinguish the effects of many distributed large pores which would be termed macropores, from the effect of several macroscopic areas of coarser material which would be termed heterogeneity. Both are present in waste rock. What does distinguish these processes is that some of the pores filled during the infiltration event were large enough that the hydraulic conductivity matched the velocity of the wetting front. The cumulative tracer mass arriving in these lysimeters during the application event was 5% of the total mass applied to them.

It can also be noted that the tracer concentration levels out early within the hydrograph response. This flattening of the BTC was found in many of the BTC's and carefully examined. It was often found to correspond to the latest recorded discernable arrival on the hydrograph. This can be explained if tracer mass is lost from these macropores or coarse zones into the surrounding porous medium during the tracer application event. This tracer mass is carried forwards when the later slowing wetting fronts carry through in the finer zones, and leads to the leveling out of the BTC.

7.5.6 No Tracer Arrival with the Wetting Front

In lysimeters (5,9,10,11 and 14), the first response during the tracer application event was a drop in the chloride concentration (Figure 7.4). Figure 7.9A presents the tracer concentration and Figure 7.9B the outflow hydrograph measured in lysimeter 11 before and after the tracer application event. During the tracer application event, the chloride concentration drops from 30 mgL^{-1} to 3 mgL^{-1}. The concentration recovers to pre-event levels within 48 hours of the tracer application, then continues to rise slowly above the background. This response demonstrates that the initial response to the tracer application was composed of water already resident within the pile.

Of particular interest is that the pathways which contributed to the first response of the hydrographs contained resident water with a lower background chloride than the flux-average during low flow rates. As the outflow became dominated by the slower flow paths at the end of the event, the tracer concentration returned to that seen in long term outflow. These data indicate that the resident soil water chemistry is not in equilibrium between different flow pathways. The fast pathways that contributed water early in the hydrograph, macropores or spatially distinct coarse zones, contained resident water which was also contained lower concentrations of dissolved weathering products. It also implies that an assumption of uniform background chloride is not strictly valid, and that separation of background and tracer flux will be difficult when chloride concentrations tail off to pre-application event concentrations.

The longer term behaviour of these lysimeters is slightly different (Figure 7.5). Lysimeters 9, 11 and 14 exhibit a slow rise in tracer concentration, whereas lysimeters 5 and 10 exhibit a more rapid rise in chloride. The BTC of lysimeters 5 and 10 indicate that tracer labeled water reached the base of the experiment in the subsequent two rainfall events. In these lysimeters, the resident water with lower background chloride present within the fastest pathways had only been within the pile for perhaps one or two events, a matter of days to a week, before it was expelled in the tracer application event. Once these faster pathways reached the base, the BTC resembles the conceptual model, and the BTC varies sharply with flux rate.

The longer slower rise in lysimeters 9, 11 and 14 may indicate that the macropores, or coarse pathways activated during the tracer application event, are less active and less significant in subsequent events. Tracer does not break through within the faster pathways in

these lysimeters until the spring of 2000, after several rainfall events. The lower chloride water resident in the fastest pathways during the tracer application event may have been in the pile for a longer time period.

7.5.7 Hydrographs and BTCs from Summer 2000

All of the BTC's presented in Figure 7.5 were examined event by event to determine the relative timing of the changes in the hydrograph and BTC. In all lysimeters, it was observed that the peak concentration gradually occurred later on the rising limb of the hydrograph, eventually corresponding to the hydrograph peak. The peak concentrations were measured in July, 2000, 9 months after the tracer was applied. In our conceptual model (Figure 7.1) this would occur approximately when the peak concentration in the fastest flow paths has moved past the plane of observation. The peak tracer concentration is generated by the flux-average of the outflow rate and tracer concentration in the fastest and medium flow paths.

Figure 7.10 presents the two types of post-peak BTC character. The behaviour typical of most of the lower flux rate lysimeters and the whole pile BTC is shown in Figure 7.10A which presents the BTC and hydrograph for Lysimeter 9 during July to October, 2000. Each event leads to higher chloride concentrations, with the peak of chloride concentration corresponding to the peak in flow rate. The chloride peak is once again tempered by the last arrivals after the flow peak to a steadier inter-event concentration. The overall inter-event concentration steadily declines. In this case, the contributions of declining chloride from the fastest flow paths, and increasing chloride from the medium flow paths average out to a chloride concentration increase over the concentration in the slow pathway at the hydrograph peak. The late arrivals from within the slow pathway are when this pathway contributes the

greatest fraction of mass, and the chloride concentrations level out briefly. The fastest pathways are past the chloride concentration peak and thus when the outflow returns to the longer duration flux-average, the concentration slowly drops.

In lysimeters 1,6,8 and 13, the BTC's changed more after the concentration peak. Figure 7.10B presents the BTC and hydrograph for lysimeter 6 for July to October, 2000. During this period, each rainfall event leads to a decrease in tracer concentration, followed by a return to a steadier tracer concentration during inter-event times. The inter-event tracer concentration drops steadily. In these lysimeters, the peak concentrations have passed in both the fastest and medium flow paths. Their tracer concentrations are below the concentrations in the slower flow paths. Thus, the rising limb and peak of the hydrograph dominated by flux from fast pathways leads to a drop in chloride, followed by a recovery to the concentration in the slowest flow paths.

7.5.8 Summary of Observations from Lysimeter Measurements

The effects of non-capillary flow paths, macropores or spatial heterogeneity and flow in the finer matrix material can all be distinguished with the BTCs from individual lysimeters. Chapter 6 indicates that there are between 3 to 12 discernable wetting front arrivals in each 2m x 2m lysimeter for each rainfall event. When the scale of observation is increased to the whole pile (8m x 8m), there are still 6-15 distinct wetting front arrivals discernable in the hydrograph from individual rainfall events. Many of the BTC features observed in individual lysimeters are also present within the whole pile BTC. The 8m x 8m scale of the whole pile is therefore insufficient to average either flow or transport properties.

7.5.9 In-Situ Tracer Measurements

Figures 7.11, 7.12, 7.13 present the chloride concentrations measured in suction lysimeter samples obtained from instrument profiles B, A and C. These profiles are located above lysimeters 13, 11 and 12 respectively. Only selected sampling dates are presented for clarity. Data are presented as profiles versus depth (panel A). The flux-averaged tracer concentration in the lysimeter underlying the profile is plotted at 5 m depth for comparison. BTC's (panel B) are plotted as tracer concentration at a single depth against the cumulative outflow volume (m^3m^{-2}) from the gravity-drained lysimeter underlying the profile (Russo et al., 1989, Wierenga , 1977). The BTC of the underlying lysimeter is presented in panel C.

The cumulative tracer mass passing each suction lysimeter was estimated from the measured BTC, the background chloride concentration and the cumulative water volume recorded in the underlying lysimeter. The results are presented in panel D. Cumulative recovery is plotted as a ratio to the total tracer applied per lysimeter. Also shown is the total outflow volume from the underlying lysimeter as a ratio to the average outflow, and the cumulative tracer in outflow.

The tracer concentrations and the timings of changes in concentrations from all instrument profiles indicate that water flow is occurring in three dimensions in spatially distinct flow pathways, some of which bypass the suction lysimeters. In profile B, (Figure 7.11) tracer progresses from 0.2m to 1.0 m in an expected fashion, arriving later, with a lower and wider chloride peak (panel B). However, the BTC's at 1.75 and 3.0 m are sharper and higher than at 1.0 m, indicating these suction lysimeters fall within a different flow pathway, with different dispersive characteristics. The outflow BTC (panel C) shows that tracer appears at the base of the CPE during the tracer application event, and peaks when the

suction lysimeter at 1.75 m peaks. The BTC peak at 4.5 m is delayed, implying this suction lysimeter lies within a much slower pathway. The tracer concentration at 4.5 m just exceeds that in the outflow at the end of the analysed period. These data indicate the fastest tracer movements occur in spatially distinct pathways that are not sampled by the suction lysimeters. There is a low probability that a rare, fast pathway will intersect with an instrument location. Similar results were noted for the measurement of water content using TDR (Chapter 6).

Figure 7.11D indicates that the calculated cumulative tracer flux passing some suction lysimeters exceeds the amount applied to the surface above the instrument profile. The concentration of tracer in all of the deeper suction lysimeters is still increasing at the end of the monitored period. Lysimeter 13 recorded the second highest volume of outflow, 1.6 times the average and thus a total tracer recovery greater than the applied mass on the 2m x 2m infiltration surface above the lysimeter can be expected from Figure 7.5C. The calculation of mass flux past near surface lysimeters is only approximate as the water flux past shallow lysimeters may be different from the water outflow at 5 m depth due to lateral movement of water into the footprint of adjacent lysimeters.

In instrument profiles A and C (Figure 7.12 and Figure 7.13), the data more clearly indicate flow in spatially distinct pathways. In instrument profile A, the tracer appears to progress downwards in two distinct pulses (Figure 7.12A). During the tracer application event, tracer appears at 1.75 m and 3.0 m at the same time tracer is recorded at 0.2m (panel 12B). By October 15, 1999 the two pulses are distinct. Tracer concentration rises at 4.5 m, and in the outflow (panel 12C), immediately following the application event. The peak in outflow concentration occurs after the peak in concentration at 4.5 m. However, the tracer

concentration in the outflow is consistently lower than the corresponding concentration at 4.5 m. The cumulative recoveries of tracer mass and total outflow volume (Figure 7.12D) indicate a range of tracer recovery that brackets the ratio of outflow recorded. Tracer recovery in outflow is lower than the tracer flux past any lysimeters. In profile C (Figure 7.13), the profile of tracer concentration has two peaks (panel 13A). Except for the short-lived spike in tracer concentration, tracer concentrations in the outflow do not change until after tracer has been recorded at 4.5 m (panel 13 B). The peak concentration at 4.5 m and in outflow appear to match in time, but outflow is again at a lower concentration than the suction lysimeter at 4.5 m. Figure 7.13D indicates lysimeter 12 reports lower than average outflow volume, and lower than average tracer recovery by the suction lysimeters and outflow lysimeter. The cumulative mass flux is similar to instrument profile B, where the outflow recovery is much lower than the recovery at 4.5 metres.

The tracer mass stored within the CPE can be calculated using the profile data in panel A of Figures 7.11, 7.12 and 7.13. Stored tracer mass was calculated from the measured chloride concentration, the estimated background chloride concentration and estimated soil water content. Water content is variable in response to infiltration events, but an approximate value of 0.1 was applied from surface to 1m depth and 0.16 after 1 m, based upon long term monitoring using TDR. The qualitative character of this calculation is insensitive to allowing water content to vary by the range recorded in TDR measurements. A second estimate of tracer mass in the CPE was determined by subtracting the calculated cumulative tracer mass in outflow from the original applied mass. The ratio of these estimates is shown in Figure 7.14. The ratio initially rises up to 8 in profile A and 3.5 to 4 in profiles B and C. It then falls below 1 in profiles A and C by October, 2000.

When the measured concentration from the suction lysimeters is assumed to apply to all the resident water, a volume-average sample, the stored mass is overestimated. This can be compared to the estimates of tracer mass flux past the suction lysimeters in panel D of Figure 7.11, 7.12 and 7.13. Within each instrument profile, the mass flux estimates calculated for individual suction lysimeters either bracket, or overestimate the calculated mass flux in outflow. The tracer concentrations derived by the suction lysimeters are therefore closer to flux-averaged samples.

The calculation of stored mass also indicates that the tracer is unevenly distributed at the pore scale within the water resident in the granular waste rock. In order to match the calculations of stored tracer mass based on the suction lysimeter data and the BTC data, the tracer concentrations determined from suction lysimeter data would only be representative of $1/8^{th}$ to 1/4 of the 16% by volume average resident water content around the suction lysimeter tip. As discussed previously in this section, the suction lysimeters collect a sample that is closer to a flux-averaged tracer concentration. The tracer mass flux is therefore dominated by a small fraction of the pore space, representing those pores with the highest hydraulic conductivity.

It was also noted in Section 7.3.6, that suction lysimeters collect a biased sample. Early in the tracer test, the largest, highest conductivity pores contain higher tracer concentrations than the flux average passing the suction lysimeter elevation. The flux created by the suction lysimeter is greater than the natural flux, and therefore the suction lysimeter samples a greater water fraction from the larger pores than the flux averaged concentration under a natural gradient. The calculation of mass flux past the lysimeter therefore uses the total water flux resulting from the true head gradient, multiplied by the

tracer concentration in the most mobile pathway only. This leads to an overestimation of tracer mass flux. Hence, the cumulative tracer mass recoveries shown in panel D of Figures 7.11, 7.12 and 7.13 indicated lower cumulative recovery in outflow compared to the flux past the suction lysimeters at the base of the pile. Later in the event, the tracer concentration within water flowing in the larger pores has already started to decline, similar to Figure 7.10. When the estimate of stored mass falls below 1 in Figure 7.14, this indicates the most conductive pore space sampled by the suction lysimeters are now relatively free of chloride compared to the overall distribution of chloride in the remaining pores.

The long time period (1 year) over which these changes in the estimates of stored mass occur indicates that the uneven tracer distribution at the pore scale persists over a long time scale. During transient infiltration, the passage of each wetting front changes the geometry of the saturated pore space as the water content increases. The mixing between the water contained within the smallest pores and the largest pores is thus slow.

Suction lysimeters are commonly used to determine the geochemistry of drainage products at existing waste rock piles. These results indicate that the samples obtained from suction lysimeters must be treated with caution. In heterogeneous waste rock, the water obtained is not representative of the fastest moving pathways within the granular matrix, nor any flow over clast-supported cobbles and boulders. These pathways are unlikely to be intercepted by any single instrument. Furthermore, the samples obtained are more representative of a flux-averaged concentration, than a volume-averaged concentration. If a total dissolved contaminant inventory is being compiled to determine long term drainage from a waste rock pile, suction lysimeters are poor (non-conservative) estimators of volume averaged concentration, or total stored dissolved mass of weathering products.

7.5.10 Residence Time Estimates

The tracer test data can be used to derive estimates of the velocity of the first moment of the tracer pulse which can be used to derive average residence time. Residence times can be estimated from: net infiltration; BTC curves from suction lysimeters; and tracer BTC's at the base of the CPE.

Average residence time for the CPE can be determined from the average annual average rainfall rate (303 mm, 1981-1997 average), average net infiltration under natural rainfall conditions (55%, Chapter 6), and using an average water content of 0.1 in the upper meter, and 0.16 in the lower four meters. The average residence time calculated is 4.4 years. Using the rainfall rate recorded during the first year of the tracer test, 487 mm, the estimated residence time is 2.8 years. This estimate assumes water moves by piston flow through the whole water content, which is in conflict with the estimates of resident tracer mass (Figure 7.14), which indicates tracer movement is dominated by a limited fraction of the pore water.

BTC data from suction lysimeters were examined to determine the cumulative outflow flux at the peak in concentration, and the cumulative outflow flux at 50% of the recovered mass or the first moment. The peak concentration always preceded the first moment, indicating preferential flow behaviour in the monitored pore fraction and non-Fickian dispersion. The cumulative outflow flux from the first moment was used to determine the cumulative outflow flux required for the first moment to reach 5 m depth. This was converted to a residence time by application of the average annual rainfall, and the estimated net infiltration rate. The result is presented in Figure 7.15, as estimated residence time against depth of sensor. It should be noted that the cumulative outflow used is that measured from the underlying lysimeters, which includes any lateral re-distribution of water.

Data from deeper sensors are more consistent, and indicate a residence time from 0.7 to 1.0 years in profiles A and C, and 4.7 years for profile B. The samples derived from suction lysimeters are biased towards the more mobile fraction of the water content, and therefore will generally underestimate residence time. The residence time estimate for profiles A and C is between 25% and 35% of the estimate from net infiltration. This is in general agreement with the discrepancy in stored tracer mass estimates which indicated 12 to 25% of the resident water content dominated tracer transport.

Data from sensors near surface, 0.2 to 1.0 m depth, indicate much higher estimated residence times. This is likely due to a variety of factors. The flux past shallow lysimeters may be poorly represented by the basal outflow in the underlying lysimeter, as the degree of lateral re-distribution of water is unknown. The shallow suction lysimeters are also within the zone of greater changes in water content due to infiltration and evaporation. During the initial infiltration of the tracer application event, water infiltration is driven by both gravity, and the capillary gradient. Early time infiltration is dominated by the sorptivity of the soil, and tracer labeled water will enter into storage depleted by near surface evaporation. Later in the infiltration event, water infiltration is dominated by gravity forces, and the infiltration capacity. That water taken up by initial sorptivity may remain longer in the near surface zone where further repeated evaporation and infiltration causes greater mixing of chloride between different pore sizes during wetting and drying cycles. Similarly discrepancies between lower near surface velocities, and higher velocities at depth have been found in other studies (Schulin et al., 1987; Butters and Jury, 1989). The wider variations in water flow velocity created by varying conditions near surface are damped with depth, and more steady water flow occurs (Destouni, 1991).

A third preliminary estimate of residence time can be obtained from the outflow BTC's. Estimation of the arrival of the first moment is difficult for individual lysimeters because the final tally of total mass reporting to each lysimeter is not known. An estimate can only be derived for the whole pile. Visually estimating an extension to the BTC in Figure 7.4 indicates an approximate arrival of the first moment at 0.5 to 0.65 m cumulative outflow flux, which corresponds to 1.8 to 2.4 years at the higher rainfall rate over the tracer test, or 3.0 to 3.9 years at the lower longer term average. This preliminary estimate favours an earlier arrival of the first moment under current infiltration conditions than indicated by the assumption of piston flow. The residence time estimate is quite close to the estimate of 2.8 years assuming piston displacement at the current rate. The actual transport occurring in the CPE is therefore not as rapid as would be suggested by the limited water content participating in transport suggested by Figure 7.14. This confirms that the suction lysimeters sample only a mobile fraction of the true tracer mass located within the CPE.

7.6 CONCLUSIONS

The tracer test was conducted to determine the physical mechanisms of flow governing the movement of water, and to determine the residence time distribution of water within the CPE. The tracer test has revealed the following:

- The hydrographs and BTC's of individual 2m x 2m lysimeters monitor the integrated arrivals of flow and tracer from multiple flow paths.
- The hydrograph and BTC of the whole pile, 8m x 8m, still contains evidence of multiple flow paths.

- Some of these flow paths are not dominated by capillary forces, and have little interaction with the granular matrix. These contribute a small proportion (<0.1%) of the total outflow.
- Some event water is able to flow 5m with a single rainfall event. This water flows within macropores or spatially distinct zones of coarser material, and proceeds at the same velocity as the wetting front. This water accounts for ~5 % of the outflow of larger rainfall events.
- The majority of the water (>90%) in outflow as the result of any individual rainfall event is pre-event water.
- During a transient tracer test, the contributions of different flow paths are temporally separated. Fast flow paths contribute more to the flux average soon after a rainfall event and slow flow paths contribute more later in the flow response. The interval between outflow samples must be flux-determined, not temporally determined. Long term monitoring of the water quality of outflow from the base of a waste rock pile (such as a in a toe-drain) on a daily or weekly basis will not represent the long term flux-average.
- Observations of tracer movement from in-situ samplers indicates that preferential tracer transport occurs both in spatially distinct areas of coarse material (macro-scale heterogeneity) and at the pore scale by the dominance of large pores in the water and tracer fluxes.
- The suction lysimeter data indicate that these samplers do not collect unbiased samples. The samples are closer to flux-averaged samples, but are biased towards the more mobile water fraction of the flow path in which the instrument is located. The fastest flow paths are likely bypassing the instrument locations. Estimates of transport properties derived

from suction lysimeter samples would lead to an overestimation of first breakthrough, and an underestimation of average residence time. The interpretation of the geochemistry of water samples collected from in-situ suction lysimeters must take this sample bias into account.

- Water contained in spatially distinct flow paths caused by porous medium heterogeneity at the field scale have different residence times, and hence different chemistry. At the pore scale, within the spatially distinct flow pathways, water in larger pores has a different chemistry than water in smaller pore spaces. The water chemistry of the outflow at the base of pile is the flux-average of the water chemistry resident within the pile. Water chemistry will change with flow rate as the proportion of the flux-average changes.
- Mean water residence time is 1.8 to 2.4 years at the rainfall rates occurring during the tracer test to date. This corresponds to 3.0 to 3.9 years at the average annual rainfall rate. The residence time distribution is expected to have a long tail.

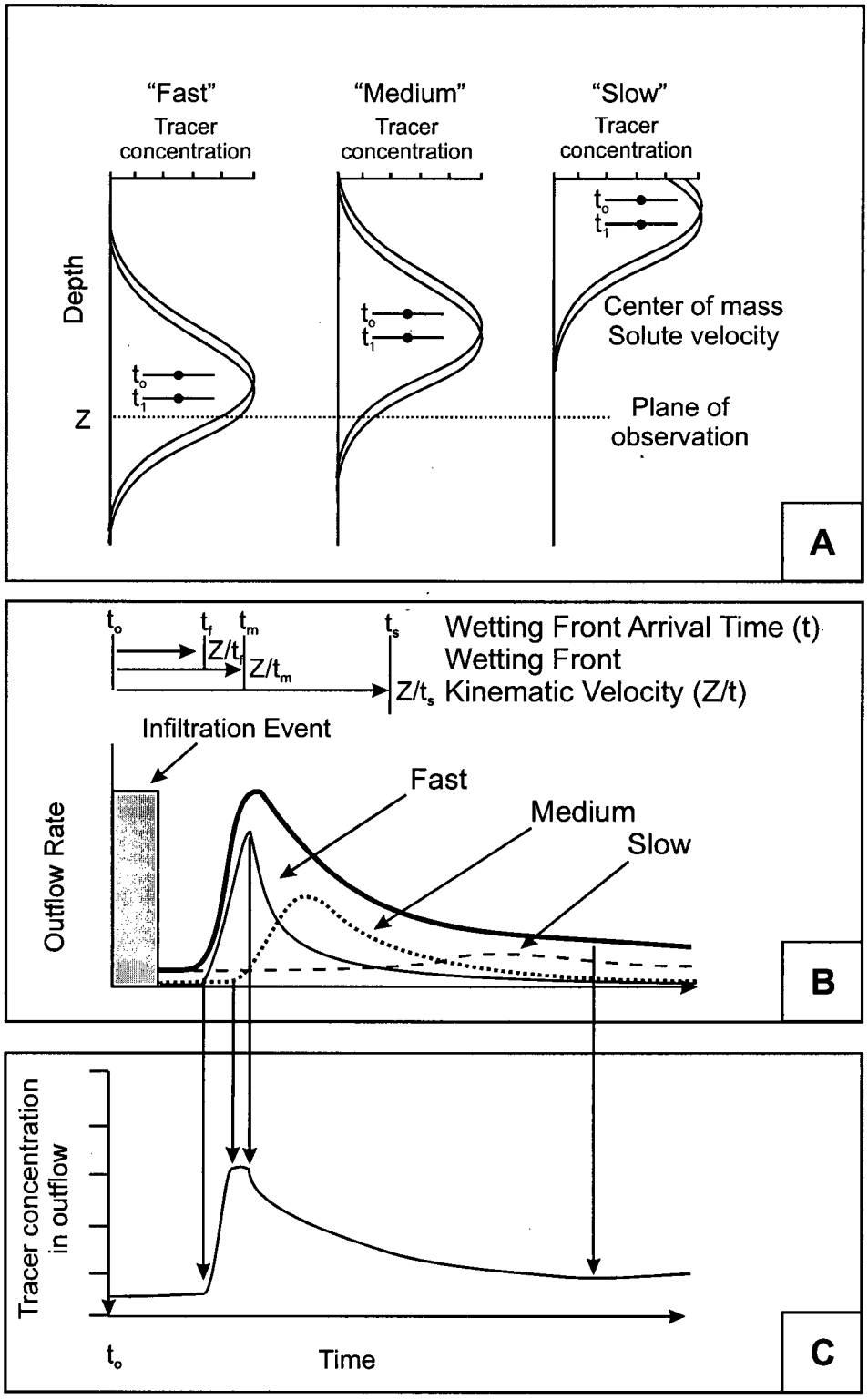

Figure 7.1: Conceptual framework of transient water and tracer movement in unsaturated heterogeneous porous media: (A) In-situ tracer profiles; (B) Outflow hydrograph and (C) flux-averaged tracer concentration in outflow.

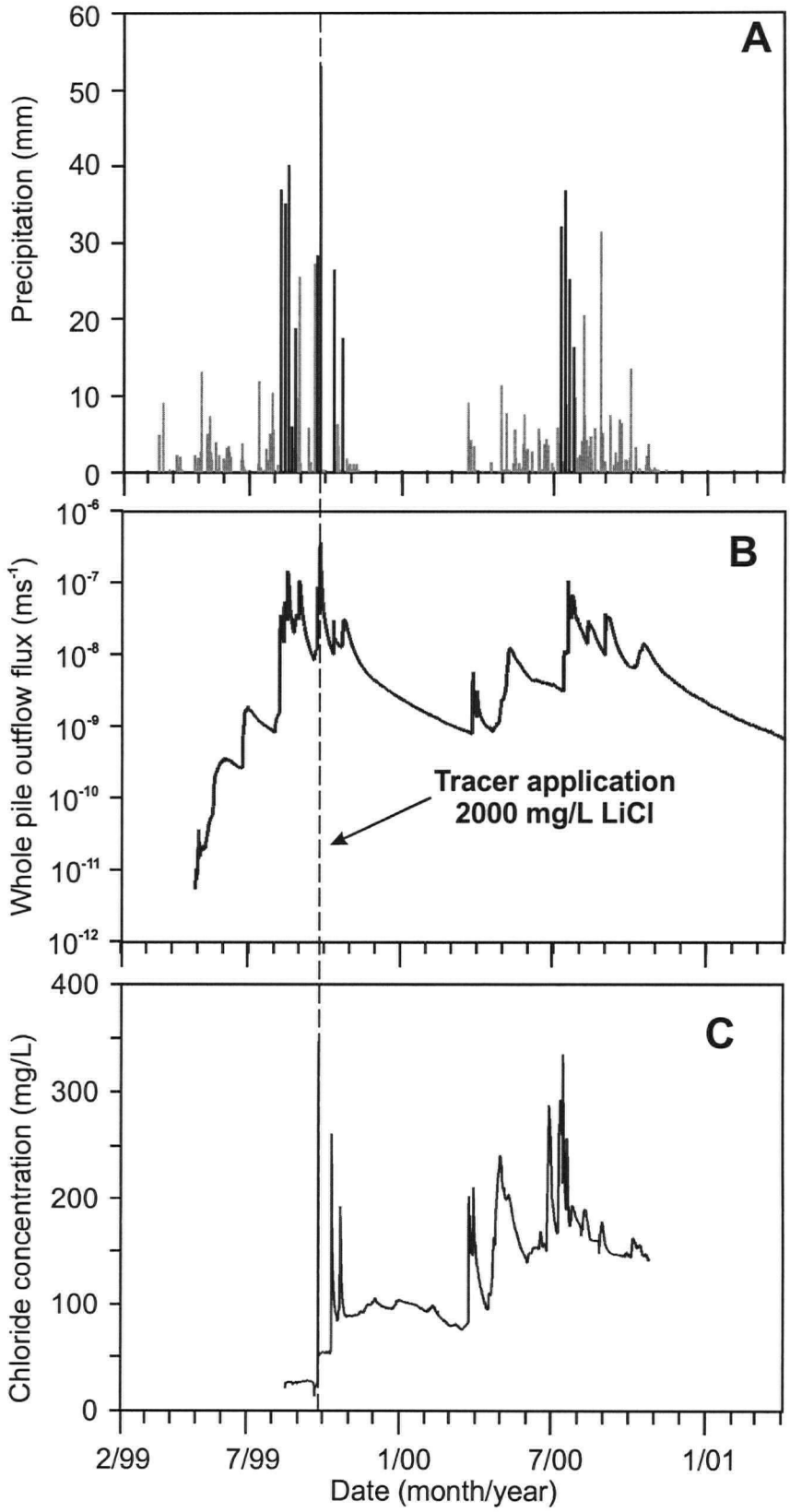

Figure 7.2: Precipitation (A), outflow flux rate (m s^{-1}) (B) and flux-average tracer concentration (C) plotted against time for the experimental period from February 1999 to March 2001.

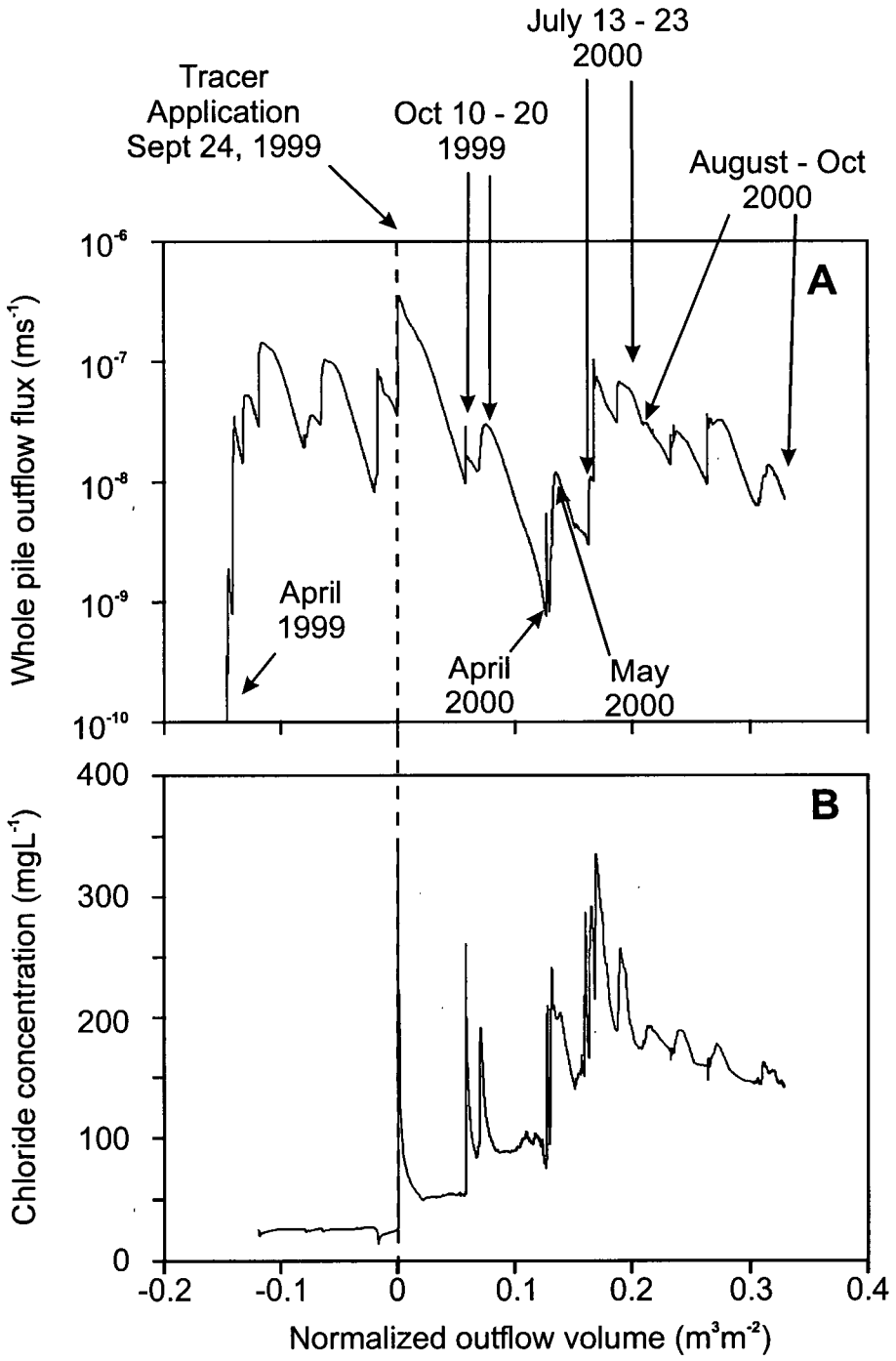

Figure 7.3: Outflow flux rate (m s^{-1}) (A) and flux-average tracer concentration (B) plotted against cumulative outflow volume normalized to cross sectional area, and zeroed at the tracer application event. The experimental period from February 1999 to March 2001 is shown.

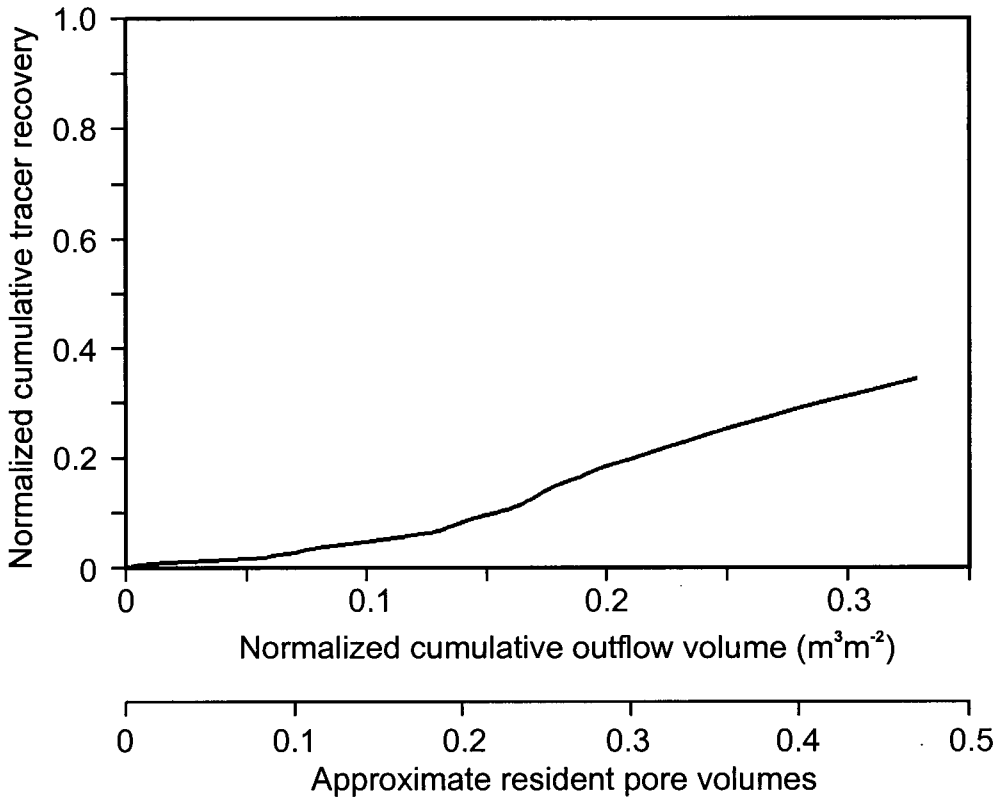

Figure 7.4: Cumulative tracer recovery in outflow of the whole CPE experiment, normalized to the mass of applied tracer.

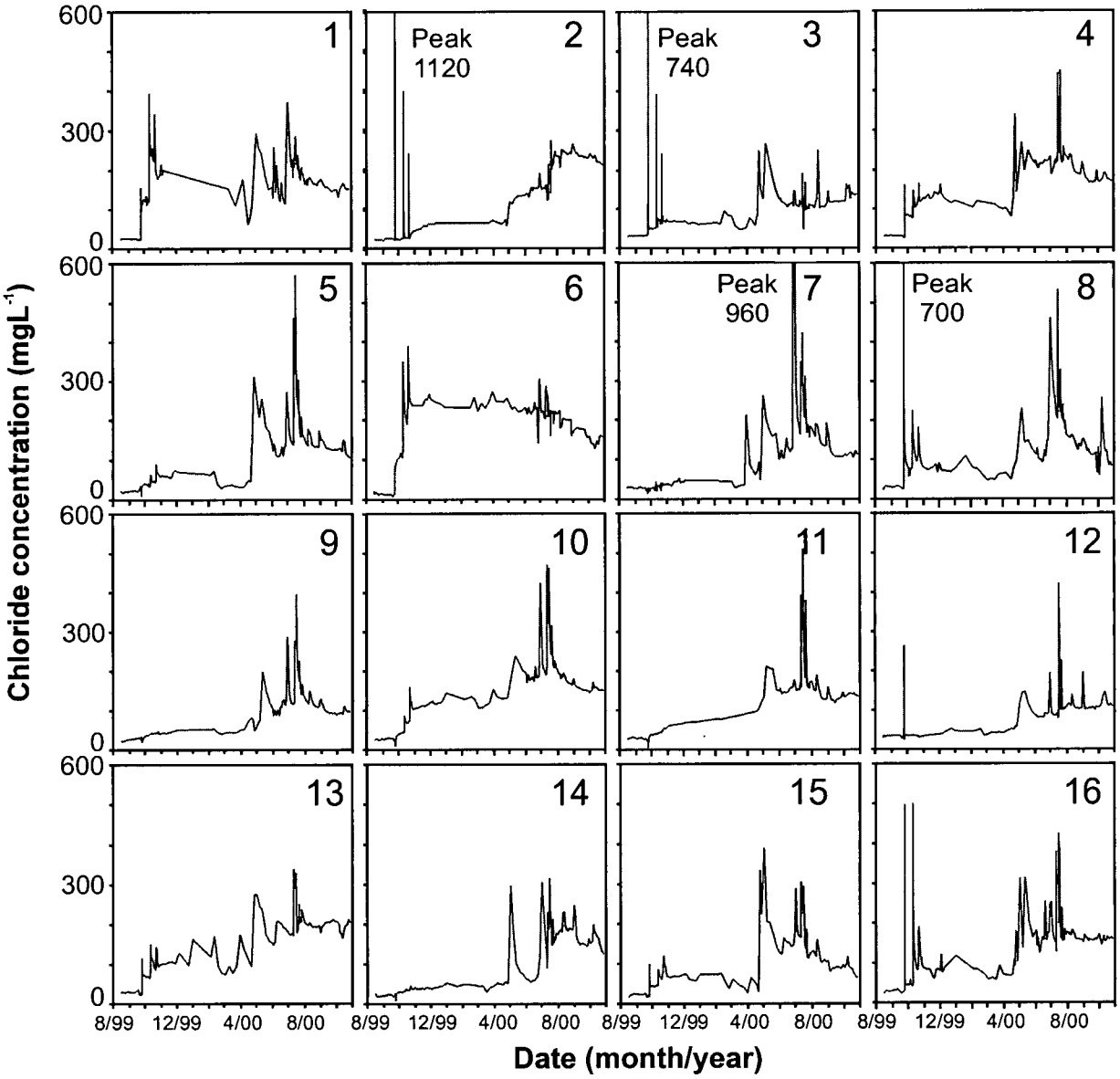

Figure 7.5: Chloride concentration in outflow plotted against time for the grid of sixteen contiguous lysimeters at the pile base.

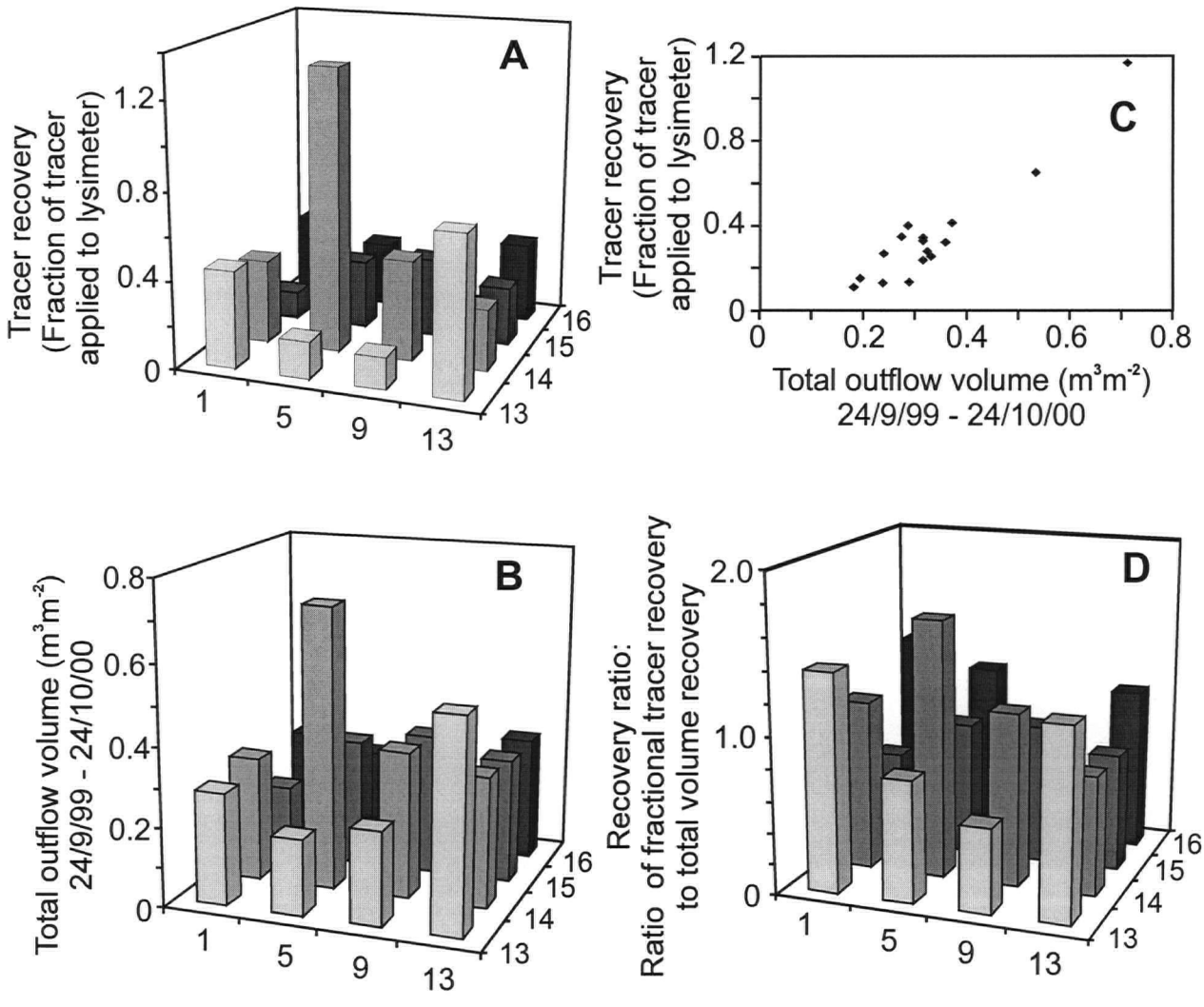

Figure 7.6: Spatial variation of tracer transport. Spatial variation in tracer mass recovery (A) and normalized outflow volume (m^3m^{-2}) (B) by lysimeter. Fraction of tracer mass recovered recovered plotted against total outflow volume (C). Spatial variation in the recovery ratio: the fractional tracer recovery divided by the normalized volume per lysimeter (m^3m^{-2})(D).

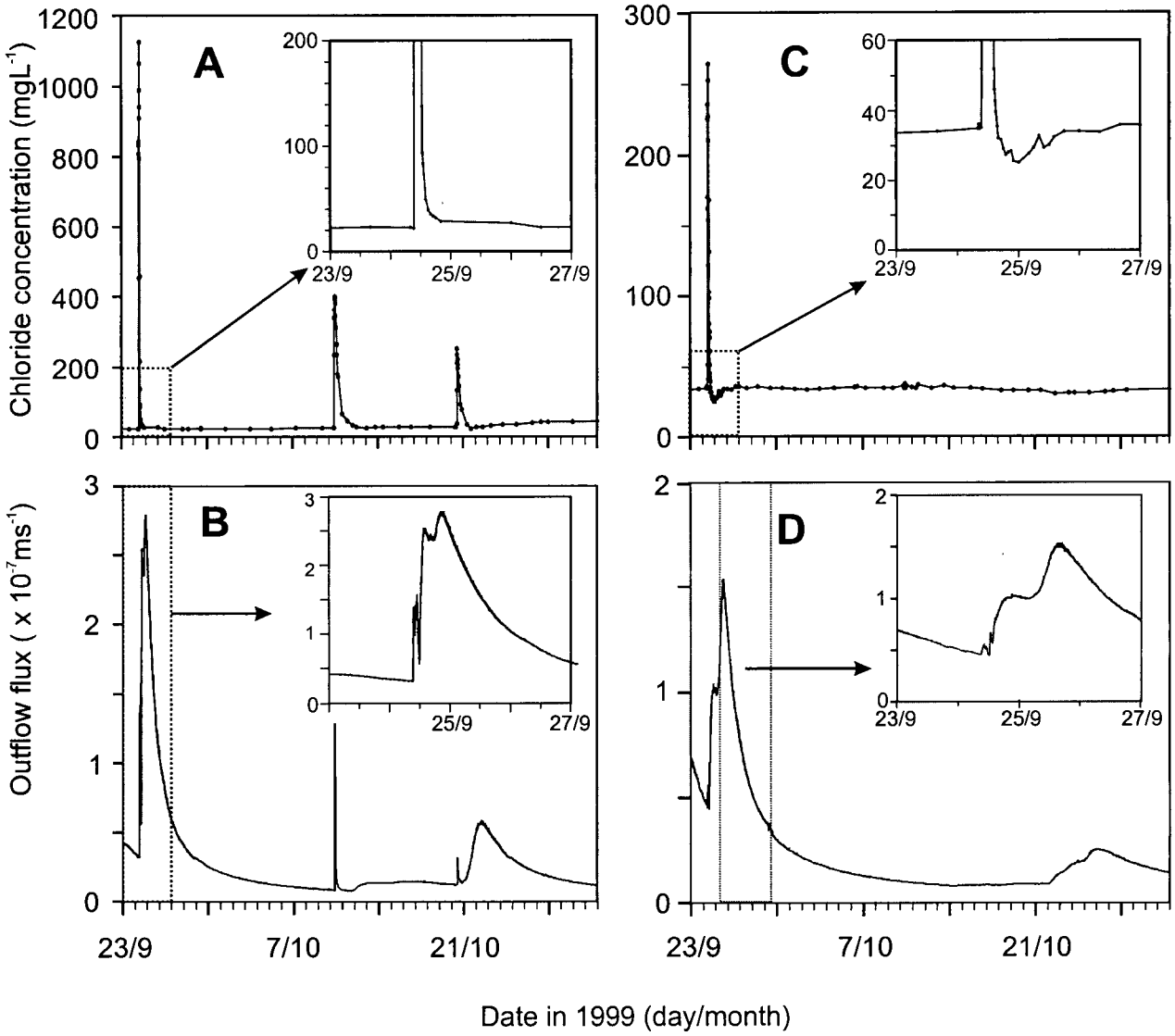

Figure 7.7: Breakthrough curves (A, C) and outflow hydrographs (B, D) for lysimeters 2 (A, B) and 12 (C, D) for the tracer application event, and two following events. Data from the tracer application event is expanded in the inset graphs.

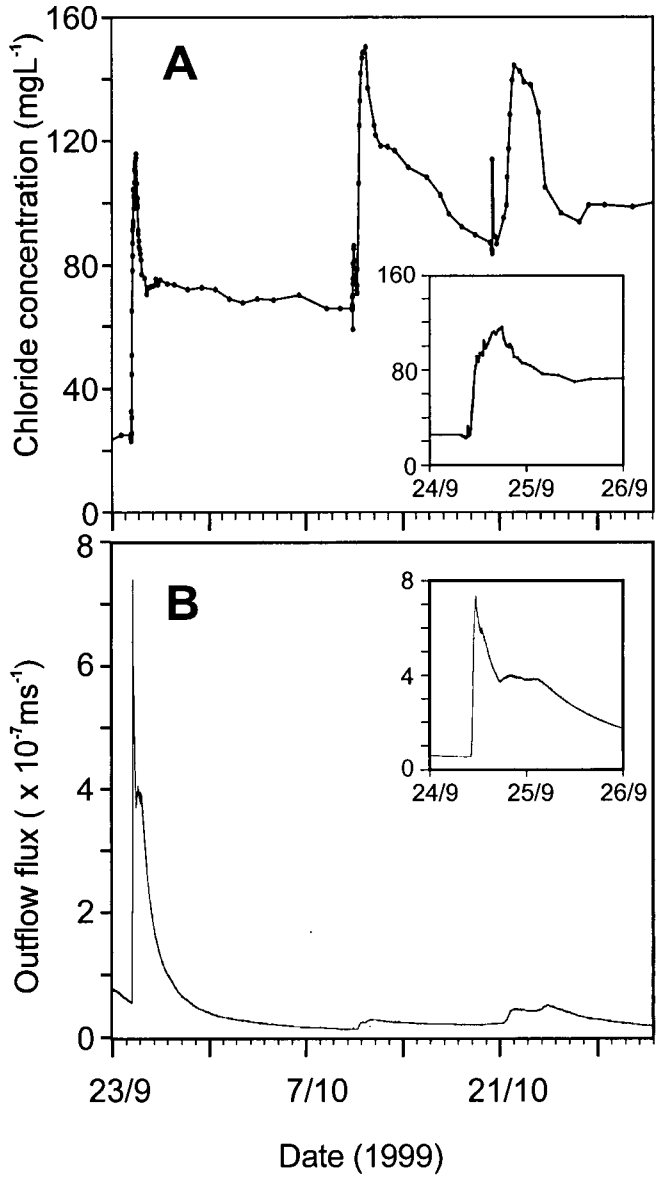

Figure 7.8: Breakthrough curve (A) and outflow hydrograph (B) for lysimeter 13 for the period of for the tracer application event and two following rainfall events. Data from the tracer application event is expanded in the inset graph.

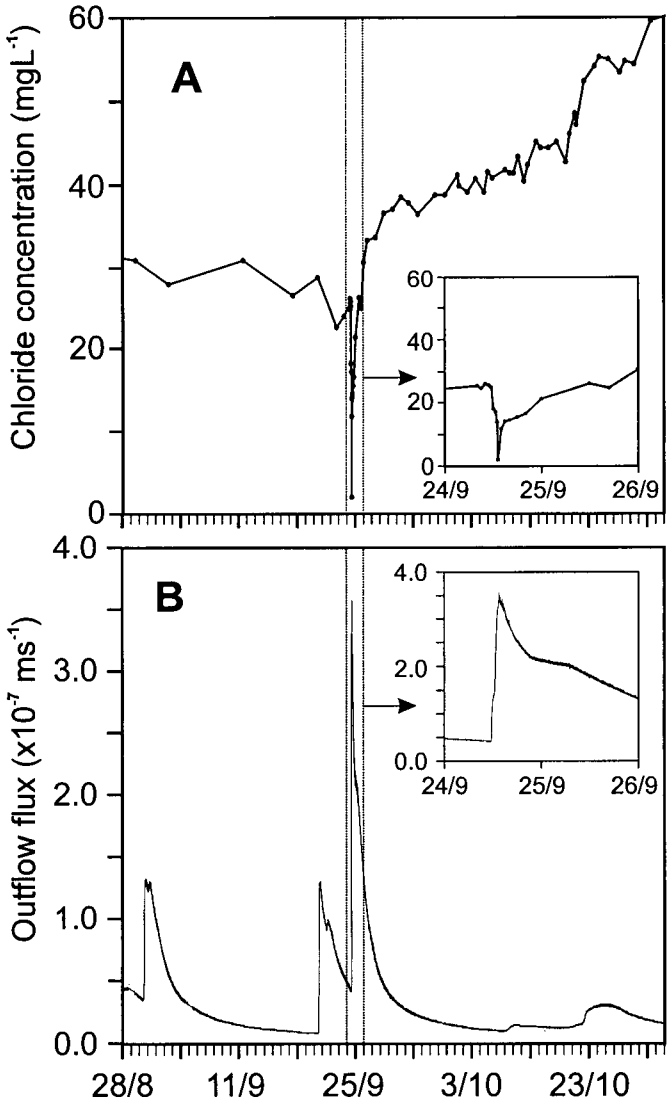

Figure 7.9: Breakthrough curve (A) and outflow hydrograph (B) for lysimeter 9 for the period of August 28 to November 1, 1999. Data from the tracer application event is expanded in the inset graph.

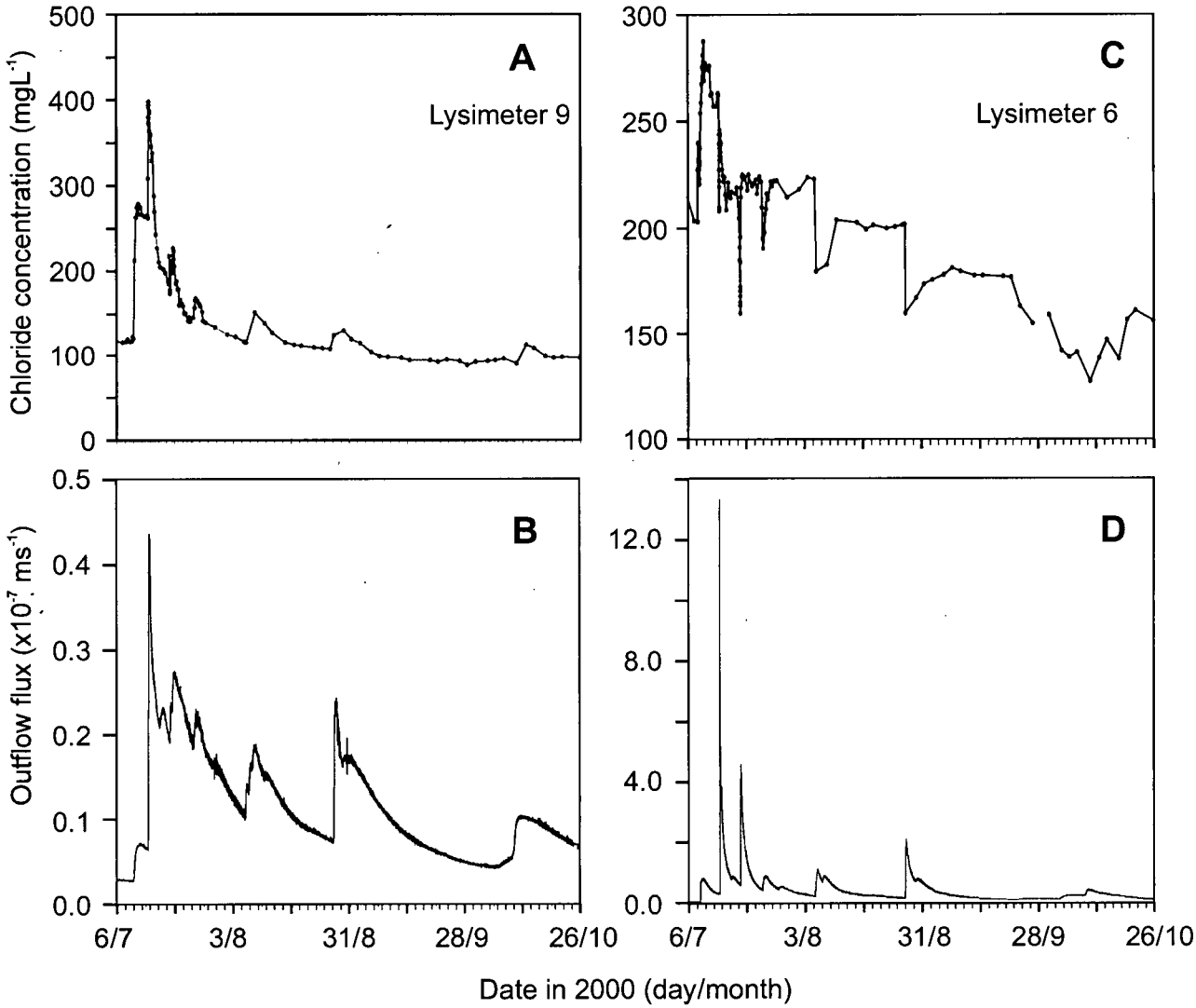

Figure 7.10: Breakthrough curves (A, C) and outflow hydrographs (B, D) for lysimeters 9 (A, B) and 6 (C, D) for the period of June 6 to October 26, 2000.

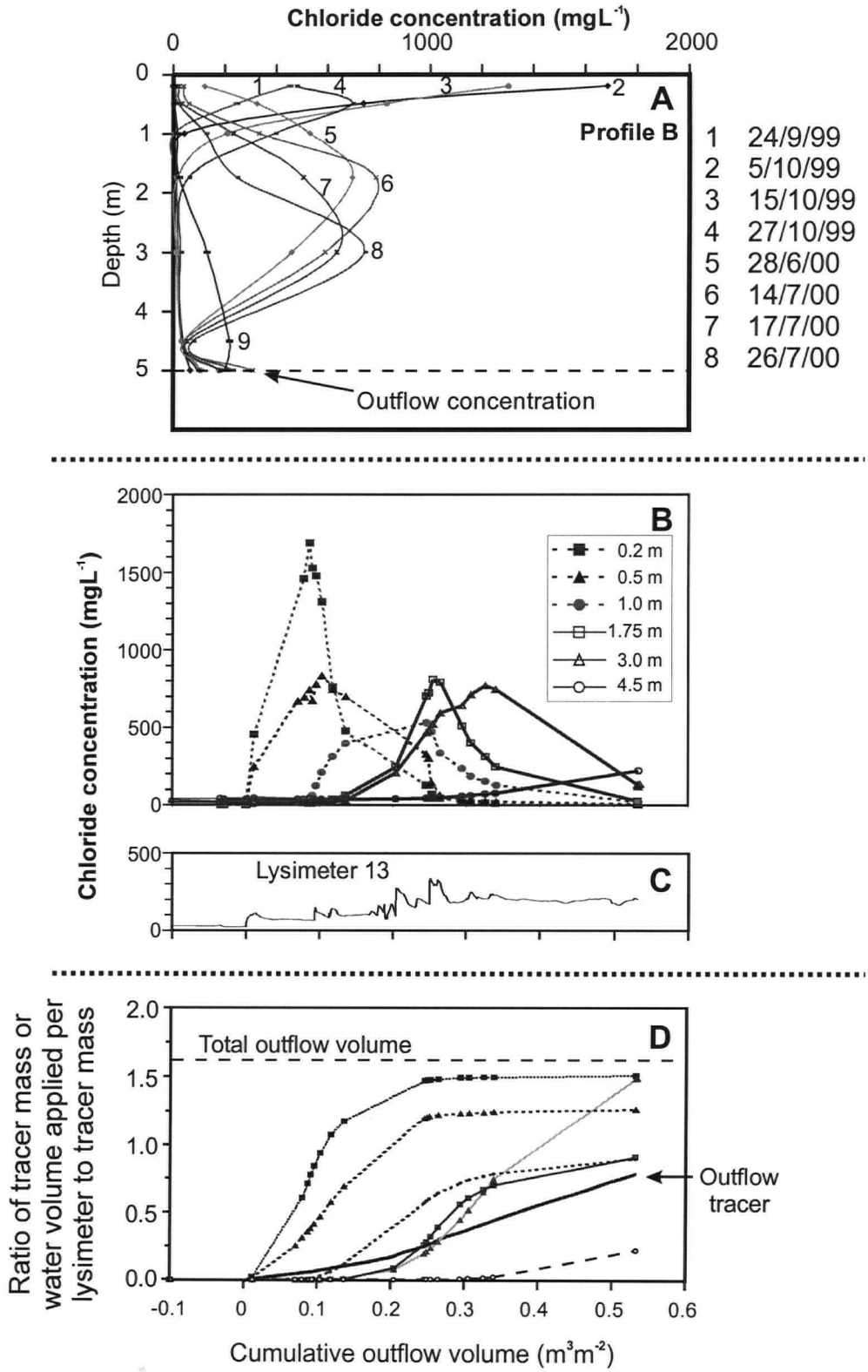

Figure 7.11: Tracer data from in-situ suction lysimeters located in instrument profile B: plotted as profiles (A); breakthrough curves (B); tracer concentration in outflow (C); and cumulative tracer recovery as the ratio to tracer applied (D). Cumulative recovery of outflow volume (D - dashed line) and cumulative recovery of tracer in outflow (D- heavy line).

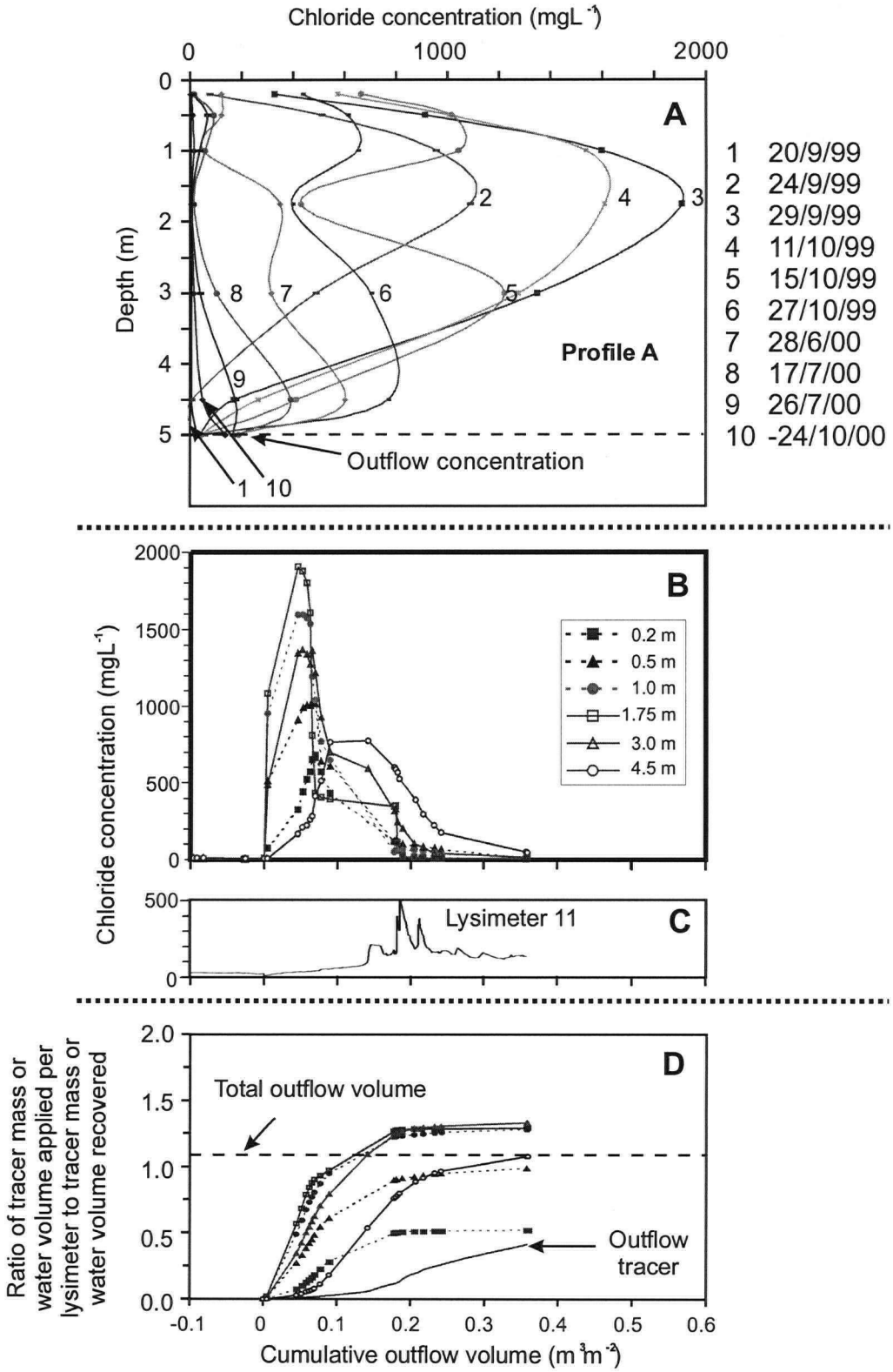

Figure 7.12: Tracer data from in-situ suction lysimeters located in instrument profile A: plotted as profiles (A); breakthrough curves (B); tracer concentration in outflow (C); and cumulative tracer recovery as the ratio to tracer applied (D). Cumulative recovery of outflow volume (D - dashed line) and cumulative recovery of tracer in outflow (D- heavy line).

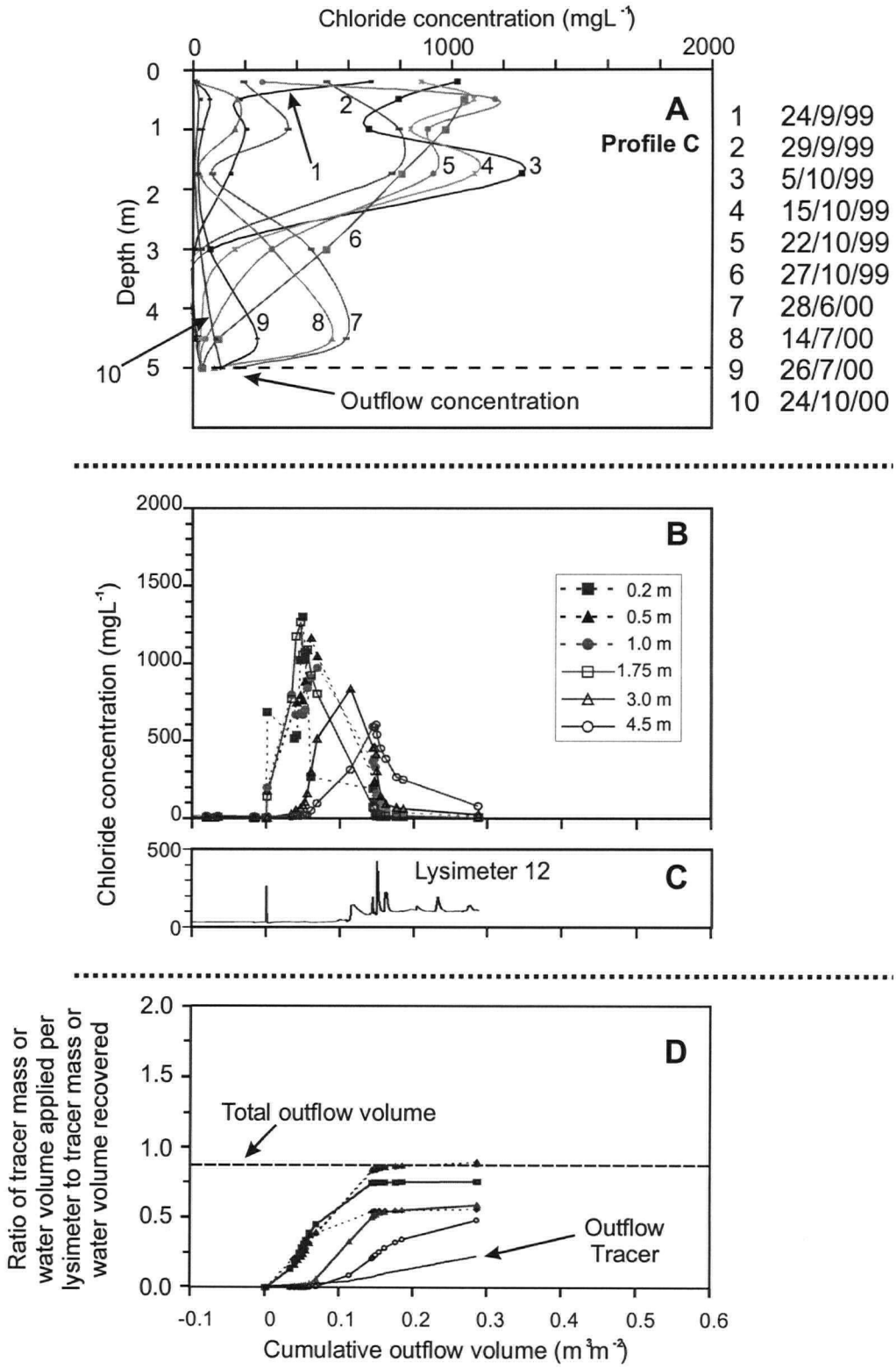

Figure 7.13: Tracer data from in-situ suction lysimeters located in instrument profile C: plotted as profiles (A); breakthrough curves (B); tracer concentration in outflow (C); and cumulative tracer recovery as the ratio to tracer applied (D). Cumulative recovery of outflow volume (D - dashed line) and cumulative recovery of tracer in outflow (D- heavy line).

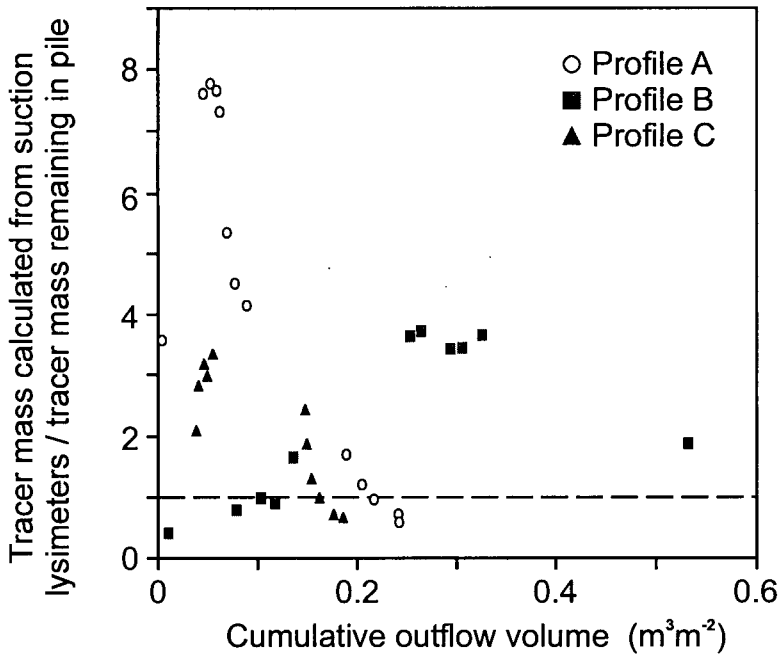

Figure 7.14: Comparison of tracer mass estimates from suction lysimeters and lysimeters for the three instrument profiles A, B, and C located above lysimeters 11, 13 and 12 respectively. Ratio of total tracer mass remaining in CPE estimated from suction lysimeter samples, divided by tracer mass remaining determined from tracer

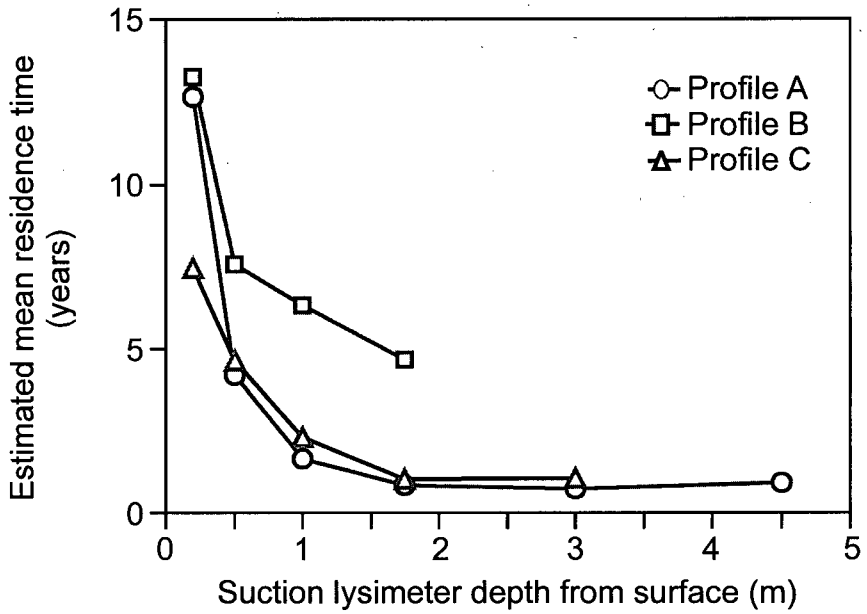

Figure 7.15: Estimated mean residence times from suction lysimeter data. Estimated residence time (years) derived from the velocity of the first moment, and estimated annual net infiltration. Plotted as a function of suction lysimeter depth.

CHAPTER 8: SUMMARY AND CONCLUSIONS

The primary purpose of this research is to fill an identified gap in the knowledge base required to address the issue of low quality drainage from coarse grained mine waste materials. The lack of understanding of flow mechanisms is the largest of the difficulties facing efforts to predict the loadings of weathering products to the environment. The main contribution of this research is therefore the data collected and the interpretation of the water flow and solute transport in the constructed pile experiment.

In addition to the water flow and transport data that was obtained, a large range of water and rock samples have been collected for the analysis of the evolution of the geochemistry of the leaching process. The field work to collect this data was undertaken as part of this research, but the analysis of these samples falls outside the scope of this thesis. When these data are analysed, further insight will be possible into the linkage between water flow, residence time, water rock interaction, and the leaching of weathering products to the receiving environment.

Several specific research objectives were outlined in the introduction to this thesis. Summaries of the results of this research that addresses these questions are presented below.

8.1 DURATION OF INITIAL WETTING PHASE

The duration of the wetting period following construction of a waste rock pile was addressed in Chapter 2. The waste rock used for the CPE was subjected to evaporation when it was moved and placed within the experiment. The data from the CPE indicate that one year's net infiltration was required for the pile to re-equilibrate. This period will vary with the initial water content of the waste rock, the weather conditions during deposition, and the

weather conditions post-deposition. The wetting up period of any large experiment can be expected to be long.

8.2 HOW ARE PHYSICAL PARAMETERS BEST MEASURED?

The measurements discussed in this thesis included water content, matric suction, material characteristic curves, and the use of suction lysimeters and lysimeters. The research presented has demonstrated that the measurement of representative physical parameters in waste rock is challenging.

This research has confirmed that TDR probe designs incorporating a resistive coating are sufficient to collect measurements of travel time within a waste rock environment. However, the data presented in Chapters 3 and 4 also indicated that measurement of travel time alone may not be sufficient to properly determine water content in materials such as waste rock, with high electrical conductivity soil water solutions. Further work is required using frequency domain analysis of the collected waveforms.

The thermal conductivity sensors tested during the operation of the constructed pile were found to be unsuccessful for measuring matric suction in the CPE waste rock environment. They would be successful in other soil environments and details of these findings were outlined in Chapter 5. Measurement of matric suction using tensiometers was more successful. The data from the constructed pile experiment indicate that soil water suctions in waste rock are likely to be low deeper within the pile, beneath the immediate pile surface. These matric suctions are within the range of tensiometers.

The data presented in Chapter 6 indicate that both laboratory and in-situ estimates of soil water characteristic curves for the CPE waste rock were difficult to interpret. The laboratory measurements did not preserve the field texture of the waste rock, and the in-situ

data was hampered by the short duration of rainfall events, and material heterogeneity at small scales. Both measurements indicate that short-duration changes of water content and matric suction occur on wetting and drying scanning hysteresis curves.

Chapters 6 and 7 found measurements of water content and matric suction within the pile poorly represent the progress of wetting fronts through the pile. In-situ instruments did not monitor the fastest flowing pathways within the pile, and a significant proportion of outflow occurs prior to any change in monitored water content. Monitoring water content and matric suction in waste rock is therefore not likely to be able to determine net infiltration and would likely underestimate the true net infiltration. Further work must be undertaken to numerically simulate the movement of water within waste rock using the measured parameters to determine the magnitude of the discrepancy.

The analysis of tracer data in Chapter 7 indicated that it is problematic what water fraction was extracted using in-situ suction samplers. They were found to sample the most mobile water fraction contained in the largest pore sizes surrounding the lysimeter tip. However, the suction lysimeter locations were bypassed by faster flow. They thus sample a small fraction of the water present, and more closely resemble a flux-average of the water chemistry within the pile.

The data derived from the basal lysimeters were more useful. The analysis of the success of in-situ instrumentation Chapters 6 and 7 indicated that these were successful in determining net infiltration, when lysimeters were large in size. The lysimeters derived flux-averaged water outflow chemistry.

8.3 WHAT PARAMETERS ARE CRITICAL? WHAT IS THE DEGREE OF SPATIAL VARIABILITY OF FLOW?

The mixed success of in-situ instrumentation indicates the need to determine net-infiltration, or further data on water movement in waste rock using lysimeters. Several indications are given in this experiment to guide future installations. The variability of outflow volume and residence time between 2m x 2m lysimeters, as presented in Chapters 6 and 7, indicates that the infiltration of water into uncovered waste rock is not well monitored by only a few small lysimeters. Variation in net infiltration was found to range by a factor of four, from 30% to 121% of precipitation. Analysis of the hydrographs for the whole pile have indicated that lysimeters greater than 8m x 8m are required to monitor uncovered waste rock. Such large experiments can be expected to require a long wetting up period due to the disturbance to the water flow created by their construction. However, the data presented in Chapter 6 also included some evidence that the scale of lysimeters required for piles covered by a low-flux cover system may be smaller.

8.4 THE FATE OF PRECIPITATION, FLOW MECHANISMS, SPATIAL VARIABITLITY, RESIDENCE TIME

Net infiltration of water through uncovered waste rock is estimated to be 55% of precipitation for a northern Saskatchewan climate. This is an average of 55% to 85% net infiltration during large summer storms, and lower infiltration during smaller rainfall events.

The data presented in Chapters 6 and 7 indicate that non-capillary flow paths are active in the CPE during larger infiltration events. For waste rock of this grain size distribution, the total volume transported is small (<0.1%). Greater prevalence of clast-supported textures and increases in surface run-off and focussed infiltration may increase the

proportion of water carried in non-capillary flow paths. This water has a residence time of hours.

Macropores are also active within the CPE. Water within these pores, or collections of pore spaces, does not mix well with the matrix water within the CPE. Some of these pores permit water flow to 5 m depth in hours within a single rainfall events. During large rainfall events, this may compose 6% of outflow. The water chemistry within these pores spaces was found to vary from water within the rest of the waste rock, and contained lower concentrations of weathering products.

The majority of water flow occurs in the granular porous media. The waste rock is highly heterogeneous, and thus the distribution of residence times is large. Mean residence time through 5 metres of waste rock is estimated to be 3 to 3.9 years at the annual average rainfall. The residence time distribution is skewed, with a narrow range of residence times faster than 3 years, and a long tail.

8.5 CHANGES IN PILE CONSTRUCTION PRACTICES

The data in Chapter 6 indicated that the installation of a low-flux cover system may decrease the spatial variability of water flow. Lower flux rates would confine flow to the finer grained matrix materials, thereby reducing, or eliminating water flow in macropores and non-capillary flow paths. Water flow in finer grained material is more easily characterized by standard laboratory methods, and would require smaller lysimeters. Further recommendations cannot be made prior to the analysis of the geochemical data.

A recommendation based on experience, rather than measured evidence, can also be made regarding the location of large experimental piles. The constructed pile was located on top of an existing pile for regulatory reasons. This design led to the creation of a micro-

climate at the top of the pile. As a result, the evaporation and weather conditions at the top of the pile may be different from the conditions experienced on a large pile surface. Any similar experiments could be improved by constructing the experiment such that the top surface of the pile was level with the top surface of an existing pile. This could be created by placing the experimental pile on the side of an existing pile. Locating the experiment on the downwind side of the existing pile would permit a stable boundary layer to be developed during wind flow over the existing pile, and carry on over the experimental surface.

REFERENCES

Annan, A.P. 1977a. Time-domain reflectrometry: Air-gap problem in a coaxial line, Report of Activities, Part B. Geological Survey of Canada, Paper 77-1B. 55-58.

Annan, A.P. 1977b. Time-domain reflectrometry: Air-gap problem for parallel wire transmission lines, Report of Activities, Part B. Geological Survey of Canada, Paper 77-1B. 59-62.

Barnett, A.P. and Dooley, A.E., Erosion potential of natural and simulated rainfall compared, Transactions of the ASAE, Vol. 15, No. 6, 1112-1114, 1972.

Bellehumeur, T., 2001, Mechanisms and spatial variability of rainfall infiltration on the Claude waste rock pile, M.Sc. Thesis, Department of Earth and Ocean Sciences, University of British Columbia.

Bennet, J.W., Garvie, A.M., Pantelis, G., Ritchie, A.I.M., Bell, A.V. and Noel, M., 1995, Comparison of measured and predicted transport processes controlling oxidation in the waste rock piles at the Heath Steele Mine Site, in *Proceedings of Sudbury '95, Mining and the Environment*, T.P. Hynes and M.C. Blanchette (editors), Sudbury, Canada, May-June, 1995, pp. 1017-1026.

Beven, K. and P. Germann, 1981, Water flow in soil macropores II. A combined flow model, Journal of Soil Science, 32, 15-29

Beven, K. and P. Germann, 1982, Water flow in soil macropores, Water Resources Research, 18, 5, 1311-1325.

Bews, B.E., M.A. O'Kane, G.W. Wilson, D. Williams, N. Currey. 1997. The design of a low flux cover system, including lysimeters for acid generating waste rock in semi-arid environments, in *Proceedings of the Fourth International Conference on Acid Rock Drainage*, Vancouver, May 31-June 6, 1997, 747-762.

Biggar, J.W. and D.R. Nielsen, 1976, Spatial variability in the leaching characteristics of a field soil, Water Resources Research, 12, 78-84.

Birchak, J.R., G.C. Gardner, J.E. Hipp and J.M Victor, 1974, High dielectric constant microwave probes for sensing soil water, Proceedings IEEE, 62(1), 93-98.

Birkham, T.K., C.A. Mendoza, M. J. Hendry, and P. Landine. 2001. Characterizing in situ reaction rates in uranium waste rock piles using O2 and CO2 gases. Applied Geochemistry (in submission).

Birkholzer, J. and Tsang, C., 1997, Solute channeling in unsaturated heterogeneous porous media, Water Resources Research, 33, 10, 2221-2238.

Boll, J, J.S. Selker, G. Shalit, and T.S. Steenhuis, 1997, Frequency distribution of water and transport properties derived from pan sampler data, Water Resources Research, 33, 12, 2655-2664.

Booltink, H.W.G. and J. Bouma, 1991, Physical and morphological characterization of bypass flow in a well-structured clay soil. Soil Science Society of America Journal, 55, 1249-1254.

Bowman, R.S. and R.C. Rice 1986, Transport of conservative tracers in the field under intermittant flood irrigation, Water Resources Research, 22, 11, 1531-1536.

Bristow, K.L., G.S. Campbell and K. Calissendorff, 1993, Test of a heat-pulse probe for measuring changes in soil water content, Soil Science Society of America Journal , 57, 930-934.

Butters, G.L. and W.A Jury, 1989, Field scale transport of bromide in an unsaturated field soil 1. Dispersion modeling, Water Resources Research, 25,7, 1583-1589.

Butters, G.L. and W.A. Jury, 1989, Field scale transport of bromide in an unsaturated soil 2. Dispersion modeling, Water Resources Research, 25, 7, 1583-1589.

Butters, G.L., W.A Jury, F.F. Ernst, 1989, Field scale transport of bromide in an unsaturated field soil 1. Experimental methodology and results, Water Resources Research, 25,7, 1575-1581.

Butters, G.L., W.A. Jury and F.F. Ernst, 1989a, Field scale transport of bromide in an unsaturated soil 1. Experimental methodology and results, Water Resources Research, 25, 7, 1575-1581.

Caron, J., S.Ben Jemia, J. Gallichand, and L. Trepanier, 1999, Field bromide transport under transient-state: monitoring with time domain reflectrometry and porous cup, Soil Science Society of America Journal, 63, 1544-1553.

Cassel, D.K., and A. Klute, 1986, Water Potential:Tensiometry, in, *Methods of Soil Analysis, Part I, Physical and Mineralogical Methods*, Klute, A. editor ,Agronomy Monograph no. 9., Second edition, 563-596.

Chow, T.L., and H.W. Rees, 1994, Effects of potato hilling on water runoff and soil erosion under simulated rainfall, Canadian Journal of Soil Science, 74, 453-460.

Christiansen, J.E., Irrigation by sprinkling, University of California Agricultural Experimental Station Bulletin, 670., 1942

CRC Press, 1994, *Handbook of Chemistry and Physics*, D.R. Lide, editor, 75th Edition, CRC Press, Boca Raton, Florida.

Dalton, F.N., W.N. Herkelrath, D.S. Rawlins and J.D. Rhoades. 1984. Time-domain reflectrometry: Simultaneous measurement of soil water content and electrical conductivity with a single probe, Science, 224:989-990.

Davis, G.B. and A.I.M. Ritchie, 1986, A model of oxidation in pyritic mine wastes: part 1: equations and approximate solution, Applied Mathematical Modeling, 10, 314-322

Davis, G.B., G. Doherty and A.I.M. Ritchie, 1986a, A model of oxidation in pyritic mine wastes: part 2: comparison of numerical and approximate solutions, Applied Mathematical Modeling, 10, 323-329

Davis, G.B., G. Doherty and A.I.M. Ritchie, 1986b, A model of oxidation in pyritic mine wastes: part 3: import of particle size distribution, Applied Mathematical Modeling, 11, 417-422

Dawson, R.F. and N.R. Morgenstern, 1995, Liquifaction flowslides in Rocky Mountain coal mine waste dumps, Phase 3, Final Report. Report by University of Alberta to CANMET SSC File No. 23440-3-9135/01=XSG, 200p.

Decker, D.L. and S.W. Tyler, 1999, Evaluation of flow and solute transport parameters for heap leach recovery materials, Journal of Environmental Quality, 28, 543-555.

Destouni, G., 1991, Applicability of the steady state flow assumpation for solute advection in field soils, Water Resources Research, 27, 8, 2129-2140.

Destouni, G., 1991, Applicability of the steady state flow assumption for solute advection in field soils, Water Resources Research, 27, 8, 2129-2140.

Devore, J.L., 1987, *Probability and Statistics for Engineering and the Sciences*, 2nd Ed., Brooks/Cole Publishing, Monterey Californa.

Dexter, A.R., 1993, Heterogeneity of unsaturated, gravitational flow of water through beds of large particles, Water Resources Research, 29,6,1859-1862.

Dirksen C. and S. Dasberg, 1993, Improved calibration of time domain reflectrometry soil water content measurements, Soil Science Society of America Journal, 57, 660-667.

Dixon, D.G. and J.L. Hendrix, 1993a, A general model for leaching of one or more solid reactants from porous ore particles, Metallurgical Transactions B, 24b, 157-169

Dixon, D.G. and J.L. Hendrix, 1993b, A mathematical model for heap leaching of one or more solid reactants from porous ore pellets, Metallurgical Transactions B, 24b, 1087-1101

Dobson, M.C., F.T. Ulaby, M.T. Hallikainen and M.A. El-Rayes, 1985, Microwave dielectric behaviour of wet soil, II, Dielectric mixing models, IEEE Transactions on Geoscience and Remote Sensing, GE-23(1), 35-46.

El Boushi, I.M. and S.N. Davis, 1969, Water retention characteristics of coarse particles, Journal of Hydrlogy, 8, 431-441.

El Boushi, I.M., 1975, Amount of water needed to initiate flow in rubbly rock, Journal of Hydrology, 27, 275-284.

Ericksson, N. and G. Destouni, 1994, Modeling field-scale transport of weathering products in mining waste rock dumps, in *Proceedings of the International land reclamationa and mine drainage conference and the third international conference on the abatement of acidic drainage*, Special Publication SP06, A-94, Bureau of Mines, Pittsburg, P.A., 50-59

Eriksson, N., A. Gupta, G. Destouni, 1997, Comparitive analysis of laboratory and field tracer tests for investigating preferential flow and transport in mining waste rock, Journal of Hydrology, 194, 143-163.

Eriksson, N., and G. Destouni, 1997, Combined effects of dissolution kinetics, secondary mineral precipitation, and preferential flow on copper leaching from mining waste rock, Water Resources Research, 33, 3, 471-483.

Feng, M and D.G. Fredlund, 1999, Hysteretic influence associated with thermal conductivity sensor measurements, in *Proceedings of the 52nd Canadian Geotechnical Conference*, 1999, 651 - 657.

Feng, M. 1999. The effects of capillary hysteresis on the matric suction measurement using thermal conductivity sensors, M.Sc. Thesis, Department of Civil Engineering, University of Saskatchewan.

Ferré, P.A., D.L. Rudolph and R.G. Kachanoski. 1996. Spatial averaging of water content by time domain reflectrometry: Implications for twin probes with and without dielectric coatings, Water Resources Research, 32 (2), 271-279.

Feyen, H., H. Wunderli, H. Wydler, A. Papritz, 1999, A tracer experiment to study flow paths of water in a forest soil, Journal of Hydrology, 225, 155-167.

Flury, M., H. Fluhler, W.A. Jury, J. Leuenberger, 1994, Susceptibility of soils to preferential flow of water: a field study, Water Resources Research, 30, 7, 1945 - 1954.

Fredlund, D. and F. Shuai. 1999. Personal Communication.

Fredlund, D.G. and A. Xing, 1994, Equations for the soil-water characteristic curve, Canadian Geotechnical Journal, 31 (4), 521-532.

Fredlund, D.G. and H. Rahardjo, 1993, "Soil mechanics for unsaturated soils", John Wiley & Sons, New York, New York, United States, 517 pp.

Fredlund, D.G., 1992, Background, theory and research related to the use of thermal conductivity sensors for matric suction measurement, in *Advances in Measurement of Soil Physical Properties: Bringing Theory into Practice*, Soil Science Society of America Special Publication no. 30., 249 – 261.

Fredlund, D.G., A. Xing, S. Huang, 1994, Predicting the permeability function for unsaturated soils using the soil-water characteristic curve, Canadian Geotechnical Journal, 31(4), 533-546

Fredlund, D.G., F. Shuai and M. Feng, 2000, Increased accuracy in suction measurements using an improved thermal conductivity sensor, in *Tailings and Mine Waste 2000, Proceedings of the 7th International Conference*, Fort Collins, January 2000, 443-450.

Friel, R. and D. Or. 1999. Frequency analysis of time-domain reflectrometry (TDR) with application to dielectric spectroscopy of soil constituents, Geophysics, 64:707-718.

Frostad, S. 1999, M.Sc. thesis, Department of Mining and Mineral Process Engineering, University of British Columbia.

Gan, J.K.M., D.G. Fredlund, A. Xing, W.X. Li, Design and data acquisition for thermal conductivity matric suction sensors, Transportation Research Record 1432, 68-75

Gelinas, P., R. Lefebvre, M. Choquette, D. Isabel, J. Locat and R. Guay, 1994. Monitoring and Modeling of Acid Mine Drainage from Waste Rock Dumps:La Mine Doyon Case Study. Mine Environment Neutral Drainage Program Report 1.14.2a. MEND Prediction Committee.

Gerke, H.H., J.W. Molson and E.O Frind, 1998, Modelling the effect of chemical heterogeneity on acidification and solute leaching in overburden mine spoils, Journal of Hydrology, 209, 166-185.

Germann, P and K. Beven, 1981, Water flow in soil macropores I. An experimental approach, Journal of Soil Science, 32, 1-13.

Germann, P.F., L. Dipietro and V.P. Singh,. 1997, Momentum of flow in soils assessed with TDR-moisture readings, Geoderma 80, 153-168.

Greenwood, K.L. and H. Daniel, 1996, A double-puncture technique for improving the accuracy of puncture tensiometer measurements, Australian Journal of Soil Research, 34, 153-159.

Gwo, J.P., P.M. Jardine, G.V. Wilson, G.T. Yeh, 1995, A multiple-pore-region concept to modeling mass transfer in subsurface media, Journal of Hydrology, 164, 217-237.

Halbertsma, J., E. van den Elsen, H. Bohl and W. Skierucha, 1995, Temperature effects on the TDR determined soil water content, in *Proceedings of the Symposium: Time-Domain Reflectrometry Applications in Soil Science*, Research Center Foulum, Sept 16, 1994, edited by L.W. Petersen and O.H. Jacobsen, Special Report 11(3), 35-37, Danish Institute of Plant and Soil Science, lyngby, Denmark.

Harvey, J.W., 1993, Measurement of variation in soil solute tracer concentration across a range of effective pore sizes, Water Resources Research, 29 (6), 1831-1837.

Hasted, J.B., *Aqueous Dielectrics*, Chapman and Hall, New York, 1973

Hatano, R. and H.W.G. Booltink, 1992, Using fractal dimensions of stained flow patterns in a clay soil to predict bypass flow, Journal of Hydrology, 135, 121-131.

Heimovaara, T.J., 1994, Frequency domain analysis of time domain reflectrometry waveforms, 1, Measurements of the complex dielectric permittivity of soils, Water Resources Research, 30(2), 189-199.

Heimovaara, T.J., E.J.G. de Winter, W.K.P. van Loon and D.C. Esveld. 1996. Frequency-dependent dielectric permittivity from 0 to 1 GHz: Time domain reflectrometry measurements compared with frequency domain network analyzer measurements, Water Resources Research, 32 (12), 3603-3610.

Herasymuik, G.M., G.W. Wilson, S.L. Barbour, and T. Smith, 1995, The characterization of hydrogic properties and moisture migration pathways of a waste rock pile, Mine Reclamation, Reclamation in Extreme Environments, in *Proceedings of the 19th annual British Columbia Mine Reclamation Symposium*, Dawson Creek, B.C., June 19-23, 1995, 234-244.

Herkelrath, W.N., Hamburg, S.P. and Murphy, F., 1991, Automatic, real-time monitoring of soil moisture in a remote field area with time domain reflectrometry, Water Resources Research, 27(5), 857-864.

Hoekstra, P. and A. Delaney, 1974, Dielectric properties of soils at UHF and microwave frequencies, Journal of Geophysical Research, 79(11),1699-1708

Hogg, W.D. and D.A. Carr (1985) "Rainfall Frequency Atlas for Canada", Canadian Climate Program, Atmospheric Environment Science, Environment Canada

Holden, N.M., Dowd, J.F., Williams, A.G., Scholefield, D., 1995, Computer control for investigating water and chemical transport in a large isolated soil block, Computers and electronics in agriculture, Vol. 12, 225-236, 1995.

Hollings, P., M. J. Hendry, R. Kirkland and R.V. Nicholson, 1999, Evaluation of the oxygen consumption method for determining the reactivity of waste rock from uranium mines of northern Saskatchewan, in *Proceedings of the 52nd Canadian Geotechnical Conference*, Regina, October 24-27, 1999, 261-264

Hollings, P., M.J. Hendry, R.V. Nicholson and R.A. Kirkland, 2001, Quantification of oxygen consumption and sulphate release rates for waste rock piles using kinetic cells: Cluff Lake uranium min, northern Saskatchewan, Canada. Applied Geochemistry, 16, 1215-1230.

Hook, W.R., N.J. Livingstone, Z.J. Sun and P.B. Hook, 1992. Remote diode shorting improves measurement of soil water by time domain reflectrometry, Soil Science Society of America Journal, 56, 1384-1391.

Jambor, J.L, and D.W. Blowes, 1994, Environmental geochemistry of sulfide mine-wastes., Mineralogical Association of Canada, Shortcourse Handbook 22.

Jardine, P.M., G.K. Jacobs, and G.V. Wilson, 1993, Unsaturated transport processes in undisturbed heterogeneous porous media, I. Inorganic contaminants, 1993, Soil Science Society of America Journal, 57, 945-953.

Jury, W.A., 1975, Solute travel-time estimates for tile-drained fields, I, Theory, Soil Science Society of America Journal, 39,1020-1024.

Jury, W.A., 1982, Simulation of solute transport using a transfer function model, Water Resources Research, 18, 363-368.

Jury, W.A., L.H. Stolzy, and P. Shouse, 1982, A field test of a transfer function model for predicting solute transport, Water Resources Research, 18,2,369-375.

Kelly, S.F., J.S. Selker and J.L. Green, 1995, Using short soil moisture probes with high bandwidth time domain reflectrometry instruments, Soil Science Society of America Journal, 59, 97-102.

Kenny, T.C., R. Chahal, E. Chiu, G.I. Ofoegbu, G.N. Omange, and C.A. Ume, 1985, Controlling constriction sizes of granular filters, Canadian Geotechnical Journal, 22, 32-43.

Knight, J.H. 1992. Sensitivity of time domain reflectrometry measurements to lateral variations in soil water content, Water Resoures Research, 28:2345-2352.

Knight, J.H., I. White and S.J. Zegelin. 1994. Sampling volume of TDR probes used for water content monitoring. In *Proceedings of the Symposium and Workshop on Time Domain Reflectrometry in Environmental, Infrastructure and Mining Applications*, Spec. Publ. 19-94 p. 93-104. Bur. of Mines, U.S. Dept. of the Inter., Minneapolis, Minn., 1994.

Knight, J.H., P.A. Ferré, D.L. Rudolph, and R.G. Kachanoski, 1997, A numerical analysis of the effects of coatings and gaps upon relative dielectric permittivity measurement with time domain reflectrometry, Water Resources Research, 33(6), 1455-1460.

Kranz, W.L., R.S. Kanwar, and C.E. Pederson, 1998, Collection and monitoring of one-meter cubic soil monoliths for leaching studies, Transactions of the ASAE, 41, 2, 333-344.

Lefebvre, R., D.Hockley, J. Smolensky, and P. Gelinas, 2001a, Multiphase transfer process in waste rock piles producing acid rock drainage 1: Conceptual model and system characterization, Journal of Contaminant Hydrology, 52, 137-164.

Lefebvre, R., D.Hockley, J. Smolensky, and P. Gelinas, 2001a, Multiphase transfer process in waste rock piles producing acid rock drainage 2: Applications of numerical simulation, Journal of Contaminant Hydrology, 52, 165-186.

Lennartz, B., J. Michaelsen, W. Wichtmann and P. Widmoser, 1999, Time variance analysis of preferential solute movement at a tile-drained field site., Soil Science Society of America Journal, 63,39-47.

Li, M., 2000, Unsaturated flow and solute transport observations in large waste rock columns, in *Proceeding of the 5th International Conference on Acid Rock Drainage*, Denver, Colorado, May 21-24 , 2000. 247-256.

Litaor, M.I., 1988, Review of soil solution samplers, Water Resources Research, 24 (5), 727-733.

Lopez, D.L., Smith, L. and Beckie, R., 1997, "Modeling water flow in waste rock piles using kinematic wave theory", in *Proceedings of the Fourth International Conference on Acid Rock Drainage*, Vancouver, May 31-June 6, 1997, 497-514.

Mallants, D., M.Vanclooster, N. Toride, J. Vanderborght, M. Th. van Genuchten, and J. Feyen, 1996. Comparison of three methods to calibrated TDR for monitoring solute movement in undisturbed soil, Soil Science Society of America Journal, 60:747-754.

Malmstrom, M.E., G. Destouni, S.A. Banwart and B.H. Stromberg., 2000, Resolving the scale-dependence of mineral weathering rates., Environmental Science and Technology, 34, 7, 1375-1378.

Maraqa, M.A, R.B. Wallace and T.C. Voice, 1997, Effects of degree of water saturation on dispersivity and immobile water in sandy soil columns, Journal of Contaminant Hydrology, 25, 199-218.

Matsubayashi, U., L.P. Devkota and F. Takagi, 1997, Characteristics of the dispersion coefficient in miscible displacement through a glass bead medium, Journal of Hydrology, 192, 51-64.

McCann, I.R., D.C. Kincaid, and D. Wang, 1992, Operational characteristics of the Watermark Model 200 soil water potential sensor for irrigation management, Applied Engineering in Agriculture, Vol. 8(5), 603-609.

McKeowen, R., S.L. Barbour, D. Rowlett, and G. Herasymuik, 2000, Characterization of the grain-size distribution for waste rock from metal mines - A review of existing grain size data and an evaluation of the implications for hydrgeologic behaviour. Canadian Society of Civil Engineers CSCE Annual Conference, Ontario, 2000, 203-209.

Miller, W.P., 1987, A solenoid operated, variable intensity rainfall simulator, Soil Science Society of America Journal, Vol. 51, 832-834

Mohanty, B.P., R.S. Bowman, J.M.H. Hendrickx, J. Simunek, and M.T. van Genuchten, 1998, Preferential transport of nitrate to a tile drain in an intermittent-flood-irrigated field: Model development and experimental evaluation, Water Resources Research, 34,5, 1061-1076.

Mojid, M.A., G.C.L. Wyseure and D.A Rose, 1998, The use of insulated time-domain reflectrometry sensors to measure water content in highly saline soils, Irrigation Science 18, 55-61.

Motorola, 1998, Product technical specifications, MPX5100 series, Motorola document service document MPX5100/D.

Murr, L.E., W.J. Schlitt and L.M. Cathles, 1981, Experimental observations of solution flow in the leaching of copper-bearing waste, in *Interfacing technologies in solution mining, Proceedings of the 2nd SME-SPE International Solution Mining Symposium*, Denver, Colorado, November 18-20, 1981, W.J. Schlitt (editor).

Newmann, L.L., G.M. Herasmuik, S.L. Barbour, D.G..Fredlund and T. Smith. 1997. The hydrogeology of waste rock dumps and a mechanism for unsaturated preferential flow, in *Proceedings of the Fourth International Conference on Acid Rock Drainage*, Vancouver, May 31-June 6, 1997, 551- 565.

Nichol, C., L. Smith and R. Beckie, 2000, Hydrogeologic behaviour of unsaturated mine waste rock: An experimental study, in *Proceedings of the 5th International Conference on Acid Rock Drainage*, Denver, Colorado, May 21-24 , 2000. 215-224.

ON Semiconductor, 2000, Semiconductor Technical Data document MPN3404/D. http://www.onsemi.com/pub/Collateral/mpn3404rev0.pdf

Or, D. and J.M. Wraith, 1999. Temperature effects on soil bulk dielectric permittivity measured by time domain reflectrometry: a physical model, Water Resources Research, 35:371-383.

Pantelis, G. and A.I.M. Ritchie, 1990, Macroscopic transport mechanisms as a rate-limiting factor in dump leaching of pyritic ores, Applied Mathematical Modeling, 15, 136-143

Pantelis, G. and A.I.M. Ritchie, 1992, Rate-limiting factors in dump leaching of pyritic ores, Applied Mathematical Modeling, 16, 553-560

Pantelis, G. and A.I.M. Ritchie, 1993, Optimising oxidation rates in heaps of pyritic material, in *Biohydrometallurgical Technologies*, A.E. Torma, J.E. Weu and W.L. Lakshmanan (editors), The Minerals, Metals and Materials Society, 1993. 731-739

Parker, J.C., M.Th. van Genuchten, 1984, Flux-averaged and volume-averaged concentrations in continuum approaches to solute transport, Water Resources Research, 20 (7), 866-872.

Pepin, S., Livingstone, N.J., Hook, W.R., 1995, Temperature dependant measurement errors in time domain reflectrometry determinations of soil water, Soil Science Society of America Journal, 59, 38-43.

Phene, C.J., D.A. Clark, G.E. Cardon, and R.M. Mead, 1992, Soil matric potential sensor research and applications, Advances in measurement of soil physical properties: Bringing theory into practice, Soil Science Society of America Special Publication no. 30, 263-280.

Phene, C.J., G.J. Hoffman, S.L. Rawlins, 1971a, Measuring soil matric potential in situ by sensing heat dissipation within a porous body: I. Theory and sensor construction., Soil Science Society of America Proceedings, 35, 27-33.

Phene, C.J., S.L. Rawlins and G.J. Hoffman, 1971b, Measuring soil matric potential in situ by sensing heat dissipation within a porous body: II Experimental results, Soil Science Society of America Proceedings, 35, 225-229.

Phillips, R.E., V.L. Quisenberry and J.M. Zeleznik, 1995, Water and solute movement in an undistrubed, macroporous column: Extraction pressure effects, Soil Science Society of America Journal, 59, 707-712.

Prazak, J., M. Sir, F, Kubik, J. Tywoniak, and C. Zarcone, 1992, Oscillation phenomena in gravity-driven drainage in coarse porous media, Water Resources Research, 28, 7, 1849-1855.

Rasmussen, T.C., R.H. Baldwin Jr., J.F. Dowd, and A.G. Williams, 2000, Tracer vs. pressure wave velocities through unsaturated saprolite, Soil Science Society of America Journal, 64, 75-85.

Reece, C.F., 1996, Evaluation of line heat dissipation sensor for measuring soil matric potential, Soil Science Society of America Jjournal, 60, 1022-1028

Robinson, R.A. and R.H. Stokes. 1955. *Electrolyte Solutions*. Butterworths Scientific Publications, London, U.K.

Roth, K, R. Schulin, H. Fluhler and W. Attinger, 1990, Calibration of time domain reflectrometry for water content measurement using a composite dielectric approach, Water Resources Research, 26(10), 2267-2273.

Roth, K., W.A. Jury, H. Fluhler and W. Attinger, 1991, Transport of chloride through an unsaturated field soils, Water Resources Research, 27, 10, 2533-2541.

Rowlett, D., S.L. Barbour, G.W. Wilson, 1999, Grain size distributions for waste rock. Canadian Geotechnical Journal, submitted.

Rudolph, D.L., R.G. Kachanoski, M.A. Celia, D.R. LeBlanc, and J.H. Stevens., 1996, Infiltration and solute transport experiments in unsaturated sand and gravel, Cape Cod, Massachusetts: Experimental design and overview of results, Water Resources Research, 32,3, 519-532.

Russo, D, W.A. Jury, and G.L. Butters, Numerical analysis of solute transport during transient infiltration 1. The effect of hysteresis and profile heterogeneity, Water Resources Research, 25, 10, 2109-2118.

Sassner, M., K.H. Jensen, G. Destouni, 1994, Chloride migration in heterogeneous soil 1. Experimental methodology and results, Water Resource Research, 30, 3, 735-745.

Sattler, P. and D.G. Fredlund, 1989, Use of thermal conductivity sensors to measure matric suction in the laboratory, Canadian Geotechnical Journal, 26, 491-498.

Schulin, R., M.Th. van Genuchten, H. Fluhler and P. Ferlin, 1987, An experimental study of solute transport in a stony field soil, Water Resources Research, 23,9, 1785-1794.

Seyfried, M.S., and P.S.C. Rao, 1987, Solute transport in undisturbed columns of an aggregated tropical soil: Preferential flow effects, Soil Science Society of America Journal, 51, 1434-1444.

Sharma, M.L. and M. Taniguchi, 1991, Movement of a non-reactive solute tracer during steady and intermittant leaching, Journal of Hydrology, 128, 323-334.

Shipitalo, M.J. and W.M. Edwards, 1996, Effects of initial water content on macropore/matrix flow and transport of surface-applied chemicals, Journal of Environmental Quality, 25, 662-670.

Shouse, P.J. and B.P. Mohanty, 1998, Scaling of near-saturated hydraulic conductivity measured using disc infiltrometers, Water Resources Research, 34, 5, 1195-1205.

Shuai, G., J. Yazdani, M. Feng and D.G. Fredlund, 1998, Supplemental report on the thermal conductivity matric suction sensor development (Year two), University of Saskatchewan, Civil Engineering Dept., Personal Communication.

Smiles, D.E. and J.R. Philip, 1978, Solute transport during absorption of water by soil: Laboratory studies and their practical implications, Soil Science Society of America Journal, 42:537-544.

Smith, L., D.L. Lopez, R. Beckie, K. Morin, R. Dawson, W. Price. 1995. Hydrogeology of Waste Rock Dumps, Final report to Natural Resources Canada, Contract 23440-4-1317/01-SQ. Available as an associated report through the Mine Environment Neutral Drainage Program.

Smith, R.E, 1982, Approximate soil water movement by kinematic characteristics, Soil Science Society of America Journal, 47, 3-8.

Spaans, E.J.A. and J.M. Baker, 1992, Calibration of Watermark soil moisture sensors for soil matric potential and temperature, Plant and Soil, 143, 213-217.

Standard Methods, 1995, *Standard Methods for the examination of water and wastewater*, 19th edition, American Public Health Association, American Water Works Association, Water Environment Federation.

Starks, P.J., 1999, A general heat dissipation sensor calibration equation and estimation of soil water content, Soil Science, 164, 9, 655-661

Thomson, S.J. and C.F. Armstrong, 1987, Calibration of the Watermark Model 200 Soil Moisture Sensor, Applied Engineering in Agriculture, Vol. 3(2), 186 - 189.

Topp, G.C., J.L. Davis and A.P. Annan. 1980. Electromagnetic determination of soil water content: Measurement in coaxial transmission lines, Water Resources Research 16(3), 574-582.

Topp, G.C., J.L. Davis and A.P. Annan. 1982. Electromagnetic determination of soil water content using TDR: I. Applications to wetting fronts and steep gradients. Soil Science Society of America Journal, 46:672-678.

Topp, G.C., M. Yanuka, W.D. Zebchuck and S. Zegelin. 1988. Determination of Electrical Conductivity using time domain reflectrometry soil and water experiments in coaxial lines, Water Resources Research, 24:945-952.

Tuller, M. and D. Or, 2001, Hydraulic conductivity of variably saturated porous media: film and corner flow in angular pore space, Water Resources Research, 37 (5),1257-1276.

Van der Raadt, P., D.G. Fredlund, A.W. Clifton, M.J. Klassen and W.E. Jubien, 1987, Soil suction measurements at several sites in western Canada, Transportation Research Record 1137, 24-35. Presented to session on Geotechnical Problems in arid regions, Transporation Research Board, Committee A2L06TRB, Washington, D.C.

Villholth, K.G., K.H. Jensen, and J. Fredericia, 1998, Flow and transport processes in a macroporous subsurface-drained glacial till soil II. Field Investigations, Journal of Hydrology, 207, 98-120.

von Hippel, A.R. (Ed.) Dielectrics Materials and Applications, MIT Press, Cambridge, Mass. U.S.A., 1954.

Ward, A., L.G. Wells, R.E. Phillips, 1983a, Characterizing unsaturated hydraulic conductivity of western Kentucky surface mine spoils and soils, Soil Science Society of America Journal, 47, 847-854.

Ward, A.D., L.G. Wells and R.E. Phillips, 1983b, Infiltration through reconstructed surface mine spoils and soils, Transactions ASAE, 26, 821-830.

Wierenga, P.J., 1977, Solute distribution profiles computed with steady-state and transient water movement models, Soil Science Society of America Journal, 41, 1050-1055.

Wierenga, P.J., R.G. Hills and D.B. Hudson, 1991, The Las Cruces trench site: Characterization, experimental results, and one-dimensional flow predictions, Water Resources Research, 27, 2695-2705.

Wildenschild, D. , K. H. Jensen, K. Villholth and T. H. Illangasekare, 1994, A laboratory analysis of the effect of macropores on solute transport, Ground Water, 32, 3, 381-389.

Wildenschild, D. and K. H. Jensen, 1999a, Laboratory investigations of effective flow behaviour in unsaturated heterogeneous sands, Water Resources Research, 35, (1), 17-27.

Wildenschild, D. and K. H. Jensen, 1999b, Numerical modeling of observed effective flow behaviour in unsaturated heterogeneous sandss, Water Resources Research, 35 (1), 29-42.

Wilson, J.A., G.W. Wilson and D.G. Fredlund, 2000, Numerical modeling of vertical and inclined waste rock layers, in *Proceedings from the Fifth International Conference on Acid Rock Drainage*, Denver, Colorado, May 21-24 , 2000. Society for Mining, Metallurgy and Exploration Inc. 257-266

Wong, D.K.H., D.G. Fredlund, E. Imre and G. Putz, 1989, Evaluation of AGWA-II thermal conductivity sensors for soil suction measurement, Transportation Research Record, 1219, 131-143.

Wraith, J.M. and D. Or. 1999. Temperature effects on soil bulk dielectric permittivity measured by time domain reflectrometry: Experimental evidence and hypothesis testing, Water Resources Research, 35 (2), 361-369.

Wyseure, G.C.L., M.A. Mojid and M.A. Malik, 1997, Measurement of volumetric water content by TDR in saline soils, European Journal of Soil Science, 48, 347-354.

Xing, A. and D.G. Fredlund, 1994, Numerical modeling of a thermal conductivity matric suction sensor, Geotechnical Testing Journal, 17 (4), 415-424.

Yazdani, A., S.L. Barbour and G.W. Wilson, 2000, Soil-water characteristic curve for mine waste rock containing coarse material, Proceedings of the CSCE Annual Conference, London Ontario, 198-202

Yazdani, A., S.L. Barbour and G.W. Wilson, 2000, Soil-water characteristic curve for mine waste rock containing coarse material, Proceedings of the CSCE Annual Conference, London Ontario, 198-202

Young, G.D. 1998a. Single diode probes. MoisturePoint™ Technical Brief 13, Environmental Sensors Inc. www.esica.com.

Young, G.D. 1998b. Calibration of profiling probes. MoisturePoint™ Technical Brief 17, Environmental Sensors Inc. www.esica.com.

Young, M.H., Fleming, J.B., Wierenga, P.J., and Warrick, A.W., 1997, Rapid laboratory calibration of time domain reflectrometry using upward infiltration, Soil Science Society of America Journal, 61, 707-712.

Young, R.A. and Burwell, R.E., 1972, Prediction of runoff and erosion from natural rainfall using a rainfall simulator, Soil Sci. Am. Proc., Vol. 36, No. 5, 827-830., 1972.

Yu, C., Warrick, A.W., Conklin, M.H., Young, M.H. and Zreda, M., 1997, Two-and three-parameter calibrations of time domain reflectrometry for soil moisture measurement, Water Resources Research, 33(10), 2417-2421.

Zegelin, S.J. and White, I., Jenkins, D.R., 1989, Improved field probes for soil water content and electrical conductivity measurement using time domain reflectrometry, Water Resources Research, 25(11), 2367-2376.

APPENDIX A:

Nichol, C, L. Smith and R. Beckie, 2000, Hydrogeologic Behaviour of Unsaturated Waste Rock: An Experimental study, 5th International Conference on Acid Rock Drainage, Denver, Colorado, May 21-24 , 2000. 215-224.

ABSTRACT

To study the hydrogeological processes that control the movement of water through unsaturated waste rock, an intermediate-scale (8m x 8m x 5m) waste rock pile has been constructed and instrumented. The constructed pile is monitored for moisture content, matric suction, temperature, matrix water chemistry, gas chemistry, gas pressure, rainfall, evaporation, discharge volume and discharge chemistry. The pile is built upon a grid of 16 contiguous lysimeters. The experiment is designed to investigate the mechanisms that create rapid water flow through a pile and its exchange with slower-moving matrix water.

INTRODUCTION

It is essential to understand how water is transported and stored in waste rock to predict the rates and quantities of mineral weathering products released to the environment. Water flow in waste rock is not well understood and represents the largest source of uncertainty in current predictive efforts. Geochemical observations or modeling alone are not sufficient to determine water flow mechanisms. The focus of this study is on obtaining detailed observations of the flow of water in waste rock which, when combined with information on primary and secondary geochemical reactions, should permit insight to the coupling between fluid flow and the release of metals from waste rock.

Observations from existing waste rock piles, and large-scale experiments, suggest that water flows slowly through a finer-grained matrix, but may also be channeled to spatially distinct pathways. The physical form and hydrogeologic characteristics of these pathways are uncertain. Rapid outflow response to rainfall events in a matter of hours has been observed through tens of metres of waste rock at Island Copper, Myra Falls, and Golden Sunlight mines (Smith et al. 1995) and in large-scale experiments by Murr (1980) and Frostad (1999). The channeling of flow to spatially distinct areas has been observed in an experiment by Murr (1980) and in tracer tests on waste rock piles by Bellehumeur (1999). Measurements of outflow chemistry indicate that differences exist between faster moving water, and slower moving water (Murr, 1980; Frostad, 1999) and that concentrations of reaction products in the first flush of outflow water following an infiltration event may be either higher or lower than concentrations in the long-term drainage from the pile.

OBJECTIVES

In the review of existing high resolution site data by Smith et al. (1995), there was no site or experiment identified where a comprehensive set of hydrogeological data were available at a temporal and spatial resolution appropriate to a detailed investigation of the hydrogeological flow mechanisms in waste rock. This paper addresses the design and presents initial results from a pile experiment constructed at the Cluff Lake Mine in northern Saskatchewan, owned and operated by Cogema Resources Inc. of Saskatoon. The mean annual temperature at Cluff Lake is 0°C, with an average annual precipitation of 439 mm. Questions related to the hydrogeology of waste rock that this research project aims to address are:

- What is the fate of precipitation onto a waste rock pile surface and how is the flow of water initiated?

- What physical mechanisms control the flow of water within a waste rock pile, and how does rapid flow relate to matrix water within the pile?
- What precipitation and surface conditions permit the initiation of rapid flow of water?
- What is the duration of the initial wetting of a pile before any release of water is to be expected?
- What is the degree of spatial variability in unsaturated flow through a waste rock pile?
- Which physical measurements of waste rock properties are critical to the characterization of flow in waste rock?

EXPERIMENTAL DESIGN

The experiment was designed to mimic the behaviour of the upper 5m of a much larger unsaturated waste rock pile. Simplified plan views and cross sections of the pile are shown in Figures A.1 and A.2. The instrumented core of the pile has a footprint of 8 m by 8 m. Conditions on the boundaries of the pile are a critical element of the experimental design.

BASE

Outflow from the base of the pile is collected in a contiguous grid of 16 lysimeters (Figure A.1). These lysimeters represent a difficult compromise between the need to collect outflow from fine matrix material and non-capillary flow paths and the desire to represent a larger unsaturated pile. In regions of the pile where capillary forces dominate, water cannot flow freely from the unsaturated material unless either a water table is formed or the water is removed by suction. Maintaining the lysimeters under suction was not considered to be technically feasible. Accordingly, a design leading to the formation of a water table at the base of the pile was chosen (Figure A.2, inset A). The pile rests on a contoured cement pad lined with a PVC geomembrane. Outflow from each 2 m by 2 m lysimeter is separately piped to an instrumentation hut where outflow is monitored using tipping-bucket rain gauges. Within each lysimeter, there is a layer of 9.5 to 25 mm screened and washed gravel. Waste rock containing fines smaller than 9.5 mm., is placed over the gravel, leading to a capillary break. The finer waste rock immediately above the gravel will wet to a higher saturation than would normally be encountered in an unsaturated pile. The gravel is coarse enough to not retain or delay water which flows from any free-draining flow pathways where capillary forces do not control flow. The gravel also provides both a rapid lateral flow path to the central drain, and a filtration capacity to prevent the movement of fines onto the lysimeter floor or into the water collection system. These fines would act as low-permeability sinks and would retain water at the base that would interfere with the interpretation of conservative tracer experiments. The piping at the base of the pile is equipped with heat tracing to allow year round operation.

Sides

In the unsaturated zone, a lysimeter with a zero-pressure boundary condition may not capture all the water which infiltrates the soil surface above. The water in the unsaturated matrix adjacent to the zero-pressure lysimeter has the same elevation head, but is still under tension. This represents a lateral head gradient which diverts flow around the lysimeter. Only by limiting lateral diversion using sides will a zero-pressure lysimeter successfully capture capillary dominated water flow, as explained in Bews et al. (1997). Preliminary unsaturated flow modeling of matrix flow in the pile was conducted prior to construction using parameters estimated from Bews et al. (1997) and Newman et al. (1997) . The modeling indicated that water recovery at the pile base would be significantly reduced, or negligible, unless sides were placed within the pile to prevent lateral diversion of water around the lysimeters. Plywood lined with a 60 mil HDPE geomembrane was used to isolate the central core of the pile, from its base to the top of the pile. The sides allow a complete water balance to be calculated, and the movement of the gas phases is reduced to one dimension. The sides provide lateral no-flow boundaries to

matrix flow which assists in making the pile mimic a portion of a larger pile. However, the sides do limit the lateral range of possible spatially-distinct flow pathways.

Top Surface

The constructed pile is 5 m high. The top surface of the pile was finished to resemble other existing piles on site which were free-dumped and then contoured to a smooth surface by limited bulldozer passes. No attempt was made to create a trafficked dump surface nor any type of compaction or artificial cover, although these may be options for later study.

Waste Rock Composition And Internal Pile Structure

The waste rock for this study was mined from the DJ Extension open pit at the Cluff Lake mine in the fall of 1996, and placed in the pile experiment in 1998. It is composed of aluminous gneisses and granitoids from the Precambrian Peter River Gneiss formation. Associated with the target uranium mineralization are sulphides of iron, copper, lead, zinc and molybdenum, with localized concentrations of nickel and arsenic minerals. Static tests on 110 samples of waste rock from the DJ Extension pit indicated: average total sulphur <0.63%; average neutralization potential of 9.2 kg $CaCO_3$/t; and NP:AP ratios ranging from 13.2 to 0.1, with an average of 2.0 (Amok Limited,1992). Further information on kinetic testing of the material in the pile is available in Hollings et al. (1999).

The grain size distribution of the 0.6m minus fraction of the waste rock is shown in Figure A.3.

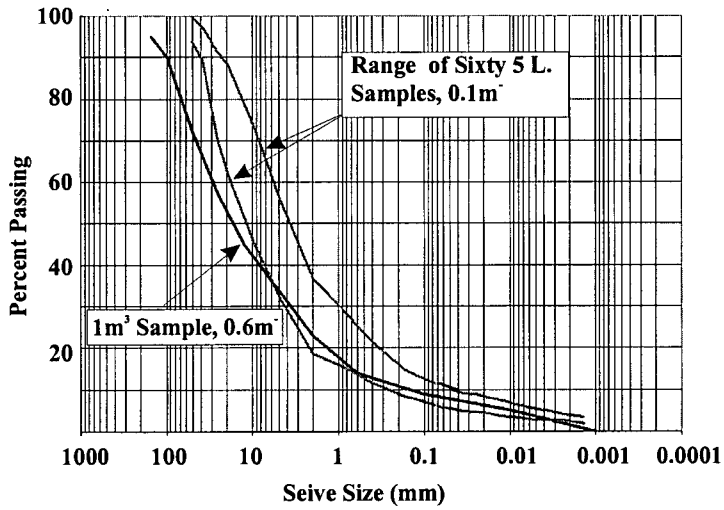

Figure A.3: Grain size of waste rock in constructed pile

Prior to pile construction, a backhoe was used to make a 15 m^3 blended composite of the 2600 m^3 of waste material used to build the pile experiment. A 1 m^3 sample of this composite was analyzed, as well as sixty 5 litre samples collected during pile construction (data from S.L. Barbour, University of Saskatchewan). The presence of delicate instrumentation within the pile limited construction methods to reworked placement of waste rock using a large excavator. The texture matches the range of textures seen in excavations of existing waste rock piles on site. It is highly heterogeneous, ranging from 1.5 m diameter boulders to clay, with areas that are matrix supported and areas with matrix-free cobbles and boulders. No attempts were made to reconstruct haul truck traffic surfaces, or the cross-bedding structures that result from end- or push-dumping.

Instrumentation

The instrumentation used to measure moisture content, matric suction, temperature and matrix soil water chemistry (Figure A.2, inset B) either all require direct contact with finer soil as part of their principle of operation, or would be damaged during construction by cobbles or boulders. The automated instrumentation primarily monitors the movement of soil water in the matrix as there are no existing instrumentation technologies for clast supported, matrix-free areas. The placement of instrumentation within the pile necessitated some care in waste rock placement to prevent damage and therefore may have resulted in rock texture that is different from un-instrumented waste rock.

Moisture content is monitored both periodically by neutron probe through aluminum access tubes placed during pile construction, and continuously using time domain reflectrometry (TDR) which relates the bulk soil dielectric to volumetric moisture content. The high concentrations of dissolved solids in the soil water necessitated the use of coated three rod, Zegelin-type TDR probes employing remote diode shorting (Knight et al. 1997; Ferre et al. 1996; Hook et al. 1992) to overcome high signal losses. The probe coating requires a non-linear correction between the apparent measured and actual bulk soil dielectric. Using a simple square root mixing model of the soil dielectric, the apparent dielectric of the water phase was found to range from 40 to 180. These values indicate a significant departure from the commonly used models of the bulk soil dielectric which assume that all dielectrics are real-valued. This effect is caused by water bound to mineral surfaces at low moisture contents and by the effect of high fluid conductance (up to 20,000 uS/cm) on the frequency-dependent complex soil dielectric at higher moisture contents. The effects of bulk soil conductance on TDR moisture measurements could be directly accounted for using a scatter function and Fourier transform approach (Heimovarra et al. 1996), but a scatter function appropriate to three wire probes is not currently available. We derived an empirical non-Topp curve calibration of measured soil bulk dielectric to moisture content. This calibration must account for the variation of soil water conductance, and was carried out using the field setup of multiplexers and cables to ensure the frequency spectra of the TDR pulse would be the consistent. The 40 cm coated probes used are capable of providing a reliable signal over 35 m cable lengths with bulk soil conductances of 3 dS/m. Shorter uncoated probes specifically designed to measure bulk soil conductance were installed in 1999.

Matric suction is monitored year round using thermal dissipation sensors with laboratory-derived temperature and sensor hysteresis corrections (Fredlund and Shuai 1999, Feng 1999). Tensiometers with pressure transducers were installed in 1999 to provide independent measurements of matric suction when air temperatures are above freezing. Temperatures are measured using commercial pre-calibrated thermistors.

Outflow water samples are collected in a cascade of mixing cells, where the water is directed through containers of increasing volume before final overflow to waste. Both instantaneous grab and longer term composite samples can be obtained without post-sampling compositing. Matrix water chemistry is monitored through the periodic manual extraction of water samples from suction lysimeters placed within the pile during construction.

Pile surface evaporation will be calculated using data from a full weather station and surface mini-lysimeters. This instrumentation was installed in the summer of 1999, but processed and calibrated data are not yet available. The measurement of pile surface evaporation and gas phase pressure and composition are under way by other researchers associated with this project, and are not discussed further in this paper.

RESULTS

The pile foundations were constructed in 1997, and the remainder of the pile constructed from June to September, 1998. Automated and manual monitoring of the pile commenced in

September 1998, and is ongoing. The experiment is currently scheduled to operate for 5 years. Summaries of rainfall, outflow, moisture content and matric suction from September, 1998 to July, 1999 are presented in Figures A.4 and A.5.

The daily total precipitation to the pile surface and the outflow rates from individual lysimeters are shown in Figure A.4. High winds remove most of the winter snowpack from the exposed pile surface, and 9 cm remained in spring, 1999. The water equivalent is indicated as precipitation when the snowpack melted March 20-22. To July 1999, outflow has been recorded from eleven of the sixteen lysimeters, but the spatial location of outflow has varied seasonally (Figure A.6).

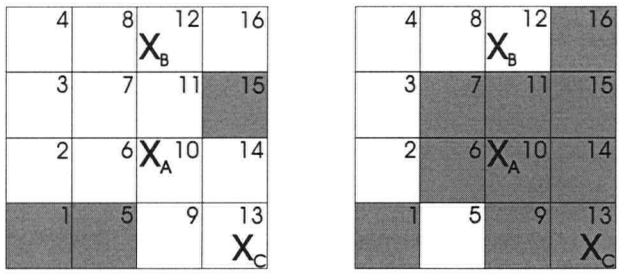

Figure A.6 : Spatial distribution of pile outflow

Outflow started in some lysimeters from 5 to 30 days following the first precipitation on the pile surface in September, 1998. In five lysimeters, no outflow has been recorded after 10 months and more than 120 mm of precipitation. To July 1999, approximately 7000 litres of water has fallen as precipitation on the pile, and 220 litres of water have exited the pile as outflow. The balance of the water has evaporated from the pile, or has entered soil moisture storage. The pile was constructed in hot summer conditions, with no rainfall during construction, and several dry surfaces were formed internally due to evaporation during pauses in construction. Overall, the waste rock may still be wetter than freshly blasted material, as it had been stored on site for 1.5 years prior to placement. The initial outflow response, which ranged from 5 days to over 10 months, indicates pile heterogeneity leads to very different initial wetting rates.

The surface temperature of the pile has varied from –22 to 28 °C, with the winter snow cover providing up to 16 °C of insulation between the air and pile surface temperature. Temperature at 0.2 m has varied seasonally from –13 to 23 °C and daily variations are observed to 0.5 m depth. Seasonal variation has led to a steady temperature decline at the base of the pile from 20 to 10 °C. Over the first winter, the pile froze to a depth of 1.5 m.

Moisture content estimated by TDR and matric suction at the center of the pile are shown in Figure A.5. Daily variations of apparent moisture content due to temperature fluctuation were used to derive a non-linear temperature correction, which has been applied to the data. Volumetric moisture contents are corrected by up to 2% due to temperature variation which is critical for deeper probes undergoing both slow temperature change and slow moisture change. The TDR response down to a depth of 1 m was affected by ground freezing, and low measurements from November to March indicate the conversion of free water to ice, which does not register as moisture content. During freezing conditions the matric suction sensors do not operate, and data is absent, or erratic.

The progress of a wetting front in the capillary-dominated matrix material can be followed by observing increases in moisture content that propagate downwards. At this profile location (lysimeter 5), the TDR data show that the initial wetting front from fall and spring precipitation events took 9 months to travel the 5 m depth to the base of the pile. The increase in

moisture content at 4.5 m depth immediately preceded the lysimeter outflow. The progress of subsequent wetting fronts to the base of the pile is recorded in the TDR response at 3 metres, through increased moisture contents on April 15 from the March 20-22 snowmelt and on 21 May due to May rainfalls. The wetting front from the rainfall event on June 21st can be traced from surface to 3 m within 45 hours from the start of rainfall. The downwards velocities of the wetting fronts are increasing following the initial wetting period.

Matric suction measurements from the thermal dissipation sensors show declines at all levels. Initial matric suction measurements were high due to intense evaporation from the pile surface at each instrument level during the time required to install each set of instruments. Suctions of several hundred kPa were created by evaporation during construction, but current matric suction measurements are less than 20 kPa below 0.2 m depth. Matric suction measurements and moisture content measurements have been combined to derive soil water characteristic curves for each sensor location. Maximum measured water contents of 16% at suctions of 0.2 kPa are well below saturation of 30 to 35% volumetric water content. The curves exibit a rapid decrease in moisture content between 0.2 kPa and 15 to 30 kPa, followed by a more gradual decline to residual moisture contents of 6 to 8% at 50 to 60 kPa. Soil water characteristic curves will be finalized following cross-referencing of thermal dissipation sensor measurements to tensiometer measurements in 1999.

Drainage and Matrix Water Chemistry

The results of this study will be combined with a coincident geochemical investigation of matrix and outflow water and waste rock mineralogy to provide a framework for prediction of environmental loadings. Initial outflow water chemistry is characterized by high sulphate (up to 40,000 mg/L), and a pH between 3 and 4. Key cations include magnesium (1500-3000 mg/L), aluminum (200-700 mg/L) and nickel (100-200 mg/L). Data indicate the pile is actively undergoing sulphide weathering, although at a rate that does not produce a significant thermal perturbation.

ONGOING AND FUTURE WORK

The field program for 1999 extended from August to October. Evaporation data collected in 1999 and beyond will allow a full water balance to be calculated. Artificial rainfall experiments using the rainfall simulator were conducted to investigate the pile hydrogeologic response to controlled inputs of water. A tracer test using lithium chloride as a conservative tracer was started to assist in determining the relationship between water outflow and matrix water within the pile. The tracer test will permit a determination of the relative proportions of tracer-tagged new water and older matrix water in the outflow following an infiltration event.

Additional analyses of grain sizes and laboratory-determined soil water characteristic and hydraulic conductivity curves will be carried out. These data will be compared to field characteristic curves from the constructed pile. Modeling of soil-atmosphere interaction and soil water flow within the waste rock will be conducted based upon the results of pile monitoring, tracer tests and the complementary laboratory determination of material properties. Sampling of both the drainage water chemistry and the chemistry of the matrix water extracted from the suction lysimeters is ongoing.

ACKNOWLEDGEMENTS

This project is part of the Waste Rock Hydrology Research Program, a joint research program initiated between the University of British Columbia, the University of Saskatchewan, Cogema Resources Incorporated, Cameco Corporation, and the Natural Sciences and Engineering Research Council of Canada. The authors would like to thank the staff of the Cluff Lake Mine for their assistance in the construction and ongoing operation of the experiment.

REFERENCES

Amok Limited. 1992. Environmental Impact Statement for the Dominique-Janine Extension, Report to Cogema Resources, Inc.

Bellehumeur, T. 1999. M.Sc. in progress, Department of Earth and Ocean Sciences, University of British Columbia.

Bews, B.E., M.A. O'Kane, G.W. Wilson, D. Williams, N. Currey. 1997. The design of a low flux cover system, including lysimeters for acid generating waste rock in semi-arid environments, Proceedings of the Fourth International Conference on Acid Rock Drainage, Vancouver, May 31-June 6, 1997, 747-762.

Feng, M. 1999. The effects of capillary hysteresis on the matric suction measurement using the thermal conductivity sensors, M.Sc. Thesis, Department of Civil Engineering, University of Saskatchewan.

Ferre, P.A., D.L. Rudolph, and R.G. Kachanoski. 1996. Spatial averaging of water content by time domain reflectrometry: Implications for twin rod probes with and without dielectric coatings, Water Resources Research, 32(2), 271-279.

Fredlund, D. and F. Shuai. 1999. Personal Communication.

Frostad, S. 1999. M.Sc. thesis, Department of Mining and Mineral Process Engineering, University of British Columbia.

Heimovaara, T.J., E.J.G. de Winter, W.K.P. van Loon and D.C. Esveld. 1996. Frequency dependent dielectric permittivity from 0 to 1 GHz: Time domain reflectrometry measurements compared with frequency domain network analyzer measurements, Water Resources Research, 32(12), 3603-3610.

Hollings, P., M. J. Hendry, R. Kirkland and R.V. Nicholson, 1999, Evaluation of the oxygen consumption method for determining the reactivity of waste rock from uranium mines of northern Saskatchewan, Proceedings of the 52nd Canadian Geotechnical Conference, Regina, October 24-27, 1999, 261-264

Hook, W.R., N.J. Livingston, Z.J. Sun, P.B. Hook. 1992. Remote diode shorting improves measurement of soil water by time domain reflectrometry, Soil Science Society of America Journal,56, 1384-1391.

Knight, J.H., P.A. Ferre, D.L Rudolph, and R.G. Kachanoski. 1997. A numerical analysis of the effects of coatings and gaps upon relative dielectric permittivity measurement with time domain reflectrometry, Water Resources Research, 33(6), 1455-1460.

Murr, L.E., 1980, Theory and practice of copper sulphide leaching in dumps and in-situ, Minerals Science and Engineering, 12(3), 121-189.

Newman, L.L., G.M. Herasmuik, S.L. Barbour, D.G..Fredlund and T. Smith. 1997. The hydrogeology of waste rock dumps and a mechanism for unsaturated preferential flow, Proceedings of the Fourth International Conference on Acid Rock Drainage, Vancouver, May 31-June 6, 1997, 551- 565.

Smith, L., D.L. Lopez, R. Beckie, K. Morin, R. Dawson, W. Price. 1995. Hydrogeology of Waste Rock Dumps, Final report to Natural Resources Canada, Contract 23440-4-1317/01-SQ. Available as an associated report through the Mine Environment Neutral Drainage Program.

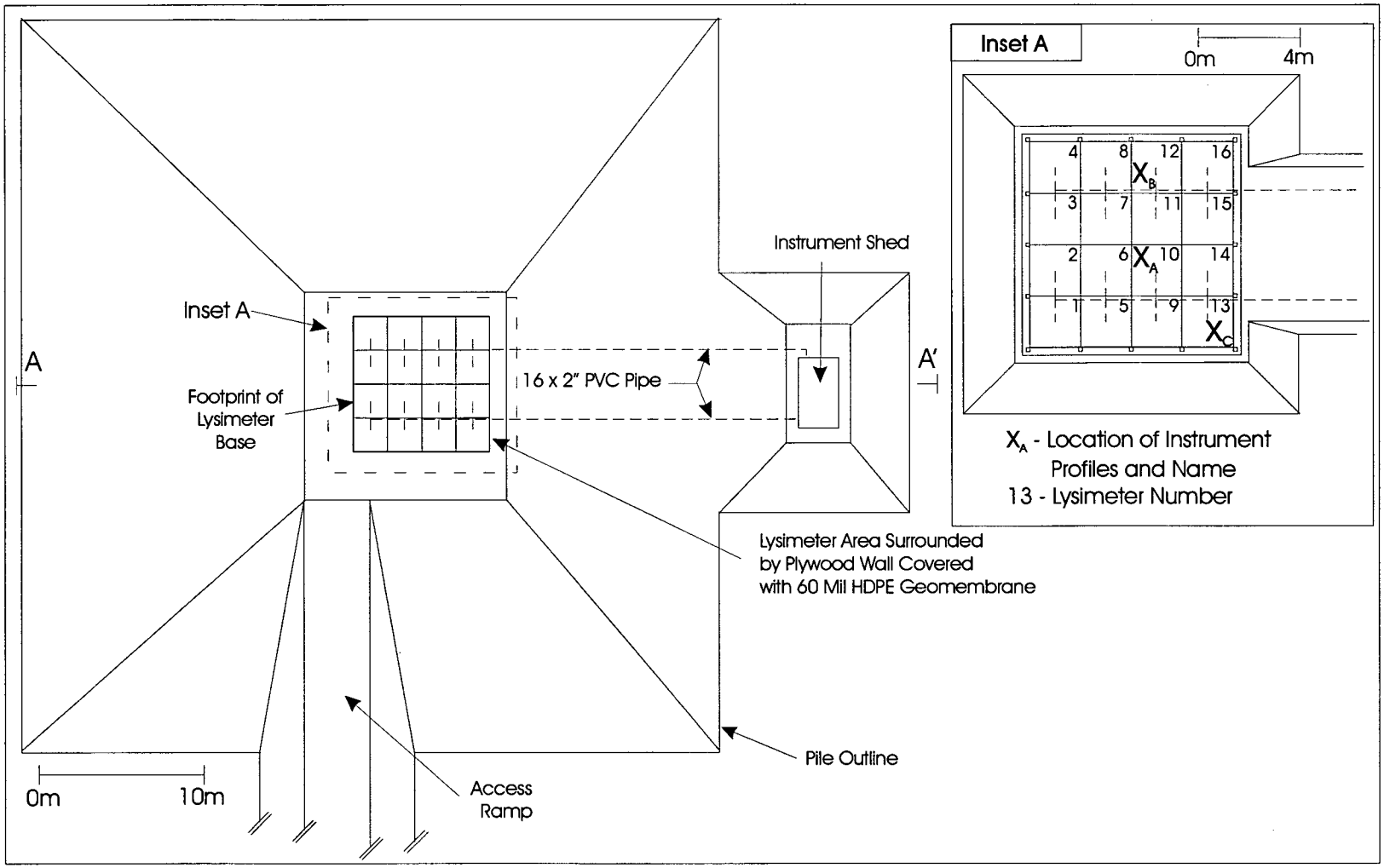

Figure A.1 : Simplified plan view of constructed pile experiment

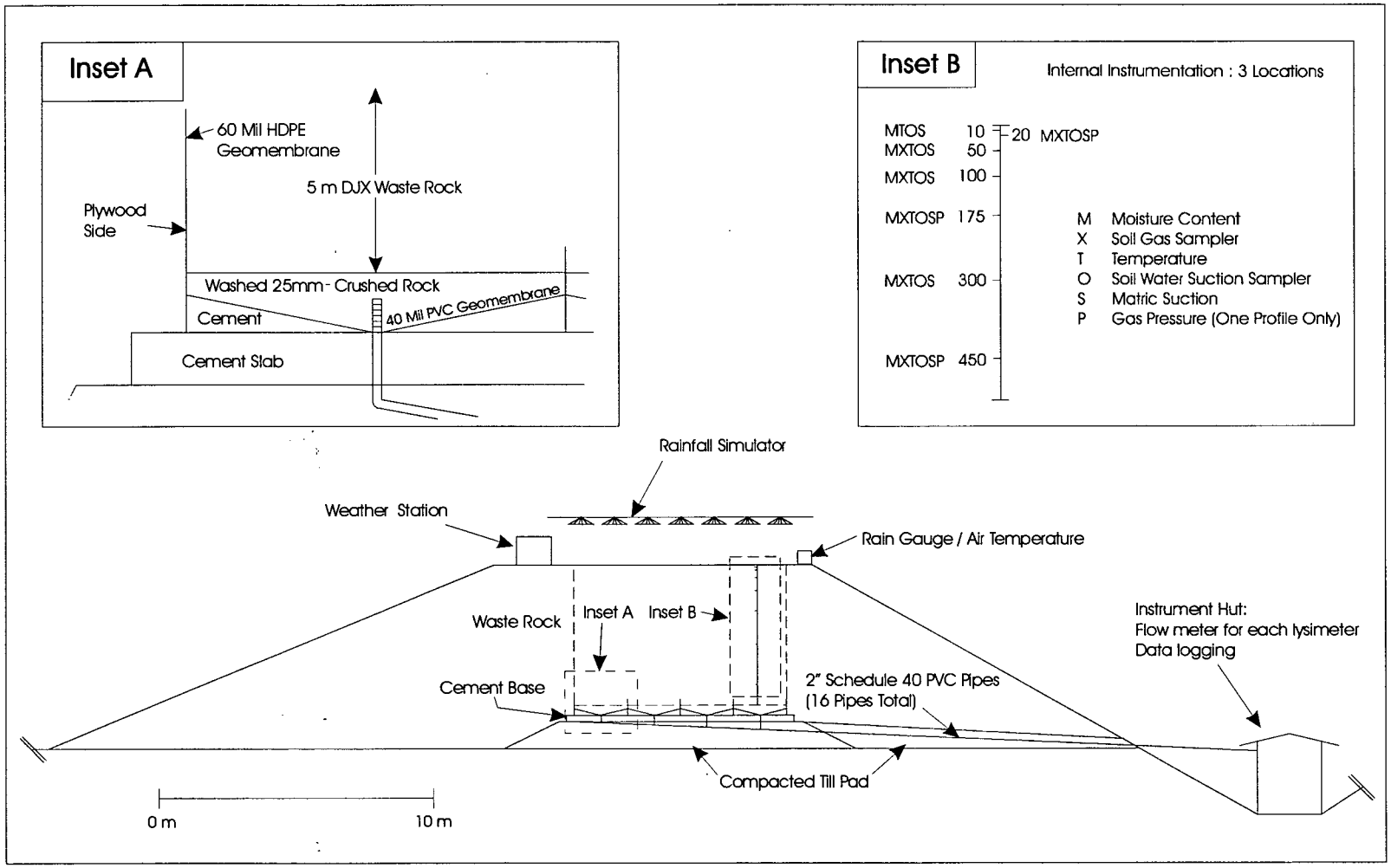

Figure A.2 : Simplified cross-section A-A' of constructed pile

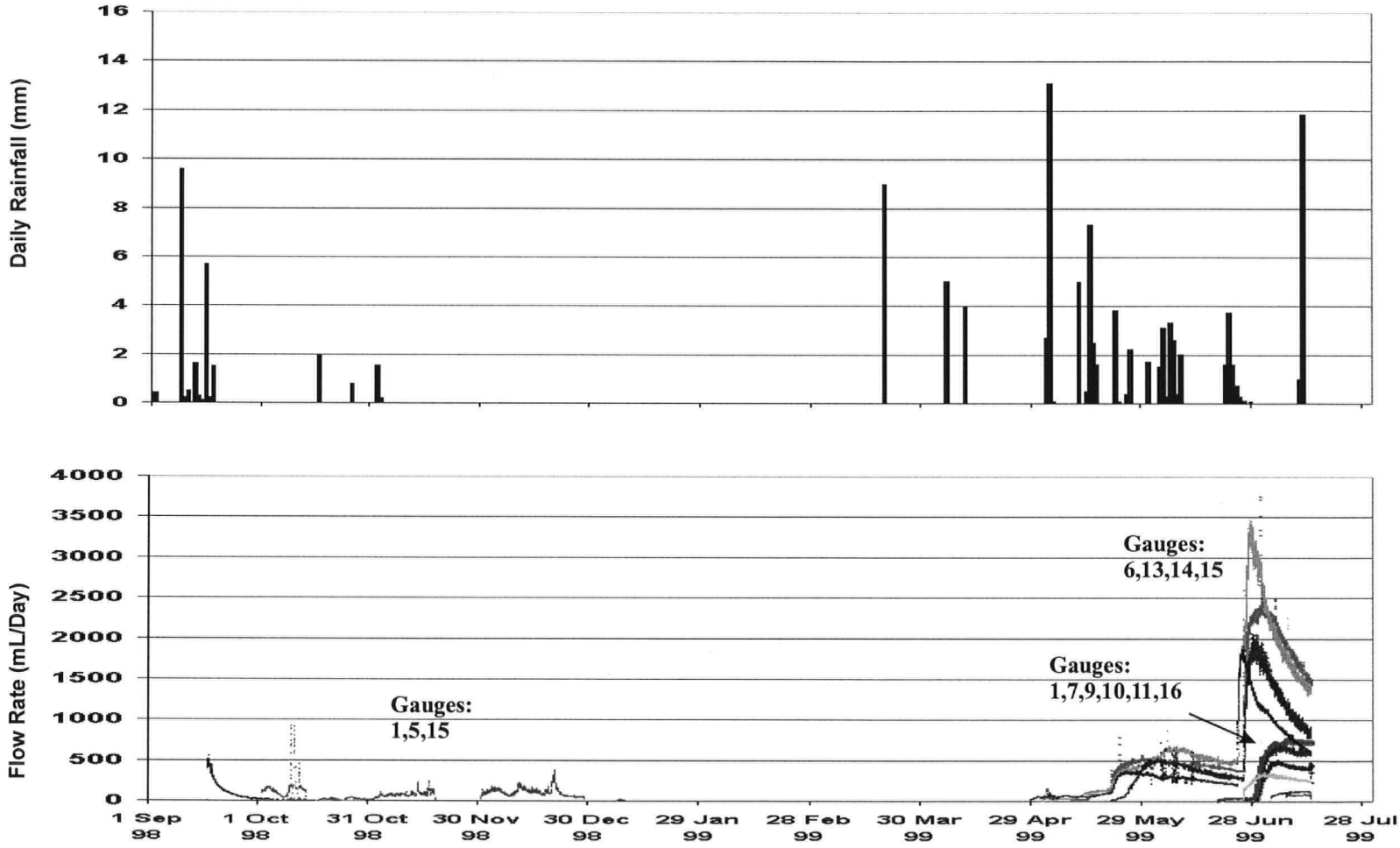

Figure A.4: Daily rainfall volume and outflow rate summary

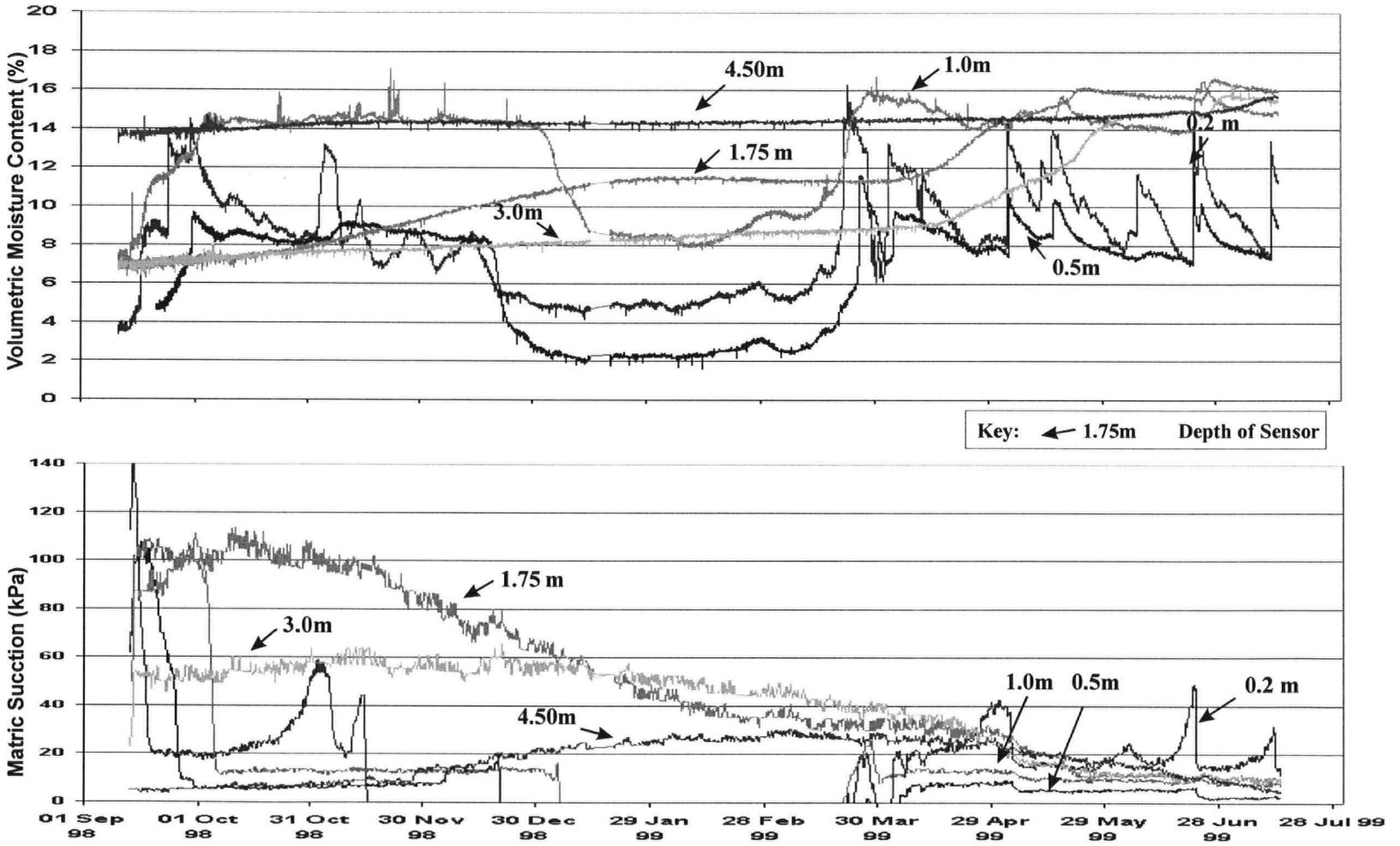

Figure A.5: Summary of volumetric water content and matric suction profile at pile center

APPENDIX B: CONSTRUCTED PILE EXPERIMENT CONSTRUCTION DETAILS

This appendix records the details of the construction of the constructed pile experiment, and presents photographs taken during pile construction.

B.1 INTRODUCTION

Cogema Resources Inc. (CRI) gave permission to start work in August 1997 on the constructed pile experiment (CPE) at their Cluff Lake minesite. During the period from the last week of August to the last week of October, the materials for the pile construction were ordered, the foundation pad was started, and some of the instrumentation was purchased. Construction resumed in late June, 1998. The concrete pad, lysimeter base, and filter gravel were completed and installed by July 14. Waste rock piling proceeded from July 14 to August 9. The instrumentation hut was installed at the pile, and all piping and instrumentation installed inside by September 12. Datalogging was started September 12, and during September and up to October 8, the system was monitored and the instrument and datalogger systems refined.

B.2 CONSTRUCTION DETAILS

B.2.1 Waste Rock Selection

Waste rock for the experiment was chosen to represent the most recently mined waste rock available on site. Mining of the DJX pit was completed in the spring of 1997. Waste rock from this pit was divided into two different categories depending upon the radiation level measured through scanning of the waste haulage trucks at the exit of the pit. Waste determined to be above the cut off grade for radioactivity was sent for disposal in the disused Claude pit as special waste. Waste rock below the cut off grade was disposed of in the adjacent DJ pit.

The waste rock selected for the project was recovered from the south-east corner of the material retained in the DJX pit (Figure B.1). Based on information from site geologists, this material was mined in the fall of 1996. The waste rock was also chosen to have a similar distribution of grain sizes to the material observed in the excavations of another waster rock pile at the Cluff site, the Claude waste rock pile. The grain size of the DJX material is known to be slightly reduced in the largest grain size fractions than the grain size of the DJ and Claude waste piles. The blasting pattern used for the DJX pile was tighter than the pattern used for the DJ and Claude pits. This was done to reduce the size of the larger boulders produced by blasting. It was found that the larger boulder sizes caused increased wear on the heavy equipment used for hauling waste. (Garfield Morin, personal comm. 1998)

B.2.2 Site Selection

The location of the proposed experiment was discussed with the site staff, and a location was picked which would not interfere with existing site operations, or future works. The experiment had to be located within an area already designated as a licensed area by the Atomic Energy Control Board (AECB) and Saskatchewan Environment and Resource Management (SERM). The top of the existing DJ waste rock pile was chosen. This pile is composed of waste from the DJ North open pit, which was later filled in using waste rock from the DJ Extension Pit. A preliminary survey of the ground surface of the DJ pile was undertaken prior to any additions being made. The general outline of the foundation pad, pipes and the overall pile was laid out, and surveyed.

B.2.3 Foundation Pad

The lower foundation pad was made using sand and gravel till from the sand and gravel crushing plant/quarry. The material was placed in small lifts of 20-30 cm using a tracked excavator. Preliminary compaction to level the newly placed material was achieved by several passes over the surface using the excavator tracks. Main compaction of the pad was carried out using a vibratory plate tamper (24"x 36"). A minimum of three passes were conducted and the finished top surface was leveled by hand and resurveyed until a reasonably level surface was achieved.

B.2.4 Pipe Trenches

The two main trenches for the drainage pipes were excavated using a small backhoe. The side trenches for the branches of the piping within the main foundation pad were hand-excavated using pick and shovel. Bedding sand was placed inside the pipe trenches to bring the ground level to the correct slopes for pipe drainage. The sand selected for placement around the pipes was a white, fine quartz sand, some gravel, which usually overlies the lower red sand and gravel till. The bedding sand was compacted using a Jumping Jack compacter. (Gasoline powered compactor with a 12"x12" plate on the bottom). The bedding sand within the side branches for the pipes was compacted using a hand plate tamper comprising a 6"x6" steel plate attached to a heavy steel rod. A minimum base of 15cm of compacted bedding sand was placed below the level of the lowest pipe, and 10 cm on either side (Figure B2). The grade of the bedding surface was determined by level surveying, and all bedding sand placed was well compacted using a Jumping Jack compactor. The pipe was laid at a grade of 3% inside the perimeter of the 9mx9m pad, and was placed at the existing ground surface grade of 5% from the outside perimeter of the main pad, to the location of the instrument hut.

B.2.5 Piping

The main drainage piping for the experiment was 2" Schedule 40 PVC. The joins were made using PVC primer, and PVC Cement. Two small diameter sample tubes were placed inside the main drainage 2" pipe. These were a 1/32" I.D., 1/16" O.D. flexible PVC tubing (Fisher Scientific: Catalog #14 176 84) and a ¼" I.D, 3/8" O.D. low density polyethylene tube (Cole-Parmer: Catalog # E-06407-06). The small diameter sample tubes were installed to permit the extraction of air samples from immediately under the lysimeter pad, and to allow the introduction of water back up inside the drainage pipes to flush and clean the drainage pipes.

Raychem self regulating heat trace (Raychem 5XL1CR, Westbourne Electric) was added to the base of the 2" schedule 40 PVC. The trace was attached to the lower side of the pipe, offset from center, and coated with a layer of aluminum duct tape (Figure B.3). The heat trace was laid from the instrument hut, to the location under the pile, where the PVC pipe turned to vertical. The main drainage pipes were bundled together for protection during final burial. The pipes were arranged in bundles, with five pipes on the bottom layer, and three pipes on the top layer. 1" thickness foam insulation was places under the five pipes, between the pipe layers, and on top of the pipes. The pipes and insulation were bound together in groups as they were assembled using duct tape and rebar reinforcing wire (Figure B.4).

B.2.6 Experiment Base

An initial concrete pad was poured, 8.6 m x 8.6 m and 250 mm thick. The concrete for the pad was standard construction mix from the on-site batch plant. The concrete was

reinforced with two layers of 9 gauge, 4" open square reinforcing mesh, and 3/8" rebar (Figure B.5). Four 8' wide strips of reinforcing mesh were laid out, and wired together with rebar wire. At five evenly placed intervals across the mesh, 3/8" rebar was wired to the mesh to form a carrying grid (Figure B.6). The mesh and rebar were terminated so that no reinforcing material came within 5 centimeters of an outer edge, or drain pipe.

The top surface of the cement was leveled with the pre-surveyed forms and floated to provide a smooth surface. The surface of the concrete was then given a roughened surface by lightly drawing a metal rake across the surface of the wet cement. This created a good gripping surface for the next layers of concrete to be applied.

Construction at the Cluff lake site was restarted in June, 1998. The concrete base with 16 drain pipes was divided in to sixteen 2m x 2m cells using 3/4" construction grade untreated spruce plywood. The dividers were 60 cm in height, and full-length (240cm) sheets were used. Adjacent sheets were joined by overlapping small pieces of plywood across the adjacent pieces of plywood and fastening with small nails. End-on joints of the internal plywood dividers to other plywood were both glued using white carpenters glue, and affixed with screws.

Sloped lysimeters bases were created inside the dividers with cement. Standard construction mix cement from the on-site batch plant was poured into the lysimeter dividers to create a sloped surface towards the drainage pipe in the center of the lysimeter. The slope was such that the outer edge is a level 20 cm higher than the center drain. The slope is circular, thus not as steep on the diagonal as it is on the other directions. A small area immediately around the 2" pipe coupling was left uncemented to allow for detailed work around the center drainage pipe (Figure B.7).

B.2.7 Sampling Tubing

The drainage pipe fixture in the center of the lysimeter was completed after the main sloped concrete was poured. The tubing inside the 2" pipe was terminated as illustrated in Figure B.8. The two tubes were threaded through holes drilled in a short piece of PVC, the tubing crossbar. The end of the 3/8" L.D.P.E. tube was covered using nylon silk screen fabric and the fabric fastened with a zap-strap tie. The 1/16" diameter PVC tube was terminated using three insert T-junctions. The three junctions were connected in a tree formation to give four terminations. The tree termination was bundled inside nylon silk screen fabric and tied using a zap-strap tie. The completed tubing crossbar was glued inside the 2" PVC immediately below the coupling collar such that the end of both small diameter sampling tubes was at an equal elevation.

The slotted drain pipe for the center of each lysimeter was prepared prior to insertion by attaching a collar of 40 mil PVC geomembrane. A section of slotted pipe was prepared with four centimeters of plain pipe below 20 centimeters of slotted pipe with 0.125 inch slots, spaced 0.125 inches apart. A 30 cm x 30 cm piece of 40 Mil PVC geomembrane was used as a collar. A hole was cut in the collar slightly smaller in diameter than the inside of the 2" PVC. This geomembrane piece was pulled upwards from the plain end of the PVC pipe, towards the slotted section of pipe. Tetrahydrofuran PVC solvent was used to glue the geomembrane to the PVC pipe. Once the slotted pipe and collar were prepared, the base of the PVC pipe was glued into the slip coupling protruding from the cement. A cement grout product (sand and cement only for a fine cement texture) was used to fill in the remaining void between the coupler and the main sloped segment of the concrete in the lysimeter.

Once the main cement and the inner collar fill cement were poured, the whole cement surface was smoothed using an angle grinder to remove all sharp edged ridges or bumps. Any holes were filled in with grouting compound.

B.2.8 Geomembrane Liners in Lysimeters

40 Mil PVC geomembrane was used to create an impermeable lining for all of the lysimeter cells. The geomembrane was purchased prefabricated as 11' x 12' panels. A 10 cm diameter hole was cut in the center of the membrane panel. This hole was fitted over the slotted PVC drain, and attached to the geomembrane collar already glued to the slotted drain pipe. The main panel and central collar were glued together using THF. The main panel was overlapped approximately 15 to 30 centimeters over the edge of the plywood lysimeter divider into the adjacent lysimeter. The first panel side to be overlapped was stapled into the plywood (Figure B9). The second panel side to be overlapped form the other side, was glued to the first panel using THF. The main panel was folded at each corner to create a continuous basin inside each lysimeter. The corner of each lysimeter was separately sealed using a small square of PVC to ensure a water-tight seal, when water was flowing downwards. The seal is may also airtight on most of the cells, but not all.

The 40 Mil geomembrane used for lining the lysimeter cells would be unlikely to withstand the direct piling of waste rock onto the membrane without tearing. Therefore, the sides of the lysimeters were additionally covered using panels of 60 mil high density polyethylene geomembrane (HDPE) (Figure B.10). For the cells within the center of the grid, the 60 mil HDPE was laid over the 40 Mil PVC, but was not attached. The interior HDPE liner was held in place by the addition of gravel and waste rock to either side of the liner. Around the edge of the lysimeter dividers, the 60 mil HDPE was laid over the inside of the lysimeter cell and bent over the top for a 10 centimeter overlap to the outside of all the lysimeters. The overlap was nailed to the plywood.

B.2.9 Washed Crushed Rock Drainage Layer

The drainage material within they lysimeter base was 25mm$^-$ crushed rock obtained from the sand and gravel plant located on site. The 25mm$^-$ was created by sieving of natural till deposits overlying the basement material. The chemical characteristics of the gravel were tested using static ABA. The drain rock was washed using a 3/8" screen, and water obtained from the Cluff Lake. The gravel was shoveled from the storage pile onto a metal screen suspended above ground on large timbers. The gravel was washed using a firehouse connected to a fire pump and a truck-mounted 500 gallon tank. The gravel was raked continuously during washing to expose all surfaces of the material. Two or three passes were made across the entire screen surface, to ensure the gravel was well washed. The screen was then tipped up to remove the gravel from the screen. The ground surface was covered with plywood to stop fines from being caught up in the washed gravel. There were some small natural wood chips in the gravel as well as fragments of plywood created by damage to the plywood mat placed under the washed gravel. As far as possible both the natural and plywood fragments were removed from the gravel.

The gravel was re-washed in the lined lysimeter cells to remove any remaining sand and silt. The gravel was shoveled out towards the lysimeter edge to expose the drainage pipe in the center. Water from Cluff Lake, supplied by the fire pump and hose, was used to wash the gravel. Sand and silt were washed down to the lysimeter base, and carried to the drainpipe in the center. Washing was continued until no further sand or silt was removed

from the gravel. The sand and silt were allowed to be washed down into the drainage pipe, and sufficient water was used to ensure that the pipe was flushed clean.

It was noticed at this time that the PVC geomembrane liner for the lysimeter cells was not perfectly smooth in all cells. Loading the gravel into the lysimeter had in some cases created wrinkles in the liner fabric. Some of these wrinkles were perpendicular to the slope of the lysimeter basins. As many of these wrinkles were removed as possible. The presence of the gravel inside the lysimeter prevented the removal of some of the wrinkles.

The gravel was leveled and evened across all of the lysimeters. The depth of gravel at the outer edge of the lysimeter was checked and was found to range from 12 to 15 centimeters in depth. Readjustment by manual shoveling was carried out to ensure a minimum 10 cm thickness everywhere and to generate a level gravel surface. The depth of the gravel in each lysimeter was checked, and the overall gravel level was between 30 and 35 centimeters below the top of they lysimeter walls.

B.2.10 Wall Construction

Walls were formed around the entire 8mx 8m divided lysimeter area using ½" treated plywood and 60 mil HDPE geomembrane on the inside of the box (Figure B.11). The wall was created in four layers, each layer 1.2 metres high (corresponding to a 4'x8' sheet of plywood on its side). For each layer, the walls were constructed prior to waste rock placement as free-standing walls, leaving a gap in one wall for access in and out of the experiment center. The waste rock would then be placed alternately inside and outside the walls, keeping the walls vertical by equal loading of the two sides.

The main wall supports were created from 3"x8" rough-cut timbers. ½" plywood was nailed to the timbers to form a solid structural wall to support the HDPE during loading of the cell. The HDPE liner was temporarily nailed across the top to the wall supports to hold it during waste rock placement. The HDPE walls were constructed using four separate panels which were overlapped 50 cm in the corners, and glued using contact cement. Three cable ducts were created on the outside of the wall to protect the instrumentation cabling.

The lowest level of HDPE wall liner was overlapped inside the HDPE of the main lysimeter grid (Figure B.12). A strip of 40 mil PVC was attached to the outside of the wall HDPE using solvent based contact cement. This PVC strip was fed to the outside of the lysimeter grid to prevent water from the plywood entering into the lysimeter grid. Each successive layer of HDPE was overlapped a minimum of 15 cm with the HDPE liner installed on the lower layer, and glued using solvent based contact cement (Figure B.13)

Wires inside the experiment walls were moved to the outside through holes cut through the walls (Figure B.14). The wires were laid down upon the ground surface and moved over to the wall. A flap was used to cover the wire where it went through the wall.

B.2.11 Waste Rock Placement

Waste rock placement started on July 12, 1998. An International 560 loader ($4m^3$ capacity) was used to move waste rock around the outside of the lysimeter grid to provide an access slope. The waste rock at the base of the lysimeter grid was placed using a Caterpillar Construction King backhoe . Waste rock in the cells around the edge of the lysimeter grid was placed using the front end loader. The front end loader bucket (0.5 m^3 capacity) was not capable of placing material all the way into the four center cells. This material was moved twice. First, the waste rock was moved from the storage beside the lysimeter to large piles located on the outside of each corner of the lysimeter grid using the front end loader. The backhoe bucket (0.1 m^3 capacity) was then used to place it within the four center cells.

Waste rock was placed to approximately 4.5 meters depth on the lysimeter pad in preparation for placement of the first instruments.

The remaining waste rock was placed over a period of 4 weeks using an International 560 loader, and a Hitachi UH30 excavator The loader was first used to build up the pile around the outside of the lysimeter grid. When the outside had been raised sufficiently to allow access, the excavator was driven up onto the pile. Material for the inside of the lysimeter grid was obtained by re-using material place outside the grid by the loader. It was found that larger material tended to fall to near the base of the slopes of the pile when dumped at the working top by the loader. Care was taken to draw material containing all grain sizes when selecting material for the inside of the lysimeter grid. The excavator bucket was drawn up from the very bottom of the pile. The excavator was able to work on two sides, south and west of the pile in order to place rock. This allowed the machine to be able to place material simultaneously on either side of any of the four the walls. Waste rock would be placed until the level inside the CPE was approximately equal to that of the next instrumentation level. The next set of instruments would then be installed. Installation of a set of instruments would take approximately 1.5 days. Similarly, setting up a new set of walls would take of the order of 1.5 days.

B.3 WASTE ROCK SAMPLING

Samples were collected at 1 m intervals from the waste rock material. A shovel was used to collect 5 liter samples of waste rock from the ground surface during construction. The sample was labeled with the cell number, and the depth elevation and stored in a sealed plastic sample bag. The samples were collected at variable times in relation to cell loading. Some were collected immediately after placement of the soil. Some were collected from the ground surface several days after placement, and had therefore experience some drying.

B.4 INSTRUMENTATION

Instrumentation was placed within three profiles within the pile as shown in Figure B.15. Instrumentation locations (Figure B.16) were installed at depths of 10, 20, 50, 100, 175, 300 and 450 centimeters inside the pile. The installation at 10 cm depth was created using TDR only. The installations at 20 centimeters and below have moisture content by TDR, matric suction by thermal dissipation sensor and temperature by thermistor. Each installation was surveyed to +/- 1cm elevation prior to installation of the instruments. Further details of instruments are included in other appendices.

B.4.1 TDR Probe Installation

The TDR probes were installed at approximately the same x-y location in each instrumentation installation. The location of the probes was measured from the south east corner of the pile . The level was checked using a survey level from the site datum location. The TDR probes were installed level, within 1 cm of the specified elevation. The waste rock at the instrumentation site was hand shoveled until it there was a flat area approximately 60 cm x 60 cm. The TDR probe was laid down on the ground surface. Stones larger than 10-25 cm in the immediate vicinity of the probe rods were removed to ensure that the probes remained unbent, and parallel. The soil immediately under and over the probe rods was loosely placed by hand. Once the probe rods were covered by a centimeter of soil, more soil was added using a shovel until the probe was buried under 10 to 15 cm of soil. This coverage was adequate to protect the probes during placement of further material using the excavator.

Uncoated TDR probes were added to the 20, 50 and 100 cm depth instrument locations on July 30th, 2000. Small holes approximately 40 x 40 cm were hand excavated in the top surface of the pile to a total depth of 100 cm. The lowest probe was placed as outlined above. The waste rock was then replaced into the hole and hand tamped to a density similar to the adjacent waste rock. The hole was filled to 50 cm depth and 20 cm depth in turn. Wiring for these probes was brought laterally 10 cm away from the probe, then upwards at the edge of the 40 cm x 40 cm hole.

B.4.2 Thermal Conductivity Sensors for Matric Suction

These probes were installed within the instrument profiles, adjacent to the TDR probes. A small hole was prepared, slightly larger in diameter than the probe, leveled so that the center of the probe body would be at the correct elevation. The soil immediately around the sensor was hand selected to remove sharp stones from directly contacting the sensor body. Care was taken not to cause compaction of the surrounding soil during preparation of the sensor location. The ceramic tip of the sensor was soaked in de-ionized water for 1 minute immediately prior to installation. A saturated paste of silica flour approximately ¼" thick was then moulded to the surface of the sensor. The sensor was placed in the hole, and the surrounding soil squeezed in to provide good contact between the surrounding soil and the silica flour. A small layer of material was added until the sensor body was covered. Further material was added using a shovel until the sensor was buried 10 – 15 cm below the waste rock surface. This cover was sufficient to protect the sensor from damage during piling of the waste rock using the excavator. The cabling from the sensor was strapped to the cables from the TDR and temperature probes to form a cable bundle. this cable bundle was hand buried prior to further piling to ensure protection from damage.

B.4.3 Temperature Probes

These sensors were installed 15 cm from the TDR probes at each installation. The sensors were placed on level ground and covered with hand picked material. Grains larger than 1 cm were removed from the soil immediately surrounding the sensors. An additional 10 – 15 cm of soil was shoveled on top of the sensors to provide protection from further piling.

B.4.4 Neutron Probe for Moisture Content

Neutron access tubes were created from 2 1/4" O.D. 1/4" I.D. Wall thickness, schedule 40 aluminum pipe. Twenty foot sections of pipe were cut to a six foot, five foot and 9 foot sections and threaded. 2" threaded Aluminum couplers were used to join the piping segments The three segments were installed with the 6' section at the base, the five foot section in the middle, and the remainder at the top. The top segment of pipe was later trimmed to be approximately 5 cm above ground surface following completion of the upper surface of the pile to the final grade. The base of the six-foot segment of pipe was sealed using a 2" PVC Shedule 40 plastic slip cap.

B.4.5 Suction Lysimeters

Nine suction lysimeters were installed in the pile to permit the extraction of soil water for chemical analysis. Suction lysimeters were installed in each instrumentation profile at depths of 450 cm, 300 cm and 175 cm below the finished surface elevation.

B.4.6 Tensiometers

Nine tensiometers were added to the pile on July 30, 2000 at depths of 20, 50 and 100 cm in each instrumentation profile. The tensiometers were SoilMoisture Inc. Jetfill Tensiometers. They were installed at the edge of the holes excavated for the installation of the uncoated TDR probes. The ceramic tip of the each tensiometer was coated in a 1/4" thick saturated paste of silica flour prior to installation. Large stones were removed from the waste rock surrounding the ceramic tip to prevent damage. The holes were backfilled and hand-tamped to the density of the surrounding waste rock.

B.4.7 Rainfall Gauge

Precipitation is measured using a Texas Electronics 525M tipping bucket rainguage, calibrated for 0.1 mm/ tip. The raingauge is mounted with its lip 50 cm above ground level attached to a small post.

B.4.8 Weather Station

A fully automated weather station was added to the pile surface in June, 1999, by collaborating researchers from the University of Saskatchewan. Wind speed, relative humidity, rainfall, air temperature and net radiation instruments are included.

B.5 PHOTOGRAPHS OF CONSTRUCTION

A series of photographs taken during construction are presented. The captions under each photograph present the photograph contents.

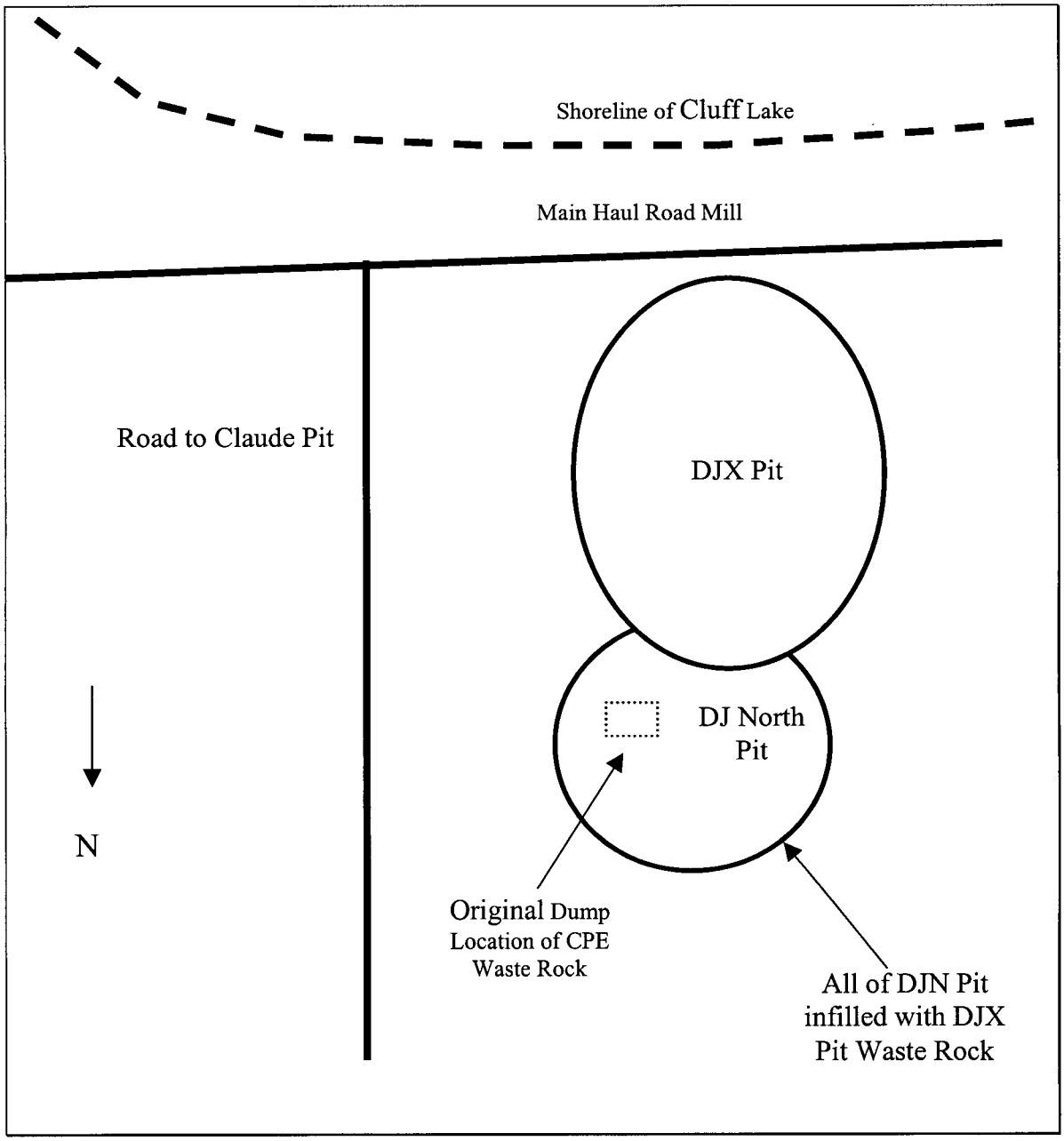

Figure B.1: Origin Location of Waste Rock used for CPE

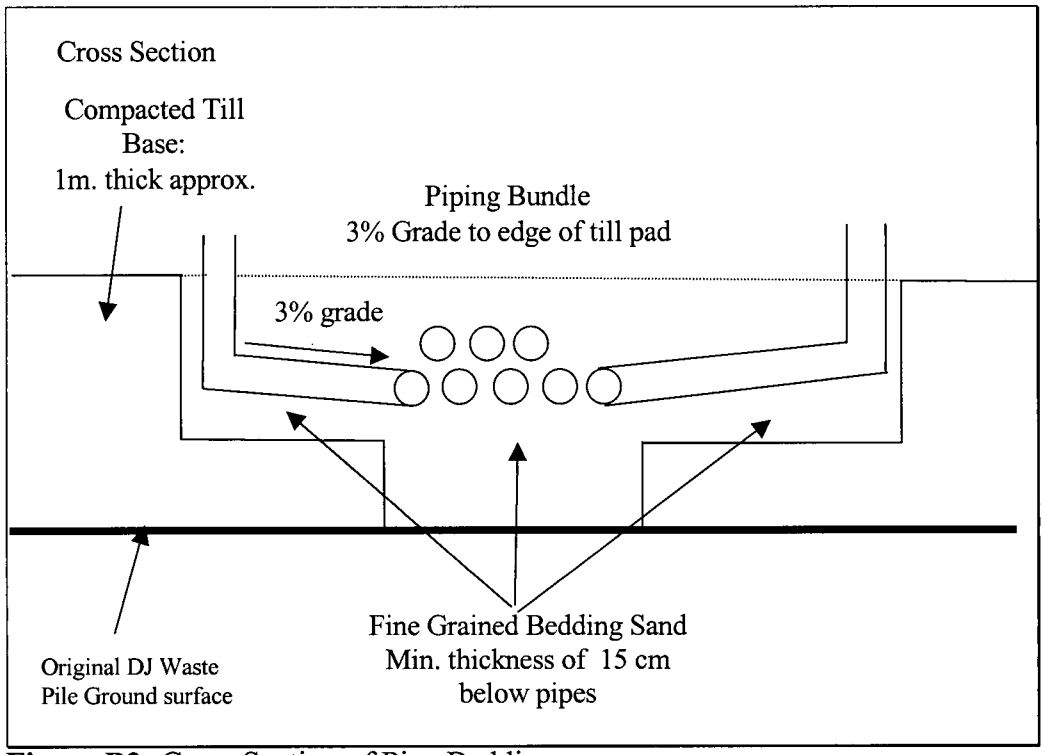

Figure B2: Cross Section of Pipe Bedding

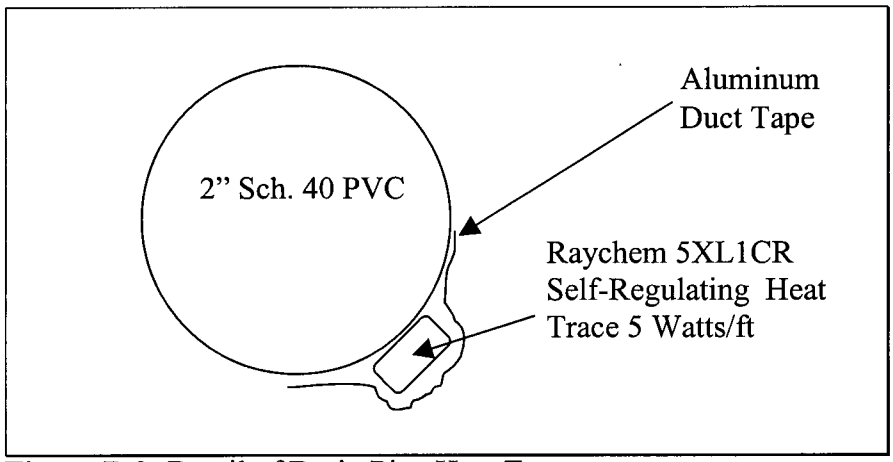

Figure B.3: Detail of Drain Pipe Heat Trace

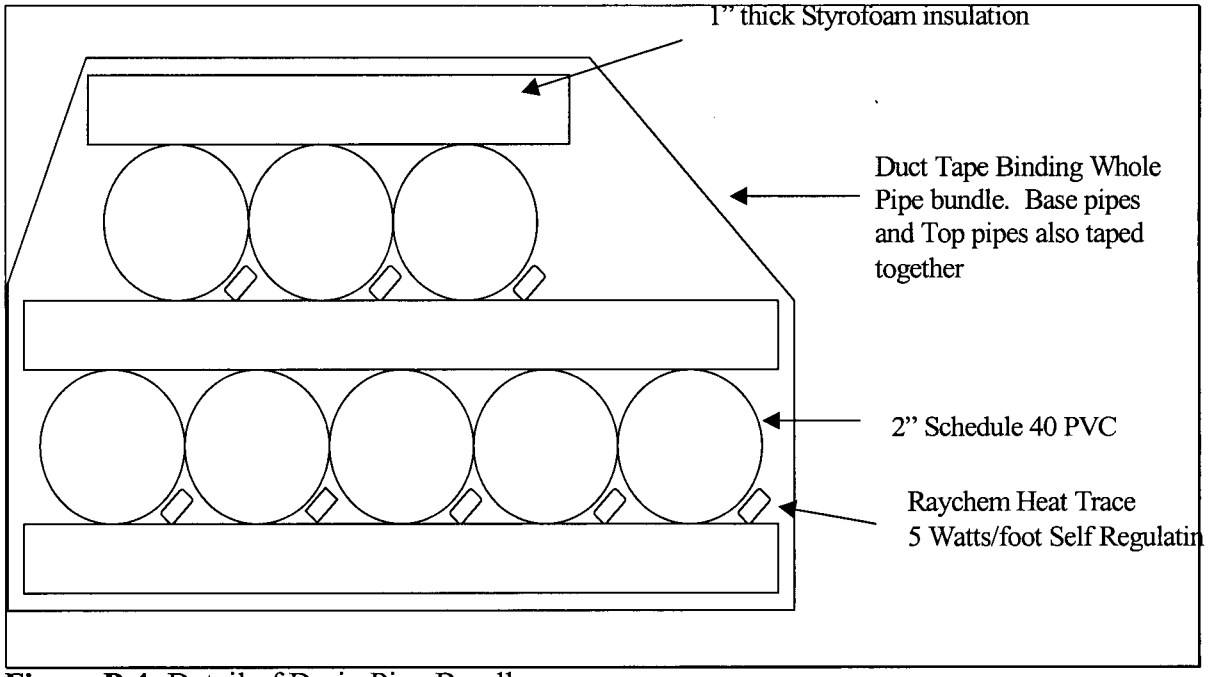

Figure B.4: Detail of Drain Pipe Bundle

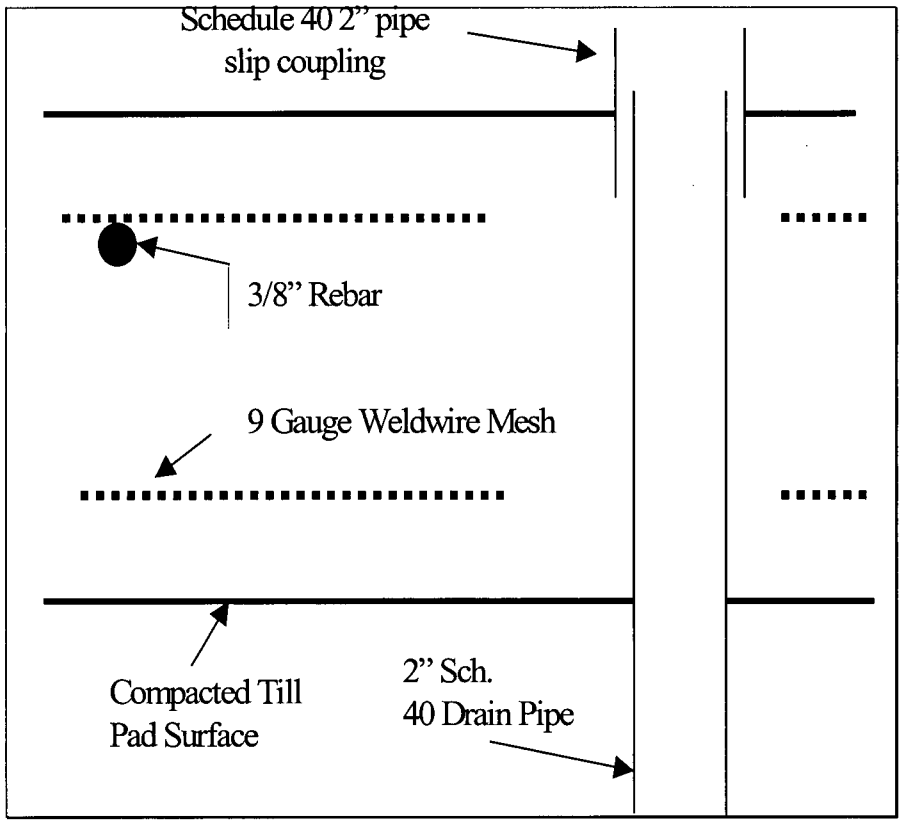

Figure B.5: Schematic Cross Section of Concrete Pad Re-enforcement

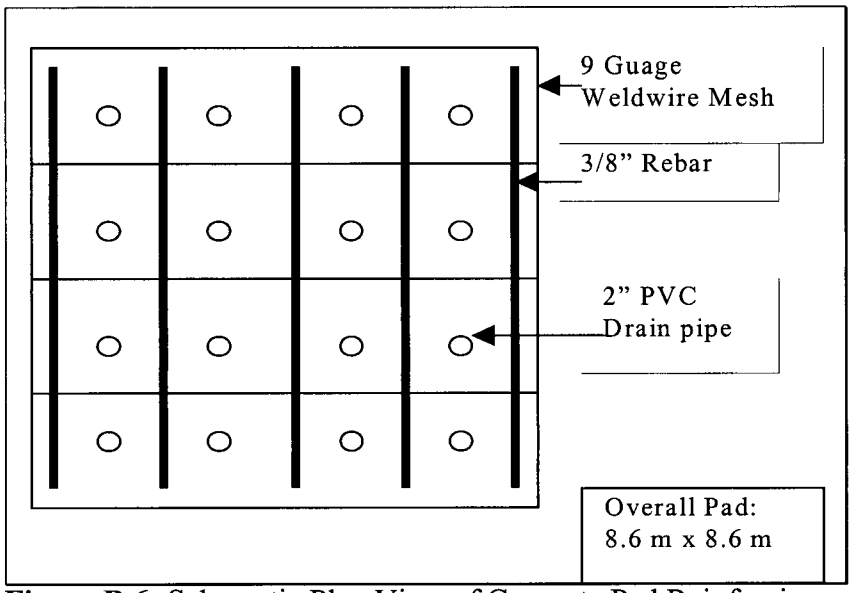

Figure B.6: Schematic Plan View of Concrete Pad Reinforcing

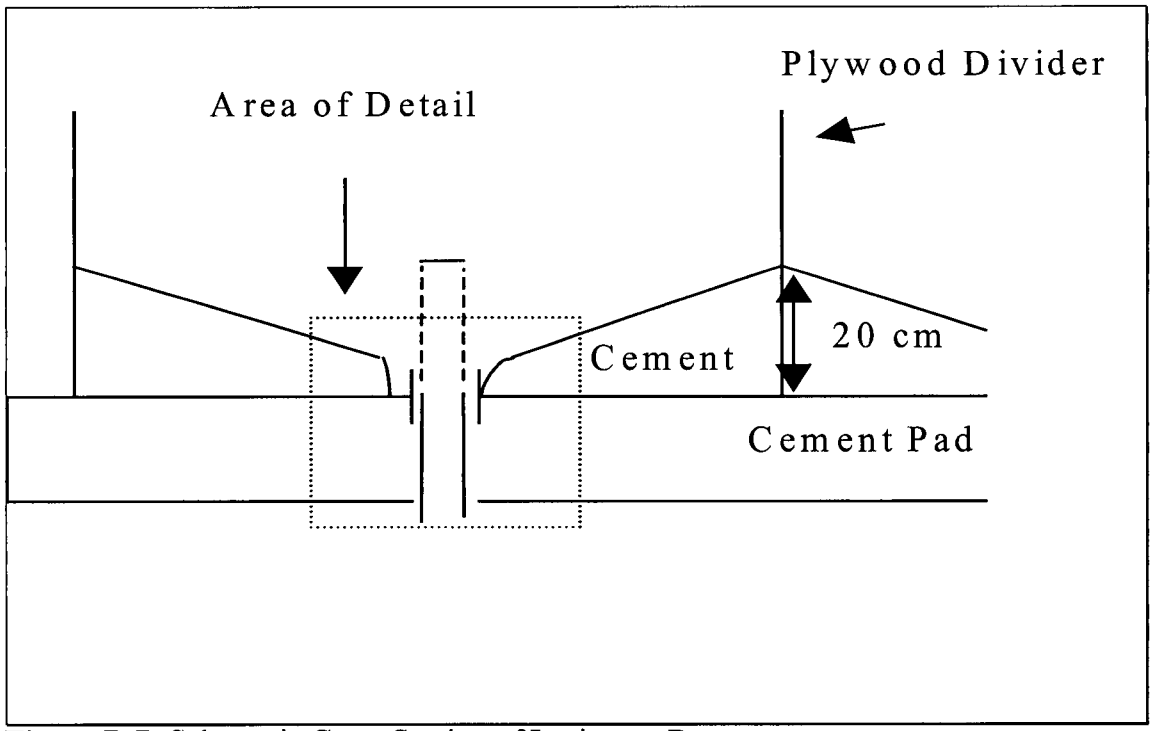

Figure B.7: Schematic Cross Section of Lysimeter Base

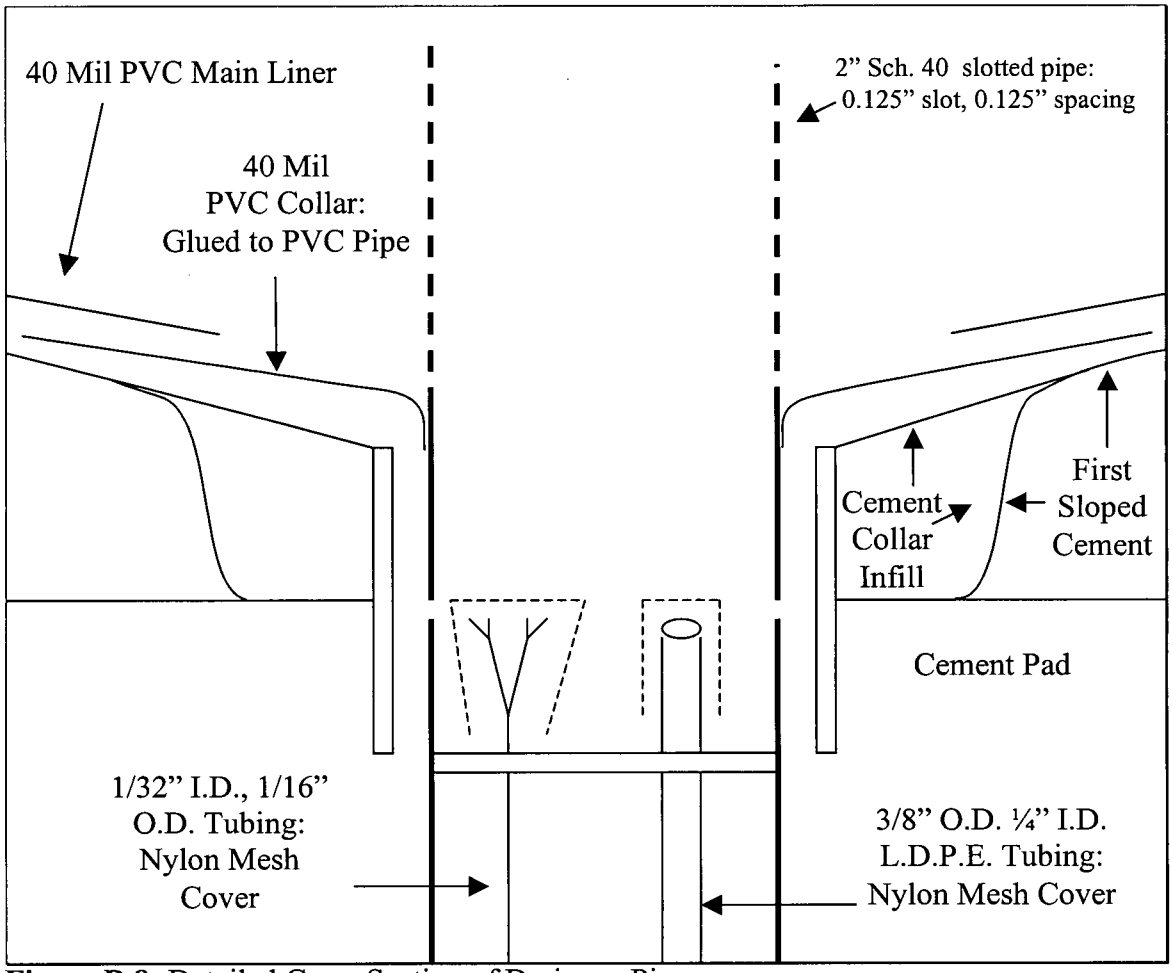

Figure B.8: Detailed Cross Section of Drainage Pipe

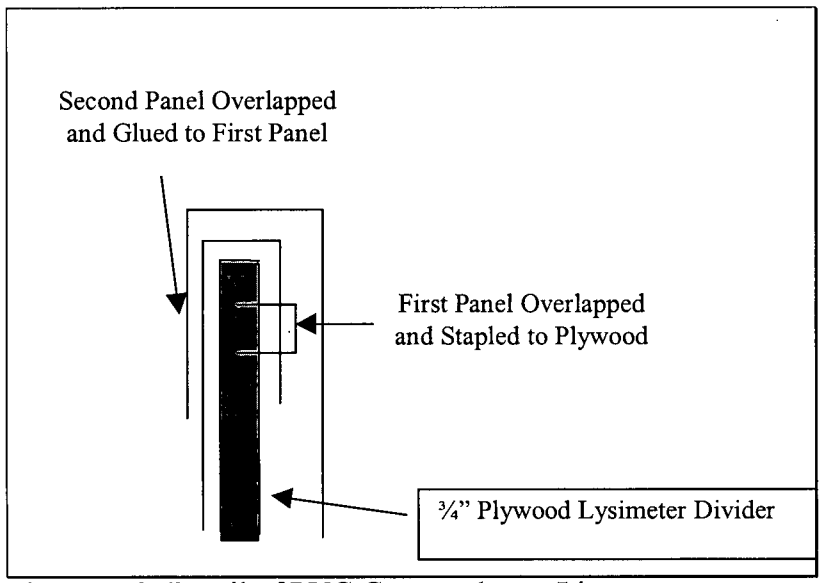

Figure B.9: Detail of PVC Geomembrane Liner

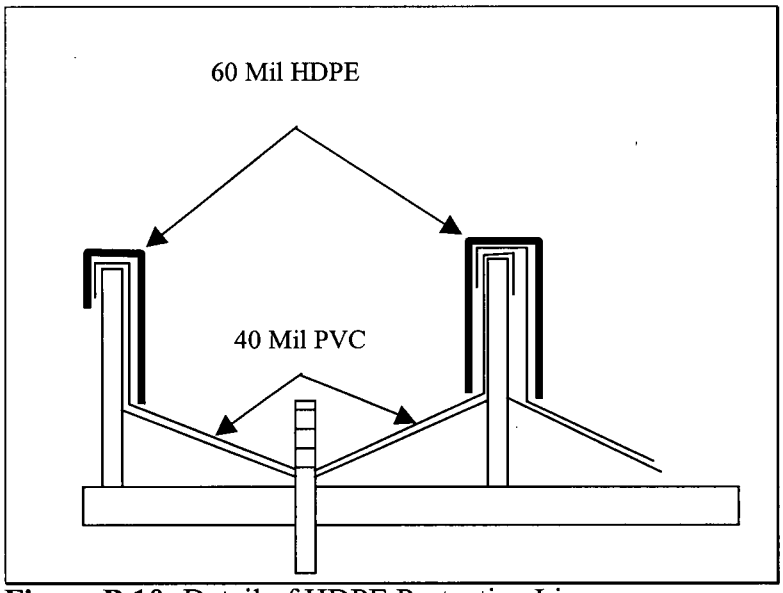

Figure B.10: Detail of HDPE Protective Liner

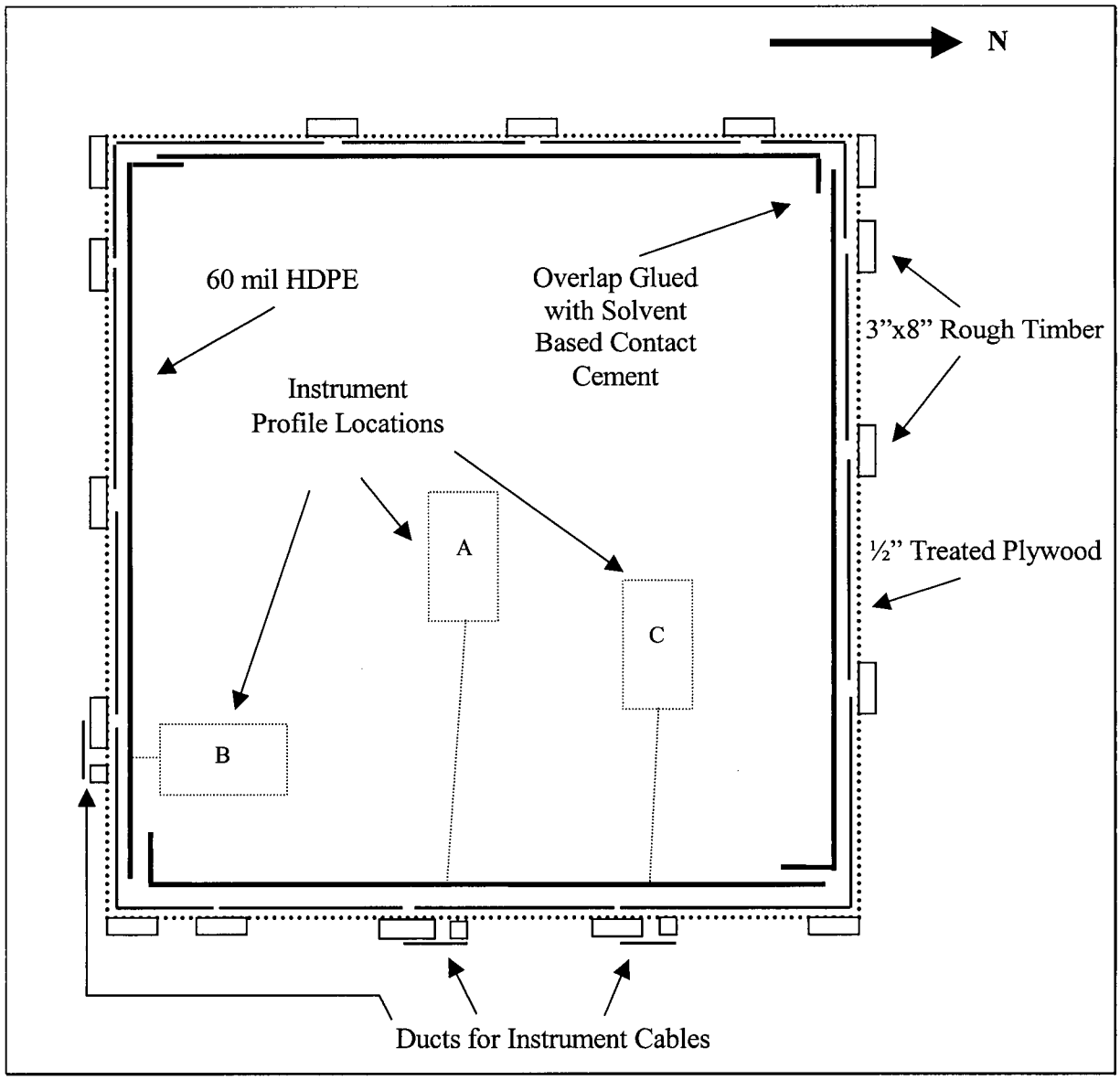

Figure B.11: Schematic Plan View of CPE Wall Structure

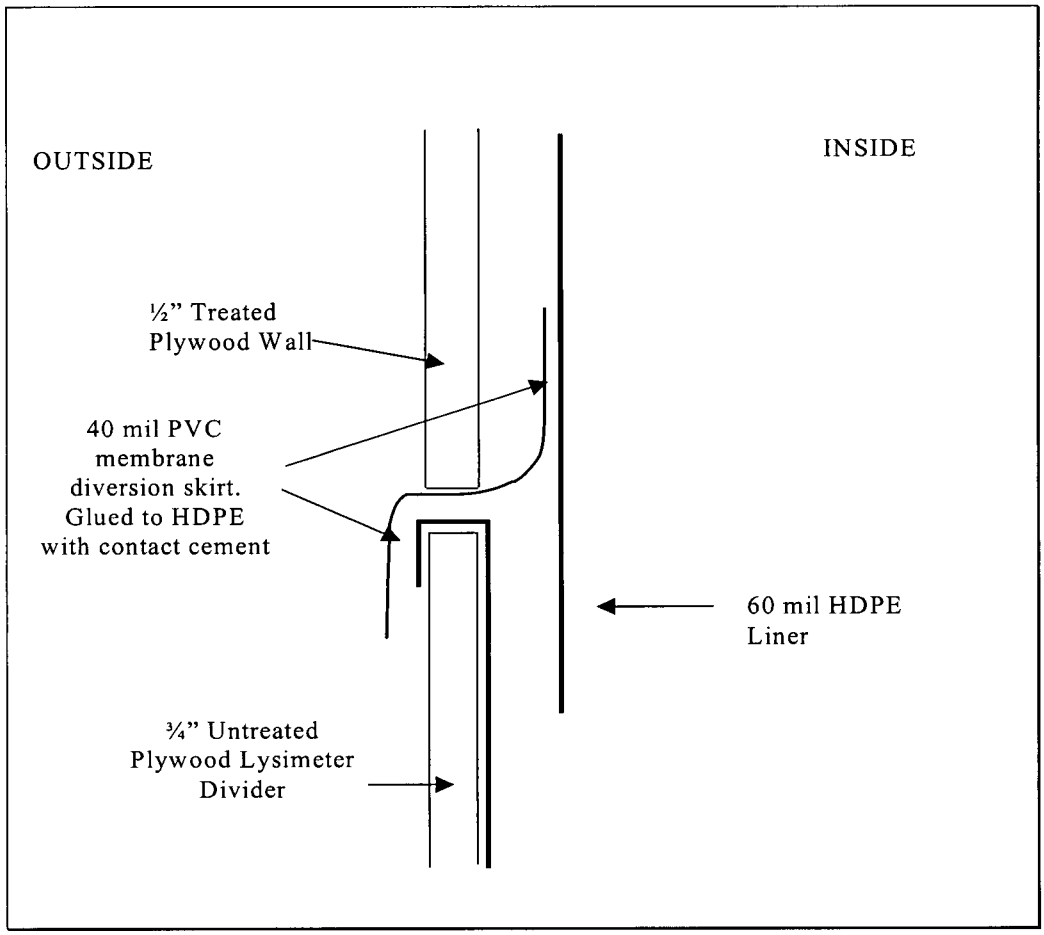

Figure B.12: Schematic Cross Section of CPE Wall and Lysimeter Base Overlap

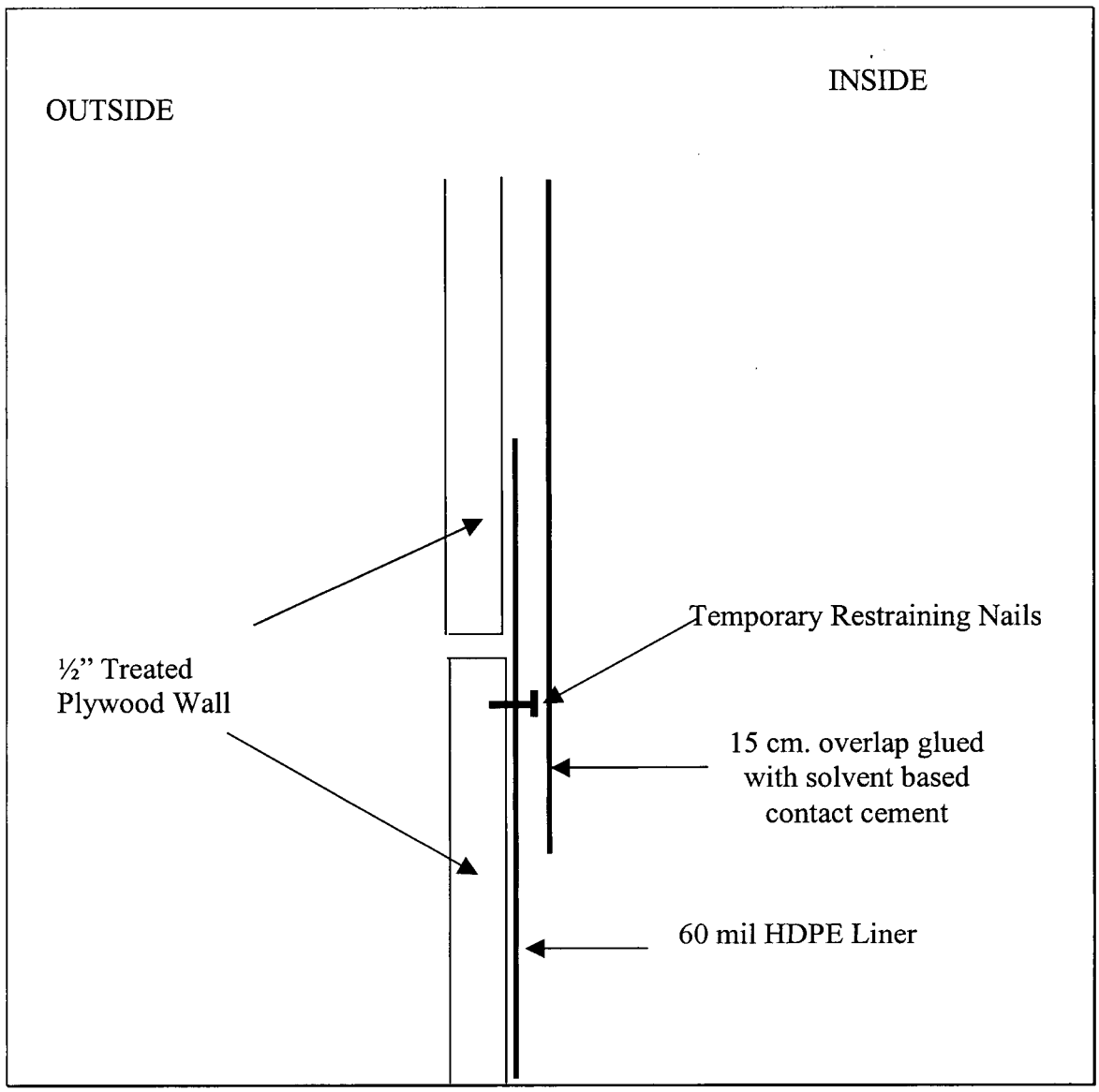

Figure B.13: Detail Cross Section of HDPE Wall Liner Overlap

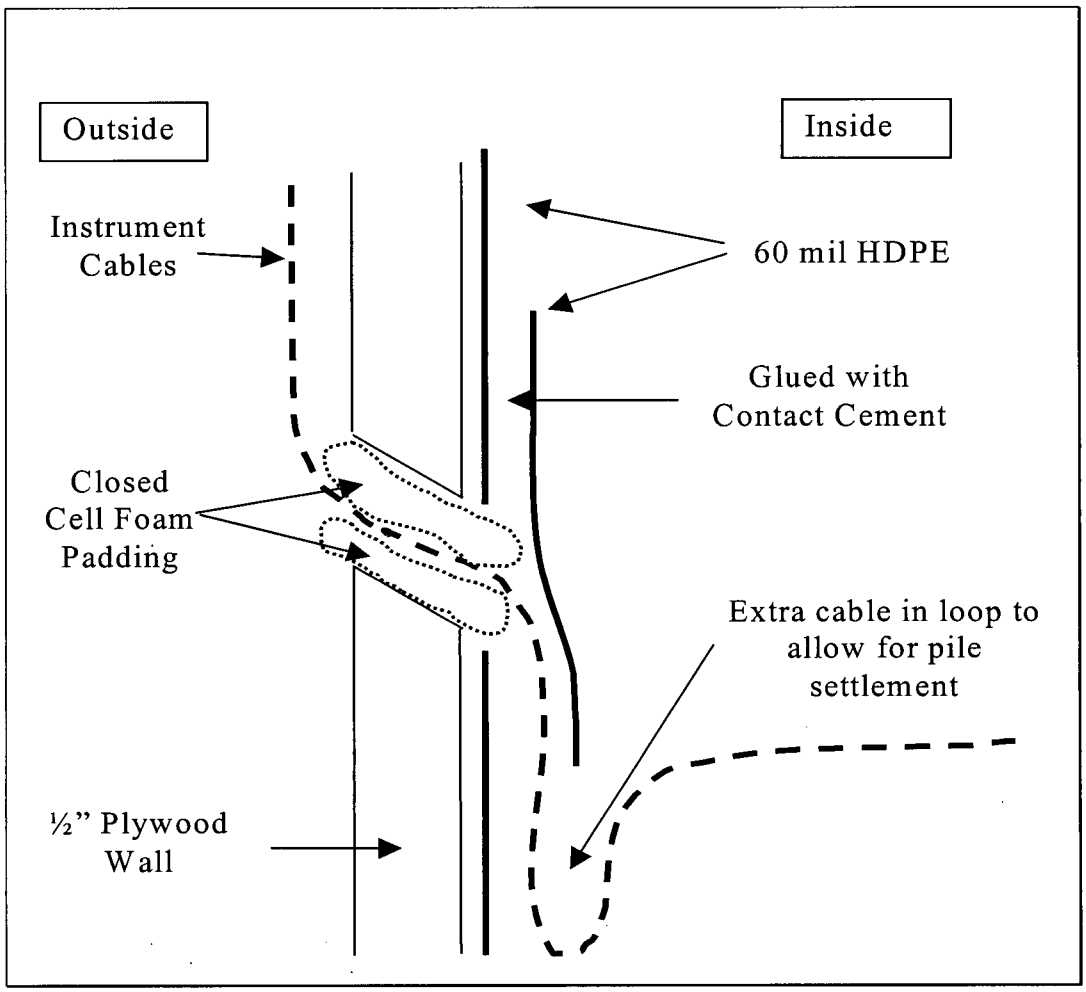

Figure B.14: Detail Cross Section of Instrument Cable Passing through HDPE Wall

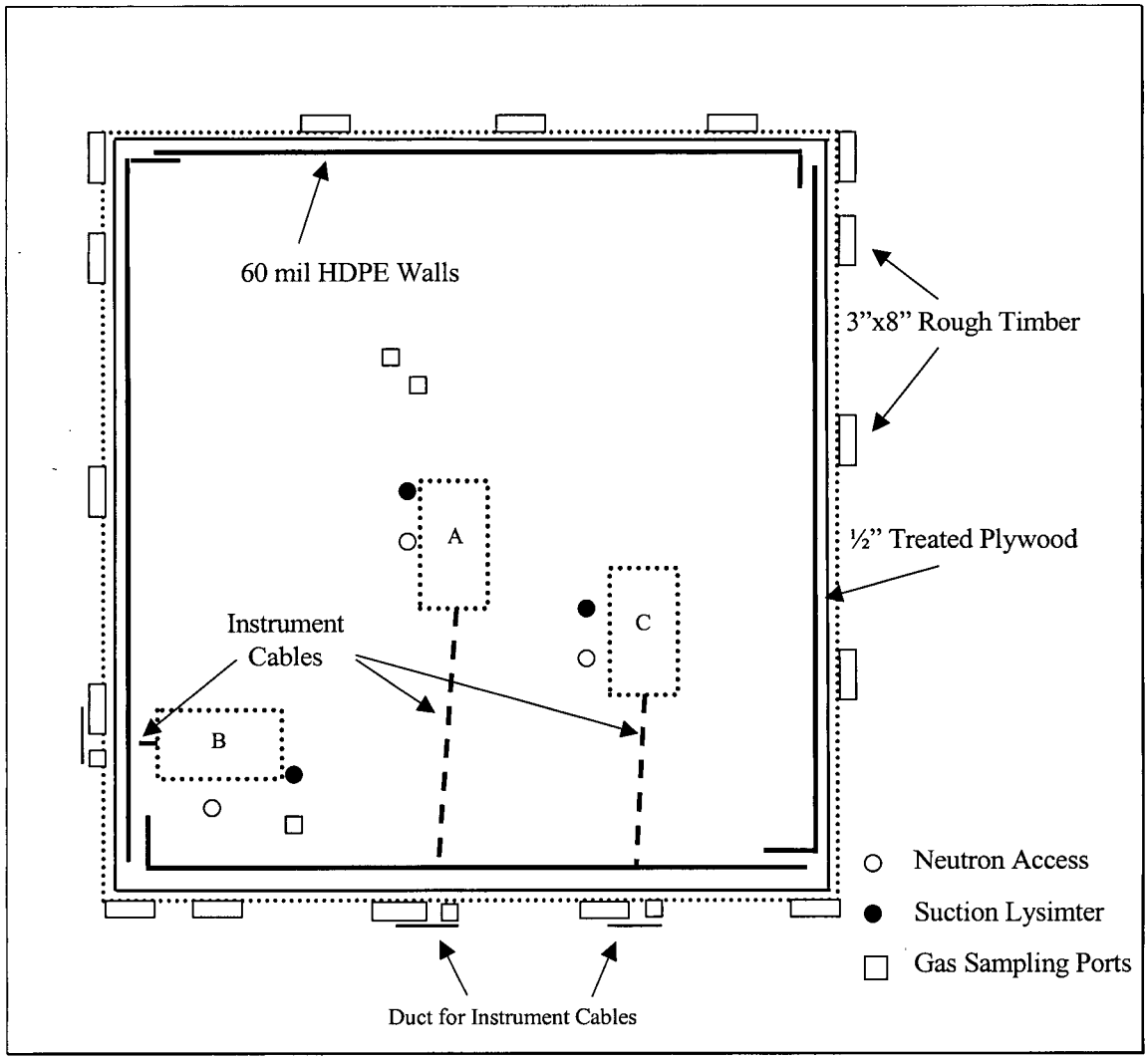

Figure B.15: Schematic Plan View of CPE showing Instrument Profile Locations

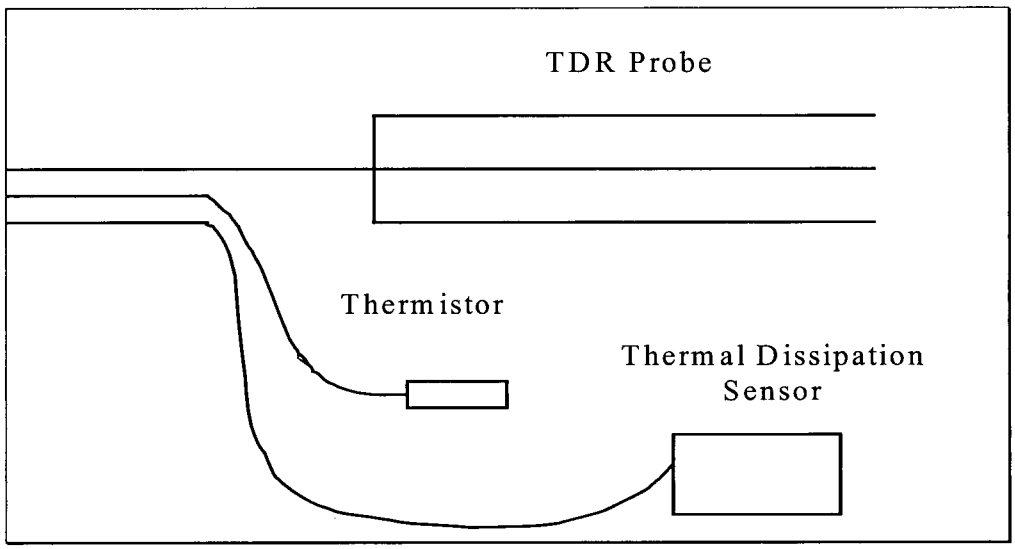

Figure B.16: Schematic Layout of an Electronic Instrumentation Installation

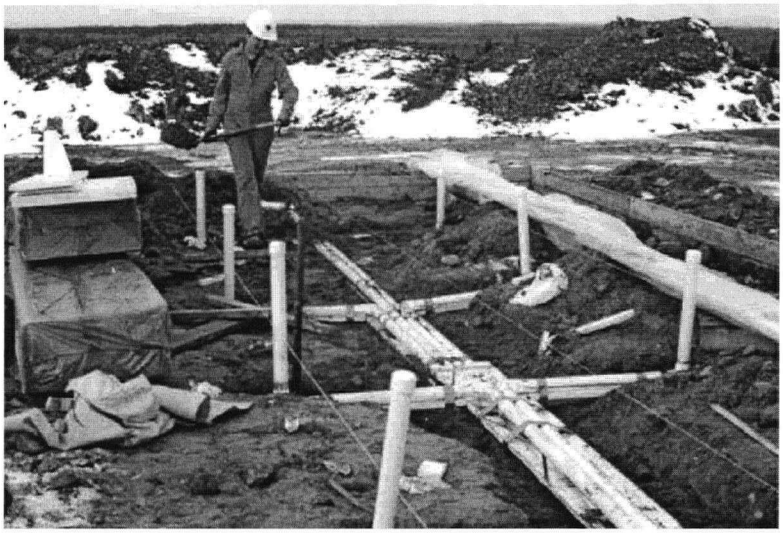

Figure B.17: Photograph of lysimeter piping at pile base.

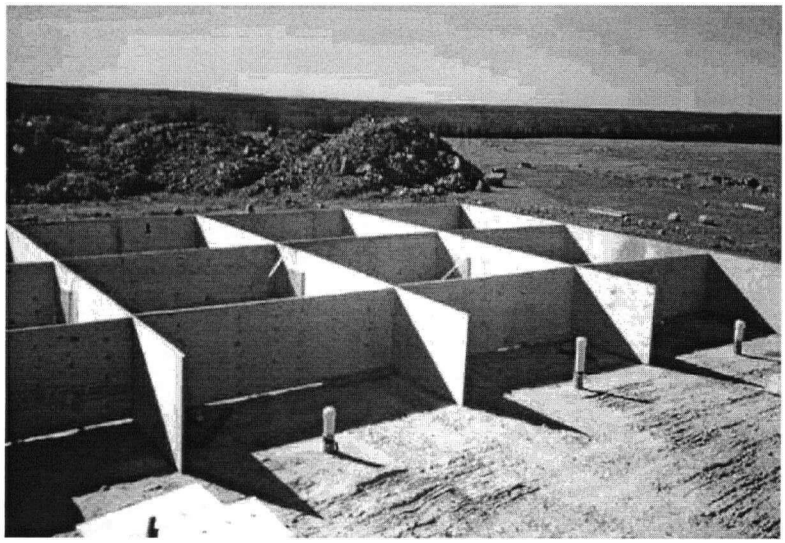

Figure B.18: Photograph of lysimeter dividers prior to installation of sloped cement.

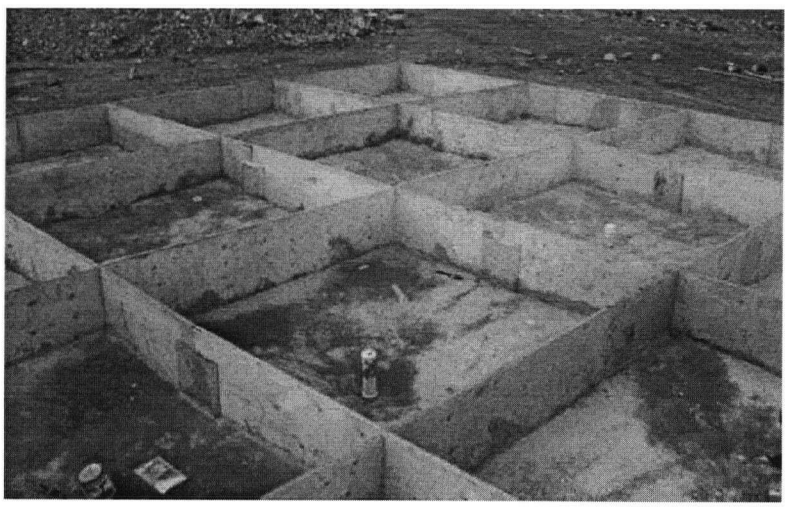

Figure B.19: Photograph of lysimeters prior to installation of geomembrane

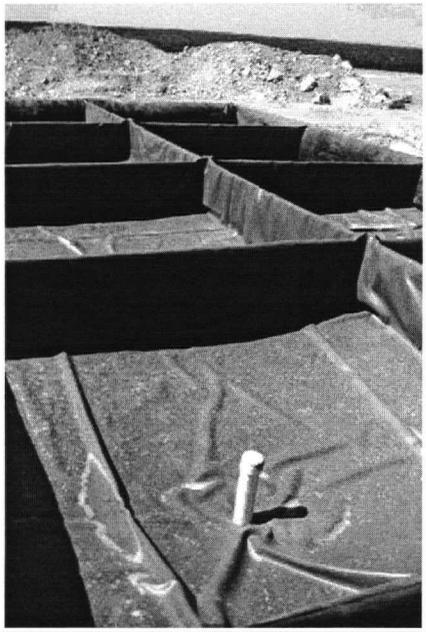

Figure B.20: Photograph of lysimeter base with PVC and HDPE geomembrane liners.

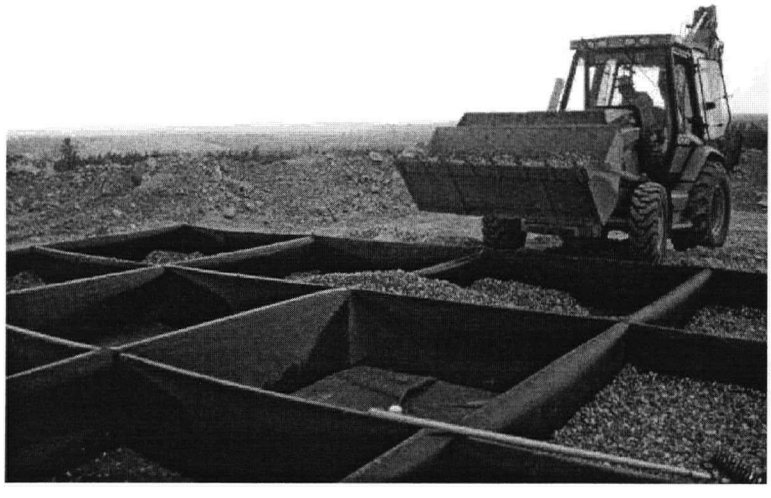

Figure B.21: Photograph of filter gravel installation.

Figure B.22: Photograph of lysimeter wall design showing support members, plywood sides, and HDPE geomembrane. Aluminum neutron probe access tubes visible, as well as PVC piping used to protect suction lysimeter tubing during installation.

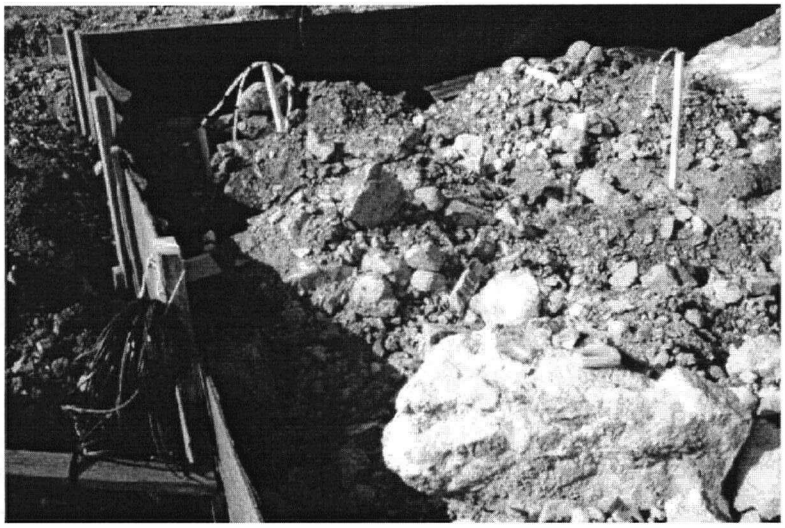

Figure B.23: Photograph showing typical waste rock texture within pile. Boulder in bottom right is approximately 1 m in diameter.

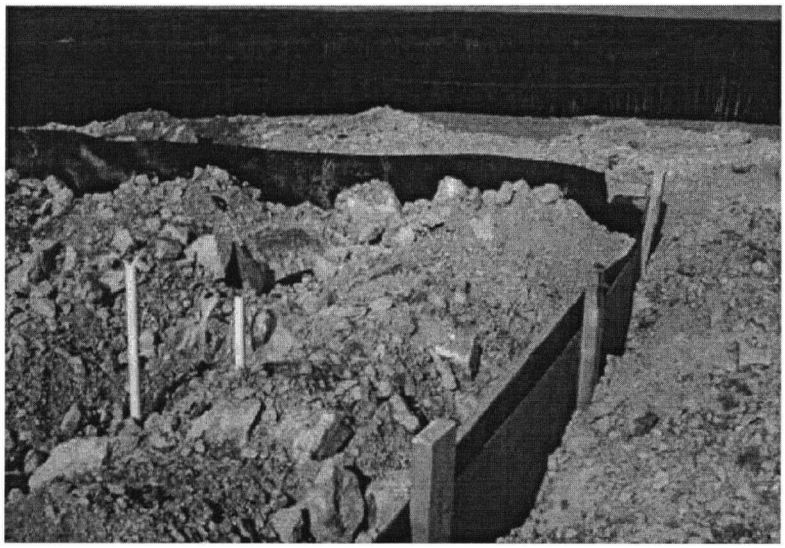

Figure B.24: Photograph showing typical waste rock texture within pile.

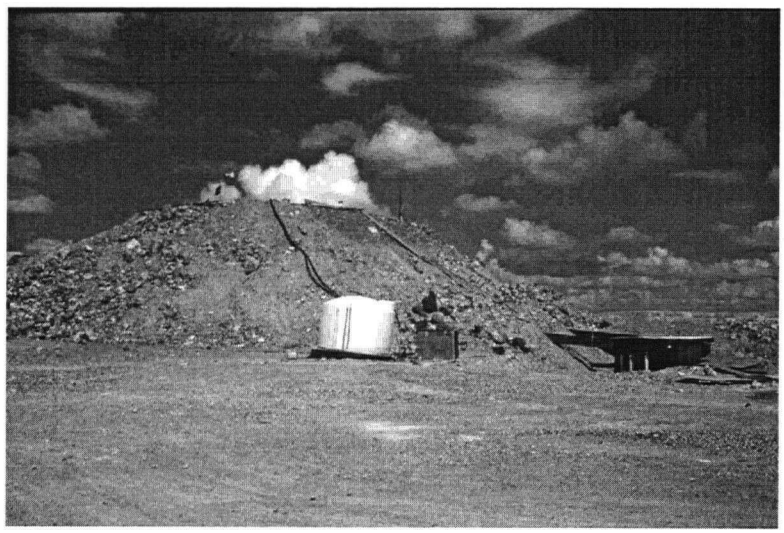

Figure B.25 Photograph of finished pile including weather station, tank for rainfall simulator and instrument hut.

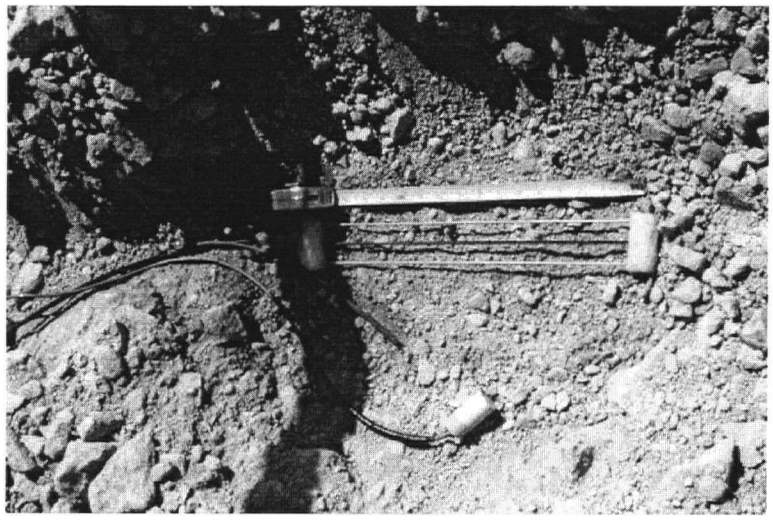

Figure B.26: Photograph of typical instrument installation with TDR probe, temperature probe and thermal conductivity sensor (top to bottom).

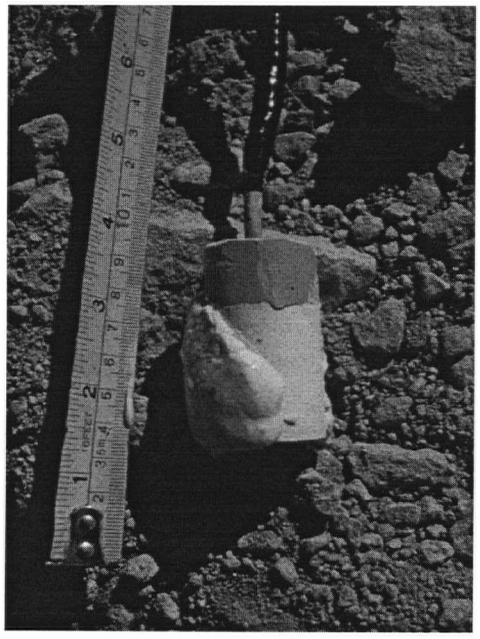

Figure B.27: Detailed photograph of thermal conductivity sensor.

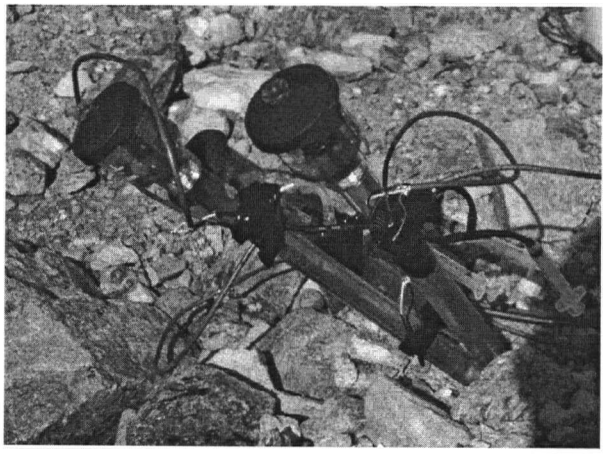

Figure B.28: Photograph of tensiometer cluster showing three Jetfill tensiometers with pressure transducers attached.

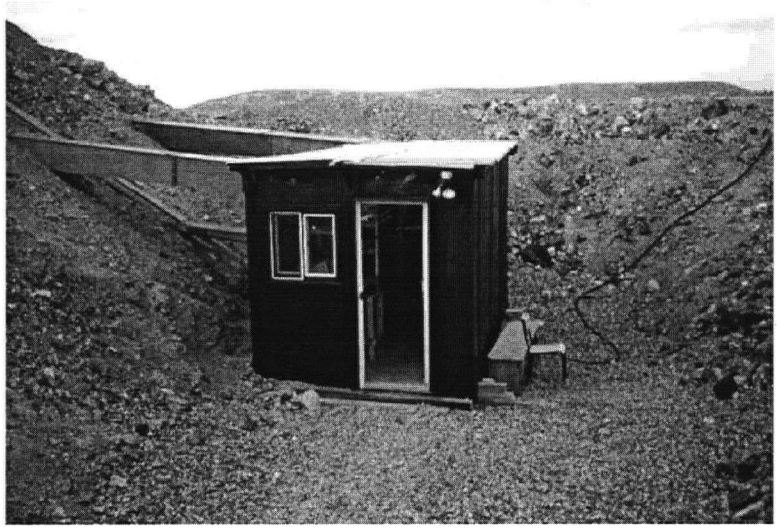

Figure B.29: Photograph of instrument hut.

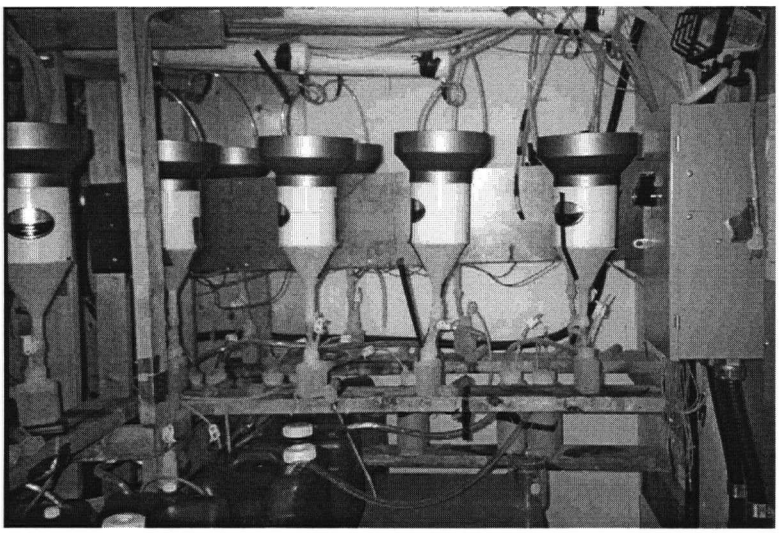

Figure B.30: Photograph of tipping bucket gauges used to monitor flow, and outflow water passive compositing system.

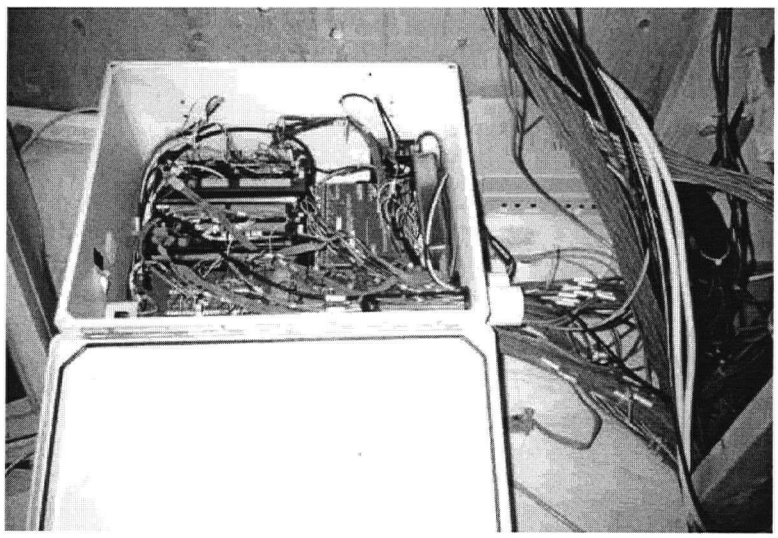

Figure B.31: Photograph of datalogging installation within instrument hut.

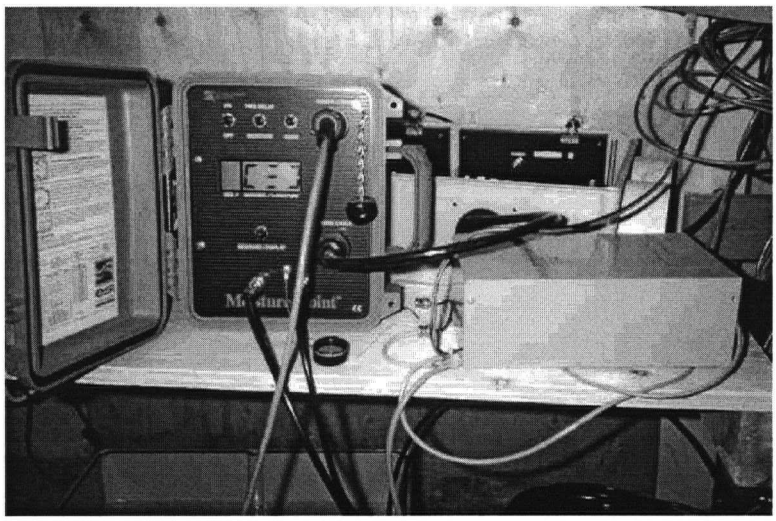

Figure B.32: Photograph of TDR measurement device, interface, and multiplexing equipment inside instrumentation hut.

APPENDIX C: CONSTRUCTED PILE EXPERIMENT: SUCTION LYSIMETERS

C.1 INTRODUCTION

This appendix presents the details of the preparation, installation, and sampling methods used to draw water samples from the suction lysimeters. The sampling procedures are written in the form of instructions.

Suction lysimeters were installed during the pile's construction in three profiles at depths of 175, 300 and 450 cm from the pile surface. The suction lysimeters are used to extract water samples from within the pile and to estimate soil water suction. They are located in the three instrument profiles and numbered as shown in Table C.1 below.

C.2 INSTALLATION DETAILS

C.2.1 Pre-installation Preparation

The suction lysimeters are Soilmoisture Equipment Model 1920L12B2M2 pressure/vacuum soil water samplers. Details of the design and installation are shown in Figure C.1 below. Prior to installation, the suction lysimeter bodies were weighed when dry, with no extraction tubing attached. They were then left to soak in de-ionized water for a twenty-four hour period and then re-weighed to estimate the volume of water contained in one pore volume of the ceramic tip (see Table C.2). The suction lysimeters were then kept stored in de-ionized water until final installation within the pile. It was found that during the storage period a volume of water (100 mls approx.) migrated through the ceramic. This water was discarded prior to the installation of the lysimeters within the pile.

The sampling tubes (1/4" O.D., 1.8" I.D. HDPE) were installed into the suction lysimeter bodies with no prior washing or preparation. One tube was cut to extend 2 cm below the base of the expansion plug at the top of the lysimeter body. The other tube was cut to extend to the base of the ceramic tip of the suction lysimeter. The top cavity of the lysimeter above the rubber expansion plug was back-filled with epoxy cement (Soilmoisture Equipment part 09800V004).

C.2.2 2.2 Installation

The suction lysimeters were installed during pile construction. The depth of the suction lysimeters was determined by level surveying to within 1 cm. A small pile of waste rock material was made approximately 15 centimeters high. Soil was scooped of this pile to create a hollow approximately 10 cm in diameter. A paste of saturated silica flour was applied to the ceramic tip prior to installation in order to insure good hydraulic contact between the lysimeter and waste rock,. The paste was made by saturating silica flour with de-ionized water. The lysimeter ceramic tip was coated with a ¼" coating of saturated silica flour paste and quickly placed inside the pre-made hole. The sides of the soil mound were squeezed in, and waste rock material was added at the sides of the hole to create a good hydraulic contact between the waste rock material and the silica flour coating on the probe. The waste rock material immediately adjacent to the suction lysimeter tip and body of was selected to remove material larger than approximately 25mm to prevent damage to the lysimeter tip.

The lysimeter was then buried using material moved manually onto the lysimeter using a shovel. This material was limited in size to particles less than 20 centimeters diameter by the nature of the shovel used to move the rock. The lysimeter was completely covered with hand moved material to a depth of 20 cm prior to the continuance of piling of any materials by an excavator.

During piling of the rock by an excavator, the tubing from the lysimeters was protected inside a 2" diameter schedule 40 PVC pipe. The sampling tubing was fed inside the pipe, and waste rock material was piled around the pipe. Once 30 to 60 centimeters of the pipe was buried, it was withdrawn and the resulting open void space was manually refilled using hand picked fine grained material. Handfuls of waste rock were manually sifted to remove larger particles (>10 mm), and the remaining material was fed into the hole until the hole was filled flush with the ground surface.

The sample tubing extended 50 cm above ground surface to allow for the attachment of sampling equipment. The tubing was terminated with flexible vinyl tubing and tubing clamps as shown in Figure C.1. A syringe body with rubber septum was added to one tube. All exposed tubing is stored under a weighted plastic bucket to shield the tubing from wildlife destruction.

C.3 SAMPLING METHOD

The following is a set of instructions which outline the sampling method used for the suction lysimters.

C.3.1 Materials needed

- Vacuum gauge fitted with syringe needle point (22 guage, 5/8")
- One 60 ml syringe per suction sampler
- Rubber septum that fits syringe body. Ends should be relatively crack-free. If dried and cracked, replace with a new septum.
- Marker pen
- Sample bottle and lids
- Notebook and pen

C.3.2 Sampling Instructions

The suction samplers are sampled by applying a vacuum to the sampler body at a suction greater than the suction in the surrounding soil. This draws water into the sampler body. The usual suction applied is 50 kPa. The sampler body is designed to hold a larger volume of sample than the tensiometers. The suction samplers will produce volumes of sample ranging from 120 to 240 mls at the 175 to 450 cm depths. The time required to produce the sample will depend upon how wet the pile is. Immediately following a rainfall event, when the pile is wetted, the samplers will produce a full sample volume in several hours. Under drier conditions, the samplers are left overnight for 16 to 24 hours. To start sampling:

- Pierce the syringe septum with the vacuum gauge syringe needle on tube B
- Attach the 60 ml syringe to tube A.
- Withdraw air from the sampler until the vacuum gauge registers 50 kPa. Use the clamp to clamp off the A tube and empty the syringe. Several syringes of air (8 to 10) will be needed to be withdrawn to achieve 50 kPa.
- With the sampler at full vacuum, leave the gauge connected and observe for a minute. Make sure the sampler is retaining vacuum.
- Clamp off all clamps, and remove the vacuum gauge from the syringe septum.
- Record the start date and time and the vacuum applied in the lysimeter sample notebook.
- Wait several hours to overnight for the sample to collect

To withdraw a sample after the sampling period:

- At the start of the sampling, zero the vacuum gauge by adjusting the calibration screw. For the manual gauge this is achieved by removing the screw in the clear gauge cover plate, and adjusting the screw on the gauge face. Tap the gauge gently to settle the needle. For the digital gauge, the calibration screw on the side is adjusted until the reading is zeroed.
- Unclamp the clamp on Tube B between the 3ml syringe body and the sampler, but do not open the clamp on Tube A. Retain the vacuum.
- Pierce the syringe septum with the vacuum gauge needle.
- Allow the vacuum gauge to come to a full reading.
- If using a dial vacuum gauge, gently tap the gauge several times to ensure the reading is stable.
- Record this reading as P1. The dial gauge can be read to 0.5 kPa. The digital gauge records to 0.1 kPa.
- Remove the vacuum gauge, and allow it to return to zero.
- Pierce the syringe septum with the vacuum gauge needle a second time.
- Allow the vacuum gauge to come to a full reading. Record this reading as P2.
- The time between vacuum measurements should be as short as possible allowing for full recovery of the vacuum gauge to a zero reading.
- The vacuum present in the sampler ($P1^2/P2$) represents an upper limit to the tension in the soil surrounding the sampler. It will only equal the tension if the sampler has come to full equilibrium.
- Once the vacuum has been recorded, remove the 3 ml. syringe body from the vinyl tubing by unscrewing it.
- Open the clamp on Tube A
- Connect the 60 ml syringe to the Tube B by screwing the syringe body into the vinyl tubing. The vinyl tubing will screw into the luer lock fitting on the syringe.
- Start to pull the sample. Pull a vacuum with the 60 ml syringe to draw the sample up from the sampler body. The sample will not be drawn up by one syringe pull. Clamp off the clamp on Tube B, remove the syringe and empty it of air. Reattach the syringe, release the clamp and pull a second syringe. The sample should start on the second syringe.
- Pull 10 mls of sample into the 60 ml syringe, then clamp the Tube B clamp. Remove the 60 ml syringe and pull the syringe open to the full open position. Swill the 10 ml of water around the syringe to wash the syringe, then discard the water. This cleans the syringe body for the new sample, and also removes any residual water that remained in the sampling tubes from the previous sampling episode.
- Reconnect the syringe and withdraw a full 60 ml syringe of sample. Clamp off Tube B
- Place this in one bottle.
- Re-connect the syringe and withdraw a full 60 ml syringe of sample. Clamp off Tube B.
- Place this in a second bottle.
- If there is sufficient sample, reconnect the syringe and withdraw at least 40 mls of sample to the syringe. This can be used to measure pH and conductivity.
- If there is still sample in the sampler, use a separate syringe to remove all of the sample. Once the syringe starts to pull air, disconnect and empty the syringe. Slowly push several syringes of air into the sampler to push the residual water within Tube B back into the sampler. The residual water will have formed small "packets" in the tubing where the

packet is held by capillary tension. Pushing the air too quickly will cause the air to break through the middle of the packet, leaving the water as a residual on the sides. The packet will then re-form. Pushing slowly will allows the packets to stay coherent and be pushed into the sampler.

- Close all clamps.
- For each sample, record the sample volume obtained. This gives an indication of soil moisture conditions near the sampler.
- The sample is split into two sample bottles. Label each bottle with the time the suction lysimeter number (SL1 to SL9), the date and time the vacuum was applied, and the date and time the sample was taken. Also add "CPE" at the bottom to indicate it was taken from the constructed pile experiment.
- The first bottle is for anion analysis. The second bottle is for cation analysis and is labeled with sampler number, dates and times and is also marked with CATIONS. Nitric acid preservative is added to this bottle from the dropper bottle stored in the fume hood in the environment deparment laboratory. Add 10 drops nitric acid using the teflon dropper bottle for a full 60 ml sample, and reduce accordingly for smaller sample sizes. Store the samples in the refrigerators in the environment lab.
- After all three lysimeters in a lysimeter bundle are sampled, coil the sampling tubes and place under the bucket to prevent wildlife damage to the tubes. Weight the bucket down with a small rock.

Profile A: Center	Profile B: North	Profile C : South Corner
T1: 20 cm	T4: 20 cm	T7: 20 cm
T2: 50 cm	T5: 50 cm	T8: 50 cm
T3: 100 cm	T6: 100 cm	T9: 100 cm

Table C.1: Location and numbering of suction lysimeters

Probe Number	Dry Weight (grams)	Saturated Weight (grams)	Mass of Water (grams)	One Pore Volume of Ceramic Tip (mls)
1	245.27	251.27	6.00	6.00
2	244.74	253.54	8.80	8.80
3	243.58	249.08	5.50	5.50
4	247.61	251.93	4.32	4.32
5	245.29	249.85	4.56	4.56
6	248.78	253.74	4.96	4.96
7	246.08	251.34	5.26	5.26
8	247.36	251.75	4.39	4.39
9	246.3	251.15	4.85	4.85

Table C.2: Pore volume of suction lysimeter ceramic tip.

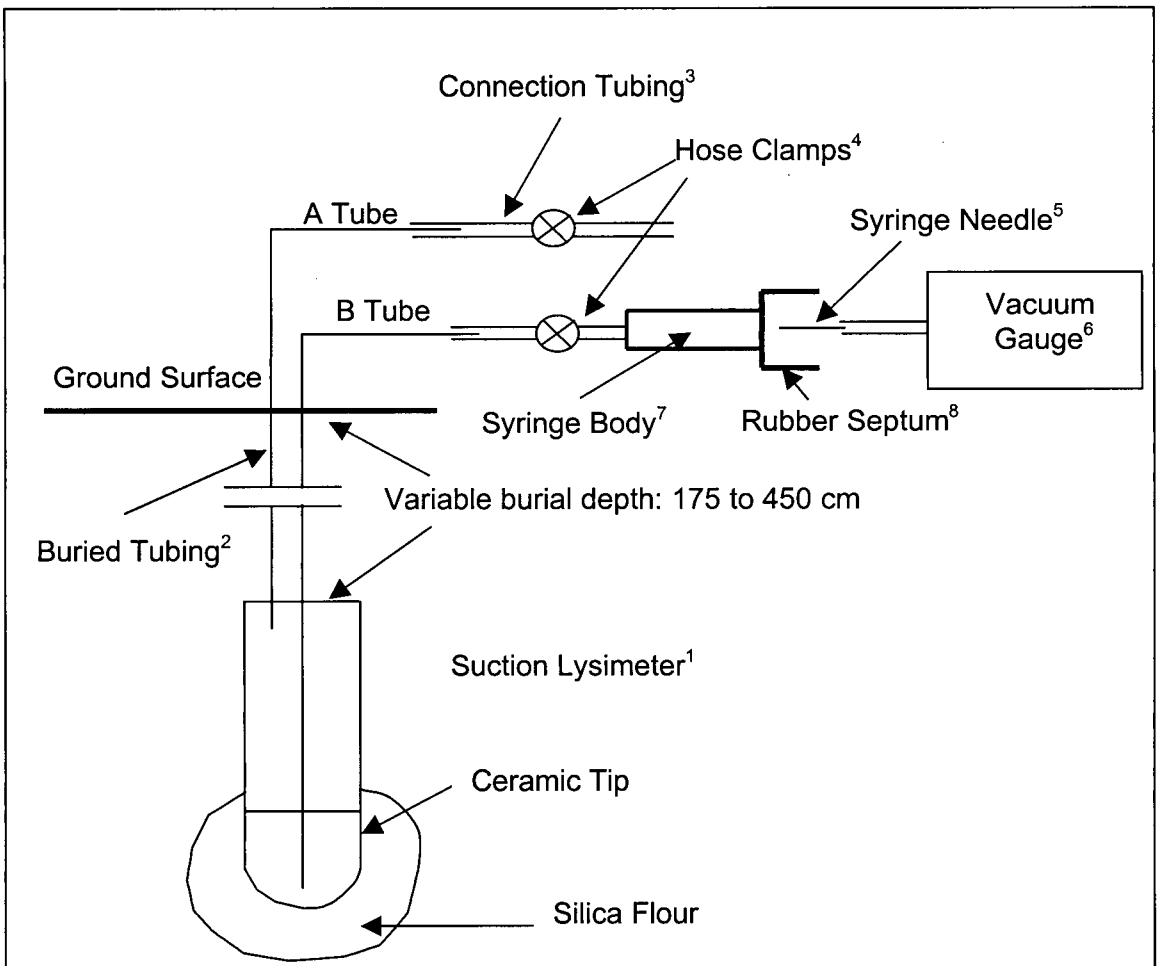

Components and Suppliers:

1. Soilmoisture Equipment Model 1920L12B2M2 pressure/vacuum soil water sampler. Hoskin Scientific, Vancouver, B.C.
2. 1/4" O.D., 1/8" I.D. HDPE tubing. Hoskin Scientific, Vancouver, B.C.
3. 5/16" O.D., 3/16" I.D. flexible vinyl tubing. Home Depot, Vancouver, B.C.
4. Adjustable hose clamp. Fisher Scientific catalog #05-869
5. Becton Dickinson & Co. 22 gauge, 5/8" syringe needle. Comes with 7.
6. Digital vacuum gauge: Micro Pneumatic Logic MPL-3200 0-99.9 kPa., Micro Pneumatic Logic, Fort Lauderdale, USA.
   Manual vacuum gauge: Soil Moisture Equipment Jetfill Tensiometer vacuum gauge
7. Becton Dickinson & Co. 3 ml Luer Lok syringe. #309585.
8. Rubber septum stopper. EQ-10075-7. UBC Chemistry department stores.

Figure C.1: Schematic outline of suction lysimeter installation.

APPENDIX D: TENSIOMETERS

D.1 INTRODUCTION

This appendix presents the details of the preparation, installation, measurement of matric suction and sampling methods used for the tensiometers. The procedures are written in the form of instructions. Also presented are the calibration details, and corrections derived for the automated measurement of tensiometer pressures using pressure transducers.

Tensiometers were installed after the pile's construction in three profiles at depths of 20, 50 and 100 cm from the pile surface. The tensiometers are used to extract water samples from within the pile and to estimate soil water suction. They are located in the three instrument profiles and numbered as shown in Table D.1 below.

D.2 INSTALLATION DETAILS

Nine tensiometers were added to the pile on July 30, 2000 at depths of 20, 50 and 100 cm in each of three instrumentation profiles. The tensiometers were SoilMoisture Inc. Jetfill Tensiometers Model Series 2725. Small holes approximately 40 x 40 cm were hand excavated in the top surface of the pile to a total depth of 100 cm. The lowest probe was placed as outlined below. Each probe was installed at the edge of the excavated hole. A small semi-circular hole at the base of the excavation was prepared by removing larger stones (>25mm) to prevent damage to the ceramic tip. The ceramic tip of the each tensiometer was coated in a 1/4" thick saturated paste of silica flour prior and placed in the prepared hole. The holes were backfilled and hand-tamped to the density of the surrounding waste rock. . The waste rock was then replaced into the hole and hand tamped to a density similar to the adjacent waste rock. The hole was filled to 50 cm depth and 20 cm depth in turn. The tensiometers are labeled T1 to T9 as shown in Table D.1 below.

D.3 TENSIOMETER SAMPLING METHOD

The tensiometers are largely used to extract water samples from within the pile. The procedure used for collecting samples from the tensiometers is presented below in the form of instructions. The tensiometers are designed as shown in Figure D.1

D.3.1 Materials needed

- Vacuum gauge fitted with syringe needle point (22 guage, 5/8")
- One 60 ml sampling syringe per tensiometer
- Rubber septum that fits 3 ml syringe body. Ends should be relatively crack-free. If dried and cracked, replace with a new septum.
- One 150 cm long, 1/16" O.D. sampling tube, with flexible, 1/8" O.D., 1/16" I.D. rubber tube end to fit sampling syringe body.
- Distilled water
- Paper towel
- Marker pen
- Spare clamps
- Sample bottle and lids
- Notebook and pen

D.3.2 Sampling Method

The tensiometers are sampled by applying a vacuum to the tensiometer body at a suction greater than the suction in the surrounding soil. This draws water into the tensiometer body. The usual suction to apply is 50 kPa. The tensiometers will produce volumes of sample ranging from 20 to 60 mls at the 20 to 100 cm depths. Typically, there is not enough sample to allow measurement of pH and conductivity. The time required to produce the sample will depend upon how wet the pile is. Immediately following a rainfall event, when the pile is wetted, the tensiometers will produce a full sample volume in several hours. Under drier condtions, the tensiometers are left overnight for 16 to to 24 hours.

To start sampling:

- Attach the refill cap to the tensiometer body. Teflon pipe tape can be applied to ensure a vacuum-tight fit.
- Pierce the 3 ml syringe septum with the vacuum gauge syringe needle.
- Attach the sampling syringe to tube B.
- Withdraw air from the tensiometer until the vacuum gauge registers 50 kPa. Use clamp B to clamp off tube B and empty the syringe. Several syringes of air may need to be withdrawn to achieve 50 kPa.
- With the tensiometer at full vacuum, leave the gauge connected and observe for a minute. Make sure the tensiometer is retaining vacuum and there are no leaks in the system.
- Clamp off all clamps, and remove the vacuum gauge from the syringe septum.
- Wait several hours to overnight for the sample to collect

To Withdraw a sample:

- At the start of the sampling, zero the vacuum gauge by adjusting the calibration screw. For the manual gauge this is achieved by removing the screw in the clear gauge cover plate, and adjusting the screw on the gauge face. Tap the gauge gently to settle the needle. For the digital gauge, the calibration screw on the side is adjusted until the reading is zeroed.
- Unclamp clamp A between the syringe body and the tensiometer, but do not open clamp B. Retain the vacuum.
- Pierce the syringe septum with the vacuum gauge needle.
- Allow the vacuum gauge to come to a full reading.
- If using a dial vacuum gauge, gently tap the gauge several times to ensure the reading is stable.
- Record this reading as P1. The dial gauge can be read to 0.5 kPa. The digital gauge records to 0.1 kPa.
- Remove the vacuum gauge, and allow it to return to zero.
- Pierce the syringe septum with the vacuum gauge needle a second time.
- Allow the vacuum gauge to come to a full reading. Record this reading as P2.
- The time between vacuum measurements should be as short as possible allowing for full recovery of the vacuum gauge to a zero reading.
- The vacuum present in the tensiometer ($P1^2/P2$) represents an upper limit to the tension in the soil surrounding the tensiometer. It will only equal the tension if the tenisometer has come to full equilibrium.

- Prepare the 1/16" O.D. sampling tube. Draw 20 mls of distilled water into the sampling syringe for that tensiometer. Connect the syringe to the small diameter sampling tube. Push the distilled water through the sampling tube to clean it, and the sampling syringe. After the distilled water, push several syringes of air slowly through the tube to remove the residual distilled water. Wipe the outside of the sampling tube with paper towel to remove water from outside.
- Remove the refill cap from the tensiometer body.
- Insert the sampling tube to the bottom of the tensiometer.
- Connect the syringe to the sampling tube and withdraw the sample.
- Split the sample into two sample bottles. Label each bottle with the tensiometer number, the date and time the vacuum was applied, and the date and time the sample was taken.
- Replace the refill cap, and close all clamps.
- Record the sample volume removed.
- The sample should be split into two bottles. One bottle for anion analysis is labeled with tensiometer number, start and end dates and times and CPE for constructed pile. The second bottle is for cation analysis. It is labeled with tensiometer number, dates and times and is also marked with CATIONS. Nitric acid preservative is added to this bottle from the teflon dropper bottle stored in the fume hood in the environment lab at City Hall. Add 10 drops nitric acid for a full 60 ml sample, and reduce accordingly for smaller sample sizes. Store the samples in the refrigerators in the environment lab.

D.4 MEASUREMENT OF MATRIC SUCTION

The tensiometers were also used for the measurement of matric suction in the pile. They were used to provide field calibration of the automated measurements conducted using the thermal dissipation sensors. Measurements of matric suction were conducted during August and September, 1999 using either manual measurement of matric suction, or automated measurement using pressure transducers. Estimates for the upper limit of matric suction can also be derived from the data collected during sampling.

D.4.1 Manual measurement

Manual measurement of the tensiometers was carried out using two methods to measure the resultant vacuum. The tensiometes were measured using the mechanical differential vacuum gauges supplied by Soilmoisture Equipment (Soilmoisture Equipment part #2060FG4). The tensiometer was configured as shown in Figure D.1 as measurement option one. The vacuum gauges were zeroed prior to installation. The body of the tensiometer was filled with distilled water and the water was de-aired by applying vacuum to the top of the tensiometer body using a vacuum pump (Soilmoisture Equipment part #2005G1). The Jet Fill cap was screwed in place. The tensiometer came to equilibrium with the surrounding soil, and the matric suction determined to 0.5 kPa by reading directly from the vacuum gauge. Over time, the tensiometer body would accumulate air, and was refilled using the Jet Fill cap mechanism.

The tensiometers were measured manually using a digital vacuum gauge (Micro Pneumatic Logic MPL-3200 0-99.9 kPa., Micro Pneumatic Logic, Fort Lauderdale, USA.) using the double-puncture technique of Greenwood and Daniel (1996). The above ground tubing was configured as shown as measurement option 2 on Figure D.1 The tensiometer was filled with water and the connection tubing including tubes A and B were filled with water. A vacuum was applied to the top of the tensiometer using a vacuum pump to de-air the water in the tensiometer. The tensiometer was filled, and the Jet Fill cap put in place.

Measurements were conducted by puncturing the rubber septum on the 3 ml syringe body with the needle of the vacuum gauge. The gauge was permitted to come to equilibrium, the measurement was recorded, then the needle withdrawn. The gauge was allowed to come to zero, then re-inserted into the tensiometer. The time between punctures was kept to a minimum to eliminate re-equilibration of the tensiometer between measurements. The two measurements of vacuum, P_1 and P_2, were recorded. The tension was calculated by (P_2^2/P_1)

D.4.2 Pressure transducer automated measurement

Motorola 5100DP integrated silicon pressure sensors were used to measure the tension within the tensiometers when attached to the tensiometer body as shown on Figure D.1 as measurement option 3. They are temperature compensated and stated to have a 2.5% maximum error over 0 to 85 degrees C. (Motorola, 1998). Pressure transducer datalogging details are given in Appendix F.

The pressure transducers were calibrated on August 15 to 17, 1999 prior to installation using the calibration configuration shown in Figure D.2. The height of the hanging water column was varied to determine the vacuum applied to the transducers. The transducers were allowed to collect data for 1.5 days while under no vacuum to determine the drift in the zero. Three sets of readings were taken with increasing, decreasing and increasing vacuum applied to the sensors. The maximum vacuum applied was 23kPa. The slope and intercept of the calibration curves to determine pressure in kPa from raw measurement voltage in mV derived from these experiments are shown in Table D.2.

The relationship between zero drift and temperature observed in the period of August 15 to 17th was not linear and showed signs of hysteresis. It was decided that all data would be collected using transducer #16 exposed to air to monitor the drift in the zero pressure voltage. Voltage measurements for transducer 16 exposed to zero pressure were collected from August 17 to October 13th, 1999. Voltage measurements for transducers 1 to 15 exposed to zero pressure were collected from September 29th to October 13th, 1999. The zero pressure voltage was plotted against temperature and it was found that a 2nd order polynomial could be fit to the data. The data for transducer 16 is shown in Figure D.3, and the zero offset determination equations are presented in Table D.3. One transducer, #15, showed very different zero offset behaviour than the others during September 29 to October 13, 1999. It is very different to its zero offset behaviour during the period of August 15 to 17, 1999. This transducer may have been connected improperly to a sealed tube during the September and October measurements, or it may have lost its on-chip temperature compensation. Using a fixed zero offset voltage led to apparent large diurnal swings in the measured suction. The temperature compensation shown in Figure D.4 was used.

The final pressure was calculated from the raw readings using the following method:

- Take five measurement 1 second apart on each transducer
- Store the average voltage measurement
- Linearly interpolate the air temperature at the time of the transducer measurement based upon the measured air temperature.
- Use the air temperature to calculate a zero offset voltage based upon the equations in Table D.3.
- Calculate the difference between the measured voltage and the calculated zero offset voltage.
- Multiply this result by the slope of the calibration equations presented in Table D.2.

- The result is the measured pressure in kPa.

D.5 REFERENCES:

Greenwood, K.L. and H. Daniel, 1996, A double-puncture technique for improving the accuracy of puncture tensiometer measurements, Australian Journal of Soil Research, 34, 153-159.

Motorola, 1998, Product technical specifications, MPX5100 series, Motorola document service document MPX5100/D..

Profile A: Center	Profile B: North	Profile C: South Corner
T1: 20 cm	T4: 20 cm	T7: 20 cm
T2: 50 cm	T5: 50 cm	T8: 50 cm
T3: 100 cm	T6: 100 cm	T9: 100 cm

Table D.1: Location and numbering of tensiometers

Gauge	Zero Offset from Gauge #16*				Linear Calibration Equation**		
	Average	Std Dev	Max	Min	Slope	Intercept	Intercept Offset from #16
1	8.10	0.59	11.34	6.52	0.0289	-7.19	-0.18
2	-2.71	0.33	-1.17	-3.84	0.0289	-6.86	0.16
3	5.07	0.36	6.67	4.17	0.0290	-7.09	-0.08
4	-3.35	0.79	-1.62	-5.18	0.0289	-6.80	0.21
5	0.98	0.31	2.34	0.00	0.0291	-7.01	0.00
6	0.32	0.38	1.50	-0.67	0.0290	-7.00	0.01
7	5.68	0.68	7.36	4.17	0.0290	-7.13	-0.12
8	4.61	0.59	6.52	2.84	0.0290	-7.10	-0.09
9	-1.78	1.19	1.00	-4.51	0.0290	-6.88	0.13
10	2.25	0.47	3.84	-0.67	0.0290	-7.03	-0.02
11	-1.59	0.53	-0.18	-3.01	0.0291	-6.93	0.08
12	-1.93	0.33	-0.68	-3.17	0.0291	-6.96	0.06
13	2.10	0.56	3.50	0.83	0.0291	-7.07	-0.06
14	0.58	1.05	3.00	-1.00	0.0290	-7.00	0.01
15	-0.96	0.47	0.50	-3.84	0.0289	-6.95	0.07
16	0.00	0.00	0.00	0.00	0.0289	-7.01	0.00

Notes:

1. * Transducer run for 1.5 days open to air pressure on both ports.
   Raw voltage readings subtracted
   from raw voltage readings for #16 to compensate for zero drift.
1. ** Linear Calibration Equation tested from 0 to 200 cm height of hanging water column
   Height of hanging water column (cm) = (Slope * Voltage Reading) + Intercept
   Matric suction (kPa) = (height of hanging water column (cm)) / 10.19784

Table D.2: Calibration equations for Motorola 5100D pressure transducers

Pressure Transducer	Best Fit 2nd Order Polynomial Coefficients y= a(x^2) + b(x) + c y= voltage at zero pressure (mV) x =air temperature (Deg.C.)		
	a	b	c
1	0.0023	0.2484	232.80
2	0.0035	0.2048	223.30
3	0.0056	0.2703	231.42
4	0.0018	0.1914	224.59
5	0.0038	0.2691	223.59
6	0.0016	0.1563	224.20
7	0.0028	0.2656	229.06
8	0.0046	0.2184	232.53
9	-0.0006	0.1424	224.39
10	0.0018	0.1961	226.28
11	0.0000	0.1606	233.32
12	-0.0009	0.2454	220.63
13	0.0020	0.3469	228.29
14	-0.0028	0.1838	228.24
15	-0.0312	-12.5050	268.66
16	0.0029	0.1949	222.40

Notes:

1. Data for transducer 1 to 15 derived from zero pressure readings from September 29 to October 13, 1999
   Over this time period, the air temperature varied from 15 to -10 degrees celcius
2. Data for transducer 16 derived from zero pressure readings from August 17 to Ocotber 13, 1999
   Over this time period, the air temperature varied from 34 to -10 degrees celcius.

Table D.3: Calibration equations to determine zero pressure calculated voltage reading (mV) from air temperature

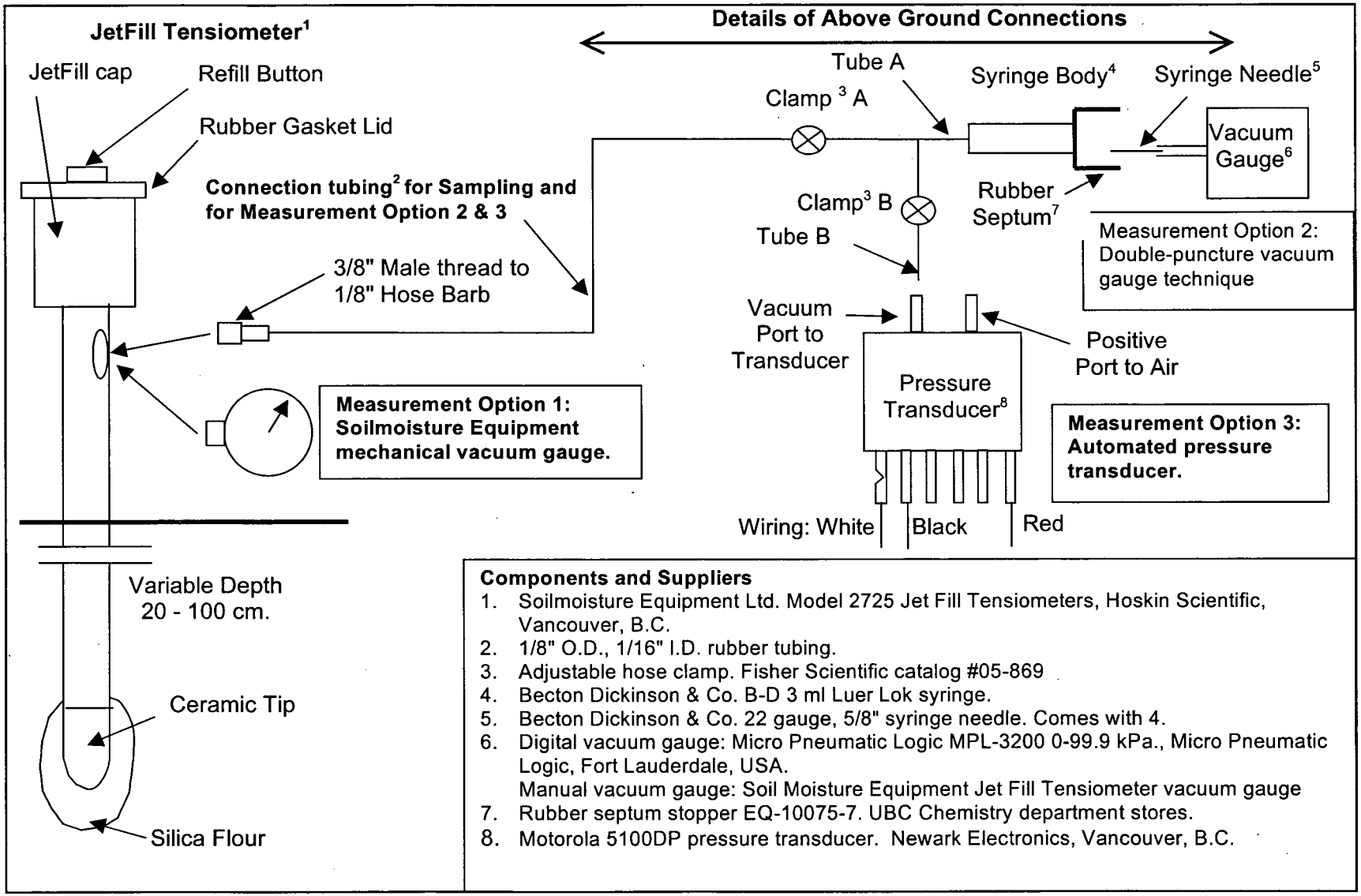

Figure D.1: Schematic of tensiometers and pressure transducers

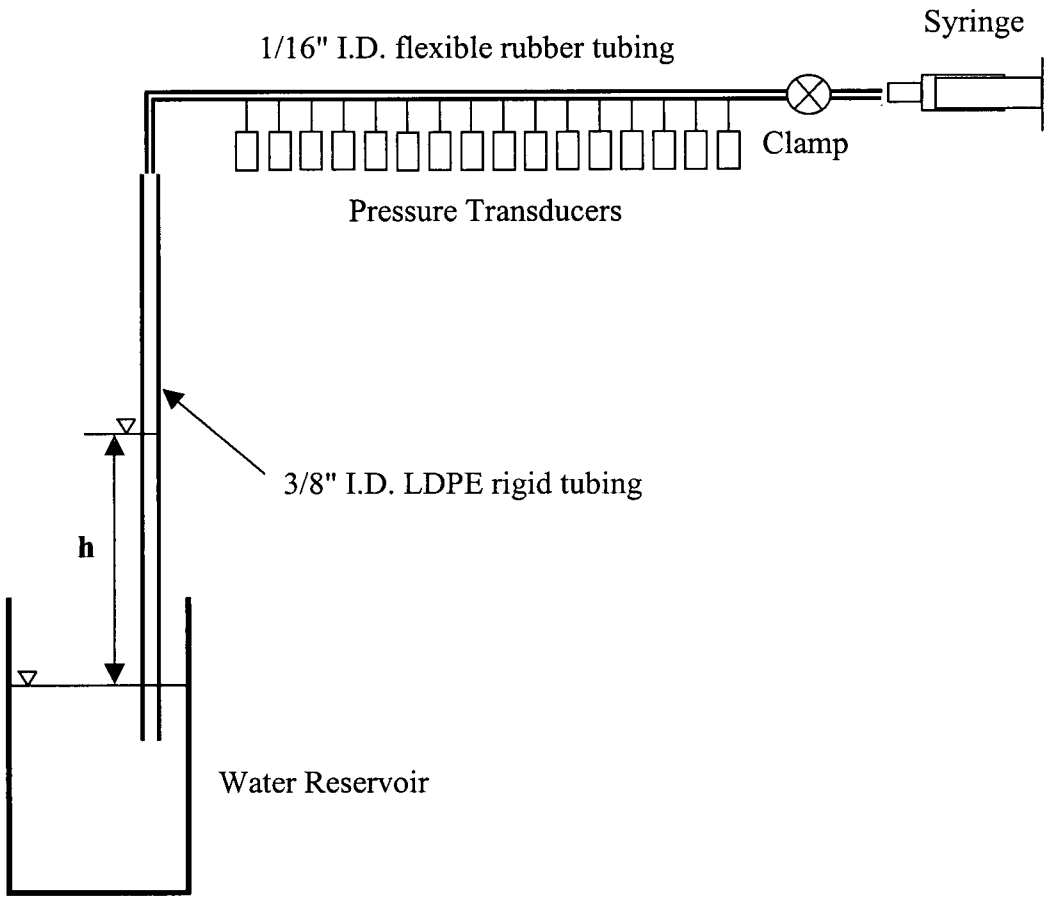

Transducer Calibration:

- Transducers connected to common 1/16" I.D. tubing.
- Water was drawn up from reservoir using syringe to create vacuum within common tubing equal to (h) in metres of water.
- (h) was increased in steps, and multiple readings collected from each ransducer.
- Several series of measurements were conducted, including overnight readings at a fixed (h) to determine temperature effect and zero drift.

Figure D.2: Pressure transducer calibration setup.

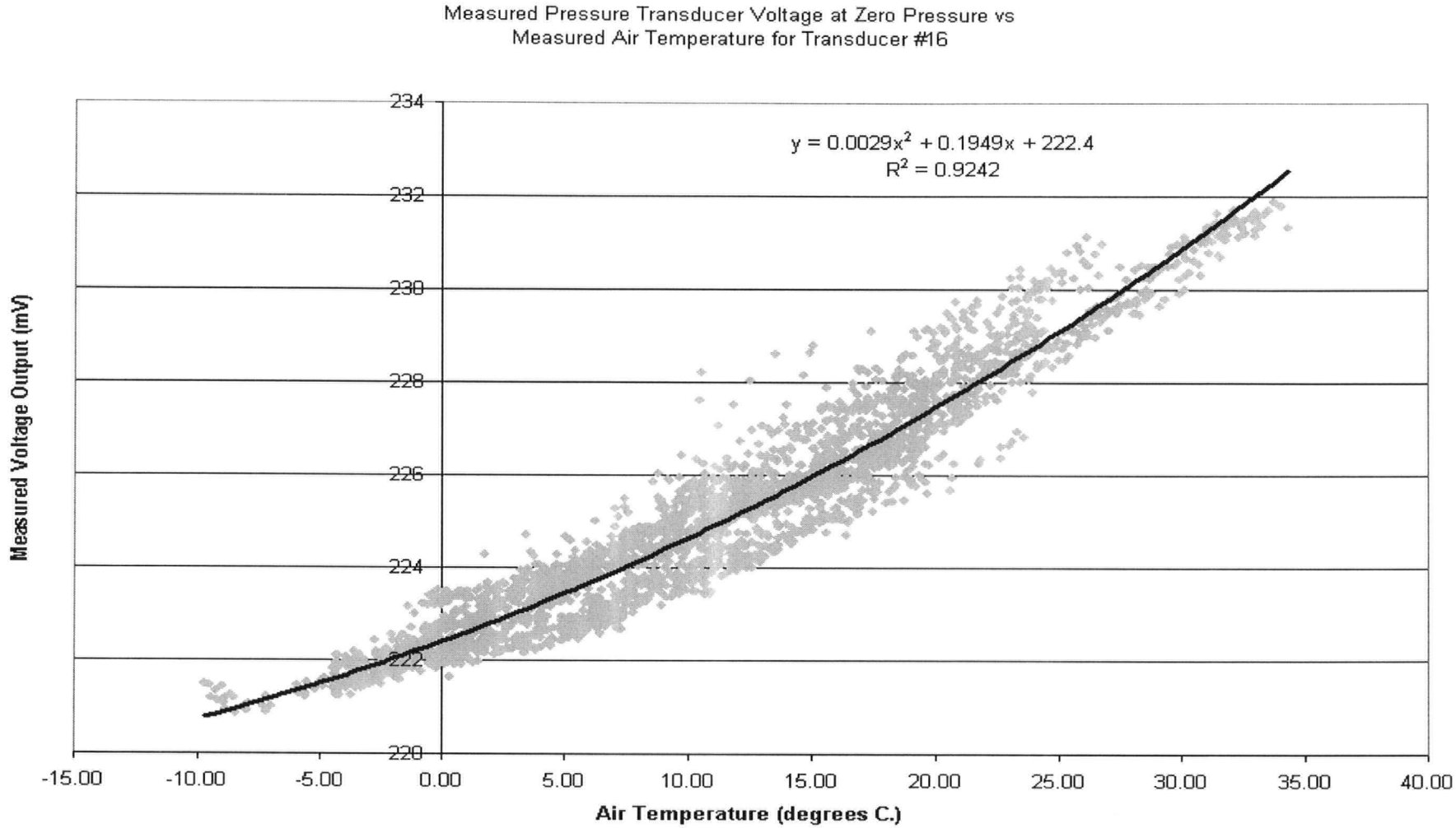

Figure D.3: Raw voltage reading of transducer 16 at zero pressure (mV) for varying temperature

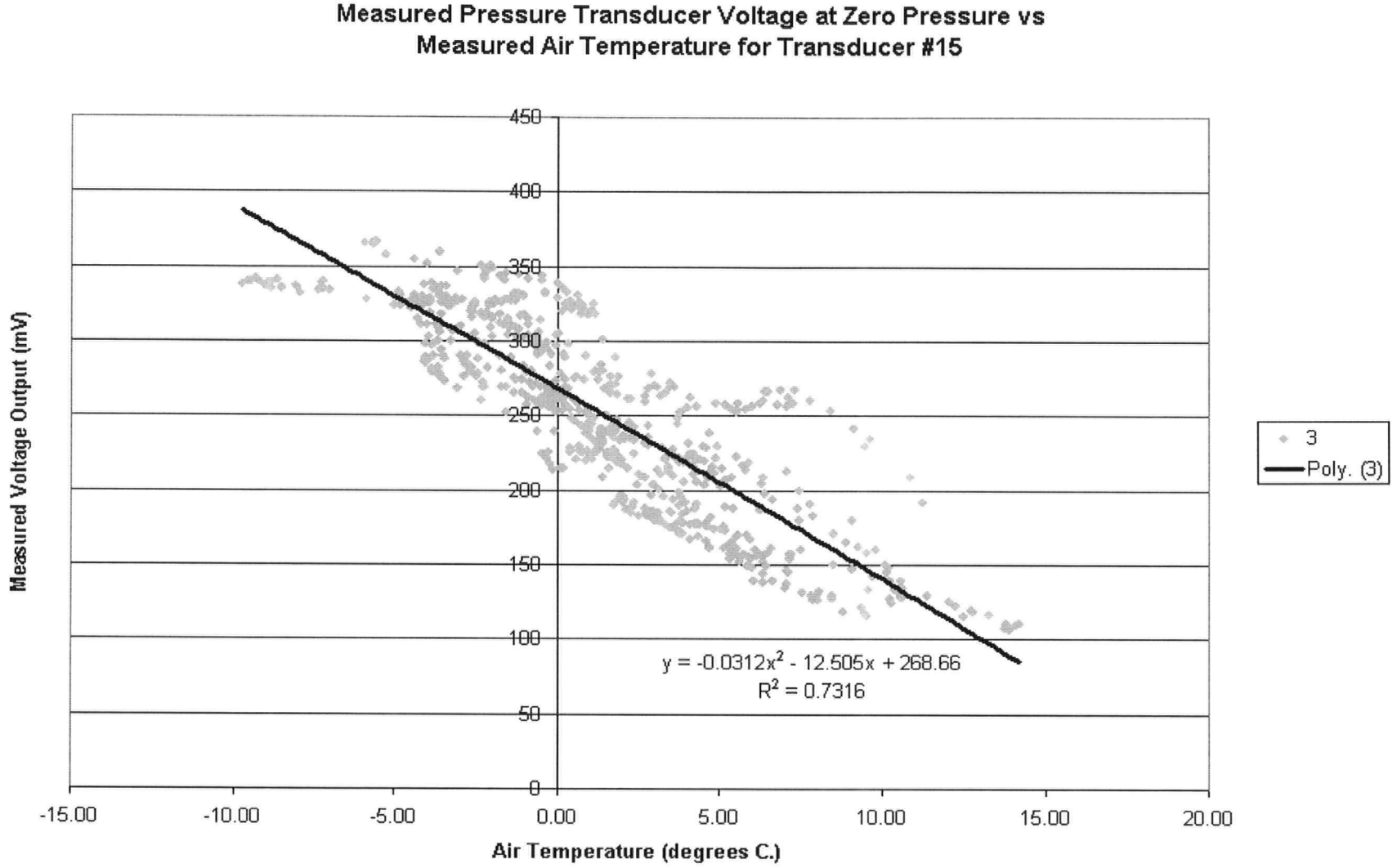

Figure D.4: Raw voltage reading of transducer 15 at zero pressure (mV) for varying temperature

APPENDIX E: CONSTRUCTED PILE EXPERIMENT: TEMPERATURE PROBES

E.1 INTRODUCTION

This appendix provides details of the calibrations undertaken to prepare the temperature probes.

E.2 CALIBRATION

The temperature probes that were installed in the constructed pile were calibrated prior to installation to determine the zero offset. The probes were connected to a Campbell CR-10X datalogger and minimum of 300 measurements were taken at a one second intervals while hanging in air, then while submerged in continuously-stirred ice water. Prior to installation in the pile, probes 1 through 19 were calibrated. Probe 20 was delivered late and was calibrated later. Probes 21 to 24 were added afterwards during subsequent work, and were not calibrated prior to installation.

E.3 RESULTS

Table 1 presents the results of the calibration. For probe 1 to 19, the zero offset was calculated by relative comparison to the data for probe #1, assuming probe number 1 is accurate. For probe 20, the zero offset was determined using the measurements in ice water.

	Calculated Temperature using Factory Calibration																			
	1	2	3	4	5	6	7	8	9	10	11	12	13	14	15	16	17	18	19	20
First Run																				
In Air	26.16	26.01	25.83	26.12	25.90													25.83	26.06	
In Ice Water	0.00	-0.07	-0.09	0.04	-0.20													-0.13	0.02	
Second Run																				
Air	20.63					20.56	20.33	20.49	20.65	20.54	20.54	20.36								
In Ice Water	-0.01					-0.08	-0.23	-0.13	0.03	-0.06	-0.02	-0.25								
Third run																				
In Air	25.18		24.88										25.41	24.88	25.04	25.14	25.14			
In Ice Water	-0.02		-0.12										-0.08	-0.12	-0.08	0.00	0.01			
Fourth Run																				
In Air																				
In Ice Water																				0.10
OffSet From Probe1																				
In Air	0	-0.16	-0.34	-0.05	-0.27	-0.08	-0.31	-0.14	0.02	-0.09	-0.09	-0.27	0.23	-0.30	-0.14	-0.04	-0.04	-0.33	-0.11	
In Ice Water	0	-0.07	-0.09	0.04	-0.20	-0.06	-0.21	-0.12	0.04	-0.05	-0.01	-0.23	-0.05	-0.10	-0.05	0.03	0.04	-0.13	0.02	0.10
Average Offset Air/Ice			-0.21	-0.01	-0.23	-0.07	-0.26	-0.13	0.03	-0.07	-0.05	-0.25	0.09	-0.20	-0.10	-0.01	0.00	-0.23	-0.04	
Spread			0.24	0.09	0.07	0.02	0.09	0.02	0.03	0.04	0.09	0.04	0.28	0.20	0.09	0.07	0.07	0.20	0.12	
Calibration Factor																				
Zero Offset	0	0.07	0.09	-0.04	0.20	0.06	0.21	0.12	-0.04	0.05	0.01	0.23	0.05	0.10	0.05	-0.03	-0.04	0.13	-0.02	-0.10

Notes:

1. Probe #1 is within 0.0001 to 0.02 degrees of zero for all calibration runs. It is considered to be accurate to reading zero degrees.
2. Probe zero offsets calibrated based upon the offset from probe #1.
3. Calibration Factor is number to be added to the raw result.
4. All measurements conducted using a Campbell Scientific CR-10X datalogger using an AC Half Bridge measurement and Polynomial conversion appropriate to an electrically noisy environment. Measurements using both the direct 107B probe instruction and the AC Half Bridge indicated that the AC Half Bridge was closer to the actual zero temperature.
5. Probe 20 could not be compared to the other probes due to a manufacturing defect. It was calibrated in ice water and the zero offset is a direct measurement against ice water.
6. All measuremenjts are the average of a minmum of 300 measurements.

Table E.1: Constructed pile experiment temperature probe calibration details

APPENDIX F: CONSTRUCTED PILE EXPERIMENT DATALOGGING

F.1 INTRODUCTION

This appendix presents a summary of the datalogging equipment and strategies used for the constructed pile experiment. It includes a history of the changes to equipment and programming as well as individual summaries and wiring diagrams.

F.2 HISTORY

The constructed pile experiment was designed to operate automatically. All measurements are conducted using Campbell Scientific CR10/CR-10X dataloggers. The main measurements are conducted using two dataloggers located within the instrumentation shed. The functions of these dataloggers have remained relatively constant, although the hardware performing the function has changed. The two dataloggers are named UBC1 and UBC2. Additional datalogging of weather conditions at the top of the pile is performed using an independent weather station containing a CR10 datalogger. The weather station was placed by another researcher, but has been operated as part of this thesis. Gas pressures within the pile are logged by another researcher using a third CR-10X located within the instrumentation shed.

The configuration of the datalogging equipment has changed over the course of the experiment. The software programming, the attached hardware and the dataloggers themselves have been altered. The datalogging protocols presented here are representative of the datalogging configuration at the end of the monitored period in October, 2000.

F.3 DATALOGGING

A flow chart of the overall datalogging strategies for dataloggers UBC1 and UBC2 is presented in Figure F.1.

F.3.1 UBC1

The UBC1 datalogger is used to operate thermal conductivity sensors to monitor matric suction, and to operate a MoisturePoint time domain reflectrometer to monitor volumetric moisture content. The wiring of the UBC1 datalogger of the TDR probes and matric suction sensors is presented in Figures F.2 and Figure F.3. Details of the matric suction sensor power supply wiring are shown in Figure F.4. Flow charts for the UBC2 logging programs are shown in Figures F.5, F.6 and F.7.

F.3.2 UBC2

The UBC2 datalogger is used to operate the rainfall gauge, temperature probes, outflow gauges and pressure transducers for the tensiometers. The datalogger was switched from a CR-10 to a CR10X on August15, 1999. The wiring and datalogger programming were not significantly altered by this change. Wiring of the UBC2 logger is shown in Figures F.8, F.9 and F.10. A flow chart of the UBC1 datalogger programs is shown in Figures F.11, F.12 and F.13.

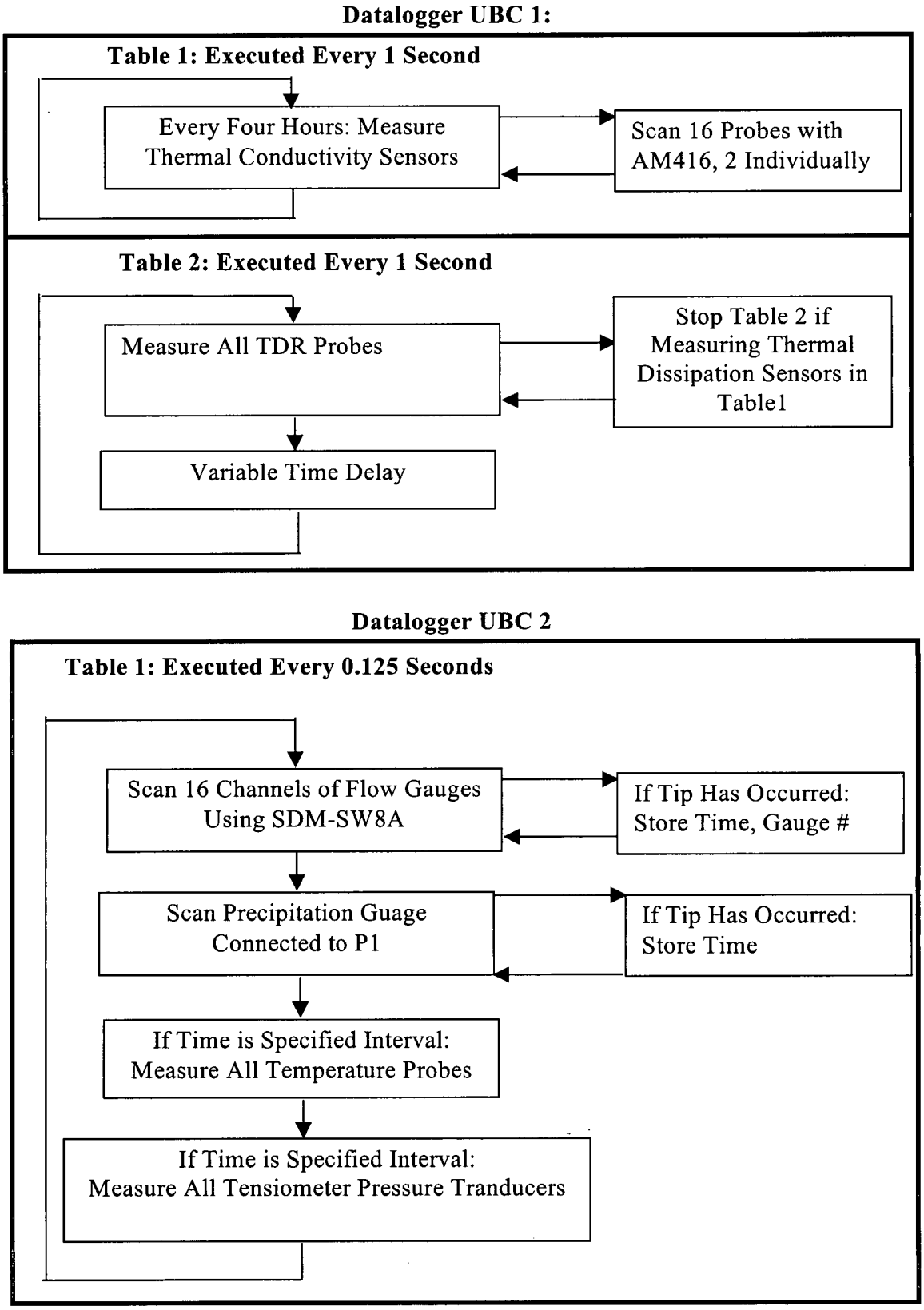

Figure F.1: Overall datalogging strategy for dataloggers UBC1 and UBC2.

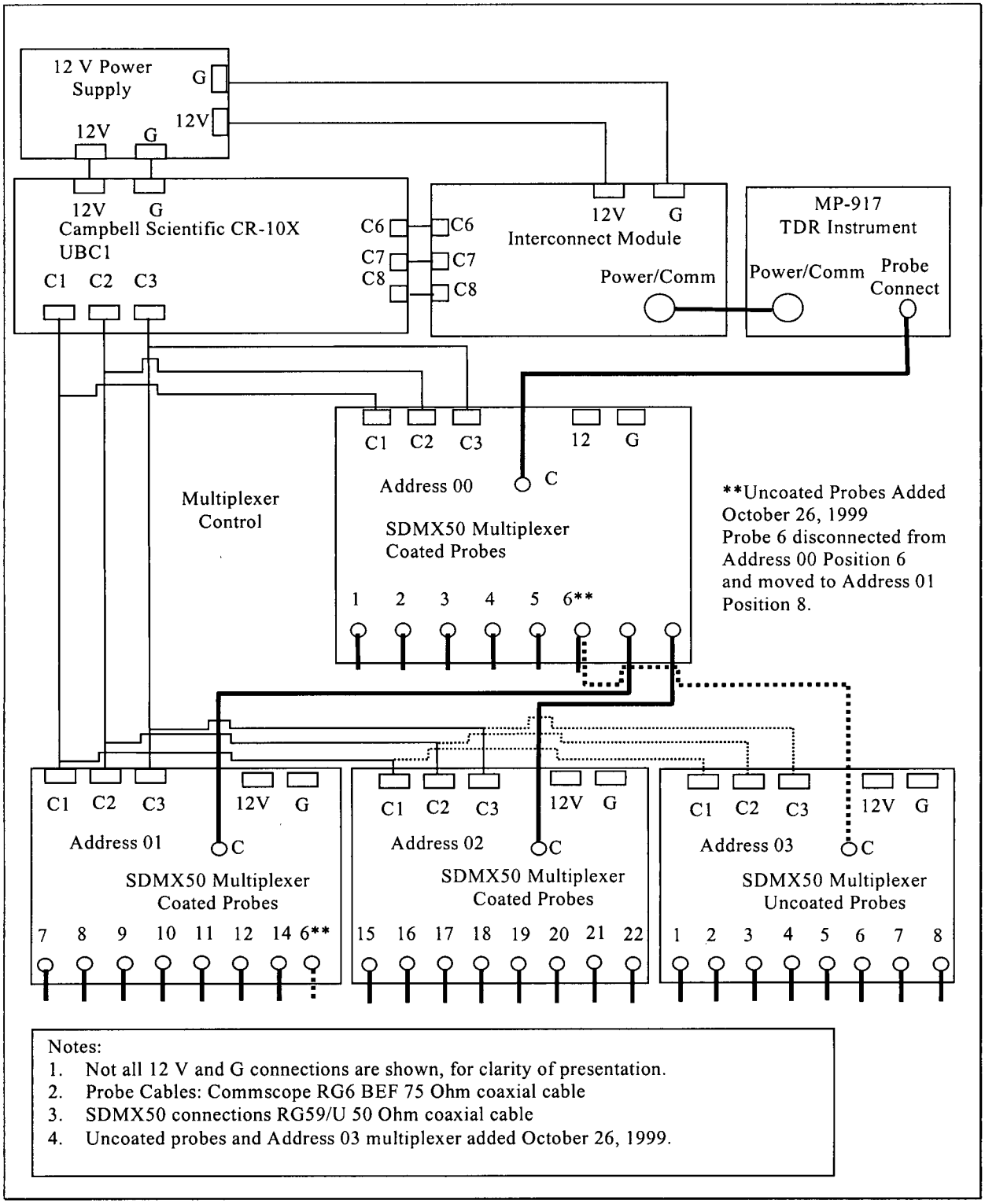

Figure F.2: Wiring layout for UBC1 datalogger: TDR probes

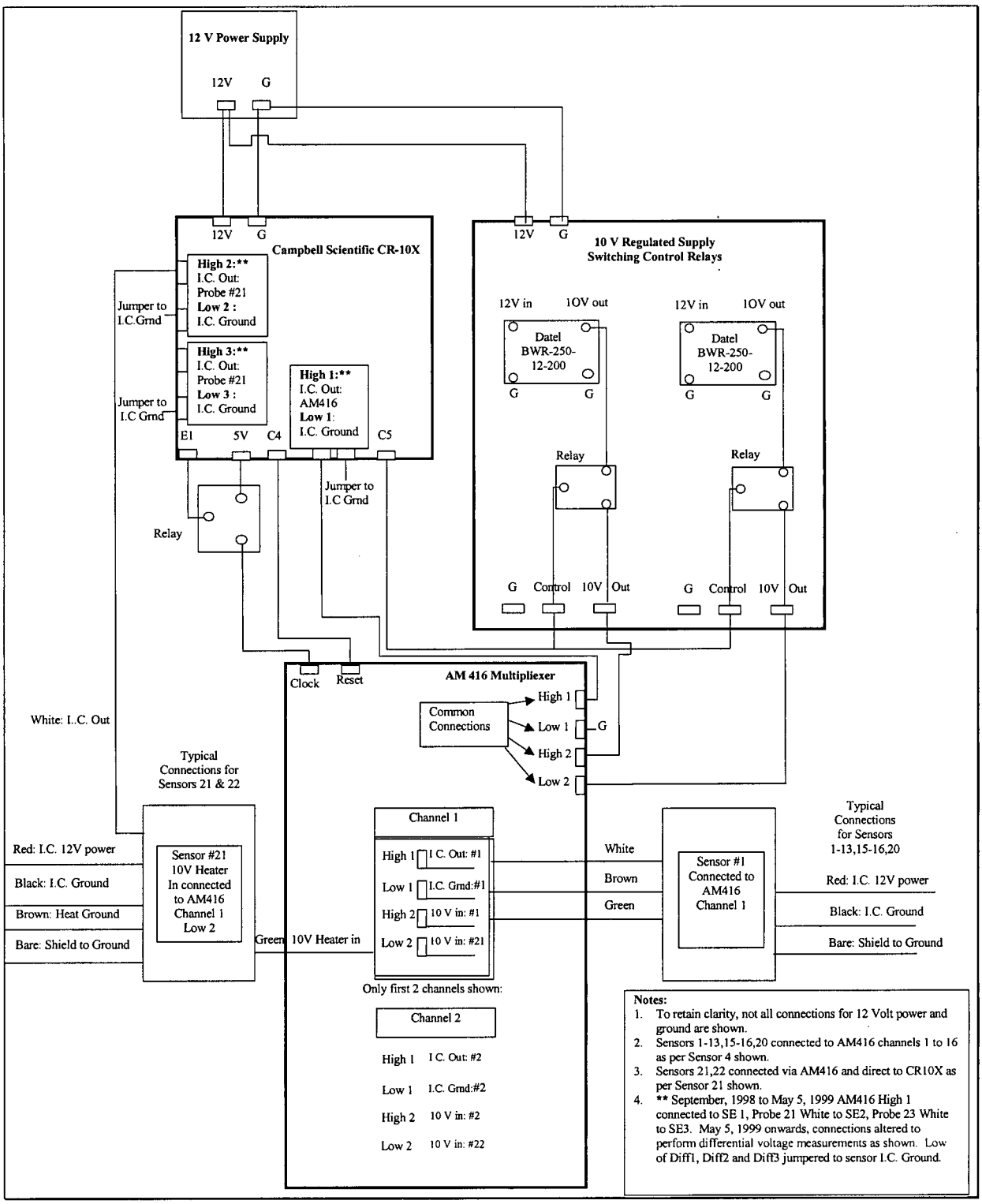

Figure F.3: Wiring Schematic for Datalogger to Thermal Conductivity Sensors

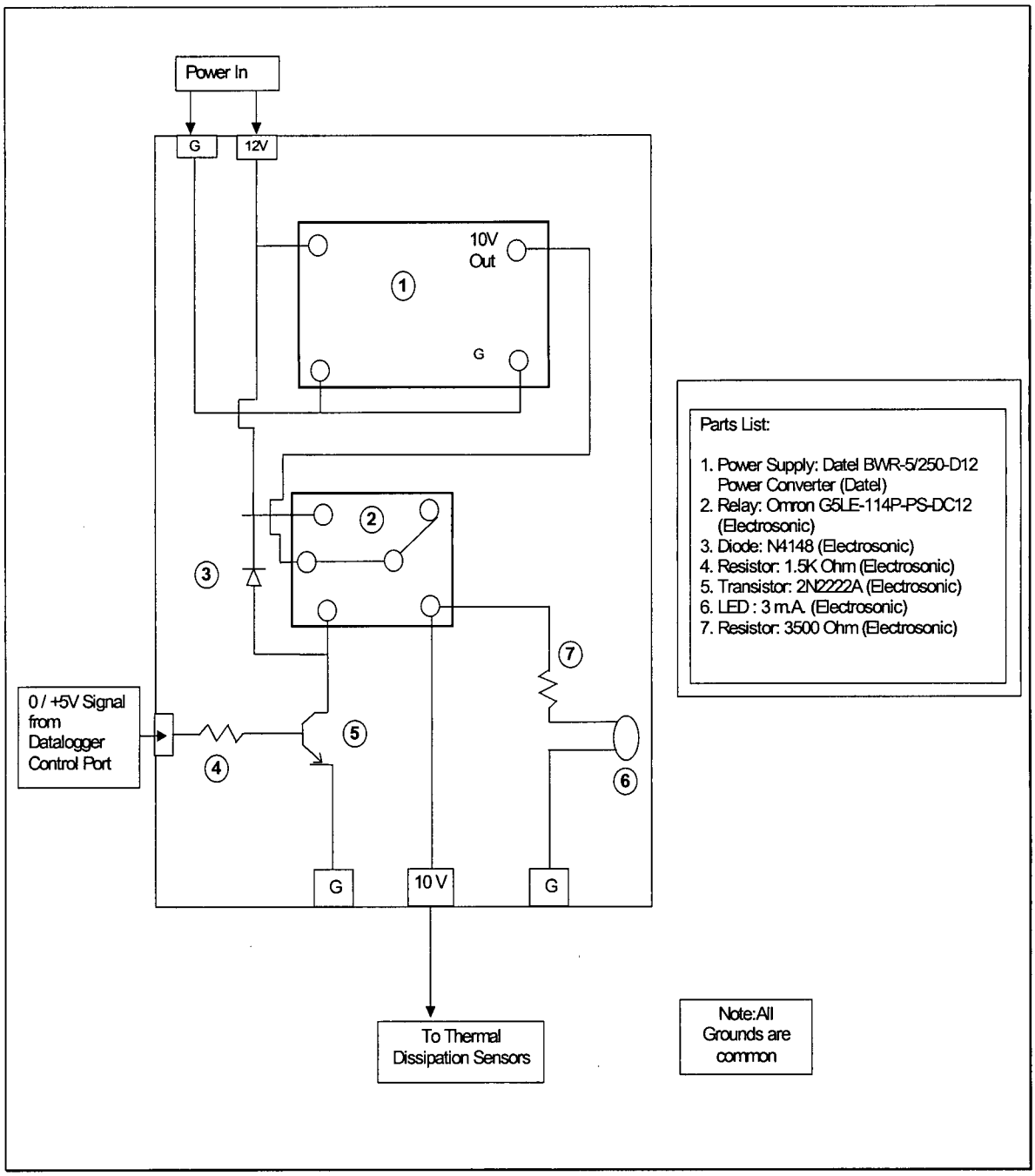

Figure F.4: Detailed Wiring Diagram of Thermal Conductivity Sensor 10Volt Power Supply

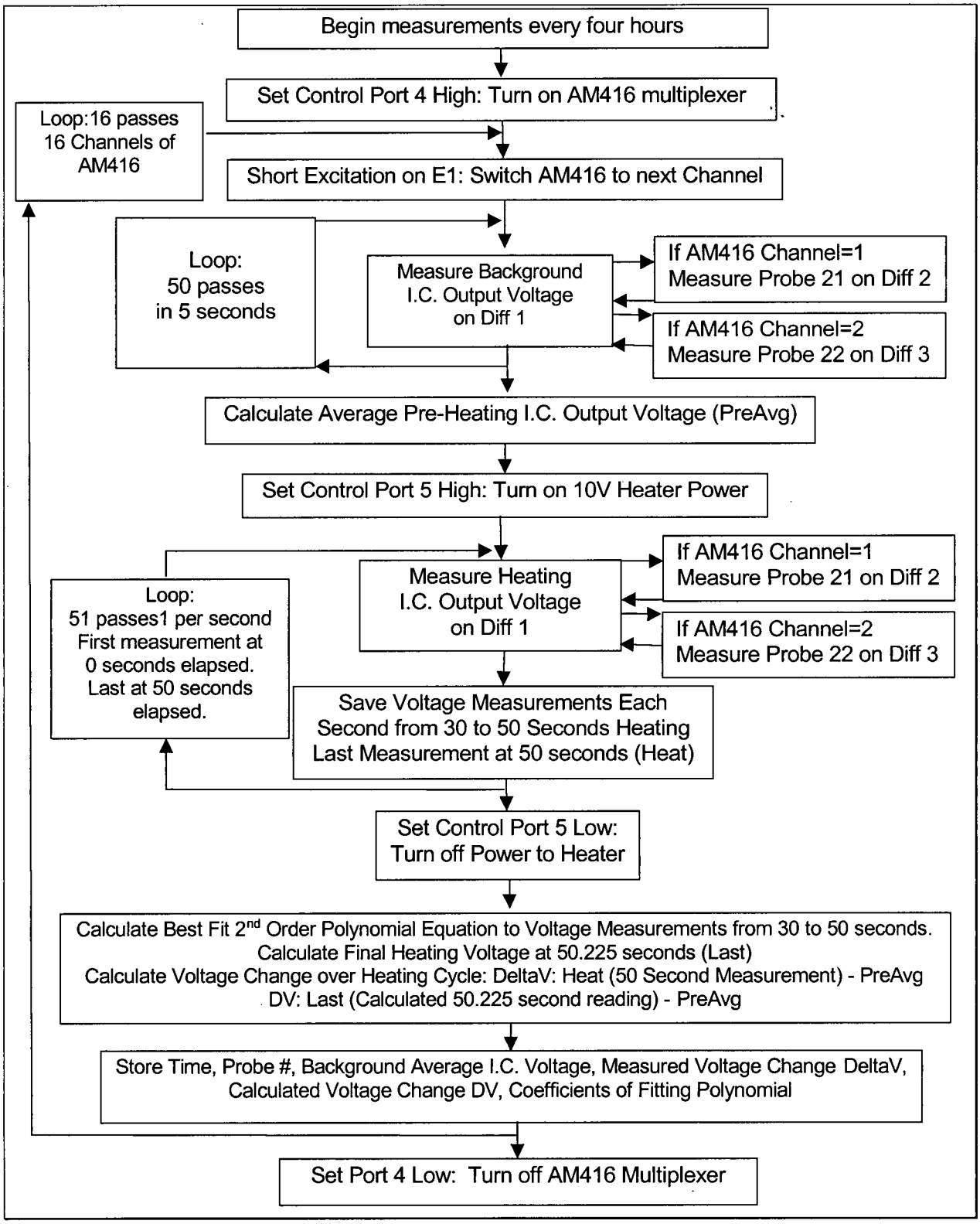

Figure F.5: Datalogger Program Flow Chart for Thermal Conductivity Sensors

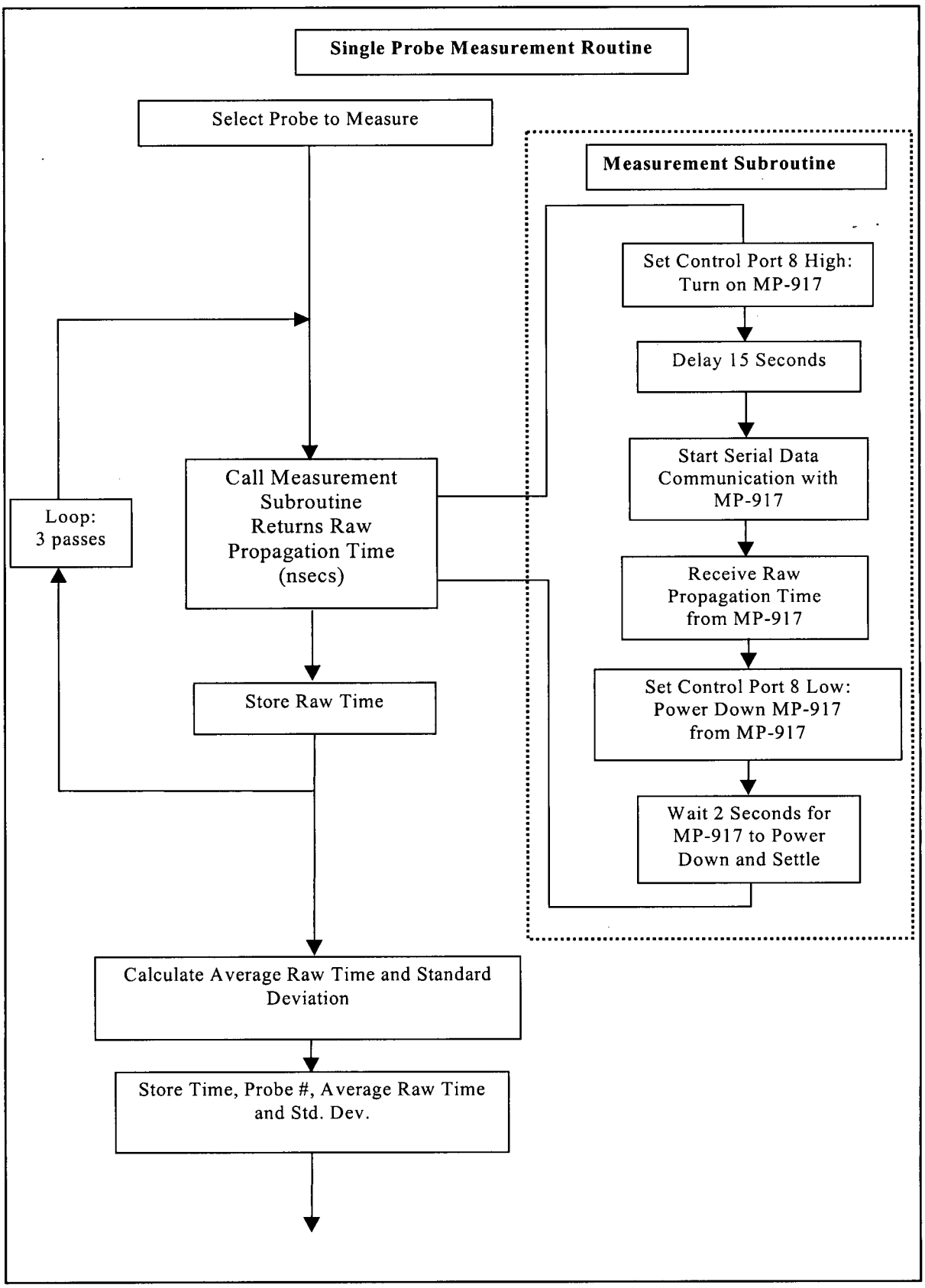

Figure F.6: Datalogger program flow chart for single TDR probe measurement

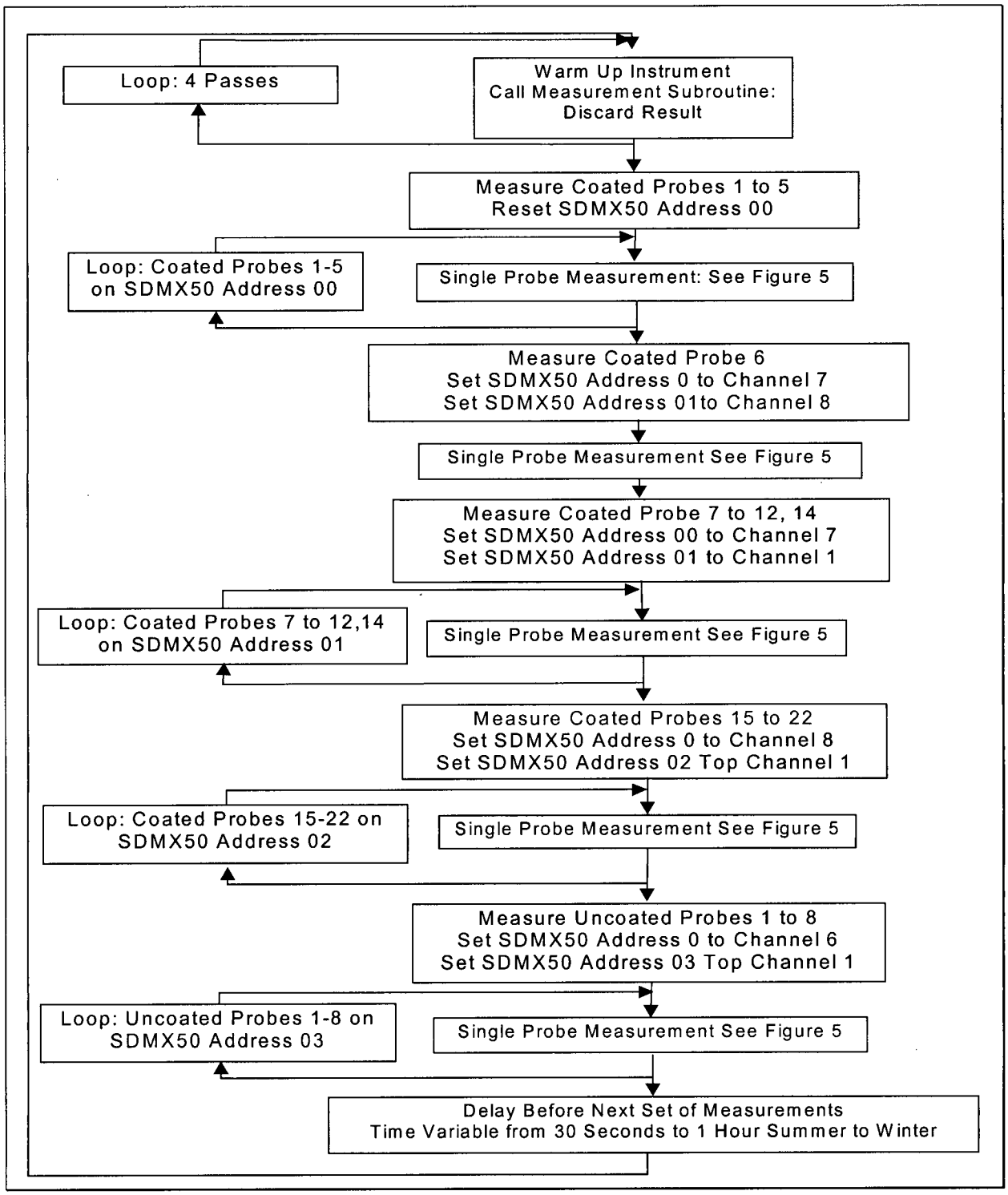

Figure F.7: Program flow chart for TDR measurement of all probes July 2000 on datalogger UBC1.

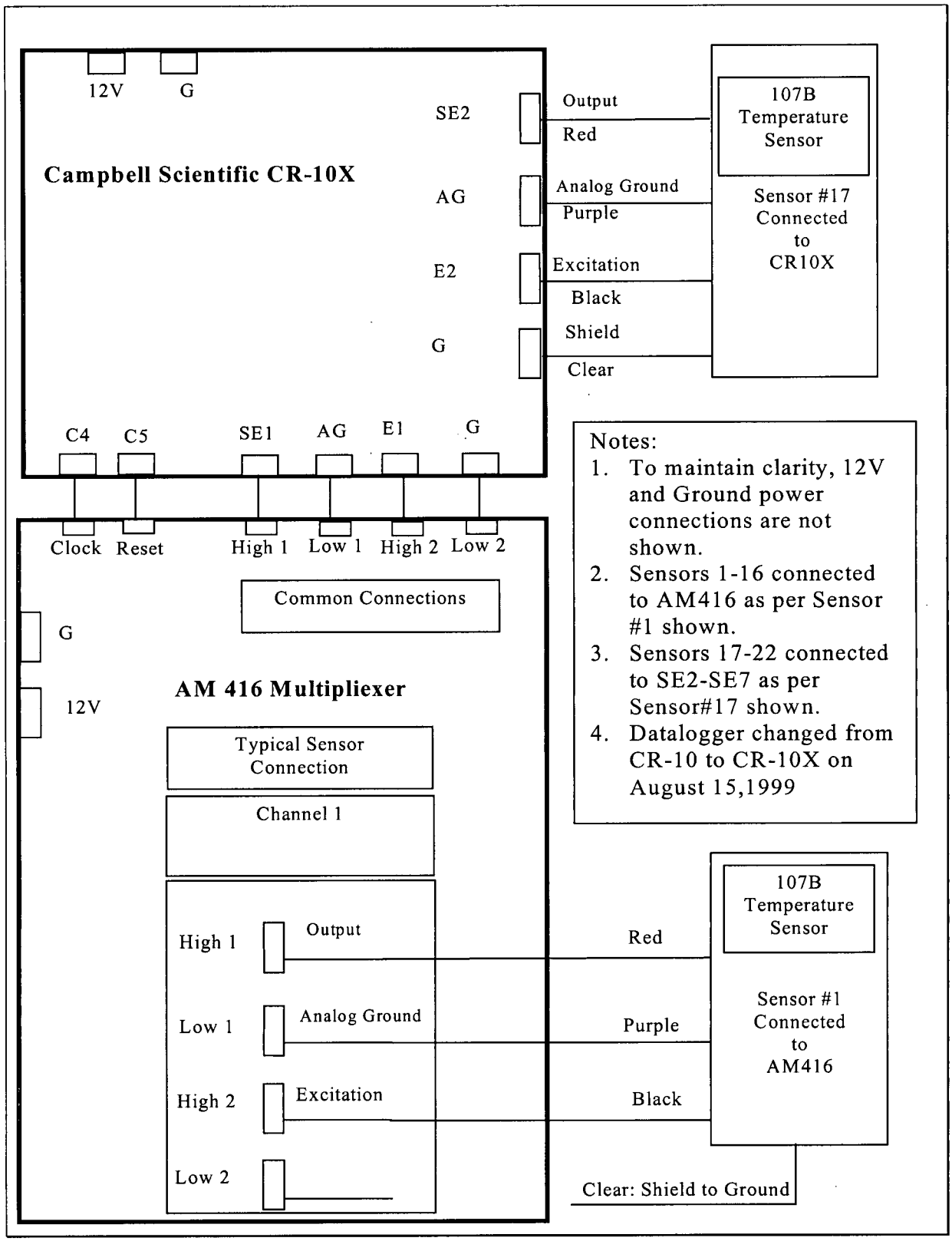

Figure F.8: Details of UBC2 wiring for temperature probes

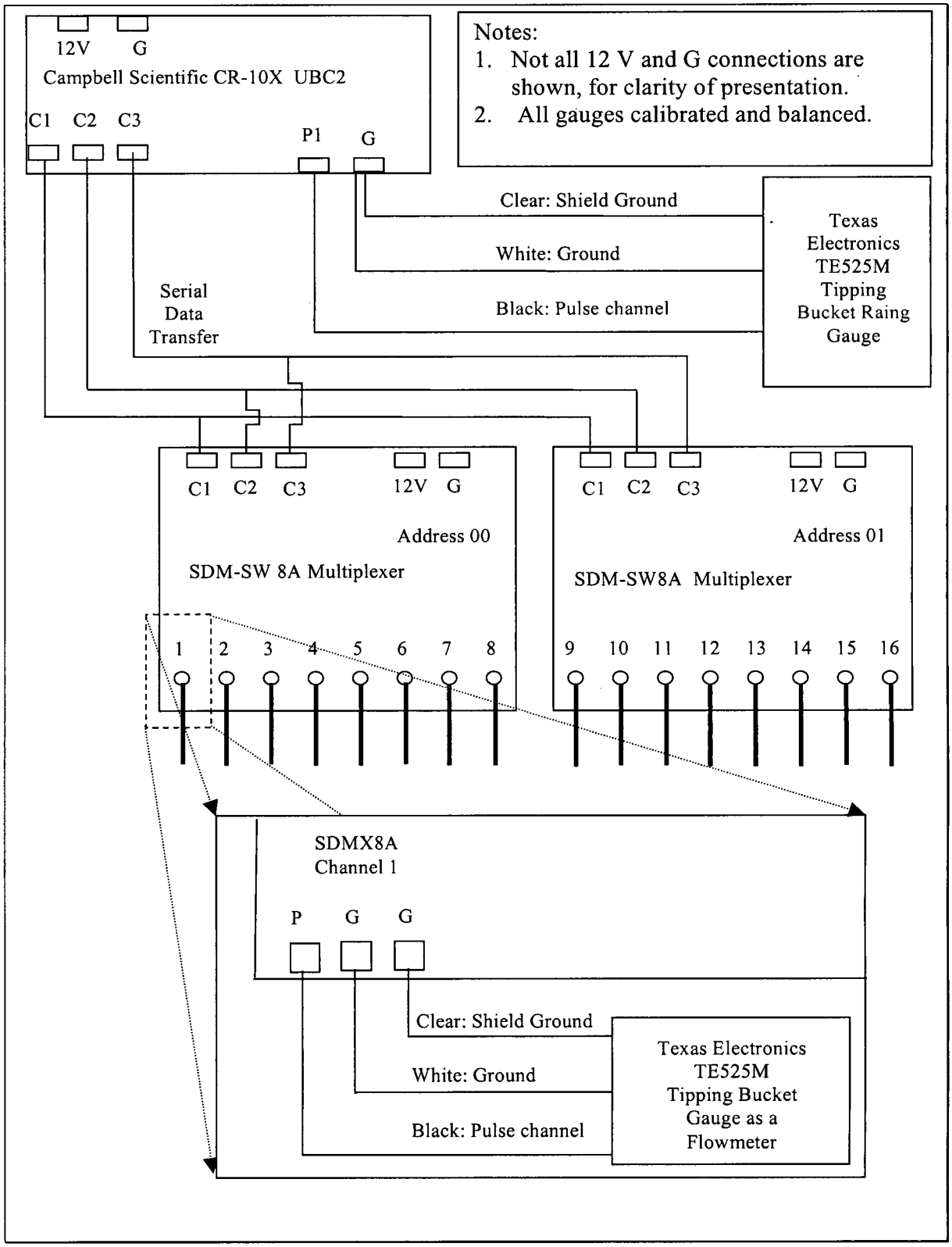

Figure F.9: Details of UBC 2 wiring for flow gauges and rain gauge.

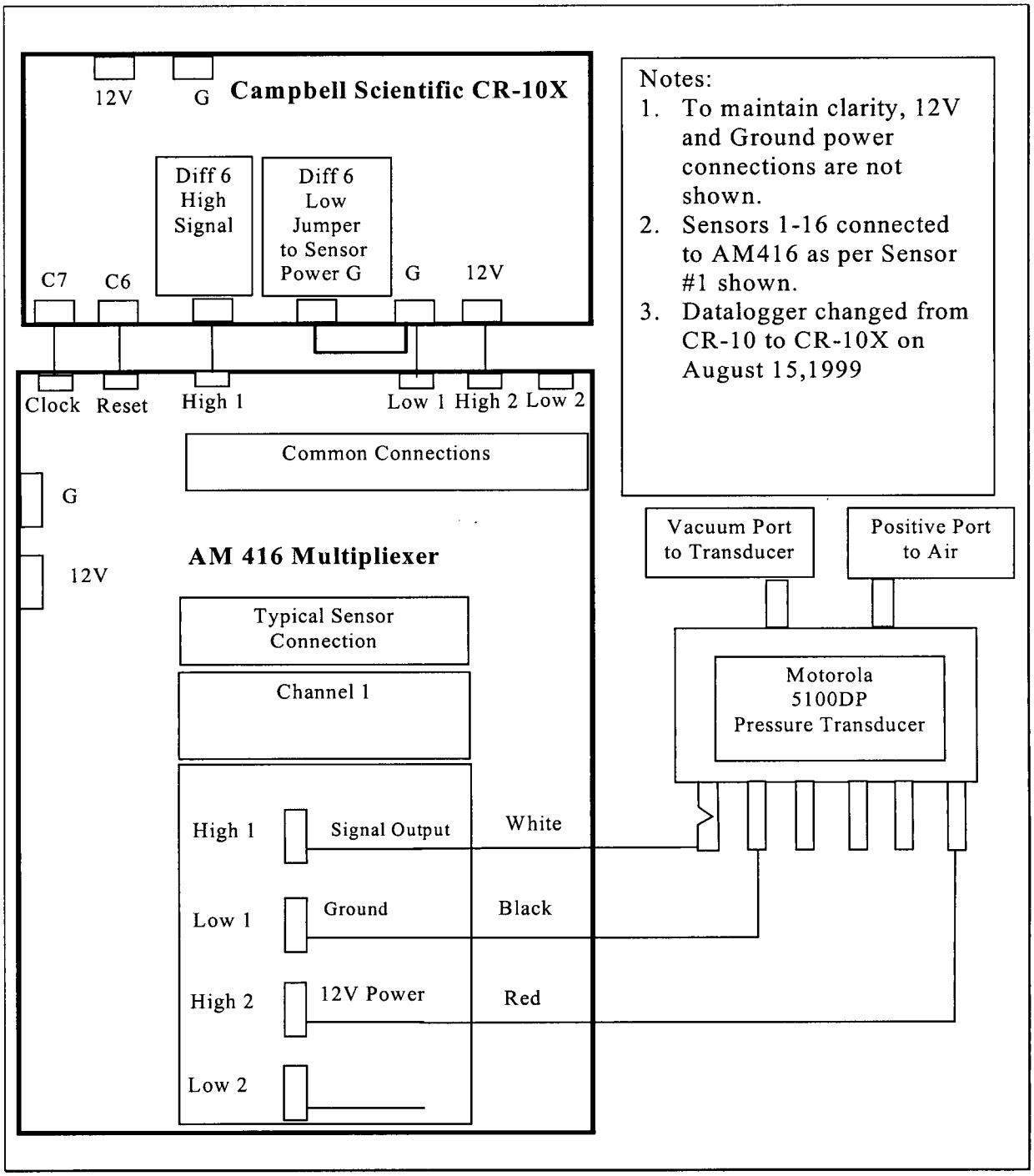

Figure F.10: Details of UBC2 wiring for tensiometer pressure transducers

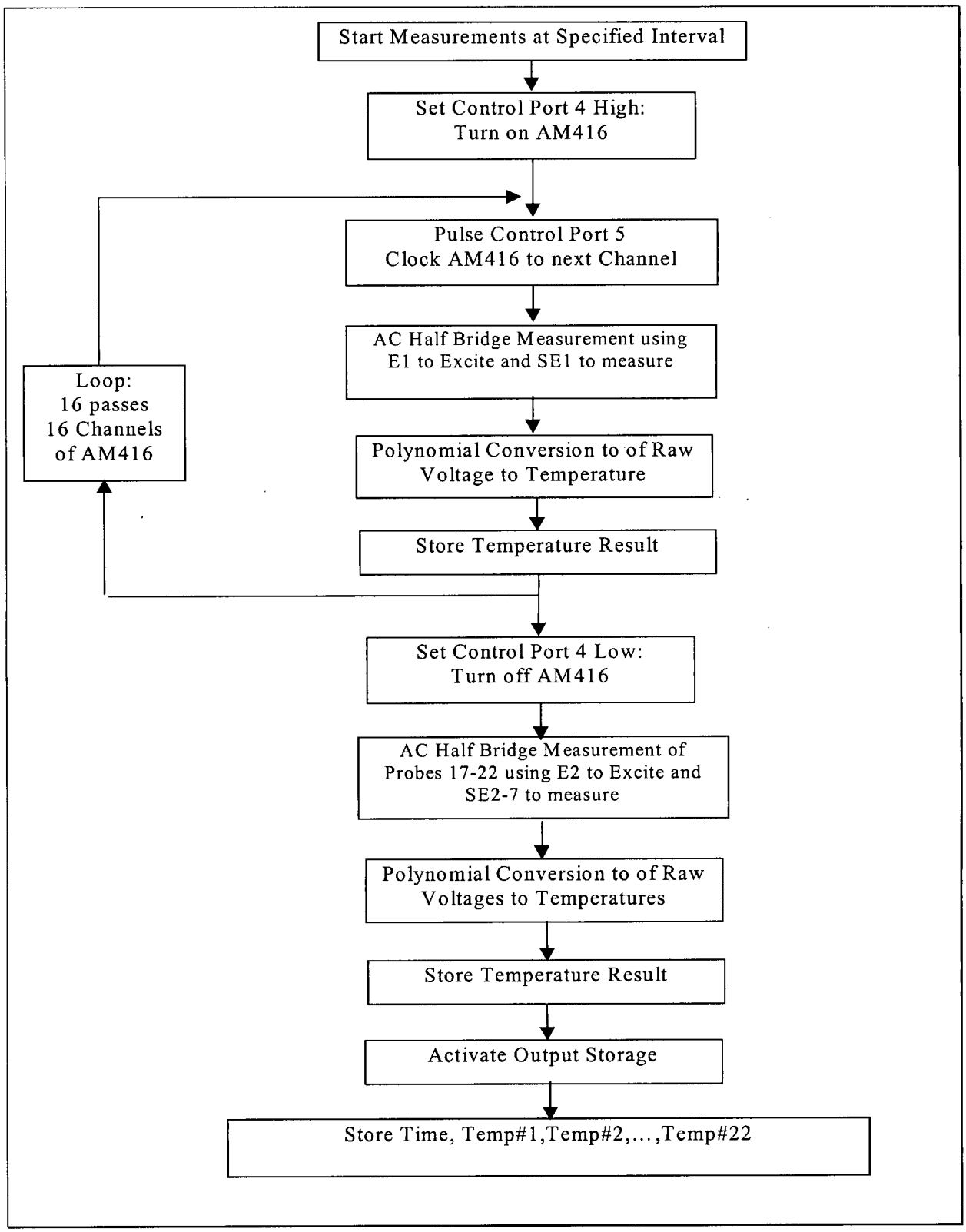

Figure F.11: Flow chart for temperature probe measurement on datalogger UBC2.

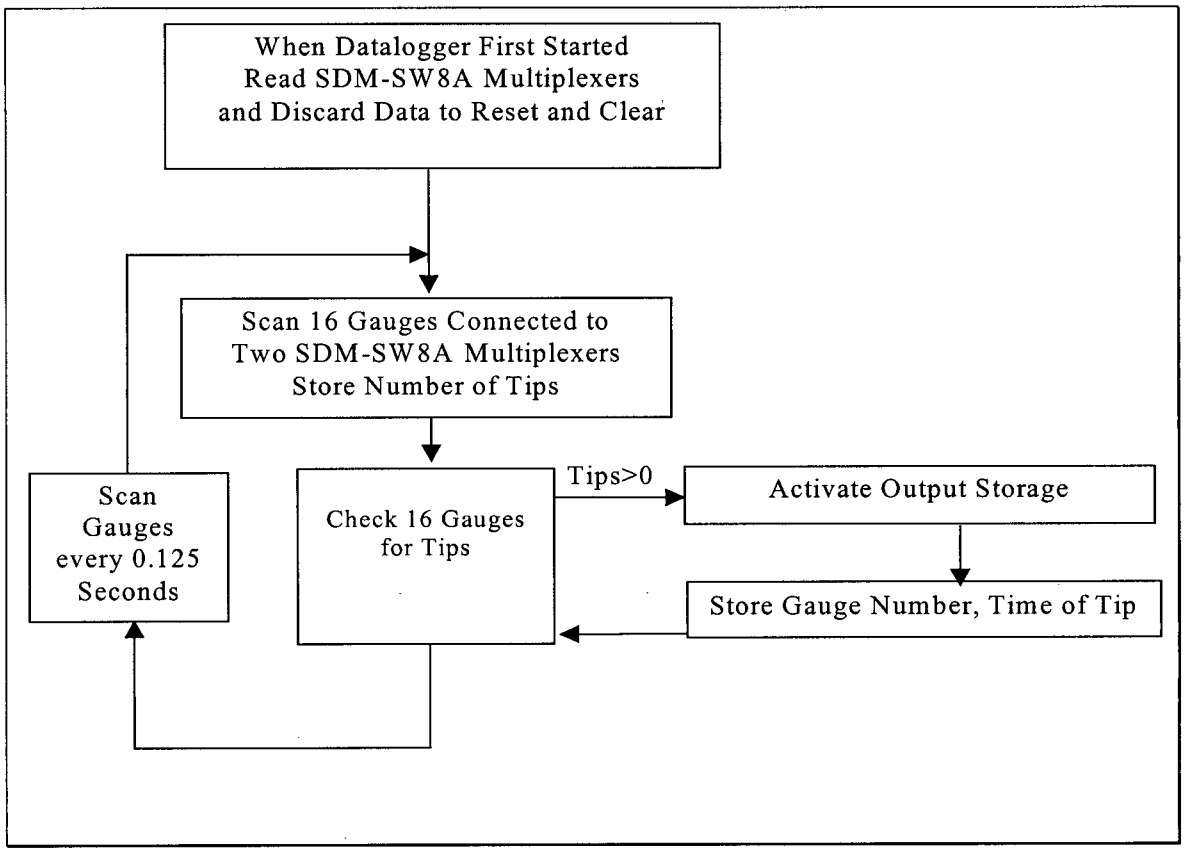

Figure F.12: Flow Chart for flow gauge measurement on datalogger UBC2.

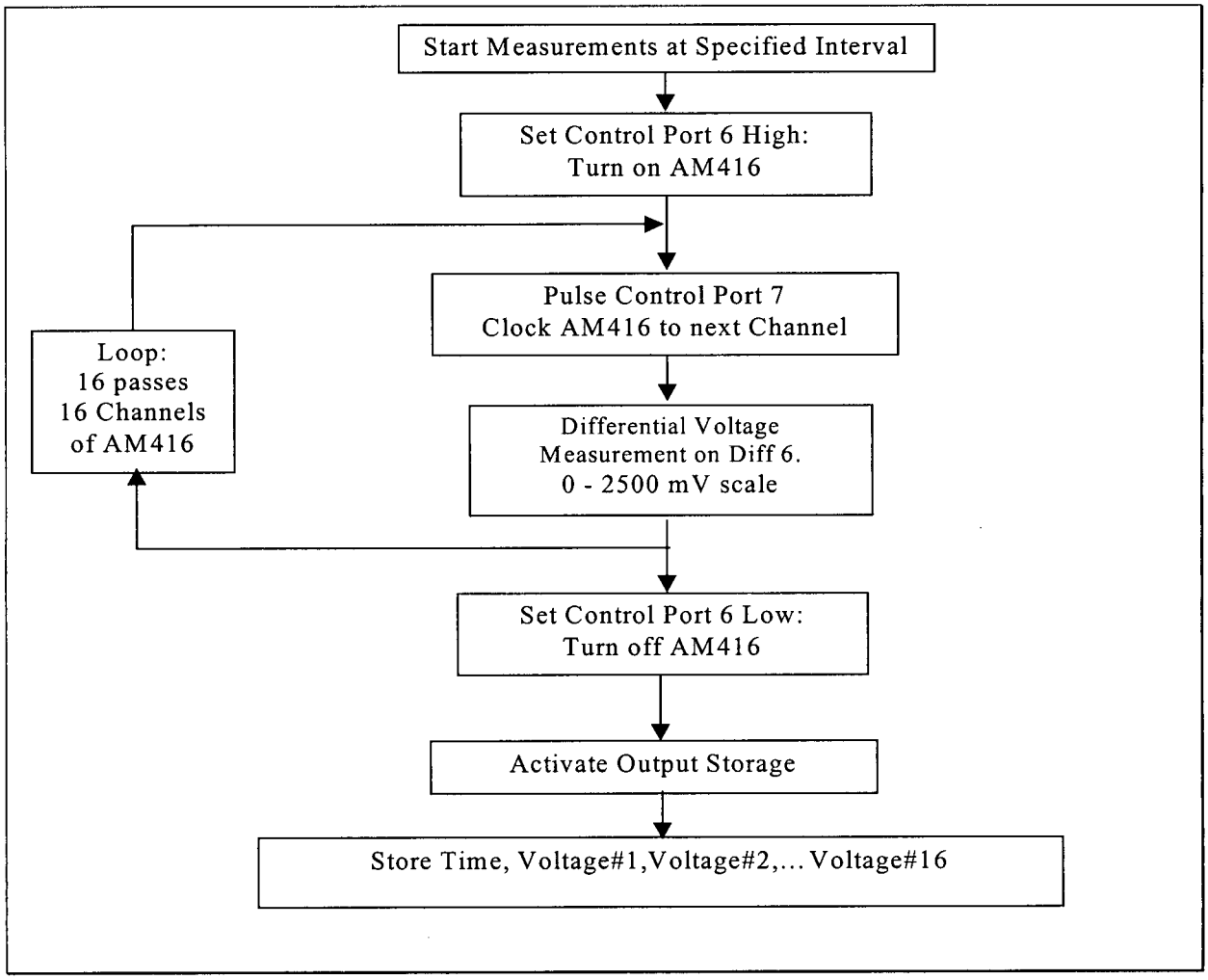

Figure F.13: Flow chart for tensiometer pressure transducer measurement on datalogger UBC2.

APPENDIX G: DEVELOPMENT OF RAINFALL SIMULATORS FOR LABORATORY COLUMN AND CONSTRUCTED PILE EXPERIMENTS

G.1 INTRODUCTION

This appendix includes an outline of the design and construction of the rainfall simulators built for the laboratory column experiment (see Appendix M), and the constructed pile experiment.

A device to simulate rainfall, and to deliver tracer-labeled rainfall, was required for both the laboratory column and the constructed pile experiment. The simulator system for the laboratory column was designed and built in the spring of 1998. It was used in 1998, 1999 and 2000. Based upon both the review of previous designs and the experience gained from the laboratory column simulator, a simulator design for the constructed pile experiment was chosen and calibrated in the summer of 1998. It was used in the summers of 1999 and 2000.

G.2 THEORY OF RAINFALL SIMULATOR DESIGN

Rainfall simulators are often used in soils research, particularly for studies of overland run-off and soil erosion. Moore et al., 1983 summarized several authors, and presented the following important characteristics of a rainfall simulator system:

1. Rainfall intensity appropriate to the region studied.
2. Uniform rainfall over the study area.
3. Rainfall application nearly continuous over the plot.
4. Drop size distribution and drop impact velocities similar to natural rainfall.
5. Random drop size over the study area.
6. Near vertical drop impact.
7. Mobility and ease of use under field conditions.

The first three criteria were considered the most important. The remaining criteria were considered to be important for studies of soil erosion. The desired characteristics were that the rainfall simulators be: automated; low maintenance; reliable; low capital cost; and capable of producing uniform, variable rate water flux to the ground surface with a maximum rate of approximately 30 mm/hr.

The review of existing work indicated that previously designed rainfall simulators fall into two broad design categories: drop type and spray type. Drop type simulators are based upon forming discrete drops using small diameter tubes connected to a low pressure reservoir. (Imeson, 1977 and Tricker, 1979). The drop size and fall rate are controlled by the tube diameter, and the head in the reservoir. Manufacturing the necessary dropper heads and maintaining the accurate low water pressures required for the tubes over the large areas of both the laboratory column and constructed pile experiment was considered to be impractical and prohibitively expensive.

Designs for spray-type simulators fall into several categories. Uniform, continuous spray designs have presented by Summner et al., 1996 and Tossel et al., 1987. These rely upon the desired rainfall intensities being deliverable using a continuous spray by a commercial spray nozzle. Controlled, variable rate designs use a variety of methods to vary the application rate A first design (Meyer and Harmon 1979, Moore et al., 1983, Hirschi et al. 1990) oscillates continuously spraying nozzles from a waste water trough, across an opening to the field plot A similar design (Morin et al. 1967, Marston 1982) rotates a perforated disc beneath the spraying nozzle, with the size of aperture, and disk rotation speed controlling the application rate. Both of these designs are successful in producing good quality, uniform, variable rate rainfall, but were

deemed to be too complicated and expensive to produce, and were therefore not selected. A third method (Shelton et al., 1985, Hinkle 1990) utilizes air injection to reduce the flow rate of water to the nozzle. By varying the water and air pressure, variable application rates are achieved. This system was not selected due to the increased cost and complexity of having two pumping systems, and because the range of rainfall intensities was not appropriate.

G.2.1 Laboratory Column

The design chosen for the laboratory study was based upon the designs by Miller, 1987 and Holden et al. 1995, who used a single nozzle type and operating pressure, but pulsed the spray on and off using a datalogger-controlled solenoid valve. This design provides an intermittent application of water, but the pulse can be kept short enough that this has a limited effect (Barnett and Dooly, 1972, and Young and Burwell, 1972, Holden et al. , 1995). Advantages of this design are:

1. The design requires a single nozzle type, height above the field plot, and operating water pressure.
2. Variation of rainfall rate does not involve altering any physical parameters of the system.
3. A single calibration of pulse timing can be used to control water application rate.
4. Moving parts are minimized.

G.2.2 Constructed Pile Experiment

The review conducted of sprayer designs for large area plots (Moore et al. 1983, Sumner et al. 1996, and Sawatsky et al., 1996) indicated that the construction of a spray nozzle based rainfall simulator similar to the laboratory column would be feasible for the constructed pile experiment. However, based upon the experience gained in building and calibrating the rainfall simulator for the laboratory column, it was decided that this type of design would be very difficult to build and calibrate. It was unlikely it would operate accurately under windy field conditions. The rainfall intensities and uniformity of commercially available garden sprinklers was checked to determine if these were appropriate.

G.2.3 Performance Evaluation

Uniformity of the simulated rainfall is reported using the Christiansen equation (Christiansen, 1942), which is used by most authors to report simulated rainfall uniformity. The equation uses data from a finite number of rainfall intensity measuring points within the tested field. The uniformity coefficient approaches 100 as the rainfall approaches complete uniformity. Previously tested rainfall simulators have achieved uniformity coefficients in the following ranges: Chow and Rees, 1994, 79 to 86 ; Miller 1987, 86 to 93; Marston, 1982, 79 to 80; and Moore et al. 1983, 80 to 83.

$$Cu = 100\left(1 - \frac{\frac{1}{n}\sum_{i=1}^{n}\left|Xi - \overline{X}\right|}{\overline{X}}\right) \qquad [G.1]$$

Cu = Christiansen Uniformity Coefficient

Xi = ith rainfall intensity measurement

$\overline{X}$ = Mean of rainfall intensity intensity measurements

n = number of measurements

G.3 DESIGNS AND CALIBRATIONS

G.3.1 Laboratory Column.

The design of the laboratory column rainfall simulator used for simulated rainfall events is shown in Figure G.1 with water supplied from the mains. Several commercially available nozzles were tested to determine the optimum nozzle for spray application. The 1/4 M8 and 1/4 LNN4W nozzles manufactured by Spraying Systems Inc. of Wheaton, Illinois, U.S.A. were selected for further testing based upon the flow rates and spray area coverage reported by the manufacturer. Each nozzle was connected to mains water supply and calibrated for spray intensity and spray uniformity using the setup shown in Figure G.2. The operation of the solenoid valve was controlled using a power relay directed by a Campbell Scientific CR10X datalogger, which was able to operate the valve to a timing interval of 0.125 seconds. Calibrations were conducted by spraying for a fixed duration, and determining the volume of water reporting to all of the rainfall collection cups. The on-off cycling rate of the solenoid valve was used to vary the rainfall intensity and the sides and roof of the spray chamber were either removed or in place to determine their effect. The results of the calibrations are presented in Table G.1

The rainfall simulator was modified as shown in Figure G.1 to permit the application of a known tracer solution to the top surface of the column experiment. Air pressure supplied by a compressor and regulator was used to drive the tracer solution out of a pressure vessel.

G.3.2 Constructed Pile Experiment

The rainfall simulator for the constructed pile experiment was based around a commercial garden sprinkler. Three types of garden sprinklers were tested and calibrated by spraying for a fixed duration and collecting rainfall in collection cups. The first calibrations done in 1998 were conducted at UBC with the system connected to a mains water supply. The system as installed at Cluff Lake is shown in Figure G.3. The results of calibrations carried out at UBC are presented in Table G.2.

G.4 DISCUSSIONS

The uniformity and rate of the sprayer system used for the laboratory column was found to be highly dependant upon the presence of sides to the spray chamber and the duration of the on/off cycle of the solenoid valve.

The maximum rainfall intensity considered for the site (30 mm/hr) was lower than most commercially available spray nozzles produce. Only those nozzles tested could come close to the desired spray rate, and have the areal coverage required for the column experiment (1m diameter at 0.64 m height). The results in Table G.1 show that the 1/4 LNN4W was the best nozzle. The other nozzles produced excessive rainfall rates, and poorer uniformity.

diameter at 0.64 m height). The results in Table G.1 show that the 1/4 LNN4W was the best nozzle. The other nozzles produced excessive rainfall rates, and poorer uniformity.

The fine spray created all of these nozzles was found to affected by the air flow patterns created by the water spray within the spray area. Different results were observed for spraying with or without top to the spray area (Table G.1, Figure G.1). The presence of a top reduce the uniformity. Plastic sides were required for the experiment to prevent water entering other areas of the lab.

The fine spray of the 1/4 LNN4W nozzle was also affected by the on/off cycle. When the solenoid valve was opened, the spray would commence with a greater concentration in the center as the pipe between the solenoid and nozzle tip came up to full pressure. The spray would reach maximum intensity with a wider spray angle during the middle of the cycle. When the valve closed, the spray angle would decrease as the pressure fell as the remaining water between the solenoid and nozzle tip was sprayed. It was determined that under fully open conditions, the spray intensity was deficient in the center of the spray field and that the on/off cycling therefore helped to fill in the center. The uniformity of the spray was therefore dependant upon a careful balance of valve open spraying to cover the edges of the spray area, and valve closure to fill in the center of the spray area. The uniformity coefficient for the 1/4 LNN4W nozzle ranges from 63 to 80, with the best uniformity achieved with a 5 second on, 0.625 second off pulsing cycle at a rainfall rate of 25 mm/hr. A uniformity coefficient of 80 is within the range of other reported rainfall simulator designs.

The system for the tracer event shown in Figure G.1 was not able to produce nozzle pressures equal to that of the water delivery from the water mains in Figure G.1. At the lower pressures, the 1/4 LNN4W nozzle did not produce a suitable intensity. The 1/4 M8 nozzle was used at the lower pressure, which reduced both the spray intensity and the spray angle of the nozzle as shown in Table G.2.

G.4.1 Constructed Pile Experiment

The results presented in Table G.3 indicate uniformity coefficients in the range of 87 to 91 for the Gardenia sprinkler using a 25 psi pressure reducing fitting, which is at the high end of reported uniformity coefficients for other rainfall simulator designs. The spray nozzle simulator used in the laboratory did not achieve spray distributions as uniform as the sprinklers. It was decided that to arrange multiple nozzles to overlap and spray under windy field conditions would be impractical and likely less accurate than the garden sprinklers. The capital expenses for equipment, and the expenditures in time to calibrate and test a multi-nozzle simulator were considered too great. The nature of the constructed pile design would also require that a nozzle and solenoid based system be tested in-situ. This would have required substantial construction to prevent water from the calibration process from entering the pile

G.5 CONCLUSIONS

The design of the laboratory column rainfall simulator was a compromise between available materials, and a tight schedule for design, calibration and operation. The single nozzle system was adequate for the experiments, but could be improved with further testing.

The rainfall simulator for the constructed pile experiment was chosen to be capable of operating under exposed weather conditions, where wind was a factor. The Gardenia Jr. and Gardenia Sr. sprinkler models were therefore chosen. It was noted that the sprinklers produced larger drop sizes than the spray nozzles which added to greater spray distribution stability under slightly windy conditions.

G.6 REFERENCES:

Barnett, A.P. and Dooley, A.E., Erosion potential of natural and simulated rainfall compared, Transactions of the ASAE, Vol. 15, No. 6, 1112-1114, 1972.

Chow, T.L., and H.W. Rees, 1994, Effects of potato hilling on water runoff and soil erosion under simulated rainfall, Canadian Journal of Soil Science, 74, 453-460.

Christiansen, J.E., Irrigation by sprinkling, University of California Agricultural Experimental Station Bulletin, 670., 1942

Hinkle, S.E., 1990, The Akron USDA-Agricultural Service portable boom mounted rainfall simulator, Transactions of the ASAE, Vol. 33, No. 3, 818-820.

Hirschi, M.C., Mitchell, J.K., Feezor, D.R., and Lesikar, B.J., 1990, Microcomputer controlled laboratory rainfall simulator, Transactions of the ASAE, Vol. 33, No. 6, 1950-1953, 1990.

Holden, N.M., Dowd, J.F., Williams, A.G., Scholefield, D., 1995, Computer control for investigating water and chemical transport in a large isolated soil block, Computers and electronics in agriculture, Vol. 12, 225-236, 1995.

Imeson, A.C., 1977, A simple field-portable rainfall simulator for difficult terrain, Earth surface processes, Vol. 2, 431-436,

Marston, D., 1982, A rainfall simulator for field determination of relative erosion potentials, Journal of the Soil Conservation Service of New South Wales, 38 (1), 31-39.

Meyer, L.D. and Harmon, W.C., 1979, Multiple-intensity rainfall simulator for erosion research on row sideslopes, Transactions of the ASAE, Vol 22, 100-103.

Miller, W.P., 1987, A solenoid operated, variable intensity rainfall simulator, Soil Sci. Am. J., Vol. 51, 832-834

Moore, I.D., Hirschi, M.C., and Barfield, B.J.,1983, Kentucky rainfall simulator, Transactions of the ASAE, Vol. 26, No. 4, 1085-1089, 1983

Morin, J., Goldberg, D. and Seginer, I., A rainfall simulator with a rotating disc, Transactions of the ASAE, Vol. 10, No. 1, 74-77 and 79.

Sawatsky, L. , Dick, W, Cooper, D, and Keys, M., 1996, Design of a rainfall simulator to measure erosion of reclaimed surfaces, Mine Reclamation, Twenty years of progress, Proceedings of the twentieth annual British Columbia mine reclamation sysposium, B.C. Technical and Research Committee on Reclamation, Kamloops, B.C., June 17 to 20, 1996.

Shelton, C.H., von Bernuth, D., Rajbhandari, S.P., 1985, A continuous-application rainfall simulator, Transactions of the ASAE, Vol. 28, No. 4, 1115-1119.

Sumner, H.R., Wauchope, R.D., Truman, C.C., Dowler, C.C. and Hook, J.E., 1996, Rainfall simulator and plot design for mesoplot runoff studies, Transactions of the ASAE, Vol. 39, No. 1, 125-130.

Tossel, R.W., Dickinson, W.T., Rudra, R.P., and Wall, G.J., 1987, A portable rainfall simulator, Canadian Agricultural Engineering, Vol. 29, No. 2.

Tricker, A.S., 1979, The design of a portable rainfall simulator infiltrometer, Journal of hydrology, Vol. 41, 143-147.

Young, R.A. and Burwell, R.E., 1972, Prediction of runoff and erosion from natural rainfall using a rainfall simulator, Soil Sci. Am. Proc., Vol. 36, No. 5, 827-830., 1972.

Parameter	Details	Experiment Number Run 1
Height		68
Duration (minutes)		22.0
Spray Cycle	On (secs) Off (secs)	constant
Remarks		no roof
Rain Rate (m/hr)	Spatial Average Spat. Avg. Std. Dev Max Min	47.67 23.52 92.89 7.40
Uniformity coefficient	Using Arith. Avg. Using Spatial Avg.	52.55 40.93
Radial Averages		
Fourth	43.5 -52.9 cm	63.94
Third	32.5 - 43.5 cm	51.65
Second	20 - 32.5 cm	47.21
First	6 - 20 cm	74.53
Center	0 - 6 cm	67.40

Notes:
1. Mains water supply at pressure of 50 Psi
2. Spatial average calculated by weighting the volume reported in each cup by the fractional area of the test surface represented by the cup.
3. Arithmetic average calculated directly from the reported volume in each cup.

Table G.1 Part I: Calibration results 1/4 M8 nozzle

Parameter	Details	Experiment Number													
		Run 4	Run 5	Run 6	Run 7	Run 8	Run 9	Run 10	Run 11	Run 12	Run 13	Run 14	Run 15	Run 16	Run 17
Nozzle height above test surface (cm)		95	64	64	51.5	64	64	64	64	64	64	64	64	64	64
Duration (minutes)		40.2	43.0	41.1	41.8	40.0	42.5	90.0	40	39.5	31	40	40	40	40
Spray Cycle	On (secs)	constant	constant	constant	constant	5	2	3	5	constant	4	5	5	4	4
	Off (secs)					0.625	2	9	0.625		0.625	0.75	0.5	0.5	0.75
Remarks		no roof Note 1	no roof	with roof	with roof	with roof Note 2	with roof	with roof	no roof	no roof	no roof	no roof	no roof	no roof	no roof
Rain Rate (mm/hr)	Spatial Average	24.86	28.29	28.68	24.11	28.23	19.44	8.17	25.04	25.14	27.50	38.85	30.44	38.65	35.92
	Spat. Avg. Std. Dev	9.65	6.30	8.82	9.28	7.51	8.13	3.11	4.94	7.05	13.72	15.69	9.59	17.16	10.19
	Maximum	40.52	39.53	44.02	42.45	40.69	33.61	13.86	33.00	38.00	58.34	65.55	49.73	70.53	54.25
	Minimum	11.26	12.62	15.41	8.66	14.02	6.38	2.61	15.82	11.45	7.58	13.56	14.92	14.02	18.99
Christiansen	Using Arith. Avg.	62.77	81.43	72.81	63.75	77.08	66.70	67.65	82.31	74.34	62.24	66.48	72.73	57.82	74.72
Uniformity coefficient	Using Spatial Avg.	66.14	81.79	73.97	67.08	77.81	65.78	67.78	83.10	76.01	60.51	65.69	74.52	62.28	75.85
Radial Averages															
Fourth ring	43.5 -52.9 cm	30.73	27.91	28.56	31.78	25.66	12.29	4.52	25.54	27.30	14.58	24.53	27.97	40.12	32.89
Third ring	32.5 - 43.5 cm	29.10	30.12	33.18	25.56	32.27	20.11	10.50	27.92	30.27	24.94	40.12	39.05	56.34	40.69
Second ring	20 - 32.5 cm	18.01	28.18	27.13	18.30	30.35	28.40	11.15	24.53	20.60	48.42	57.70	30.52	27.18	41.14
First ring	6 - 20 cm	13.84	25.39	22.39	12.99	22.27	19.73	6.78	18.71	16.77	28.15	38.03	17.74	17.18	24.30
Center cup	0 - 6 cm	12.61	22.29	16.29	13.43	17.63	14.89	5.02	15.82	16.02	20.42	29.39	16.73	14.02	20.34

Notes:

1. Cups 50, 70 had drip problems. Average of other cups substituted
2. Several cups had drip problems. Average of other cups substituted.
3. Mains water supply at pressure of 50 Psi
4. Spatial average calculated by weighting the volume reported in each cup by the fractional area of the test surface represented by the cup.
5. Arithmetic average calculated directly from the reported volume in each cup.

Table G.1 Part II: Calibration results for 1/4 LNN4W nozzle

Sprinkler	Pressure (psi)	Average Rainfall Rate (mm/hr)	Standard Deviation (mm/hr)	Christiansen Uniformity Coefficient[1]	Number of Rainfall Cups	Rainfall Cup Pattern
Gardenia Jr	50	12.2	3.5	75	37	A
Gardenia Jr	25	9.6	1.2	91	37	A
Gardenia Jr	25	8.6	1.2	88	53	B
Gardenia Sr.	50	6.7	2.0	75	37	A
Gardenia Sr.	25	5.4	0.8	87	37	A
Gardenia Sr.	25	7.3	1.1	89	53	B
Nelson 3400	50	12.0	5.3	67	37	A
Nelson 3400	25	9.2	2.0	86	37	A
Nelson 3400	25	9.3	3.1	78	53	B

Notes:
1. Pressure of 50 psi at sprayer from direct connection to water mains
2. Pressure of 25 psi at sprayer created using commercial pressure reducing fitting.
3. Sprayer placed in the middle of an 8m x 8 m test spray area.
4. Rainfall collection cups placed at the following locations:

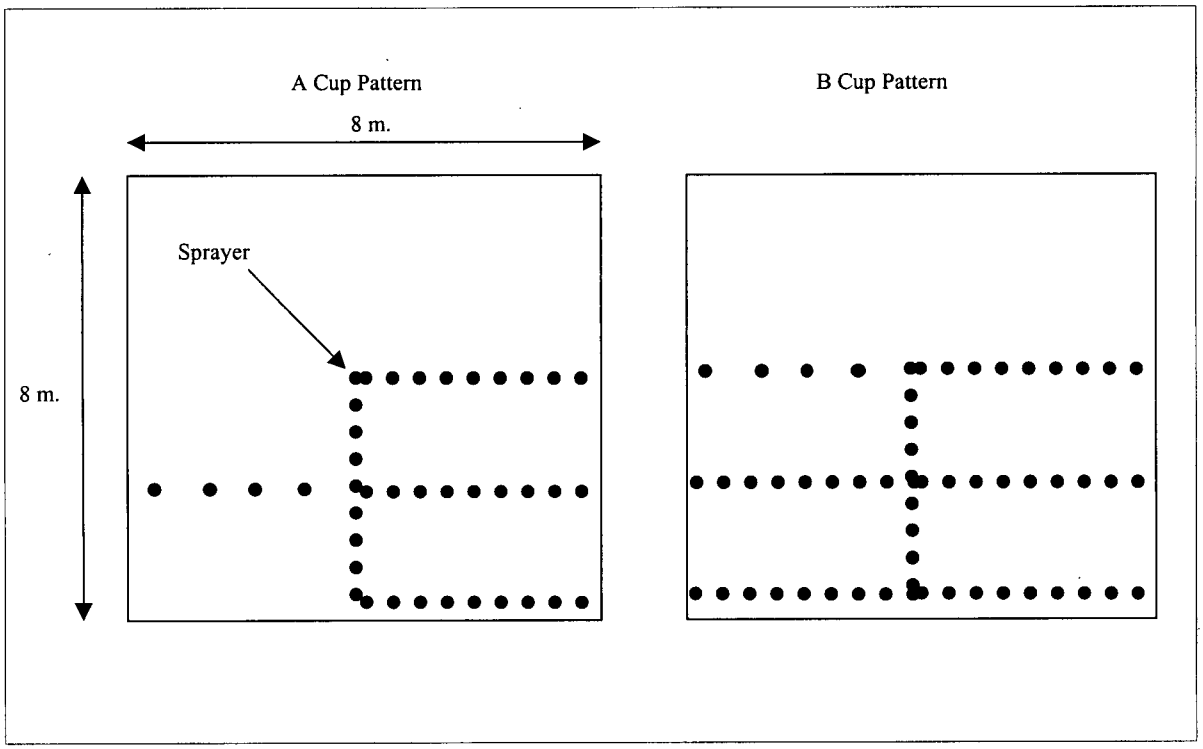

Table G.2: Calibration results for commercial garden sprinklers

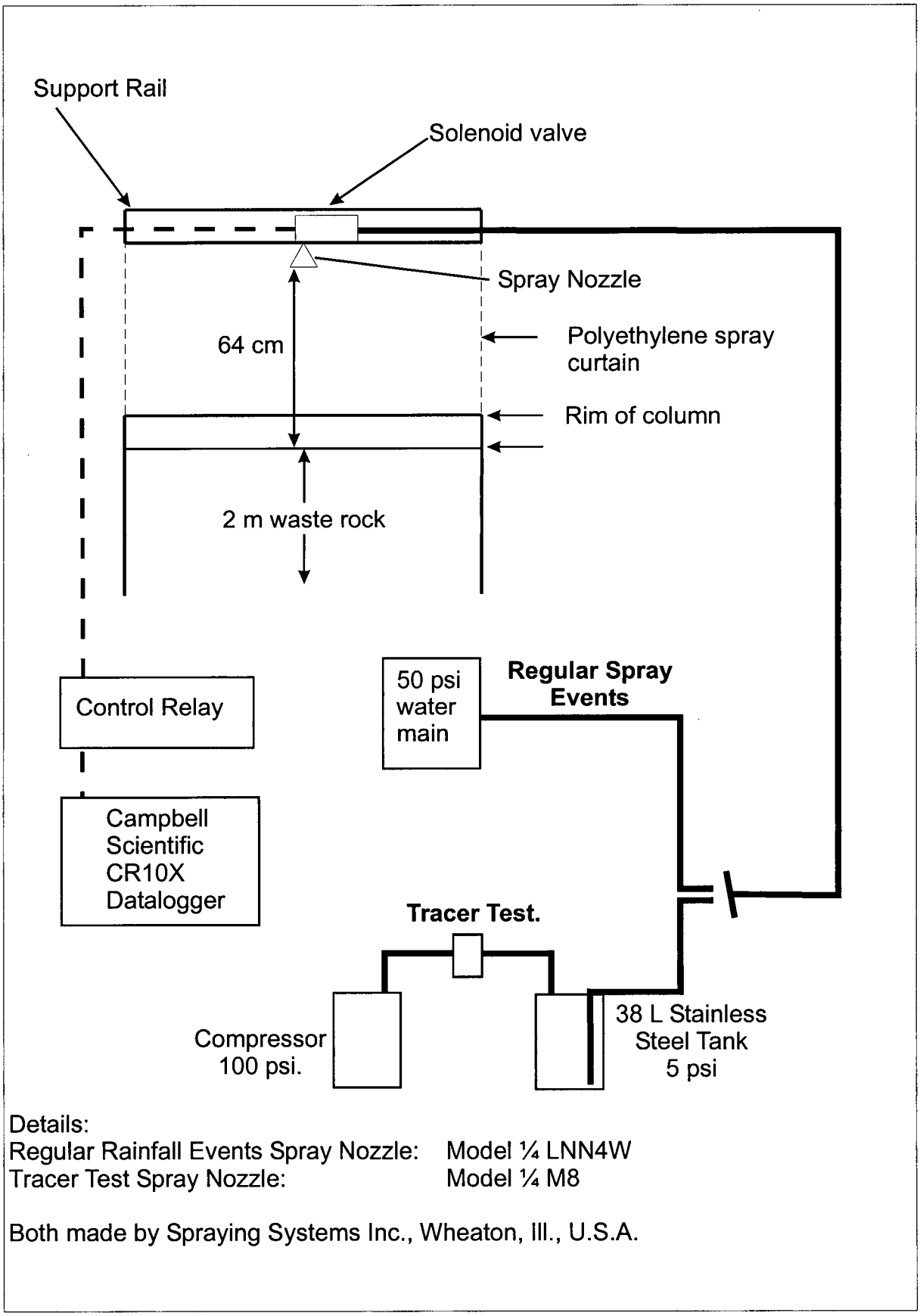

Details:
Regular Rainfall Events Spray Nozzle: Model ¼ LNN4W
Tracer Test Spray Nozzle: Model ¼ M8

Both made by Spraying Systems Inc., Wheaton, Ill., U.S.A.

Figure G.1: Laboratory column rainfall simulator design

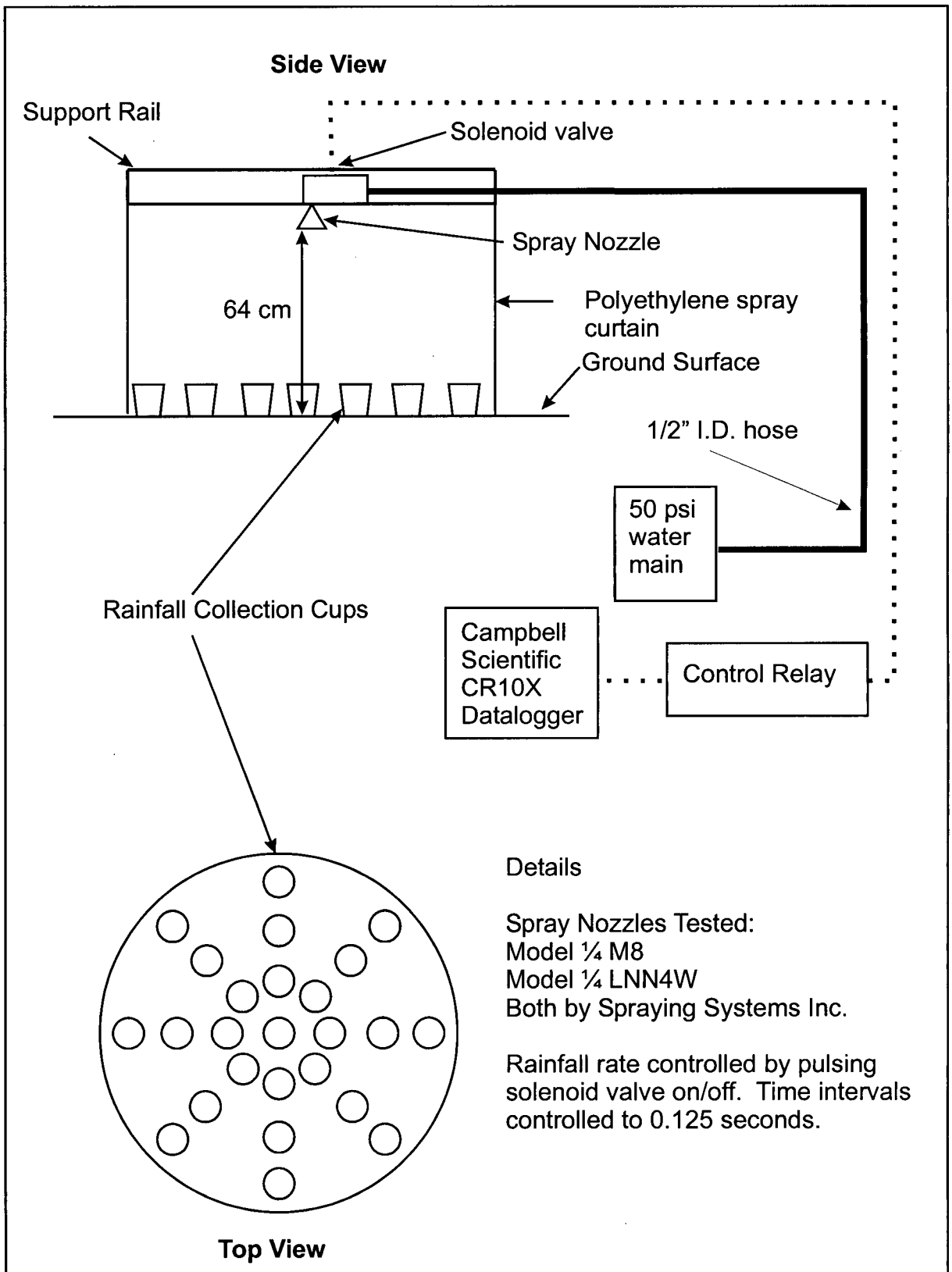

Figure G.2: Laboratory column rainfall simulator calibration setup

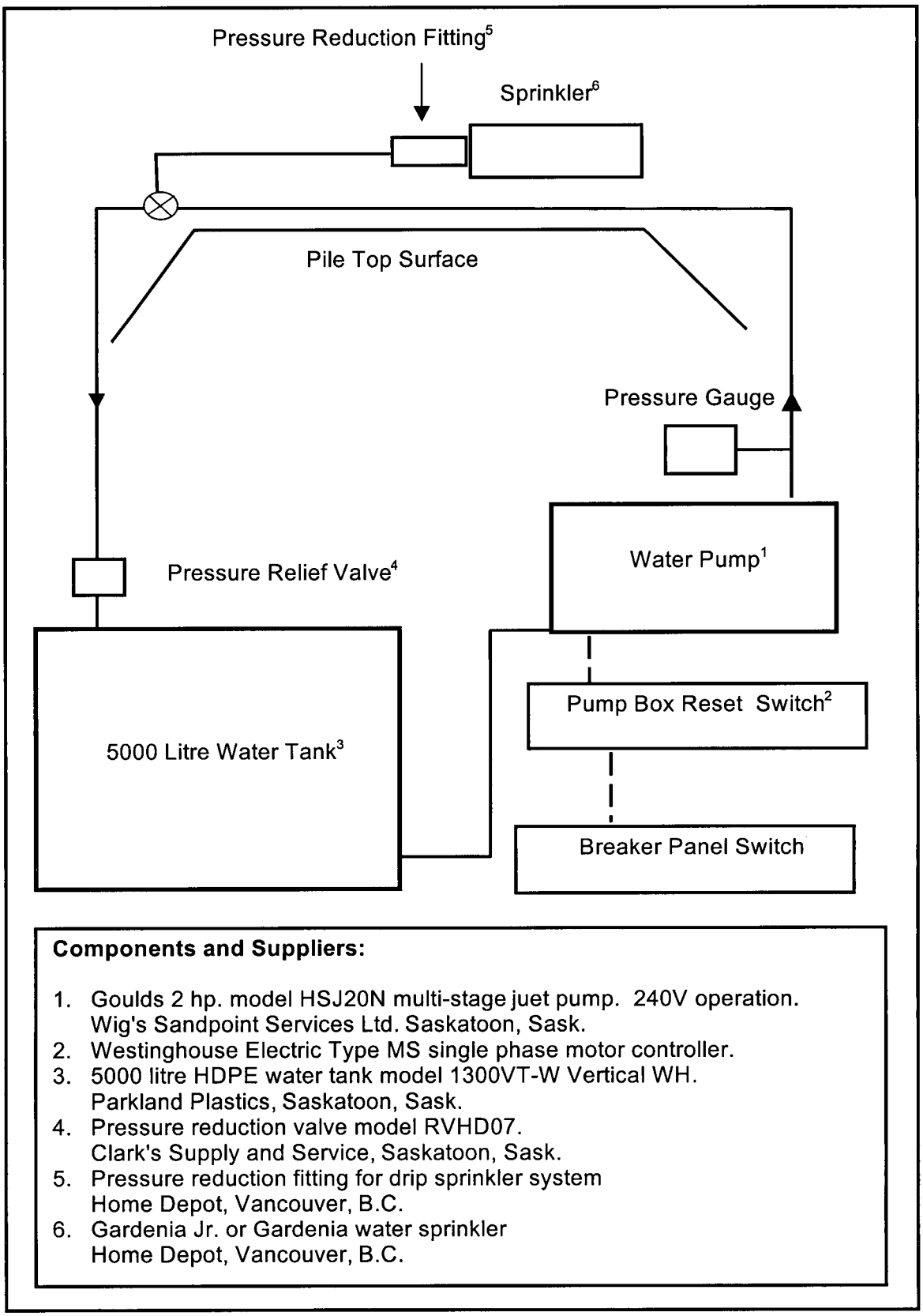

Components and Suppliers:

1. Goulds 2 hp. model HSJ20N multi-stage juet pump. 240V operation.
   Wig's Sandpoint Services Ltd. Saskatoon, Sask.
2. Westinghouse Electric Type MS single phase motor controller.
3. 5000 litre HDPE water tank model 1300VT-W Vertical WH.
   Parkland Plastics, Saskatoon, Sask.
4. Pressure reduction valve model RVHD07.
   Clark's Supply and Service, Saskatoon, Sask.
5. Pressure reduction fitting for drip sprinkler system
   Home Depot, Vancouver, B.C.
6. Gardenia Jr. or Gardenia water sprinkler
   Home Depot, Vancouver, B.C.

Figure G.3: Schematic layout of constructed pile experiment sprayer system.

APPENDIX H: INSTRUCTIONS FOR OPERATING CONSTRUCTED PILE EXPERIMENT RAINFALL SIMULATOR AND CONDUCTING AN ARTIFICIAL RAINFALL EVENT

H.1 INTRODUCTION

The constructed pile experiment at Cluff Lake is designed such that artificial rainfall can be created on the top of the pile to supplement the natural rainfall at the Cluff Lake site. The system involves a water supply, pump, and sprayer system. This appendix contains the protocol for carrying out an artificial rainfall event, written as instructions for a person at the Cluff Lake site.

H.2 SPRAYER SYSTEM DESIGN:

A overall schematic of the sprayer system was presented in Figure G.3. Details of the piping connections are presented in Figure H.1.

H.3 ASSEMBLING THE SPRAYER SYSTEM:

H.3.1 Pump

The water pump is drained and removed from the system during the winter to prevent freezing and damage to the pump. To connect the pump:

- Bring the pump to the pump box.
- Place the pump in the pump box, input towards the tank, wiring towards the switch. Do not bolt the pump down
- **TURN OFF THE BREAKER SWITCH TO THE PUMP IN THE INSTRUMENT SHED.**
- **TURN OFF THE RESET SWITCH IN THE PUMP BOX**
- Remove the cover from the pump wiring panel
- Connect the blue and red wire to the two outer wiring connections on the pump. It does not matter which is connected to which side.
- Connect the bare copper wire to the green pump ground screw.
- Replace the cover on the pump wiring connections

H.3.2 Piping

- Connect the 1-1/4" I.D. ABS pipe from the tank to the pump intake.
- Connect one of the 1-1/2" I.D. ABS pipes from the pipe loop on the pile to the output of the pump.
- Connect the pressure relief valve and 90-degree elbow fitting to the descending end of the 1-1/2" I.D. ABS pipe loop returning from the top of the pile. The relief valve is connected such that the pressure adjustment screw is in line with the descending pipe from the top of the pile (Figure H.1). The pressure gauge will be perpendicular to this pipe.
- Connect the 1-1/2" ABS pipe tank return flow pipe to the pressure reduction elbow.
- Once both lines are connected, bolt the pump to the floor of the pump box.

H.3.3 Testing

- Close all hose connections at the top of the pile

- Screw the pressure adjustment screw on the pressure reducer all the way anti-clockwise to reduce the pressure.
- Turn on the pump
- The pump will come up to speed, and the pressure should gradually increase to 40 to 50 psi. on the pump gauge.
- Hold the discharge pipe to the tank to prevent excessive jostling caused by air passing through the pressure reducer. Once the air has been expelled, the flow should be smooth, with a steady pressure at the pump.
- Adjust the pressure reducer screw inwards (clockwise) to bring the pump pressure to 55 psi.
- The loop at the top of the pile is now pressurized and ready for spraying.

H.3.4 Water Supply

Water is obtained from Cluff Lake using the green TEREX water buggy. Speak to the Mine Captain or the above ground crew supervisor about obtaining water. Fill the tank to full each time. After the water has been delivered, use the dip net to remove large floating particles from the water. After several events, use the brush to remove sediment from the bottom of the tank, and drain the tank to remove this material.

H.3.5 Sprayers

There are two sprayer types available, Gardenia Jr. and Gardenia Sr. sprayers. The sprayers, pressure reducers and hoses are all stored in the Environment department trailer.

H.3.6 Rainfall Cups

There are 16 rainfall collection cups made from 1 litre sample bottles. The cups are stored in the Environment department trailer. Before each rainfall event these are placed within their respective cells. The volume reporting to each cup is measured to determine the distribution and volume of rainfall. The cups may need to be weighted down to prevent being tipped over by the wind. Rocks can be taped to the outside of the cups, or placed inside the cups. They are 72 mm in inside diameter. Each 4.902 mls reporting to the rainfall cups corresponds to 1mm of rainfall.

H.4 CONDUCTING A SPRAY EVENT

- Choose a day with low wind velocity. The wind speed is normally lowest during the early morning (8 am - 10 am.).
- Connect the pump and hoses
- Obtain a full tank of water. Remove the larger debris.
- Place all 16 rainfall measurement cups on the surface in their respective cells..
- Connect the required sprayers to the hose connections on the pile. Make sure all connections are tight and do not leak.
- Check the rainfall skirt at the edge of the pile which diverts water off the exposed wall.
- Align the sprinklers so the spray is perpendicular to the predominant wind direction
- Turn on the pump system
- Note the starting time, and commence spraying.
- Use another sprayer to periodically wet the ground surface under the net radiometer on the weather station.
- Adjust the sprayer(s) to ensure even coverage of the pile

- During the spray event, the water volume in some of the rainfall cups can be checked. If need be, use a hand held sprayer to augment the rainfall volume in areas receiving lower rainfall.
- Spray for the required time.
- Collect a water sample from one of the hose connections at the top of the pile.
- Not the ending time and end the spray event.
- Wait ½ to 1 hours for the surface to dry before collecting all rainfall cups and measuring the volumes collected.
- Convert the volume to mm rainfall using 4.902 mls = 1mm rain. Calculate the average rainfall in mm, the standard deviation and Christiansen coefficient of variability of the rainfall.

H.5 TROUBLESHOOTING/ HELPFUL HINTS

- SPRAY IS LOW: Check the fast-connect fitting at the sprayer for debris and clean if necessary.
- SPRAY IS LOW: Try using a different hose connection point. In July 2000, the west connection seems to be partly clogged, use the east and south connections.
- TWO SPRAYERS: Make sure the sprayers are offset slightly. If they line up, the sprays will intersect close to the sprayers and cause extra rainfall to the cell containing the sprayers.
- WIND: Do not conduct rainfall events if the wind is too strong. Try to conduct them early in the morning to get still air.
- WIND: The sprayers must always be aligned with the sides of the pile to gain coverage. They should be perpendicular to the predominant wind direction.
- LEAKS: Check to make sure the connections to the sprayer are not leaking in any way and tighten if necessary.
- LEAKS: Check to make sure the black pressure reducing fitting at the sprayer is not leaking from the weep hole. If it is, use a different fitting.
- SURFACE: Try to minimize walking on the pile surface when it is very wet. The pile surface will compact easily when wet, which should be avoided. Try to walk on stony areas if possible.

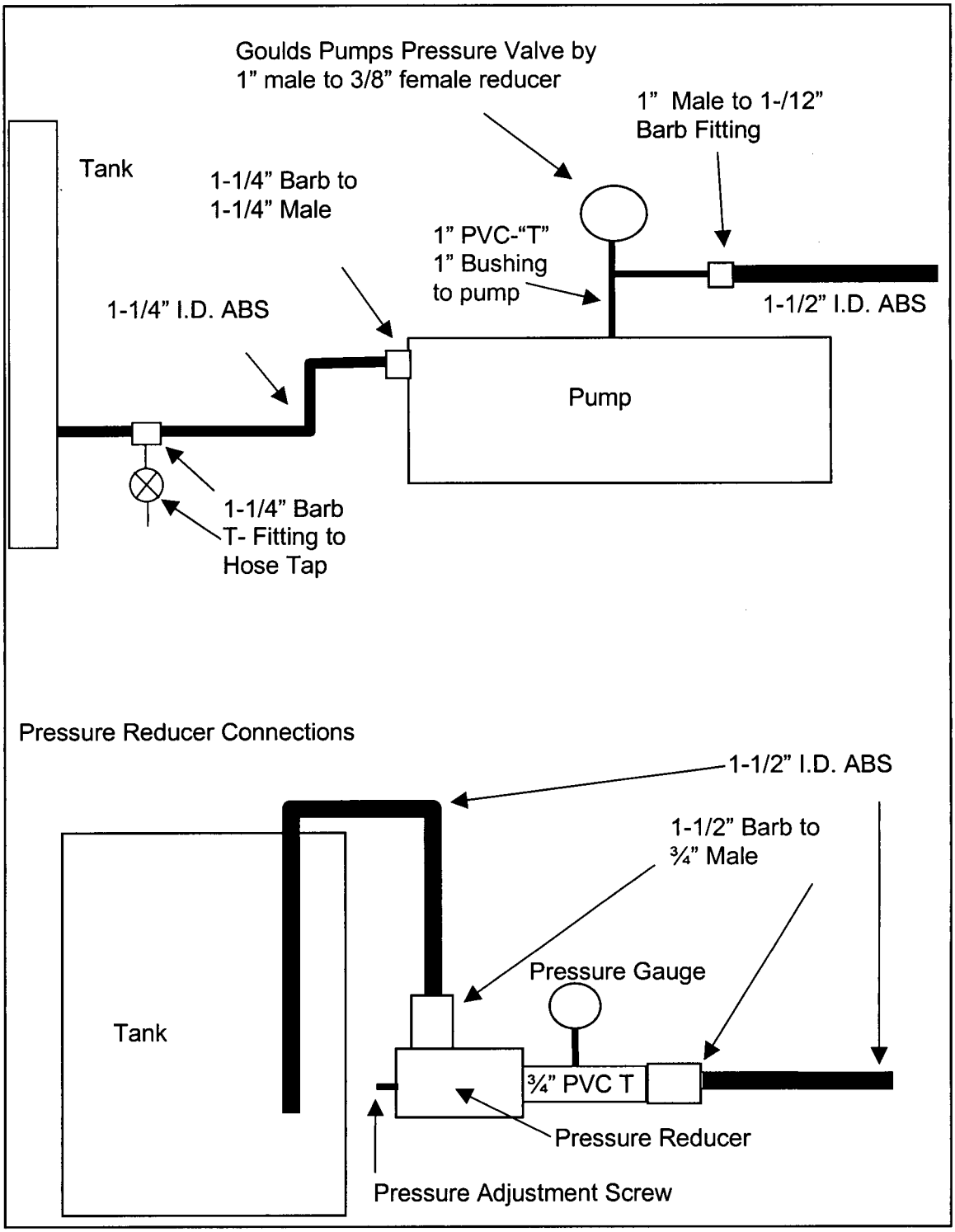

Figure H.1: Details of piping layout.

APPENDIX I: CONSTRUCTED PILE EXPERIMENT TDR PROBE CALIBRATION DETAILS

I.1 INTRODUCTION

Both coated and uncoated TDR probes are installed in the constructed pile experiment. Prior to installation, a series of measurements were taken using each probe to determine the characteristics of the probe coatings, and to determine the probe head/end offset correction (Chapter 3 and 4).

I.2 METHOD

Calibration measurements were conducted in air, oven-dried silica sand, and de-ionized water. The sand or water was placed in a 20-litre plastic pail, 30 cm diameter. Probes were fully covered by the sand or water. A MoisturePoint MP-917 TDR instrument (MTDR) was used to collect travel time measurements in each media using the automated fitting routines included in the instrument firmware. Stable readings were achieved by ensuring the MTDR instrument was appropriately warmed up. The instrument warm-up time for each individual measurement was set to 15 seconds. In addition, a minimum of five measurements were taken and discarded prior to recording calibration data. Gain settings were set 2 for the probe head and 2 for the probe end, which matches the gain settings used for the probe head and end for measurement of waste rock in the constructed pile experiment. A minimum of twenty measurements were taken for each probe calibration setup, and the average and standard deviation of the measured travel times were taken.

I.3 RESULTS

Tables I.1 and I.2 present the data recorded. Included are the calculated travel times in water and air.

Parameter	Average	Probe Number 1	2	3	4	5	6	7	8	9	10	11
Probe Length (mm)	390.091	389	389	390	391	390	**390***	390	391	386	390	389
Calculated tcair [(2L/c)* (Kair)^0.5] (nsecs)	2.603	2.596	2.596	2.603	2.609	2.603	2.603	2.603	2.609	2.576	2.603	2.596
Measurements in oven dried silica sand (tods)												
Measured Raw Average Time (nsecs)	4.848	4.869	4.817	4.885	4.872	4.972	4.884	4.851	4.839	4.845	4.848	4.749
Standard Deviation	0.030	0.011	0.008	0.015	0.018	0.052	0.068	0.016	0.097	0.016	0.010	0.016
Measurements in de-ionized water (tw)												
Raw Average Time (nsecs)	13.782	13.728	13.662	13.600	13.624	13.626	13.565	14.363	13.752	13.523	13.666	13.494
Standard Deviation (nsecs)	0.020	0.023	0.016	0.008	0.017	0.015	0.021	0.015	0.011	0.015	0.019	0.019

Parameter	Average	Probe Number 12	13	14	15	16	17	18	19	20	21	22
Length (mm)	390.091	**390***	392	389	385	390	394	**390***	391	393	392	391
Calculated tcair [(2L/c)* (Kair)^0.5] (nsecs)	2.603	2.603	2.616	2.596	2.569	2.603	2.629	2.603	2.609	2.623	2.616	2.609
Measured travel time in oven dried silica sand (tods)												
Measured Raw Average Time (nsecs)	4.848	4.740	4.770	4.792	4.844	4.810	4.898	4.875	4.899	4.863	4.905	4.835
Standard Deviation	0.030	0.013	0.019	0.041	0.014	0.047	0.036	0.007	0.051	0.060	0.046	0.010
Measured travel time in de-ionized water (tw)												
Raw Average Time (nsecs)	13.782	13.724	14.519	13.391	13.496	13.491	13.729	13.629	13.657	14.621	14.599	13.750
Standard Deviation (nsecs)	0.020	0.015	0.018	0.017	0.118	0.018	0.016	0.013	0.010	0.016	0.011	0.016

Notes:

1. MoisturePoint TDR system used. 15 second warm up time. Automated remote diode shorting routine used to locate probe head and probe end transitions.
2. * Probe length not measured, assigned average of all probes. Probe length indicates length of exposed rods.
3. L = length of probe, c= speed of light in a vacuum, K = dielectric constant
4. Dielectric constant of oven dried sand estimated using an uncoated TDR probe: 2.7
5. Dielectric constant of probe coating estimated from calibration experiments (Chapter 3): 2.8
6. Water temperature 21 Deg. C. Dielectric constant of water (Kw) 79.994. (Young, 1998)

Table I.1: Constructed Pile Experiment: Calibration Details of Coated TDR Probes

Parameter	Average	Probe 1	2	3	4	5	6	7	8	9	10
Probe Length (mm)	119.8	122	119	115	122	118	120	121	121	120	120
Measurements in Air (tair)											
Measured Average Travel Time (tair, nsecs)	1.528	1.518	1.522	1.553	1.524	1.490	1.551	1.489	1.571	1.508	1.554
Standard Deviation	0.024	0.013	0.021	0.012	0.020	0.073	0.011	0.020	0.023	0.020	0.025
Calculated Travel Time [(2L/c)* (Kair)^0.5] (tcair, nsecs)	0.799	0.814	0.794	0.767	0.814	0.787	0.801	0.807	0.807	0.801	0.801
Probe Head/End Offset (nsecs) (tair-tcair, nsecs)	0.728	0.704	0.727	0.786	0.709	0.702	0.750	0.681	0.764	0.707	0.753
Measurements in oven dried silica sand (tods)											
Measured Average Travel Time (nsecs)	2.028	2.036	2.023	2.043	2.020	1.988	2.039	1.969	2.100	2.029	2.040
Standard Deviation	0.009	0.008	0.010	0.009	0.009	0.008	0.008	0.008	0.008	0.010	0.013
Measurements in de-ionized water (tw)											
Measured Average Travel Time (tw, nsecs)	8.424	8.539	8.378	8.313	8.482	8.324	8.441	8.427	8.527	8.453	8.361
Standard Deviation	0.016	0.012	0.022	0.015	0.017	0.021	0.010	0.018	0.017	0.017	0.011
Water Temperature (Deg C)	18.650	18.7	18.7	18.7	18.7	18.7	18.6	18.6	18.6	18.6	18.6
Water Dielectric Constant	80.860	80.86	80.86	80.86	80.86	80.86	80.86	80.86	80.86	80.86	80.86
Calculated Travel Time [(2L/c)* (Kw)^0.5] (tcw, nsecs)	7.189	7.321	7.141	6.901	7.321	7.081	7.201	7.261	7.261	7.201	7.201
Probe Head/End Offset (tw - tcw, nsecs)	1.236	1.218	1.237	1.412	1.161	1.243	1.240	1.166	1.266	1.252	1.160

Notes:

1. MoisturePoint TDR system used. 15 second warm up time. Automated remote diode shorting routine used to locate probe head and probe end tra
2. Probe length indicates length of exposed rods.
3. L = length of probe, c= speed of light in a vacuum, K = dielectric constant
4. Dielectric constant of oven dried sand estimated using an uncoated TDR probe: 2.7
5. Dielectric constant of water from Young, 1998.

Table I.2: Constructed Pile Experiment: Calibration Details of Uncoated TDR Probes

APPENDIX J: CONSTRUCTED PILE EXPERIMENT: THERMAL CONDUCTIVITY SENSOR CALIBRATION AND MEASUREMENT DETAILS

J.1 INTRODUCTION

The thermal conductivity sensors installed in the constructed pile experiment were manufactured and calibrated by the research group of Dr. Del Fredlund at the university of Saskatchewan. This appendix documents the calibration equations provided with the sensors, the additional calibration equations calculated to account for sensor hysteresis, and details of the measurement routines used.

J.2 METHODS

J.2.1 Measurement cycle and fitting equation

The thermal conductivity sensors record the temperature rise occurring at the core of the sensor body as the result of the application of a fixed heat pulse to the center of the sensor. The heat is generated by a resistor which is provided power for a fixed time interval (50.225 seconds) by a 10 V constant voltage power supply. The temperature at the core of the sensors is monitored before the heating cycle, and during the heating cycle using an integrated circuit temperature sensing chip. Output from the I.C. temperature sensor is a voltage signal. All measurements of the output voltage were recorded using a Campbell CR10/10X datalogger using a 0 – 2500 mV voltage range differential voltage measurement between the I.C. temperature chip ground and I.C. temperature chip output. All measurements were done with a 60 Hz rejection filter to eliminate electrical noise from other instrumentation and electrical wiring. Calibrations conducted by Dr. Fredulund's group were conducted using the power supplies to be installed in the constructed pile experiment.

Following the sensor heating cycle, the final sensor temperature recorded at 50.225 seconds. Dr. Fredlund's group used a fitting equation based upon Xing and Fredlund (1994) to fit a curve to the last twenty points of the heating curve, and calculated the final temperature at 50.225 seconds. This improves resolution by averaging out the error associated with a single measurement. This equation was replaced using a second order polynomial fitting equation of the form (Devorre, 1987):

$$V' = \hat{\beta}_2 t^2 + \hat{\beta}_1 t + \hat{\beta}_0 \qquad [J.1]$$

where :

$$\hat{\beta}_1 = \frac{s_{1y}s_{22} - s_{2y}s_{12}}{s_{11}s_{22} - s_{12}^2}$$

$$\hat{\beta}_2 = \frac{s_{2y}s_{11} - s_{1y}s_{12}}{s_{11}s_{22} - s_{12}^2}$$

$$\hat{\beta}_0 = \overline{V} - \hat{\beta}_1 \overline{t} - \hat{\beta}_2 \overline{x^2}$$

$$s_{1y} = \sum t_i V_i - n\overline{tV}$$
$$s_{2y} = \sum t_i^2 V_i - n\overline{t^2}\,\overline{V}$$
$$s_{11} = \sum t_i^2 - n\overline{t}^2$$
$$s_{12} = \sum t_i^3 - n\overline{t}\,\overline{t^2}$$
$$s_{22} = \sum t_i^4 - n(\overline{t^2})^2$$

t = Time after heating started (seconds)

V = Measured sensor output voltage

V' = Calculated sensor output voltage

J.2.2 Calibration:

Sensors were calibrated using the following method (F. Shuai, personal comm., 1998). The sensors were placed in a chamber with a pressure plate at the base, and kaolinite clay to make contact between the sensor and the pressure plate. The sensors were first vacuum saturated to 100% saturation. The sensors were then dried to a matric suction of approximately 400 kPa. The sensors are then re-wetted to 0.1 kPa, and held at this suction for several days. The sensors were then subjected to progressively greater matric suctions from 0.1 kPa to 400 kPa, and measurements were taken to determine the change in output voltage of the I.C. chip over the heating cycle at each matric suction. Suction measurements and calibrations are cut off for matric suctions greater than 400 kPa because of the very long equilibration times required for the sensors.

Based on this work, calibration equations to describe the drying curves obtained during calibration were provided of the form:

$$\psi = \left[\frac{b \cdot (\Delta V - a)}{c - \Delta V}\right]^d \qquad [J.2]$$

ψ = matric suction (kPa)

ΔV = measured output voltage rise

a, b, c, d = fitting parameters

The parameters of this curve have physical meaning (Feng, 1999):

A is the water content, or voltage output corresponding to zero suction
C is the water content, or voltage output when the suction is infinite
B defines the horizontal position of the curve
D defines the slope of the central linear portion of the curve.

J.2.3 Sensor hysteresis

Calibrations were performed for drying conditions only. No data points were measured during wetting of the sensors from dried. The response of the sensors is affected by hysteresis (Chapter Five, Feng, 1999). An estimation of the wetting curve based upon the drying curve was made based upon the data contained in Feng, 1999. Feng (1999) measured drying, wetting and scanning hysteresis curves for thermal conductivity sensor with the same ceramic as the sensors used in this study. The measured drying and wetting curves are presented. This data was used to derive estimates for the a,b,c and d curve fitting parameters for calibration curves for our sensors under wetting conditions.

The following method was used:

1) The drying curve for each sensor was plotted using Equation J.2 and using a, b, c ,and d from the drying curve measurements provided with each sensor.
2) Values of output voltage were picked for 100,200 and 300 kPa. These drying curve values were divided 1.55, 1.35 and 1.5 respectively, based on the measured drying and wetting curve data presented in Figure 4.10 of Feng (1999, page 87).
3) These points were assumed to lie upon a wetting curve of the form of Equation J.2. The values of a, b, c and d for the wetting curve were manually altered until the fitting curve satisfied two conditions: (1) the fitted wetting curve passed through the points defined by Step 3 and (2) the subsequently calculated values of drying suction/wetting suction must had a similar pattern to Graph 4.10 of Feng, (1999)

J.3 RESULTS

The fitting parameter for measured drying conditions, and the fitting parameters for wetting conditions estimated using the method above are presented in Table J.1.

J.4 REFERENCES:

Devore, J.L.,1987, *Probability and statistics for Engineering and the Sciences*, 2nd Edition, Brooks/Cole Publishing Company, Montery California.

Man Feng, 1999, The effects of capillary hysteresis on the matric suction measurement using thermal conductivity sensors, M.Sc. Thesis, Department of Civil Engineering, University of Saskatchewan.

Xing, A. and D.G. Fredlund, 1994, Numerical modeling of a thermal conductivity matric suction sensor, Geotechnical Testing Journal, 17, 4, 415-424.

Measured Laboratory Calibrations
Drying Curve Parameters

Probe Number	A Factor	B Factor	C Factor	D Factor
1	54.1	87.88	85.34	1.16
2	40.59	145.34	67.55	1.02
3	52.99	185.47	78.44	0.93
4	61	79.1	86.68	1.08
5	44.3	251.45	63.07	0.84
6	69.54	78.04	107.62	1.15
7	85.82	227.18	124.8	0.97
8	71.31	209.26	105.35	0.91
9	43.36	68.15	79.82	1.37
10	33.05	657.57	64.57	0.75
11	29.44	4452.85	59.03	0.56
12	56.32	313.78	107.26	0.86
13	39.19	76.66	70.27	1.08
15	50.35	390.99	79.51	0.75
16	51.68	59.25	95.58	1.23
20	53.04	395.26	79.18	0.78
21	73.01	145.22	109.37	0.92
22	53.51	106.72	88.73	1.02

Estimated Wetting Curve Parameters

Probe Number	A Factor	B Factor	C Factor	D Factor
1	54.1	44.49	85.34	1.26
2	40.59	67.02	67.55	1.11
3	52.99	79.35	78.44	1.01
4	61	38.08	86.68	1.18
5	44.3	98.23	63.07	0.91
6	69.54	39.28	107.62	1.25
7	85.82	100.67	124.8	1.06
8	71.31	87.87	105.35	0.99
9	43.36	38.30	79.82	1.49
10	33.05	229.48	64.57	0.82
11	29.44	1087.29	59.03	0.61
12	56.32	125.28	107.26	0.94
13	39.19	36.90	70.27	1.18
15	50.35	136.45	79.51	0.82
16	51.68	31.18	95.58	1.34
20	53.04	143.63	79.18	0.85
21	73.01	61.56	109.37	1.00
22	53.51	42.20	88.73	1.16

Notes:

1. Estimated wetting curve parameters derived using drying curve suction to wetting curve suction ratios estimated by Man Feng, 1999, "The effects of Capillary Hysteresis on the Matric Suction Measurement Using the Thermal Conductivity Sensors", M.Sc. thesis, Department of Civil Engineering, University of Saskatchewan.
2. Parameters are the parameters of the fitted calibration curve :

$$\psi = \left[\frac{b \cdot (\Delta V - a)}{c - \Delta V}\right]^d$$

ψ = matric suction (kPa)

ΔV = measured output vol tage rise

a, b, c, d = fitting parameters

Table J.1: Drying and wetting calibration curves for thermal dissipation sensors.

APPENDIX K: CONSTRUCTED PILE EXPERIMENT: TIPPING BUCKET GAUGE CALIBRATION

K.1 INTRODUCTION

The volume and rate of outflow from the constructed pile experiment was monitored using model 525MM tipping bucket rain gauges manufactured by Texas Electronics of Dallas, Texas. The manufacturer's information states the gauges have a linear calibration in the range of 0 to 10 mm/hr. (Campbell Scientific, 1998). This corresponds to a flow rate through the gauge of 0 to 0.132 mls/sec. (0 to 11.4 L/day), or one tip every 36 seconds. Tipping rates in excess of 1 tip per 36 seconds were expected during the experiment. A detailed calibration of all 16 gauges was performed to determine the equation relating flow rate to tipping time for flow rates between 0.132 mls/sec and 10 mls/sec.

The time taken for the tipping bucket mechanism to tip creates a non-linear relationship between tip time and flow rate. The time for the bucket to rotate from the filled side to the empty side allows more water to enter the filled side of the bucket before the bucket passes through a horizontal position and the inflow starts to fill the empty side of the bucket. The time for the bucket to pass from one rest position through horizontal to the opposite rest position may take 0.3 to 0.6 seconds (Marsalek, 1981), reducing as the flow rate increases. The extra volume of water added to the already filled side on each tip increases as the flow rate increases and thus the time between tips becomes non-linearly related to flow rate. Theoretical discussions of the derivation of non-linear equations are presented by Marsalek, 1981 and Simic and Maksimovic, 1994. A practical calibration similar to this work is presented by Barfield and Hirschi, 1986.

A first calibration was carried out when the gauges were installed in September 1998. During the period of September 1998 to July 2000, the tipping bucket mechanisms underwent several maintenance repairs and design retrofits. During each repair, the position of the tipping bucket mechanism calibration screws were recorded using a vernier scale, and these positions were re-instated after all repairs were finished. In order to confirm that the repairs had not disturbed the original factory calibrations of the tipping buckets, a second calibration was performed in July 2000.

K.2 METHODS:

K.2.1 Gauge Balancing

All gauges were mounted within the instrumentation shed of the constructed pile experiment as shown in Figure K.1. The tipping bucket mechanism is located within an outer gauge casing, as shown in Figure K.2. Details of the design changes are shown in Figure K.3. The calibration screws are factory calibrated to control the volume which will be contained within each side of the bucket when it tips. The tipping bucket mechanism is fixed to the outer body of the gauge and if this outer body is not aligned vertically, then the tipping mechanism will record a different volume for each side of the bucket.

Prior to each calibration the vertical alignment of the outer bodies of all gauges were adjusted to ensure the volume recorded by each side of the tipping bucket mechanism was equal. To balance the gauge, a constant flow rate of water was introduced to the tipping bucket gauge and the time of each tip was observed. The adjustment point (Figure K.1) was moved laterally until the tip time and hence bucket volume, was equal for both sides of the tipping bucket mechanism. The alignment guide was used to record the gauge body alignment during the balancing process, and the final alignment when balanced. Between calibrations, the gauge bodies were re-balanced whenever required.

K.2.2 Flow Rate Calibration.

A constant head device was used to provide a constant flow rate of water to each tipping bucket gauge. The flow rate from the constant head device was measured by collecting all water from the gauge over a fixed time period. The start and end time of the flow rate measurement period was coordinated with the exact time of a bucket tip. This ensured that the volume of water from an even number of tips was measured. The delivered flow rate was calculated from the total volume collected divided by the duration of the collection period. The flow rate was measured over a minimum of twenty tips of the bucket. Flow rates were varied from 0.1 to 10 mls/sec. The real clock time of each tip was collected to an accuracy of 0.125 seconds using a Campbell CR10X datalogger connected to the 16 gauges using two Campbell Scientific SDM-SW8A multiplexers. 0.125 seconds is the maximum time resolution possible using the configuration of multiplexers used.

It was observed that at higher flow rates, the direction of water flow into the collection funnel of the gauge affected the measured tipping rate by creating imbalance between the two sides of the bucket. The force of the water pouring to the base of the collection funnel created spiraling flow through the funnel opening. This led to the water flow into the tipping bucket mechanism not being centered over the tipping bucket. All flowing water from the constant head device, and all outflow monitored during normal operations, was introduced to the side of the gauge funnel parallel to the hinge axis of the tipping bucket mechanism to eliminate spiral flow and ensure that any forces generated by the water flow from the funnel to the tipping bucket were directed parallel to the hinge axis, and would not lead to unbalanced tips.

Details of the field procedures are included at the end as a set of instructions: "Instructions for Outflow Monitoring and Maintenance".

K.3 RESULTS

Figures K.4 through K.7 present the data from the September 1998 calibration, and the July 2000 calibration. The data from all 16 gauges has been composited and presented in Figures K.4 through K.7. A composite calibration equation is derived and presented in each figure based upon the data collected from all 16 gauges. A summary of the individual equations for each graph are presented in Table K.1. Table K.2 presents the percentage differences between a composite calibration equation derived from all the data from the sixteen gauges, with the individual calibration equations for each gauge. Table K.2 also presents the average standard deviation, expressed as a percentage, for the measured tip times for all of the flow rates for each gauge.

Based upon the reported gauge dimensions and the stated degree of accuracy (Campbell Scientific, 1998), a point was added for each gauge to represent operation under low flow rate conditions . The flow rate at 10mm/hr is 0.132 mls/sec or 1 tip per 36 seconds. This was assigned a calculated of 4.73 mls/tip based upon the stated gauge dimensions (Campbell, 1998). Figures K.4, K.5 and K.7 present the data with this factory calibration point added. Figures K.4B and K.6 present the graphs with these added points removed.

Figure K.7 presents the results from September 1998 and July 2000. The composite calibration curves derived from the data collected from all 16 gauges are presented. The two calibration lines are nearly coincident.

K.4 DISCUSSION

All of the calibration equations use calculated tip time, and not the raw tip time data. The time between tips for a single tip (left-right or right-left) were found to be affected by slight imbalances of the gauge body. The calculated tip time used for the calibration was half the combined intervals of two single adjacent tips. Two tips represents one cycle (left-right-left or right-left-right) of the tipping bucket mechanism. This helps to cancel out any residual imbalance in the gauge body.

The results above were used to determine if the calibration of all of the gauges, and of individual gauges had been changed by the rebuilding and retro-fitting process. The first minor gauge repairs and rebuilding occurred September 19, 1999 and more extensive repairs were undertaken April 16 - 19, 2000

The data from all 16 gauges appeared to fall very close to the composite calibration equations derived from all data (Figures K.4 to K.7). Table K.1 presents both the individual calibration equations and the equations derived by combining all calibration data. The equations derived from September 1998 and July 2000, including the added factory calibration point, have the same exponent and a constant which is 3.9% higher for the July 2000 data. A specified recorded tip time will correspond to a 3.9% higher actual flow rate using the July 2000 equation. This indicates that the September 1998 composite calibration should be replaced with a new equation for later data.

Table K.2 presents the data used to determine if the flow rate could be calculated using a single composite calibration equation, or whether individual calibration equation should be used. Table K.2 also presents the results of calculations estimate the expected error in the flow rate equations. In Table K.2, the maximum difference, minimum difference, average difference and average of the absolute differences between the composite calibration equations, and the individual calibration equation are presented for the range of flow rates observed during the 1999 and 2000 field season. The final two columns present the standard deviations of the calculated tip times averaged over all of the calibration runs for each gauge.

A composite equation will be appropriate if the variations between the individual equations were created only by uncertainty in the measured parameters of volume and tip time. There are random uncertainties in the measured parameters used to derive the 6 to 9 points on each individual calibration graph. These uncertainties will lead to slightly different calibration equations even if each gauge is systematically identical. If the only differences in calibration equations are caused by random uncertainties, then a composite equation derived from 100 to 130 measurements from 16 identical gauges will be more accurate than the individual equations derived from 6 to 9 points. The data on table two was used to assess the hypothesis that the only variations between gauges were caused by random uncertainty.

The September 1998 data indicates that gauges 12, 14 and 16 varied the most from the composite equation with absolute differences of 6.4%, 5.1% and 6.5% respectively. The average standard deviation of calculated tip times for the September 1998 is 3.1%. This can be used to represent the average uncertainty in the measurement of a calculated tip time. The differences between the individual calibration equations for gauges 12, 14 and 16 and the composite equation are greater than the uncertainty in the calculated tip time. This indicates the differences between the equations for these gauges and the composite are the result of systematic differences between these gauges and the rest of the gauges. These systematic differences may be slight differences in the bucket volumes, imbalance of the gauges, or other physical differences between gauges.

The July 2000 data indicates greater difference between individual gauges and the composite calibration equation. Gauges 2, 6 and 10 have the greatest average absolute

differences between the individual equations and the composite equation of 20.3%, 7.4% and 10.4%. For gauges 2 and 10, these differences are substantially greater than average uncertainty of the calculated tip time, indicating systematic physical differences between these gauges and the other gauges. The average uncertainty in the calculated tip time for gauge 6, 7.5%, is of the same order of magnitude in the difference between the individual calibration equation and the composite equation, 7.4%. It is possible that there is less systematic difference between gauge 6 and the other gauges than the difference with the composite equation would suggest.

The data from September and July 2000 indicates that the individual calibration equations should be used for all 16 gauges. The composite equations are not appropriate to represent all of the gauges.

The estimates of uncertainty in the calculated tip times increase from September 1998 to July 2000. Combined with the 3.9% average change in the composite equation, this indicates increased wear on the gauges is leading to altering calibrations, and greater uncertainty in the calculated flow rates.

An estimate of the overall uncertainty in the flow rate can be made using the data in Table K.2. An assumption is that if the average absolute difference between individual equations and the composite equation is greater than the uncertainty in the calcualted tip time then the gauge is systematically different than the others. The differences between the remaining gauges and the composite equation are the result of random uncertainties only, with the composite equation being a more accurate estimate of the true calibration equation. For September 1998, the average absolute difference for these gauges is 1.8%, and for July 2000, is 2.7%. This compares to the uncertainty in measuring the calculated tip time of 3.1% and 4.5%. The estimates of the uncertainty are therefore that a single flow measurement may therefore be within 3.1% for September 1998 and 4.5% in July 2000, and a well average calculated flow rate may be within 2% in September 1998 to 3% for July 2000

K.5 CONCLUSIONS

Based upon the discussion above, a composite equation derived from the data for all 16 gauges is not appropriate for the calculation of the flow rate from individual gauges. There are systematic physical differences between the mounting and internal calibration settings of the individual gauges which make the use of individual calibration equations derived from a limited number of calibration points more accurate than a composite equation derived from more calibration points from all gauges.

The flow rate is calculated using the following algorithm:

1. The clock time of each single tip is recorded to 0.125 seconds.
2. Five tip times, A,B,C,D,E are examined.
3. The intervals between A-C, B-D, and C-E tips are determined.
4. The calculated tip time is the average of these three intervals divided by two.
5. For calculated tip times of more than 36 seconds, the flow rate is 4.73 mls/calculated tip time.
6. For calculated tip times of less that 36 seconds, the flow rate is determined from:
   $$\text{Flow Rate (mls/sec)} = \text{Constant (Calculated tip time in seconds)}^{\text{Power}}$$
7. The constant and power are determined from the individual calibration equations for each gauge.
8. The equations from the September 1998 calibration is used for September 1998 to April 2000.

9. The equation from the July 2000 calibration is used for April 2000 onwards

Using this algorithm, the uncertainty in the flow rate is estimated to be approximately 3.1% using the September 1998 data, and 4.5% using the July 2000 data.

K.6 REFERENCES

Barfield, B.J. and M.C. Hirschi, 1986, Tipping bucket flow measurements on erosion plots, Transactions of the ASAE, American society of Agricultural Engineers, , 29, 6, 1600-1604.

Campbell Scientific, 1998, TE525 Tipping bucket rain guage, user manual

Marsalek, J. , 1981, Calibration of the tipping-bucket raingage, Journal of Hydrology, 53, 343-354.

Simic, M. and Maksimovic, C., 1994, Effect of siphon control on the dynamic characteristics of a tipping bucket raingauge, Hydrological Sciences, 39, 1, 35-46.

K.7 INSTRUCTIONS FOR OUTFLOW MONITORING MAINTENANCE AND CALIBRATION

Cleaning Outflow Pipes

Each outflow pipe has a 3/8" O.D., ¼" I.D. HDPE tube which terminates in a filter screen at the top of the outflow pipe immediately below the lysimeter base. These can be used to flush out the outflow pipes. The pipes should be flushed out each spring.

- Ask permission to borrow two peristaltic pumps from the Environment trailer.
- Connect silicone peristalitic pump tubing from a pail of water to the ¼" O.D. flushing tubing from the first outflow pipe to be flushed.
- Place a spring clamp on this tubing just below the connection to the flushing tubing.
- Insert this silicone tubing in a peristaltic pump
- Remove the outflow piping from the top of the flow gauge.
- Connect a tube from the outflow pipe back to the pail of water.
- Turn on the peristaltic pump to pump water from the pail, up the flush tubing, then back to the pail.
- Turn the peristaltic pump on high. It may take several minutes for the outflow to start.
- Once the outflow has started, allow it to continue for 5 minutes, then turn off the peristaltic pump and close the clamp to prevent the flushing tubing from losing its water.
- Allow the water to drain from the outflow pipe. Experience has shown that flocculated precipitate will accumulate in the tail end of the water draining out.
- Repeat the flushing and draining cycle several times until no more precipitate is noted from the outflow.
- Discard the water from the pail.
- Connect to another flushing tube, and repeat.
- Use two peristaltic pumps to flush two outflow pipes simultaneously.
- Flushing all 16 outflow pipes will likely take 2 days.

Outflow Gauges

The outflow gauges suffer from several problems:

- Unbalanced gauges.
- Dissolution of the upper funnel
- Corrosion of the wires to the magnetic switch
- Dissolution of the supporting frame for the calibration screws
- Dissolution of the holding screws and nuts which hold the tipping bucket in place.
- Disintegration of the paint covering of the outer case, and dissolution of the case.

Balancing Outflow Gauges

The gauges should always be checked for balance to make sure they are measuring equal volumes of water from each side of the bucket.

- Use the "Flow Calculator _____.xls" spreadsheets to process the data and examine the flow
- rate.
- If any gauges show different tip times for each side, then adjust their positions.
- Record the current position by noting where the holding bracket meets the measurement tape on the holding frame.
- Loosen the holding bolt, and slide the gauge left of right. Try 2 mm to start.
- Record the new setting
- Reprocess the flow data and examine the effect.
- Continue until the gauge is balanced.
- For minor adjustments, the gold funnel can be "skewed" by tilting it from level. This will cause minor changes in the balance of the funnel.
- If the gauge has reached the end of the possible movement left or right on the mounting board, then the calibration screws may have been moved out of position. See the dismantling instructions below.

Cleaning Ouflow Gauges.

The tipping bucket gauges will require periodic cleaning to remove precipitate from the internal mechanisms, and to ensure proper operation.

- Remove the outflow tubing from the top of the gauge. Use tubing to divert the outflow to a bucket.
- Note the gauge number, date and time that maintenance started in the log book.
- Remove the gold funnel. Flush with fresh water to remove any precipitate.
- Check the condition of the funnel.
- The outflow tubing should be not be resting on bare aluminum. The aluminum should either be covered in silicone sealant, or plastic. This will prevent dissolution of the aluminum by the outflow waters.
- Examine inside the gauge.

- Remove the wires to the switch. Use sandpaper to clean the contact to remove corrosion products. Use a sharp knife or the edge of a screwdriver blade to clean the contacts on the tippng bucket mechanism.
- Reach inside the gauge to the base, under the tipping mechanism, and check the calibration screws. These may loosen.
- If the calibration screws are loose remove the internal mechanism by removing the two outer screw and nuts from the base of the gauge casing.

Rebuilding the mechanism.

If the calibration screws have loosened, then the internal tipping bucket mechanism will need to be rebuilt:

- Remove the wiring from the mechanism
- Remove the outer bolts/nuts from the bottom of the casing to release the mechanism.
- Measure and record the height of the calibration screw from the base plate using a vernier caliper. Measure to two decimal places in mm. Eg; 14.55 mm
- Check where the calbration screw hits the tipping bucket. There should be a distinct mark whre the calibration screw should hit.
- If the calibration screw is shifted off this mark then loosen the holding nuts slightly and slide the calibration screw sideways until it hits the proper mark. Re-tighten the nuts. Check the screw height.
- If the nuts or washers holding the calibration screw are corroded, replace with STAINLESS STEEL replacements.
- Coat all internal parts with silicone sealant. Make sure the coating does not interfere with the level of the where the base of the mechanism meets the casing.
- If the holding screws or nuts are corroded, replace with STAINLESS STEEL.
- Replace the mechanism back in the gauge, tighten the holding screws.
- Connect the wiring.
- Rebalance the gauge.
- If the calibration screws had shifted significantly, re-calibrate the gauge.

Gauge Calibration

Should be done each year in spring. Then, clean, readjust , rebalance and maintain the gauges and repeat the calibration procedure.

- There is a white bucket with hose connections in the Environement trailer.
- Two of the hose connections are a refill line, and an overflow.
- Use a perstaltic pump to pump water in the refill, and direct the overflow back to the source bucket.
- The third hose, has a screw valve attached. This is used to create a constant flow.
- Place the outflow hose in the gold funnel of the first gauge. Place the hose so the discharge is perpendicular to the tipping bucket mechanism. At higher flow rates, discharge on the sides of the funnels parallel to the bucket mechanism will cause unbalanced readings.
- Start outflow from the third hose.
- Start with 10 to 20 mls/minute.
- After the flow has stabilized, prepare to measure the flow rate.

- Wait for the tipping bucket mechnism to tip. Immediatelly place a collection beaker under the gauge, and note the time to the second from the datalogger clock.
- Wait until 150 to 300 mls of sample have collected in the beaker. Remove the beaker exactly on a tip, and record the time to the second.
- Record the volume collected
- Repeat with increasing flow rates up to 400 mls/min. Try 10,20,50,100, 150 etc mls/min
- Process the data by locating the tip information for each collection period.
- Determine the tip time for each gauge by taking the time for two tips to occur, and dividing by two. If the gauge is not exactly balance, then the tip time for each side will be different. However, the tip time for two tips should be the same regardless of which side it started from. Use the two tip time divided by two.
- Plot the flow rate in mls/minute against the tip time. Fit a power law relationship using excel.

Calibration Equation of the Form:
Flow Rate (mls/second) = Constant * (Calculated Tip Time)^ Power

Where calculated tip time is half the time of two tips of the tipping bucket mechanism.

Gauge	September 1998 Flow Rate vs Tip Time With fixed point			September 1998 Flow Rate vs Tip Time Without fixed point			July 2000 Flow Rate vs Tip Time With fixed point			July 2000 Flow Rate vs Tip Time Without fixed point		
	Constant	Power	r2	Constant	Power	r2	Constant	Power	r2	Constant	Power	r2
1	7.1259	-1.1139	0.9994	7.1217	-1.1134	0.9990	7.3525	-1.1313	0.9994	7.4150	-1.1458	0.9993
2	7.2556	-1.1308	0.9992	7.3532	-1.1512	0.9990	7.9738	-1.2190	0.9987	7.8126	-1.1015	0.9990
3	7.2394	-1.1287	0.9987	7.3882	-1.1516	0.9977	8.0453	-1.1384	0.9978	7.9928	-1.1314	0.9970
4	6.7510	-1.1155	0.9988	6.9274	-1.1432	0.9988	7.7553	-1.1421	0.9951	7.7794	-1.1464	0.9931
5	7.7690	-1.1484	0.9990	7.8817	-1.1630	0.9986	7.2931	-1.1365	0.9990	7.4671	-1.1705	0.9994
6	7.0859	-1.1237	0.9993	7.1580	-1.1381	0.9991	6.5710	-1.1066	0.9983	6.7590	-1.1101	0.9219
7	7.2316	-1.1409	0.9987	7.3937	-1.1628	0.9991	7.4887	-1.1334	0.9989	7.5313	-1.1404	0.9983
8	7.3468	-1.1437	0.9985	7.5421	-1.1770	0.9988	7.3458	-1.1115	0.9989	7.3077	-1.1055	0.9987
9	7.6722	-1.1526	0.9990	7.9047	-1.1809	0.9994	7.8813	-1.1479	0.9997	7.9345	-1.1586	0.9995
10	7.2007	-1.1378	0.9988	7.3493	-1.1643	0.9992	8.5034	-1.1361	0.9985	8.2842	-1.1016	0.9992
11	7.4534	-1.1309	0.9988	7.4534	-1.1309	0.9988	6.9655	-1.1120	0.9998	7.0043	-1.1190	0.9997
12	7.2274	-1.1079	0.9993	7.1456	-1.0949	0.9992	7.4955	-1.1315	0.9996	7.5232	-1.1364	0.9994
13	7.5007	-1.1345	0.9988	7.5748	-1.1433	0.9980	7.9809	-1.1518	0.9994	8.0327	-1.1617	0.9991
14	7.2707	-1.1133	0.9993	7.2367	-1.1070	0.9990	6.8474	-1.1124	0.9980	6.8869	-1.1219	0.9971
15	7.4117	-1.1355	0.9995	7.5021	-1.1490	0.9995	7.8601	-1.1483	0.9997	7.9381	-1.1611	0.9997
16	6.8627	-1.1333	0.9976	6.8627	-1.1333	0.9976	7.8338	-1.1513	0.9982	7.9287	-1.1668	0.9973
Average	7.2753	-1.1307		7.3622	-1.1440		7.5746	-1.1381		7.5998	-1.1362	
Std Dev	0.2611	0.0130		0.2912	0.0242		0.5024	0.0262		0.4427	0.0240	
Best fit to all data	7.2618	-1.1296	0.9983	7.3451	-1.1426	0.9973	7.5457	-1.1296	0.997	7.5411	-1.1288	0.9951

Table K.1: Summary of calibration equations

Gauge	Maximum Flow Rate Observed				Percent difference between flow rate calculated from individual calibration equations and flow rate calculated using calibration equation derived from all data Within flow rate ranges observed. All equations using fixed point.								Calculated Tip Times Measured during Calibrations	Calculated Tip Times Measured during Calibrations
					September 1998 Data				July 2000 Data				Std Dev as percent September 1998 Average of All Runs	Std Dev as percent July 2000 Average of All Runs
	1999 (mls/sec)	2000 (mls/sec)	1999 (L/day)	2000 (L/day)	Max Difference	Min Difference	Average Difference	Average Absolute Difference	Max Difference	Min Difference	Average Difference	Average Absolute Difference		
1	3.36	0.29	25	290	3.83	-0.80	2.49	2.52	-3.03	-3.15	-3.10	3.10	3.57	2.95
2	1.16	0.41	35	100	-0.28	-0.52	-0.44	0.44	-15.86	-23.41	-20.34	20.34	2.03	3.63
3	0.93	0.21	18	80	0.02	-0.14	-0.04	0.05	3.75	3.30	3.51	3.51	3.36	7.17
4	2.89	0.41	35	250	-2.19	-5.88	-3.30	3.30	-0.43	-1.74	-1.20	1.20	3.03	3.96
5	1.16	0.19	16	100	3.80	-0.02	1.29	1.29	-5.45	-5.72	-5.59	5.59	2.34	2.68
6	8.10	7.23	625	700	-0.33	-2.59	-0.88	0.88	-5.40	-21.63	-7.41	7.41	2.37	7.51
7	1.39	0.69	60	120	-2.07	-4.39	-3.61	3.61	-1.53	-2.10	-1.89	1.89	3.95	6.10
8	3.01	0.46	40	260	0.05	-3.84	-2.71	2.71	3.91	1.73	3.02	3.02	1.77	3.76
9	0.69	0.21	18	60	0.72	-2.74	-1.44	1.52	-1.25	-2.21	-1.77	1.77	1.94	3.36
10	2.31	0.46	40	200	-1.68	-3.73	-3.10	3.10	10.95	10.09	10.43	10.43	2.43	3.83
11	1.62	0.64	55	140	2.46	2.16	2.26	2.26	-1.65	-4.09	-2.60	2.60	7.26	6.71
12	0.61	0.41	35	53	7.61	4.39	6.35	6.35	-1.15	-1.34	-1.26	1.26	3.72	3.99
13	2.89	0.69	60	250	2.85	1.48	1.89	1.89	1.00	-2.36	-1.10	1.25	5.21	3.74
14	0.87	0.35	30	75	6.17	3.25	5.10	5.10	-3.46	-4.97	-4.10	4.10	2.97	4.85
15	0.87	0.29	25	75	0.93	-0.08	0.29	0.30	-1.23	-2.62	-2.01	2.01	2.42	3.27
16	1.97	0.69	60	170	-5.90	-6.75	-6.48	6.48	-0.71	-3.98	-2.76	2.76	1.57	4.29
Average	2.11				1.00	-1.26	-0.15	2.61	-1.35	-4.01	-2.39	4.51	3.12	4.49
Std. Dev.	1.84137				3.38	3.21	3.35	2.00	5.56	8.17	6.30	4.90	1.46	1.53

Table K. 2: Comparison of Individual Gauge Calibration Equations with a Single Calibration Equation derived from all data.

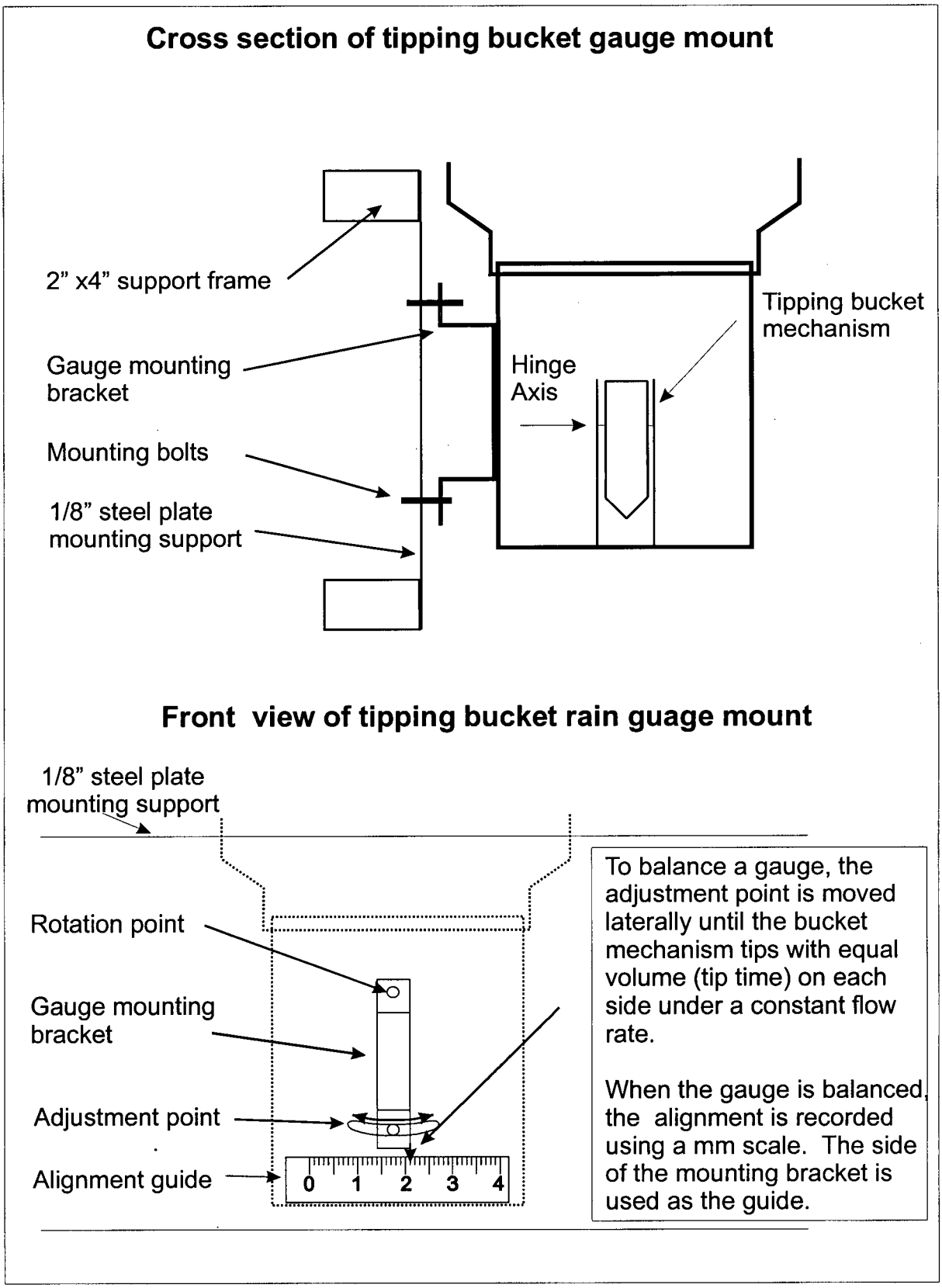

Figure K.1: Details of flow gauge installation

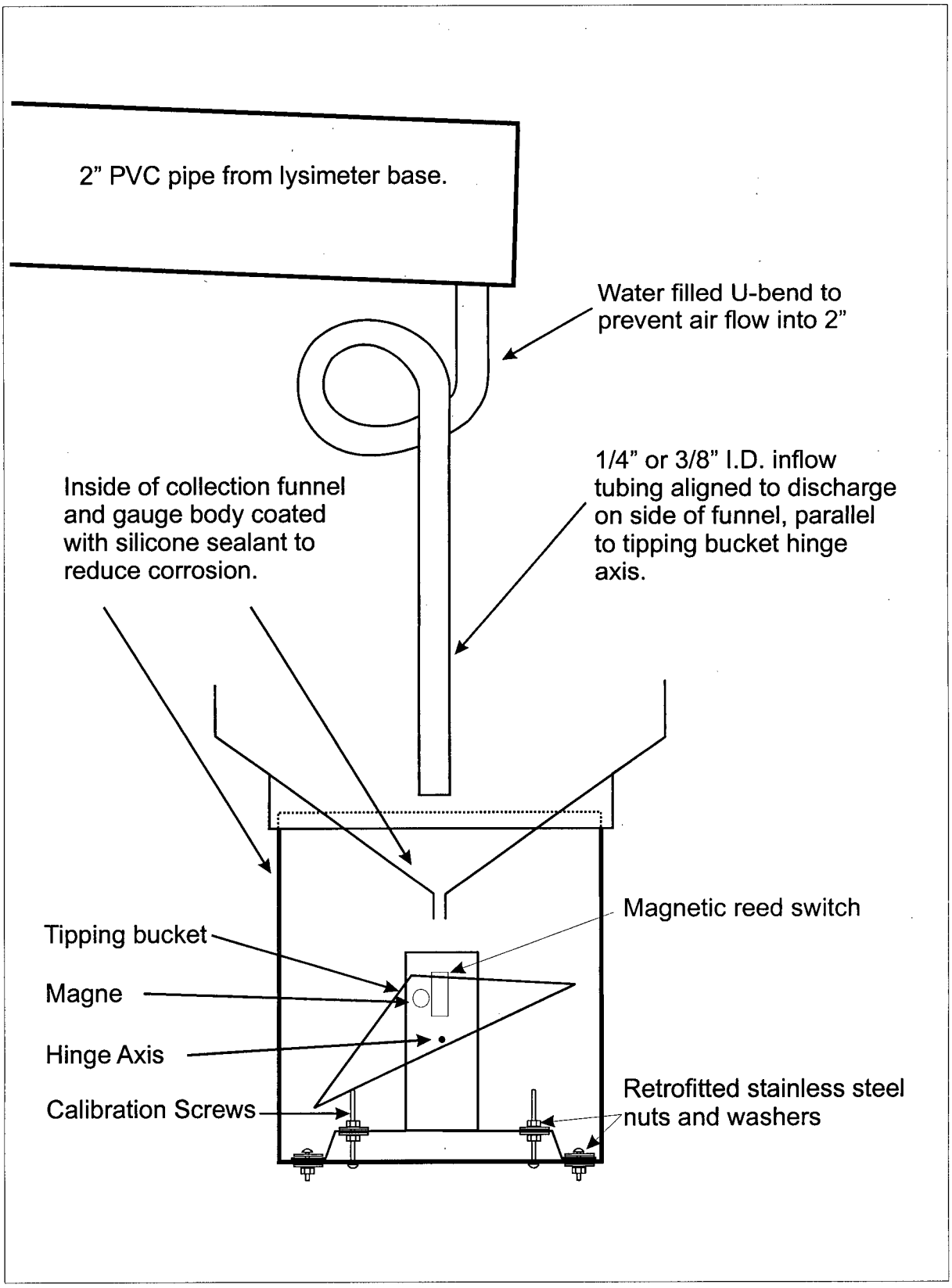

Figure K.2: Front view of tipping bucket rain gauge

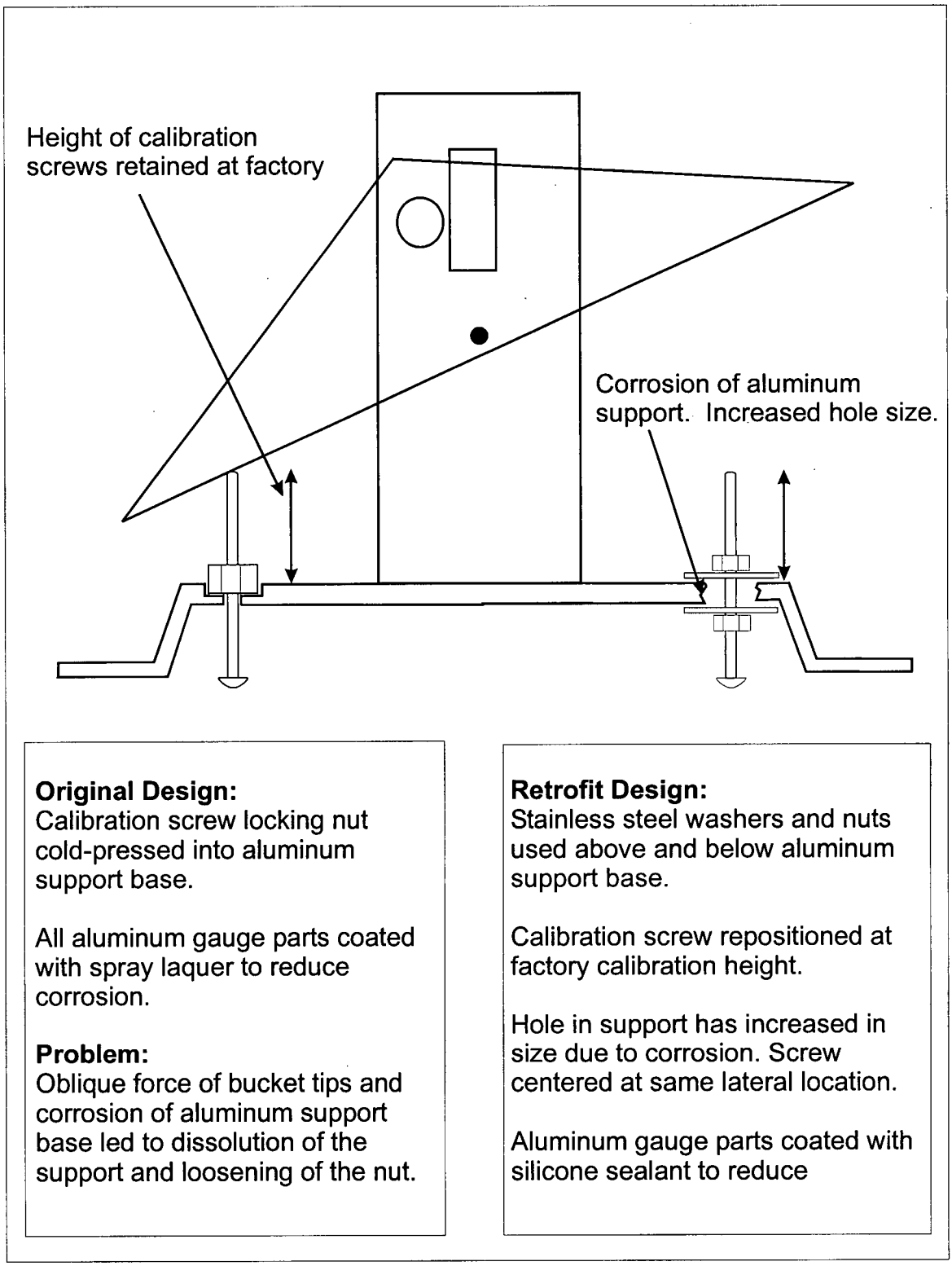

Figure K.3: Details of tipping bucket mechanism design changes

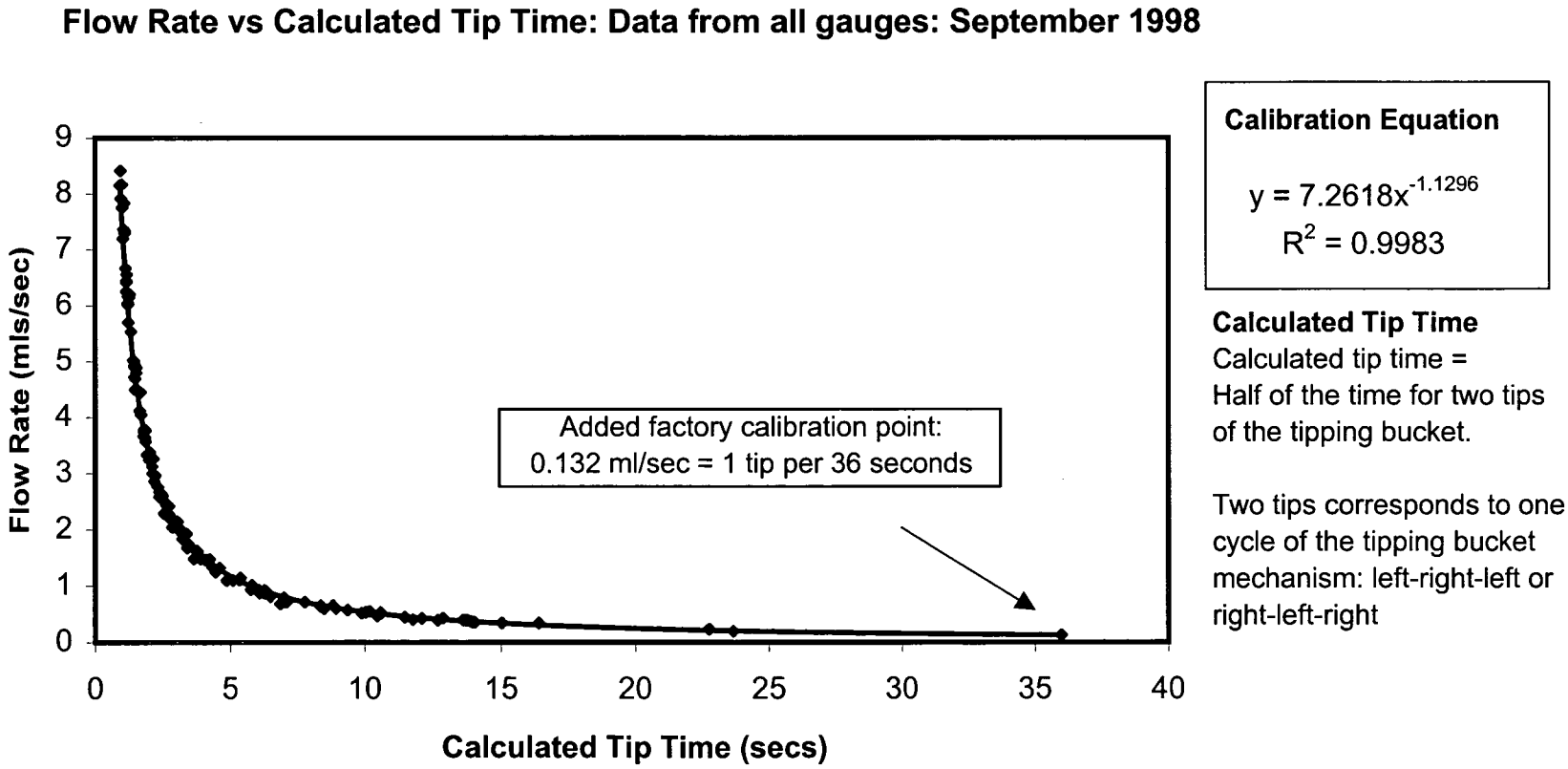

Figure K.4: September 1998 calibration summary

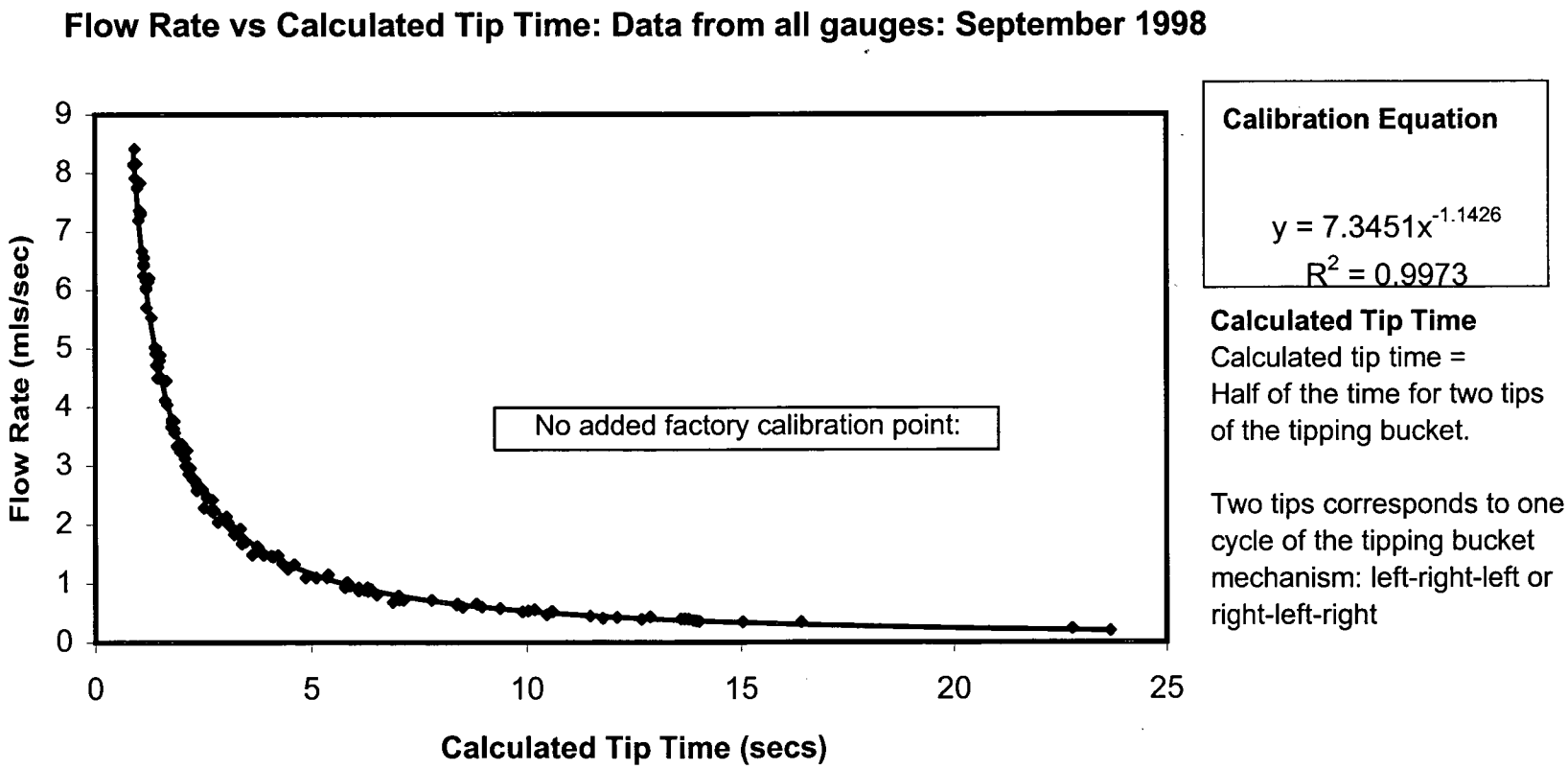

Figure K.4B: September 1998 calibration summary

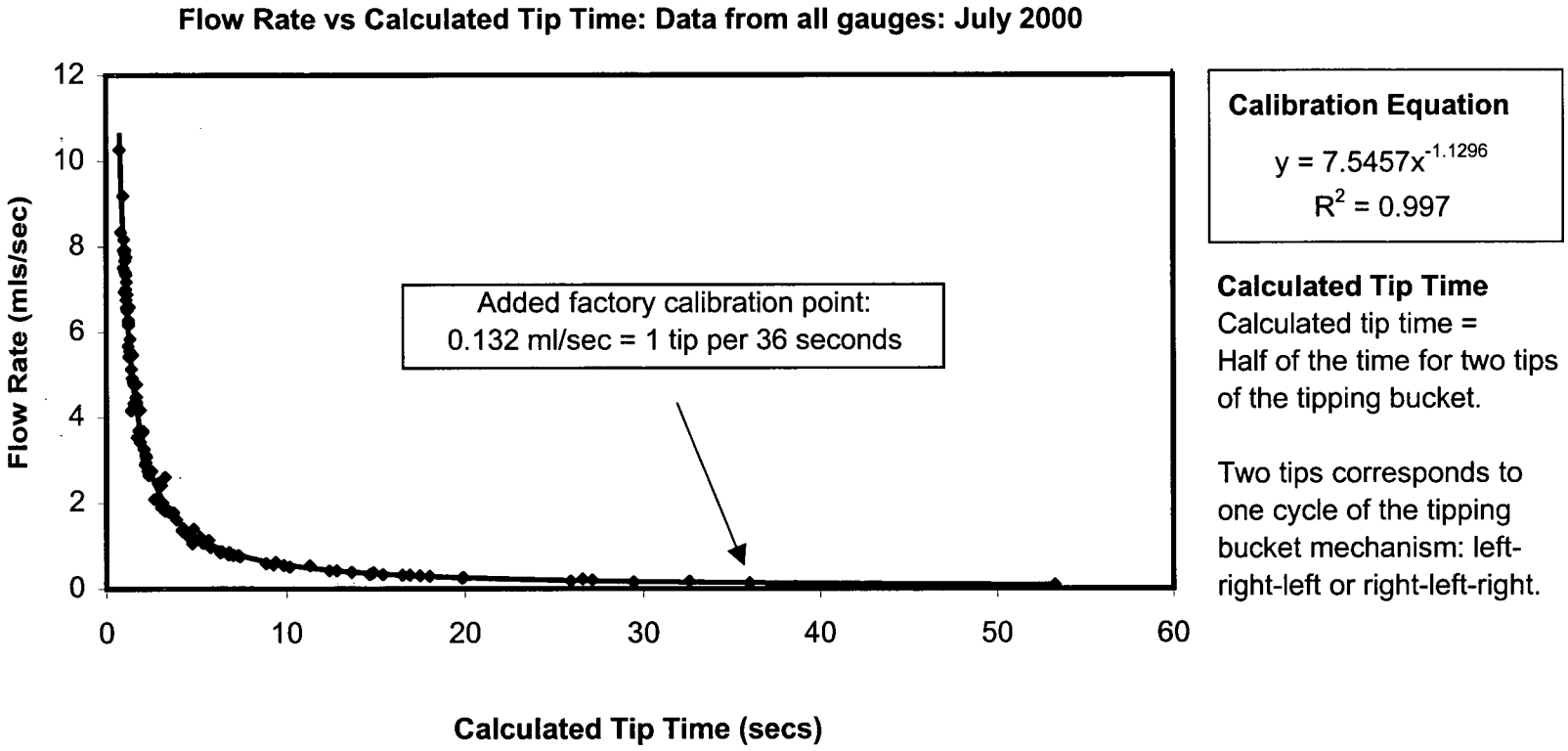

Figure K.5: July 2000 calibration summary

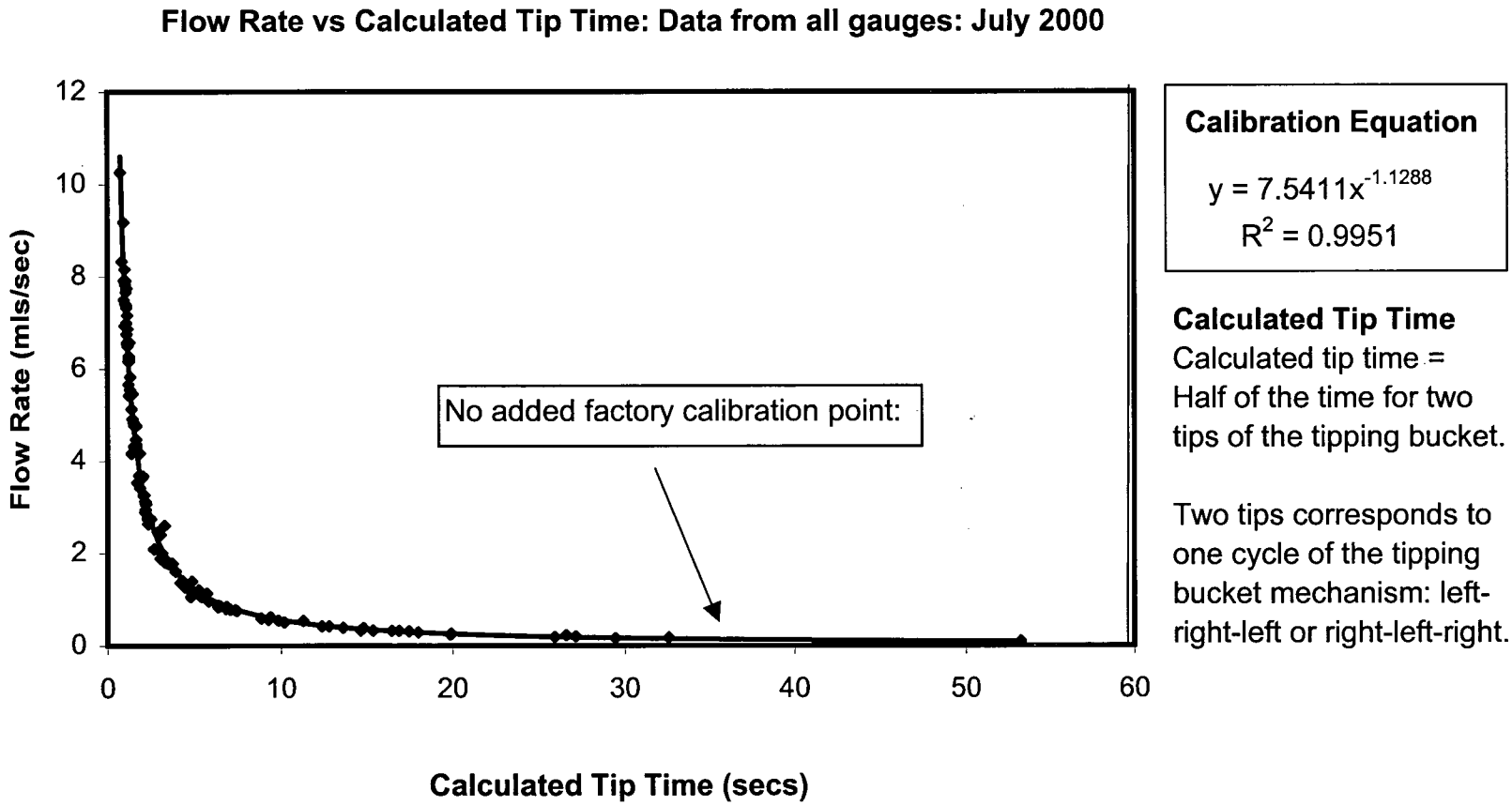

Figure K.6: July 2000 calibration summary

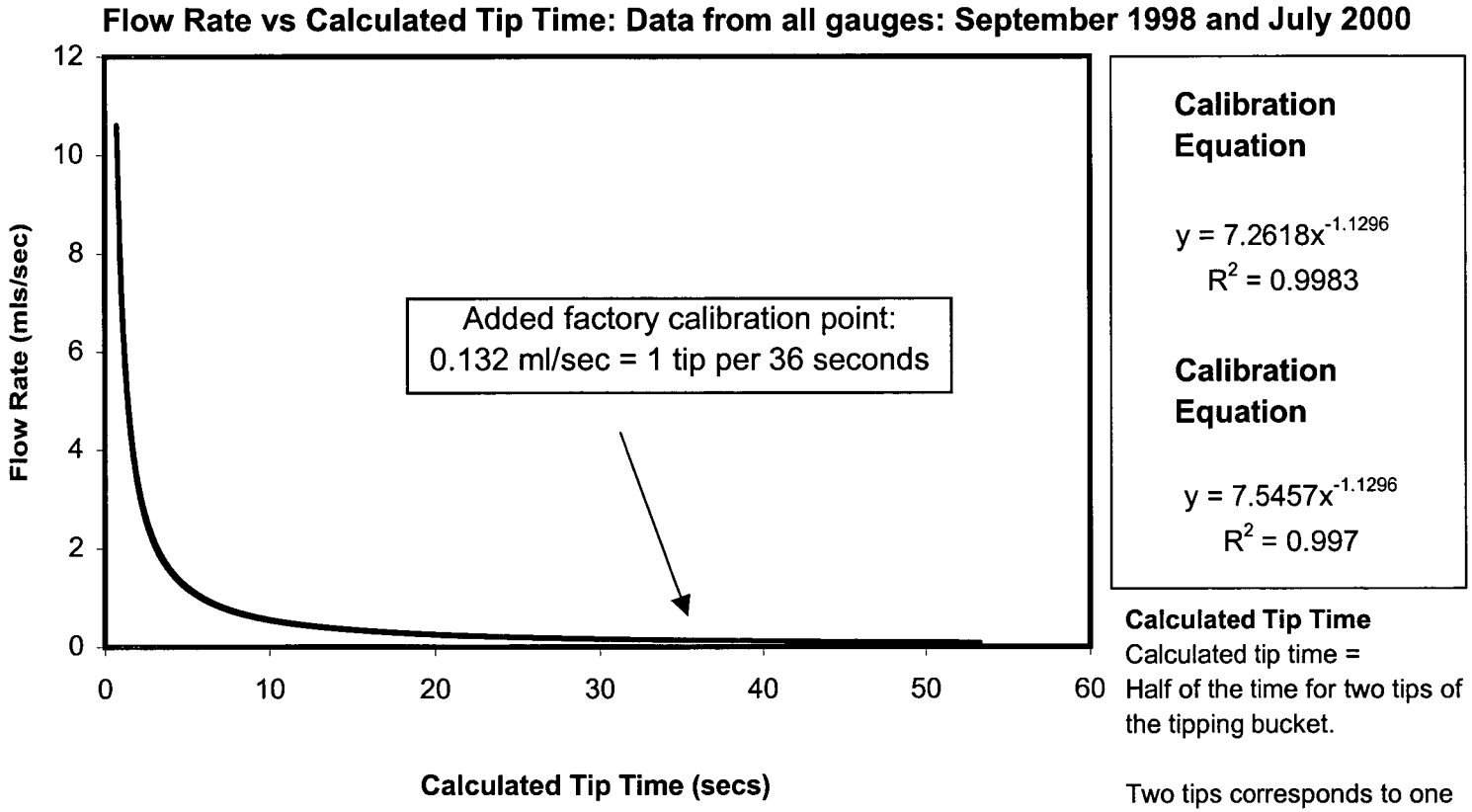

Calculated Tip Time
Calculated tip time = Half of the time for two tips of the tipping bucket.

Two tips corresponds to one cycle of the tipping bucket mechanism: left-right-left or right-left-right.

Figure K.7: September 1998 and July 2000 calibration comparison

APPENDIX L: MEASUREMENT OF DISSOLVED CHLORIDE IN WATER SAMPLES FROM THE CONSTRUCTED PILE EXPERIMENT

L.1 INTRODUCTION:

The common methods available for the analysis of chloride ion in water are gravimetric methods, titrimetric methods, selective ion electrodes, ion chromatography and spectrophotometric methods. Summaries of the available methods are found in ASAE (1982), ASTM D512-89 (1989), Orion Research Incorporated (1990) and Standard Methods (1995).

Each method was reviewed to determine the most appropriate for the determination of chloride ion in water samples from the constructed pile experiment and laboratory experiment. The requirements were: low cost per sample for reagents and expendable items; low capital cost for necessary equipment, short time of analysis per sample thus allowing high daily throughput; minimal interference effects from other chemical species expected to be found in the samples; and the ability to analyse the expected background chloride concentrations (5 to 40 mg/L).

Titration and gravimetric methods were considered to be too slow to allow efficient processing of large numbers of samples. Ion chromatography was eliminated due to slow sample processing, machine accessibility, high cost per sample, high capital cost for a new chromatography column and poor detection limit. The concentrations of sulphate found in the outflows (5,000 to 40,000 mg/L) would necessitate large dilutions of all the samples to reduce the sulphate concentration to within the range acceptable to the ion chromatograph. Including the necessary, the detection limit for chloride would be of the order of 25 to 50 mg/L, which exceeded the expected background chloride concentration.

The ion selective electrode methods were rejected on the basis of the potential for interference effects (Standard Methods, 1995, Orion Research Incorporated, 1990). A tracer test in waters of similar chemistry was conducted by the University of Saskatchewan at the Key Lake Mine (S.L. Barbour, pers. comm., 1997). An ion selective electrode was used for initial sample analysis for bromide, but the researchers were unable in to reliably compensate for interference effects and found it necessary to use ion chromatography for the final results.

Based upon the criteria outlined above, it was determined that the mercuric thiocyanate spectrophotometric method for chloride, presented in several variations in Standard Methods (1995), and Hach (1997), was the most suited to the requirements. This method allows for rapid sample analysis, a minimum of sample preparation, reasonable cost per sample, reasonable cost for necessary equipment, portability to the field site, and adaptability of the method to overcome site specific difficulties.

L.2 METHOD DEVELOPMENT

L.2.1 Method Introduction

The mercuric thiocyanate method is based upon the creation of a coloured ion complex and the measurement of the absorbance of the sample solution using a spectrophotometer to determine the concentration of this ion complex. The colour reagent used contains mercuric thiocyanate, ferric nitrate, nitric acid and a nonionic surfactant, polyoxyethylene 23 lauryl ether (Brij 35) (Standard Methods, 1995). The presence of chloride ion in the sample creates soluble mercuric thiocyanate. The free thiocyanate ion then combines to produce red-coloured ferric thiocyanate. The colour intensity of the final solution is proportional to the amount ferric thiocyanate and hence, of chloride added. The reaction of chloride with the colour reagent is temperature-dependant, time-dependant, and

light sensitive. All measurements of both standards and samples must therefore be conducted under identical conditions to minimize these dependencies.

The lab procedure used was modified from the methods outlined in Standard Methods (1995) and Hach (1997). The Hach (1997) method is an all manual procedure whereas Standard Methods (1995) presents the analysis as performed in a sealed, automated system where samples and reagents are delivered by calibrated peristaltic pump. The ratio of colour reagent to sample solution varies from 1:12.5 in Hach (1997) to 3:1 in Standard Methods (1995). Increasing the ratio of colour reagent volume to the volume of sample containing chloride increases both the detection limit and the colour saturation limit to shift the entire method detection range upwards. The reagent volume to sample volume ratio of 3:1 from Standard Methods (1995) was modified to 30:1 to provide a working range from 0 to 400 mg/L using manual pipetting of the reagent and sample into a disposable cuvette.

L.3 METHOD DETAILS.

The laboratory method used to analyse samples is outlined below. For more detail on reagent preparation, see Standard Methods (1995).

L.3.1 Stock solutions:

Mercury stock solution:

- Fisher Scientific Ltd. Catalog #LC16720-1 0.42% Mercuric Thiocyanate in methanol.

Ferric iron stock solution:

- 202 grams ferric nitrate and 21 mls nitric acid in 1 litre filtered solution.

Chloride distilled water standard solutions:

- Solutions of NaCl prepared to 10,20,30,40,50,70,100,200,300, 400, 500, 700, 1000, 2000, 3000, 4000 mg/L chloride in distilled water.

L.3.2 Chloride colour reagent:

- 150 mls mercury stock solution
- 150 mls ferric iron stock solution
- 0.5 mls polyoxyethylene 23 lauryl ether (BRIJ 35 – Fisher Scientific Catalog #BP345-500)
- made up to 1 litre of solution

L.3.3 Working colour reagent solution

- 125 mls of colour reagent was stored in a wide mouthed amber glass bottle for daily use. This was refilled at the start of each measurement session from the 1 L stock bottle.

L.3.4 Individual Sample Measurement Method:

- Hach DR/2010 spectrophotometer adjusted to measure absorbance using continuous lamp operation.
- Spectrophotometer tuned to 455 nm and warmed up for 20 minutes.
- Spectrophotometer then zeroed using a 1.5 ml disposable cuvette (Fisher Scientific Catalog #14-385-942) containing 1 ml of colour reagent.
- 1 ml of colour reagent pipetted into a 1.5 ml disposable cuvette.
- Cuvette placed in spectrophotometer and the absorbence recorded as reagent absorbence, (RA).
- Cuvette removed from spectrophotometer and returned to rack.

- 33.3 ul of sample water pipetted into cuvette at a known time.
- Parafilm streched over the top of the cuvette and once sealed, the cuvette is gently rocked several times to mix the sample and reagent.
- Sample is returned to cuvette rack.
- After exactly 2 minutes, the cuvette is placed back in the spectrophotometer and the absorbence recorded as sample absorbence (SA)
- The absorbance is calculated as the sample absorbance minus the reagent absorbance (SA-RA)

The actual chloride concentration in the sample is determined by preparing a calibration curve from the analysis of standard solutions.

L.4 DETERMINATION OF APPROPRIATE CALIBRATION STANDARDS.

A series of experiments were conducted to evaluate the method precision, accuracy, and to determine the nature of any background interference effects present in the samples from Cluff Lake. The repeatability of the measurement of a calibration curve was assessed by comparing the calibration curved derived for several sets of distilled water standards, and is presented in Figure L.1. The portion of the calibration curve for 0 to 70 mg/L is shown. (UBC method development c)

L.4.1 Spike Recovery using distilled water standards

The accuracy of spiking a solution with a known amount of chloride was determined by spiking a 20 mg/L distilled water standard using other distilled water standards to make sample solutions with total concentrations of 20 to 110 mg/L. Distilled water standards were used as calibration standards, and two best fit non-linear calibration curves were fitted to the calibration standards data for 0 to 50 mg/L and 50 to 400 mg/L. The concentration of each sample was calculated based upon the calibration curves, and was compared to the theoretical amount of chloride spiked to each sample. (UBC Method Development A) One measurement was taken of each calibration standard, and three measurements were taken of each sample. Figure L.2 presents the percent error in the calculated sample recovery against the chloride spike added. The magnitude of percent error in sample spike recovery, for an average of three sample measurements, ranges from 0.8% to 11% with an average error of 5.8%. For a single measurement of the sample, the magnitude of percent error in sample spike recovery ranges from 0.5 to 18%, with an average error of 6.0%.

L.4.2 Sample Dilution using distilled water standards

The accuracy of diluting samples using adjustable pipettors was assessed by diluting distilled water standards from the range of 100 to 400 mg/L by 1:11. Distilled water standards were used as calibration standards, and a best fit non-linear calibration curves were fitted to the calibration standards data for 0 to 50 mg/L and 50 to 400 mg/L. The accuracy of the dilutions was determined by comparing the concentrations calculated from the standards, to the known concentrations of dilutions. (UBC Method Development B)

In one set of experiments, three measurements were taken of each calibration standard and of each sample. Figure L.3 presents the percent error in the calculated sample concentrations against the known concentrations. The magnitude of the percent error for the average of three sample measurements ranges from 0.2% to 2.6% with an average of 1.1%. The magnitude of the percent error for a single measurement ranges from 0 to 3.6%, with an average of 1.25%. When only a single calibration standard measurement was used to derive

the calibration curves, the magnitude of the percent error for average of three sample measurements ranges from 0.5% to 4%, with an average of 2%. For a single measurement of the sample, the magnitude of the percent error ranges from 0.5 to 5.5, with an average of 2.2%.

In a second experiment,, one measurement was taken of each calibration standard, and three measurements of each diluted sample. Figure L.4 presents percent error in the calculated sample concentrations against the known concentrations. The magnitude of the percent error for the average of three measurements ranges from 2.2% to 6.3%, with an average of 4.5%. The magnitude of the percent error for single measurements ranges from 0 to 10.4%, with an average of 4.5%

L.4.3 Spike recovery in Cluff Lake samples

The magnitude of background interferences in the Cluff Lake samples were assessed by carrying out a series of experiments to determine spike recovery efficiences. Three outflow streams from the constructed pile experiment were chosen to be used. Bulk solution electrical conductivity was used to determine the lysimeters with the lowest (OG6) and highest (OG9, OG12) concentrations of dissolved solids. Sets of experiments were carried out for each lysimeter. In each experiment, samples of raw outflow were spiked with known amounts of chloride to raise the chloride concentration up to 393 mg/L above background. A spiked sample was prepared by taking 1 ml of raw sample and adding 100 uL of distilled water standard ranging from 0 mg/L to 4000 mg/l. UBC Method Development C. Table L.1 presents a summary of results from the three sets of experiments Figure L.5 presents the theoretical chloride concentrations against the measured absorbance for the spiked samples and the known concentrations aborbance of the distilled water standards against measured. Figure L.6 presents the percent error in spike recovery against the known spike addition for all the data using best fit equations to distilled water standards to calculate sample concentrations. Figure L.7 presents the same data from outflow lysimeter #9 only.

In the third set of experiments conducted January 13th and 14th, 1999, samples from OG6 (Sept 22, 18:37 and October 13, 12:00) and OG9 (September 22, 18:37) were spiked with chloride. Samples with total chloride greater than 90 mg/L were then diluted 1:11 and re-measured using distilled water standards as calibration standards. Figure L.8 presents the percent error in spike recovery against the known total chloride concentration for the samples from lysimeter 6, 9 and 12.

L.5 DISCUSSION

The data presented in Figure L.1 clearly show that the calibration curve for distilled water standards varies between different measurement sessions. The general slope of the calibration curve is more consistent than the intercept of the curve. Laboratory experience shows that the calibration curve varied as the colour reagent was used during a laboratory measurement session. Variations were also noted between different batches of colour reagent made from the stock solutions, and different batches of reagent placed into the daily usage bottle from the stock solution bottle. These variances may be due to temperature changes within the lab, evaporation of methanol from the reagent, exposure of the reagent to light during analysis or variations in the preparation of the reagent. An attempt was made to reduce the aging of the colour reagent by using a airtight storage system, and delivering the reagent using an airtight syringe. It was found that this method of delivery created micro-bubbles within the reagent which clung to the cuvette wall, leading to erratic measurements. Based upon laboratory experience, a calibration was expected to be valid for a time period of

approximately 2 hours. The procedure adopted was: measure a set of standards; measure 30 to 50 samples; repeat the calibration standards; measure 30 to 50 samples; repeat the calibration standards . The average values of the standards from either side of the sample measurements was used to derive the calibration curves for those samples.

The estimates of error in the spike recovery and dilution tests indicate that for a single measurement of the calibrations standards, and a single measurement of a sample, these techniques can be carried out to an average percent error of 6% and 4.5% respectively. Maximum percent errors for an single sample measurement were 18% and 10.4% respectively.

The data from spike recovery test on Cluff samples indicate that distilled water standards are not appropriate for undiluted Cluff Lake samples. The measured samples from Cluff Lake (Figure L.5) show a S-curve type shape, compared to the smooth C-curve shape of the distilled water calibration standards. The magnitudes of the average percent errors in the spike recoveries are much larger than the errors observed during spike recoveries on distilled water standards (Table L.1). The range in errors in spike recoveries for OG12 is greater than OG6, which is consistent with higher concentrations of dissolved solids in the OG12 outflow sample. The data presented in Figures L.6 and L.7 indicate systematic errors in the calculation of the spike recoveries when using distilled water standards to derive calibration equations. All of the lysimeters tested (6, 9 and 12) show a systematic change in the estimated error between 65 and 363 mg/L spike addition (see Figure L.6). Figure L.7 highlights the presence of a systematic trend in the data from lysimeter 9. These data indicate the presence of background interference in the method due in some way to the interaction of the other chemical constituents in the samples with the method reagents.

This data led to the determination that known addition calibration standards were better standards for the measurement of chloride in the Cluff Lake outflow samples. For each outflow lysimeter, a sample was selected from prior to the application of any tracer. In this sample, the background geochemistry capable of creating interference effects was assumed be present at full strength with only background concentrations of chloride (10 to 40 mg/L approx.). 1 ml aliquots of sample were spiked with 100 uL of distilled water standards to derive standards ranging from +0 mg/L to +363 mg/L chloride. The concentration (Co) of the original sample was determined using triplicate analysis using distilled water standards as calibration standards. The concentrations of the known addition standards were determined by adding the known spike addition to the measured Co value. The addition of water labeled with the tracer lithium chloride would act similar to a spike addition. It is assumed the remainder of the geochemistry of the sample will progress in a manner similar to the progression without the chloride addition. The outflow samples after the tracer was added are therefore of a similar background chemistry to the sample used for the known addition standards. The known addition of chloride is therefore similar to the addition of chloride through the tracer.

The results of dilution tests on the spiked Cluff Lake samples (Figure L.8 and Table L.1) indicate that the magnitude of the errors in the diluted Cluff Lake samples are higher than those achieved when diluting distilled water standards. These samples were spiked and then diluted, so the errors are expected to be higher than for spike addition only (Figure L.2) or for sample dilution only (Figures L.3 or L.4). The data presented in Figure L.8 shows no systematic trend in errors as was observed for the spike additions at lower concentrations (Figure L.6 and L.7). This indicates that the dilution of the Cluff Lake samples by 1:11 removes the interference effects of the background water sample chemistry. Diluted Cluff Lake samples can be measured using distilled water standards as calibration standards.

L.6 CONCLUSIONS

The data presented indicate that the analysis of samples with total concentrations of chloride less than 400 mg/L should be carried out using known addition standards. These are made by spiking aliquots of a field sample containing background chloride levels with known amounts of chloride delivered using distilled water standards. For samples with chloride concentrations greater than 400 mg/L, and less that 4400 mg/L, the concentration of total chloride in the sample can be determined by diluting the sample by 1:11 and using distilled water standards as calibration standards.

L.7 REFERENCES:

ASAE, 1982, Methods of soil analysis Part 2 Chemical and Microbiological properties, 2nd Edition, American Society of Agronomy, Soil Science Society of America, 2nd Edition.

ASTM D512-89, (1989) Standard test methods for chloride ion in water, American Society of for Testing and Materials, 1989 Annual Book of ASTM Standards.

Hach, 1997, Chloride mercuric thiocyanate method, method 8113, DR/2010 Spectrophotometer handbook, Hach Company.

Orion Research Incorporated, 1990, Model 94-17B chloride electrode and Model 96-17B combination chloride electrode instruction manual, Orion Research Incorporated, Laboratory products group.

Standard Methods, 1995, Standard Methods for the examination of water and wastewater, 19th edition, American Public Health Association, American Water Works Association, Water Environment Federation.

Experiment	Lysimeter	Number of calibration standards measurements	Number of sample measurements	Range of chloride spike added (mg/L)	Measured starting chloride concentration Co (mg/L)	Dilution
Experiment 1	6	2	1 to 3	0 to 90	15.3	none
All Data	12	2	1 ot 3	0 to 90	34.0	none
Experiment 2	6	2	1 to 2	0 to 363	17.5	none
All Data	12	2	1	0 to 363	32.2	none
Experiment 3	6	1	2 to 4	0 to 363	15.7	none
All Data	6	1	2 to 3	0 to 90	222.0	none
	9	1	2 to 3	0 to 363	23.6	none
Experiment 4	6*	1	2 to 4	90 to 393	15.7	1:11
Spike Ranges	6	1	2 to 3	90 to 393	222.0	1:11
90 to 393 mg/L	9	1	2 to 3	90 to 393	23.6	1:11

Notes:
* distilled standards were not repeated for diluted sample measurements. Standards from undiluted spike samples was used.

Experiment	Average magnitude of percent error in spike recovery based on average of 1 to 3 measurements	Maximum magnitude of percent error in spike recovery based on average of 1 to 3 measurements	Minimum magnitude of percent error in spike recovery based on average of 1 to 3 measurements	Average magnitude of percent error of spike recovery based on individual measurements	Maximum magnitude of percent error of spike recovery based on individual measurements	Minimum magnitude of percent error of spike recovery based on individual measurements
Experiment 1	2.4	4.2	0.5	4.1	9.5	0.5
All Data	5.0	14.6	1.2	8.1	18.8	0.6
Experiment 2	14.7	39.7	0.8	15.4	41.5	0.8
All Data				6.3	13.9	0.2
Experiment 3	3.0	11.3	0.0	4.0	17.6	0.0
All Data	7.1	23.6	0.3	7.4	32.1	0.3
	3.4	10.2	0.3	3.6	13.7	0.2
Experiment 4	15.8	33.3	5.8	15.7	61.9	4.4
Spike Ranges	3.7	5.3	2.3	5.4	10.3	0.7
90 to 393 mg/L	6.9	19.4	1.3	7.2	23.9	0.5

Table L.1: Summary of estimated errors for known chloride spike recoveries in Cluff Lake constructed pile experiment outflow samples

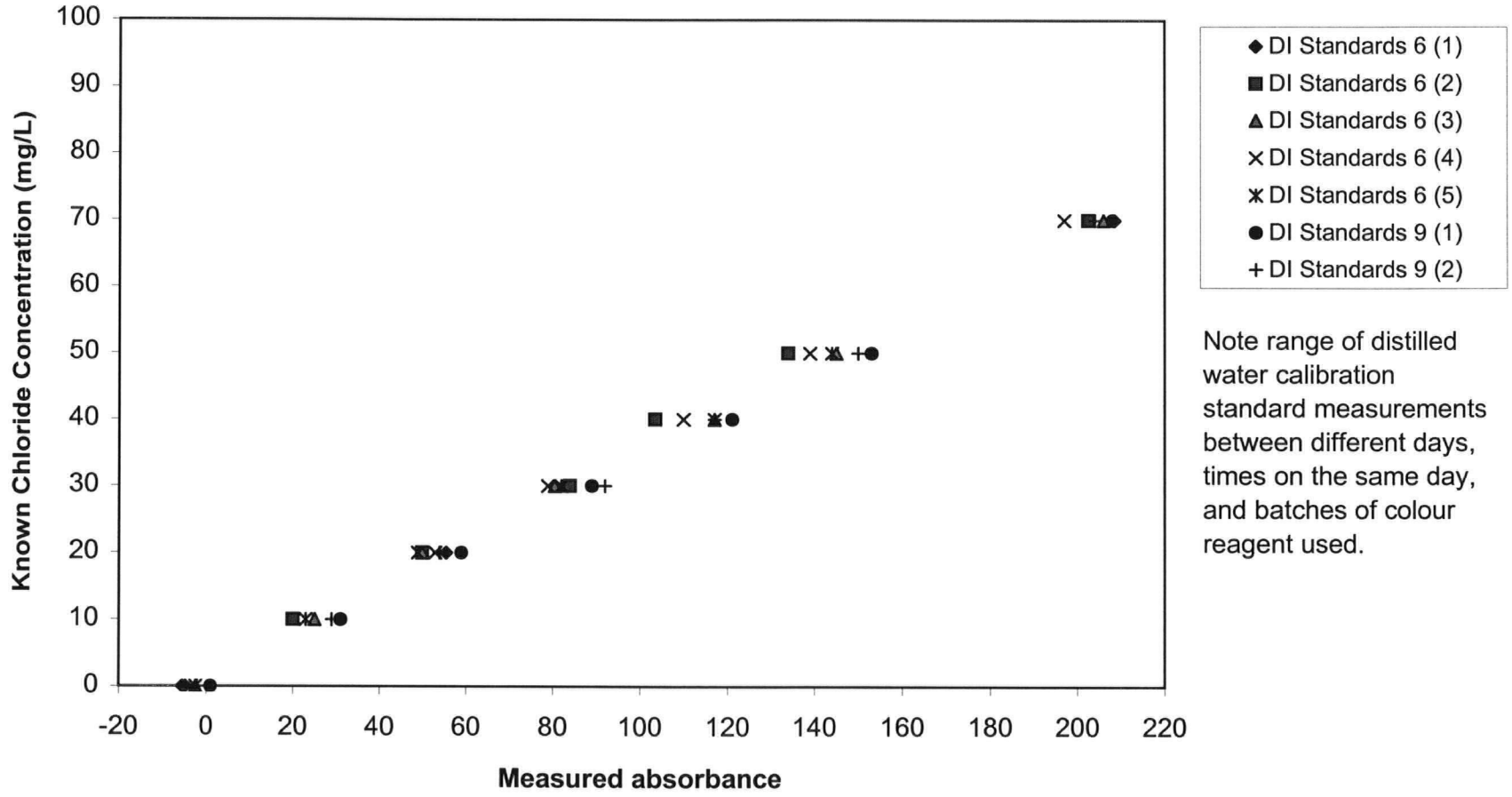

Figure L.1: Comparison of distilled water standards measured as calibration standards on different days.

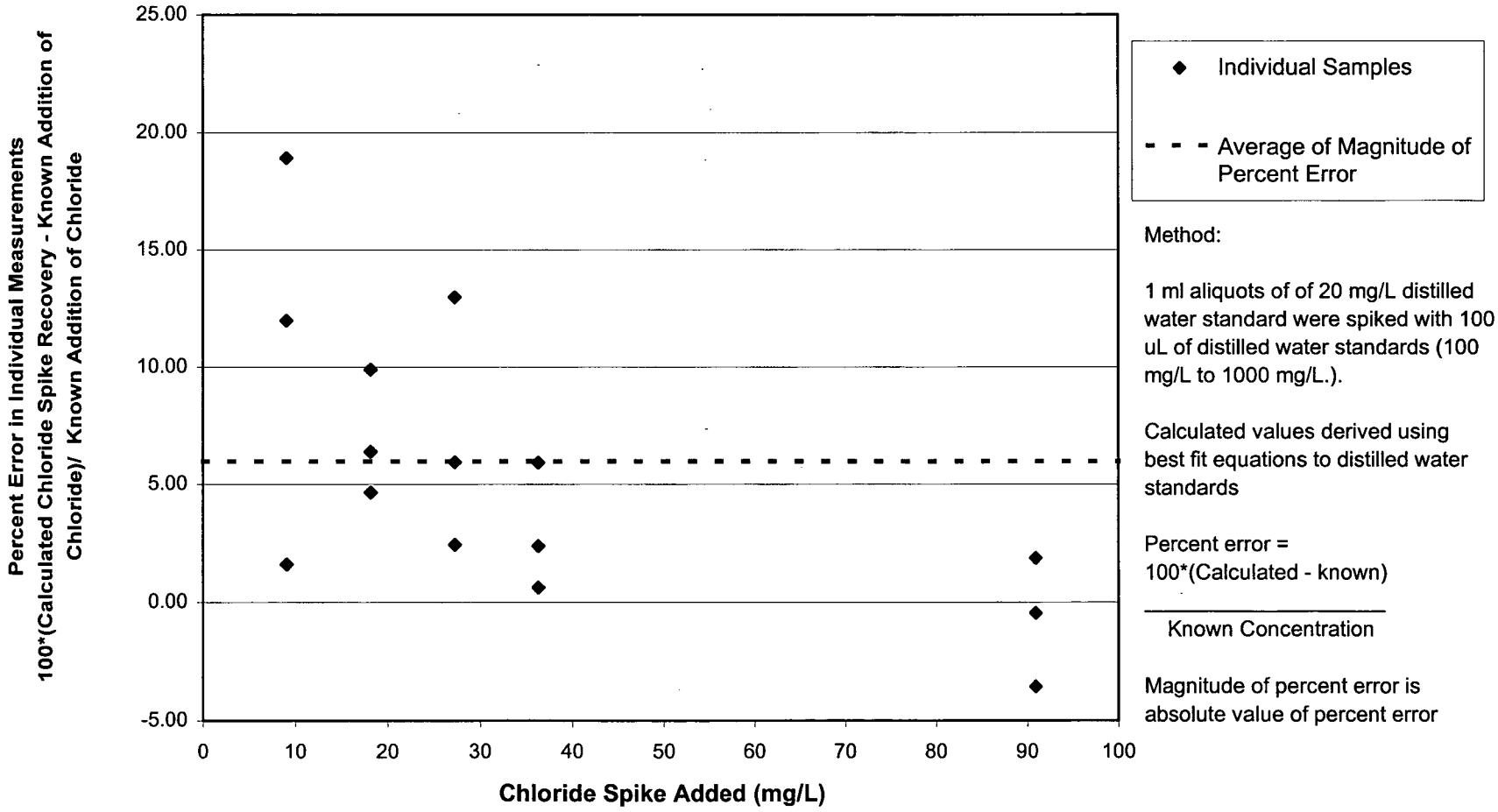

Figure L.2: Accuracy of Spike Recovey Distilled Water Standards

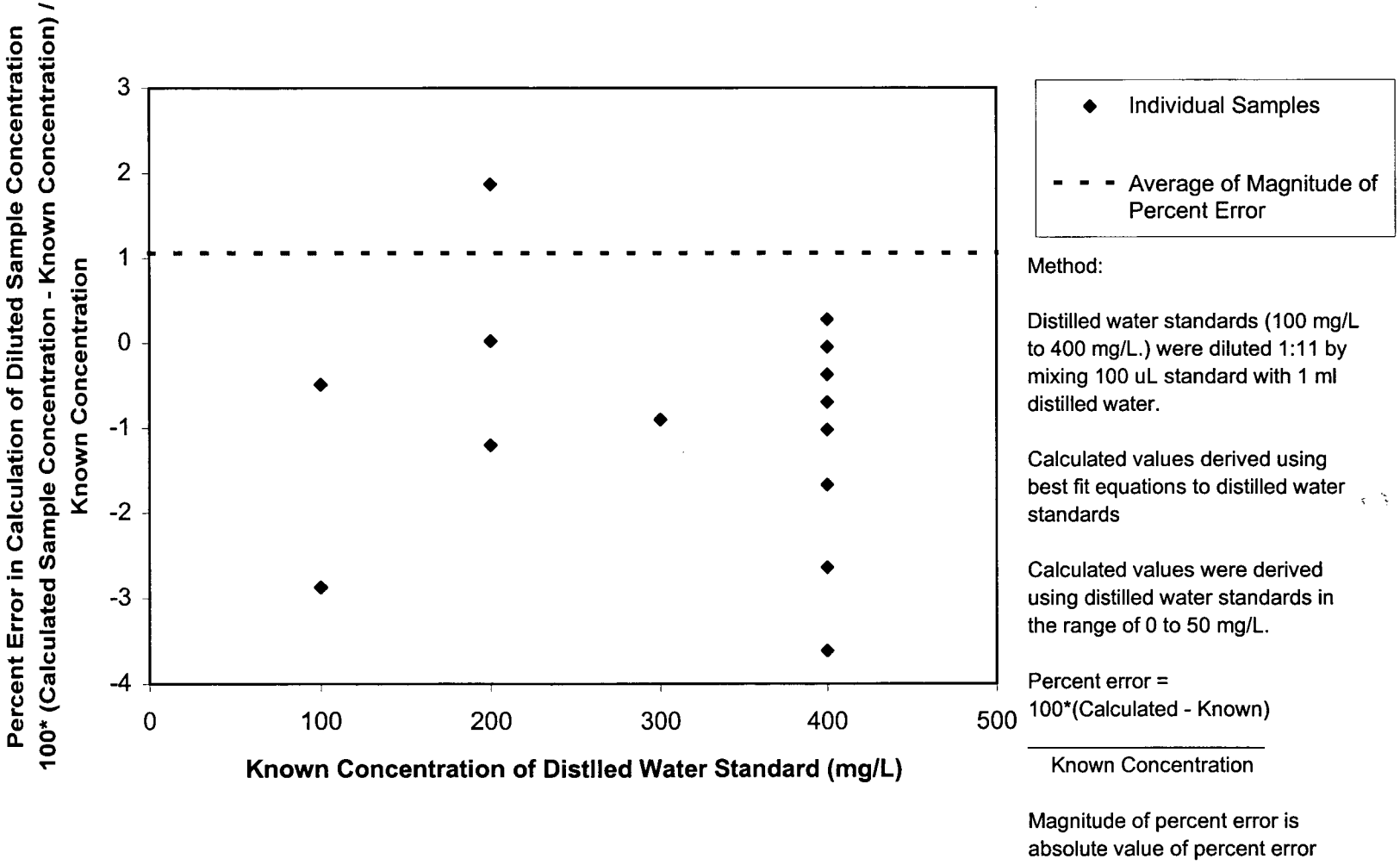

Figure L.3: Accuracy of sample dilution using distilled water standards: Experiment #1

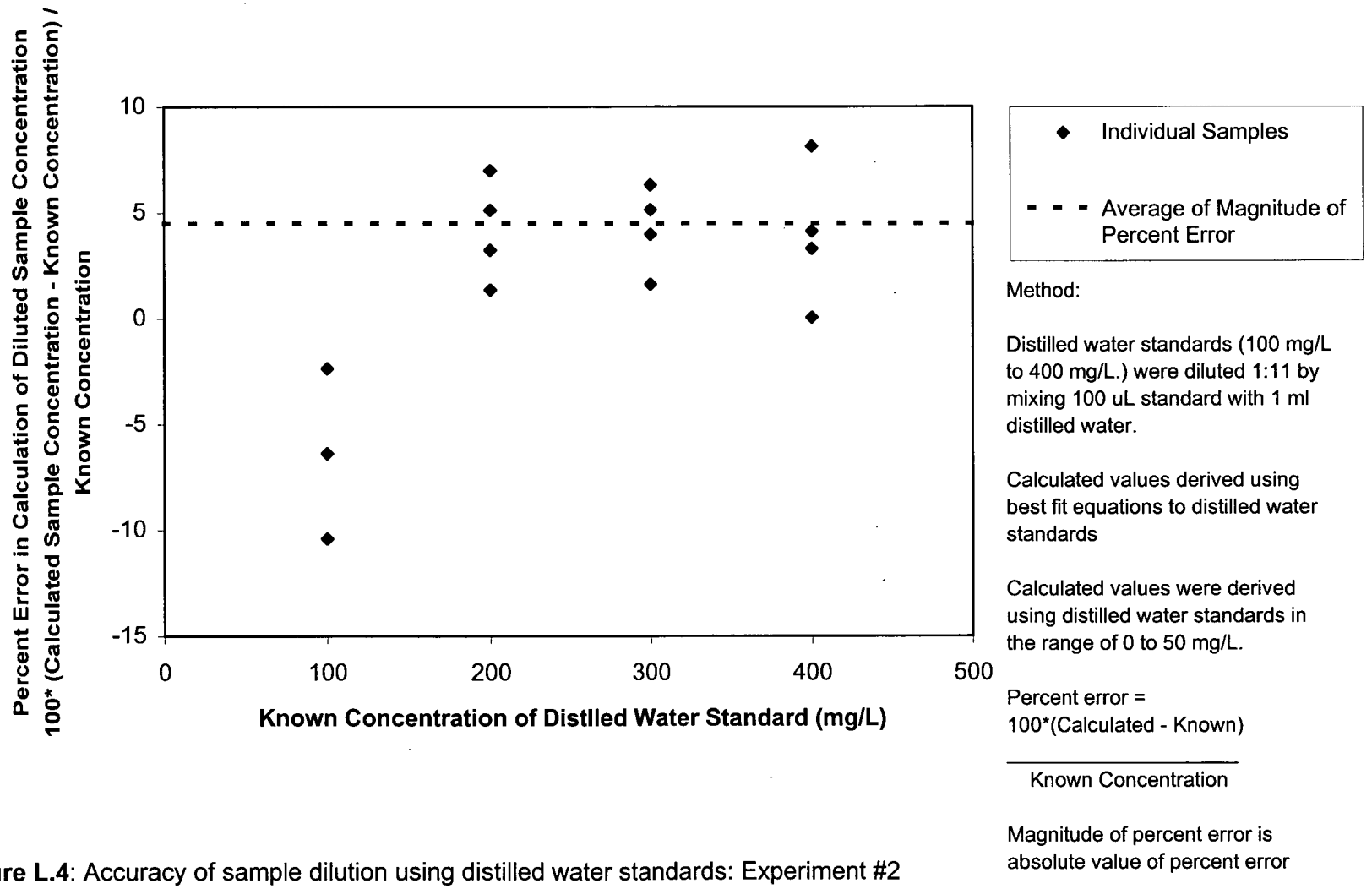

Figure L.4: Accuracy of sample dilution using distilled water standards: Experiment #2

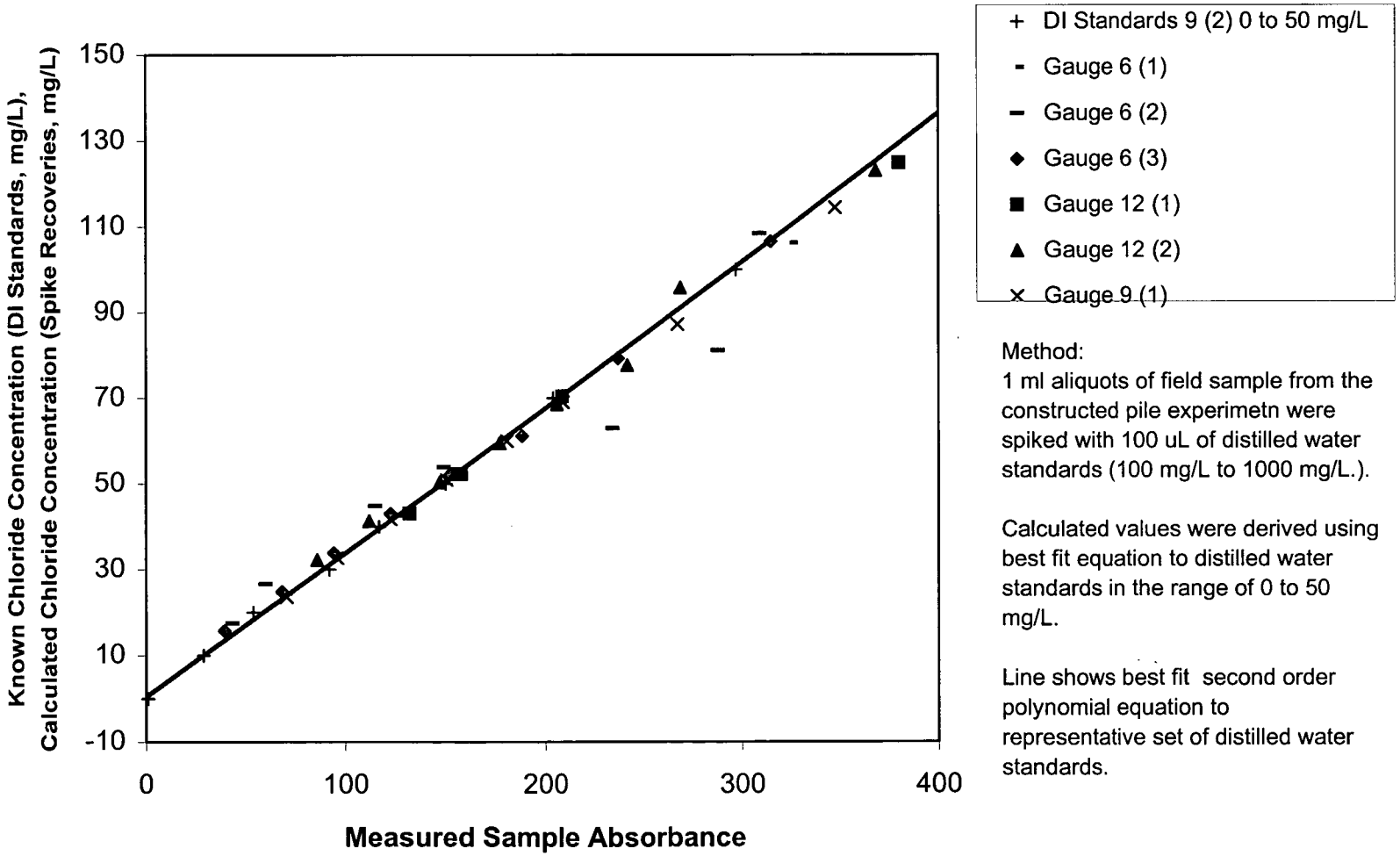

Method:
1 ml aliquots of field sample from the constructed pile experimetn were spiked with 100 uL of distilled water standards (100 mg/L to 1000 mg/L.).

Calculated values were derived using best fit equation to distilled water standards in the range of 0 to 50 mg/L.

Line shows best fit second order polynomial equation to representative set of distilled water standards.

Figure L.5A: Analysis of background interferences: Comparison of constructed pile experiment spiked sample spike recovery to distilled water standards as calibration standards

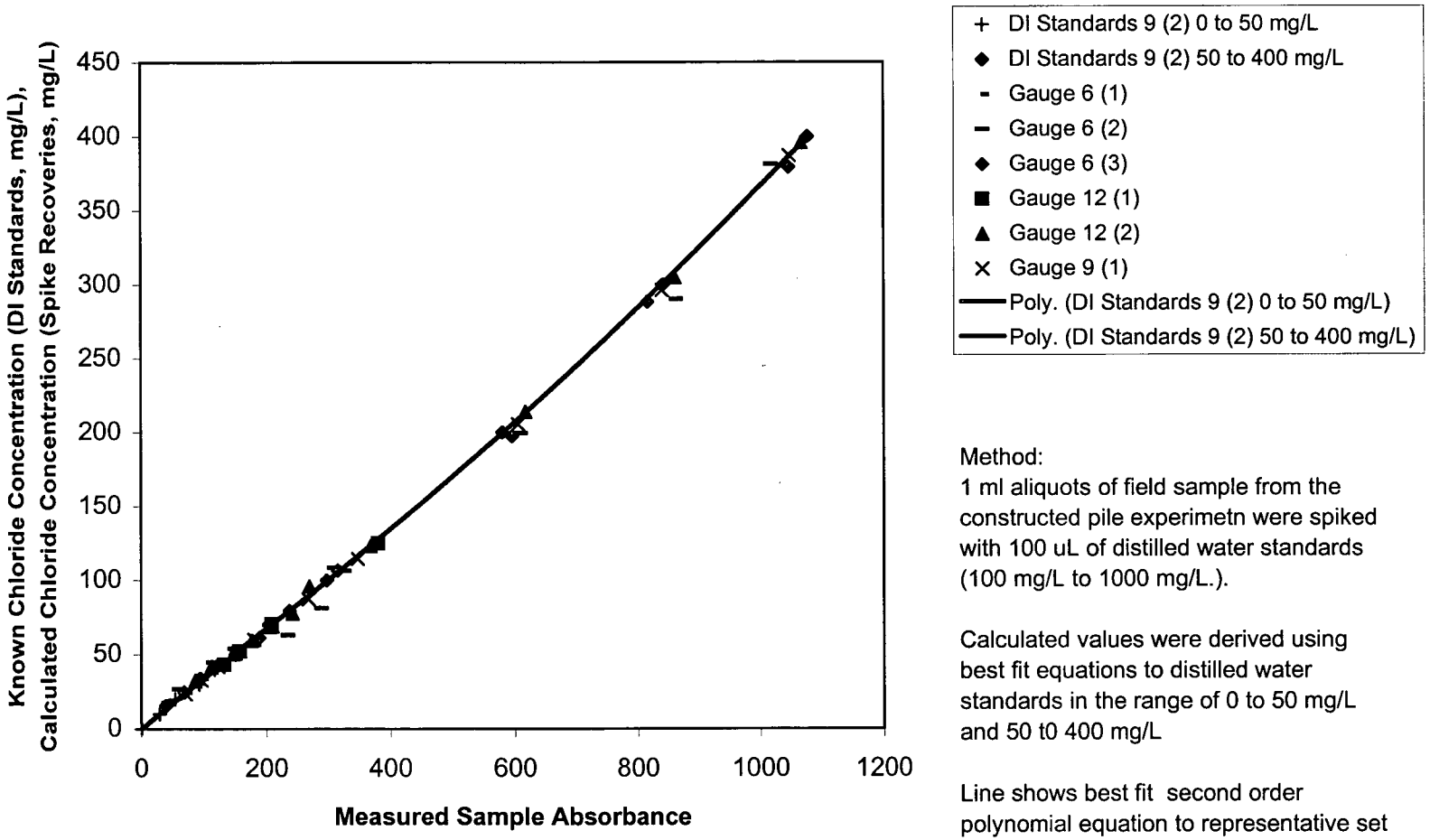

Method:
1 ml aliquots of field sample from the constructed pile experimetn were spiked with 100 uL of distilled water standards (100 mg/L to 1000 mg/L.).

Calculated values were derived using best fit equations to distilled water standards in the range of 0 to 50 mg/L and 50 t0 400 mg/L

Line shows best fit second order polynomial equation to representative set of distilled water standards.

Figure 5B: Analysis of Background Interferences: Comparison of constructed pile experiment spiked sample spike recovery to distilled water standards as calibration standards

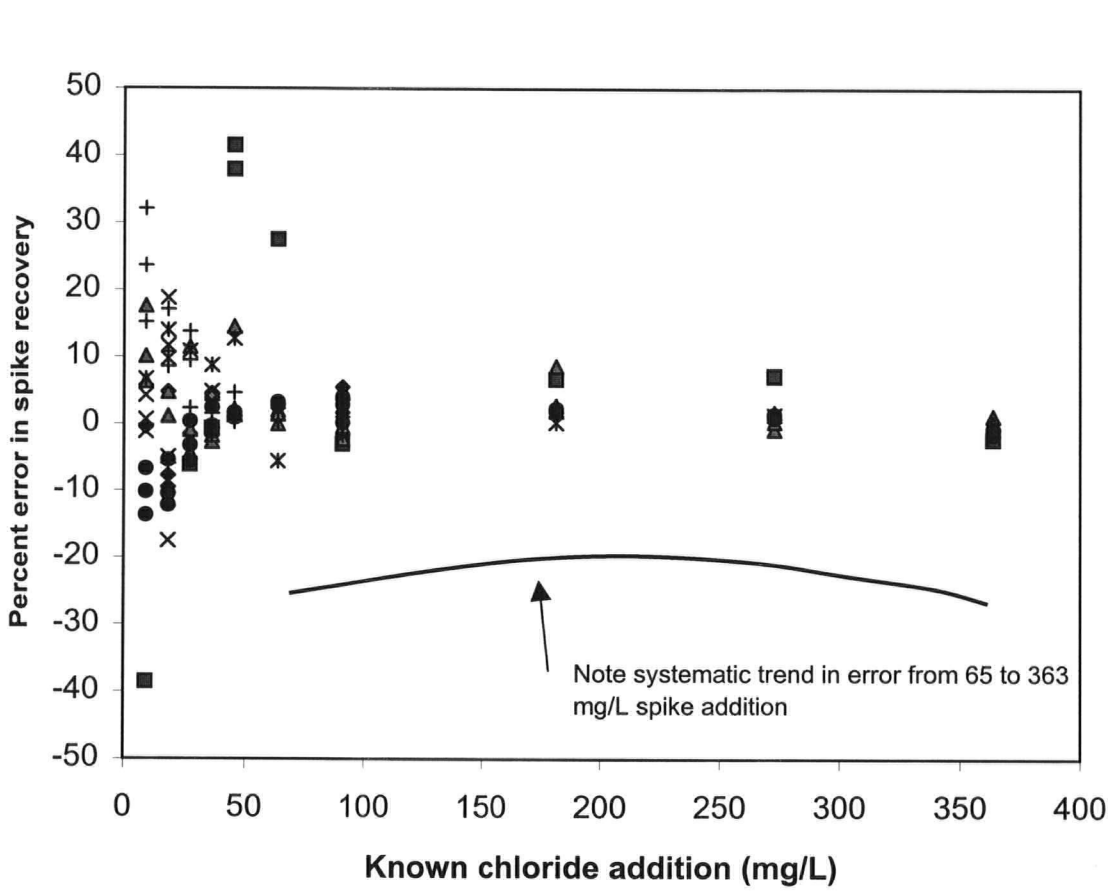

◆ Gauge 6 - Jan 6
■ Gauge 6 - Jan 11
▲ Gauge 6 - Jan 13
× Gauge 12 - Jan 6
✱ Gauge 12 - Jan 11
● Gauge 9 - Jan 13
+ Gauge 6B - Jan 13

Method:
1 ml aliquots of field sample from the constructed pile experimetn were spiked with 100 uL of distilled water standards (100 mg/L to 1000 mg/L.).

Calculated values were derived using best fit equations to distilled water standards in the range of 0 to 50 mg/L and 50 t0 400 mg/L

Spike recoveries calculated from calculated concentration - calculated concentration of 0 mg/L spike addition.

Percent error =
100*(Calculated spike- Known spike)

Known spike addition

Figure L.6: Analysis of Background Interferences: Percent error in spike recovery for constructed pile experiment spiked sample calculated using distilled water standards as calibration standards.

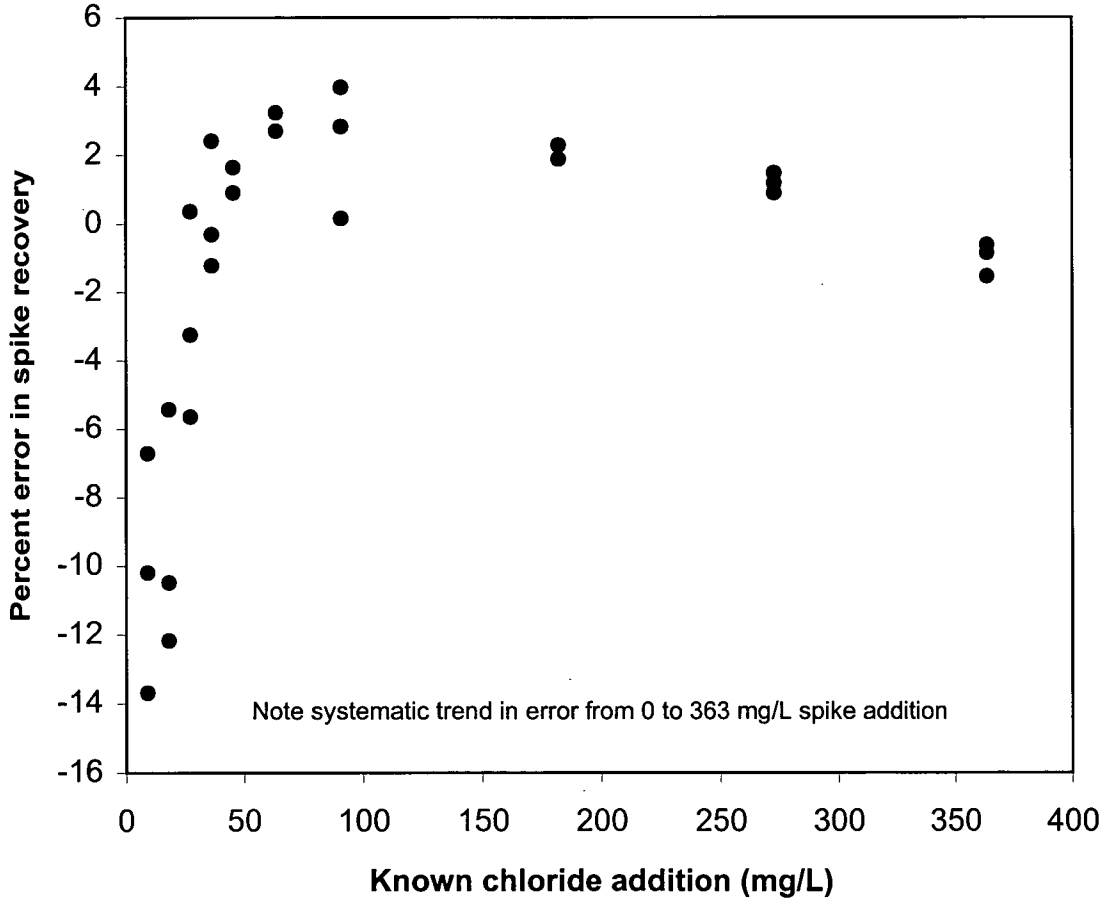

● Gauge 9 - Jan 13

Method:
1 ml aliquots of field sample from the constructed pile experimetn were spiked with 100 uL of distilled water standards (100 mg/L to 1000 mg/L.).

Calculated values were derived using best fit equations to distilled water standards in the range of 0 to 50 mg/L and 50 t0 400 mg/L

Spike recoveries calculated from calculated concentration - calculated concentration of 0 mg/L spike addition.

Percent error =

$$\frac{100*(\text{Calculated spike- Known spike})}{\text{Known spike addition}}$$

Figure L.7: Analysis of Background Interferences:Percent error in spike recovery for constructed pile experiment spiked sample calculated using distilled water standards as calibration standards. Gauge 9 data only.

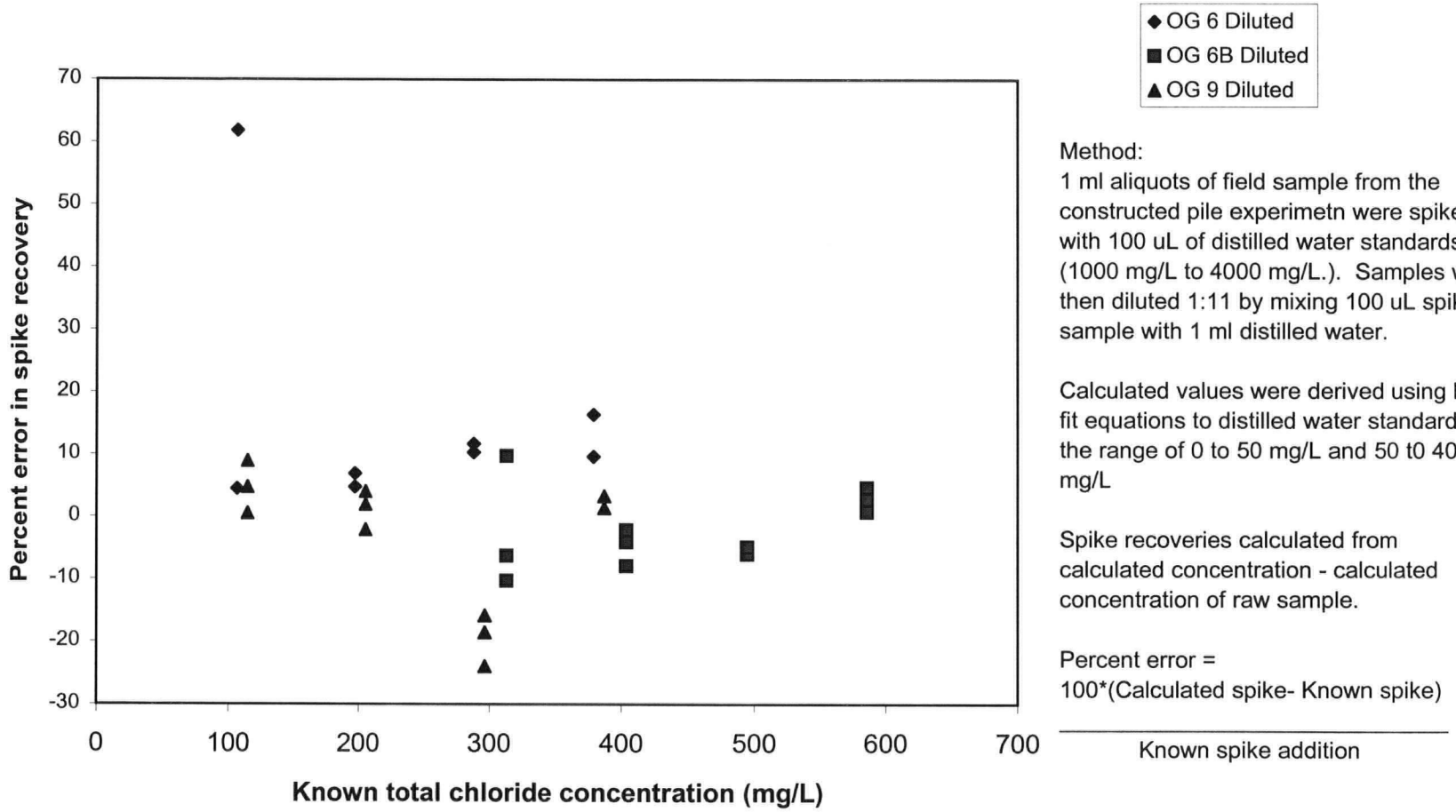

Figure L.8: Analysis of effect of dilution on Cluff Lake samples background interference: Percent error in spike recovery for diluted constructed pile experiment spiked samples calculated using distilled water standards as calibration standards. Samples spiked with 90 to 363 mg/L, then diluted 1:11

APPENDIX M: LABORATORY COLUMN EXPERIMENT DETAILS

M.1 INTRODUCTION

In addition to the constructed pile experiment, a laboratory column experiment was conducted using the same waste rock as the constructed pile experiment. This appendix provides some limited details of the construction of the column experiment and of the monitoring equipment used. Selected results of infiltration experiments are presented. Details of the rainfall sprayer system used on the laboratory column were presented in Appendix G.

M.2 EXPERIMENTAL CONSTRUCTION

The waste rock was shipped to the University of British Columbia in 200 L drums in the fall of 1997. Construction of the laboratory column was undertaken in the spring of 1998. The column was constructed from three sections of 42" nominal diameter reinforced fiberglass pipe, and a section of 1/4" transparent lexan. A schematic plan of the laboratory column is presented in Figure M.1. A schematic of the datalogging equipment and sprayer system are shown in Figure M.2. Photographs of the pile during construction are presented in Figures M.3 to M.5.

Waste rock was placed within the column experiment by hand using buckets. A maximum grain size of 0.4 m was used. During placement of the waste rock, sixteen tensiometers and sixteen coated TDR probes were installed to monitor conditions within the experiment and the progression of wetting fronts through the experiment. Tensiometers were monitored manually using manometer tubes. TDR probes were monitored automatically using a MoisturePoint MP917 TDR instrument datalogged by a Campbell Scientific CR10X datalogger. The outflow from the base of the pile was monitored both manually by measurement of outflow volume by gravimetric and volumetric means, and automatically using a tipping bucket rain gauge connected to the datalogger.

M.3 EXPERIMENTAL PROGRAM AND RESULTS

Five infiltration events were created ranging from 5mm/hr to a 20 l ring infiltrometer test during the period of June 1 to June 10, 1998. Two additional rainfall events were created during 1999. The outflow hydrograph in response to events 1 to 3 is shown in Figure M.6. The response to event 4 is shown in Figure M.7.

A large increase in discharge from the experiment base was not noted until after event 3. The initial two rainfall events created wetting fronts that could be monitored by changes in matric suction and water content. However, these slow moving wetting fronts were overtaken by subsequent rainfall events.

The responses to events three and four both indicate multiple wetting front arrivals and subsequent flow peaks, similar to that noted in Chapter 6. This indicates the presence of sufficient heterogeneity with the experiment to lead to the progress of multiple wetting fronts.

Estimates of matric suction and water content from the column experiment were combined to derive estimates of the in-situ soil water characteristic curves (SWCC) at each paired instrument location similar to the analysis in Chapter 6. Details of the matched matric suction and water content data for two instrument locations near the column surface are presented in Figure M.8. This data indicates that the majority of the wetting and drying trends observed in the laboratory column experiment followed wetting and drying scanning hysteresis curves, and that the matched data can not be used to determine boundary wetting

or drying curves. There are several temporal trends in the data which are physically impossible, such as increases in tension at the same time as rising water content. These responses indicate that the wetting front arrived at slightly different times at the tensiometers and TDR probes, located approximately 20 cm apart.

M.4 CONCLUSIONS

The laboratory column experiment showed outflow responses similar to that observed in the individual lysimeters of the constructed pile experiment, indicating preferential flow was occurring at small scales. The in-situ water content and matric suction data indicates that the scale of heterogeneity was small enough to cause variations in wetting front propagation over lateral distances of 20 cm. Similar to the constructed pile experiment, the in-situ data can not be used to derive SWCC data. The dominance of scanning hysteresis behaviour will substantially increase the effort required to undertake any numerical simulation of these results.

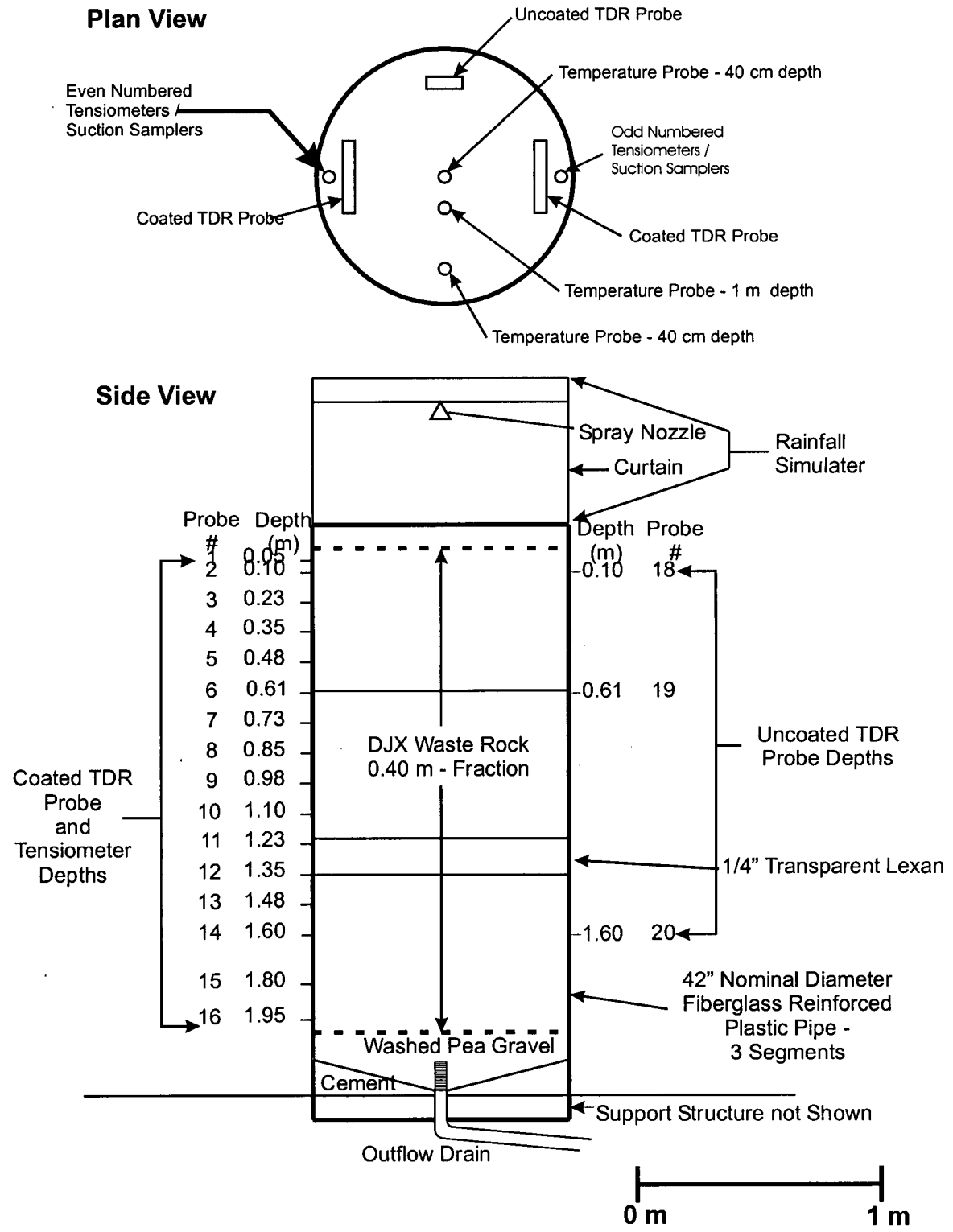

Figure M.1: Plan and Side Views of Laboratory Column Experiment

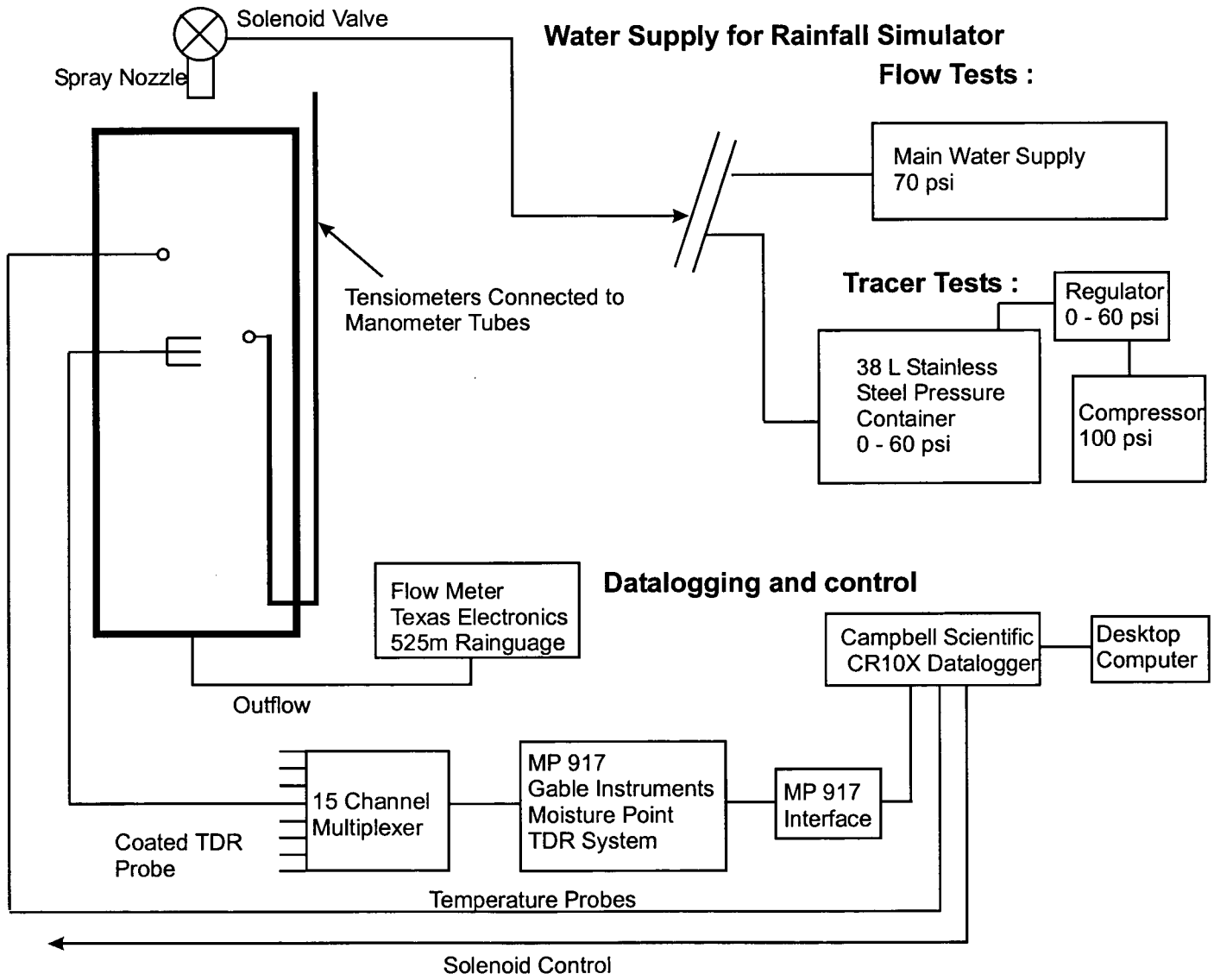

Figure M.2 Schematic layout of lab experiment controls and datalogging

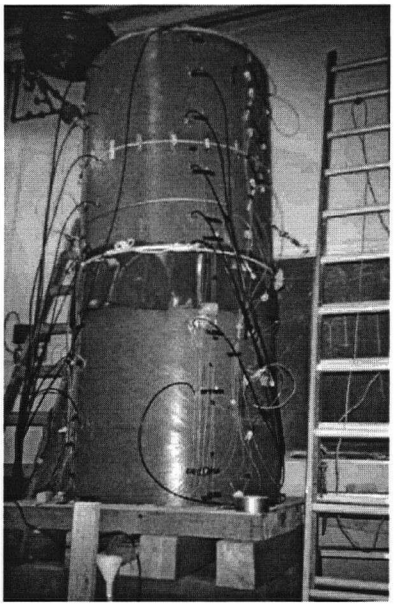

Figure M.3: Photograph of laboratory column experiment. Transparent lexan window is covered by grey plastic.

Figure M.4: Photograph of laboratory column experiment base.

Figure M.5: Photograph of waste rock placed inside laboratory column experiment. The closed cell polyethylene foam used to line inside of pile is visible.

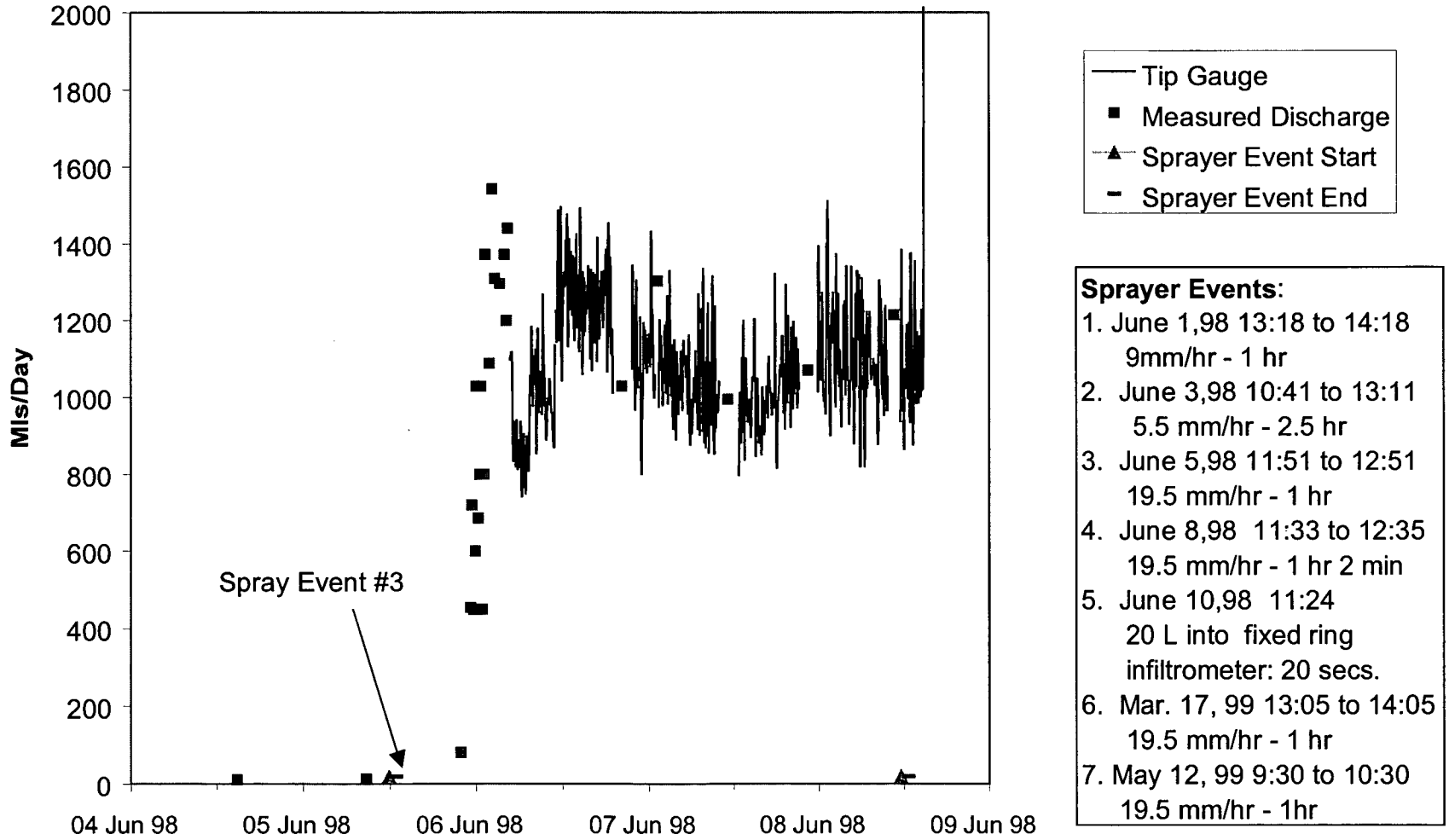

Figure M.6: Outflow hydrograph from laboratory column experiment in response to rainfall events 1 through 3.

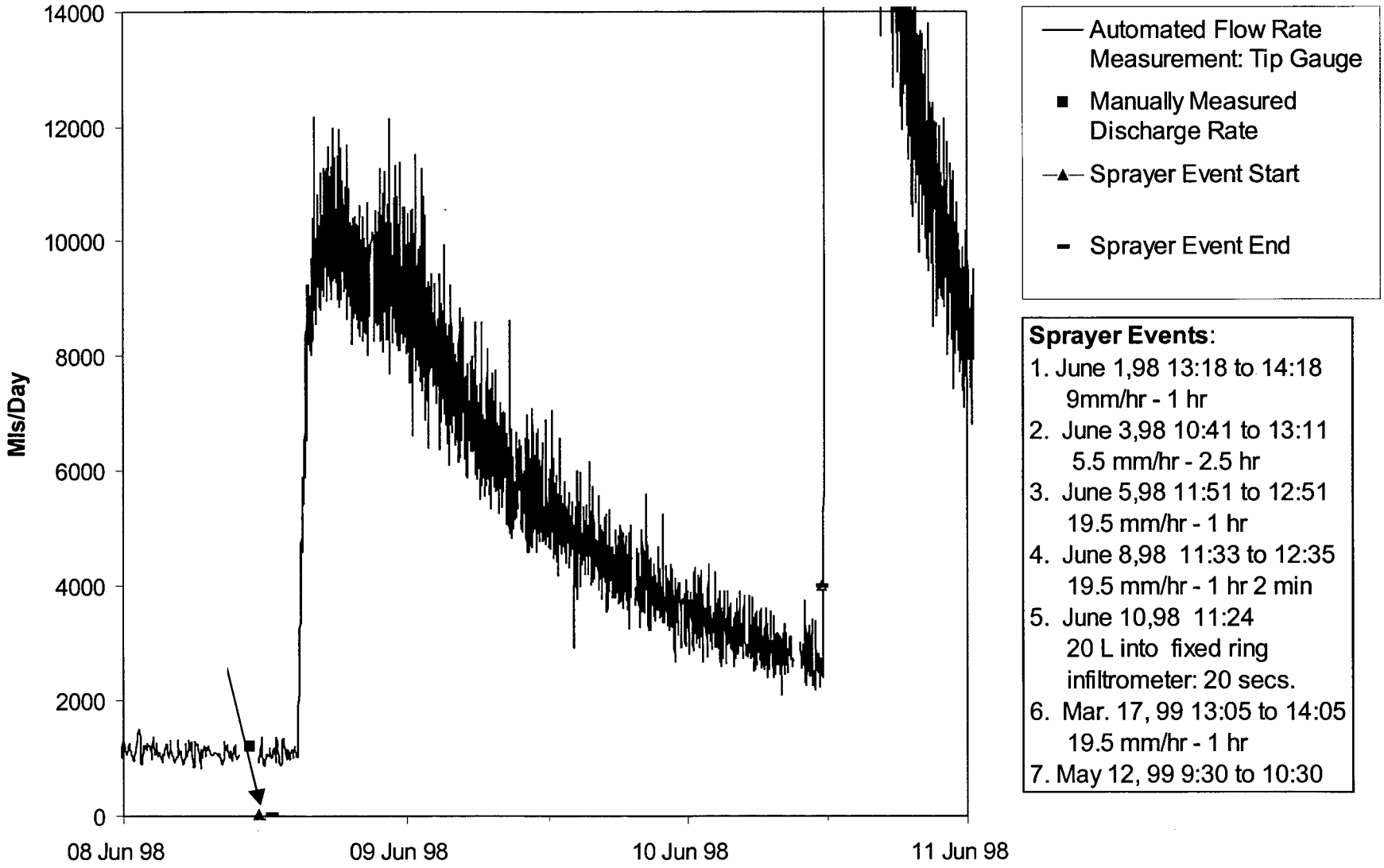

Figure M.7: Outflow hydrograph from laboratory column experiment in response to rainfall event 4.

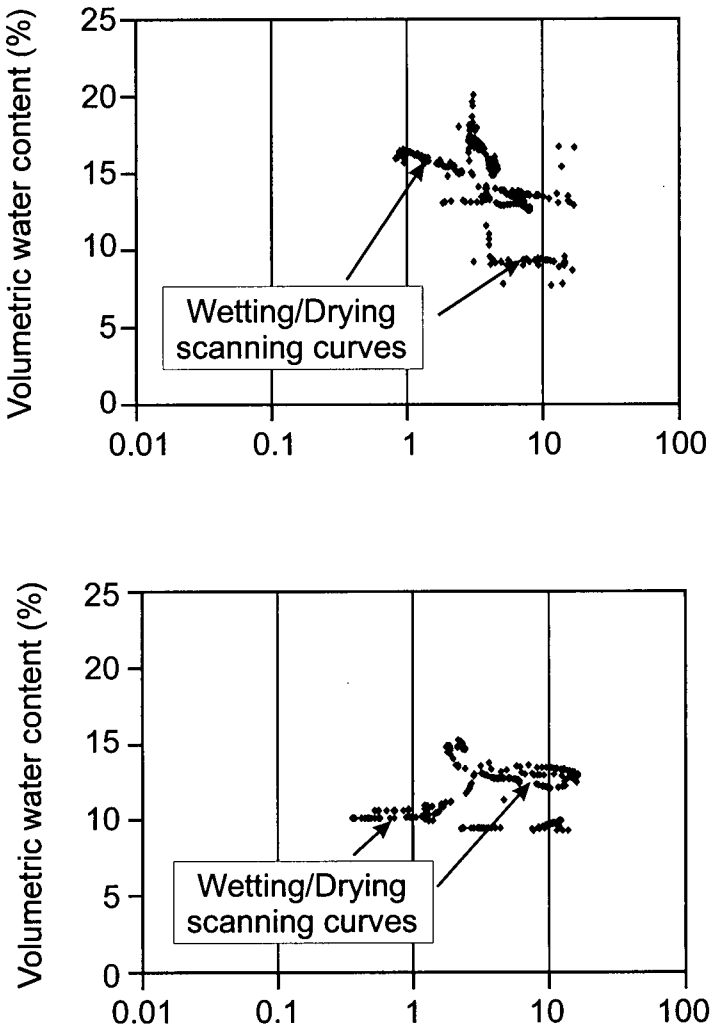

Figure M.8: Matched matric suction data from tensiometers and water content data from TDR probes for laboratory column experiment during rainfall events 1 to 5.